

NASA TM-84894

NASA-TM-84894 19830003736

# Advances in Planetary Geology

---

LIBRARY COPY

JAN 25 1993

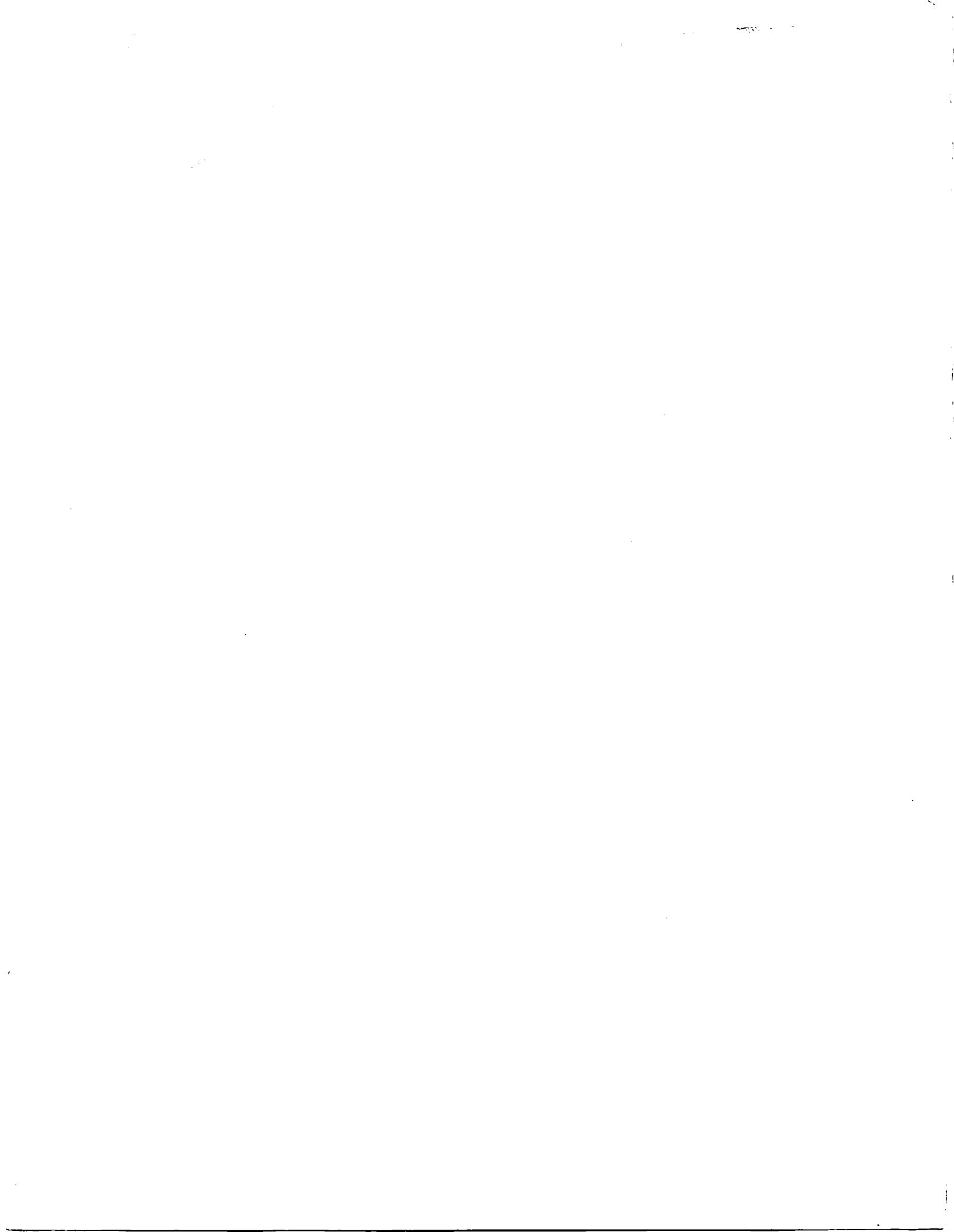
LANG.

...TER

LIBRARY, NASA  
HAMPTON, VIRGINIA

September 1982

**NASA**



# Advances in Planetary Geology

---



## FOREWORD

This document is a compilation of reports from Principal Investigators and their Associates of NASA's Office of Space Science and Applications, Earth and Planetary Exploration Division, Planetary Geology Program. The reports present research that adds to our knowledge of the origin and evolution of the solar system and to our understanding of the earth as a planet. Advances in Planetary Geology was established as a complement to "Reports of Planetary Geology Program" and to professional journals. This document provides a method of publishing research results which are in a form that would not normally be published elsewhere such as lengthy research reports, progress reports, Ph.D. dissertations, or master's theses.

Joseph M. Boyce  
Discipline Scientist  
Planetary Geology Program  
Office of Space Science  
and Applications

To Contributors:

A wider variety of manuscripts can be accommodated by Advances in Planetary Geology than by most journals. Particularly appropriate are complete theses, dissertations, and research reliant on extensive presentations of data. All contributions must be of direct interest to planetary geologists and must be of high quality. Manuscripts must be typed single spaced in a camera-ready format and sent to:

Alex Woronow  
Lunar and Planetary Laboratory  
University of Arizona  
Tucson, AZ 85721

## CONTENTS

### SECTION I:

THE INTERCRATER PLAINS OF MERCURY AND THE MOON: THEIR NATURE, ORIGIN, AND ROLE IN TERRESTRIAL PLANET EVOLUTION.	1
Martha Ann Leake	

### SECTION II: REPORTS OF THE "PLANETARY GEOLOGY INTERN PROGRAM."

	537
Planet-Crossing Asteroid Survey	541
Carlos A. Atallah	
Possible Applications of Time Domain Reflec- tometry in Planetary Exploration Missions	545
Steve Heckendorn	
Assessing the Volcanic Probability of Martian Landforms	556
Maureen M. O'Toole	
The Effects of Varying Surface Roughness on Aerodynamic and Aeolian Processes	559
Lynn M. Reding	
Morphology of Volcanoes	565
Henry J. Shuver	
Two Methods for Determining Volumes for Explosion and Impact Craters	568
Alejo N. Verdes	
Ejecta Distribution Around a Small Lunar Crater	574
Stephen J. Wetzel	





**SECTION I**



THE INTERCRATER PLAINS OF MERCURY AND THE MOON:  
THEIR NATURE, ORIGIN, AND ROLE  
IN TERRESTRIAL PLANET EVOLUTION

by  
Martha Alan Leake

---

A Dissertation Submitted to the Faculty of the  
DEPARTMENT OF PLANETARY SCIENCES  
In Partial Fulfillment of the Requirements  
For the Degree of  
DOCTOR OF PHILOSOPHY  
In the Graduate College  
THE UNIVERSITY OF ARIZONA

1981

#### ACKNOWLEDGMENTS

This research was conducted in partial fulfillment of the requirements for the Degree of Doctor of Philosophy in The Department of Planetary Sciences of The University of Arizona, Tucson, Arizona. Financial support as a graduate research assistant was provided primarily under NASA Grant NSG-7146 to Professor Robert G. Strom, my thesis advisor. I owe a great debt to Professor Strom for his kindness, patience, and understanding. It has been a pleasure to work with him in interpreting the exciting images so freshly returned from space.

I also owe great thanks to Mike Malin and Carl Allen, who with Bob Strom, pioneered use of the mapping scheme used here; to Drs. Laurel Wilkening, Alex Woronow, Mike Drake, John Sumner, and Robert Butler, members of my advisory committee; and to Gail Georgenson, Coordinator of Special Collections of the Space Imagery Center of the Lunar and Planetary Laboratory. B. Van Praag, K. Denomy, G. McLaughlin, and D. Fugate were invaluable in the preparation of the manuscript's text, figures, and photographs.

I am also greatly appreciative of the help and support offered by my colleagues, friends, and family. In particular, I thank Dr. Mirene Hazebrouck and my parents, Dr. and Mrs. James R. Leake.

This work is dedicated to the continued health and vitality of planetary science.

## TABLE OF CONTENTS

	Page
ABSTRACT . . . . .	9
1. INTRODUCTION . . . . .	11
Justification . . . . .	13
Method . . . . .	18
Synopsis of Results . . . . .	19
Organization of the Dissertation . . . . .	20
2. GEOLOGIC MAPPING OF MERCURY AND THE MOON . . . . .	21
Materials and Techniques of Geologic Mapping and Analysis . . . . .	23
Mapping Strategy of the U.S. Geological Survey . . . . .	23
Materials and Techniques of Lunar Mapping . . . . .	27
Materials and Mapping Techniques for Mercury . . . . .	46
Geologic Map of Mercury's First Quadrant . . . . .	58
Correlation of Map Units . . . . .	58
Material Units . . . . .	60
Structure . . . . .	84
Albedo and Color of Mercury's Surface . . . . .	99
Initial Conclusions from Geologic Mapping of Mercury . . . . .	107
Geologic Map Analyses of the Lunar Intercrater Plains . . . . .	110
3. CRATERING HISTORIES OF THE INTERCRATER PLAINS . . . . .	142
Methods Summary . . . . .	143
Data Presentation . . . . .	144
Signatures of Geologic Processes on a Crater Population . . . . .	146
Saturation and Equilibrium . . . . .	147
Direct Basin Impact . . . . .	148
Basin Impact--Periphery . . . . .	148
Ballistic Plains Emplacement . . . . .	149
Volcanic Plains Emplacement . . . . .	149
Endogenic Craters . . . . .	150
Isostatic Equilibration . . . . .	150

TABLE OF CONTENTS--Continued

	Page
3. CRATERING HISTORIES OF THE INTERCRATER PLAINS-- <u>Continued</u>	
Differential Preservation and Degradation Due to Target Properties . . . . .	151
Initially Degraded Craters . . . . .	152
Erosion by Infiling with Dust or Ejecta . . . . .	153
Tectonic Processes . . . . .	153
Gravity and Strength Scaling . . . . .	154
External Processes: Changes in the Bombarding Population . . . . .	154
Secondary Cratering on the Moon and Mercury . . . . .	155
Secondary Cratering From Fresh Lunar Craters . . . . .	156
Secondary Cratering by Lunar Basins . . . . .	164
Secondary Cratering on Mercury . . . . .	167
Discussion of Additional Studies of Secondary Cratering . . . . .	172
Cratering Histories of the Lunar Intercrater Plains . . . . .	175
Crater Statistics of Selected Lunar Areas . . . . .	176
Crater Statistics of Sectors of the Southern Highlands . . . . .	187
Crater Statistics on Divided Sectors . . . . .	197
Discussion . . . . .	201
Summary of Lunar Crater Statistics . . . . .	207
Cratering Histories of the Intercrater Plains of Mercury . . . . .	209
Statistics of Selected Areas . . . . .	209
Statistics of the Geologic Map Area . . . . .	223
Discussion and Summary of Mercurian Crater Statistics . . . . .	240
4. GEOLOGIC MAP ANALYSES: CORRELATION OF GEOLOGIC AND CRATERING HISTORIES . . . . .	244
Specific Areas Illustrating Volcanic and Ballistic Plains Emplacement Mechanisms . . . . .	244
Volcanic Plains . . . . .	255
Ballistic Emplacement . . . . .	259
Discussion of Mapping Bias . . . . .	261
Areal Coverage by Craters and Plains on Mercury . . . . .	265
Unit Coverage over the Entire Geologic Map . . . . .	266
Unit Coverage of the Quadrangles . . . . .	276
Paleologic Maps of Mercury's First Quadrant . . . . .	279
The Caloris Connection . . . . .	279
The "Post-Caloris" Surface . . . . .	284

TABLE OF CONTENTS--Continued

	Page
4. GEOLOGIC MAP ANALYSES: CORRELATION OF GEOLOGIC AND CRATERING HISTORIES-- <u>Continued</u>	
The "Caloris" Surface . . . . .	291
The "Pre-Caloris" Surface . . . . .	295
Summary . . . . .	299
The Lunar Intercrater Plains: Synthesis of Geologic and Cratering History . . . . .	300
Origins . . . . .	301
Similarities and Contrasts of the Lunar to Mercurian Intercrater Plains . . . . .	305
5. REMOTE SENSING AND PHYSICAL DATA OF MERCURY AND THE MOON . . .	309
Remote Sensing Observations of Mercury . . . . .	309
Spectrophotometric Measurements . . . . .	310
Thermal Infrared Data . . . . .	312
Orbital Data and Implications . . . . .	313
Magnetic Field . . . . .	314
Remote Sensing Observations of the Moon . . . . .	316
Age and Petrologic Data from the Apollo 16 Site . . .	317
Compositional Data . . . . .	318
Physical Data . . . . .	321
6. THERMAL HISTORIES OF MERCURY AND THE MOON . . . . .	323
Thermal Histories of Mercury . . . . .	323
Compositional Constraints of Mercury's Surface and Interior. . . . .	325
Basic Thermal Evolution Models . . . . .	330
Lunar Thermal Evolution: Some Comparisons . . . . .	344
Lunar Thermal Evolution . . . . .	345
Comparisons with Mercury . . . . .	349
7. DISCUSSION OF THE NATURE, ORIGIN, AND ROLE OF THE INTERCRATER PLAINS OF MERCURY AND THE MOON . . . . .	353
Summaries of Results . . . . .	353
Mercury . . . . .	354
The Moon . . . . .	360
Implications for Terrestrial Planet Evolution . . . . .	366
Scarp Formation and Magma Source Depth . . . . .	366
Relative and Absolute Ages of the Intercrater Plains . . . . .	371

TABLE OF CONTENTS--Continued

	Page
7. DISCUSSION OF THE NATURE, ORIGIN, AND ROLE OF THE INTERCRATER PLAINS OF MERCURY AND THE MOON-- <u>Continued</u>	
Summary of Surface Histories as Shaped or Recorded by the Intercrater Plains . . . . .	376
The Role of the Intercrater Plains . . . . .	379
Future Work . . . . .	380
APPENDIX A: DESCRIPTION OF UNITS TO ACCOMPANY THE GEOLOGIC TERRAIN MAP OF MERCURY'S FIRST QUADRANT . . . . .	383
APPENDIX B: AREAL MEASUREMENT OF MERCURY'S FIRST QUADRANT . . .	390
APPENDIX C: MEASUREMENT AND ERRORS OF CRATER STATISTICS . . . .	400
APPENDIX D: CRATER STATISTICAL DATA . . . . .	413
APPENDIX E: ESTIMATED THICKNESS OF EJECTA DEPOSITS COMPARED TO CRATER RIM HEIGHTS . . . . .	471
APPENDIX F: CONSTRUCTION OF THE PALEOGEOLOGIC MAPS . . . . .	475
APPENDIX G: THERMAL MODELS OF MERCURY . . . . .	477
APPENDIX H: ALTERNATIVE THERMAL HISTORIES . . . . .	489
APPENDIX I: TANGENTIAL STRESS FACTOR . . . . .	498
APPENDIX J: CHRONOLOGY OF SURFACE HISTORY OF MERCURY . . . . .	499
APPENDIX K: CHRONOLOGY OF SURFACE HISTORY OF THE MOON . . . . .	505
REFERENCES . . . . .	508



## ABSTRACT

Various origins have been proposed for intercrater plains on Mercury and the Moon which lead to divergent thermal, tectonic, and bombardment histories. The relative ages of various geologic units and structures place tight constraints on their origin and thus provide a better understanding of the geologic histories of these bodies. Crater statistics, a re-examination of lunar geologic maps, and the compilation of a geologic map of a quarter of Mercury's surface based on plains units dated relative to crater degradation classes were used to determine relative ages. This provided the basis for deducing the origin of intercrater plains and their role in terrestrial planet evolution.

Mercury's extensive intercrater plains span a range of ages contemporaneous with the period of heavy bombardment. Most intercrater plains predate scarp formation and the formation of the hilly and lineated terrain. The age of the hilly and lineated terrain is identical to that of its probable progenitor, the Caloris basin impact. Post-Caloris plains--smoother in texture, less extensive, and confined to crater depressions--formed as cratering waned and scarp formation progressed.

This research indicates that mercurian intercrater plains are volcanic deposits interbedded with ballistically emplaced ejecta and reworked by basin secondaries and smaller impacts. A greater proportion of ejecta may comprise lunar intercrater plains. Neither the

lunar nor mercurian intercrater surface is primordial because each preserves pre-plains crateriforms.

Ancient volcanism on Mercury is evidenced by (1) widespread plains distribution, (2) structurally controlled deposition, (3) embayment of craters and basins, (4) associated (but tentative) volcanic landforms, (5) losses of small craters, and (6) uncorrelated plains and crater coverage. The limited range of mercurian ejecta reduces the resurfacing potential relative to that of lunar craters. Crater densities are affected by intercrater plains emplacement, additions of secondaries, ancient basin impacts, and target physical properties.

"One-plate" thermo-tectonic models best explain the geologic characteristics recognized in this study. Thermal expansion during core formation causes global extension and widespread volcanic extrusions; subsequent cooling and radial contraction form compressional scarps. Younger plains-forming materials issue from magma reservoirs in subsurface tensional zones tapped by impact fractures. The age and stress environment of these volcanic plains suggest a source greater than 40 km depth and a composition different from that of the intercrater plains.

## CHAPTER 1

### INTRODUCTION

Half the observed surface of Mercury consists of flat-lying to rolling terrain which surrounds clustered or isolated large craters. It was designated the "intercrater plains" by Trask and Guest (1975). High densities of smaller craters, 5 to 15 km in diameter, pit the plains' surface. The major exposure of Mercury's observed intercrater plains occurs on its first quadrant (imaged prior to encounter by the Mariner 10 spacecraft), as illustrated in Fig. 1. A similar intercrater plains unit of far more restricted extent occurs on the Moon, in the southern nearside highlands; this unit is mapped as the "Pre-Imbrian Pitted Plains" by Scott (1972). Fig. 2 shows that this plains unit lies south and southwest of the Nectaris basin.

The similarity of plains' morphology on these two planets is not reflected in the physical properties of the Moon and Mercury. Mercury is much denser, slightly larger, and has a higher surface gravity than the Moon, as noted in Table 1. These properties, as well as heliocentric distance, orbital parameters, and rotational period show that Mercury differs from the Moon in its composition, solar insolation, and exposure to distance-dependent forces or bombarding populations within the solar system. Inasmuch as the surfaces of atmosphereless bodies record their geologic and bombardment history,

Table 1: Physical Data of Mercury and the Moon

Parameters	Mercury	Moon
Mass (Earth = 1) <sup>a</sup>	0.055	0.0123
Equatorial Radius <sup>b</sup>	2439 km	1738 km
Mean Density	5.44 g/cm <sup>3</sup>	3.343 g/cm <sup>3</sup>
Equatorial Surface Gravity	370 cm/sec <sup>2</sup>	162 cm/sec <sup>2</sup>
Escape Velocity <sup>b</sup>	4.25 km/sec	2.38 km/sec
Effective Temperature <sup>c</sup>	440° K	270° K
Temperature Extremes	100°K to 725°K	94°K to 390°K
Bond Albedo <sup>d</sup>	0.10	0.07
Geometric Albedo: average <sup>d</sup>	0.16 ± 0.03	0.13
normal extremes	0.13 to 0.23	0.11 to 0.16
Magnetic Dipole Moment <sup>e</sup>	4.9 (+ 0.2) 10 <sup>22</sup> Gauss cm <sup>2</sup>	---
Semi Major Axis <sup>a,f</sup>	0.387 AU 57.9·10 <sup>6</sup> km	~1 AU 0.3844·10 <sup>6</sup> km <sup>f</sup> from Earth
Eccentricity	0.206	0.055
Inclination to Ecliptic	7° 00'	5° 09'
Mean Orbital Velocity	47.90 km/sec	1.03 km/sec
Sideral Period of Revolution <sup>a</sup>	86.0 days mean solar time	27.32 days mean solar time
Aphelion Distance	69.8·10 <sup>6</sup> km	0.4055·10 <sup>6</sup> km
Perihelion Distance	46.0·10 <sup>6</sup> km	0.3633·10 <sup>6</sup> km
Rotation Period: Synodic <sup>a</sup>	176.0 days mean solar time	29.53 days mean solar time
Sideral <sup>a</sup>	58.6 days mean solar time	27.32 days mean solar time
Sideral Period <sup>b</sup>	87.97 days	
Synodic Period <sup>b</sup>	115.88 days	
Inclination of Equator to Orbit (Obliquity) <sup>a</sup>	near 0°	1° 32'

a. Data from Frontispiece Proc. Lunar Planet. Sci. Conf. 9th, Vol. 3 from cover, compiled by Ray Newburn, 1978.

b. Data from Strom (1979)

c. Thermal data from Morrison (1970) and Chase et al. (1976)

d. Data from Dzurisin (1977b)

e. Data from Ness (1978)

f. Geocentric orbital parameters for the Moon, in "a."

this dissertation thus constrains the internal and external evolution of Mercury and the Moon by determining the nature, origin, and "role" of the intercrater plains surfaces.

#### Justification

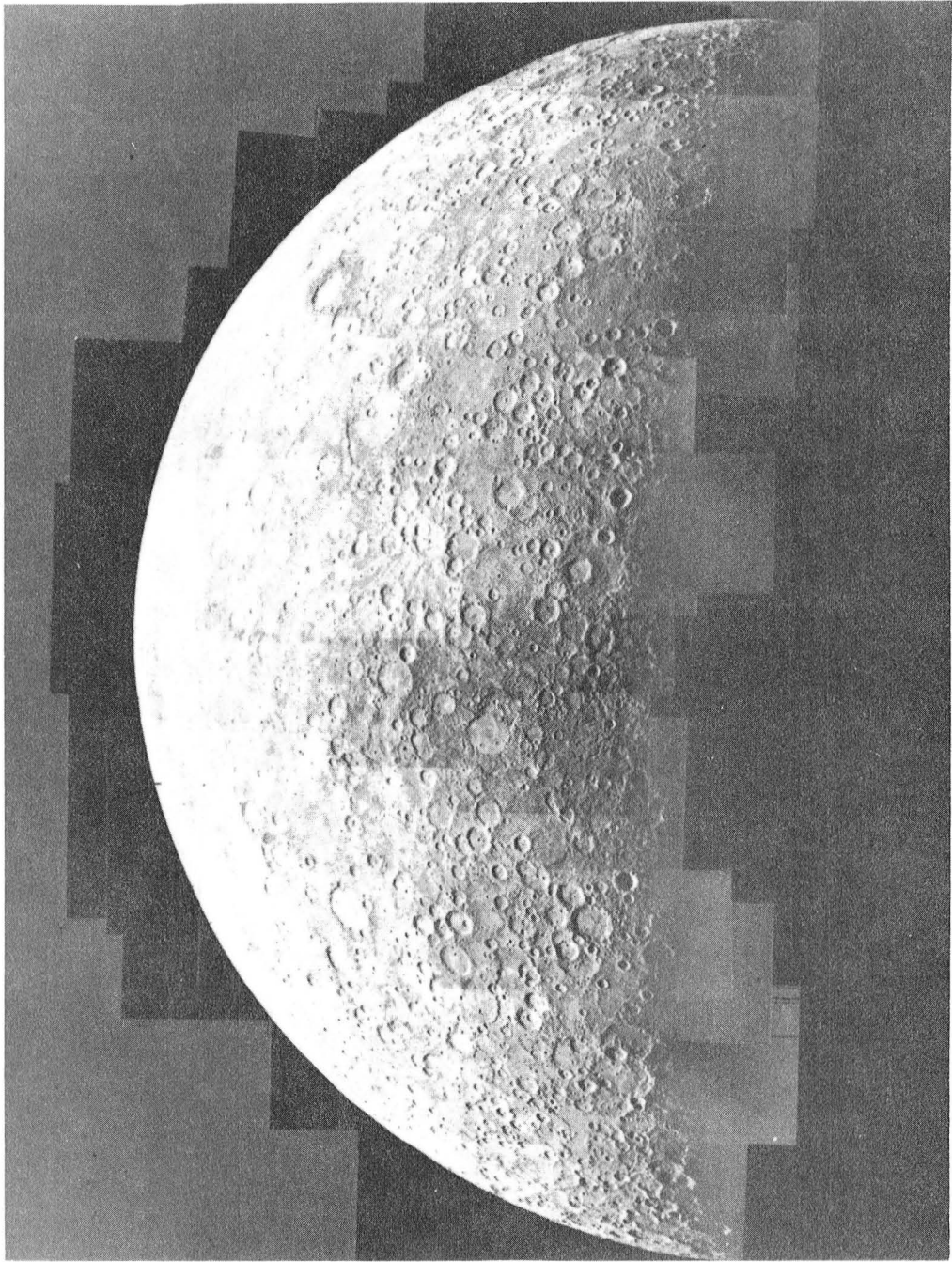
The above statement expresses the major justification of this research. Such a determination is not easily accessible. On both the Moon and Mercury, the areas mapped as intercrater plains are themselves diverse, and the relative ages of various units remains obscure; the morphologic similarities among the plains may or may not imply genetic similarities. By determining the relative ages of the intercrater plains, one could evaluate the three major theories of their origin: (1) a primordial surface remaining after accretion (Oberbeck et al., 1977), or a remnant secondary surface which formed after global melting and crustal solidification (Malin, 1976a); (2) late planetary volcanism associated with ongoing differentiation of the planet during bombardment (Murray et al., 1975; Strom, Trask, and Guest, 1975b; Trask and Strom, 1976; and Strom, 1977); and (3) ballistic deposition of ejecta from crater- and basin-forming impacts (Howard, Wilhelms, and Scott, 1974; Head, 1974; Wilhelms, 1976a; and Oberbeck et al., 1977).

Complications occur in determination of the bombardment history of the intercrater surface, because resurfacing by volcanic or ballistic plains emplacement will locally reset or alter the cratering

Fig. 1. Photomosaic of the Incoming Side of Mercury

Mercury's first quadrant, viewed as Mariner 10 approached the planet, has large expanses of intercrater plains and clusters of heavily cratered areas as shown in this mosaic, prepared from 70 medium to high resolution images. The bright crater with the dark halo near the northwest limb is Lermontov, 160 km in diameter. Near the left center of the disk is Kuiper, a rayed crater 60 km in diameter. Mercury's evening terminator occurs at  $10^{\circ}$ W longitude; the limb occurs at  $90^{\circ}$ W longitude, approximately. Fig. 10 illustrates the geologic map boundaries and latitude-longitude system.

North at top.



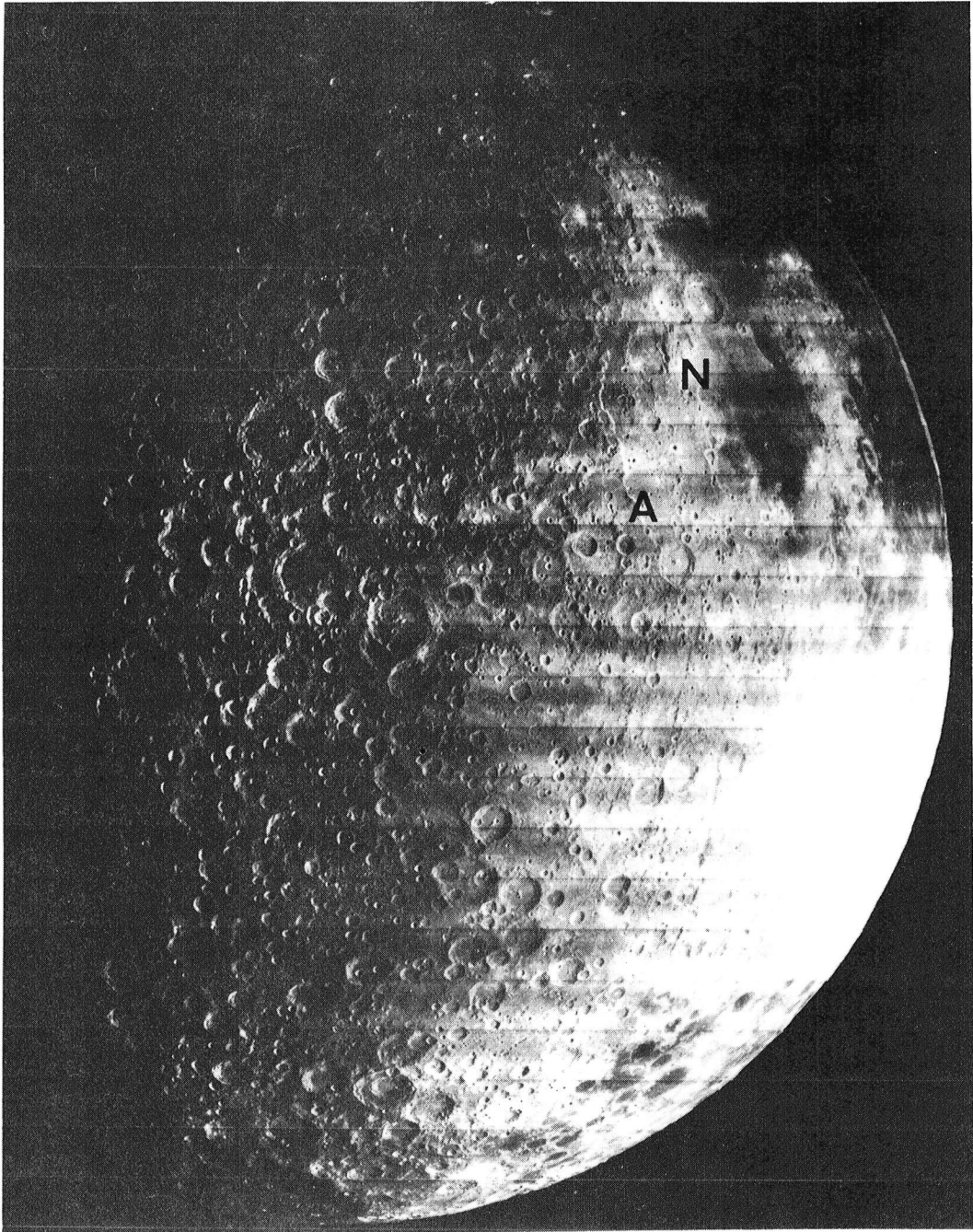


Fig. 2. Southern Highlands of the Moon

Lunar intercrater plains lie southwest of the Nectaris basin (N), beyond its topographic rim, the Altai Scarp (A), 435 km in diameter. Radial valleys extend 1.0 - 1.6 R from the basin center; the plains lie between 1.6 R to 3.6 R.  
Lunar Orbiter IV 95-M. North at top left.



record. In addition, although secondary cratering may aid in determining relative ages, it also adds spurious craters to the primary crater population. Because many of the small craters superposed on the plains are similar in morphology to secondary craters, i.e. they are elongate and arrayed in chains sometimes radial to large craters or basins, many of the plains are thought to be older than the superposed clusters of large craters, collectively known as the heavily cratered terrain (Trask and Guest, 1975). However, this observation does not uniquely distinguish among the major theories of plains formation.

Other surface alterations may be associated with volcanism or ballistic deposition. Thermal anomalies in the crust could, by decreasing crustal viscosity, contribute to the disappearance of basin structures (Schaber, Boyce, and Trask, 1977; Bastin, 1974). Continued erosional bombardment by smaller impacts, in addition to mass wasting and seismic disturbances from larger impacts, could create a plains surface in situ (Trask, 1976a; Malin, 1976b; Schultz and Gault, 1975a,b, 1976).

The intercrater plains of the Moon, as well as those on Mercury, appear to embay or bury older craters, weakening support for the first hypothesis for plains formation. Both surfaces record irregularly shaped craters interpreted to be secondaries of distant craters and basins. Yet, the lunar intercrater unit, unlike most of the lunar surface, lies far from the reworking of young lunar basins, and therefore may aid in distinguishing volcanic from ballistic origins. Because of their limited extent, the lunar intercrater

Pre-Imbrian Plains also may offer a less diverse range of morphologies and relative ages than do their mercurian counterparts. In summary, by determining the relative ages and origins of the intercrater plains, one can constrain the thermal and bombardment history of these two planets, and possibly determine the flux and origin of the bombarding projectiles.

#### Method

Photointerpretation, geologic mapping, and cratering studies comprise the principal tools through which the intercrater plains are examined. Mariner 10 and Lunar Orbiter IV imagery provide the principal data sources. Both data sets, however, suffer from similar limitations. Mariner 10 imagery of Mercury covers only ~45% of the planet's surface; resolution and sun angle vary widely. The lunar southern highlands were imaged by Lunar Orbiter IV and earth-based photography only; the highlands were not overflown in the Apollo missions. From Mariner 10 and Orbiter IV photographs, the first quadrant of Mercury was mapped, and the existing maps of the lunar regions were examined. Crater statistics of large regions and selected smaller areas were collected. The nature of the intercrater plains is also intricately woven into the fabric of the surrounding units. Therefore, Mercury's heavily cratered terrain, its hilly and lineated terrain, and its smooth plains were compared to the intercrater unit. The lunar maria, the Imbrian light plains, the Nectarian plains, and the terra

surfaces were similarly examined and fitted into the framework of the pitted plains surface. The detail and extent of the mapping and map analysis, the integration of cratering statistics, and the intercomparisons of mercurian and lunar units are unique to this research.

### Synopsis of Results

The intercrater plains of Mercury represent a primarily volcanic surface interbedded with ballistically emplaced ejecta of craters and basins and reworked by basin secondaries and small craters. The lunar unit is similar, possibly a product of pre-Imbrian highlands volcanism, but has more interbedded ejecta deposits than the mercurian plains, in part because of its proximity to the Nectaris basin. Neither intercrater plains surface is primordial, but rather suggestive of an intermediate stage of volcanism usually occurring exterior to craters and basins, but sometimes localized to ancient basin floors.

Plains emplacement appears to be greatest during the heaviest phases of bombardment, prior to the Caloris impact on Mercury, and prior to the Imbrium impact on the Moon. Both plains and crater coverage decrease with time, but not in the kind of matching proportions which would suggest plains formation by ejecta deposition alone. Other evidence--plains distribution, morphology, stratigraphic relationships, and tentative identifications of volcanic features--favor the volcanic origin for mercurian and lunar intercrater plains. The

cratering records on Mercury are confused by these multiple resurfacing episodes during the heavy bombardment.

The plains formation ("igneous") chronology, the tectonic history, the cratering record, and remote sensing results are used to set constraints on thermal histories. These may then be used to predict or test for compositional variations during planetary differentiation, and to identify profitable areas for further research.

### Organization of the Dissertation

The next two chapters describe the nature of the intercrater plains derived from geologic mapping and crater statistics. The initial sections of Chapter 2 examine in detail the correlation of crater classification systems for the Moon and Mercury, so that a firm base can be prepared for later comparisons. The study of mercurian and lunar units will follow parallel formats, with the lunar unit used as a foil for the mercurian unit. The cratering chapter (Chapter 3) first presents expected statistical signatures of geologic processes, then proceeds to examine crater statistics of the Moon and Mercury. Chapter 4 synthesizes cratering and geologic histories, and evaluates the major theories for the plains' origin. Compositional data and thermal models in Chapters 5 and 6 complement the geologic syntheses to better define the origin of the plains and their part in terrestrial planet evolution. Implications and the "role" of the intercrater plains are discussed in the concluding Chapter 7.

## CHAPTER 2

### GEOLOGIC MAPPING OF MERCURY AND THE MOON

This chapter presents the geologic framework of the intercrater plains on Mercury and the Moon as determined through geologic mapping. The strategies used in such mapping are discussed first. Then, because the degree of crater degradation is applied to both mapping and crater statistics, the correlation of degradation classification of lunar and mercurian craters is thoroughly addressed. Different imaging systems can potentially affect this classification, and are therefore also discussed. The techniques used in mapping Mercury are discussed in Section 2, followed by presentation of the Geologic Map of Mercury in Section 3. Material units, structure, and relevant albedo and color data are discussed therein. Preliminary conclusions regarding plains' origins are given there, and in the Description of Units (Appendix A) accompanying the map. The last section of this chapter presents the mapping analyses of the lunar intercrater plains, including tentative conclusions of their origin.

Early in the analysis of the imaging data of Mercury, geologic mapping was used to help synthesize the data. Murray et al. (1974b) produced a preliminary geologic map in addition to determining crater statistics on the general map units. Trask and Guest (1975) followed with the Preliminary Geological Terrain Map of Mercury in which they defined the intercrater plains unit and postulated that it predates the

heavily cratered terrain. Detailed geological maps of Mercury's quadrangles are now being published by the U.S. Geological Survey. They may use a new mapping strategy suggested by Malin (1975) which is used in this work and described in the following section. Similarly, studies of the intercrater plains of the Moon depend heavily on geological maps of the lunar southern highlands and related areas, as well as upon studies of crater densities and morphologies, as described below.

In this analysis, emphasis is focused on the comparatively localized area of intercrater material on the nearside southern highlands of the Moon, and on the widespread intercrater surface of the incoming side, or first quadrant, of Mercury. Although geologic mapping of terrestrial quadrangles is rarely influenced by geologic events in the other hemisphere, such might be the case for the Moon and Mercury, because the planets are smaller and the geologic processes (impact cratering, mass wasting, tectonism, and volcanism) are globally more uniform than on the Earth. However, the uninvestigated parts of Mercury and the Moon are quite different from the investigated areas, principally because of large basin events and their associated plains. Studies of Mercury's second quadrant and the lunar farside, as reported in the literature, fill this potential information gap in the intercrater plains analysis.

Intercrater plains and smooth plains similar to those of the first quadrant also occur in Mercury's second quadrant, but in different areal proportions. For instance, smooth plains nearly dominate

the Caloris hemisphere. Although both intercrater and smooth plains may have similar origins on each quadrant, they appear to represent a different history of plains emplacement. Processes associated with the Caloris impact are probably the primary factor which may have altered these histories.

The lunar pitted plains in the Maurolycus area form the only major exposures of terrain similar to the intercrater plains of Mercury. Areas of Nectarian plains in farside basins are less extensive with respect to younger plains materials. These farside plains are studied through recent regional geologic maps. Basin distribution and crustal thickness may also affect the dichotomy in intercrater plains distribution seen on the near and farsides of the Moon. Thus, the other regions of the two planets are not ignored; the author is cognizant of the northern plains units on Mars as revealed by Mariner 9. Later sections address this problem more fully through comparisons of regions dominated by the intercrater plains with those in which the plains are apparently a minor unit.

#### Materials and Techniques of Geologic Mapping and Analysis

##### Mapping Strategy of the U. S. Geological Survey

The mapping of Mercury and the Moon has as its basis the geologic mapping of the earth--a base in techniques and rationale expressed by Wilhelms of the U.S. Geological Survey (USGS) in his monograph, "The Geologic Mapping of the Second Planet," (1972).

"Terrestrial stratigraphic practice," he states, is built upon the concepts of (a) geological units formed either by a discrete process or over a discrete interval of time, and (b) sequence of formation. That is, when a "younger unit overlaps or embays an older unit, or the contact of a younger unit cuts across the contact between the two older units," (Wilhelms, 1972, p.6), one can determine the units' relative age within the rock stratigraphic column. Photogeologic data quality and age or character of the unit may force the mapper to rely on secondary characteristics, such as crater densities and morphologies, rather than on primary characteristics such as flow fronts. When the data are primarily photographic, as for the Moon and Mercury, overlap and transection relationships are most useful. However, the principle of uniformitarianism, in which "older terranes are likely to be degraded equivalents of younger, demonstrably bedded ones," (Wilhelms, 1972, p. 8), is applied cautiously to the plains materials, for it is not clear if the intercrater plains are simply degraded smooth plains. Because of the uniformity of meteoritic erosion over the surface of Mercury, and the lack of an atmosphere, Trask and Guest remark, "We may assume that on Mercury, surface morphology reflects the age, composition, lithology, and mode of formation of the underlying rock unit. To a much greater extent than the earth, therefore, we may recognize different rock units by their surface characteristics," (Trask and Guest, 1975, p. 2461).



In relating local units to the total stratigraphic record, the mapper uses "extensive and synchronous datum planes," like the secondary craters and ejecta blankets of Imbrium, Orientale, and Caloris. If such extensive marker horizons are not available, secondary features such as superposed crater densities or crater morphology are applied to the larger area from the reference area, under the assumption, that "morphology partly indicates state of preservation," (Wilhelms, 1972, p. 8). On Mercury's first quadrant, one must use degradational states or crater densities, for many of the existing datum planes are model dependent (e.g. first quadrant features interpreted to be related to the Caloris basin of the second quadrant), non-synchronous (plains formation), or restricted in area (most ejecta blankets). This also holds to some extent on the lunar southern highlands, where the plains lie far from the Imbrium and Orientale marker horizons.

Wilhelms states that the USGS attempts to "map materials, not physiographic forms," resulting in stratigraphy and not geomorphology. However, the units mapped here are a mixture of terrain and time-stratigraphic units, somewhat analogous to the lunar material units, yet not strictly the rock stratigraphic units common in terrestrial mapping. The lunar geologic systems are: Copernican, Eratosthenian, Imbrian, and Pre-Imbrian; the latter system is now divided into Nectarian and Pre-Nectarian (Stuart-Alexander and

Wilhelms, 1975). The mercurian systems, which are presented in subsequent sections, are: Post-Caloris (Class 1 and Class 2, defined below), Caloris (Class 3), and Pre-Caloris (Class 4 and Class 5), in order of increasing age. Unlike the lunar systems, where the marker horizon forms the base of the period, the mercurian system proposed here places the Caloris marker horizon at the "top" of the crater and plains Class 3 period, or at the base of the Class 2 period (the Post Caloris System).

It is USGS policy to avoid the "interpretative bias" by portraying units as they appear physically, not hypothetically, thus extending the "map's usefulness beyond the acquisition of new data." Lines delineating unit boundaries must be reproducible, "unit names must be objective," (p.10), and description of physical characteristics must be separate from interpretation of those features. For example, small craters radially distributed around a larger crater may be described as satellitic craters, rather than "secondary" craters, a name which presumes an origin for these features. Age assignments must be clearly stated and reproducible; surface properties should be quantified where possible. Wilhelms concludes that a planet's surface is mapped to "learn and communicate," (p.13), a practice adopted here. In the mapping process, one's observations are filtered, organized, tested, and generalized.

## Materials and Techniques of Lunar Mapping

Materials. The materials used in the analysis of the lunar intercrater plains include a variety of imagery, maps, and catalogues of lunar crater data. Lunar Orbiter IV imagery covers the southern highlands at photographic resolutions of about 100 meters at sun elevations of  $0^{\circ}$  to  $24^{\circ}$ , depending on latitude. More specific data on Orbiter IV imagery is given in Chapter 3 and in the accompanying figures and tables of crater statistics in the Appendix. Supporting data include imagery from other Orbiter missions and, for comparisons, the Apollo mission photography of the light plains, the maria, and the farside plains. High resolution Orbiter IV and V photos were used in studies of Copernicus and Langrenus, discussed in Chapter 3.

A second set of materials uses the 1:1,000,000 scale quadrangle maps of the Geologic Atlas of the Moon series (U.S. Geol. Surv. Misc. Inv. Geol. maps). The four quadrangles enclosing the intercrater plains designated by Trask and Guest (1975) are Maurolycus (Scott, 1972), Hommel (Mutch and Saunders, 1972), Clavius (Cummings, 1972), and Tycho (Pohn, 1972). Bordering quadrangles of interest include Rheita (Stuart-Alexander, 1971) and Rupes Altai (Rowan, 1971). The four central maps were compared to Orbiter IV and to earth-based imagery to ascertain unit boundaries, contacts, relative ages, etc., to understand the mappers' observations and interpretations. The common boundaries of the quadrangle maps were examined to determine consistency of unit ages and interpretation. These maps were then

compared to the Geologic Map of the Near Side of the Moon, a 1:5,000,000 scale map independently constructed by Wilhelms and McCauley (1971). The Pre-Imbrian Plains unit on that map combines several different units of the lower scale maps (pitted plains, Imbrian cratered plains, ridged terra, etc.); the constituent units were examined for mutual similarities and for similarities to the intercrater plains of Mercury. (See Table 6 in the last section of this chapter.) The nearside maps are structured about the four lunar geologic time systems noted above. The Nectarian and Pre-Nectarian systems appear in more recent maps, the limb and farside 1:5,000,000 series: West Side (Scott, McCauley, and West, 1977), the East Side (Wilhelms and El-Baz, 1977), the Central Far Side (Stuart-Alexander, 1978), and the North Side (Lucchitta, 1978). Plains units which could possibly be related to or analogous to the pre-Imbrian plains (pIp) unit were studied on each of the large scale maps.

The geologic map data were augmented by crater statistics on diameter, degradation class, morphologic type, and other data found in the Lunar and Planetary Laboratory Catalog of Lunar Craters (Wood and Andersson, 1978a). Other materials used include charts from the System of Lunar Craters (Arthur et. al., 1963, 1964, 1965, 1966), the Lunar Earthside Chart (LMP-1), the Farside Chart (LMP-2), and South Polar Chart (LMP-3), and the Lunar Orbiter IV Atlas and Gazetteer (Gutschewski, Kinsler, and Whitaker, 1971).

Crater Degradation Criteria from the Moon to Mercury. The

relative age of craters is often expressed by their extent of degradation. On the premise that all (primary) impact craters begin as fresh crateriforms and become progressively degraded, degradation can be roughly quantified and correlated with age.

The USGS system used in Mercury mapping (see Strom, Malin, and Allen, 1978; and McCauley et al., 1978) is built upon work by Pohn and Offield (1969) who proposed a 7.0 to 0.0 continuum in which a 7.0 rating is given to a fresh, sharp-rimmed rayed crater and 0.0 rating is given to a severely degraded crater. Lunar craters of three size groups (diameters less than 20 km, 20-45 km, and greater than 45 km) were judged according to the degradation of the following features: rays, radial ejecta, satellitic craters, rim crest sharpness, terracing, interior radial channels, polygonality, rim texture, and, for smaller craters, the geometry of the interior shadow. The change in these features with age is interpreted by Pohn and Offield (1969) in Fig. 3. As one can see, rim sharpness was considered the most significant criteria, especially for the larger craters. The non-linear relative age scale, determined by non-linear erosional processes, is affected by at least three variables--rock strength, volcanic materials, and proximity aging. The latter, also called proximity weathering, occurs when fresh craters are severely degraded by large impacts in the immediate vicinity. This catastrophic degradation belies the true age of the affected crater. Similar uncertainties apply to relative age dating on other planets.

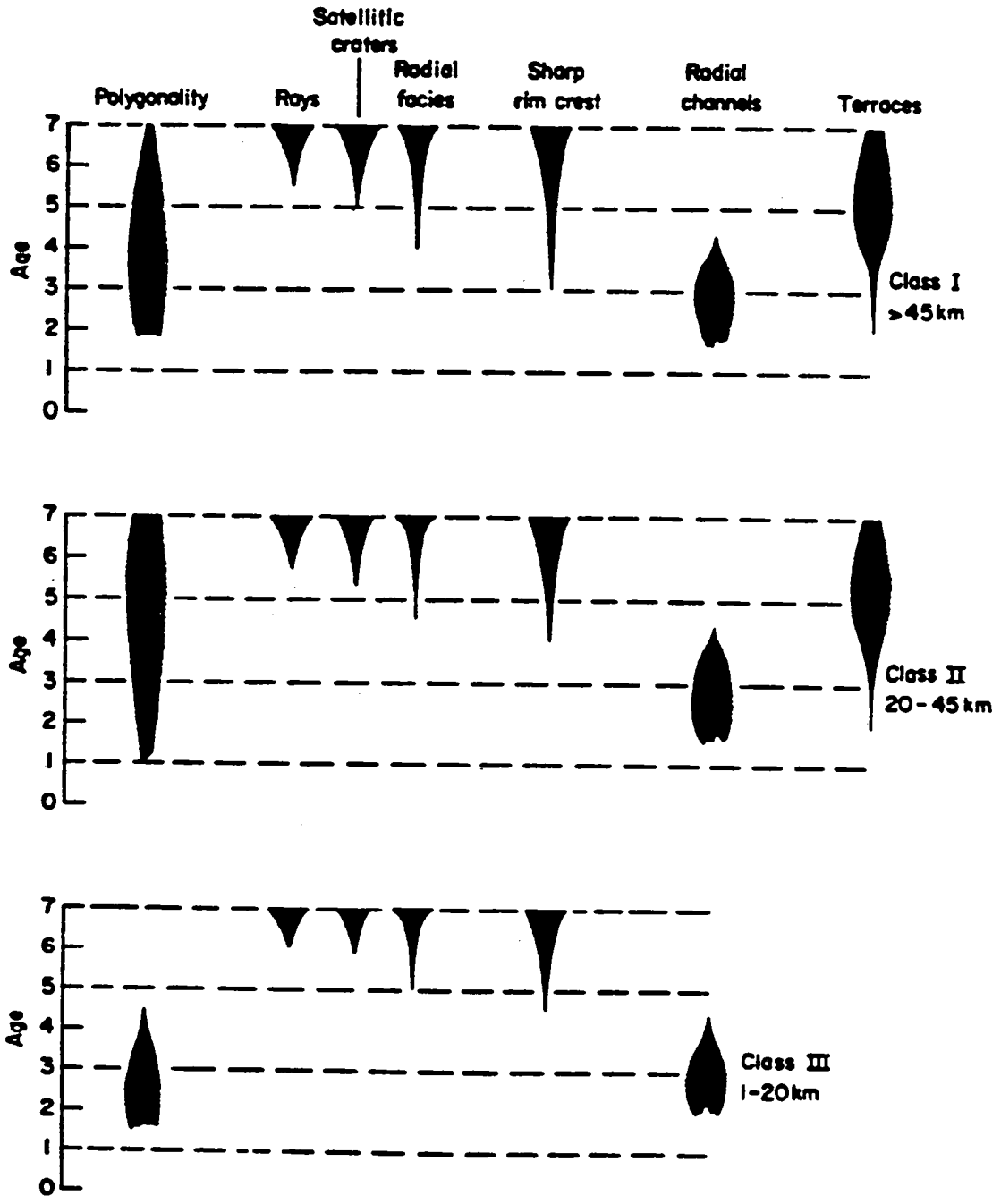


Fig. 3. "Changes in Diagnostic (Lunar) Crater Features With Age"  
 From Pohn and Offield (1969)

Offield and Pohn (1969) demonstrate that small craters "age" more quickly than the larger structures (Fig. 3; also see Fig. 1 of Strom et al., 1978). Craters of diameters between 8 and 15 km were considered the best to use when dating surface units; larger craters were often too scarce for accurate statistics and small craters tended to show a false older age. Generally, surfaces dated by the Offield and Pohn (1969) technique corroborate surface ages determined by geologic mapping except in those areas with significant numbers of endogenic craters or in areas likely to have undetected secondary craters. The following table compares the Pohn and Offield (1969) system to the geologic time systems used in the lunar mapping, adapted from Wilhelms and McCauley (1971). Note the rather good time resolution possible in the Pohn and Offield morphologic continuum shown in Table 2.

Table 2: Age Classification Comparisons

USGS System Name	Symbol	Pohn and Offield "Age"
Late Copernican	Cc <sub>2</sub>	7.0 -- 6.5
Early Copernican	Cc <sub>1</sub>	6.4 -- 6.0
Eratosthenian	E	5.9 -- 5.5
Late Imbrian	Ic <sub>2</sub>	5.4 -- 4.8
Early Imbrian	Ic <sub>1</sub>	4.7 -- 4.2
Late Pre-Imbrian	pIc <sub>3</sub> (N)	4.1 -- 3.0
Middle Pre-Imbrian	pIc <sub>2</sub> (N, pN)	2.9 -- 2.0
Early Pre-Imbrian	pIc <sub>1</sub> (pN)	1.9 -- 0.0

- a. The Early Middle Pre-Imbrian is the proposed time of the Nectaris event. Symbols and names would then change to Nectarian (N) and Pre-Nectarian (pN).



The degradation class "filter" has been applied to other crater studies, one of which is the Lunar and Planetary Lab (LPL) Catalog of Lunar Craters, and another, the USGS degradation spectrum applied to Mercury's craters. Both are five class systems, but ranking is oppositely numbered: USGS designates Class 5 craters as the youngest and freshest, and Class 1 as oldest, while in the LPL system used here, Class 1 is freshest and Class 5 most degraded. Degradation criteria differ slightly as discussed below.

The five-class system developed by Arthur et. al. (1963) at LPL and used in the current Catalog of Lunar Craters (Wood and Andersson, 1978a) and in the Brown University Mercury Crater Library (Cintala et al., 1976) has as its main criteria rim sharpness and as secondary criteria rim completeness and brightness under high sun angle illumination (see Wood, Head, and Cintala, 1977). Smaller craters have greater symmetry and regularity than larger lunar craters of the same class. Rim degradation occurs with successive impacts, large and small; by Class 3 (C3--LPL), rims are "broken and poorly defined." Ruins characterize Class 4 (C4) structures, while Class 5 (C5) objects "are so battered and fragmentary, or so subdued, that they sometimes are not easily recognized as former craters," (Wood and Andersson, 1978a).

Craters classified by the LPL scheme do not fall into distinct groups of the Pohn and Offield dating method, as shown in Table 3,

adapted from Wood and Andersson (1978a). Represented are 106 craters. The last column gives the name of the USGS system equivalent to the Pohn and Offield morphologic age.

Table 3: LPL Degradation Class Comparisons

Pohn & Offield Morphologic Age	LPL Class					USGS System Name
	1	2	3	4	5	
7.0 -- 5.0	52	7	1	0	0	CE to Ic <sub>2</sub>
4.9 -- 4.0	7	15	3	1	0	Ic <sub>2</sub> to pIc <sub>3</sub>
3.9 -- 3.0	0	0	10	2	0	pIc <sub>3</sub>
2.9 -- 2.0	0	0	2	3	1	pIc <sub>2</sub>
1.9 -- 0.0	0	0	1	1	0	pIc <sub>1</sub>

The differences result from the different criteria used for each classification system. Advantages of the LPL system include its greater ease and speed of application, the adequate "degradation resolution," and the improved statistics within classes. A great amount of other data is available for each crater classed in the LPL Catalog.

Using the decreasing depth of craters with age, due to filling, Wood (1979) has determined the general absolute ages of the LPL crater classes. His crater ages are presented below in Table 4, with

estimates of percent shallowing of the crater from a pristine Tycho-type depth-diameter ratio. Fig. 4 interrelates these ages with major lunar events.

Table 4: Crater Age and Shallowing

LPL Class	Pohn and Offield Age	Percent Shallowing	Absolute Age
1	7.0 -- 5.0	0	0 -- 3.5 b.y.
2	4.9 -- 4.0	23	3.5 -- 3.9
3	3.9 -- 3.0	40	4.0 <sup>a</sup>
4	2.9 -- 2.0	59	4.1 <sup>a</sup>
5	1.9 -- 1.0	76	4.2 <sup>a</sup>

a. These are the approximate ages of the middle of the crater-forming period (Wood, 1979), in billions of years before present.

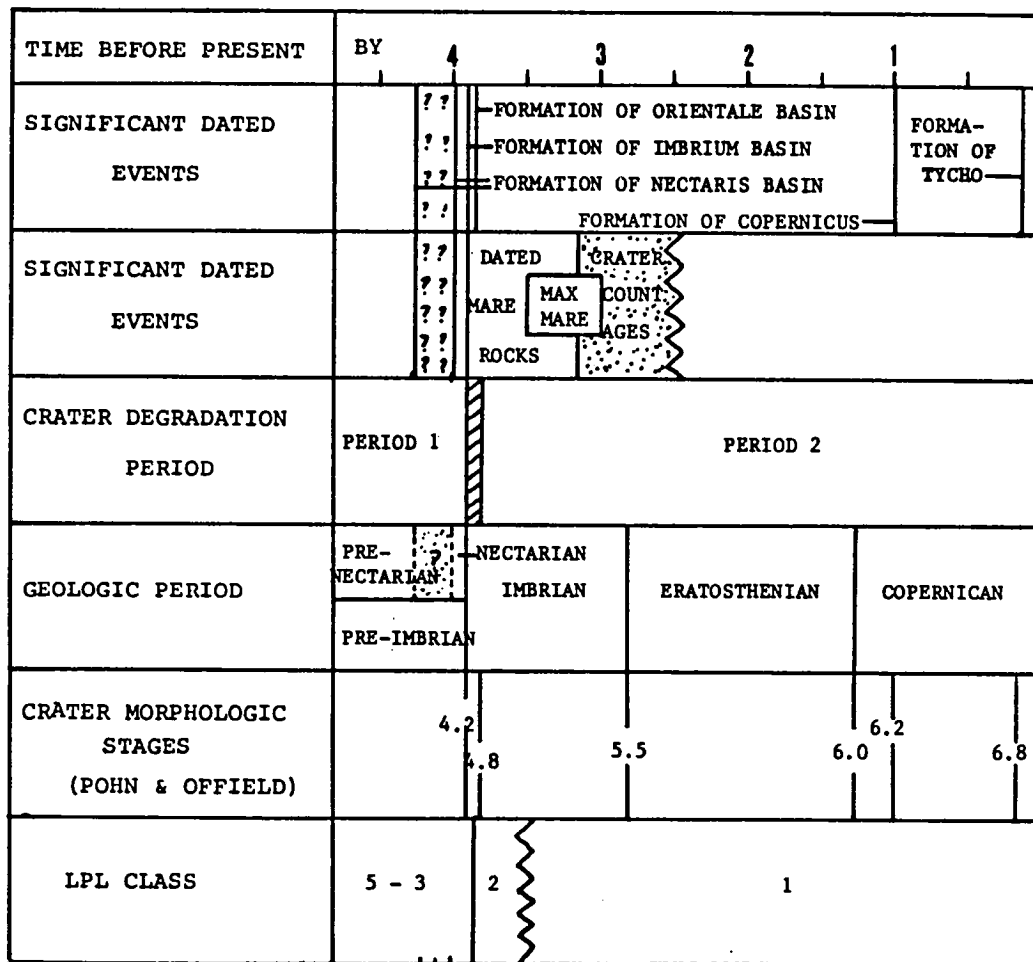


Fig. 4. Major Events in Lunar Surface History From Wood et al. (1977)

Crater degradation Period 1 is much more severe and intense than Period 2; see Head (1975) and Wood et al. (1977). The queried area spans 4.25 to 3.98 ae., the proposed ages for the Nectaris impact and the marker horizon dividing Pre-Nectarian and Nectarian geologic periods (Stuart-Alexander and Wilhelms, 1975). Adapted from Wood et al. (1977).

The mercurian degradation criteria as determined by the Brown-LPL system are schematically presented in Fig. 5 (Wood et al., 1977). The U.S. Geological Survey places more emphasis on interior feature preservation (such as central peaks and terraces), superposed craters, and infilling and various ejecta facies, while weighting rim sharpness slightly less heavily (McCauley et al., 1978). The broader criteria, somewhat similar to those used by Pohn and Offield, are necessitated by the decreased resolution of Mercurian imagery and the increased gravity of the mercurian surface.

Mercury's gravitational field probably acts to restrict the range of ejecta facies--both continuous and discontinuous deposits (Gault et al., 1975). For craters of diameter  $D_r$  less than 300 km, Gault et al. find that the width of the continuous ejecta deposit

$R_{cb}$  is

$$R_{cb}/D_r = 0.44 - 10^{-3} \cdot D_r$$

for Mercury and

$$R_{cb}/D_r = 0.68 - 1.5 \cdot 10^{-3} \cdot D_r$$

for the Moon. A greater amount of ejecta deposited on the rim wall may increase its relative resistance to degradation by increasing the amount of material which must be degraded. Hence, "raised rims" may be a more persistent feature for the mercurian crater than the lunar crater. Basins and craters are classed differently because of the increasing preservation of features of larger sizes and of larger formation energies (See Fig. 1 of Strom et al., 1978).

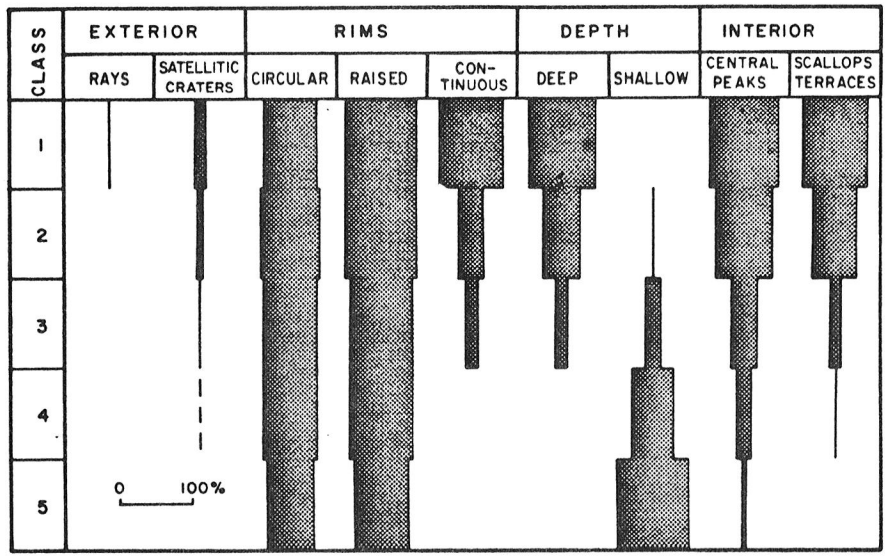


Fig. 5. "Changes in Diagnostic Degradation Features With Age For Mercurian Craters (LPL Class)" From Wood et al. (1977)

Note the persistence of circular and raised rims for mercurian craters. Compare with Fig. 3 from Pohn and Offield's (1969) study of lunar craters.

Summary of Morphologic Criteria for Mercury. The morphologic criteria used in the mapping and crater analysis of Mercury are essentially like those of the USGS with an LPL numbering system. The five degradation states are determined by (1) rim sharpness and completeness; (2) preservation of interior features such as terraces, slumps, central peaks or peak rings, and the plateau region inside the rim; (3) preservation of ejecta facies, including rays, secondary craters and troughs, and the continuous ejecta blanket; and (4) the number of superposed craters. The system was designed to be consistent with current USGS practices as well as current LPL studies of size-degradation distributions. Emphasis is retained on rim sharpness so that this hybrid LPL system is analogous to that used by Wood et al., (1977), i.e. Brown University's catalogue of mercurian craters. A "sixth" class, representing the C5' ("C-five-prime") structures, has been added to indicate vague circular depressions of inferred ancient crater and basin rims. Fig. 6 presents crater degradation types for an area of the lunar southern highlands; Fig. 7 shows the analogous mercurian crater types.

Dependence of Degradation Classification on Imagery Systems.

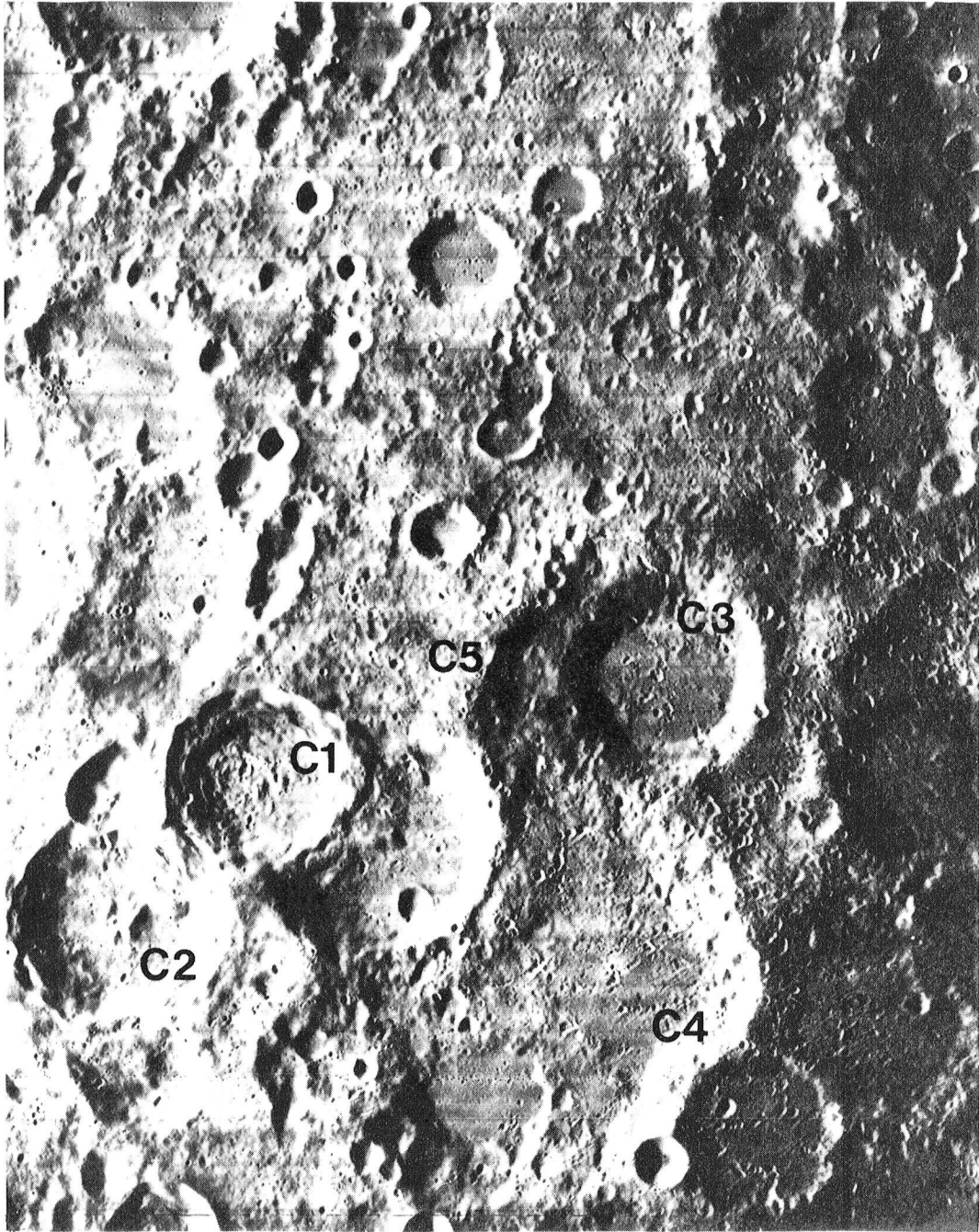
Orbiter IV photos of the southern highlands (such as Fig. 6) were compared to earth based photos of the same highland region, plates G11 and H11 of the Consolidated Lunar Atlas (Kuiper et al., 1967). In general, a criterion based on rim sharpness enables the viewer to

Fig. 6. Degradation Classes of Lunar Craters

Area east of Tycho (with North at bottom). Crater names are C1 Nasereddin; C2 Miller; C3 Saussure; C4 Orontius; and C5, a saucer-shaped crater under Saussure. Note Imbrian secondaries (thick arrows) and the secondaries of Tycho (thin arrows). The latter form chains of small craters radiating from a point off the photo at right center. Pre-Imbrian Plains (pIp) occur in a small area at top center of this photo.

Lunar Orbiter IV 112-H2. North at bottom. Nasereddin is 52 km in diameter.





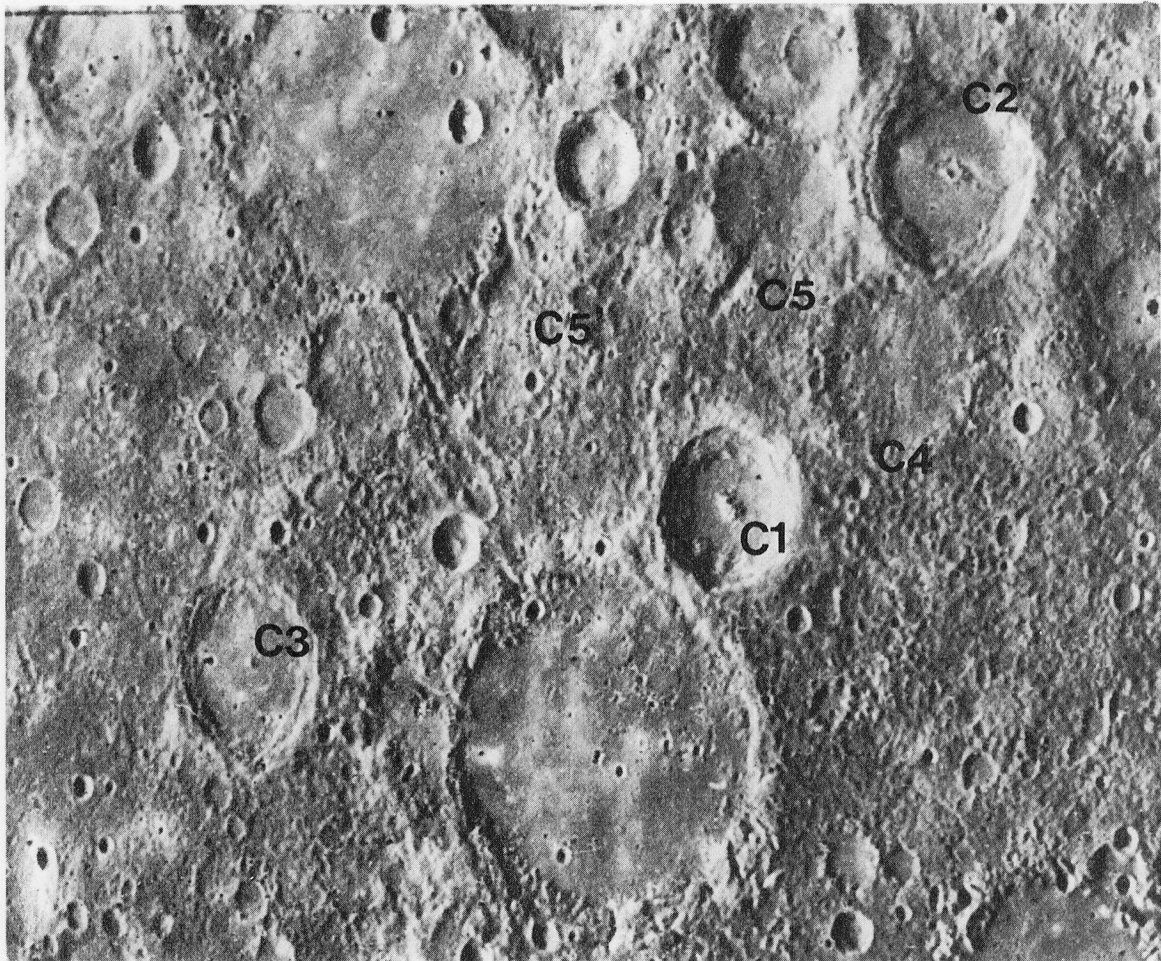


Fig. 7. Degradation Classes of Mercurian Craters

The region near Ibsen (large, 160 km crater at lower center) and Imhotep (large 160 km crater at upper left center) includes all crater types from C1 (freshest) to C5 (most degraded). C5' craters are tentatively marked.

Note secondaries of the C1 crater (100 km diameter) on the floor of Ibsen. The scarp cutting the C2 crater at upper right deflects around the central peak within the central depression. The trace of the scarp on the east crater wall suggests that it represents a normal fault (see Scott et al., 1980).

FDS 27363. North at top.

properly classify the large craters at lower resolution, even through the ejecta blanket and secondaries are harder to distinguish. Wood and Andersson (1978a) compared their classifications of 1200 craters in the new LPL catalog based on Lunar Orbiter (and Apollo) imagery, to the older System of Lunar Craters (Arthur et al., 1963, 1964, 1965, 1966), which used only earth based photography. Seventy two percent of the 1200 craters common to each catalogue were assigned the same classes in the 1-5 LPL degradation system, while the remainder differed by one class higher or lower. Reproducibility at differing illuminations showed a standard error of  $\leq 0.2$  class units, (Wood and Andersson, p. 27). In other words, degradation classification did not fluctuate greatly under changing resolutions (or illuminations) from earth based imagery of the Moon to Orbiter IV imagery, for craters  $\geq 7$  km diameter.

A similar comparison was made between Orbiter IV photo 103 H1, the earth-based Atlas plates A5 and B10, and Mariner 10 image FDS 2286 of the area around Aristoteles. The resolution available on much of the Mariner 10 lunar and mercurian imagery is very similar to earth based photography of the Moon. However, many small craters visible in the higher resolution Orbiter photo are not visible at the lower resolution of the Mariner image, therefore affecting the completeness of crater statistics at small diameters. Schultz (1977) estimates that 50% of the craters on smooth surfaces visible on Orbiter imagery

are not detected on the Mariner 10 photo if they are smaller than 2.5 pixels, the so-called "resolution limit." If the background terrain is hilly, nearly 90% of these smaller craters are lost. Schultz cautions that statistical studies of craters should be limited to those of diameters twice as large as the resolution limit, or about 5 pixels. That practice is adopted here.

Other effects of lower resolution and vidicon imagery are noticeable when trying to determine crater class or morphologic type, especially for small craters. Rim sharpness remains an excellent criteria when reinforced by other relative age criteria. Superposition, embayment, and transection relationships, however, also become more obscure as resolution decreases from 100 m to 1-3 km. Secondary craters of primaries less than 50 km in diameter are nearly undetectable except at the highest resolutions. Slump features are either enhanced or lost, and crater recognition varies with terrain background as well as with lighting. Diameters of the smaller craters, less than 5 pixel units, are larger by up to 25%; rayed and haloed craters are also overestimated in diameter (Schultz, 1976a).

For the larger craters, degradation classes are fairly reproducible between earth-based, Orbiter, and Mariner imagery. In comparing degradation classes that would be assigned to lunar craters on the Mariner 10 photo with those previously determined by Wood and Andersson, the following observations are made. Class 1 craters retain their class status, especially when the craters are rayed, haloed, or lie on top of the dark maria. Class 2 craters with sharp rims but some

detectable superposed craters are easily identified (and remain C2). Class 3 craters have quite battered rims, and seem to span a larger range of stages of degradation. Most of the rims remain intact, however, and this observation is readily made at Mariner 10 resolution. Smaller craters are much harder to classify on Mariner 10 imagery, for, as Schultz noted, they all appear fairly sharp and bowl-shaped, except where there are obvious superposed craters. Clues to small crater degradation states, such as interior shapes and shadows (Pohn and Offield, 1969), are much harder to detect on highland areas than on mare.

Highly degraded craters, if identifiable, have moderately reproducible class assignments. The more battered and incompletely rimmed of the Class 4 craters may be classed as C5 structures on the Mariner 10 photos. The most degraded class, Class 5, are unambiguously C5 craters if they are recognized at all. It is uncertain what status the "ancient circular depressions," the C5' forms detected on Mercury, would have on the Moon. Some might be Class 5 structures; others would receive no designation because of their vague nature. Buried craters under high sun lighting tend to be lost in the Mariner 10 imagery. Features which are linear, such as rilles and scarp faces, are often not lost, even when their width is one-fourth the resolution limit (Schultz, 1976a), with the exception of features extending east--west, parallel to solar illumination.

The intercomparison of these three imaging systems correlates the loss in feature recognition and changes in apparent crater degradation classes and morphologies with the loss in resolution; this loss can be quantified, as Schultz has shown. Fortunately, some of the Mariner 10 imagery is of higher, 100 meter, resolution, enabling one to compare feature recognition and crater degradation within the Mariner 10 imaging system.

The Discovery Scarp Mosaic illustrates the effects of a change in resolution within the Mariner 10 imaging. The mosaic, centered about the crater Rameau (~50 km diameter), consists of four high resolution, third encounter pictures (FDS 52881-4) in the center, surrounded by moderately high resolution photos from the first encounter, (FDS 27397-9, 27393, 27386). One can see the increase in number of recognizable small craters and general detail in the central scarp region. The degree of degradation of the moderate size (20 km) craters appears to increase slightly as resolution drops, but larger craters, like Hesiod's northern neighbor, retain enough detail to be classed according to degradation state. The Discovery Scarp area is discussed later in this chapter and illustrated in Fig. 8.

#### Materials and Mapping Techniques for Mercury

Materials. A photomosaic base of moderate to high resolution (0.5 to 1.5 km) Mariner 10 imagery (Fig. 1) was used to construct the Geologic Terrain Map of Mercury's first quadrant (Fig. 9).

The scale of this "Perspective Projection" is approximately 1:7,700,000; a working scale of 7.74 km per mm was used to measure features parallel to the limb of the mosaic. Features of 40 km (5 mm) and larger were included in the geologic terrain map; smaller features were included if they proved useful in the map interpretation. Source data for this project were: Mariner 10 imagery from all three encounters, photomosaics and stereo pairs prepared by JPL/IPL, and published color and albedo data. Outgoing, post-encounter images (of the second quadrant) were used mainly for comparative purposes. A diagram of the map boundaries appears in Fig. 10.

Techniques. In the mapping technique used here, crater groups are classified first. The youngest craters of the area or cluster are delineated using their continuous ejecta blanket as the extent of this material unit. Secondary cratering appears to rework the local terrain rather than add substantial amounts of new material from the target area and bolide. Many craters can still be identified after being bombarded with secondary craters and continuous ejecta deposits of other craters and basins (Trask and Strom, 1976). Even on the lunar surface with its lower gravity, the proportion of country rock mixed with primary crater ejecta and redeposited as secondary and tertiary ejecta outweighs the target material (Oberbeck, 1975; Oberbeck and Morrison, 1976; Oberbeck et al., 1977; and Morrison and Oberbeck, 1978). As noted, mercurian gravity tends to concentrate the continuous ejecta blanket closer to the crater rim (Gault et al., 1975). Ejecta

Fig. 8. Discovery Scarp Mosaic--Intercrater Plains

Crisper features in central area of mosaic result from higher resolution images (0.8 km to 0.9 km) than the surrounding images (average resolution 1.4 km).

Discovery Scarp transects Rameau (R), a C2 crater of 55 km diameter, and two C3 craters north of Rameau. This section of the scarp roughly parallels the contact between a P4 unit to the west and a P3 unit to the east. P2 plains embay the northern end of Discovery Scarp at top left.

Because Discovery Scarp does not alter the craters it transects, the scarp is likely to be tectonic, and another example of mercurian thrust fault scarps. The graben-like structure at the southern end of the scarp may be a remnant of the planet's expansion, or can be interpreted as a pair of facing thrust faults, a remnant of the planet's contraction. The domical feature (arrow) noted by Malin (1978) appears to be Class 2 in age (about the same age as the scarp). Note the intracrater scarp in crater A, north of Hesiod.

FDS 528881-4 in center; FDS 27386, 27393, 27397-9 around the edges. North at top.





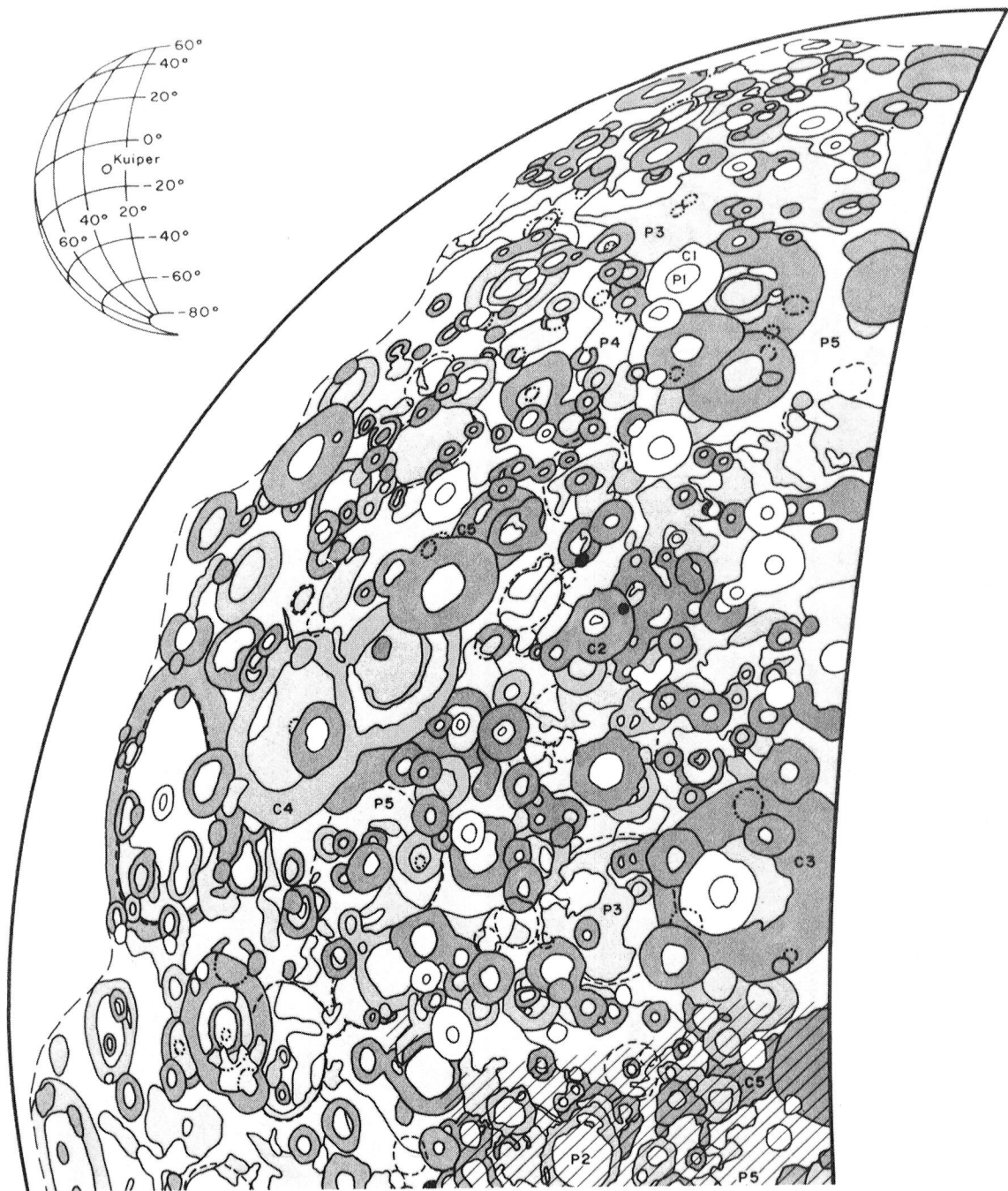


Fig. 9. Geologic Terrain Map of the Incoming Side of Mercury

- a. Northern Section. The southern section and correlation of units are continued on the next page. Color copies of this map will be distributed to Principal Investigators and other interested persons.

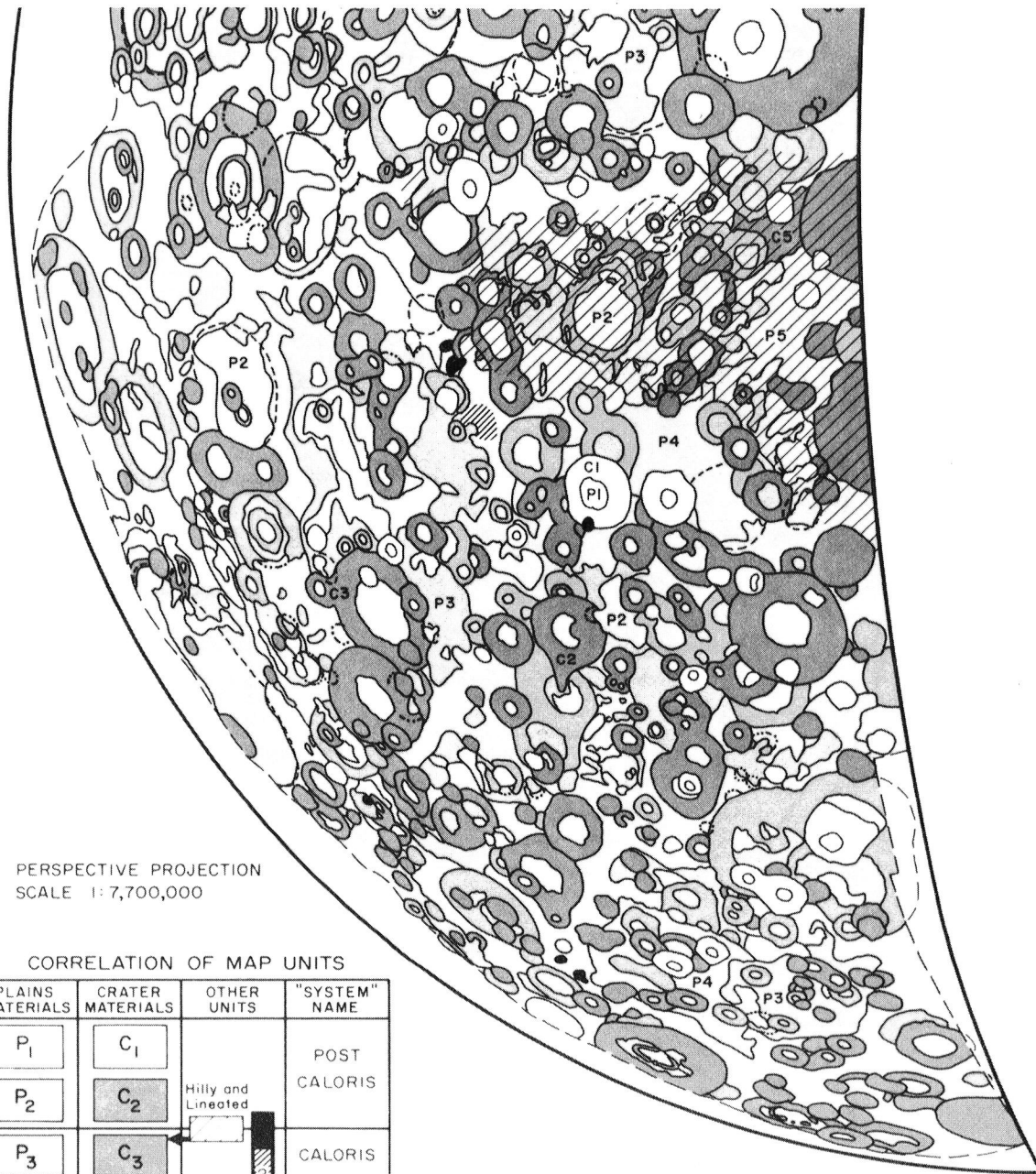


Fig. 9. Geologic Terrain Map of the Incoming Side of Mercury

b. Southern Section

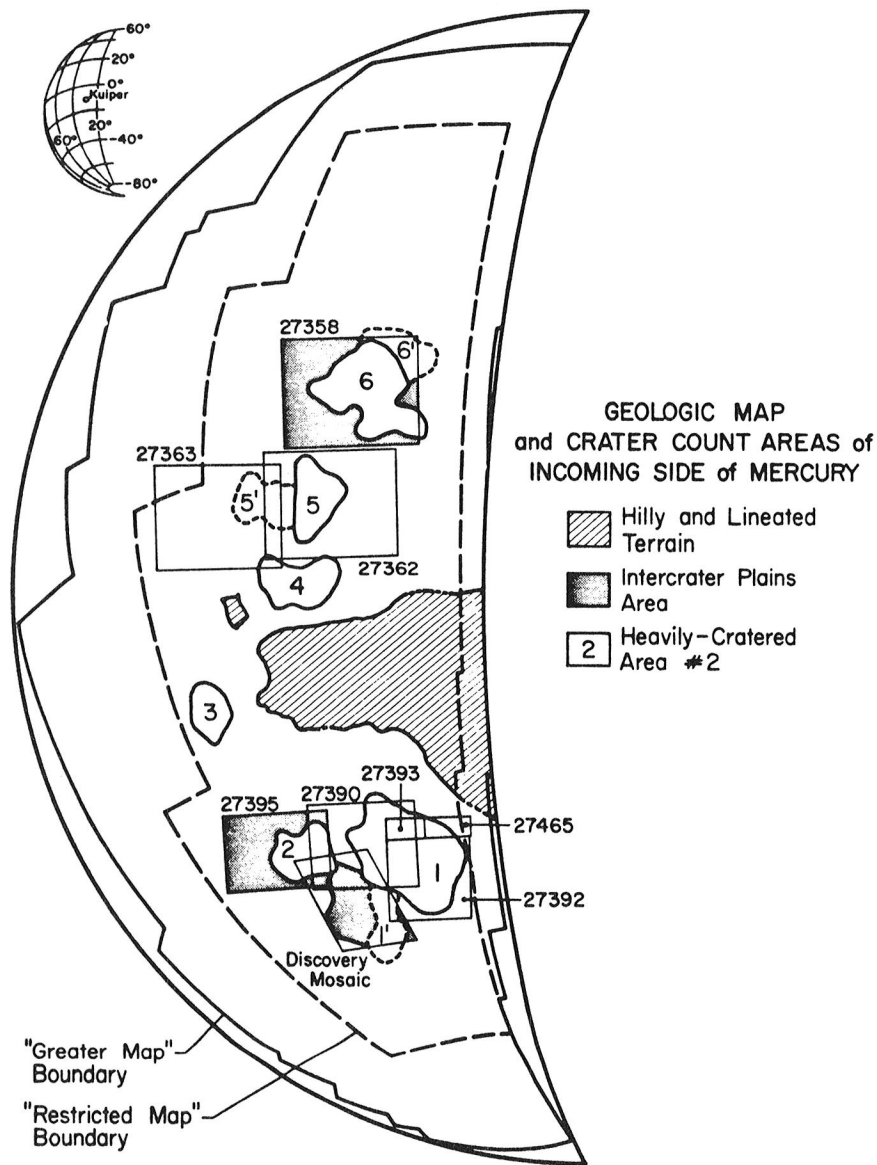


Fig. 10. Boundaries of Geologic Map and Crater Count Areas of the First Quadrant of Mercury

Boundaries are marked for the General Map Area ( $1.0284 \cdot 10^7 \text{ km}^2$ ) and the Restricted Map Area ( $4.985 \cdot 10^6 \text{ km}^2$ ); the latter more closely conforms to the "discriminability limits" used by other authors. Crater statistics ( $D \geq 5$  to 7 km) were gathered for heavily cratered areas 1, 2, 5, 5', and 6 (and part of 6'), and for intercrater regions surrounding areas 1, 2, and 6. Area 2 intercrater plains were subdivided into 8 regions roughly corresponding to map units (see Fig. 63 and Appendix D). FDS numbers are given for each footprint. North at top.

from secondary and tertiary impacts is likewise concentrated close to their rims. Color-ratio images of the surface may confirm that compositional variations are confined to the continuous ejecta blanket, if a variation in surface and substrate exist (Hapke et al., 1975).

Boundaries of craters underlying the freshest crater or cut by its secondaries were delineated next. When two or more craters appeared to be degraded approximately to the same extent, with few clues as to which of the craters was the older, the pair or group was included in one crater material boundary. Where an emplacement sequence was obvious, but the crater's degradation state was similar or of the same class, crater materials were separately drawn, although the unit classes were equivalent. The crater units indicate a sequence of emplacement as well as degradational groups; however, degradational classes over the entire incoming side are as consistent with these classes as possible. Sequencing within the cluster of large craters on Mercury's surface is less difficult than determining the degradation class of craters isolated in the plains. Superposition of basin and crater secondaries or ejecta could not always be applied, so their relative ages depended more heavily on morphologic criteria such as described earlier.

Mapping and relative age dating of plains units followed the determination of crater boundaries and sequences. Smooth plains were outlined first. Boundaries of plains areas of similar texture and

apparent crater frequency were outlined next. Contacts, in general, were hard to establish at the resolution of most of the Mariner 10 imagery. Poor resolution in the northern limb regions makes unit boundaries and relative ages more questionable. Albedo transitions sometimes accentuate the contact, but are not common. More often, superposed crater densities, surface textures, and abrupt termination of crater troughs and chains delineated plains boundaries.

Once the rough physical limits of the various plains units were established, the time limits of plains formation were determined by the relative ages of the oldest craters which overlie the plains' surface and the youngest crater which is overlain or embayed by the plains (Malin, 1975). Plains which overlie a C3 crater but are cratered by a C2 crater or its ejecta are classified as P3 plains. Impact melt surfaces inside a C3 crater are also designated P3 plains material. Although plains units can be thought of as an extensive marker horizon, embaying craters and other plains, they are not as useful as crater ejecta blankets for the former could well lack simultaneity and uniformity of origin.

Plains units varied in both lateral and vertical extent. Some were thin enough to recognize rough, more highly textured, older plains material beneath. The degree of burial of subjacent topography often increased toward a central area; this is interpreted as a thickening or deepening of deposits, sometimes associated with indistinct depressions. Buried craters were noted with dot-dash symbols if

their rims were still distinctly crateriform; rims of the ancient, vague depressions were less certain and denoted with long dashed lines. Stereo pairs available for the southern half of the incoming side of Mercury helped in recognition of buried craters, contacts, tectonic features, and in determining relative thicknesses of plains units. High resolution photography and stereo pairs were used to insure consistency and continuity of plains surfaces across the first quadrant.

Because lighting conditions change so drastically across the incoming quadrant, plains units of similar ages often do not appear to have similar textures. Crater and plains units near the limb may be less well defined because of high sun angles where relief appears much more subdued and crateriforms are more difficult to recognize. Bright patches from small recent craters and swaths of ray material contrasted against the darker background of smooth plains on the limb areas (e.g. Copley). Although resolutions of the second Mercury encounter were poorer and sun angles were greater, it was still possible to recognize the older intercrater plains units by the high densities of small bright crater rims. Relief and texture on the terminator, on the other hand, are often exaggerated by shadowing, as can be seen in the secondary crater fields of old basins (e.g. Fig. 12, the basin surrounding Hitomaro) and the texture and roughness of units underlying the smoother plains near the terminator.

The hilly and lineated terrain is a tectonic modification of pre-existing terrain units, rather than a separate material unit. The region was closely examined using much of the high resolution photography, and its surface was compared to those in bordering areas. Craters and plains emplaced before and after the modification event were established. Map units were extended inward from the surrounding regions. The relative age of the youngest affected crater sets the lower age limit for the hilly and lineated area. Likewise, the age of the oldest unmodified crater in the zone, preferably near the area of greatest damage, sets an upper time limit to this event.

The last materials mapped were dome materials and rimless depressions (see Chapter 4, "The Caloris Connection"). It is not likely that all domical features are recorded here, especially those smaller than 40 km. (For instance, Discovery Dome, north of Rameau below the rim of a smaller crater cut by the scarp, is not marked; see Malin, 1978).

Tectonic Features. Although tectonic features are not included in the terrain map presented here, they were mapped separately and used in the subsequent analysis (next section). Comparisons of the tectonic overlay were made to maps of Strom et al. (1975b) and Dzurisin (1977a, 1978), both of whom studied Mercury's tectonic framework in order to define its thermal, rotational, and surface histories. No distinction was made between arcuate, lobate, and linear



scarps. Lineations were also mapped, including linear crater chains, fault traces, linear segments of crater rims, the lineations within the hilly and lineated terrain, troughs, valleys, and linear ridges. The tectonic overlay was then compared with the completed and colored geologic terrain map to determine ages of scarp formation relative to crater and plains ages. Scarps which transect craters and plains offer another means to check the relative ages of these units.

A "Restricted Area" map was compiled which excluded far northern, southern, and extreme limb regions, therefore reducing any errors in plains and crater classification and measurement resulting from exaggerated terminator relief or loss of resolution and high sun angle illumination near the limb. The area of the Restricted Map, the General Map, the hilly and lineated region, and the areas designated for cratering studies were calculated from the bounding latitudes and longitudes (Appendix B). These regions are illustrated in Fig. 10.

The finished geologic map was transferred to the appropriate USGS Shaded Relief Map bases, with somewhat finer detail than possible in the photomosaic base. Plains areas were then measured using a planimeter. The area in  $\text{cm}^2$  was tallied for 5 or 10 degree latitude strips and converted to  $\text{km}^2$  using an average of the printed scale lengths of the bounding latitudes. "Exterior" and "interior" plains of all five ages were then computed and are presented and discussed further in Chapter 4. Errors in areal measurements are described in Appendix B.

## Geologic Map of Mercury's First Quadrant

### Correlation of Map Units

The map units are correlated in morphology and time of emplacement as illustrated in Fig. 11 (reproduced from the terrain map). In general, the five plains units are considered "coeval with" the youngest of the five crater units they embay. The hilly and lineated unit was formed in the late Class 3 or early Class 2 period, possibly by seismic activity generated by the Caloris impact, which also occurred between the Class 2 and Class 3 periods (McCauley et al., 1978). The "system name" is derived from this hypothesized link. Craters and plains of Classes 1 and 2 are "Post Caloris" features, while those of Classes 4 and 5 are "Pre-Caloris" features; the Class 3 units, although they are mostly pre-Caloris in age, are designated the "Caloris" features.

The temporal formation of other landforms overlaps this dating scheme. Dome materials range in apparent age from very old Class 4, pre-Caloris ages, to fairly young Class 2, post-Caloris age. Buried craters have indeterminate ages; they are at least as old as the surface which covers them. Rimless depressions may be younger than the material in which they appear, especially if the feature formed by collapse without subsequent resurfacing. Vague circular depressions often underlie the P5 surface, and are designated C5', implying ages equal to or greater than C5. These craters must have formed on an even older surface, as also noted by Malin (1976b).

PERSPECTIVE PROJECTION  
 SCALE 1: 7,700,000

CORRELATION OF MAP UNITS

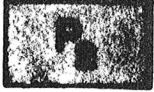

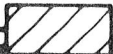

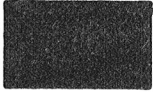

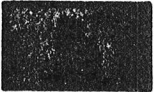
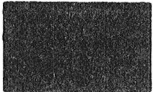

PLAINS MATERIALS	CRATER MATERIALS	OTHER UNITS	"SYSTEM" NAME
<div style="border: 1px solid black; padding: 5px; text-align: center;">P<sub>1</sub></div> 	<div style="border: 1px solid black; padding: 5px; text-align: center;">C<sub>1</sub></div> 	Hilly and Lineated 	POST CALORIS
			
		Dome Mat. Circular Depressions 	PRE CALORIS

Fig. 11. Correlation of Map Units from the Geologic Map

Circular depressions are the C5' units; dome materials are denoted by heavy diagonal lines where queried. Age of the Caloris event has been independently determined to be the same age as that of the hilly and lineated terrain (McCauley et al., 1978; see text).

Ages of tectonic features are described in a later section.

#### Material Units

Crater Materials. Crater materials are divided into five formal degradation classes (C1-C5) and one informal class (C5'), as described in the preceding section. Figs. 12 and 13 illustrate the type areas for the C1 through C5' structures. The materials mapped (i.e. rim and floor materials) depend somewhat on size and position, in that the map detail for 40 km structures (especially near the limb) is necessarily less than for larger structures nearer the terminator.

Many materials comprise the freshly formed crater. These include the central peak, floor, wall, rim crest, exterior rim, continuous and discontinuous ejecta facies. Central peak-type materials are not mapped unless they form basin rings. They are therefore included in the appropriate class of crater material. Floor materials usually are mapped as plains; impact melts form plains coeval with the crater. The remaining landforms, except for the discontinuous ejecta facies, are included as crater materials. These materials and morphologic features are now discussed.

Very fresh and/or rayed craters have crisply defined rims and interior forms (central peaks or peak rings, and terraces), with very few to no superposed craters greater than about 10 km diameter. The rim crest materials are usually circular in plan, sharp, and continuous; however, a sharp but discontinuous rim is noted for Hitomaro

(Fig. 12b), and a polygonal plan following the local lineament direction is noted for Kuiper (Fig. 78). Central peak materials vary with crater size, and begin to appear in craters as small as 10 km (Cintala, Wood and Head, 1977). Peaks are sometimes angular or linear in plan; craters of 70 to 140 km diameter often have circular arrays of hills or hummocks, grading to incomplete peak rims with larger size (as described below).

A continuous, thick blanket of material, radially ridged to hummocky with dunes, extends from the rim crest to 1/2 to 1 radii beyond the rim. Some rayed craters have unusually large, continuous and smooth blankets of material, extending 2 to 4 diameters from the primary's rim. The slope of the continuous deposit is concave to linear from the rim crest to the surrounding surface; fresh craters on basin floors appear to have conical deposits when viewed in stereo. Relief of the continuous deposit varies with the underlying topography; the above examples occur on smoother surfaces. Continuous deposits are hummocky in the hilly and lineated area; they are lobate and extended when they fall within a larger basin (where the crater is superposed on the rim of a larger crater or basin). The edge of the deposit forms a distinct toe, similar to that of a landslide, extending a full radii or more onto the depression's floor.

Discontinuous deposits--linear troughs, or chains of satellite craters--extend downrange a maximum of 3 to 5 radii from the

Fig. 12. Crater Degradation Classes C1, C2, and C4

- a. C2 crater Mahler at top left (M). Secondaries of C1 Hitomaro (Fig. 12b) crater Mahler's floor. Secondaries from Mahler crater the floors and rims of the C4 craters Kenko (K; 90 km in diameter) and Balagtas (B; 100 km in diameter) to the east. Secondaries from the C3 basin to the north superpose the C4 craters' rims, but not their floor materials, indicating that the latter are P3 in age. The crater at lower center is C5 in age.

FDS 27427. North at top.

- b. C2 crater Hitomaro, 105 km diameter, contains the type area P1 plains. Note that very few craters superpose either the plains or Hitomaro's sharp, but discontinuous rim. The larger basin surrounding Hitomaro is C3 age; its peak ring has been largely destroyed by Hitomaro and its secondaries. Arrows mark the double ring structure noted by De Hon (1976).

FDS 27430. North at top. This area lies immediately north of region shown in Fig. 12a.

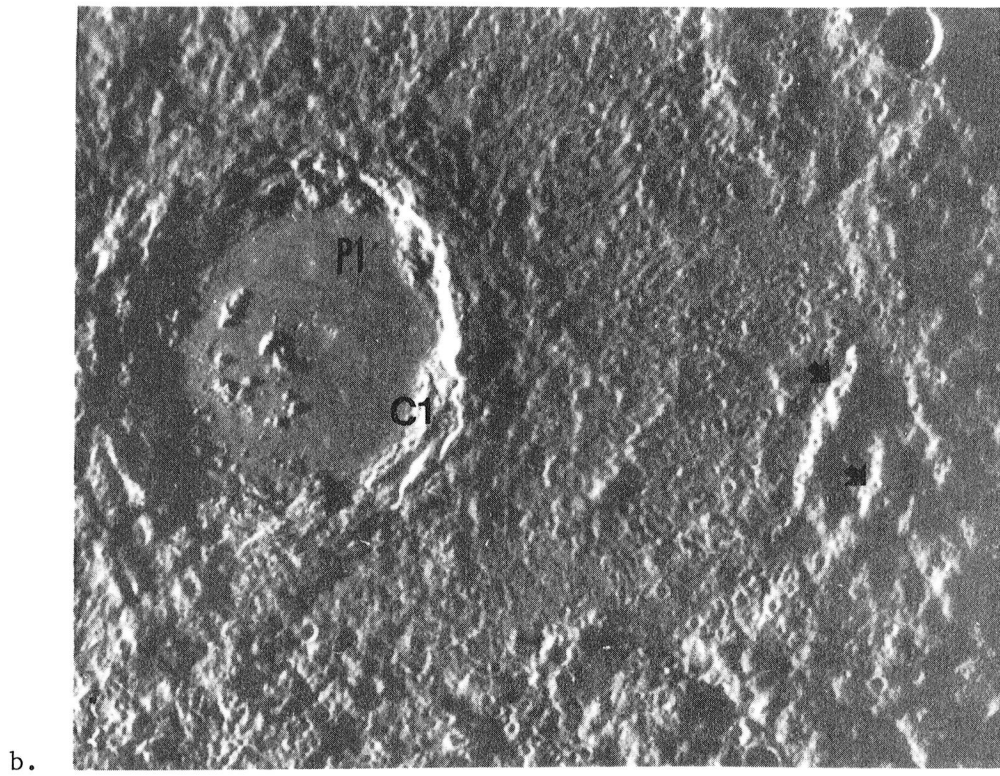
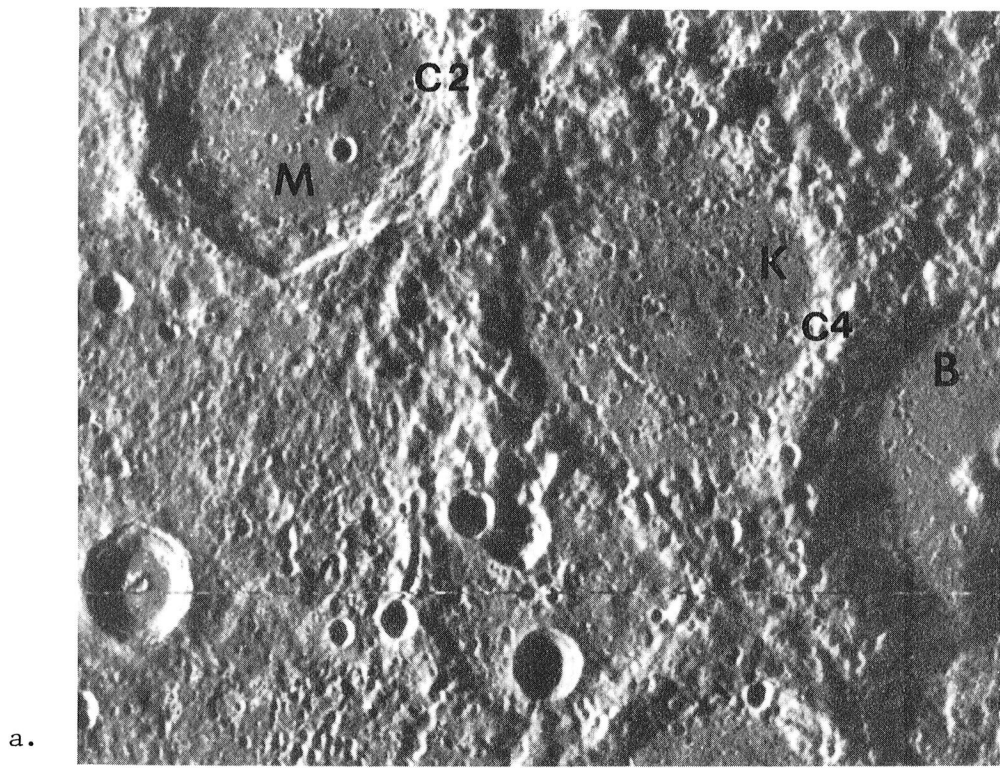


Fig. 13. Crater Degradation Classes C3 and C5'

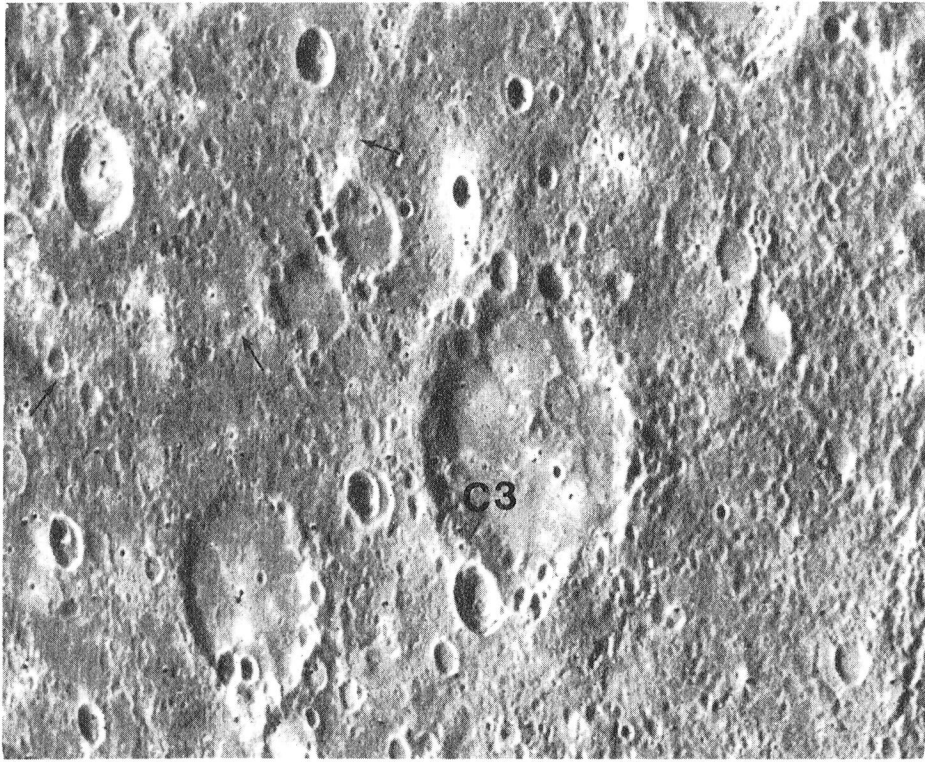
- a. C3 craters, 60 and 93 km in diameter, lie west of Ibsen in P4 intercrater plains. Rims are subdued and cratered. Large C5' basin to the northwest (top left, arrows) has scarp-like rims which align with the global lineament directions.

FDS 27425. North at top.

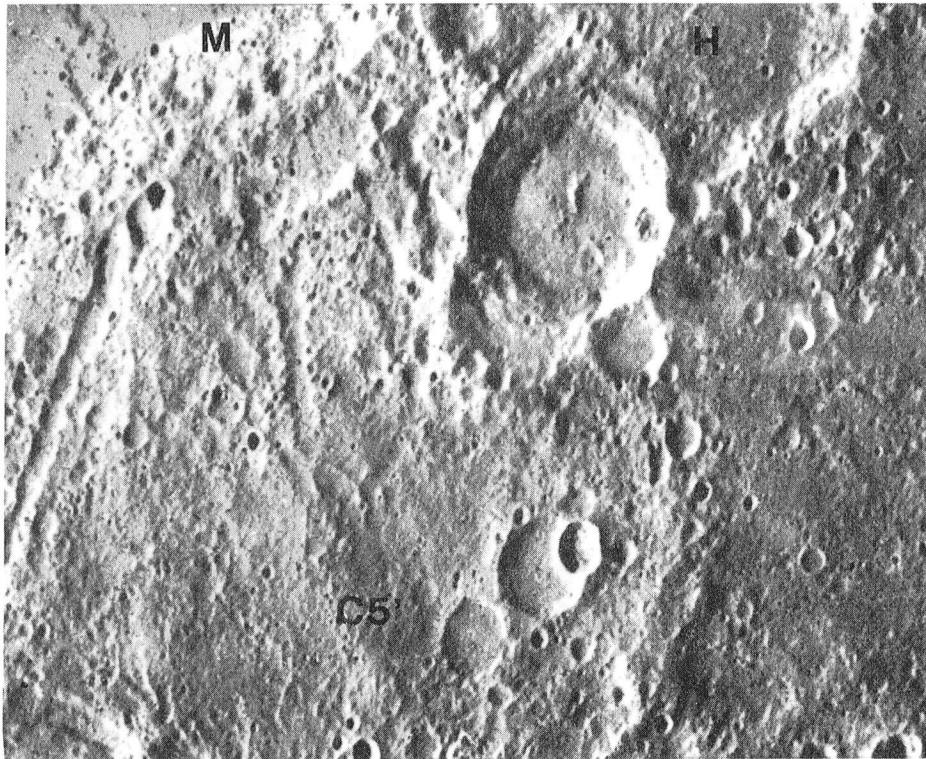
- b. C5' craters of about 50 km and 100 km in diameter lie south of Murasaki (M) and Hiroshige (H). Rims are highly subdued and buried by intercrater plains and ejecta of the larger craters. This area best illustrates a possible example of ballistically emplaced plains.

FDS 27432. North at top.





a.



b.

primary crater's center. The satellitic craters are less subdued at greater ranges and have greater depth/diameter ratios (Mouginis-Mark, 1978). They often extend inward and superpose the continuous deposits or the crater rim. Further description of this material is given in the secondary cratering section of the next chapter.

Morphologic data for fresh mercurian craters indicates that their depths (d) vary with diameter D as follows: for  $D \leq 9.8$  km,  $d = 0.176 D^{0.98}$  and for  $D \geq 9.8$  km, depth  $d = 0.91 D^{0.26}$  (Malin and Dzurisin, 1977). The width of the continuous deposits has been noted earlier. Other morphologic data (floor width, rim width, rim height, swirl features, terrace onset, slump onset, and frequency of these features) are found in Gault et al. (1975), Wood and Head (1976), Malin and Dzurisin (1977, 1978), Smith (1976), Smith and Hartnell (1978), Cintala et al. (1977), and others.

The fresh (C1) features are interpreted as young impact craters surrounded by ballistically emplaced ejecta deposits. Rayed craters are the youngest examples. The continuous blanket of material about the rim is interpreted as ballistically emplaced ejecta followed by a debris surge (Oberbeck, 1975); the discontinuous material is ejected at higher angles to the horizontal and greater velocities, thus landing at greater ranges from the ejection site (Shoemaker, 1962). Some high angle material is expected to fall close to the rim of the crater, producing craters on top of the continuous ejecta blanket or cutting the rim.

Central peak materials are interpreted to be local rock uplifted by seismic rebound, or toes of slump blocks from the crater walls. Peak ring origin is still controversial; see Hale and Head (1979a,b) and Hale (1979). Fresh, but non-rayed craters might have undergone some modifications of rim, walls, and floor due to slumping, mass wasting associated with smaller bombardments and tectonism, and volcanism at a late stage in Mercury's history, during which molten materials were extruded through fractures beneath the crater floor.

"Shadowing" of ejecta deposits of ray craters suggests very low angle ejection (although the "shadows" may be confused with dark ejecta, Schultz, 1976c). Rayed craters are obviously very high energy impacts, with consequently greater distributions of ejecta deposits. Cintala (1979a,b) suggests that the high energy impacts have shallow depths of burst, with lower ejection angles and greater ranges. The resulting crater may be shallower.

The fresh crater's morphologic characteristics are modified as the crater ages, as discussed in the preceding section. The type-craters illustrate the increasing degrees of shallowing, rim degradation, loss of crispness in terraces and central peaks, and embayment by surrounding plains deposits. Basin-size craters are subject to isostatic equilibration of the rim and basin floor. Convex, lobate aprons of material extend from the rims and rings of older basins onto the adjacent floor materials; a greater amount of such material is noted when the adjacent floor is deeper.

These features are in part the result of slumping and mass wasting. The width of the exterior basin or crater rim not only varies with size as noted above, but also with age, the elevation of surrounding terrain, and processes affecting the surrounding plains (subsidence, infilling). The oldest, most indistinct structures, designated the Vague Circular Depressions (C5'), are often filled with smoother materials (see also Fig. 85).

Some large, fresh craters (from 70 to 140 km) have an inner ring of peaks, hills, or hummocks interpreted to be the incipient peak ring of craters of sizes intermediate between simple central peak craters and double ring basins. Material between the hills and crater wall is often rougher, radially or concentrically ridged, and may have a higher crater density (as can be noted in Figs. 14 and 15). It is termed a "peak ring plateau" because it is raised above the region interior to the incipient peak ring. The interior depression is surrounded by an inward facing scarp which drops from the plateau level usually just inside the hilly area. A central peak is often present, sometimes located off center within the depression (Fig. 15a). The smoother materials which occupy this area are usually flat lying, but sometimes concave upward at the scarp face, and at the base of the central peak. The peak ring of Brunelleschi (Fig. 15a) lies acentrically inside the scarp and smooth material covers the entire crater floor. The depth of the inner depression decreases with the extent of

the smooth material (Fig. 14b), especially when the latter extends into the higher plateau area. (That is, the height difference between plateau and depression decreases.) The peak ring and inward facing scarp vary from 0.3 to 0.5 times the rim diameter, as shown in Table 5.

Significance of this morphology is (1) P1 or P2 material interior to craters may have two distinct facies, hummocky or smooth, depending on crater size and possibly underlying topography, (2) intermediate size craters may fill with plains material from within, either by extrusion of volcanic material into the deeper central depression of the crater, or by mass wasting of material off the steeper slopes of the central peak and inner scarp wall, and (3) plateau material may be older, while the inner material may be continually resurfaced. An extreme example of this morphology is the basin Homer, 320 km diameter, C4 age, with a plateau of P4 material 1 km below the rim (Zohar and Goldstein, 1974) and an inner depression (about 2-3 km depth) filled with material of P3 age.

Table 5 below lists the fresh transition-size craters with the typical morphologies described above.

Fig. 14. Fresh Crater "Transition Morphologies," C2

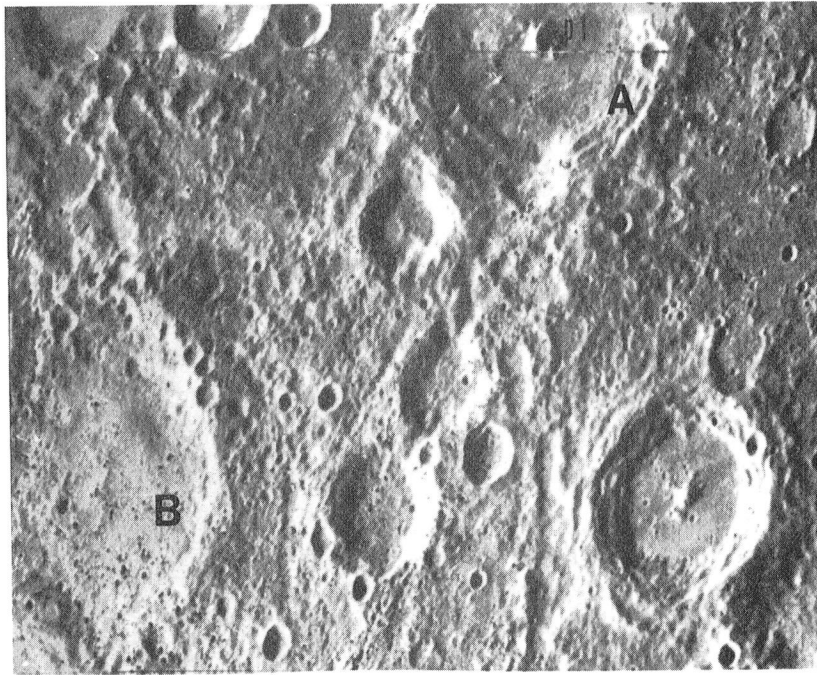
- a. C2 crater, about 100 km diameter at top center of photo (A). Smooth plains (P1) surround a central peak but lie in a depressed region of roughly circular plan, surrounded by a plateau of hummocky P2 plains which are faintly radially striated. Hills at the inner scarp edge may form an "incipient peak ring."

Secondaries from Kuiper, to the southwest, crater the floor of the C2 crater and Byron (B). The rim of a large C5 crater lies immediately west of the crater A. Fig. 43 is a high resolution image of this transition morphology crater.

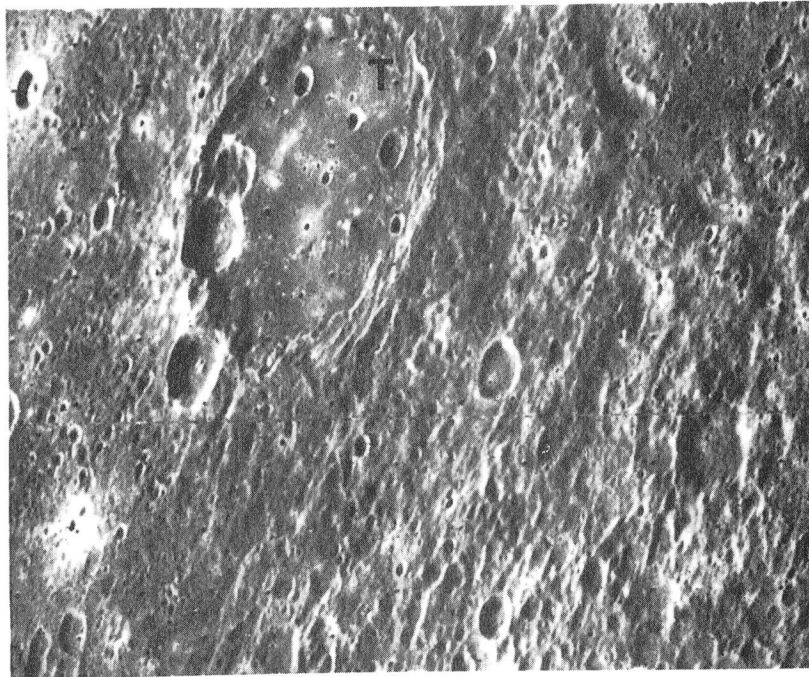
FDS 27436. North at top.

- b. Titian, a C2 crater of 115 km diameter. Its inner peak ring is flanked by a plateau of slightly hummocky material and an inner area (slightly depressed in radar cross section, Zohar and Goldstein, 1974) of smooth plains. Note its distinct ejecta blanket; just north of this area, the ejecta blanket appears to have finger-like lobes.

FDS 27437. North at top.



a.



b.

Fig. 15. Fresh Crater "Transition Morphologies," C2 and C3

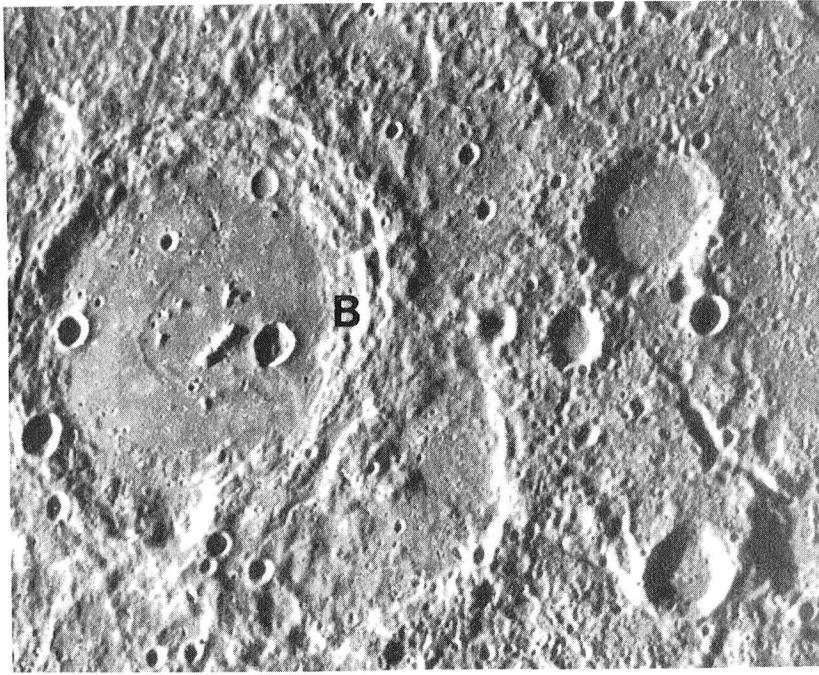
- a. Brunneleschi, a C3 crater, 140 km in diameter, lies at left center. The entire crater floor is flooded with smooth material, including a broad plateau surrounding an interior facing scarp and shallow inner depression. The plateau scarp is cut by an off-center peak ring. Floor materials partly inundate slumped debris from the walls of the southern inner rim. Brunneleschi is at the larger extreme of the 70 km to 140 km size range of craters in "transition" from central peak crater morphology to peak ring basin morphology.

FDS 27435. North at top.

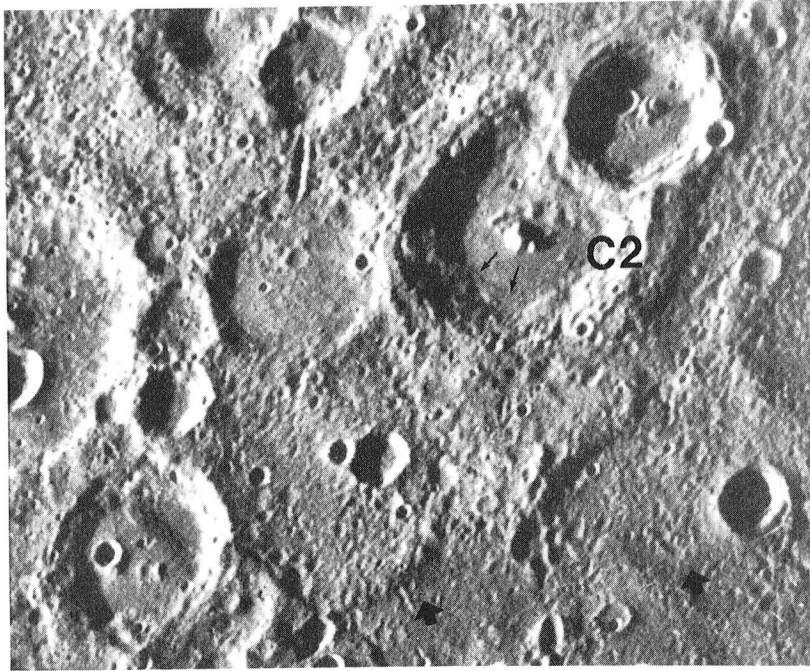
- b. Unnamed C2 crater southwest of Donne occurs near the center of photo. Smooth plains surround the central peak within a shallow depression. The rugged scarp encircling the peak may be part of the wall materials; small arrows trace the scarp. A similar morphology is noted in Donne. Smooth P2 and P3 plains embay the depression at lower right (thick arrows); some of the plains appear to be limited by the broad ridges.

FDS 27438. North at top. The unnamed crater is about 75 km in diameter.





a.



b.

Table 5: Transition Size Craters

Location (lat.° long.° )	Crater Name	Class	Diameter (D ) km	Inner Scarp Diameter	Outer/Inner Material #	Peak Material *
(-9.5,34)	(South of Byron)	C2	61	25	P2	cp,sc
(76,103)	(South of Bach)	C3	68-70	25-29?	P2	cp,sc
(-70.5,69.5)	Camoës	C2	70	28	P2	sc,cp
(1.0,17)	(SW of Donne)	C2	71-90	43	P1	cp,sc
(11,21)	Asvaghosa	C1	80	35	P1/P1	cp,pr
(-19,31)	(east of Imhotep)	C2	84	(28)	P2	cp,sc
(5,25)	"dome" crater	C3	85	27	P3/P2	h = pr
(3,14)	Donne	C1	90	41	P1	sc,cp,sc
(0.5,23.5)	Lu Hsun	C2	95	40	P2/P1	cp,h=sc
(-76,135)	Van Gogh (?)	C2	95	34	P2	cp,pr
(-5,29)	(North of Kuiper)	C2	97	31	P2/P1	cp,h=sc
(-16,16)	Hitomaro	C1	105	(45)	P1	cp,pr
(-3,42.5)	Titian	C2	115	50 (25?)	P1	pr
(23.5,22.5)	Ts'ai Wen-chi	C1	120	60	P1/P1	h,cp
(-8.5,22.5)	Brunelleschi	C3	140	46	P1	cp,h,sc
(-79.5,136)	Bernini	C3	145	45	P3	pr,cp,r
(4,34)	Handel	C2	150	65-70	P2	pr

\* Peak Material:

cp = central peak

h = hills

sc = inner scarp

pr = peak ring

r = ridge

P1/P1 = hummocky and smooth P1 material in outer/inner floor of crater

P2/P1 = material of outer/inner floor

# Diameter of named craters from Atlas of Mercury, Davies et al. (1978).

Plains Materials. Type areas for the five plains units are illustrated in Fig. 12 (P1), Fig. 16 (P2), Fig. 17 (P3), and Fig. 18 (P4 and P5). The plains units within the hilly and lineated region are shown in Fig. 19. As can be seen in these figures, plains morphologies vary extensively across the first quadrant of Mercury.

As classified here on the basis of age relative to degradational class of included or superposed craters, different morphologies are exhibited by the same age of plains material.

Geologic mapping established that the intercrater plains defined by Trask and Guest (1975) actually differ in relative age, comprising the P3 through P5 units (Fig. 17,18). The oldest plains are the most extensive. The P5 material is heavily cratered, hummocky, pitted by secondaries of C4 and C5 basins, and sometimes subdued when located outside of large, young craters. It often occupies higher elevations than younger plains units, but also buries, and follows the topographic contours of, the vague shallow circular depressions (C5'). Superposed craters include a wide spectrum of sizes, with 5-15 km diameters the most common at moderate resolutions. Pockets of smooth material lie within depressions in the plains units, often filling the superposed craters. Slightly younger intercrater material has a reduced size spectrum of superposed craters, although densities are just as high, as shown in Chapter 3. P4 plains are leveler than the P5 materials, and sometimes continuous with ejecta blanket facies of C4 craters. P4 material is also elevated above younger plains units.

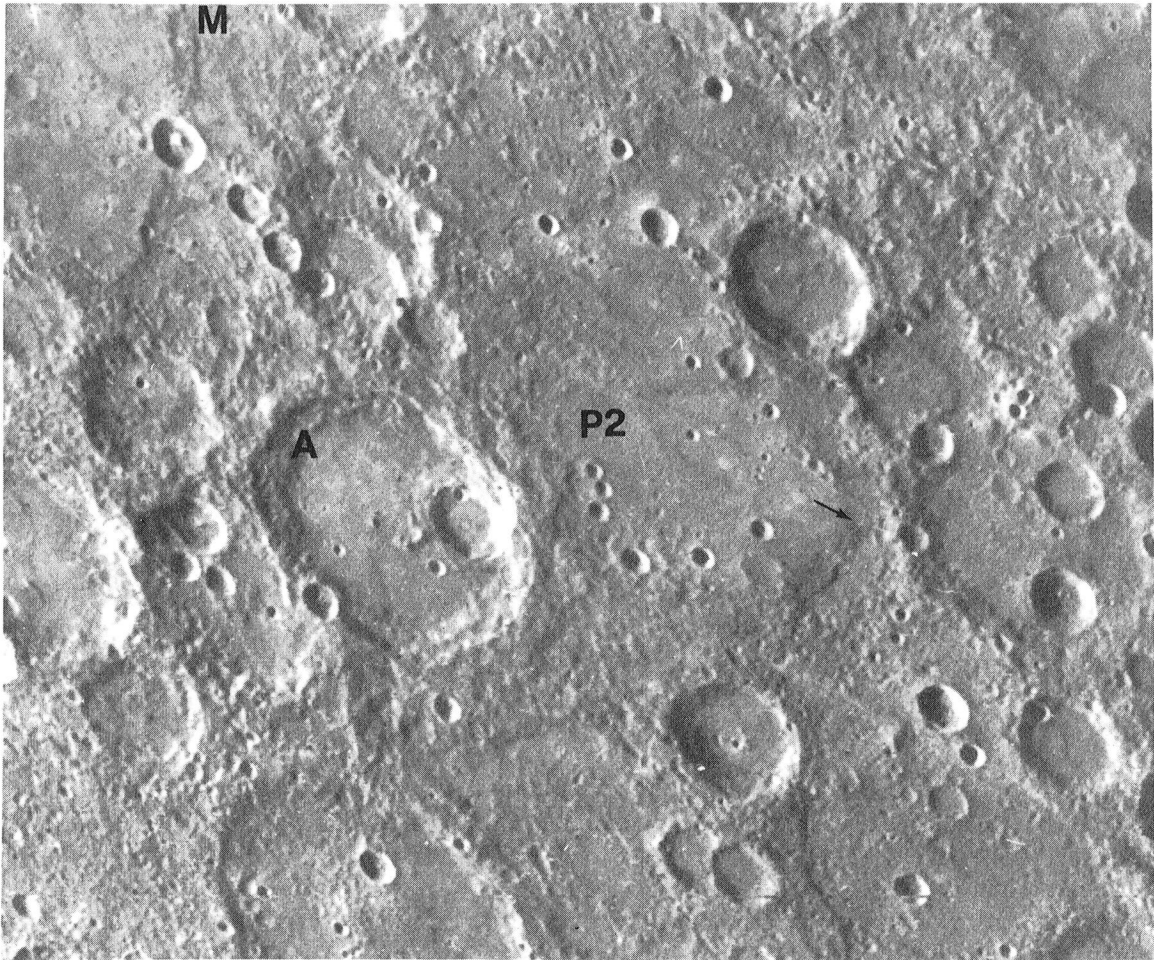


Fig. 16. P2 Plains Materials in Andal Area

P2 plains materials embay the interior of Andal (A) and its ejecta blanket to the east. Buried craters of various sizes can be detected beneath P2 and P3 materials.

Note the scarps in the area: west of Andal, a fresh C1 crater superposes Mirni Rupes (M; top left); to the east, P2 plains embay the northern end of Discovery Rupes. Such superposition relationships are used to constrain the ages of scarp formation.

FDS 27386. North at top. Andal is 90 km in diameter.

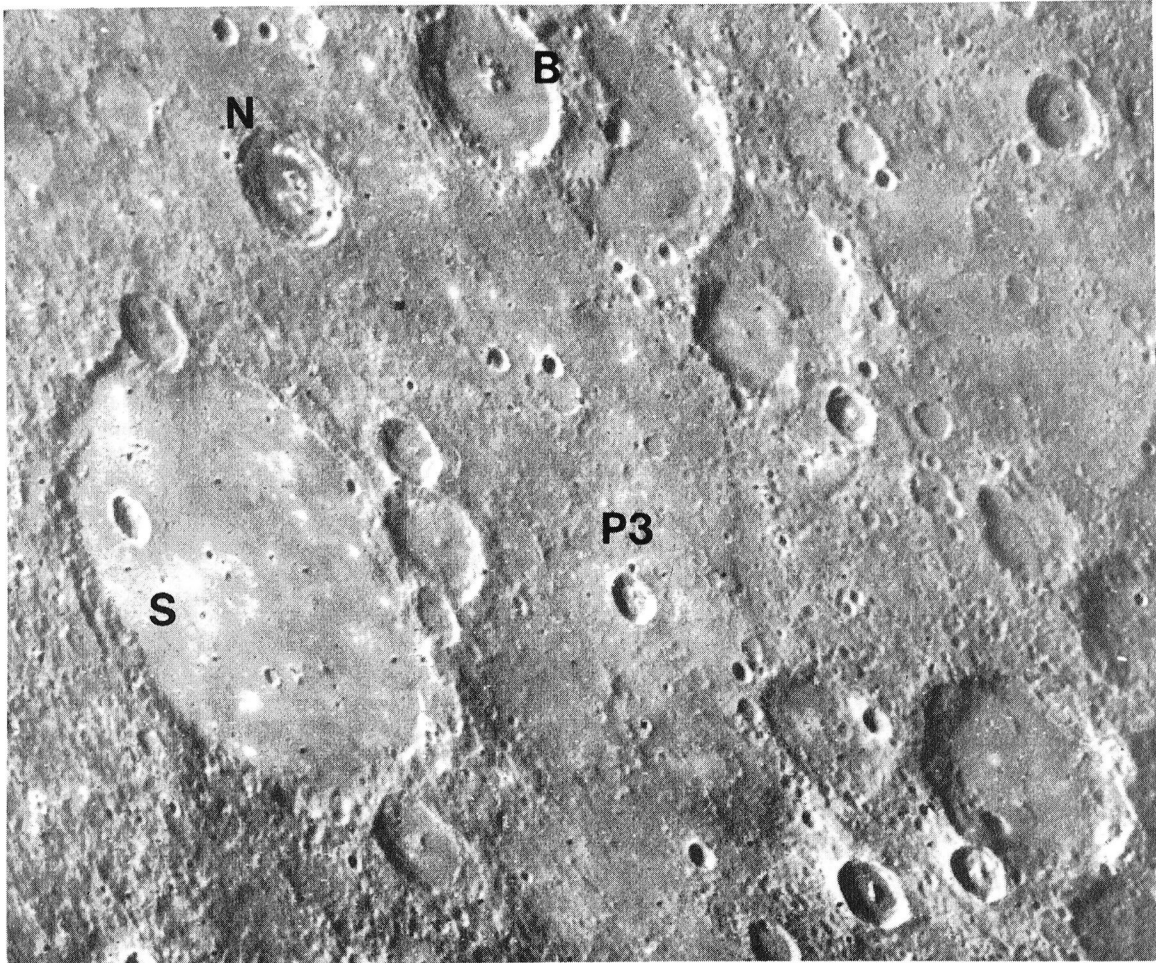


Fig. 17. P3 Plains Materials in Schubert Area

P3 plains east of Schubert (S), a C3 basin 160 km in diameter, overlie its ejecta sculpturing and may embay a large ancient depression noted by Malin (1976b). The P3 materials may overlie some ballistically emplaced debris from Schubert. P2 plains lie within Schubert; P4 plains occur on a plateau to the east and are overlain by Schubert's secondaries to the west.

Note the morphology of rim deposits and ejecta facies of the crater at top center (B). The shelf with the lobate toe may be characteristic of all crater rims formed by impacts onto the rims of pre-existing craters. Rim destruction may involve landslides as well as ejecta deposition. Nampeyo (N; 40 km diameter) has dark floor deposits.

FDS 27387. North at top.

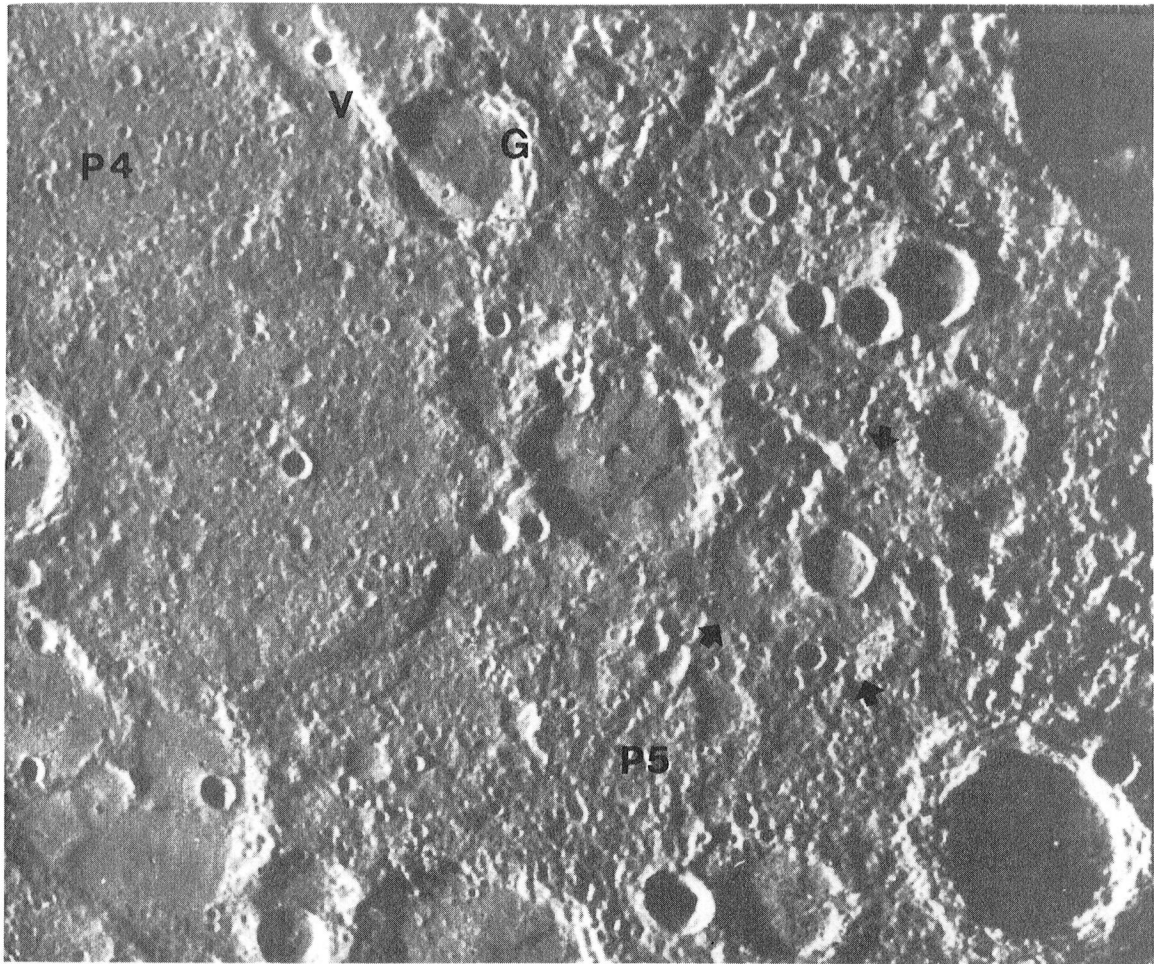


Fig. 18. P4 and P5 Materials in Vostok Rupes Area

P4 plains west of Vostok Rupes (V) are level but heavily cratered; P5 materials to the south are more heavily cratered. Highly degraded crateriforms (arrows) occur near the border of the hilly and linedated terrain. The crater Guido d' Arezzo (G; 50 km in diameter) is laterally offset by Vostok Rupes, and is shortened perpendicular to the strike of the scarp; this is interpreted as a 10 km westward heave of a thrust fault of estimated dip 25 to 45 degrees to the east. (See Strom et al., 1975 b.)

FDS 27381. North at top. Rilke, lower right corner, is 70 km in diameter.

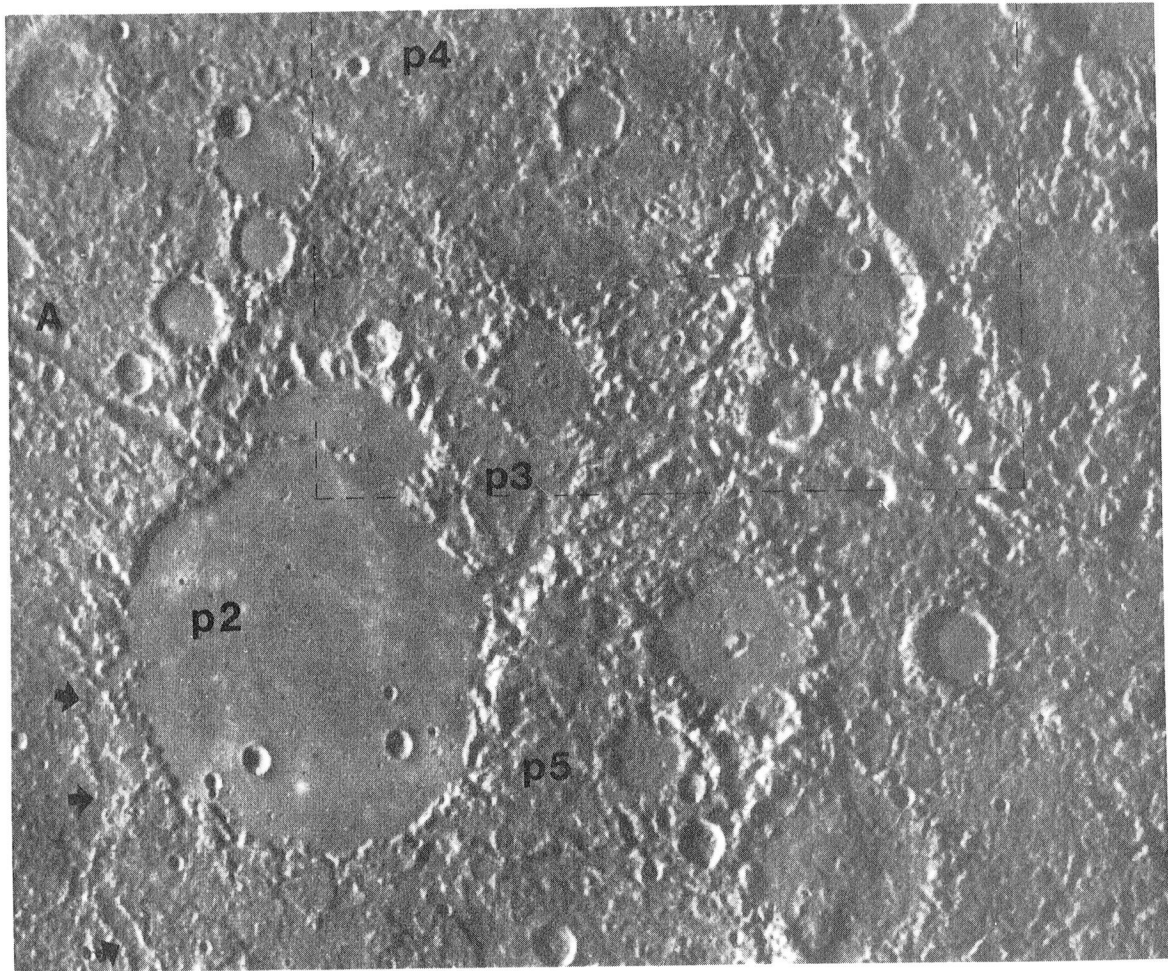


Fig. 19. Plains Materials of Hilly and Lineated Area

Larger crater in left center is Petrarch, 160 km in diameter, C4 in age. P2 plains in Petrarch were emplaced after the event which disrupted its rim and wall materials. Hummocky P3 plains are interpreted to be older materials emplaced prior to the disruption event. Hills and rim segments of this region are 0.1 to 1.8 km in height and 10 km in width (see Trask and Guest, 1975).

Radial valleys to the northwest (Arecibo, A) and northeast of Petrarch are filled with deposits mass-wasted from the walls, but embayed only slightly by materials from the P2 plains in the large craters. A sinuous valley of unknown origin extends from Petrarch to the south (arrows).

FDS 27370. North at top. Outlined area denotes the boundaries of FDS 27423, illustrated in Fig. 90.

Morphologic and albedo variations within the intercrater plains P5 and P4 are less marked than between younger units. This is, in part, due to the homogenizing process of continued impacts. Apparent albedo variations in P5 material may be spurious and result from changing illumination angle. The added roughness from secondary craters of young basins and craters may obscure the ancient features of P5 materials. Some materials mapped here as P5 plains (as around Rodin, Fig. 21) are mapped elsewhere as young, rough terra (See DeHon, Scott, and Underwood, 1980; DeHon, Underwood, Scott, 1977). (Note that albedo variations did not necessarily dictate placement of geologic units or contacts.)

Younger plains units have two basic morphologies which apparently depend on the thickness of the deposit relative to the relief of the underlying surface. These units appear "smooth," gently rolling to level, when the underlying surface is smooth or highly subdued, or when the deposit itself is thick (Fig. 16). The second type of unit appears rougher and discontinuous when overlying hummocky and ridged topography (Fig. 85). The smoother deposits occur in crater and basin interiors and irregular depressions; the latter occur in ancient C5' basins, and regions scoured by basin secondaries. P3 plains material may have a third morphology if the thicker and more massive deposits are divided into cratered and less cratered units, as, for example, in the Santa Maria Rupes area (Fig. 20) and the Bach regions (Fig. 26) respectively.



The plains units P5, P4, and Santa Maria Rupes-type P3 comprise the intercrater plains described by Trask and Guest. As mapped, and illustrated in Fig. 80 (Chapter 4), P4 plains appear to embay Chekov (C4) and a C5 crater nearby. P3 plains embay the ejecta blanket of Schubert (C3) (Fig. 17), Ma Chih-Yuan (C4) (Fig. 84), and completely bury 30 to 60 km craters in the Victoria Quadrangle. P5 plains appear to bury C5' and some C5 units, although the extent of the rim degradation makes this relative age uncertain. The C5' structures must overlie an even older unit. Thus the intercrater plains span a range of relative ages, but are not primordial.

P2 materials are found most often as smooth plains interior to C2 craters or older crateriforms. Less often P2 plains fill regions exterior to craters in a thick smooth blanket (as outside of Andal, Fig. 16) or thinner deposits in multiple depressions outside of younger craters (as outside of Handel, Fig. 85). P2 materials embay some arcuate scarps. P1 materials predominantly occur in C1 craters (Fig. 12b) but also are identified in inner depressions of fresh, transition-size craters (Fig. 14a) and possibly on top of a dome-like crater rim (Fig. 80). P1 materials may comprise the bright halo deposits of rayed craters which extend two to four diameters from the primary's rim. Ray material may instead be emplaced on smooth P1 deposits.

The different morphologies may signify different origins, namely: ballistically emplaced deposits in shallow, discontinuous depressions in a field of secondary craters; impact melt interior to craters of the same age; or volcanic flooding of older craters and deeply depressed regions within older intercrater plains. Underlying topography may appear as gentle swells and ridges, or as "islands" of rim remnants in an otherwise level surface. Depressions and ridges may be preserved by viscous flow; level plains may be formed by ballistic deposits, often accompanied by seismic events or continued redistribution by small craters. Although few of the older plains materials remain as "impact melts" within the C4 and C5' craters, they may be interpreted as above, as volcanic or ballistic deposits. Embayment relationships, their widespread distribution, and association with tentative volcanic landforms described below favor a volcanic origin.

Other Materials. Other material units include buried craters, the ancient circular depressions (a type of buried crater?), rimless depressions, and dome materials. Craters are buried by P5 through P2 units (Fig. 20), and occasionally completely inundated under the continuous ejecta blankets of larger basins. The C5' structures are commonly buried by P5 and P4 materials, but Malin (1976b) suggests that simple degradation of these crateriforms may produce the intercrater plains material (see Fig. 85). Rimless depressions are found in crater floors and usually associated with tectonic features (scarps,

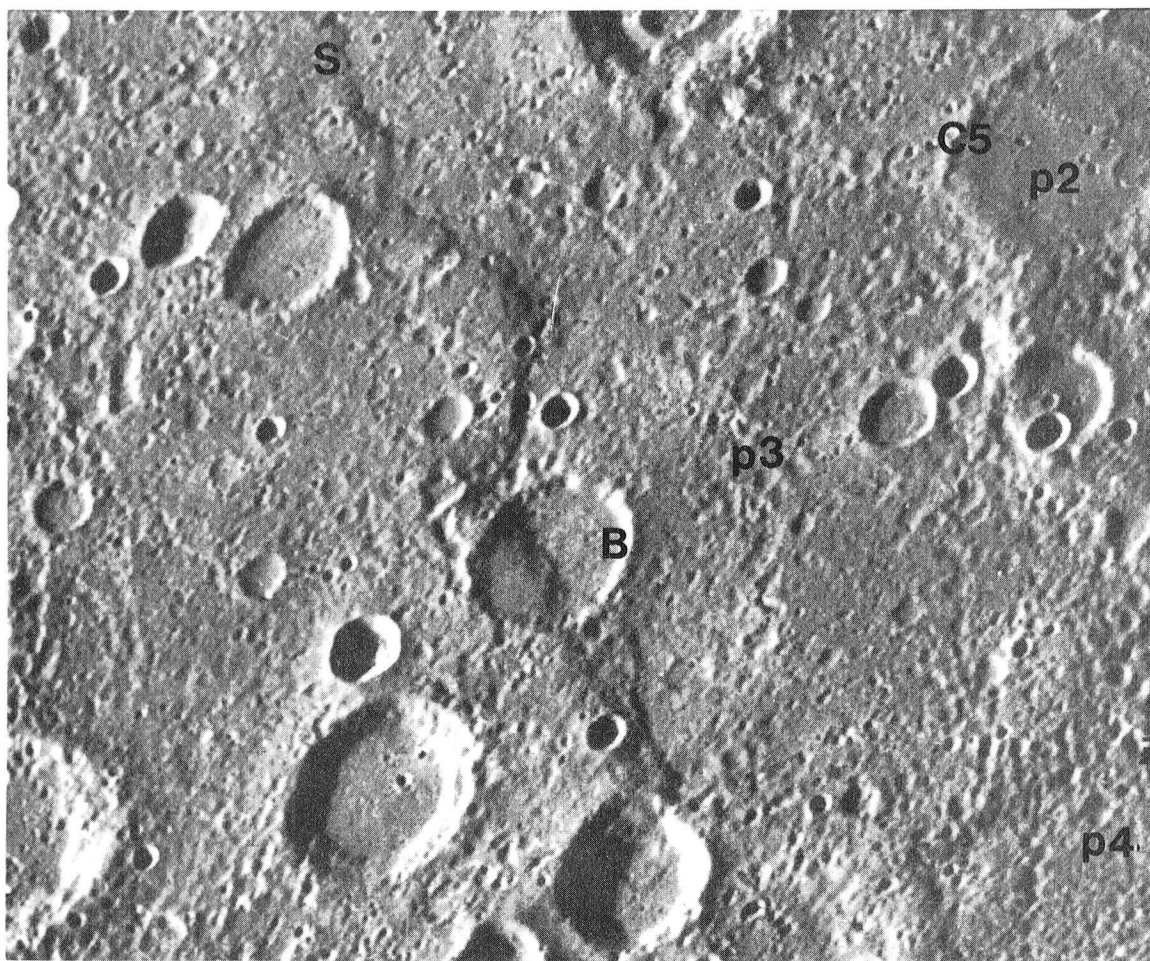


Fig. 20. Santa Maria Rupes Area--Buried Crater at Upper Right

Different classes of craters and plains are shown here in the region of Santa Maria Rupes (S). Smooth P2 plains fill and bury part of the rim of a 46 km crater (C5) at top right of the frame. P3 plains in the central region are surrounded by hummocky P4 materials. Note the abundance of irregular, breached craters aligned in chains or clusters. The scarp transects C3 and C4 craters and appears to be overlain by a small C2 crater at its southern end; its age is thus Class 2 or late Class 3. P2 plains in the C4 crater at the center of the picture may have been deposited on a level surface prior to the scarp forming event.

FDS 27448. North at top. Crater B is approximately 30 km in diameter.

ridges, or faults), and interpreted to be collapse pits (Fig. 21). Volcanic features usually occur in the vicinity. Domes appear rounded, convex-up to plateau-like; Malin identifies a conical feature in H-12 quadrangle (Malin, 1978). Heavily cratered domes, of class 3 or 4 in age, are pitted (Figs. 22-24) but sometimes surrounded by low albedo, smoother materials (Fig. 23a). One group of older domes is aligned north-south (Fig. 89). Dome materials are, in most cases, interpreted to be volcanic and mark the closing of a vent source. Ridges like Mirni Rupes may be closed fissure vents (Fig. 27; see Dzurisin, 1978).

### Structure

The tectonic fabric of Mercury's first quadrant has been described by Strom et al. (1975b), Cordell (1977) and Dzurisin (1977a). Definition and descriptions of these features are adapted from Dzurisin's work. Stress patterns and their interpretations are further discussed by Melosh (e.g. 1977a,b) and Melosh and Dzurisin (e.g. 1978).

Structures noted in this preliminary informal mapping include escarpments (or "scarps", undifferentiated by type), faults, ridges, lineaments, troughs, sinuous valleys, domes, rimless depressions, and ancient circular depressions. The last three features are discussed above. Basic characteristics, ages, and interpretations of the other structures are discussed below.

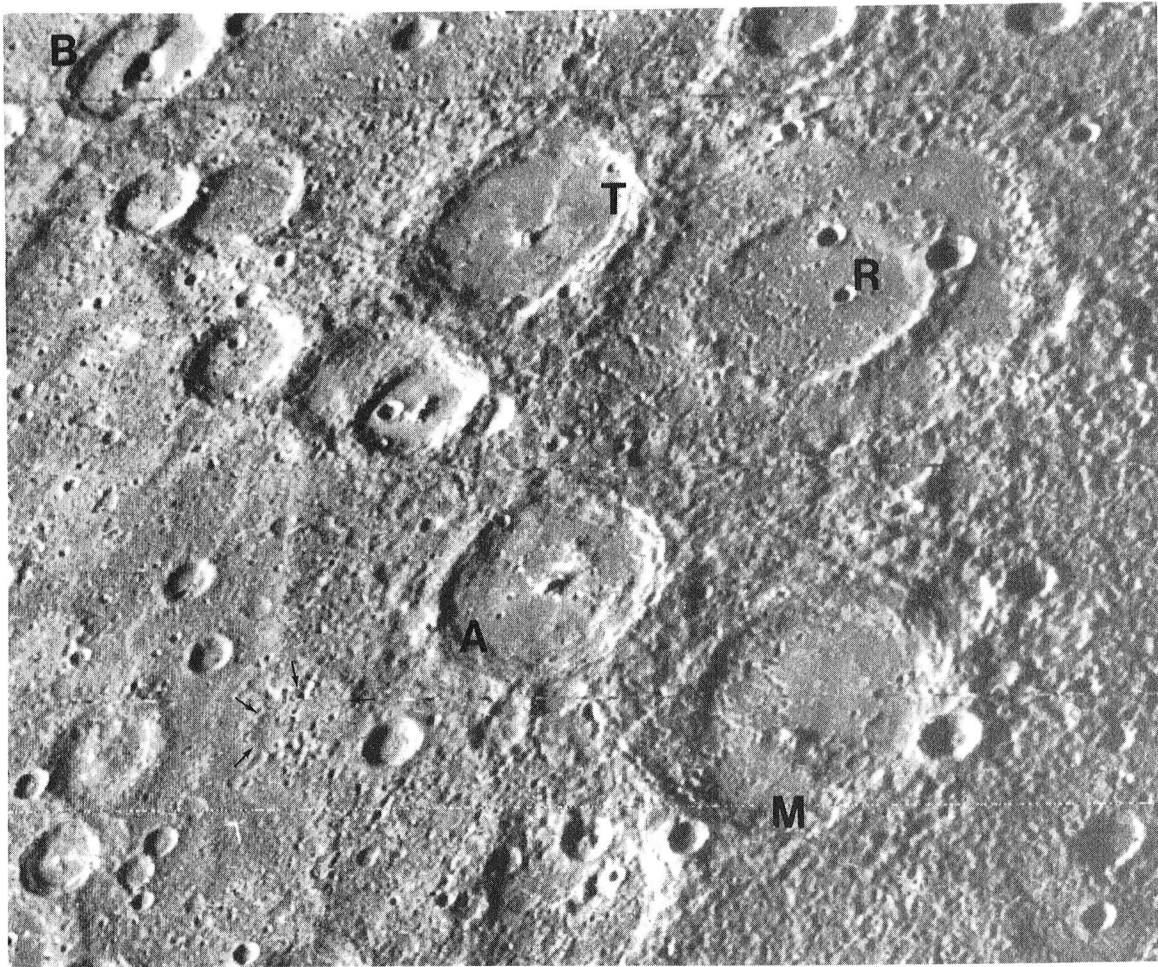


Fig. 21. Rodin Complex--High Relief Plateau of Older Plains

Rodin, a C3 basin of 250 km diameter, is superposed by Moliere (M; C3) Abu Nuwas (A; C2), and Ts'ai Wen-chi (T; C1). Part of the plateau may consist of ejecta from this cluster of craters. Buried craters are visible southwest of Ts'ai Wen-chi and west of Abu Nuwas. The latter one lies on the plateau's edge; half of its rim is embayed by the smoother P3 materials west of the plateau. Arrows denote this crater.

Note the morphology of the basin ring and rim of Rodin (R) farthest from the superposed craters; compare the lobate apron of debris to that of Ma Chih-Yuan, a C4 basin illustrated in Fig. 84.

The rimless depression in the C2 crater B at upper left is probably a collapse pit formed after plains emplacement, concurrently with the formation of the transecting ridge, Antoniadi Dorsum.

FDS 27342. North at top right. Abu Nuwas is 115 km in diameter.

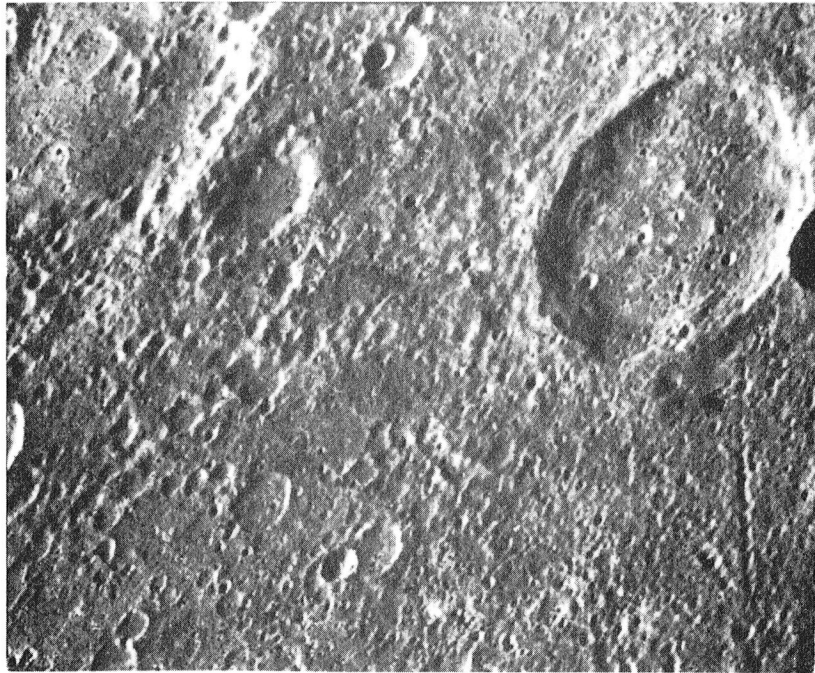
Fig. 22. Domical Feature and Contact Zone East of Handel

- a. Domical feature (thick arrow) on the south rim of this 85 km crater has a central rimless depression. Associated tectonic or mass wasting features occur as layers or terraces on the eastern dome mass, inside and outside of the crater rim. The dome sits on the intersection of the crater's rim and a linear contact zone separating two surfaces of nearly similar age (Fig. 22b). The crater chains south of the large crater are radial to Lu Hsun. The C5' structure illustrated in Fig. 85 lies to the southwest.

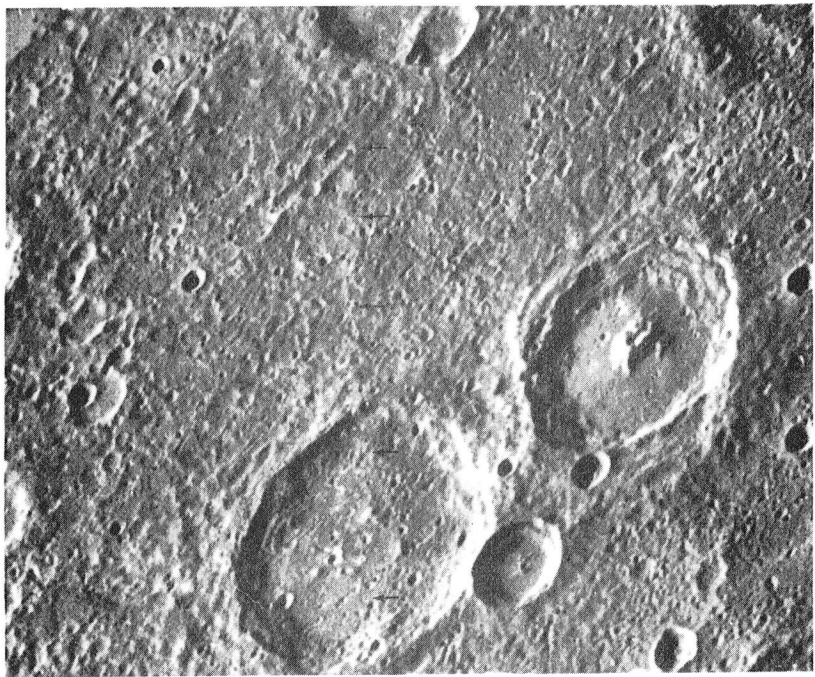
FDS 27449. North at top.

- b. Linear contact zone trending north-south cuts the 85 km crater of Fig. 22a (arrows). There is little to no height difference across this feature to support an interpretation as a fault scarp. Chains of large craters from Homer (or Handel?) appear to be terminated at the contact. The region traversed by the linear feature is the floor of an ancient circular depression centered on the C3 crater north of the C3 "dome" crater (see Fig. 24 for sketch map of area and Fig. 9, in pocket; also see Malin, 1976b).

FDS 27444. North at top. This image adjoins Fig. 22a, with (b) north of (a). A mosaic of the linear contact zone also contains images FDS 27440, 27442, 27443, 27453, and 27458.



a.



b.

Fig. 23. Domical Features on Rims of Ancient Craters

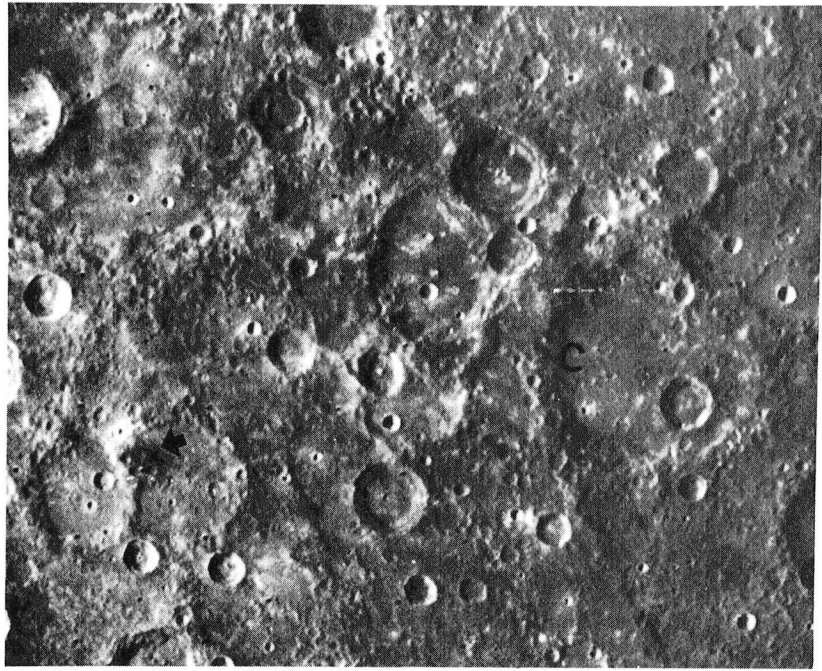
- a. Domical feature near the left center of the photograph (arrow) is located on the overlapping rims of a C4 and C5 crater. The dome material is low in albedo, highly cratered or pitted, and flanked by smooth plains within the C5 crater. The entire area is south of Bramante (C3). The C5 crater Coleridge (C) is 110 km in diameter and retains a raised rim.

FDS 166663. North at top.

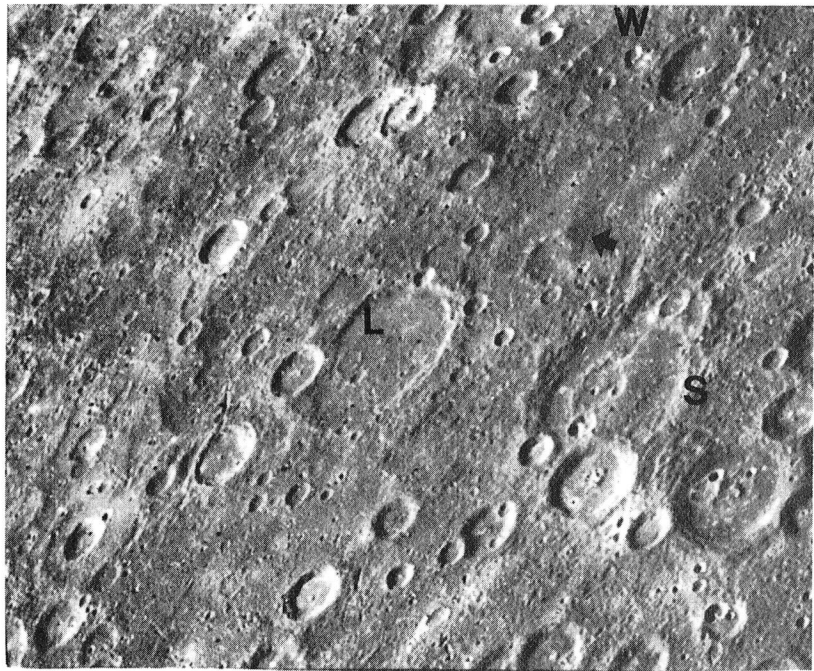
- b. Domical feature located on a crater rim (arrow) in region which may be an ancient circular depression filled with younger plains. Wren basin (W; 215 km in diameter) can be seen at top center. Li Po (L; 120 km diameter) lies in the center of the image; Sinan, 140 km diameter (according to the Atlas, Davies et al., 1978), lies just east of Li Po. The latter is C4 in age; Sinan is C3. Wren is a C4 basin.

FDS 27343. North at top.





a.



b.

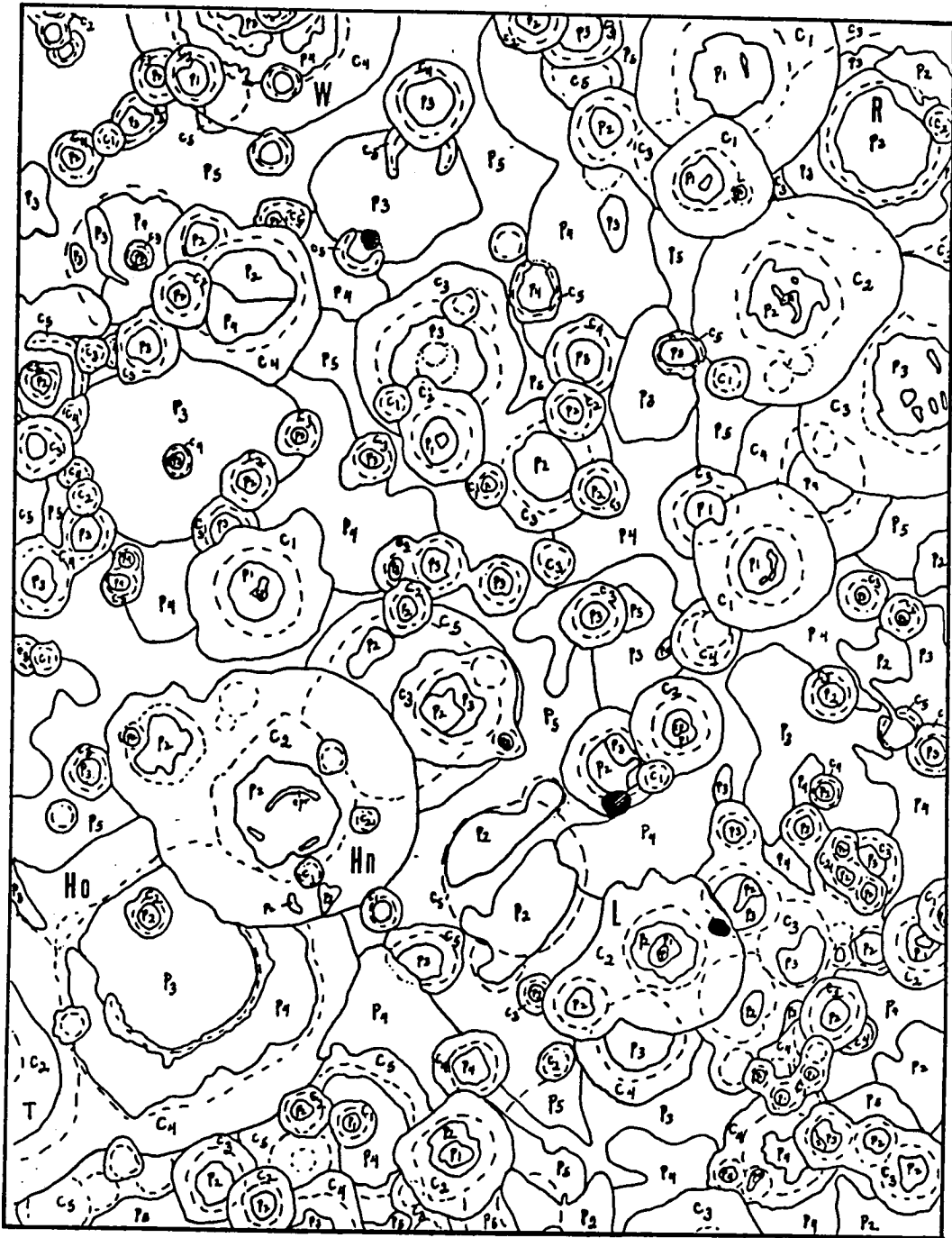


Fig. 24. Dome Location in the Homer - Handel Area: A Sketch Map

Drawn on Shaded Relief Map H-6 base. Domical features are shaded black; the dome of Fig. 22 lies nearest center right. Units are described in Figs. 9 (in pocket) and 11. Abbreviations are Hn--Handel, Ho--Homer, L--Lu Hsun, W--Wren, and R--Rodin. Short dashed lines are crater rims; long dashes are C5' structures.

Dzurisin defines scarps as "relatively steep, cliff-like slopes of considerable lateral extent separating terrain lying at different levels," (Dzurisin, 1977a, p. 8). Most are arcuate to irregular in plan, and convex in profile. Scarps often transect crater walls, floors, and the surrounding plains units without altering those landforms. With a few exceptions noted later, albedo and crater densities do not change across the scarp face. A few craters are shortened perpendicular to the strike of the scarp (e.g. Guido d'Arrezo on Vostok Rupes, Fig. 18). Strom et al. (1975b) interpret these features as tectonic, high angle reverse faults or thrust faults. Because they are apparently globally distributed (Strom et al., 1975b), the scarps may signify global compressive stresses due to cooling of Mercury's core or lithosphere. A radial contraction of 2 km was computed by Strom et al. (1975b).

Based on scarp ages of Class 3 through Class 1, determined by transection and superposition relations, the onset of scarp formation (and global compression) appears to be early in the Class 3 period, continuing through to the Class 1 period. Most scarps are Class 2 in age. Cordell (1977) finds a dearth of scarps in the latitude of the hilly and lineated area; no such lack is registered here, although the scarps do appear damaged. Thus scarp formation may have begun prior to the formation of the hilly and lineated area (and by implication, as defended later, the impact forming the Caloris basin). However, if the scarps are purely tectonic, their formation minimally disturbs the

existing hilly topography, similar to the minimal disturbance of transected crater rims.

Intracrater scarps have various origins. Scarps adjacent to and facing the inner wall along the floor perimeter may be thrusts of consolidated floor material over the materials of the wall-floor contact (as north of Hesiod, Fig. 8). Irregular scarps within smooth plains confined to older craters may be flow fronts of lava (Fig. 89; Strom et al., 1975b), or landslides of debris from superposed impacts (Fig. 17). Some scarps form circular depressions interior to the incipient peak ring (see Crater Materials; Fig. 14a).

Tensional features are regional or rare, isolated occurrences on Mercury's surface. The hilly and lineated zone and the interior of the Caloris basin are the only two regions of extensive normal-type faults, fractures, and graben. A few normal faults and graben are tentatively identified exterior to the hilly and lineated region on the first quadrant. One of the two normal faults (see Scott, Underwood, and DeHon, 1980) deviates around a central peak, paralleling the circular inner scarp of a C2 crater (Fig. 7); the other borders a smooth plains region and may have resulted from drainage of a lava pool (see Fig. 25b, Renoir south). A few features appear to be ancient, 10-15 km graben: southeast of Bramante (Fig. 81), near Discovery Scarp at Rameau (Fig. 8), east of Schubert (Fig. 17), and south of Ts'ai Wen-chi (Fig. 21). These features could also be a pair of thrust faults,

or plateau-scarp combinations. Each lies within P3, P4, or P5 plains; in two or three cases, younger plains are confined within the graben-like feature. No firm relative age can be set.

Although scarps are primarily tectonic in origin, two possible exceptions are noted by Malin (1976b) and Dzurisin (1977b); near Holberg (Fig. 26) and in Renoir (Fig. 25). They are interpreted as volcanic for the following reasons: (1) albedo changes across the scarp trace, (2) craters transected by the scarp are visibly mantled and subdued, and (3) plains units of different age are divided along the scarp trace. A volcanic origin is reaffirmed in this mapping. Some major scarps such as Fram Rupes are closely associated with volcanic features, and may be linked with an episode of volcanism (Fig. 84). Other scarps strike along unit boundaries, although they are tectonic features; differential strength of the two materials may define the fault surface.

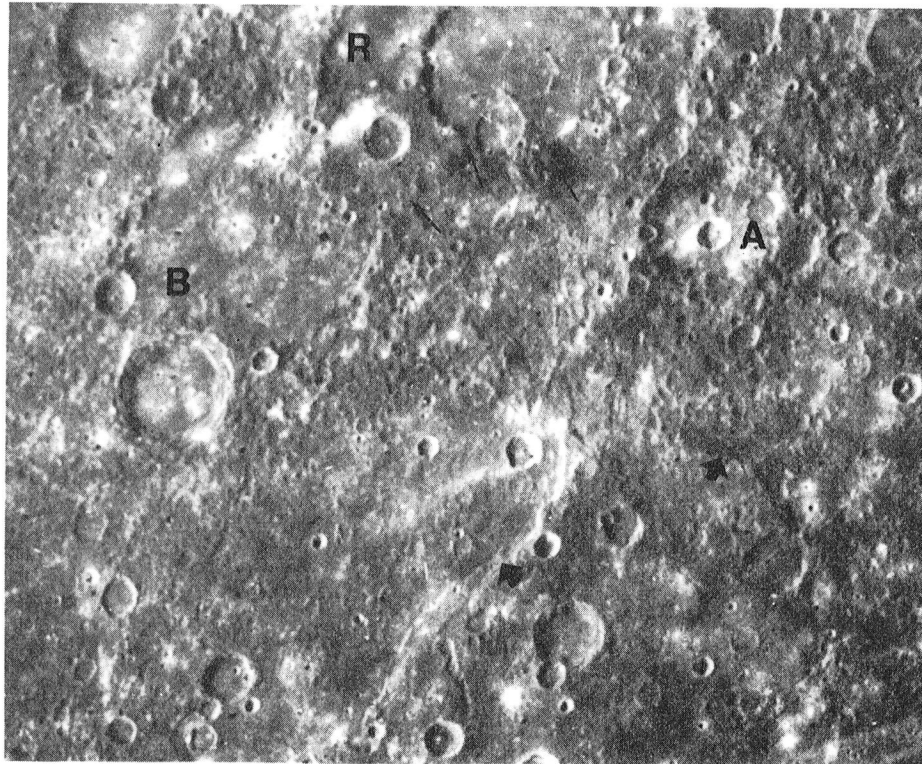
Fig. 25. Renoir Basin Area

- a. Renoir (R), a double ring C3 basin of 220 km diameter, exhibits a variety of features interpreted to be volcanic. Smooth materials filling crater A appear to flank both sides of its thin, crenulated rim, and extend down onto the outer and inner rings of Renoir, ending in a rough lobe near the inner ring. Equal in age but smoother P2 materials fill the west part of the outer plateau and the inner basin area, flooding two craters. Dzurisin (1977a,b) finds an albedo difference between the rough textured material (arrows) along a different contact zone than mapped here. Crater B to the west (C5 age) also has been flooded with plains subsequent to the formation of Renoir and the formation of a small crater on its floor. Secondaries from Renoir scour the plains to the southwest.

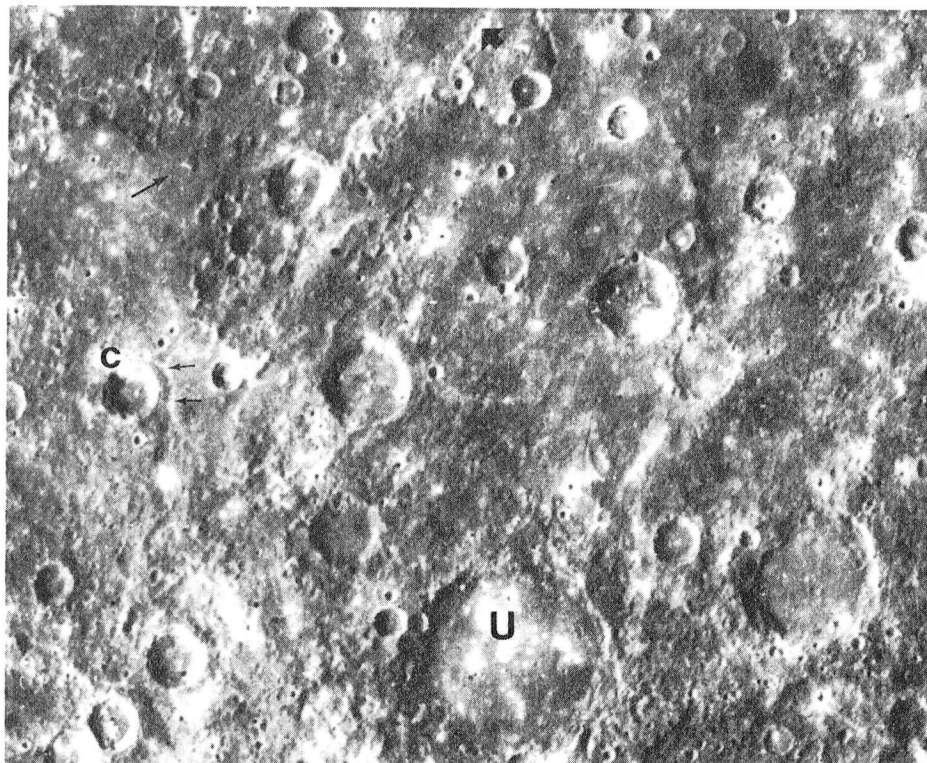
FDS 166649. North at top.

- b. Part of the plains to Renoir's south. The older plains appear to have been raised to form a lobate scarp (thick arrows), while smooth materials have collected at the base of the scarp. From a high plateau to the southwest, smooth material "spills" down (long arrow) into the depressions south of Renoir, flooding low areas at the base of the scarp and embaying Renoir's crater chains. The crater C at center left appears to be faulted along its east rim (short arrows); this normal-type fault may be associated with the emplacement or drainage of the smooth plains just north of it.

FDS 166650. North at top. Unkei (U) is 110 km in diameter.



a.



b.

Fig. 26. South Polar Mosaic SP - 7 of Bach Region

Features of the Bach Quadrangle (H-15) are illustrated in this mosaic and subsequent images. The C3 basin Bach (B) is 225 km in diameter. Note that it did not destroy the smaller craters near its rim with ejected debris. Fresh crater Van Gogh (V) at lower center superposes two double ring basins: Cervantes, C5 in age, 200 km in diameter (C), and Bernini, a C3 central peak basin of 145 km in diameter (Br).

A large C5' basin may lie north of Bach, but was not mapped here. Basins buried by P3 plains appear to retain the double ring structure; P2 plains lie within the inner depression. Other local depressions in P3 materials are filled with smooth P2 plains.

Ridges in the Bach Quadrangle may be tectonic structures or buried crater rims. Scarps are usually tectonic, but the feature perpendicular to Adventure Rupes (A) at arrows displays variations in albedo and crater density across it, and is interpreted as a volcanic flow front (see Dzurisin, 1978). Other features referred to in the following illustrations are Coleridge (Co), Khansa (K), Boccaccio (Bo), and Ma Chih-Yuan (M).



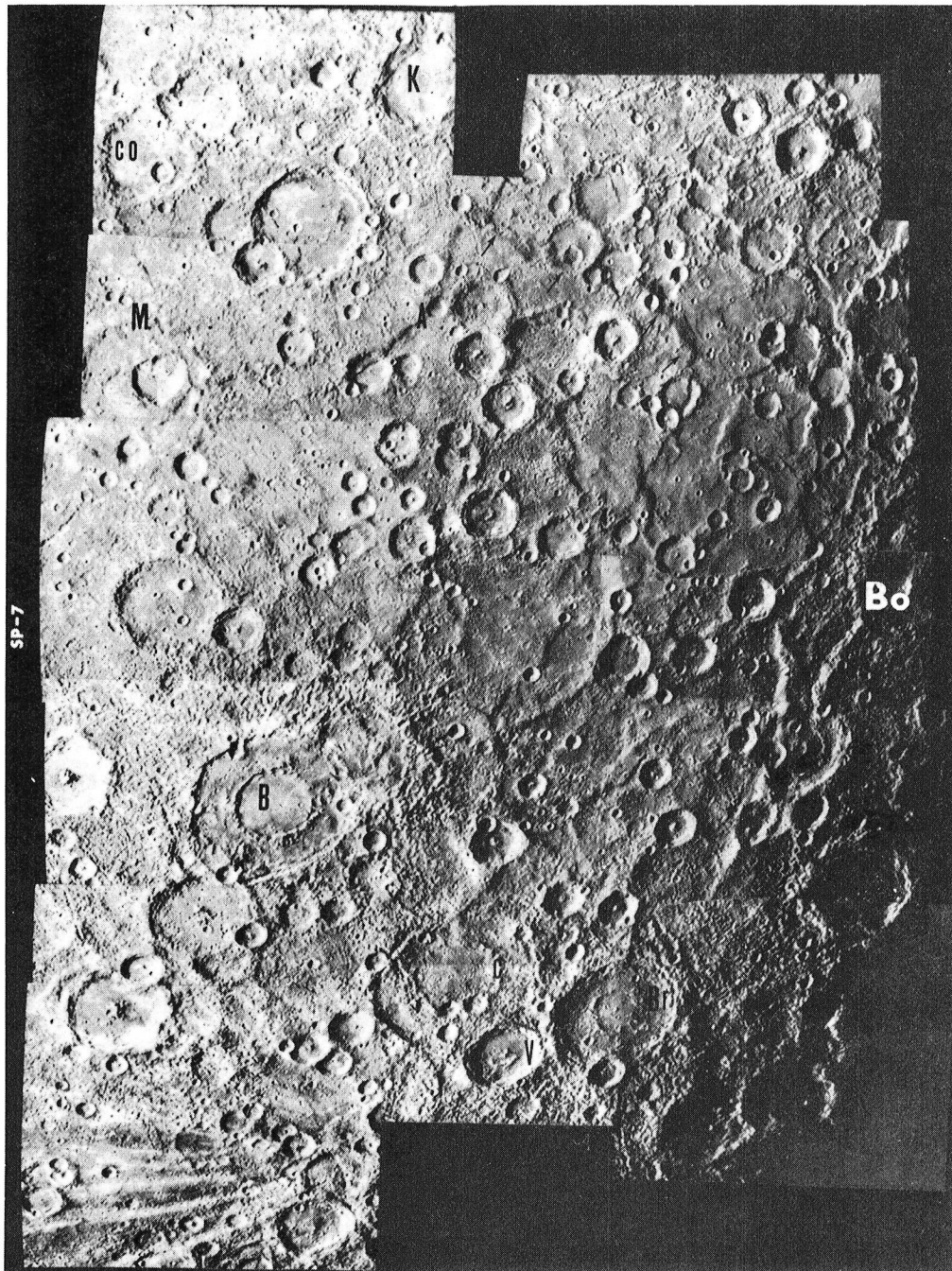


Fig. 26. South Polar Mosaic SP - 7 of Bach Region

Ridges have various morphologies. Linear to arcuate ridges, like Mirni Rupes (Fig.27), may be sites of extrusion of plains material surrounding the ridge. Broad, rounded ridges transecting smooth P3 materials of the Bach Quadrangle (Fig. 26) are probably tectonic features because of their great height (Strom et al., 1978); but rows of craters along the ridge summit, and destruction and embayment of craters transected by the ridge, argue for associated volcanism. These ridges appear to have domical cross sections. Ridges near Santa Maria Rupes have a subdued, rim-like profile; they may overlie a C5' structure recognized by De Hon (1978) (Fig. 20). Antoniadi Dorsum, associated with the collapse pit noted earlier (Fig. 21), may be a source region for the smooth plains of the southern Victoria Quadrangle.

Lineaments (defined earlier) are found mainly in older plains materials--P5, P4, and P3 units--as well as in all ages of craters. Few lineaments are found in smooth plains materials unless underlying topography is visible or if linear scarps or ridges transect the plains. Polygonal rim segments occur on C5' through C1 craters. Melosh and Dzurisin (1978) interpret these features as part of an ancient stress pattern formed during intercrater plains formation, prior to scarp formation. The lineament pattern may have resulted from stresses produced during tidal spin-down, i.e., the relaxation of the equatorial bulge of a more rapidly spinning planet. Tidal spin-down of

Mercury may produce thrust faults in equatorial regions, strike-slip faults at mid-latitudes, and normal faults at the poles. The latter may be suppressed if the planet is also cooling and undergoing global compressional stresses (Melosh, 1977a; Melosh and Dzurisin, 1978; and Pechmann and Melosh, 1979). Expansion due to planetary heating following core formation may have produced globally isotropic grabens and rifts, while contraction during cooling of the planet may have produced the globally isotropic thrust faults (scarps).

Linear troughs, sinuous valleys, and radial valleys have varied origins. Linear troughs are common in the hilly and lineated area and result from the destructive event which formed this terrain (Fig. 19). The troughs are oriented along the global lineament directions, suggesting that failure occurred along zones of structural weakness. Widening of the trough may occur through mass wasting. Troughs which are formed on crater rims or along a linear rim segment may be secondary crater chains from adjacent primary impacts. Slumping is an alternative explanation.

#### Albedo and Color of Mercury's Surface

In addition to stratigraphy and structure, albedo and color data from Mariner 10 should be incorporated into any theory of Mercury's surface history. Other remote sensing data are presented in Chapter 5.

Mercury's general surface reflectance is lunar-like, with a geometric albedo of  $0.16 \pm 0.03$ , slightly higher than that of the Moon,

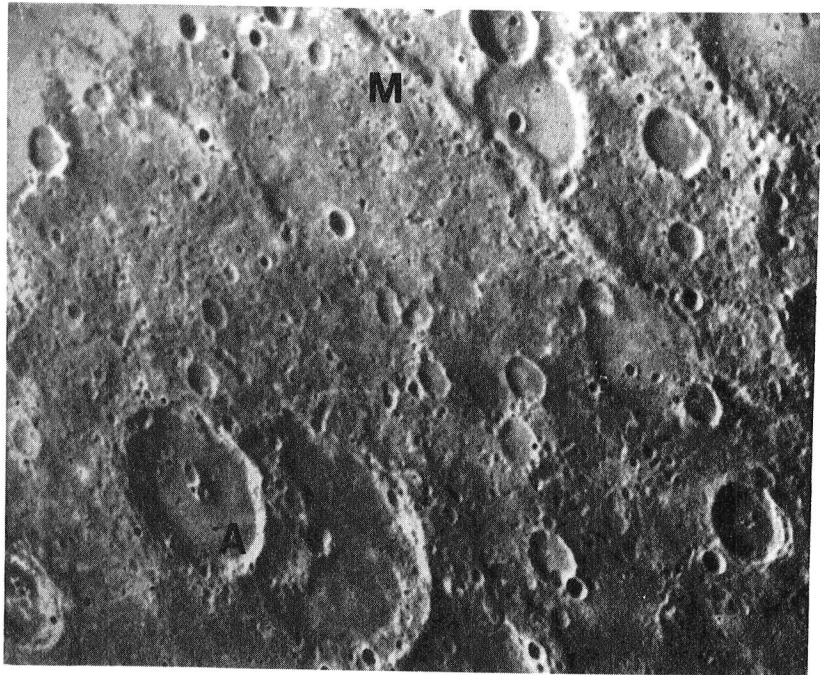
Fig. 27. Ridge Materials of Mirni Rupes and H-15 Regions

- a. Linear ridges like Mirni Rupes (M) may have been fissures through which plains-forming materials were extruded late in the expansional stage of the planet's thermal history, or they may be materials "squeezed up" during the early compressional stage. Craters transected by the ridge appear to have massive deposits within them, although no lateral or transverse movement is noted along the ridge strike. (See Dzurisin, 1978.)

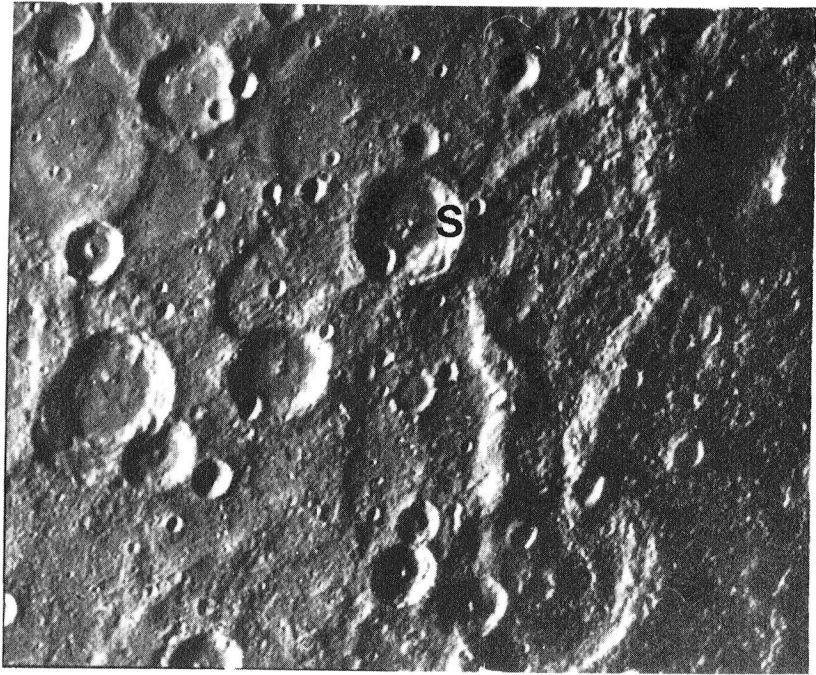
FDS 27420. North at top. Crater A at lower left is 60 km in diameter.

- b. The ridges near Boccaccio (in terminator of H-15 Quadrangle) are topographically high, domical in cross section, and have rows of craters along their summits. Crater rims appear to be altered where transected by the ridge.

FDS 166688. South Pole lies near the lower right corner of the image. The crater in center, Sadi (S), is 60 km in diameter.



a.



b.

0.13 (Dzurisin, 1977b). Surface contrasts, in albedo and color, are less on Mercury than on the Moon, more akin to the weak contrasts of the lunar highlands than to the significant contrasts of lava flows on the mare (Murray, Dollfus, and Smith, 1972; Hapke et al., 1975; Whitaker, 1972). The albedos of Mercury's major units are very similar: 0.18 in the P3-P5 intercrater plains, 0.17-0.18 in the heavily cratered terrain (C3-C2), and 0.15 for the smooth plains around and in Caloris (probably P3 to P1 plains; Dzurisin, 1977b). The lunar mare and terra highlands have geometric albedos of 0.11 and 0.16 respectively (Dzurisin, 1977b; Murray et al., 1974b). Dzurisin (1977b) concludes, that because of the similar albedos of Mercury's three major surface units, homogenizing processes have affected most of Mercury's surface as recently as sometime within the Post Caloris period.

The absence of contrast in albedo caused Hapke et al. (1975) to conclude that there are no large regions characteristic of concentrations of metallic iron or bare rock. Albedo, polarimetry, ultraviolet, and infrared data are consistent with a silicate-like surface whose upper centimeters form a fine, intricately structured regolith (e.g. Morrison, 1970; Dollfus and Geake, 1975; Chase et al., 1974, 1976).

Variations in albedo do occur, however, in both young and old units. Young, smooth P2 plains may be dark, with albedos of 0.13, or

bright, with albedos of 0.23. Dzurisin (1977b) finds that neither bright nor dark smooth plains are intrinsic to crater interiors (as intracrater plains) and that no sequence of albedo variations occurs between these types of smooth plains. This implies that the homogenizing process is not strictly a function of bombardment history, nor simply a brightening or darkening of the surface with age. Some of the youngest units have the brightest albedos: rays, 0.23, and bright patches on crater floors, 0.44 (Fig. 28).

Local variations in albedo occur across two scarps, one perpendicular to Rendezvous Rupes, and the other entering Renoir's inner ring (Dzurisin, 1977b). Lack of an albedo change across most scarps supports their tectonic origin. Albedo changes in the young and old terrains provide partial support for their proposed volcanic origin.

Color contrasts on Mercury reach variations of 25% in the OR/UV ratio, as opposed to 45% on the Moon (Hapke et al., 1980b). Bright and dark patches of red and blue materials which occur within craters do not appear to be impact melts (Dzurisin, 1977b). Fresh craters and rays on Mercury are mostly blue and have a high albedo (Hapke et al., 1975). This color-albedo combination is inconsistent with Ti-rich materials from Mercury's subsurface soils. Some basins with blue rims contain red floor materials emplaced well after the basin's formation; the color difference and delayed infilling probably reflect a compositional difference produced by endogenic processes.

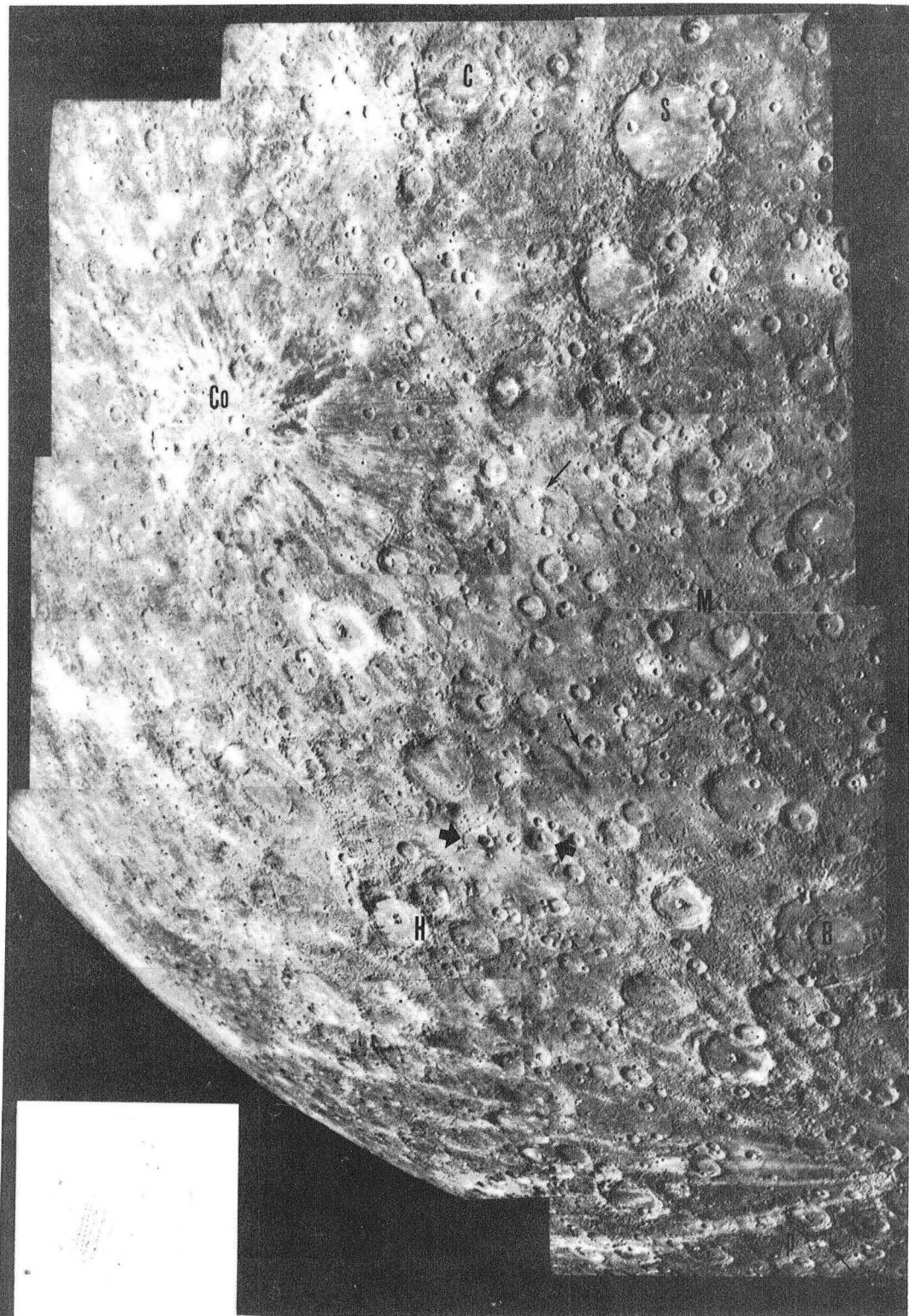
Fig. 28. South Polar Mosaic SP-3: Albedo Features

Locations of various features and rayed craters noted in the text and succeeding figures: S--Schubert; C--Chekov; M--Ma Chih-Yuan; B--Bach; H--Hawthorne volcanic area; thin arrows--dome materials; thick arrows--rimless depressions; P--Pourquois-Pas Rupes and Hero Rupes area, with conical formation nearby; and A--crater near Shevchenko with multiple layers of plains on the floor.

Albedo features near Copley (Co) suggest that the rayed crater was formed by an impact into dark deposits flooding an ancient basin. This C5' basin may be 500 to 700 km in diameter. Rayed crater north of Hawthorne is located on an anomalously smooth area and appears to have excavated both light and dark materials.

North at top.





Four dark halo craters east-southeast of Caloris have red halos, blue and red floor materials, but rays of the same color as the surrounding terrain. These craters have excavated deep-seated materials of a composition unlike the surrounding surface. (The change in color approximately coincides with the change from continuous ejecta deposits to discontinuous ejecta. The latter is hypothesized to consist primarily of local materials, and thus is consistent with the indistinct rays.) Two craters with massive central peaks occur on the periphery of the 800 km basin surrounding Lysippus. Their rare, red-colored rays are the reddest features observed on Mercury (Hapke et al., 1980 a,b). The craters may be endogenic, resulting from differentiation and intrusion of magma into a crust punctured by the large impact (Schultz, 1977).

Most color boundaries on Mercury show little or no correlation with geologic unit or topographic boundaries (Hapke and Rava, 1980). There is a higher degree of chemical homogeneity compared to the Moon, "at least as far as those elements which affect color, particularly iron, are concerned" (Hapke et al., 1980a, p. 394). In some cases it appears that the compositionally distinct units were formed prior to cratering. In other cases, postulated young volcanic units do not differ in color (and composition?) from older surrounding materials. Whether this is inconsistent with volcanically or ballistically derived plains units is not clear, since lunar color maps show that regions of different origins (highland and mare) may have the same

"color," and regions of different color (i.e. composition), such as mare basalts, may have broadly similar origins.

Widespread variations in color occur between the Caloris smooth plains and the intercrater plains of the second quadrant. The yellower smooth plains may consist of more iron-(FeO) rich soils. Intercrater and smooth plains of the first quadrant are blue-green and yellow respectively.

In summary, albedo and color data constrain geologic history in several ways. Some process has insured that all major units or materials are homogeneous in albedo and nearly so in color. Different color ratios and changes in albedo across scarps and within crater floors indicate that composition may vary in such ways that a volcanic origin is supported. In some cases, units of distinctive color differences are young, suggesting that the homogenization process is less active with time, and thus may be related to the decline in bombardment and ejecta distribution. This poses the question of whether this indirectly supports ballistic plains formation. Color differences or compositional differences are also sometimes ancient, predating existing geologic events. Overall, however, the ancient surface is fairly homogeneous in composition.

#### Initial Conclusions From Geologic Mapping of Mercury

The planet Mercury is affected by both impact cratering and its associated deposition and reworking, and by volcanism. The intercrater plains (P5, P4, and P3) appear to be volcanic surfaces

interbedded with ballistically emplaced ejecta and some mass-wasted debris. Tentative volcanic landforms are identified--domes, some scarps, some ridges and flow fronts--which have ages similar to those of the intercrater units. Stratigraphic relationships which suggest a volcanic origin for the intercrater and some younger smooth plains (P3, P2, and P1) include: delayed infilling of cratered basins (sometimes with materials of distinct color or albedo), embayment of crater rims and interiors, albedo differences across scarps associated with unit contacts, and alterations of morphology of embayed craters. Smoother plains are sometimes isolated from younger craters by tracts of older terrain and lie within older basins. Minor amounts of ballistic deposits may thinly cover rough topography outside of large, young basins (e.g. Handel?). In only a few cases, however, do these deposits lie on topographic elevations as well as depressions, as would be expected for ballistically emplaced materials. Younger smooth plains are concentrated in topographic depressions; intercrater plains may occupy depressed areas (C5') but their preservation is in part attributed to their plateau-like elevated positions with respect to surrounding terrain.

Plains morphology is not uniquely related to plains age. From the degradation sequence P1 to P5 one may infer that P5 materials were once formed like P1 plains and subsequently degraded to their present state. This may occur only if bombardment of the original material

does not build up substantial deposits of younger material, and if subsequent volcanism does not embay or bury P5 relief (like the C4 secondaries) in the low lying areas. The P5 plains are remarkable in that they do represent such "preserved" areas. Their elevation and the restricted ballistic range of ejecta may insure their preservation. A primordial surface is unlikely; P5 plains often bury the C5' structures which in turn cover a more ancient surface. In conclusion, geologic mapping of Mercury's first quadrant suggests that many exposures of both intercrater and smooth plains (P5-P1 units) formed through volcanic processes.

Lineaments are found in the intercrater plains and are apparently ancient. Most scarps are globally distributed, tectonic features formed in Class 3 to Class 1 periods. A majority formed during Class 2 crater and plains formation. Normal faults and grabens are rare, but a few examples are tentatively identified; the graben-like features may be older than scarps, possibly concurrent with Class 4 to Class 3 age. Ridges and domical structures may be associated with the last stages of intercrater plains emplacement; rimless pits are associated with scarp-forming tectonics. Intercrater plains emplacement occurred during the formation of C5', C5, C4, and C3 craters. Smoother plains P1 and P2 were emplaced during formation of more sparsely distributed C2 and C1 crateriforms.

The detailed crater production history will be discussed in the next chapter, and incorporated into the preliminary geologic history outlined here.

## Geologic Map Analyses of the Lunar Intercrater Plains

In order to accurately define the nature of the lunar intercrater unit, the Near Side map of Wilhelms and McCauley (1971) was locally redrawn and modified to highlight the Pre-Imbrian Plains, as shown in Fig. 44 in the next chapter. The general 1:5,000,000 scale map was then compared to the 1:1,000,000 scale maps, principally the Maurolycus, Hommel, Clavius, and Tycho Quadrangles, to determine what specific units comprised the pre-Imbrian plains (pIp) mapped by Wilhelms and McCauley (1971). (This intercomparison was outlined in the first section of this chapter.) Fig. 29 illustrates the pIp exposures on the four quadrangles. The individual quadrangle map units which comprise these exposures are listed in Table 6; note the variety of "textures" and assigned ages of these units. Most of these materials are illustrated in the Orbiter IV photographs which follow.

The collective characteristics of these areas describe a level plains unit of primarily Nectarian (middle to late Pre-Imbrian) age, heavily cratered with 1-10 km craters, some of which have irregular shapes similar to that of secondary craters. The type area of the pIp is located southwest of Nicolai (labelled N in Fig. 30). The entire expanse of the intercrater pIp unit lies within 1.6 to 3-3.6 basin radii from the center of Nectaris, using 435 km as the radius of the Altai Scarp (Wilhelms, Hodges, and Pike, 1977). The plains extend between clusters of larger craters (e.g. the cluster around Maurolycus

and Barocius) and embay some smaller craters of middle-to-late pre-Imbrian age (Fig. 30). Fewer craters over 40 km diameter seem to occur within the pIp exposures than within other highland areas, such as those west and north of this area.

Though its contacts are obscure, the pre-Imbrian plains appear to embay the Janssen Formation and thus may postdate the emplacement of Nectaris' ejecta (Scott, 1972; Stuart-Alexander, 1971). Fig. 31 illustrates the textural difference between the pre-Imbrian Janssen (pIj) unit and the pIp unit. Subdued to sharp 5-15 km secondaries from Imbrium are superposed on the plains' northern extension (Figs. 30, 32). Secondaries from the Nectaris Basin underlie the Janssen Formation, forming ridges radial to the Altai Scarp; faint lineations and buried crateriforms trending northeast within the plains suggest that they too overlie Nectarian secondaries and sculpture. The northern pitted plains lie within 150 to 300 km of the Altai Scarp, and therefore may contain greater amounts of embedded ejecta, or thinly overlie these materials at their margins.

However, the degradation of the crater Zagut may suggest otherwise. Zagut, an 84 km crater which lies 100 km east of the northern-most exposure of the pIp unit, appears to be cratered by Nectarian secondaries (Fig. 32). Scott (1972) and Wilhelms and McCauley (1971) assign it an early pre-Imbrian age. Despite its age, and its proximity to the Altai Scarp (within 150 km), its western rim

Fig. 29. Pre-Imbrian Plains Locations on Quadrangle Maps of Lunar Nearside Southern Highlands

Stippled areas represent the Pre-Imbrian Plains mapped by Wilhelms and McCauley (1971) as distributed on the following four Quadrangle Geologic Maps: Tycho, upper left; Maurolycus, upper right; Hommel, lower right; and Clavius, lower left.

Marked craters are Tycho (Ty), Werner (W), Stofler (S), Licetus (L), Maurolycus (Mr), Barocius (Br), Rabbi Levi (RL), Nicolai (N), Pitis-  
cus (P), Baco (B), Ascelpi (A), Hommel (H), Tannerus (T), Mutus (Mu),  
Jacobi (J), Cuvier (Cv), Zach (Z), Clavius (Cl), and Maginus (Mg).

Table 6 (text) lists the various units mapped within each quadrangle which are collected under the Pre-Imbrian Plains designation of Wilhelms and McCauley (1971).



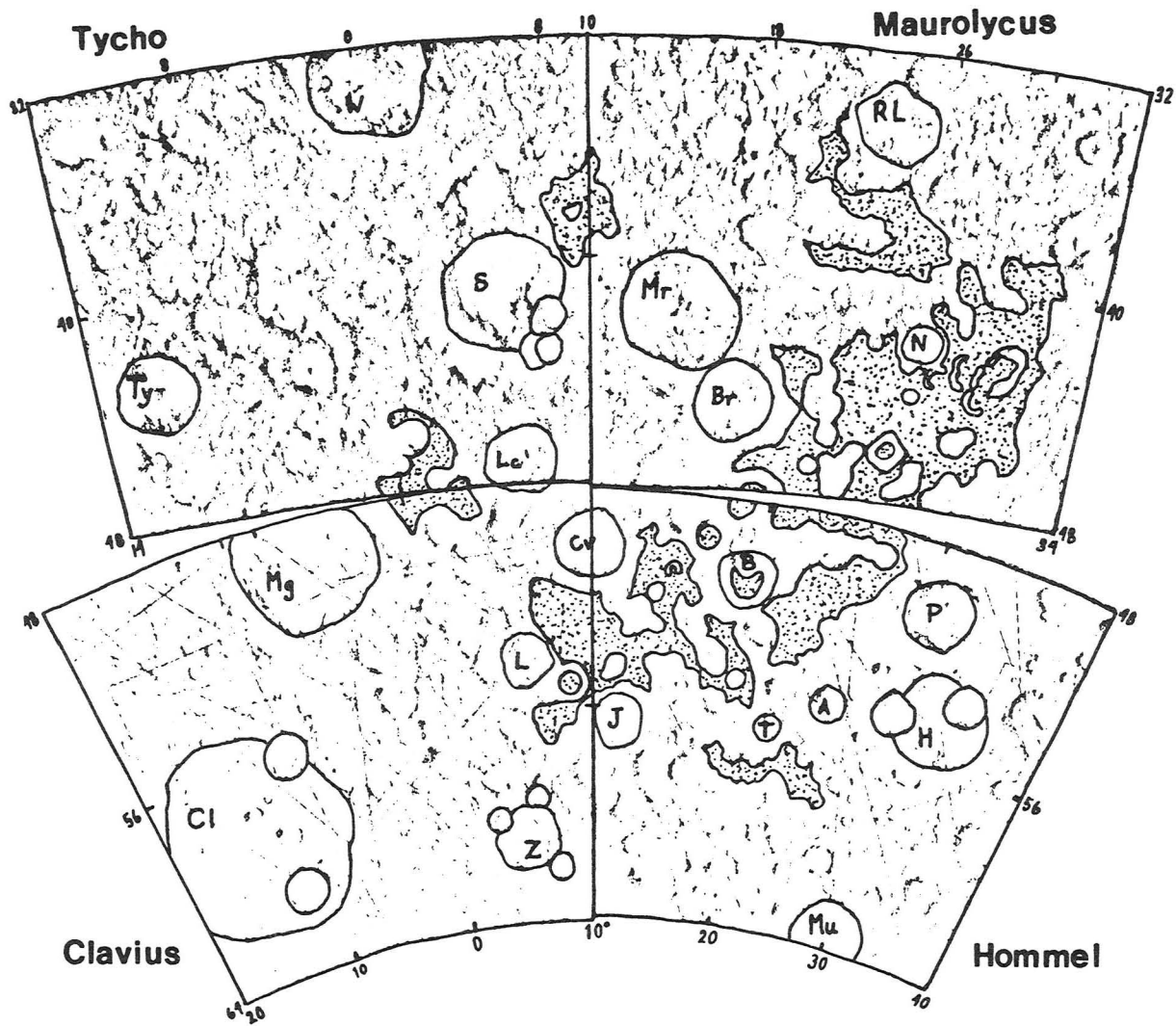


Table 6: Quadrangle Map Units Assumed Under Title  
"Pre-Imbrian Plains"<sup>a</sup>

Quadrangle (Author)	Unit Symbol	Unit Name	Age <sup>b</sup>	Location of Unit Center
Maurolycus (Scott, 1972)	pIp	Material of Pitted Plains	pI <sub>3</sub>	27° E, 44° S
	pIt	Terra Material	pI <sub>2</sub>	21° E, 36° S 21.5 E, 39.5 S 20° E, 38.5 S 20° E, 44° S
Hommel (Mutch and Saunders, 1972)	pIp	Highly Cratered Plains Material	pI <sub>2</sub> - pI <sub>3</sub>	14° E, 51° S 26° E, 48° S
	pIrt	Ridged Terra Material	pI <sub>1</sub> -pI <sub>2</sub>	26° E, 50.5 S
	pIst	Smooth Terra Material	pI <sub>2</sub> -pI <sub>3</sub>	22° E, 52° S 19° E, 54.5 S 22° E, 58° S
	IpC	Cratered Plains Material	I <sub>1</sub>	12° E, 54° S
Clavius (Cummings, 1972)	IpC	Plains Material, Cratered	I <sub>1</sub>	9° E, 54.5 S 1° E, 48° S
	It	Terra Material, Hilly	I	9° E, 52.5 S
	Ips	Plains Material, Smooth	I <sub>2</sub>	(small patches)
Tycho (Pohn, 1972)	pIp	Plains Material	pI <sub>3</sub>	1.5 E, 47° S 9.5 E, 39° S
	IpIt	Hilly Terra Material	pI <sub>3</sub> -I <sub>1</sub>	9° E, 39.5° S
Rheita (Stuart- Alexander, 1971)	pIp	Plains Forming Material	pI <sub>2</sub> - pI <sub>3</sub>	58° E, 44° S

<sup>a</sup> On the Map of the Near Side of the Moon (Wilhelms and McCauley, 1971), the Pre-Imbrian Plains type area is located at 22.5 to 25° E longitude, and 44° to 45.5 S latitude.

<sup>b</sup> Standard lunar stratigraphic nomenclature. In Hommel and Clavius Quadrangles, the Pre-Imbrian is divided into Upper and Lower, noted here by pI<sub>2</sub>-pI<sub>3</sub> and pI<sub>1</sub>-pI<sub>2</sub> respectively. Older units are numbered "1," and younger units "2" or "3."

is relatively undamaged. This preservation suggests that Janssen Formation deposits in this region are not as destructive or as voluminous as they are south and southwest of Nectaris (Fig. 34). However, Rowan (1971) maps Zagut as a post-Nectarian crater; the radial troughs and lineations are interpreted to have formed from tectonic activity some time after the basin impact. If so, there is little reason to conclude that ejecta deposits from Nectaris were unsubstantial in this area. Other factors in this debate are introduced shortly.

Nectarian secondaries are also found on the rims of the larger, older craters surrounding the plains farther south: Cuvier, Vlacq, and Mutus are some examples. The pIp unit appears to embay the rim materials of these craters. Although the relative age of this unit is thus established as Nectarian, obscure contacts and variable small crater densities across the mapped pre-Imbrian plains suggest that this surface was formed in successive episodes. The variety of unit ages of Table 6 supports this.

Near Nearch and Mutus, within a generally depressed area, rims of buried craters are slightly visible (Fig. 33a). The thickness of the plains appears to vary over the Hommel and Maurolycus quadrangles, and is the result of some structural control. Smooth Imbrian plains deposits lie on crater floors and depressions within the older plains units. Large scale blocks and their associated vertical movements may

Fig. 30. Nicolai Area: Type Area of the Pre-Imbrian Plains and Selected Areas 1 and 2

Rectangular region outlined at center left is the type area for the Pre-Imbrian Plains (Wilhelms and McCauley, 1971). Pre-Imbrian Pitted Plains mapped by Scott (1972) occupy most of the lower two-thirds of the photograph. The lower third of the photo was used for crater statistics of the Lockyer G area (Selected Area 1), denoted LG, and the Spallanzani Area (Selected Area 2), denoted S. Note the arcuate chain of fresh Imbrian secondaries at top center, north of Nicolai (N). Striations and crater chains east of Nicolai are radial to the Nectaris basin and form parts of the Janssen Formation exposure. Arrows indicate the two regions sampled by Pieters (1979) in studies of highland spectra.

Lunar Orbiter IV 88 H2. North at top. Nicolai is 42 km in diameter.

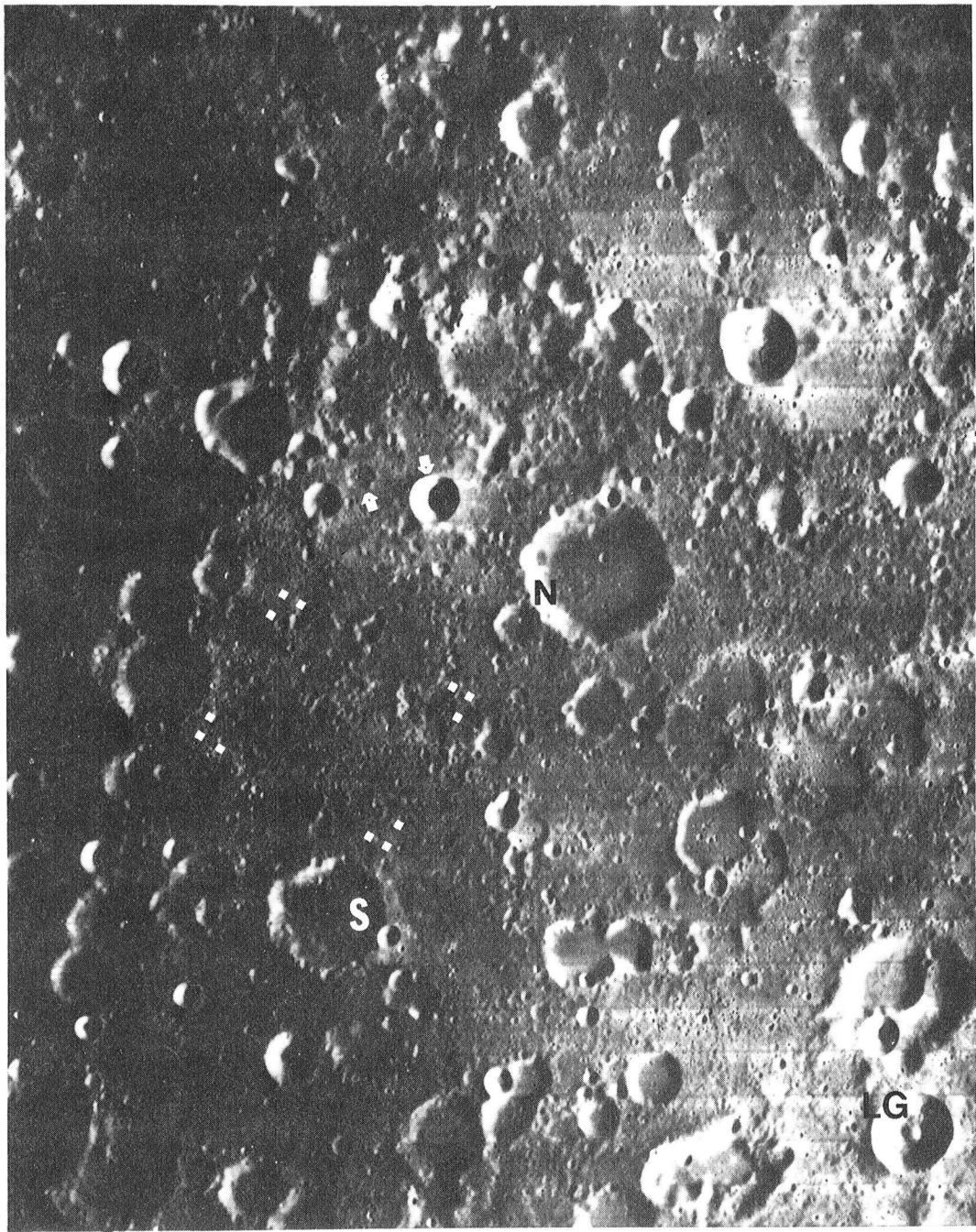


Fig. 31. Janssen Formation Contact With Pre-Imbrian Pitted Plains

Crater chains and ridges radial to Nectaris (trending north-northeast to upper right) are characteristic of the Janssen Formation (pIj), Nectaris' ejecta blanket. The crater Janssen (J) contains the pIj type area; rilles cross its floor.

Pre-Imbrian Pitted Plains embay the Janssen Formation along a contact traced by arrows (see Scott, 1972, and Figs. 29 and 44). The Lockyer G area (LG) crater statistics may be affected by small craters within the Janssen Formation. The thick arrows denote craters southeast of Nicolai (N) which are roughly aligned radial to Nectaris, embayed by the pitted plains unit (pIp), and filled by younger plains. According to Wilhelms (1976b), these craters may be secondaries of Nectaris.

Lunar Orbiter IV 83 H2. North at top. Lockyer (L) and Nicolai (N) are both C2 craters, 34.3 km and 42 km in diameter respectively.

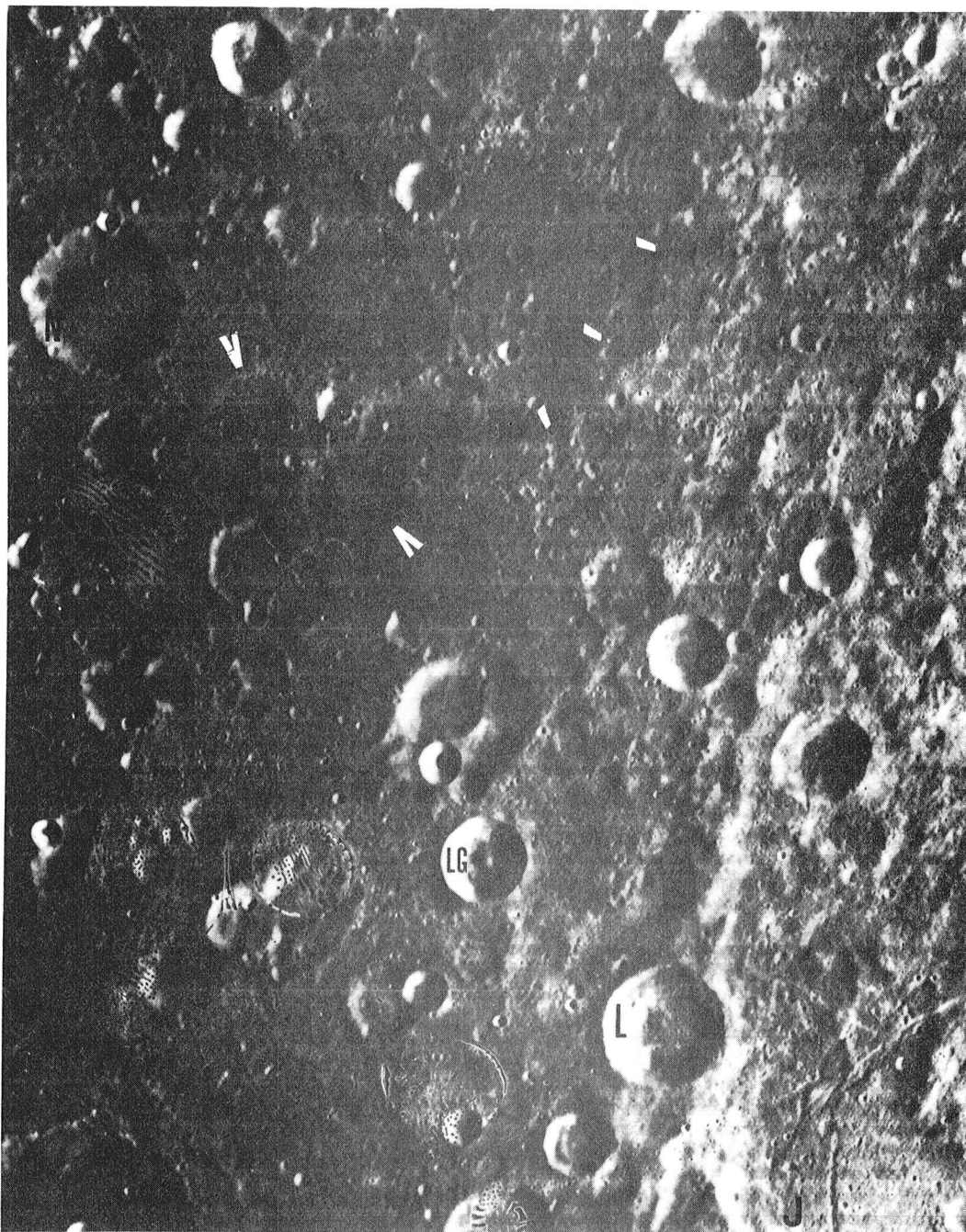


Fig. 31. Janssen Formation Contact with Pre-Imbrian Pitted Plains

Lunar Orbiter IV 83 H2

Fig. 32. Zagut Area East of Altai Scarp--Northern  
Limit of Pitted Plains

Patches of Pre-Imbrian Plains occur in the lower center of the photograph. Note that the rim of Zagut (Z) appears to be scoured by craters radial to Nectaris (thin arrows); this is interpreted to mean that Zagut pre-dates the Nectaris impact and was cratered by Nectaris' secondaries. Other interpretations are discussed in the text.

Many of the 5-15 km craters in chains or clusters and which appear to be fresher than the Zagut lineaments are secondaries from Imbrium, north-northwest of this region.

Lunar Orbiter IV 88 H1. North at top. Zagut is 84 km in diameter. Rabbi Levi (RL) is 81 km in diameter.



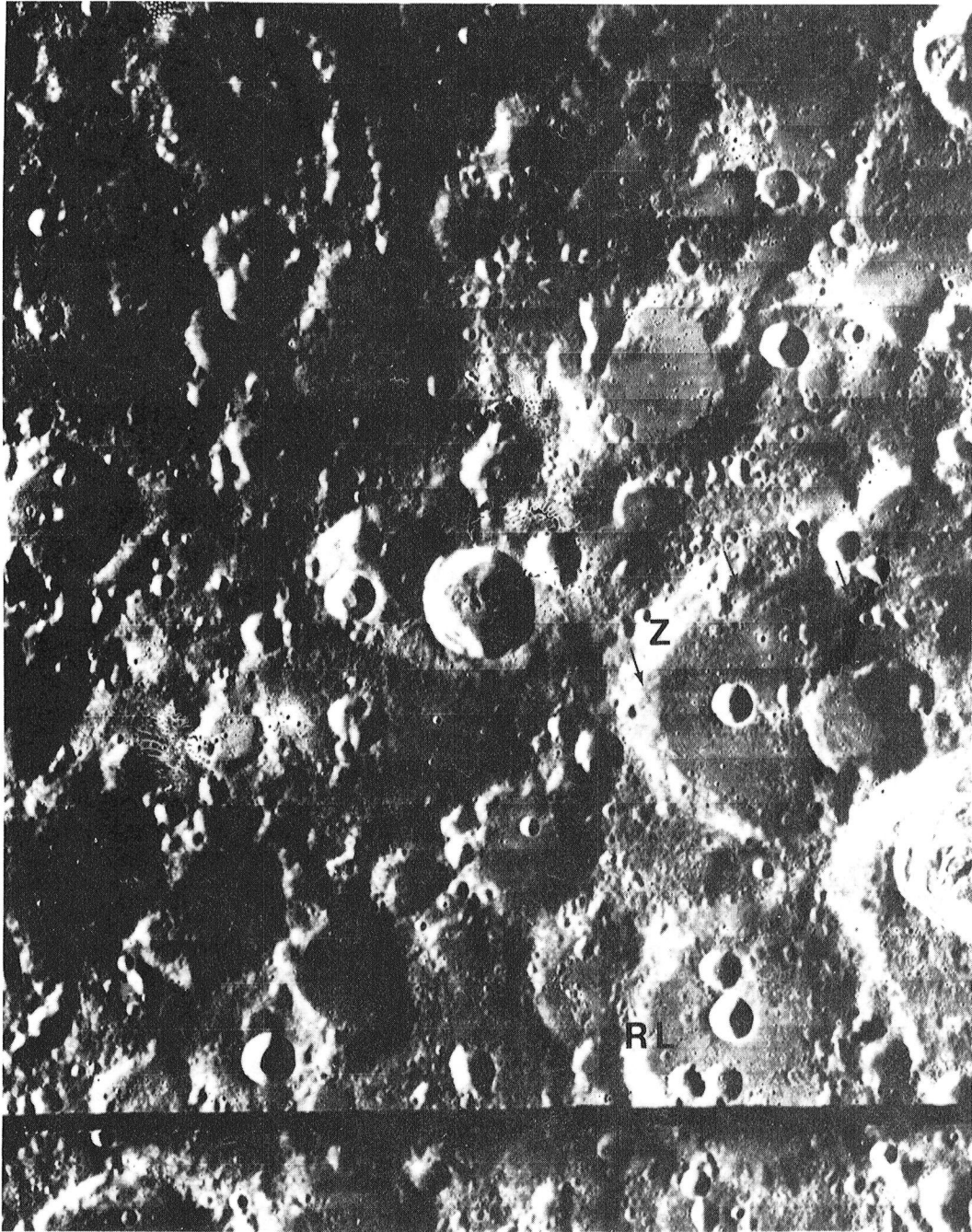


Fig. 33. The Southern Extent of the Lunar Intercrater Plains

- a. Intercrater plains of the Ascelpi (A) and Mutus (M) area. Plains of several ages are shown in this photograph: Pre-Imbrian Plains occupy the upper left corner and a small zone in the left center. Pre-Imbrian terra--both smooth and ridged--form plains units in the upper left quarter of the photo. Imbrian age plains occur in center and lower right; note how these plains units embay and bury older craters (thin arrows). Mutch and Saunders (1972) find that the plains emplacement in this region (The Hommel Quadrangle) is structurally controlled by fault block uplifts (thick arrows). Hommel occurs at top right center (H).

East of Mutus, Imbrian plains (Ip), apparently flow lobes from the south, embay two breached craters. High crater densities on this material indicate it may be older than other Ip units. Strom (1977) includes this feature and similar smooth pre-Imbrian terra and Imbrian plains to the south of this region within the Moon's intercrater plains units.

Crater statistics were sampled in the Ascelpi and Tannerus (T) region (upper left corner of photo) and in the Mutus flow lobe area. These Selected Areas 3 and 4 are marked by corner lines. Statistics within the two regions are discussed in Chapter 3.

Lunar Orbiter IV 82 H3. North at top. Diameters of Ascelpi and Mutus are 42.5 km and 77.6 km respectively.

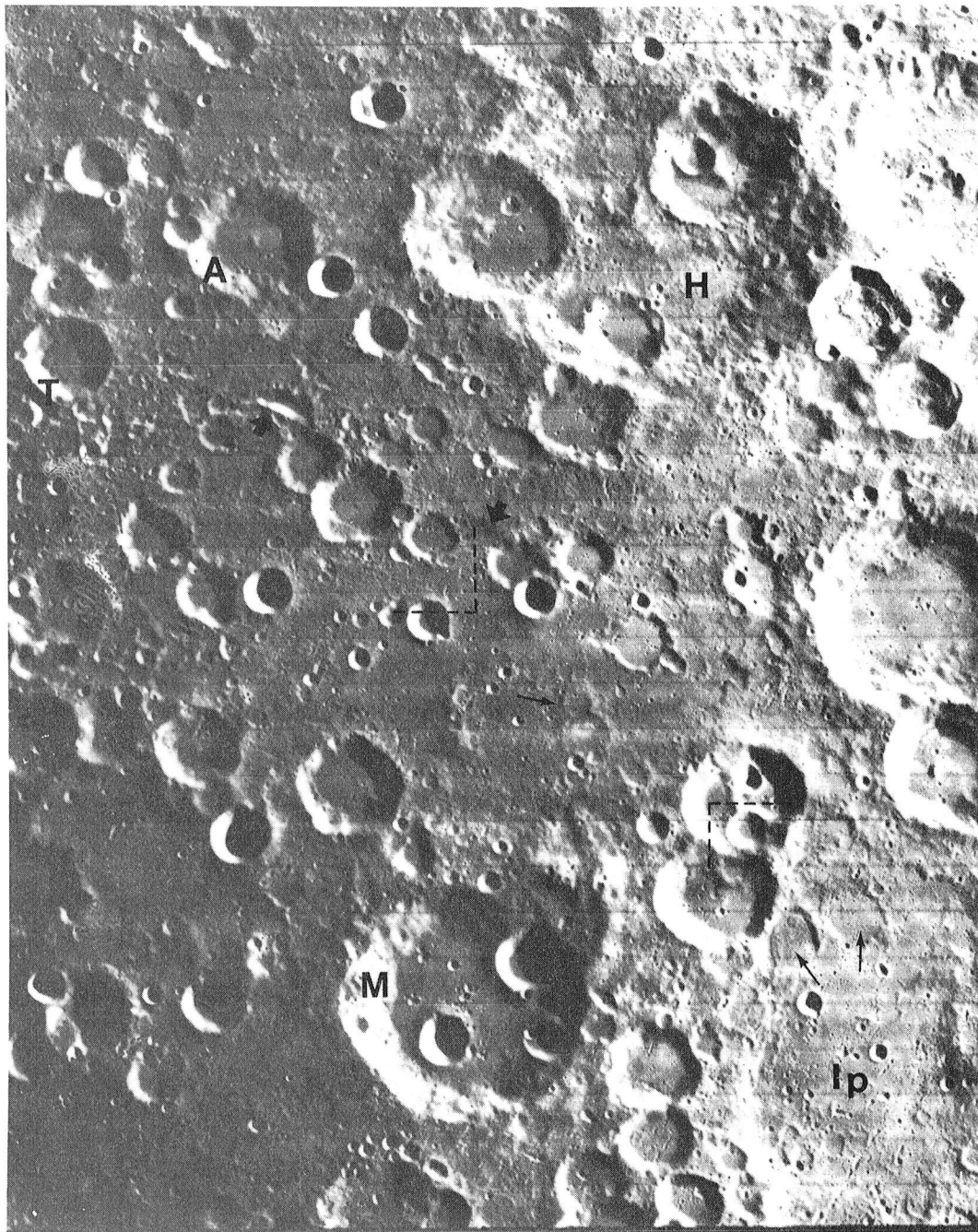


Fig. 33. The Southern Extent of the Lunar Intercrater Plains--  
Continued

- b. Jacobi (J) and Lilius (L) area Pre-Imbrian Plains. This region lies south of the area illustrated in Fig. 6 (also with south at top), and adjacent to the area of Fig. 33a. Pitted plains to the right of Jacobi and in crater A are mapped as pre-Imbrian in age (Wilhelms and McCauley, 1971); those left (east) of Jacobi are mapped as Imbrian highly cratered plains (Mutch and Saunders, 1972). Buried craters (arrows) are discernible. Compare the cratered plains units with the smooth Imbrian plains within Cuvier (Cv).

Cratering statistics were gathered in the southwest portion of this photograph (the upper right quarter). Many of the units represented here are characteristic of the Clavius region which Strom (1977) uses as a standard lunar highland area.

Lunar Orbiter IV 112 H1. North at bottom. Lilius and Jacobi, both C3 craters, have diameters of 61.1 km and 68.1 km respectively.

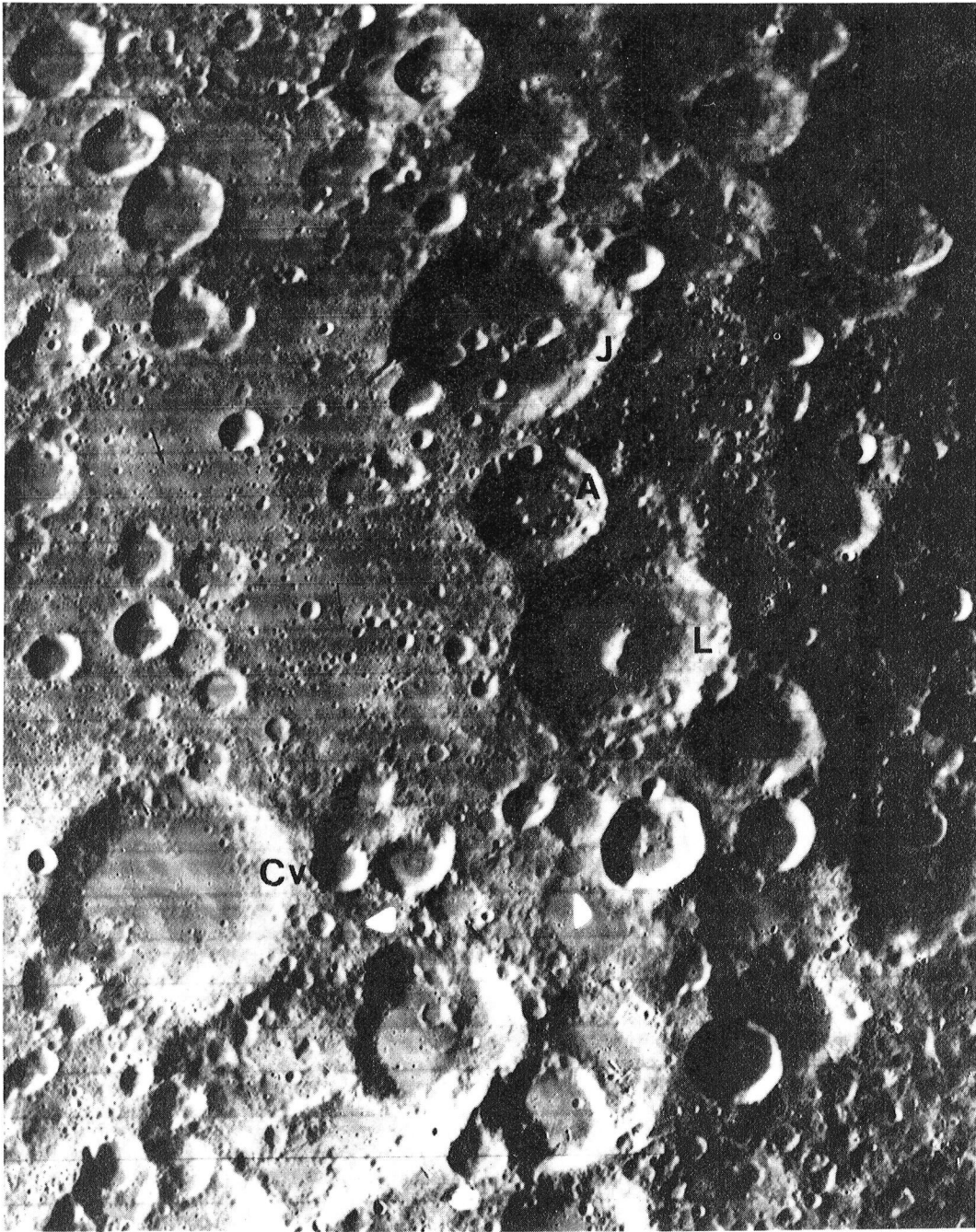
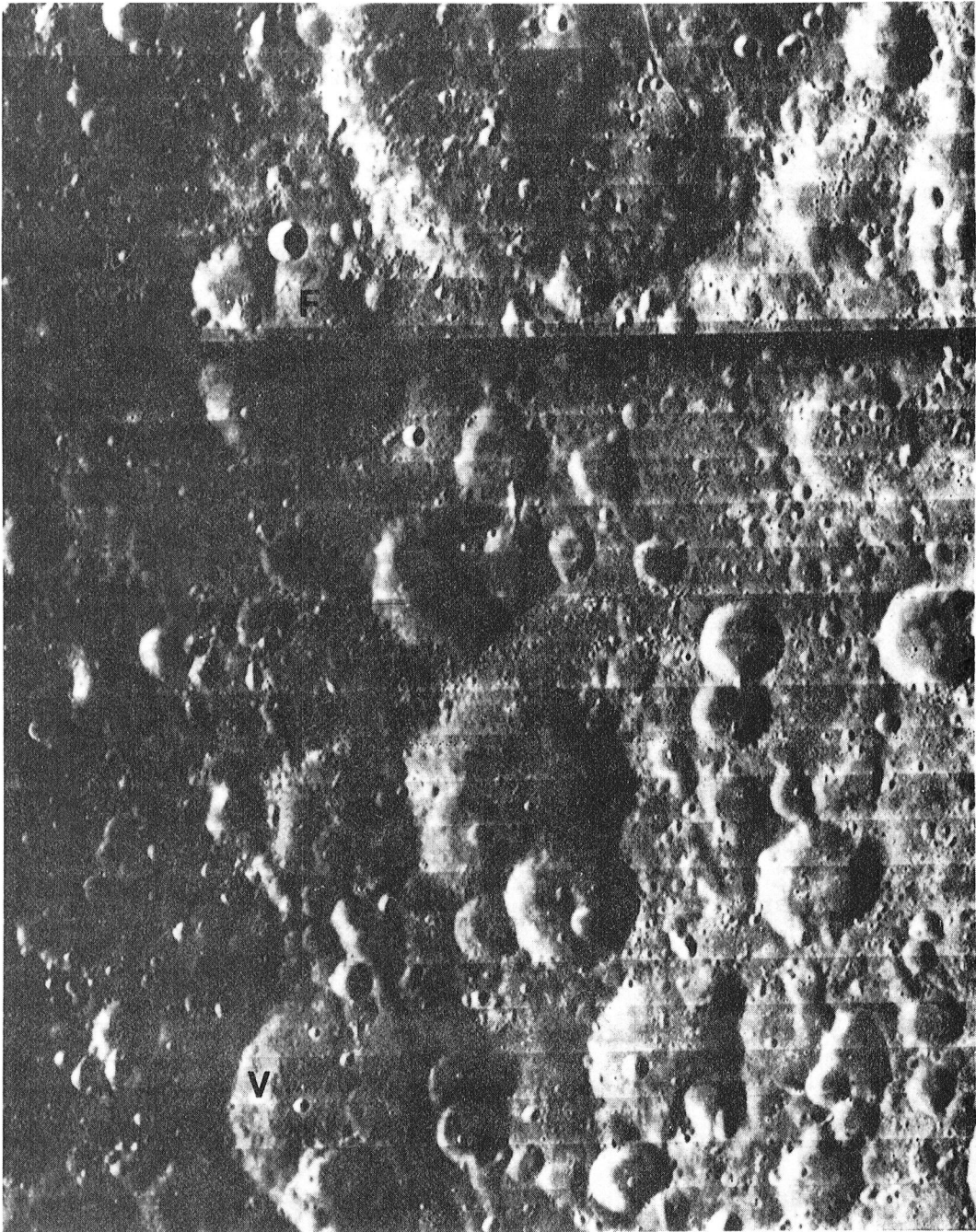


Fig. 34. Nectarian Intercrater Terrain Near Fraunhofer and Furnerius

Furnerius, the large crater at top center of frame, contains post-Imbrian mare deposits. The terrain west of Fraunhofer (F) and south of Furnerius is Nectarian in age, and has pitted and rolling topography. Although its appearance is quite similar to pre-Imbrian pitted plains (see Stuart-Alexander, 1971), it is surrounded by Nectaris' secondaries and ridges of the Janssen Formation. Wilhelms and El-Baz (1977) suggest that this "Nectarian Terra" is therefore basin-associated ejecta. Wilhelms (1976b) further suggests that the pre-Imbrian plains of Fig. 30 are ejecta facies of Nectaris.

Secondaries of Nectaris superpose the C3 crater Vega (V), helping to establish the early C3 age for the Nectaris impact event. The pitted plains are late C3 to early C2 in age.

Lunar Orbiter IV 76 H1. North at top. Fraunhofer is 56.8 km in diameter. Vega is 75.6 km in diameter.



have controlled older plains deposition within the Hommel quadrangle (Mutch and Saunders, 1972). Structural lineations are generally more subdued under the pre-Imbrian plains units compared to those within the Imbrian-Pre-Imbrian terra (IpIt) of the Clavius Quadrangle (Cummings, 1972). This region is similar to the western Jacobi area of Fig. 33b.

Tentative volcanic features are associated with the plains. The volcanic landforms in the region include domes of Imbrian and pre-Imbrian age, rilles within Tannerus (a floor-fractured crater?), and a maar-type crater Lockyer G. These latter features are Imbrian age or younger. A possible flow lobe mapped as Imbrian smooth plains embays a breached crater east of Mutus (Fig. 33a; Mutch and Saunders, 1972; Strom, 1977). This plains feature may be older, perhaps Imbrian-Nectarian (INp) in age.

Other units south of Nectaris, variously labelled pitted plains or Nectarian terra, have characteristics similar to the pre-Imbrian plains features, yet they are more clearly associated with the Janssen Formation; Wilhelms and El-Baz (1977) interpret these units as ballistically emplaced, smooth-lying deposits from Nectaris. (See also Wilhelms, 1976b.) Fig. 34 and Fig. 35 display Nectarian plains units south of Fraunhofer and in the Biela-Watt region east of Nearch respectively; note the lineations radial to Nectaris.

Areal coverage by plains material within the southern highlands area appears to decrease--or at least fluctuate--with time.



Although plains areas were not measured, one can note the following trends. Young Imbrian plains decrease in their scattered areal extent away from the major basins Imbrium and Orientale (see Fig. 44). For example, Ip units are more extensive north of Werner (Oberbeck et al., 1974, 1975, 1977; Howard et al., 1974).

Farside highlands show a general increase in plains with time, i.e. Imbrian plains are more common than Nectarian plains (Stuart-Alexander, 1976; Gifford and El-Baz, 1979). The latter units are most often found in the interiors of pre-Nectarian craters (e.g. Gagarin, Fig. 36), and basin remnants (e.g. Lomonosov-Fleming; Stuart-Alexander, 1976). The nearside southern highlands contain more pre-Imbrian (or Nectarian Np) plains than Imbrian plains; some characteristic of the nearside and farside surfaces (like their different crustal depths and basin ages) may have altered their plains emplacement history. The location of farside plains within basins and the observed lower densities of large craters in the pIp region--analogous to the decreased crater densities in the South Polar-Aitken basin as observed by Wood and Gifford (1980)--suggest that the nearside unit lies within an ancient basin, previously unrecognized. See last section of this chapter.

To afford some comparison with the geologic map and relative age studies of Mercury, degradation classes (LPL) were plotted onto the Near Side base map. Class 3 craters dominate the entire area;

Fig. 35. Smooth Plains and Nectarian Sculpture  
Near Biela and Watt

East of Hommel, Nectarian intercrater terrain extends beyond Watt (W) to Biela (B). Nectarian secondaries have cratered the rim of Vlacq (V) and produced the ridges noted west of Watt. The plains south of Watt are pitted with small craters, lack obvious sculpture, and are quite similar to the pre-Imbrian plains to the northwest.

Lunar Orbiter IV 52 H2. North at top. Biela (C2) is 76.2 km in diameter. Watt (C3) is 66.3 km in diameter.

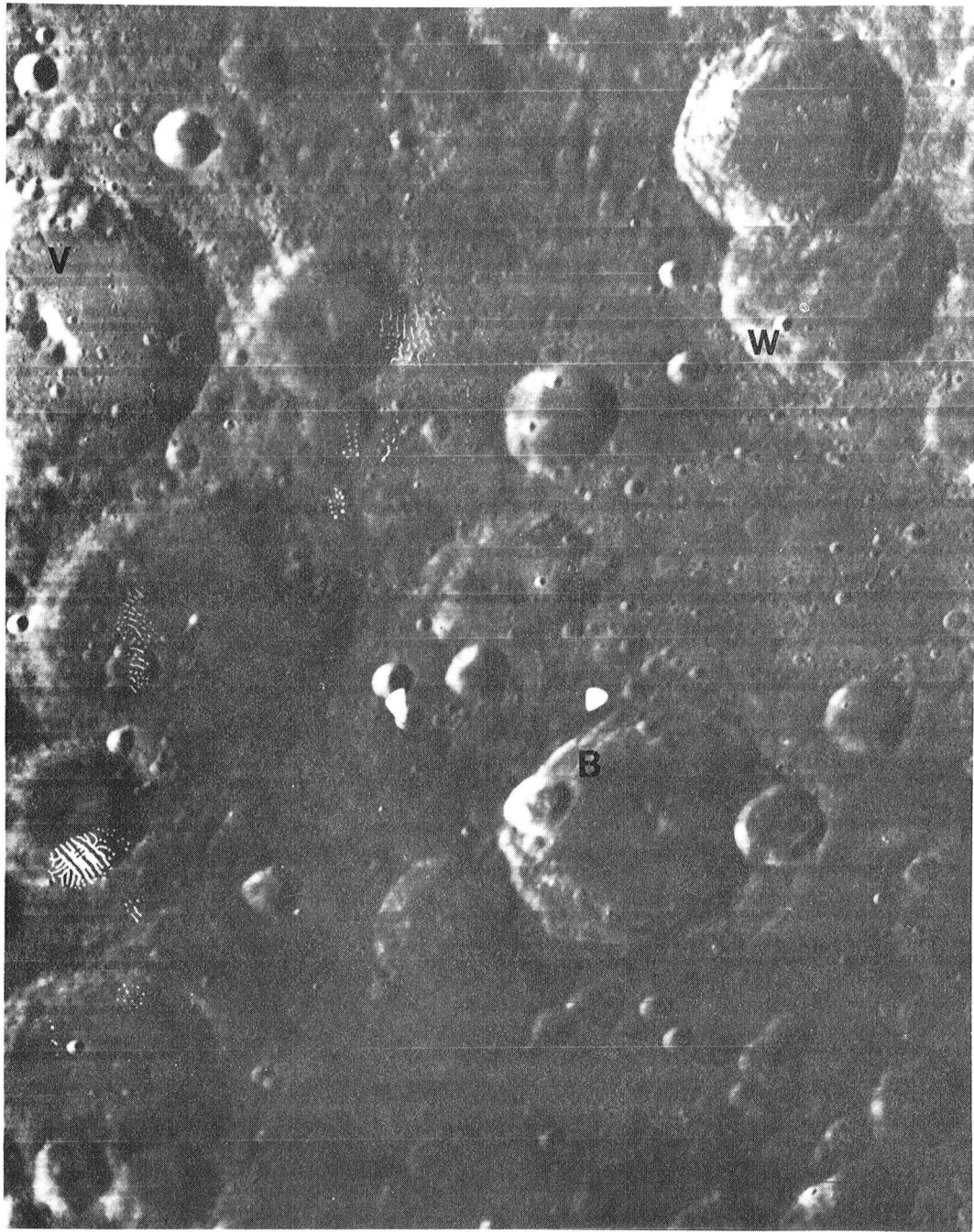


Fig. 36. Far-Side Lunar Highlands and Nectarian Plains

The oldest smooth plains units, the Nectarian plains (Np), often are found within old basins and large craters such as Gagarin (G; 230 km in diameter) on the lunar farside, rather than in extensive intercrater tracts as on the lunar nearside. Note that the Nectarian plains do not cover the most heavily cratered areas visible in this farside region.

Grooved terrain, analogous to Mercury's hilly and lineated terrain (Fig. 19), surrounds the Mare Ingenii (MI) area. The disrupted region lies antipodal to the Imbrium basin.

Lunar Orbiter II 75 M. This view toward the south (at top) encompasses much of the South Polar-Aitken Basin.



fresher craters become more numerous to the south pole and more degraded craters (Classes 4 and 5) become more abundant toward the north, nearing the Imbrium and Nectaris basins. (See also Ronca and Green, 1969.) From embayment and transection relationships, the pre-Imbrian plains appear mainly as a P3 surface. Interpretations are "broad" because the LPL and USGS degradation criteria do not always produce the same crater ages relative to adjacent units (see Chapter 2, Section 1). The Janssen Formation could be interpreted as a P3 (to P4?) surface, and the pre-Imbrian ridged terra a P4 surface, while the smooth Imbrian plains range from P2 to P3 age. Subdued Imbrian secondaries overlying the area fall within Class 3, narrowing the relative "Class 3" age of the plains; however, fresher looking Imbrian secondaries are given Class 2 ages. Mare surfaces to the north are likely to be designated P2 or P1.

Dated in this manner, the lunar intercrater plains--the pIp unit--display a narrower range of relative ages than their Mercurian counterparts. On Mercury, the intercrater plains are P5 through P3 units; the smooth plains are P2 to P1 surfaces. The lunar intercrater plains are P3 units, and the smooth light plains (Ip units), are P3 to P2 in relative age. Inclusion of the pre-Imbrian terra surfaces would broaden this lunar plains spectrum to P4 intercrater surfaces.

The overwhelming consensus of interpretations of the pre-Imbrian plains, prior to the Apollo 16 mission, favored volcanic

plains, lava or ash flows produced in an episode of pre-mare, pre-Imbrian volcanism (e.g. Scott, 1972; Wilhelms and McCauley, 1971). Volcanic landforms, variable unit depth, embayment relationships, and other stratigraphic data were cited as evidence for a volcanic origin. The age of the pre-Imbrian plains was not considered to be obscured by possible endogenic craters (Mutch and Saunders, 1972). Pohn (1972) interpreted the terra and possibly the plains within the Tycho quadrangle as mainly volcanic, but possibly interbedded (or composed of) crater and basin ejecta, "a deep regolith developed in situ." Many interpreted the pIp unit as an older equivalent of the Imbrian plains (including the Cayley Formation).

Pohn's cautious interpretation was a precursor to the post-Apollo 16 views recorded in all later maps and analyses. Following the discovery of the breccia dominated, ballistically-emplaced Cayley plains, interpretations of all plains formation swung to basin and crater related origins (e.g. Oberbeck et al., 1974, 1975; Head, 1974, 1976a). Volcanic hypotheses, though not completely dismissed (Stuart-Alexander, 1976; Wilhelms and El-Baz, 1977; Scott et al., 1977), were outweighed by growing evidence for plains formation by ballistic deposition of crater and basin ejecta. The pre-Imbrian plains unit was then considered to be a deposit of the Nectarian basin of a more subdued nature (smooth, with fewer ridges) than the basin's lineated, but ancient ejecta blanket, the Janssen Formation (Howard et al., 1974; Stuart-Alexander and Wilhelms, 1975). Comparisons were

made to the ejecta blankets and secondary craters of Imbrium and Orientale (Wilhelms, 1976b; Wilhelms et al., 1977).

The West Side map of the Orientale basin (Scott et al., 1977) was studied to determine the nature of the ejecta deposits of the basin, and compare it to the Nectaris area. Secondary craters as large as 30 km form overlapping "chains and clusters radial and peripheral to the basin," (Scott et al., 1977). They are subdued close to the basin rim on the inner Hevelius facies, as if mantled, and both overlie and underlie areas of the outer Hevelius facies. Very few secondaries are superposed on the highly lineated inner facies which begins at the Cordillera Scarp and extends to 3 basin radii from the center of Orientale. Morphology of the outer facies varies from swirly and lineated to hummocky and smooth; its outermost boundary is indistinct and extends a basin radii beyond the inner facies, i.e. from 3 to 4 radii from the basin center.

As noted by Woronow, Strom, and Rains (1979), craters within 300 km of the Cordilleran Scarp are severely affected: 40% of craters greater than 50 km in diameter are obliterated.

The extent of either facies may vary because of the oblique impact of the projectile (Scott et al., 1977; Wilhelms, 1980; Gault and Wedekind, 1978). An impact from the northeast may have caused the following morphologic features: (1) decreased width of the inner and outer ejecta (Hevelius) facies to the northeast (uprange of the impact



trajectory); (2) increased width of knobby facies to the southwest (downrange) which extends past the outer ejecta facies; (3) secondaries abundant to the northwest, southwest, and possibly southeast, but fewer to the northeast (some features to the northeast are buried under Oceanus Procellarum); (4) disrupted ring and rim scarp to the southwest, but better defined concentric ring system to the northeast; and (5) extensive valley formation perpendicular to and downrange of the impact trajectory. These factors can be applied to the Nectaris Basin, assuming it was formed by an impact from the southwest.

Smooth Imbrian plains lie on top of the outer facies at the edge of the inner Hevelius facies; numerous patches of plains lie in areas bordering the ejecta deposits of Humorum and Imbrium to the east and north respectively.

The late pre-Imbrian pitted plains appear well displaced "temporally" from the early middle pre-Imbrian impact forming the Nectaris basin (Scott, 1972; Offield and Pohn, 1969). Evidence supporting this conclusion are (1) superposition of the Janssen Formation by the pIp, (2) burial and embayment of Nectarian secondaries and ridges, (3) burial of circular 3-5 km craters, (4) occupation of lower-level fault blocks and depressed regions, and (5) embayment of craters of early to late middle pre-Imbrian and flows of ages of middle pre-Imbrian to early Imbrian, including the flow lobes east of Mutus (Strom, 1977).

Because the pre-Imbrian plains are within a basin diameter of Nectaris, the level surface of the plains may at least reflect the subjacent extension of the Janssen Formation or other smoother ejecta deposits. The abundant 10 to 20 km craters in the area may be secondaries from Nectaris; those identified by Wilhelms (1976b) are middle to late pre-Imbrian in age.

However, some of the evidence reviewed here is consistent with a basin related origin (Wilhelms, 1976b; Howard et al., 1974; Moore, Hodges and Scott, 1974; Wilhelms et al., 1977; and Wilhelms, Oberbeck, and Aggarwal, 1978). Although not definitive, the evidence includes the obscure contacts of the pIp unit with the Janssen Formation, the ambiguous relative ages of the proposed basin secondaries and post-basin, pre-plains craters, and the absence of well identified pre-Imbrian volcanic features. (Younger Imbrian age features were noted; they include the floor-fractured crater Tannerus, and the maar-type crater Lockyer G.)

As was noted in the discussion of the West Side map of the Orientale basin, late arriving basin secondaries may overlie, or escape mantling by, the outer ejecta facies, which may vary in texture from lineated to smooth; alternatively, basin secondaries may be mantled by the basins' later ejecta deposits.

Two puzzles remain. The first is that the time interval between Nectaris basin formation and intercrater plains formation is

still undetermined. Secondaries from Imbrian provide a well defined upper marker horizon but tend to obscure the observations of older details. A second puzzle is that the plains occupy an area lacking the large craters which are so abundant elsewhere in the southern highlands. The missing craters do not appear to lie beneath the plains, as their rims would be higher than the lineations from Nectaris which do appear faintly at the pitted plains margins. Neither have these craters been destroyed by the Nectaris basin impact, for alleged pre-Nectarian craters closer to the basin (like Zagut? See Rowan, 1971 and Scott, 1972) are still quite intact and visible. Plains distribution on the farside suggests that nearside old plains might lie within the confines of a very old, unrecognized basin. (Detection of Lomonosov-Fleming, South Polar Aitken, and other farside basins is remarkable enough that such an unrecognized structure on the nearside is unlikely or quite remarkable.) The effects of an ancient basin-forming impact are discussed in the next chapter.

Thus the pitted plains--the pre-Imbrian plains--may have various origins, or stages of formation, as yet unclear. The area occupied by the plains has not escaped basin influences of Nectaris, nor even entirely of Imbrium, but at least the area is not dominated by the younger Imbrium impact. Relegating an origin to the older plains based on its morphologic similarities to younger plains may not be justified (and may not be applicable to Mercury!) A volcanic

origin is not excluded, and indeed supported by many features, although the dominant presence of basin related material and processes is recognized for the lunar highlands. A range of ages is spanned by the lunar plains units, and the position of the intercrater plains within that spectrum indicates that it (1) is not a primordial surface and (2) was emplaced over an extended period of time, perhaps overlapping the Nectaris and Imbrian basin impacts.

The preferred interpretation of the mapping is that the pre-Imbrian plains may well be a volcanic surface, one which has substantial amounts of basin and local ejecta superposed on or underlying these deposits. The unit's placement in topographic depressions, its extended formational age, and burial of craters, suggests that volcanism is structurally controlled. Ancient basalts would have been intruded into locally thin regions of the crust such as ancient basins or faulted provinces. The Nectaris impact though has greatly affected the pIp region, and its ejecta may have collected in such topographic depressions.

Note in Proof. In a recent map of the South Side of the Moon, Wilhelms, Howard, and Wilshire (1979) propose the existence of a 680 km diameter basin encompassing the pre-Imbrian plains region. The basin is named after the crater Mutus and Vlacq which superpose its southern rim remnants. Wilhelms et al. (1979) argue that the Nectarian plains (pIp) units within the basin are merely collections of ejected basin and crater debris. It is argued here, and throughout, that the ancient basin site may also structurally control the emplacement of volcanic materials, in particular those extruded into shallower areas of the lunar crust.

## CHAPTER 3

### CRATERING HISTORIES OF THE INTERCRATER PLAINS

The intercrater plains of Mercury and the Moon are defined, in part, by their high densities of small craters. The crater size-frequency statistics presented in this chapter may help constrain the relative ages and origins of these surfaces. To this end, the effects of common geologic processes on crater frequency statistics (Sections 2 and 3) are compared with the diameter-frequency distributions of the intercrater regions of the Moon (Section 4) and Mercury (Section 5). Such analyses may determine whether secondary craters dominate the distribution at small diameters, and whether volcanic plains or ballistic deposits form the intercrater surface.

Determining the mass-frequency distribution and flux of the impacting population is a more difficult problem. The necessary information—such as scaling relationships between projectile energy and crater diameter, the relative fluxes of solar system objects, and the absolute ages of surface units—is model dependent and poorly constrained, especially for Mercury. Only general comments can be made about the bombarding population and its changes relative to geologic events in the planet's history.

## Methods Summary

The collection of cratering data from planetary imagery is fairly straightforward, consisting of determining the number of craters  $N$  of diameter intervals  $\Delta D$  on a surface of area  $A$ . Diameter, degradation class, presence in a chain or cluster, the underlying units, and the approximate position were determined for each crater larger than a limiting diameter on the selected Mariner 10 images and the Lunar Orbiter IV photographs.

Appendix C reveals measurement techniques and errors. In its first section, I discuss the preparation of the base photograph, measurements of crater diameters and the sampled area, and the instruments used. Among the errors discussed in the second section are those related to sun angle, scale factors, degradation classification, and biases in crater recognition. Most of these errors are more serious for the Mariner 10 images than for the Lunar Orbiter IV photographs, because of the poorer resolution of the Mariner images. For instance, areas derived with a scale factor in km per pixel (or TV line) were not equal to areas derived from the longitude and latitude of the region's boundaries on the Shaded Relief Maps. Because of slight changes in the classification criteria used in the crater assignments and the geologic mapping of Mercury, degradation classes of large craters within the selected regions of Mercury were judged to be (usually) one class younger when mapped, using the revised LPL

scheme, than when the crater was classified using the lunar LPL criteria. The shift in classes involved some C4 and C3 craters which were mapped as C3 and C2. Further details are discussed in the appendix; the degradation criteria are discussed in Chapter 2. Uses of different scale factors and degradation criteria for Mercury's selected regions do not change the conclusions drawn in Section 5.

#### Data Presentation

Tabular and graphical presentation of the data follow the guidelines set by the Crater Analysis Techniques Working Group (1978). Tables of diameter frequency data and supporting information appear in Appendix D. These tables list, for each area A, the number of craters  $N(D)$  within a diameter bin of limits  $D_1$  and  $D_2 = D_1 \cdot (2)^{\frac{1}{2}}$ . The mean diameter of the logarithmic bin is then  $\bar{D} = (D_1 \times D_2)^{\frac{1}{2}}$  or  $D_1(2)^{\frac{1}{4}}$ . A standard diameter  $D_1$  of  $(7/2^3)$  km is used here. Supporting data include the image identification, image source, image processing, the photo scale, regional boundaries, measuring instruments used and their accuracy, the lower diameter limit sampled, and notes on picture quality or special problems.

Most of the data are displayed throughout the chapter as Area Plots or, in regions of general interest, as Cumulative Size-Frequency Plots. Both abscissa and ordinate of the graphs are equally scaled to the log base 10. The diameter is plotted along the abscissa at the geometric mean of the diameter bin,  $\bar{D}$ . The left-hand side ordinate of



the Area Plot is the function  $P(\bar{D})$ , the percent coverage of area A by N craters within the diameter bin of  $\bar{D}$ . Percent coverage is represented by the formula:  $P(D) = (100 \pi \bar{D}^2 N) / (4A)$ . The right-hand side ordinate of the Area Plot is the Relative Size Frequency factor,  $R(D)$ . When the bin widths of the Relative Size Frequency Plot equal those for the Area Plot, as they do here, the two values are related by the expression,  $R(D) = 0.0365 P(D)$ . The cumulative size-frequency distribution displays the integral of the differential size-frequency distribution  $F(D)$ . The slope of the differential distribution is called the population index "a," where  $N = bD^a$ , or  $F(D) = bD^a$ . The relative size frequency distribution ratios the function  $F(D)$  to a reference distribution  $S(D)$ , commonly  $D^{-3}$ . Thus, if  $F(D) \propto D^{-3}$ , the slope of the Area Plot and the Relative Size Frequency Plot will be zero, i.e.

$$d(\log R(D))/d(\log D) = 0$$

A line of "-3 slope" has been used by Gault (1970) and others to designate some fraction of equilibrium or saturation of the cratered surface. On the Area Plot, a distribution of differential index  $a = -3$  will be horizontal. Positive slopes on the Area Plot represent indices of  $a > -3$ , and negative (downward left to right) slopes of the Area Plot represent indices of  $a < -3$ . Mathematical formulation of these functions are presented in the Workshop booklet noted above and reviewed in Appendix C.

A Poisson error distribution is assumed for the crater population. Frequency values and their 1 sigma error bars are thus:  $\log ((N \pm N^{1/2})/A)$  for the Cumulative Plot;  $\log (R \pm R/N^{1/2})$  for the Relative Size Frequency Plot; and  $\log (P \pm P/N^{1/2})$  for the Area Plot, (Crater Analysis...Group, 1978). The Area Plot format is emphasized in this work because it readily shows deviations from theoretical saturation or equilibrium distribution, i.e., deviations from the horizontal (Woronow, 1977a; Strom, 1977). Goodness-of-fit tests and regressions lines were not calculated. Area Plot slopes, where given, are estimates derived from slope of the linear part of the curve over a specified diameter range.

#### Signatures of Geologic Processes on a Crater Population

A surface which records all impacts upon it, without any one impact obliterating another, records the production population. The size-frequency distribution of the production population may take any form on the area or cumulative plots; the lunar post-mare population, for instance, forms a near-horizontal line (-2.8 slope) on the area plot at 0.1% coverage (Strom, 1977).

Degradation criteria as specified in Chapter 2 often indicate the age of the crater. By extension, the size-frequency distribution of a certain crater class may represent the population statistics for craters of a common age. However, the size of the crater, the distance of large and young events, and the criteria used for fresh craters

weaken this correlation. The first two factors refer to rapid degradation of small craters and proximity weathering, explained in Chapter 2. Area plots of C1 craters classified on the basis of continuous and sharp rims will not be equal to area plots of C1 craters classified on the degree of infilling by dust or ejecta (Woronow, 1979a).

The effects of common geologic processes on the total crater distribution and the degradation class distributions are summarized below. Secondary cratering is described in Section 3.

#### Saturation and Equilibrium

When the crater size-frequency distribution no longer changes with time, as impacts accumulate, the cratered surface reaches either saturation or equilibrium, depending on whether the obliteration process consists of simple overlap of crater rims, or additional processes respectively (Woronow, 1977a; Gault, 1970). The distribution of a saturated surface yields only general information on the generating function.

If the saturated distribution is horizontal ( $a = -3$ ), the generating function was negatively inclined,  $a < -3$ . If the saturated distribution is sloped upward, the generating function may also have been positively sloped, with  $-3 < a \leq -2$ . The value of the population index  $a$ , the slope of the area plot, and the magnitude of  $P(D)$  increase as the surface reaches saturation.

### Direct Basin Impact

Craters of all ages (classes) and sizes are destroyed within the excavation cavity. Crater densities are reduced by a factor which decreases with the age of the basin relative to the age of unaffected areas. The excavation cavity may suffer further resurfacing by volcanic extrusions. Wood and Gifford (1980) discuss the crater density reductions caused by the South Polar Aitken impact.

### Basin Impact--Periphery

A basin impact produces the most severe form of proximity weathering just outside the basin rim. Lunar studies (Strom, 1977) indicate that losses of small craters near the basin rim will steepen the area plot of that region by reducing  $P(D)$  at small  $D$ . The percent obliteration within the continuous ejecta blanket of the basin is greatest for the smallest craters; within 300 km ( $0.6 R$ ) radially outward from the Cordillera Scarp of Orientale, fully 80% of the craters 8 - 12 km in diameter are destroyed by the basin's continuous ejecta deposits (Woronow et al., 1979). (One may expect that similar destruction extends 278 km from the 870 km Altai Scarp of Nectaris.)

Severe degradation of large craters will increase abundances of C4 and C5 craters above normal levels; the extent of degradation decreases outward from the basin rim (Ronca and Green, 1969). Beyond the continuous ejecta blanket, one expects additions of basin secondaries; they may exceed the primary crater population, as shown in the next section (Wilhelms et al., 1977, 1978; Oberbeck et al., 1977; Woronow et al., 1979).

### Ballistic Plains Emplacement

A crater population affected by this mechanism may exhibit characteristics of basin proximity weathering, with its associated degradation, and volcanic plains emplacement, with its elimination of small and shallow craters. The degree of burial decreases radially away from the basin. This "signature" will be examined later in this chapter.

### Volcanic Plains Emplacement

Flood plain type flows will eliminate small craters and old shallow craters whose rim heights are less than or equal to the flow depth. Rims of larger craters are left intact although the interior and exterior of the crater may be embayed. The resultant area plot will steepen below a certain diameter, although densities and degradation classes of larger craters should not change. The resurfacing will eliminate most secondary craters. The lunar post-basin, pre-mare area plot exhibits the effects of mare flooding (Strom, 1977).

Typical crater distributions on Imbrian plains surfaces have roughly constant coverage of 1% to some diameter; coverage decreases abruptly for greater diameters. The size of the sampled area may determine the transition diameter. Mare areas have similar distributions, but about a tenth the magnitude of Imbrian plains. Nectarian plains sampled by Neukum and Horn (1976) and Beals and Tanner (1975) have higher levels of constant coverage. (See also Neukum, König, and Arkani-Hamed, 1975a; and Neukum et al., 1975b.)

## Endogenic Craters

Rimless, collapse-pit craters in a terrestrial volcanic lava field are represented by an area plot which reaches maximum coverage at some diameter possibly related to flow depth, and decreases in coverage for larger and smaller diameters. Such an addition to existing small crater coverage may increase the apparent age of the surface (Greeley and Gault, 1979). Size and degradational class characteristics are uncertain. Volcanic eruptions may produce secondary craters very close to the "primary" crater rim (e.g. Hartmann, 1967).

## Isostatic Equilibration

This process will eliminate larger craters and basins from the population; smaller crateriforms are unaffected over the same time-scale. The time for isostatic adjustment, as applied by Schaber et al. (1977) to Mercury's basins,

$$t_e = (20\eta)/(\rho gw)$$

varies directly with viscosity  $\eta$ , inversely with the half-width of the landform  $w$ , the density  $\rho$ , and the gravity  $g$ . A basin will adjust (i.e. lose its vertical relief) much more quickly than its secondaries. The loss of basin coverage decreases the slope of the area plot and makes that of the cumulative plots more negative at the higher diameters. Basins, of course, may be eliminated by both large and small impacts long before attaining isostatic equilibrium (e.g. South Polar Aitken and Mare Australe).

## Differential Preservation and Degradation Due to Target Properties

Consolidated and unconsolidated targets, like mare basalt and terra megaregolith respectively, differently affect morphology and preservation of superposed craters (Cintala et al., 1977; Thompson et al., 1979; Head, 1976b; and others). Pike, Roddy, and Arthur (1980) find that the transition diameter from simple to complex craters varies with the planet's gravity and target strength: Mercury's value of 16 km indicates its surface is "hard" or consolidated rather than extensively brecciated. Cintala et al. (1977) note a similar effect.

Craters formed in a megaregolith eject less blocky material (possibly reducing the secondary crater sizes), have less consolidated rims, and are degraded more quickly than craters formed in a consolidated surface by a similar projectile. Such processes may affect craters as large as 12 km on the Moon (Thompson et al., 1979). This effect may be offset by the smaller size of craters formed in more consolidated materials under the same gravity and velocity factors.

Craters formed in layered targets reflect the strength of the materials which form the more substantial portion of (i.e. dominate) the crater wall (Aggarwal and Oberbeck, 1979; Schultz, Greeley, and Gault, 1977; and Oberbeck and Quaide, 1968). When craters are better preserved, their coverage  $P(D)$  rises. Thus penetration of a lava flow overlying a megaregolith which overlies bedrock alternately raises, lowers, and raises coverage by small craters at increasingly larger diameters which are some multiple of each layer's depth (see also Young, 1975). This factor may vary from 5 to 8 depending on the depth-diameter relation used. This differential preservation may not apply to large craters. Schultz et al. (1977) set this limiting diameter at about 2 km. Scott (1977) discusses other mechanisms (higher impact velocities and ejection angles) which increase the preservation of secondary craters on Mercury. Shallow secondary craters--formed in lower energy impacts--may be differently affected by target composition and layering than primaries of the same diameter. (See the gravity and strength scaling section.)

#### Initially Degraded Craters

Secondary craters and volcanic craters may be formed in degraded states, artificially increasing abundances of similar size craters of the same degradational class (Oberbeck, 1975; Morrison and Oberbeck 1975, 1978).



## Erosion by Infilling with Dust or Ejecta

Infilling by dust or widely distributed ejecta, in addition to crater obliteration by overlap, reduces abundances of small and older craters. Degradation class area plots will not be parallel, since craters which are degraded to older classes (i.e., filled by dust) are more likely to be obliterated by continuing impacts. The limit of maximum coverage attainable before reaching equilibrium or a steady state is reduced by atmospheric erosional processes. Changing atmospheric conditions may cause changes in the area plot and its level of equilibrium (e.g. Woronow, 1977b, 1979a,b).

## Tectonic Processes

Mass wasting is likely to be associated with normal and thrust faulting and with impact generated seismic waves. The resulting rim degradation (or rejuvenation) and infilling may be severe enough to alter the degradation-class statistics. The area plot will steepen if smaller craters are destroyed; at larger diameters, C5 populations may be filled by the degradation of craters contemporary with the tectonic event. Modification may be localized, focused on antipodal areas, or global (Schultz and Gault, 1975a,b, 1976; Hughes, App, and McGetchin, 1977; O'Donnell, 1978). Unless collapse depressions form, no craters are expected to be added to the existing population, unlike the effect of a basin impact. Effects such as those described above for erosional infilling by dust are to be expected for mass wasting.

## Gravity and Strength Scaling

Mercury's higher gravity and the expected higher velocities of projectiles impacting its surface may have offsetting effects on crater size. Gault et al. (1975) document how gravity affects the range of ejecta and possibly the morphology of mercurian craters, although the latter effects are disputed by Malin and Dzurisin (1977, 1978). The scaling of crater diameter with gravity or target strength is still not well defined (e.g. Gault and Wedekind, 1977; Gaffney, 1978). Strength scaling is responsible for the differential preservation of small craters (Schultz et al., 1977). In this case, diameter is a function of the one-third power of kinetic energy. For targets of no strength, or for large craters, gravity scaling requires that diameter vary with the one-fourth power of kinetic energy (or the negative fourth root of gravity). The experimentally derived value lies between these functions;  $D \propto g^{-.165 \pm .005}$  at fixed velocity and energy (Gault and Wedekind, 1977). The restricted range of ejecta on Mercury will reduce infilling of craters distant from the impact, reduce the radial extent of proximity weathering from basins and craters, and will reduce the width of the continuous ejecta blanket (Gault et al., 1975). Ranges of ejecta on the Moon and Mercury are illustrated by Strom (1979).

## External Processes: Changes in the Bombarding Population

Externally imposed changes in the crater statistics will result from changes in the impacting population--its size-frequency

distribution, its flux, or its source. These changes may be recorded in crater statistics if the above affects can be minimized (especially partial losses of craters) or utilized (especially the completely resurfaced areas): e.g. Guest and Gault, 1976; Whitaker and Strom, 1976; Oberbeck et al., 1975. Increased flux or increased size of the bombarding objects may increase degradation rates and alter the general type of degradation (e.g. Head, 1975). Flux rates, however, can only be determined if absolute ages are available for craters or the surfaces on which they lie (e.g. Hartmann, 1977).

The geologic and external processes which affect crater statistics, as presented above, will be used to determine the processes affecting lunar and mercurian crater populations. The most important of these may be basin formation and volcanic flooding, although other effects are anticipated. Note that differential preservation may indicate both lava flows (consolidated layers) or basin ejecta deposits (unconsolidated layers).

#### Secondary Cratering on the Moon and Mercury

In this limited study of secondary cratering, two large, lunar craters were chosen whose secondaries are superposed on adjacent mare regions. Ideally, the objectives were to (1) quantify the addition of secondary craters to a post-mare production population, and (2) apply that algorithm to secondary cratering in the lunar highlands. Significant studies of secondary cratering from basin sized impacts are

reviewed, with particular focus on the Nectaris basin. Some characteristics of secondary cratering on Mercury are also discussed. To apply the lunar studies to the mercurian surface, the effects of increased gravity and impact velocities must be evaluated.

#### Secondary Cratering From Fresh Lunar Craters

Mare areas northeast of Copernicus (95 km in diameter) and northwest of Langrenus (136 km in diameter) were divided in annuli of width equal to one or one-half the primary crater radii (e.g., Fig. 37). Within each annulus, crater diameters, degradation classes, and distances to possibly interfering primaries were noted. The most important results of the data are enumerated below. Secondary crater diameters are scaled to the diameter of the primary, and ranges are scaled to the radius of the primary and measured from its center.

In the Langrenus area, to a distance of 6 R, craters of sizes 0.01 D to 0.04 D have nearly equal coverage of  $\sim 2.5\%$  (Fig. 38). The post-mare background averages 0.1% coverage (Strom, 1977). Fresh secondaries (C1 and C2) reach a maximum coverage only one fourth the combined total for craters which are 0.03 to 0.04 the primary diameter.

The maximum coverage for secondaries of a certain size and range (Fig. 39) occurs for craters of 0.03 D (0.026D to 0.05D) within a radial range of 1.5R to 2.0R from Langrenus and 2R to 3R from Copernicus. The greater scaled range of the Copernicus secondaries

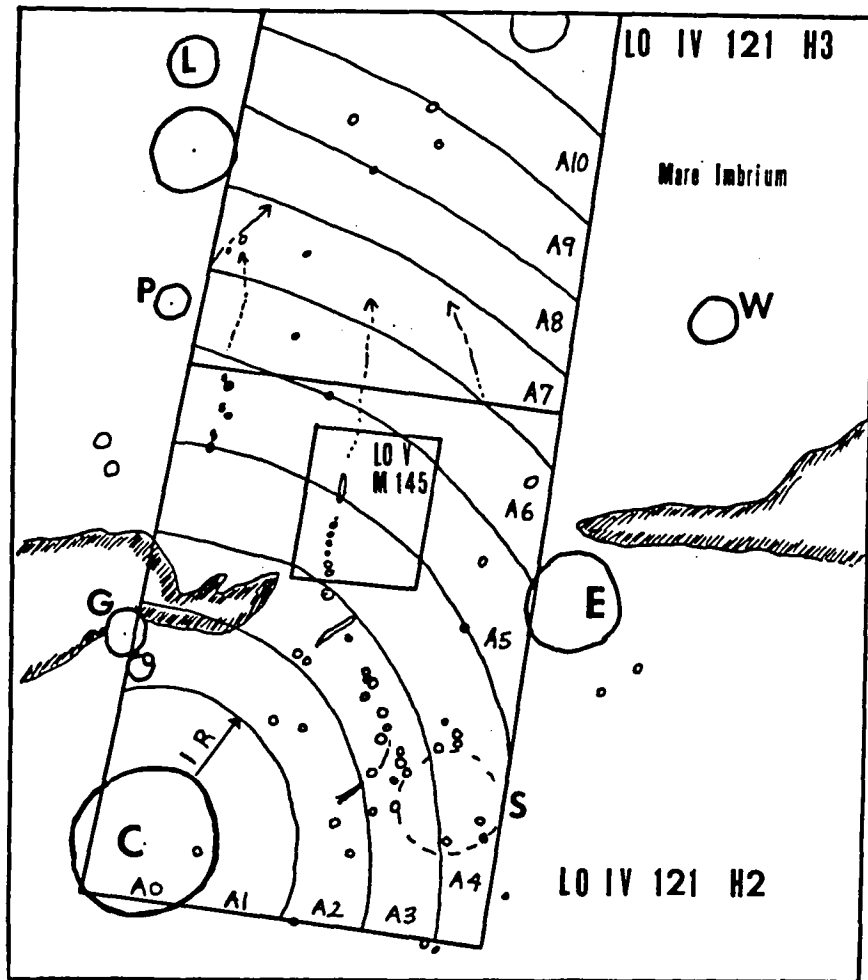


Fig. 37. Sketch Map of Copernicus Area Used In Secondary Crater Study

Annuli of one Copernican radius (47.5 km) in width extend north of Copernicus into Mare Imbrium. Craters greater than 2.45 km were tallied in Annuli A0 - A3, greater than 1.84 km in A4 and A5, and greater than 1.22 km in A6 - A9. Total area =  $1.069 \cdot 10^5 \text{ km}^2$ . Abbreviations are: C - Copernicus, E - Eratosthenes, S - Stadius, G - Gay Lussac, P - Pytheas, L - Lambert, and W - Wallace. Stippled regions are highland massifs. Statistics for this region can be found in Tables D16 and D17 of Appendix D. Langrenus area is similarly divided, but annuli are 0.5 R in width; see Tables D14 and D15.

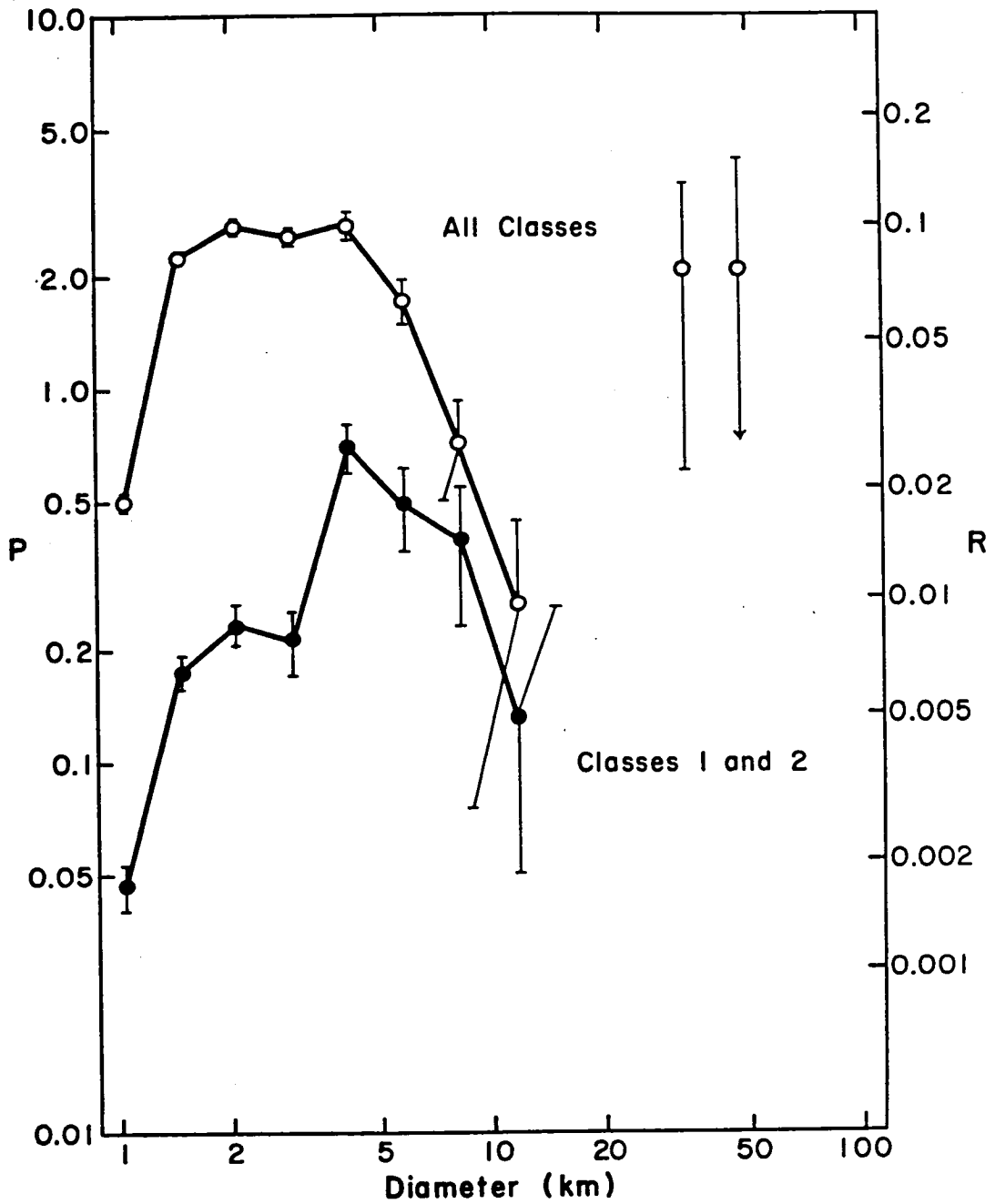


Fig. 38. Crater Coverage of Mare Region Northwest of Langrenus

Percent coverage  $P(D)$  by craters of mean diameter  $\bar{D}$  km in Mare Fecunditatis, northwest of Langrenus. Right ordinate  $R(D)$  is the Relative Frequency Factor discussed in text.

suggests that the Copernicus impact was more energetic than the Langrenus impact, although other factors may be involved (e.g. slumping, Settle and Head, 1979; Melosh, 1977c).

As the secondary size increases, the range of peak coverage decreases, moving inward to the rim of the primary, as expected from earlier studies of Shoemaker (1962) and Oberbeck and Morrison (1974). Early in the impact event, more highly shocked comminuted material is ejected at higher velocities from regions near the center of the transient crater; this material travels to the greatest ranges and impacts after the rim-forming ejecta. Larger fragments are ejected at lower velocities from regions closer to the transient crater rim. The volume of material ejected increases with time, and with the expanding radius of the shock front, forming the rim and continuous ejecta blankets (Oberbeck and Morrison, 1974, 1976; Shoemaker, 1962).

Craters nearest the primary rim are more degraded; presumably, the debris surge blankets the area following secondary excavation. Fresher secondaries in a particular size group reach peak coverages at greater radial ranges, usually 1 R farther, than more degraded craters of that size. The greater diversity in degradation class found at greater ranges results from (1) lack of debris surge blanketing and (2) increasing significance of the local primary population.

Allen (1979) shows that the average maximum secondary diameter is  $(0.04 \pm 0.006) D$  and its range is  $2.8D^{0.89}$ , i.e. about 3.3-3.4 radii from the primary crater. (Compare Fig. 11 of Wilhelms et al. (1977), who find that secondary range is  $5.2 R_p^{0.9}$ , where  $R_p$  is the radius of the primary.) Allen finds that maximum secondary size and range vary nearly linearly over three orders of magnitude from 100 m to 250 km. Copernicus and Langrenus are included in his sample. Note (on Fig. 39) that the craters contributing the greatest areal coverage at 1.5R to 2.0R are only slightly smaller, 0.03 D, than the maximum size secondary, 0.04 D.

Percent coverage of the maximum size secondary peaks at a range of 2.5 R- 3.0 R with coverage P(D) one half that of the more numerous smaller secondaries. The last substantial contribution of the larger secondaries, about 2%, occurs within the range 3.0 R to 3.5 R, consistent with that determined by Allen (1979). At that range, the numerically dominant secondaries of diameters 0.01 D contribute 2.6% coverage.

Although secondary densities of Langrenus and Copernicus differ in detail, perhaps due to different impact energies, age, or target consolidation, plots of their number density distributions versus range in primary diameters are similar (Fig. 40). Number densities ( $N/\text{km}^2$ ) of secondaries are highest for small craters of



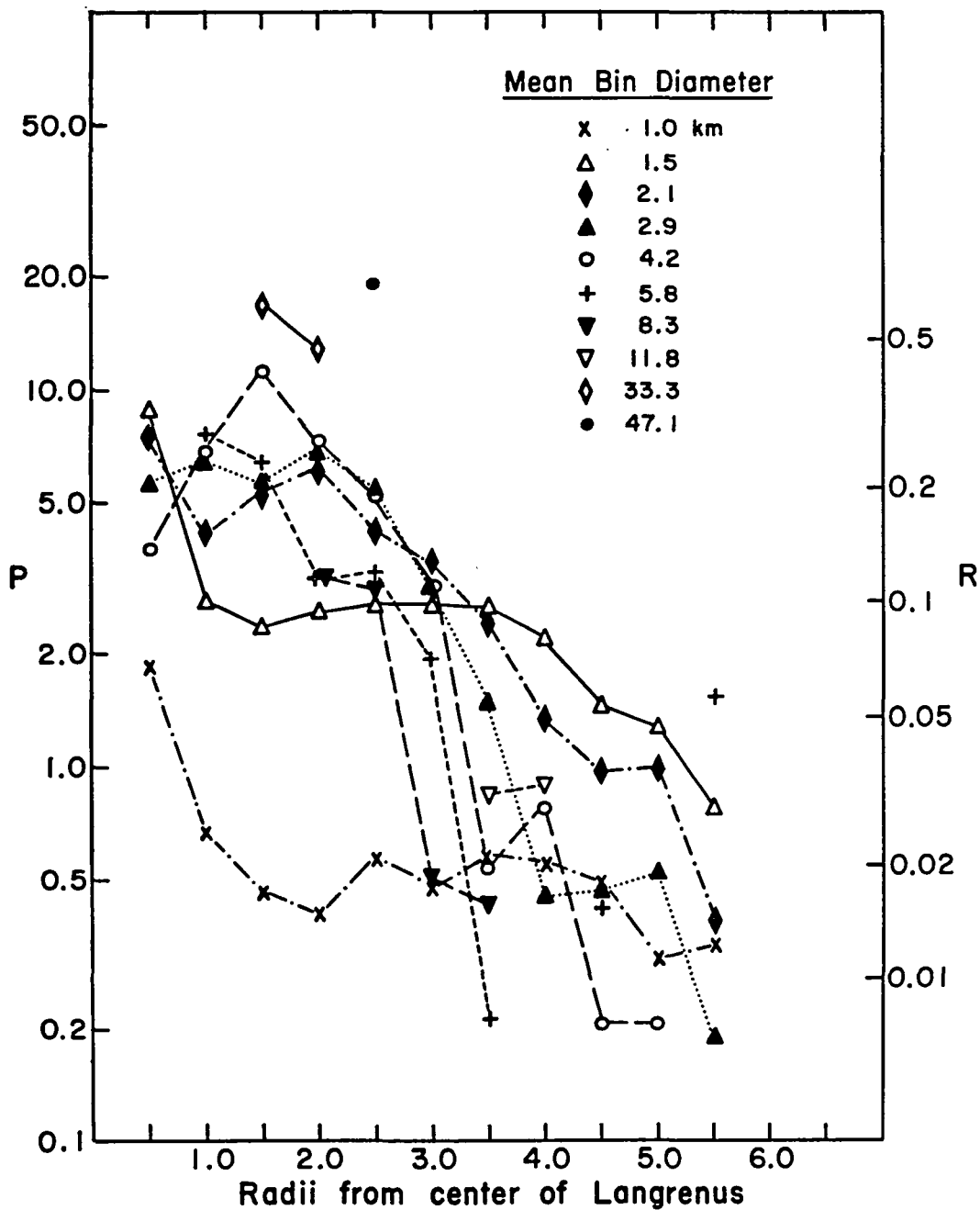


Fig. 39. Coverage by Specific Size Crater Within Specific Range From Langrenus

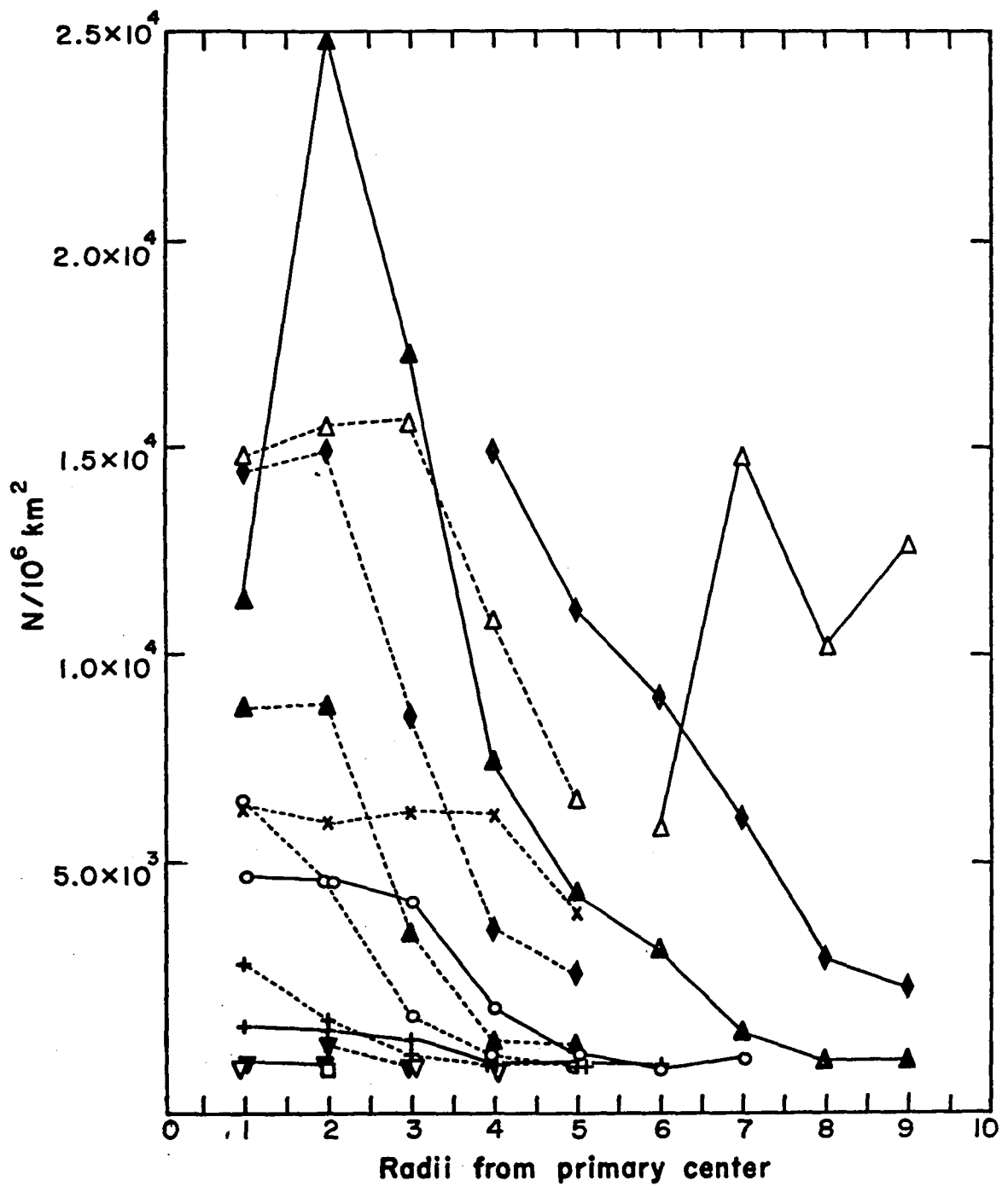
Craters larger than 8.3 km are likely to be primaries unrelated to the Langrenus impact. Such "field" craters are included in these statistics. The relation of these crater sizes to primary crater Langrenus (D = 136 km) is given in the table accompanying Fig. 40.

Fig. 40. Areal Densities ( $N/km^2$ ) of Specific Size Crater Within Specific Range of Langrenus and Copernicus

Solid line refers to Copernicus data where range of 1.0 radius is 47.5 km. Dashed line refers to Langrenus data where range of 1.0 R is 68 km. Note the variation in cut off diameter for Copernicus number densities; see Fig. 37. The table below lists mean diameters expressed as a fraction of the primary crater diameters,  $D_L = 136$  km for Langrenus and  $D_C = 95$  km for Copernicus. Symbols are the same as those used in Fig. 39.

Diameter of Secondary as Ratioed to Primary

$\bar{D}$ (km)	$\bar{D}/D_L$	$\bar{D}/D_C$
1.0	0.01	0.01
1.5	0.01	0.02
2.1	0.02	0.02
2.9	0.02	0.03
4.2	0.03	0.04
5.9	0.04	0.06
8.3	0.06	0.09
11.8	0.09	0.12



diameters  $0.01 D$  at a range of  $2 R$  to  $3 R$  from the primary's center (see also Gault et al., 1975). Numerical density calculations imply that degraded craters of the smallest measured diameter are most common well outside the continuous ejecta blanket, at ranges greater than  $2.5 R$ . Inside that range, slightly larger but still degraded craters are most abundant.

#### Secondary Cratering by Lunar Basins

Secondaries of lunar basins have lower scaled sizes and ranges than those of large lunar craters; this factor is partly dependent on the basin ring chosen to represent the crater's diameter (see Wilhelms et al., 1977). Studies of Orientale show that fresh secondaries of sizes  $0.01$  to  $0.02$  times the basin's outer scarp-diameter contribute significant coverage at ranges of  $2$  to  $3.2$  times the radius of this scarp (Woronow et al., 1979). Smaller secondaries (above the  $7$  km limit of the LPL catalogue) contribute marginally detectable coverage within that range, and secondaries larger than  $0.02 D$  are insignificant at ranges beyond  $3.2 R$  (see also Wilhelms et al., 1977, and Allen, 1979).

When scaled to the Altai Scarp of Nectaris (Table 7), the range of significant bombardment by Nectarian secondaries of scaled size  $11$  to  $19$  km in diameter extends from  $890$  km to  $1390$  km, encompassing much of the northern pre-Imbrian plains. As noted in Chapter 2, Wilhelms (1976b) has identified probable secondaries of Nectaris in

Table 7: Scaled Secondary Diameters and Ranges for  
Orientale and Nectaris Basins

Parameter	Basin Ring Values in Kilometers					
	N1	N2	N3	01	02	03
$D_p$ *	400	600	870	480	620	940
$D_s = 0.01 D_p$	4.0	6.0	8.7	4.8	6.2	9.4
$D_s = 0.03 D_p$	12.0	18.0	26.1	14.4	18.6	28.2
$D_s = 0.04 D_p$	16.0	24.0	34.8	19.2	24.8	37.6
1.5 R	300	450	652.5	360	465	705
3.0 R	600	900	1305	720	930	1410
4.0 R	800	1200	1740	960	1240	1880

\* Ring diameters from Wilhelms, Hodges, and Pike, 1977

$D_p$  = Diameter of primary; R = Radius of primary

$D_s$  = Diameter of secondary

N = Nectaris; 0 = Orientale

this region. The shallow, degraded secondary craters closer to the basin rim may be more easily embayed by subsequent deposits than the fresher, deeper secondaries at greater ranges. These results suggest that Nectaris' secondaries should be apparent in the LPL statistical data, especially at ranges of 2R to 3R from the basin center. Secondaries are numerous south and southeast of the basin. The Janssen Formation extends  $2.7 R_A$  from Nectaris' center; Rheita Valley (formed by Nectaris' secondaries) extends 1.3 R to 2.7 R. (The pIp exposures begin at 1.6 R.)

The magnitude of coverage by secondaries of Imbrium and Orientale, averaged over the nearside lunar surface, reaches 1.0% and 0.5% respectively, nearly 2 to 5 times greater than coverage of Imbrian-age primaries (Wilhelms et al., 1978; see Fig. 41). The resulting population of 5-15 km Imbrian-age craters is dominated by basin secondaries (Fig. 42).

Wilhelms has recently noted (1980) that basin morphology is often irregular because of oblique impact of the projectile; Nectaris may be such an example. The ejecta distribution and secondary distribution visible today (the Janssen Formation and the Rheita Valley, for instance) are indeed surficially asymmetric, indicating an impact from the southwest. This has some serious implications, some of which are related to the Zagut degradation problem. If the region now occupied by the pitted plains southwest of the basin is in the forbidden zone

uprange of the trajectory, it may have been spared substantial amounts of both continuous and discontinuous ejecta (Gault and Wedekind, 1978). The pre-Imbrian pitted plains may not embay a great thickness of the ballistically emplaced continuous deposits of Nectaris (the pIj unit), as Scott (1972) had concluded. On the other hand, if these deposits are embayed by the pre-Imbrian terra and the pitted plains, there is less reason to conclude that the deposits are asymmetric, and the impact oblique.

#### Secondary Cratering on Mercury

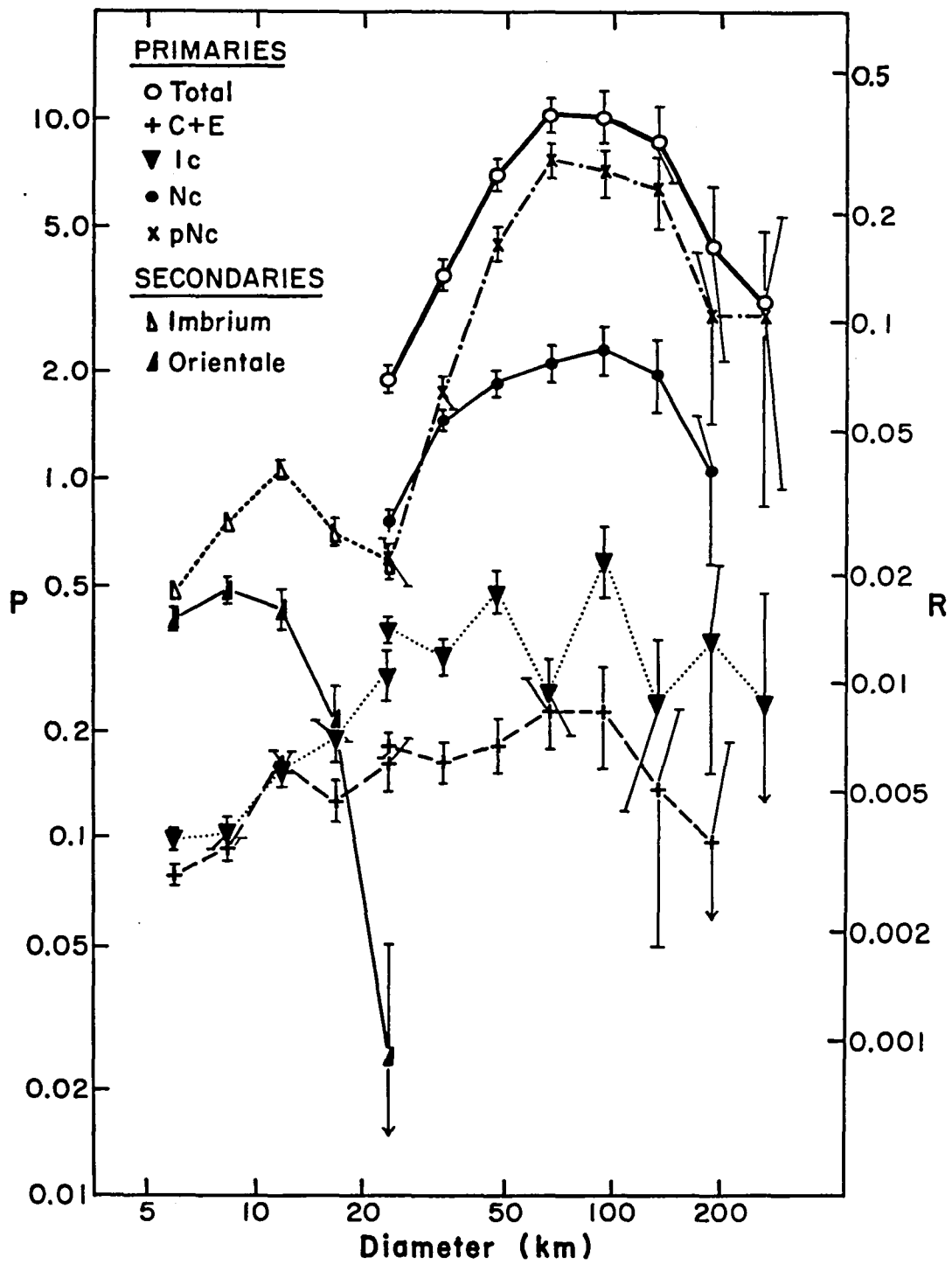
Secondary cratering on Mercury differs from that on the Moon in the following ways: (1) Range of continuous and discontinuous deposits is less on Mercury (due to its higher gravity, Gault et al., 1975); (2) secondaries reach a larger size relative to the primary crater (this study); and (3) secondaries are better preserved (Scott, 1977; Trask, 1976a,b).

Mercury's secondaries are often superposed on the continuous ejecta blanket and so closely spaced that they form broad, radial troughs; both effects may result, in part, from high ejection angles. Higher impact velocities, which cause ejection velocities of debris to be 50% higher on Mercury than on the Moon (Scott, 1977), and higher ejection angles contribute to preservation of secondary craters on Mercury. With greater energy and a steeper descent, the ejected mass produces a larger and deeper secondary, which is less easily degraded than its lunar counterpart.

Fig. 41. Crater Coverage of Lunar Surface From  
Wilhelms et al. (1978) Data

Primary craters of different time stratigraphic ages were sampled by Wilhelms et al. (1978) using specific criteria to exclude possible secondaries. Four age groups are represented by statistics for craters greater than 20 km: Copernican and Eratosthenian (C + E), Imbrian (I), Nectarian (N), and Pre-Nectarian (pN), from youngest to oldest respectively. Younger primaries and secondaries are included in statistics from 5 - 20 km over a limited area of the nearside. The data were rebinned and are presented in the areal coverage format above. Note the high coverage by secondaries of Imbrium (Isc) and Orientale (Isco) on the lunar nearside. Further discussion in Section 3 of this Chapter.





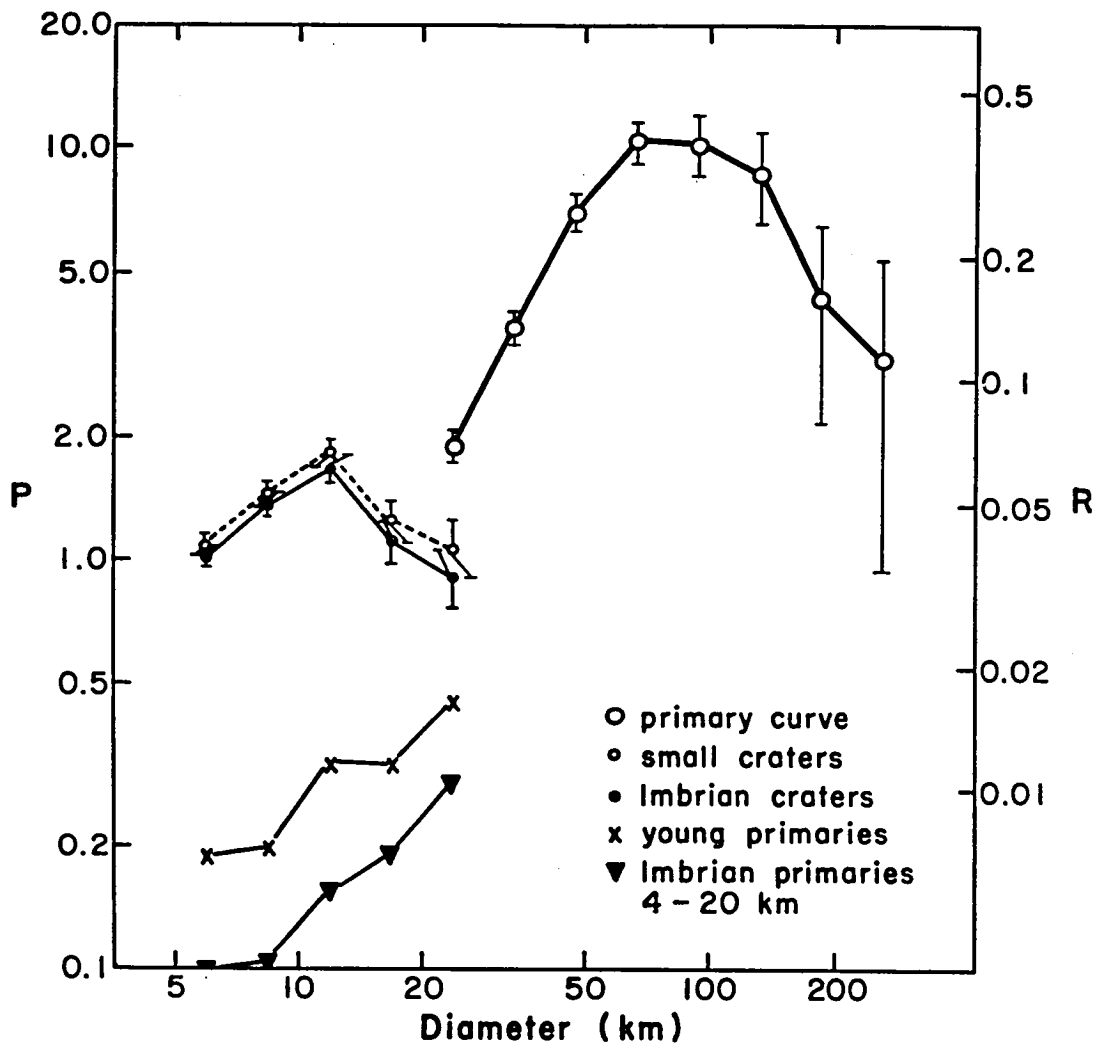


Fig. 42. Total Crater Coverage of Lunar Surface Using Wilhelms et al. (1978) Data

Large primaries include Copernican through pre-Nectarian craters; small (5-20 km) craters include secondaries and primaries from Copernican to Imbrian systems. Gap between total primary curve and total small crater curve may be due to Nectarian and pre-Nectarian primaries (and secondaries) less than 20 km in diameter. Wilhelms et al.'s data show an apparent "secondary hump" for lunar craters of 10 - 15 km diameter.

The secondary crater's ejecta is also constrained. The concentration of tertiary ejecta may reduce the distribution of locally excavated, plains-forming material (Oberbeck, 1975). The fresh, large craters Mozart and Ts'ai Wen-chi, for example, do not appear to produce plains material around their periphery.

Maximum areal density of secondaries (Chapter 2) occurs at 2.4 R to 2.5 R from the primary crater center (Mouginis-Mark, 1978; this distance is about .12 R from the edge of the continuous ejecta blanket). Gault et al. (1975) show that the mercurian range (2R to 3R) is less than the analogous distance for lunar craters, 2.5 R to 4R. The enhanced destructive effects of this concentration of ejecta on Mercury is offset, over a large area, by the ejecta's more limited extent (Malin and Dzurisin, 1977; Woronow, 1977 a,c). The resurfacing potentials of mercurian craters and basins do not appear to be as great as those of lunar craters and basins. Small pre-impact structures are noted even under the concentrated continuous ejecta blankets of larger craters and basins, such as Caloris, Bach, and the basin under Hitomaro (Strom et al., 1978).

In a preliminary survey of secondary craters on Mercury, the largest secondaries were found to be 0.07-0.05 times the primary crater diameter; some are as large as 0.1 D. Smaller secondaries are, of course, more common. In other respects, they are like lunar secondaries: they overlap downrange, have weak interference ridges

(herringbone patterns, Oberbeck and Morrison, 1974; and Oberbeck and Aggarwal, 1977), and become deeper downrange (Mouginis-Mark, 1978; see Fig. 43). The maximum range of large secondaries is 5 R from the primary's center. Linear troughs radial to large basins extend to distances of 3R to 4R from the basin's center. Close to the basin rim, some troughs appear to be filled by continuous ejecta deposits.

The rayed craters form exceptions to those comments. They have remarkably large, "smooth," continuous ejecta blankets which extend 3R to 5R from the primary center (as compared to 1.88 R for normal fresh craters studied by Gault et al., 1975). Their ejecta, however, is not sufficient to fill adjacent older craters of half their size. High resolution images of Mozart suggest that rays are concentrations of unresolved secondary craters, extending outward tens of diameters. A high velocity, low angle ejection, as suggested by Cintala (1979 a,b), from rayed craters, e.g. at  $10^\circ$  from the horizontal and at 2.25 km/sec, will project material  $\sim 1000$  km (from Fig. 6b in Strom, 1979). Allen (1977) argues that rays include primary ejecta, as well as tertiary material. The diameter-frequency distribution of the rayed craters on Mercury and the Moon suggest that they are a high energy subset of the fresh crater population (the post-Caloris craters on Mercury, and the C1 craters of the Moon).

#### Discussion of Additional Studies of Secondary Cratering

Opinions on the contribution of secondary cratering to a primary population vary markedly but usually reflect an assessment (and

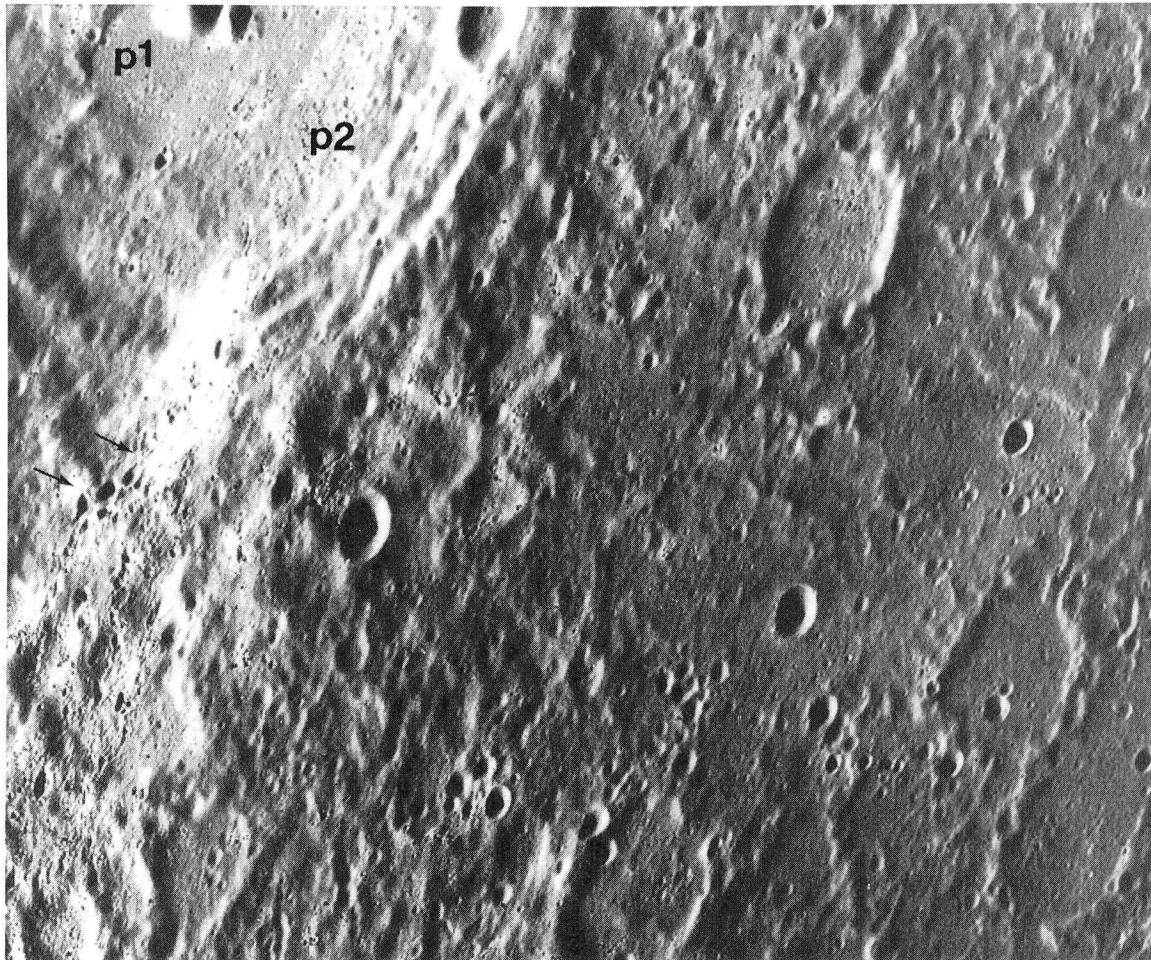


Fig. 43. Secondary Craters from Kuiper Superposed on Rim of Fresh "Transition-Size" Crater

Secondaries from Kuiper (along left edge of photo) are arranged in clusters and radial chains, overlap downrange, and have discernible herringbone patterns. Interference ridges (arrows) occur downrange of the secondaries. High albedo material of the ray is apparently associated with secondary cratering. The largest Kuiper secondaries visible here are 2.5 to 3.3 km diameter, or 0.04 - 0.05 times Kuiper's diameter of 60 km.

This high resolution photo of Fig. 14a shows the incipient peak ring shelf and the inner depression. The outer shelf materials, mapped as P2 plains, are more rugged and cratered than the P1 deposits of the central depression. Both units, however, are cratered by secondaries of the C1 crater Kuiper.

FDS 27474. North at top. The flat floored crater at top right is 18 km in diameter.

avoidance) of local contributions. Gault (1970) calculates that secondary cratering from a hypothesized impact flux would not be substantial until after one billion years of bombardment, i.e. after substantial numbers of larger bodies had impacted the surface. The Nectarian age of the pre-Imbrian plains may represent 4.2 to 3.9 b.y. of bombardment, but only 0.2 to 0.6 b.y. in that interval spanning the heaviest impact flux.

Although Schultz et al. (1977) conclude that effects on crater distributions due to secondaries are minimal and only local, they too avoid secondary material. Similar diameter-density distributions for small craters (5-500 m) were found in highland and mare areas, showing a dependence on regolith depth and not on additions of secondary craters. The opposing viewpoint is held by Wilhelms: as shown in Chapter 2 above, additions of basin secondaries appear to overwhelm the primary crater population from 5 km to at least 20 km diameter (Wilhelms, 1976b, 1979; Wilhelms et al., 1977, 1978).

Studies of Langrenus and Copernicus suggest that the addition of secondaries is noticeable in the mare, where background coverage is 0.1%. If the ratio of secondaries to a primary is the same in the highlands as in the mare, one expects greater numbers of secondaries in the heavily cratered highlands. They may contribute to the 2% to 4% "background" coverage noted in the highland areas. More substantial coverage from secondaries of 0.03 D may elevate P(D) in the vicinity

of large fresh craters. Such local contributions may be illustrated in the lunar (and mercurian) selected area statistics.

How significant is secondary cratering on Mercury? Trask (1976a, p. 473) notes that "The observed population of larger craters and basins 50 km in diameter and larger yield a background density of secondaries slightly below those shown in Fig. 1." His statistics for the southern polar region are illustrated by Strom (1977) reproduced in Fig. 49 of the next section. The "hump" in the mercurian curve at 15 km diameter has thus been interpreted as partly due to secondary craters from primaries in the heavily cratered terrain which have diameters 10 to 20 times larger than the secondaries. Recent statistics of Woronow, Strom, and Gurnis (1980) show no "hump." However, the studies completed here suggest that there are significant contributions of degraded craters below 10-15 km which appear to be secondaries. Watkins' (1980) statistics of the young craters of the Caloris plains also show a minor increase in crater density at 15 km, but few "primary-size" (source) craters.

#### Cratering Histories of the Lunar Intercrater Plains

Hypotheses advanced for the origin of the intercrater plains of the lunar nearside are similar to those proposed for the intercrater plains of Mercury. The position of the lunar unit, far from the youngest known basins, suggests a primitive surface (Oberbeck et al., 1977). Yet proximity to Nectaris argues for an origin through deposition of ballistically emplaced ejecta (Howard et al., 1974; Wilhelms,

1976b). Finally, morphologic similarities to volcanic plains, plus mineralogical evidence in other regions of the Moon, have revived the pre-mare volcanism hypothesis (e.g. Strom, 1977).

Cratering studies were divided into three programs. The first studies diameter/density distributions of craters greater than 1-3 km in diameter for selected plains and terra units of the intercrater region. A second study utilized existing diameter and degradation data (Wood and Andersson, 1978a) for craters over 7 km in four regions separated by the 45° S latitude and the central meridian. The third study entailed dividing three quadrants examined by Strom (1977) into heavily cratered and non-heavily cratered areas, similar to plains and crater divisions on Mercury, and computing diameter-degradation statistics for those areas.

#### Crater Statistics of Selected Lunar Areas

The first program of cratering studies presents statistical data on the pre-Imbrian pitted plains (pIp) and adjacent units for five areas located generally outside the large, overlapping crater clusters (Fig. 44). Data on diameter, degradation class, floor diameter, shadow length, and presence in a chain or cluster were collected for craters of 1-3 km diameter and greater, thus extending the 7 km diameter limit accessible with the LPL Catalog of Lunar Craters (Wood and Andersson, 1978a).

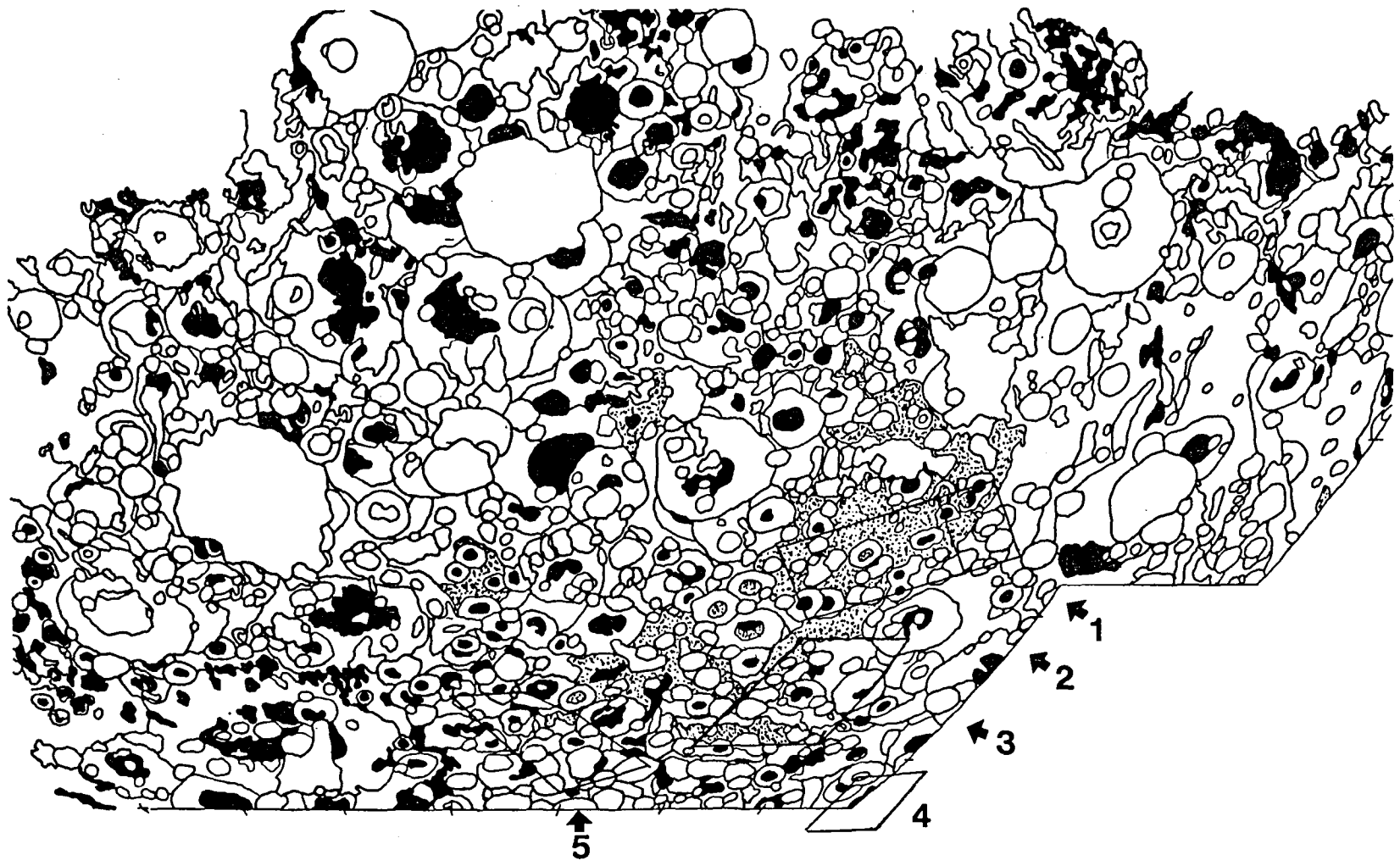


The individual pre-Imbrian pitted plains units were found to differ little in density distribution from the other pre-Imbrian to Imbrian-age surfaces studied. These surfaces include pre-Imbrian terra near Spallanzani, pre-Imbrian ridged terra and pre-Imbrian smooth terra near Ascelpi, Imbrian smooth plains east of Mutus in the "flow lobe" area, and Imbrian cratered plains. All are included in the Pre-Imbrian Plains of Wilhelms and McCauley (1971). Their area plots are commonly V-shaped, with peaks in coverage for craters of diameter 1.5 km to 2.5 km and 14 km to 28 km. Areal densities in the pitted plains were usually greater than that of other units for craters of diameters 1-5 km, but lower than other units for craters greater than 10 km.

When combined, the southern highland selected regions' area plot (Fig. 45, with key to symbols, Fig. 46) shows constant coverage between 3.5 - 7 km, with peaks at  $\bar{D}$  equal to 3 km and 17 km. The average slope of this plot is represented by an index of -2.7. The non-pitted plains (non-pIp) units show a broad peak in coverage from diameters of 10 to 28 km. The area plot (Fig. 47) is nearly identical to the combined southern highlands because non-pIp units comprise most of the selected areas. Degraded craters contribute heavily to the small crater population; C3 craters dominate over the entire diameter range. The pitted plains area plot (Fig. 48) is roughly horizontal at a high level of coverage. (Its constant coverage may have resulted from averaging two out-of-phase V-shaped plots.)

Fig. 44. Locations of Selected Regions and Imbrian and Pre-Imbrian  
Plains of Lunar Southern Highlands Adapted From  
Wilhelms and McCauley (1971)

Black regions indicate Imbrian plains (Ip) units; stippled regions are pre-Imbrian (pitted) plains (pIp) as mapped by Wilhelms and McCauley (1971). Outlined areas selected for crater statistical studies are: Area 1 - Lockyer G; Area 2 - Spallanzani; Area 3 - Ascelpi; Area 4 - Mutus Flow Lobe; Area 5 - Jacobi. See also Fig. 29. Mare Nectaris is located near top right.



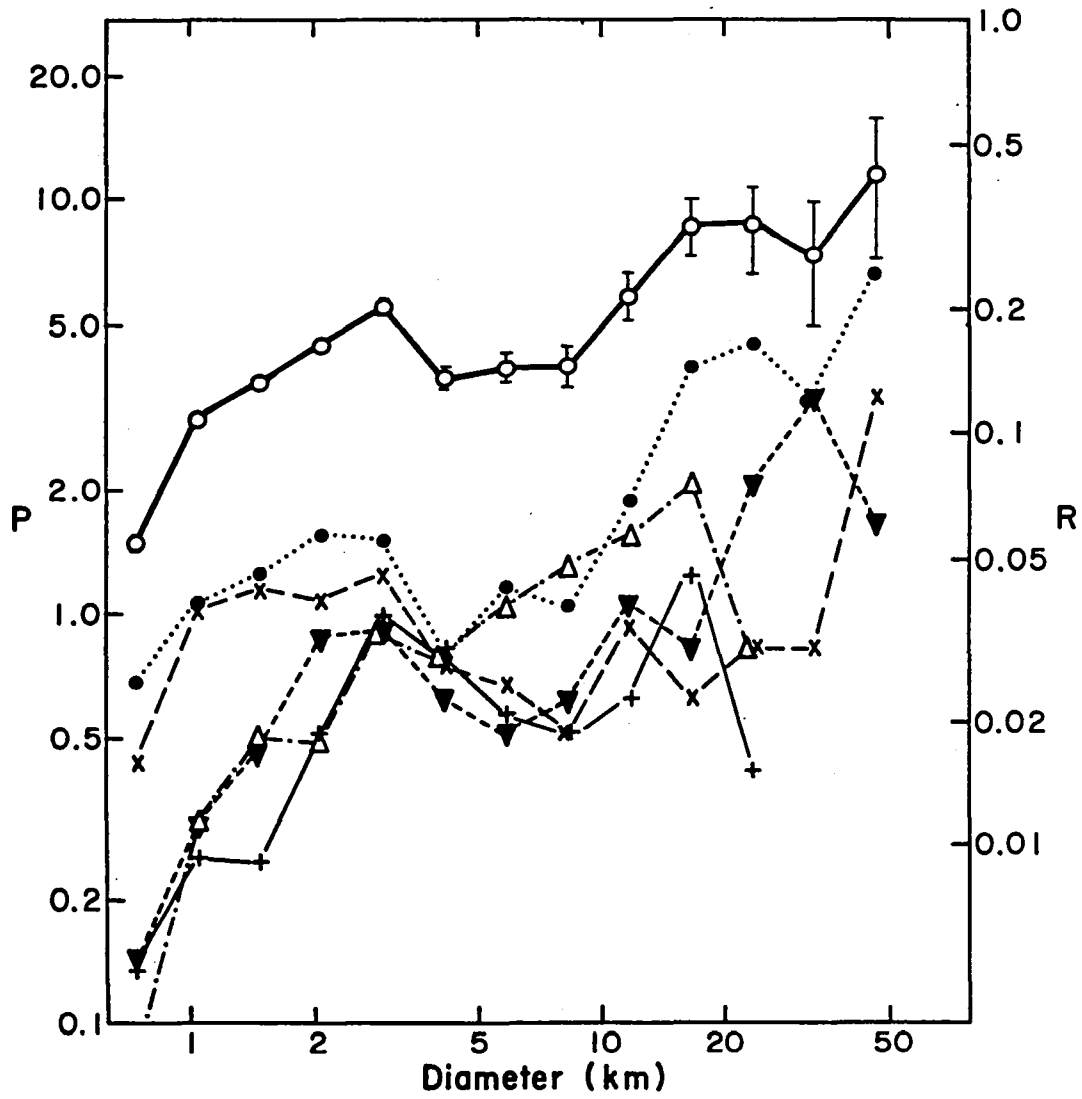


Fig. 45. Crater Coverage of Selected Regions in the Lunar Southern Highlands

Key to symbols given in the following figure. Data given in Appendix D, Table D6.

**Key to Symbols  
on Cumulative and Area Plots**

LPL Crater Class	Symbols
$C_1$ Freshest	+-----+
$C_2$	▽-----▽
$C_3$	●.....●
$C_4$	x-----x
$C_5$ Most Degraded	△-·-·-△
$C_5 + C_5'$	▲-·-·-▲
<hr/>	
Total      All classes, $\pm 1\sigma$	○-----○
Total      Hilly and lineated terrain	⬤-----⬤
Total      All classes except $C_5'$	*-----*
<hr/>	
Post Caloris $C_1 + C_2$	▽-----▽
Caloris $C_3$	●.....●
Pre Caloris $C_4 + C_5$	△-----△
$C_4 + C_5 + C_5'$	▲-·-·-▲

Fig. 46. Key to Symbols on Cumulative and Area Plots

These symbols are used in all subsequent plots of crater statistics of the mercurian and lunar surfaces.

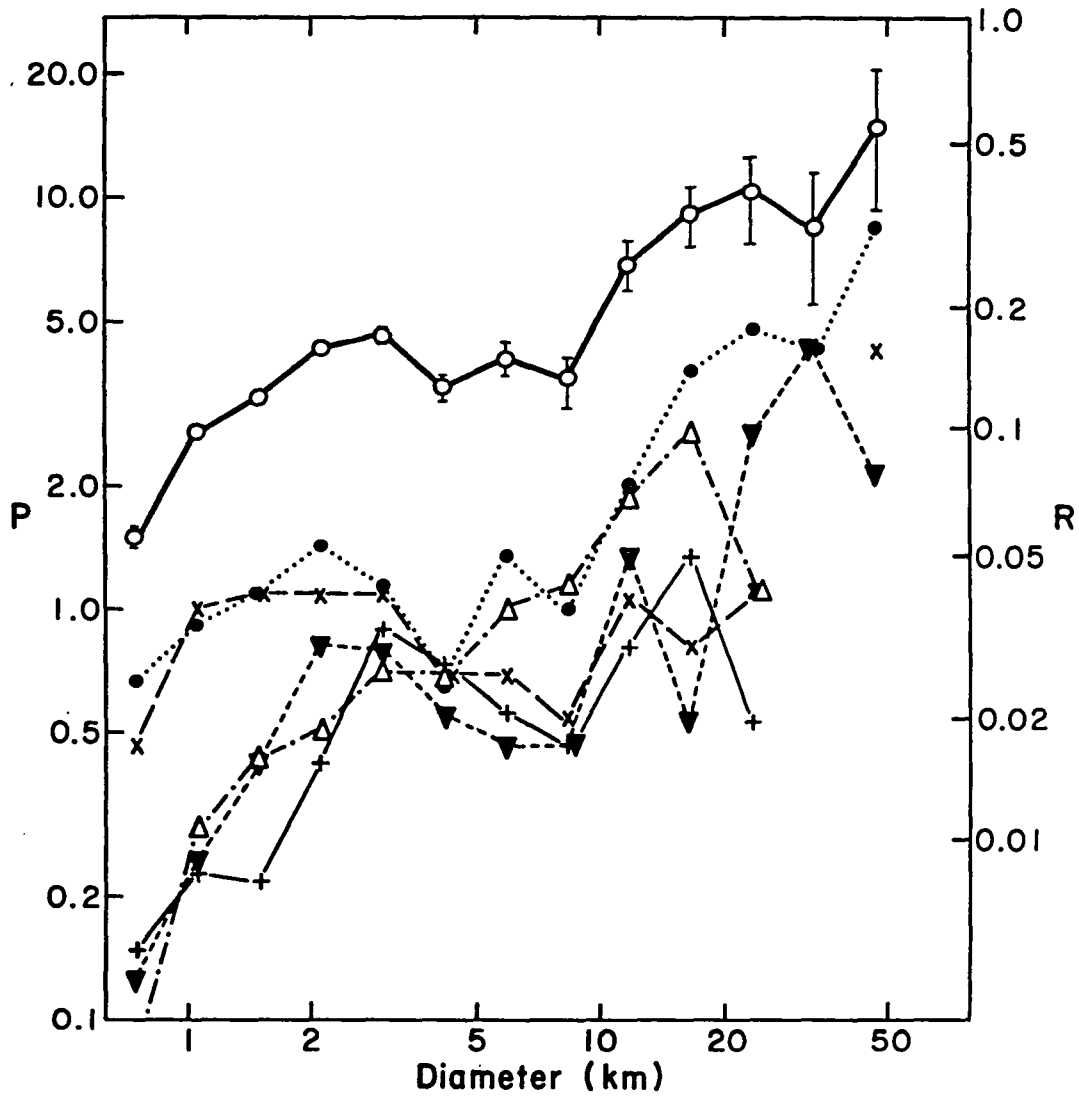


Fig. 47. Crater Coverage of Selected Regions Exclusive of Pitted Plains

Data presented include pit units of Areas 1 and 2, all units of Areas 3, 4, and 5; see Table D8 of Appendix D. (Symbols in Fig. 46.)

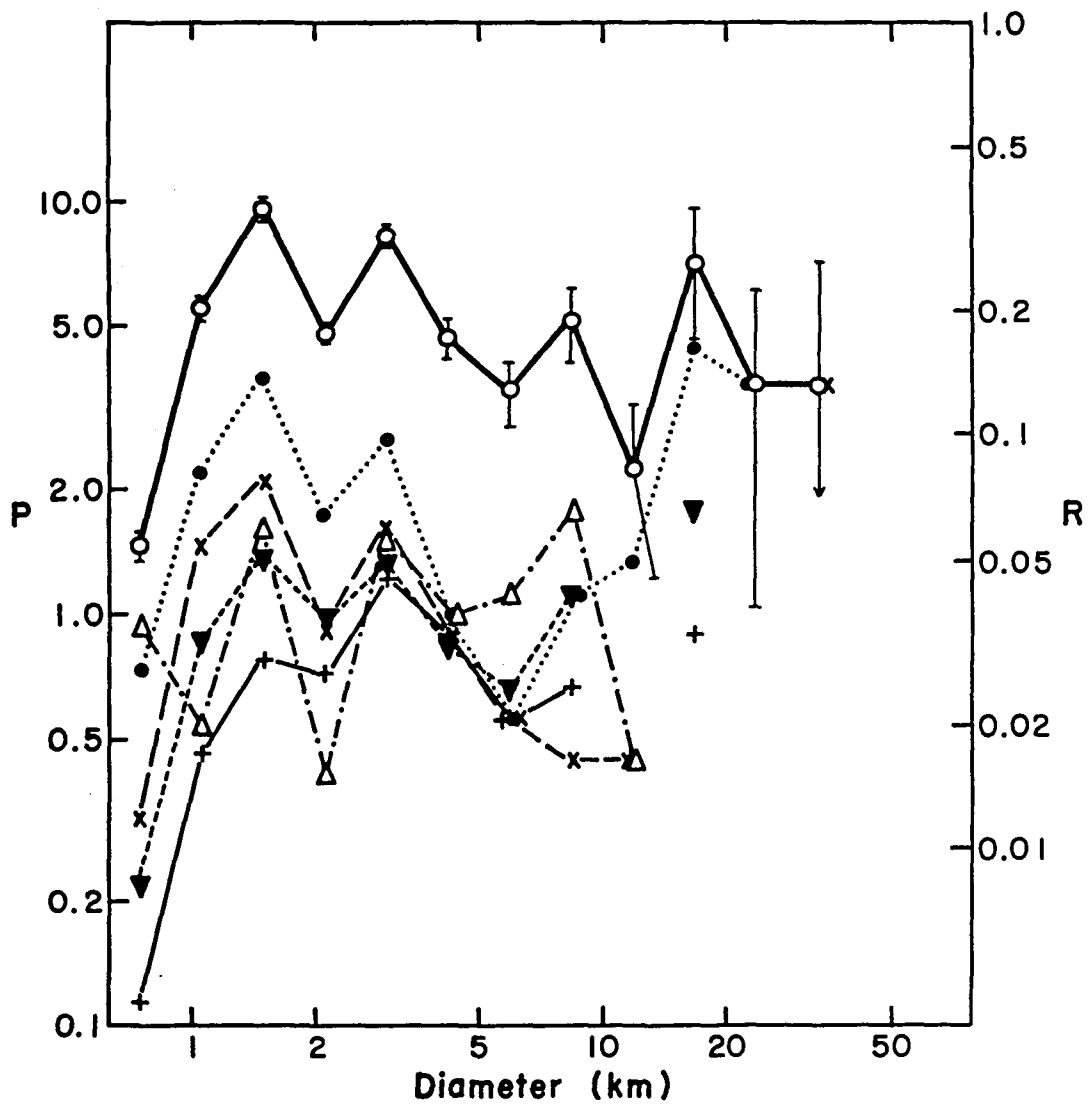


Fig. 48. Crater Coverage of Pre-Imbrian Pitted Plains

Statistics of pIp units of Areas 1 and 2 are presented; see Table D7 of Appendix D. Poor statistics at large diameters are a result of the smaller area sampled and the exclusion of large craters from the pitted plains (pIp) unit of Scott (1972).

The magnitude of coverage at small diameters on these plots may not be unusual. Area plots of crater statistics of central highland plains (Ip unit; statistical data in Greeley and Gault, 1970) show a constant coverage at comparable magnitudes,  $P(D) = 4\% - 6\%$  from diameters of 14 meters to 1 km. However, the combined area coverage by craters of diameters of 7 km to 30 km exceeds values determined by Whitaker and Strom (1976) and Strom (1977) for the central lunar highlands (see Fig. 49).

The principal enigmatic feature of the crater distributions in these selected areas, also noted by Mutch and Saunders (1972) and Young (1975), is that small-crater densities on the plains units are higher than on the terra units. The older terra are not able to retain, or do not have, a great abundance of small craters. Even C1 coverage on the plains exceeds that on the non-pIp units, although both units are nearly equal in average age and both are emplaced prior to the C1 craters. Another major characteristic of the pre-Imbrian plains is precisely their lack of large craters; the size of the "larger" craters may unfortunately depend on the observer's or mapper's definition.

The nearly zero slopes of the combined and pitted plains area plots do not suggest losses of craters by volcanism, ballistic deposition, or tectonic destruction (Sec. 2). Instead, the statistics of



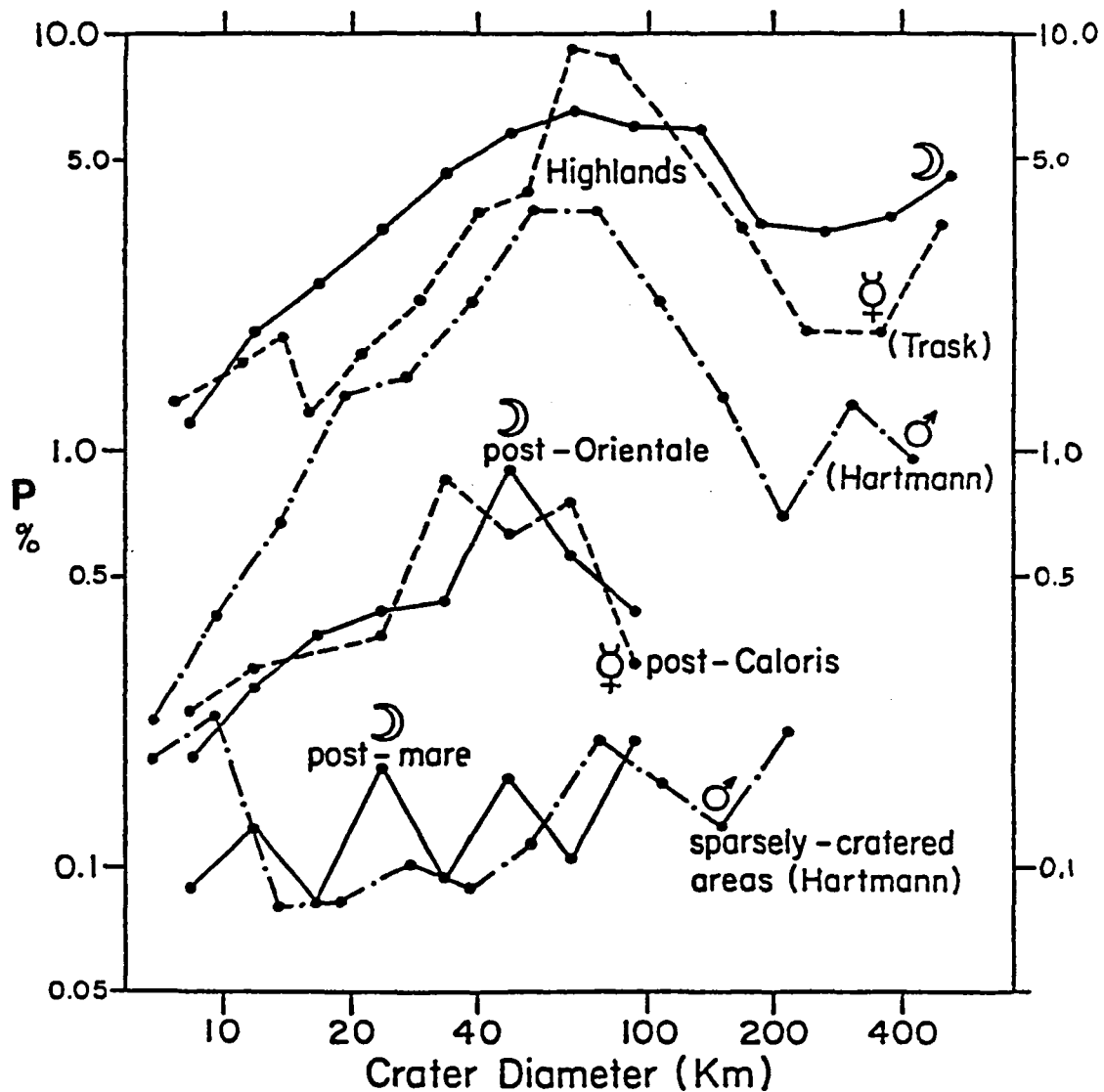


Fig. 49. Crater Coverage of Planetary Surfaces From Strom (1977)

Lunar curve plotted by Strom (1977) displays highland statistics of 7-150 km craters in Clavius Region from the LPL Catalog (Wood and Anderson, 1978a). Larger craters and basins were sampled over the entire lunar surface. Note that  $P(D)$  values over the 7-30 km size range are much less than those of selected regions (Fig. 45, 47, 48). These data are discussed later in this section.

selected areas suggest that secondary cratering and differential preservation determine the V-shaped plot. If volcanism and resurfacing had occurred, small-crater densities have been subsequently increased by either of the two above mechanisms (secondary cratering and preservation on a consolidated surface). Although the diameters sampled here may be too large to apply theories of differential preservation (Schultz et al., 1977), the V-shaped plot may reflect a deep unconsolidated layer sandwiched between two consolidated layers. The lower layer may be bedrock, and the upper layer, the pitted plains surface. Nectaris ejecta and the megaregolith may comprise the middle layer (Aggarwal and Oberbeck, 1979; Thompson et al., 1979; Hartmann, 1973; Oberbeck and Quaide, 1968; and Young, 1975).

If the relative peaks in the area plots are due to secondaries, one expects source craters of 25 to 30 times the diameter of craters at the peak in coverage; 30 km to 90 km primaries and a primary of about 510 km diameter. The large craters of the southern highlands and the Nectaris basin are the probable sources of these secondary craters. The major factors affecting any secondary population in any locality are the size, age and distance of the primary, and the age of the surrounding surface (the intercrater plains) relative to the primary crater. These factors will be further assessed in the large-crater statistics of the next section.

## Crater Statistics of Sectors of the Southern Highlands

In a second cratering study, crater statistics from the LPL Catalog (Wood and Andersson, 1978a) were compiled in four general areas divided by the central meridian and latitude  $45^{\circ}$  S (Fig. 50). Northern and southern extents were  $24^{\circ}$  S to  $75^{\circ}$  S and east to  $40^{\circ}$  -  $60^{\circ}$  E, west to  $30^{\circ}$  -  $50^{\circ}$ . The regions are labelled C, D, S, and T starting clockwise from the northwest quadrant. Region S encloses most of the pre-Imbrian plains units, "D012" corresponds to the Werner area of Strom (1977), and "T012" corresponds to his region about Clavius. (Region "C01" includes Tycho.)

The percent coverage of crater material can be computed by summing the P(D) values for all diameter bins over a certain set of diameters. The cumulative coverage by craters greater than 40 km diameter was depressed in the areas dominated by pre-Imbrian plains (S123) relative to regions around Clavius (T012) to the west and Werner (D123) to the north. Large craters cover from 20% to 32% of the intercrater regions, compared to 46% to 53% in the peripheral areas, including an area just east of the central meridian from Licetus to Simpelius (S0). Coverage by craters of 7-40 km diameter is slightly larger for the intercrater areas (26%) relative to surrounding zones (18% - 22%). The comparison of cumulative crater coverage confirms one's visual impression that the intercrater areas have fewer large (40 km and greater) craters and an abundance of smaller craters.

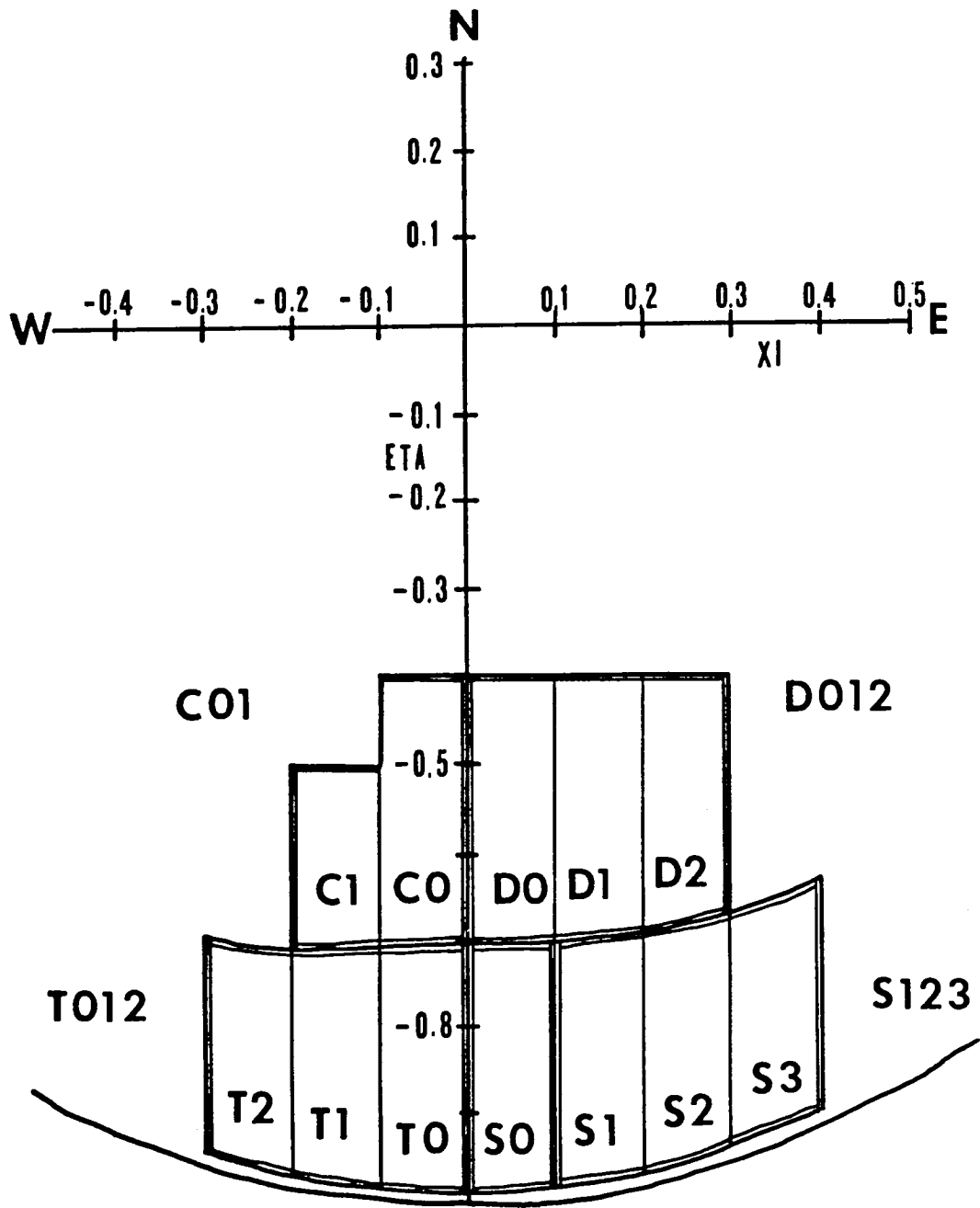


Fig. 50. Locations of Southern Highlands Sectors C, D, S, and T

Orthographic Eta-Xi projection of lunar nearside adapted from Wood and Andersson (1978a). Informal sector names are: C01 "Tycho," D012 "Werner," S123 "Cuvier" (pre-Imbrian plains area), S0 "Jacobi," and T012 "Clavius."

Differences in the area plots of crater distributions on these surfaces (Fig. 51-55) are quite apparent; their interpretations, however, are not. Slopes of area plots of the C01, D012, and T012 quadrants agree with the curves of Strom (1977) for nearly equivalent regions (see also composite in Fig. 56). Within the Clavius area the density of small 7-20 km craters increases westward; presumably these could be Orientale or Humorum secondaries. No such systematic rise occurs eastward toward Nectaris in the S quadrant, although densities of 14 to 28 km craters are higher than those of the Clavius area. A more positively sloped plot (index  $a = -1.6$  from 12 to 56 km) was determined for the S0 sector. In this region, densities of larger craters 33-80 km were higher than those of the T012 region; small craters were abundant, but less so than the S123 region to the east. Major exposures of pre-Imbrian plains occur in the S123 sector.

Strom's (1977) analysis of the intercrater plains shows that their mode of degradation is similar to that of volcanic flooding and unlike that of areas dominated by Cayley-like deposits on the periphery of basins (Sec. 2). The region which may be affected by volcanic flooding is in the southernmost part of the S quadrant, nearly out of range of the Nectaris ejecta. This area may not be completely analogous to the intercrater--pIp units studied here. However, the characteristics of volcanic flooding (steep slopes and a lack of C5 craters on the area plot) may be applicable to the S123 region if

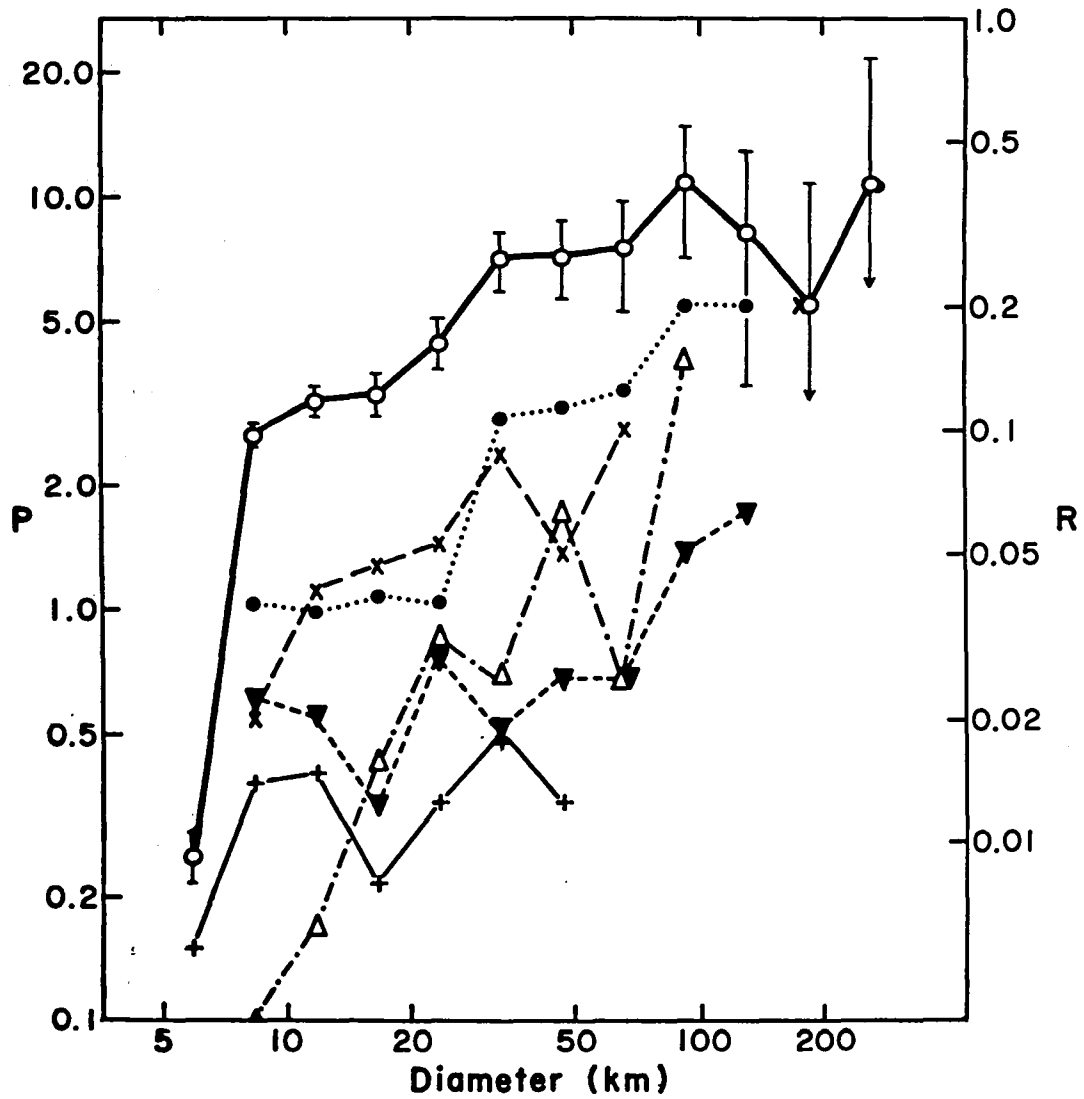


Fig. 51. Clavius Region (T012) Crater Coverage

Statistics of region cited by Strom (1977) as representative of southern lunar highlands. See also Fig. 56. Symbols given in Fig. 46.

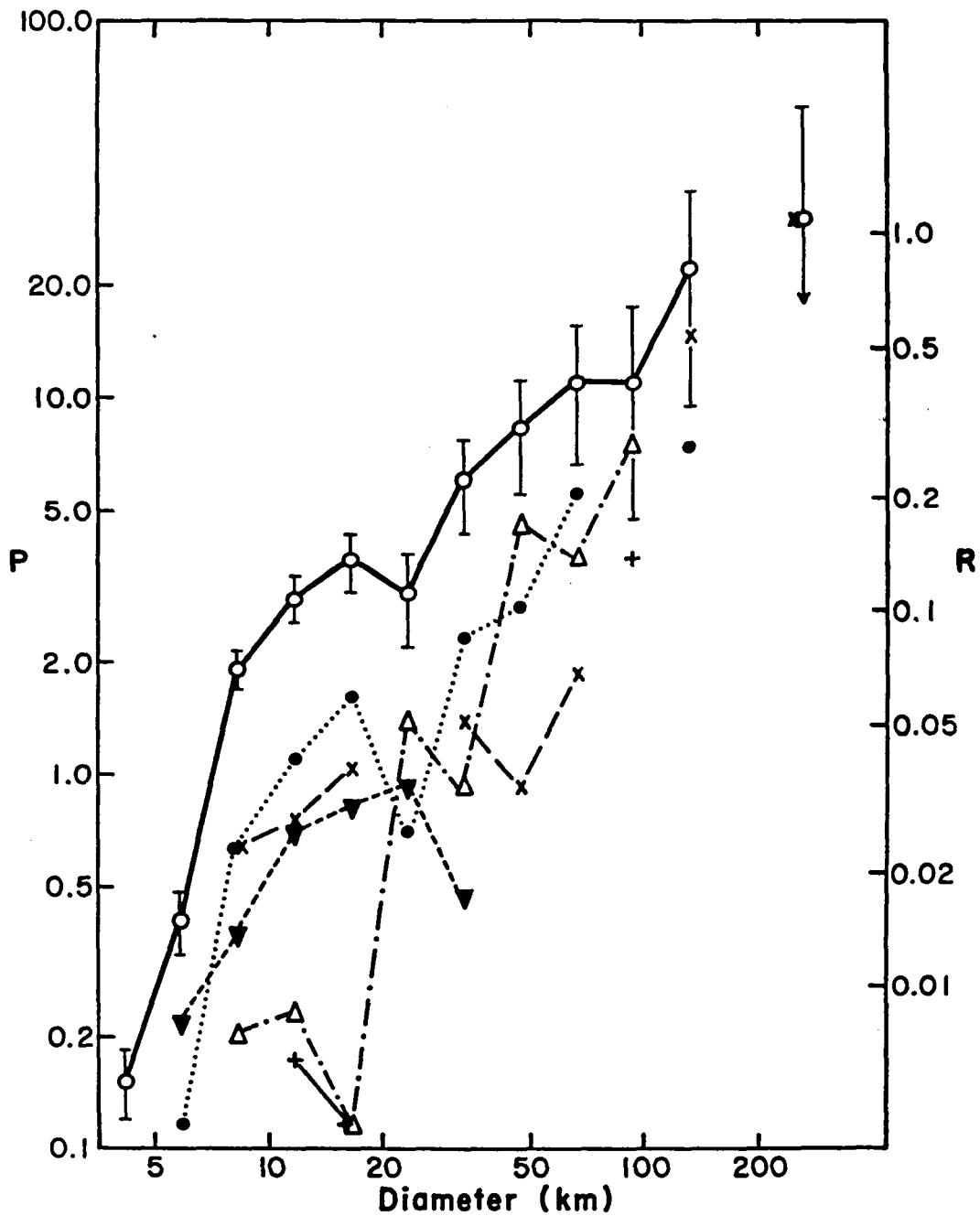


Fig. 52. Tycho Region (C01) Crater Coverage

Note apparent increase in slope of curve. Increase in coverage by large C5 craters and decrease in coverage by small C3 and C2 (Imbrian) craters may be the result of destruction and resurfacing by debris from the Imbrium impact.

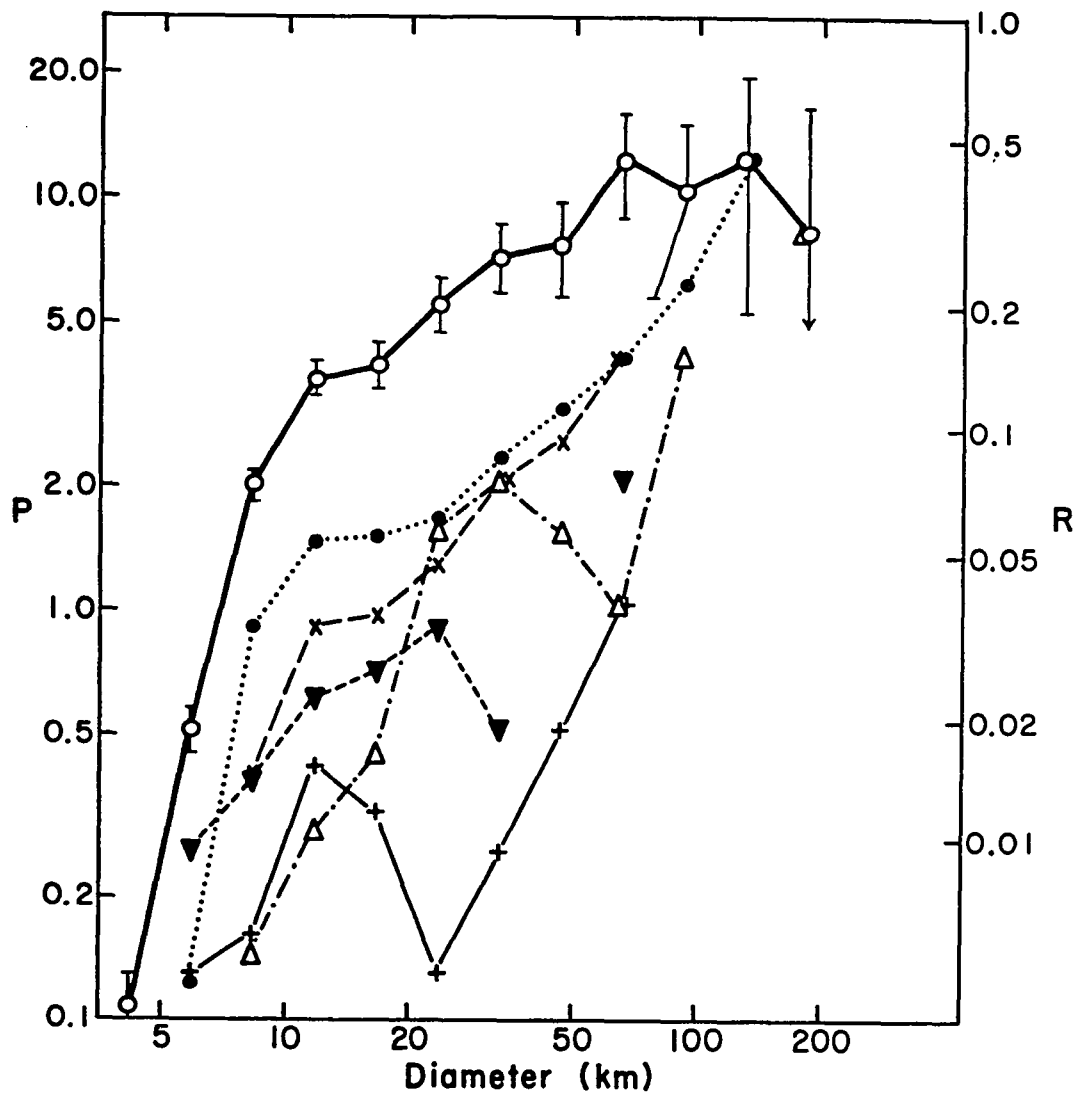


Fig. 53. Werner Region (D012) Crater Coverage

Increased coverage by large ( $\geq 20$  km) degraded craters, increased numbers of 10-15 km Imbrian craters, and deficiencies of 7-10 km craters relative to the T012 area may indicate degradation, resurfacing, and burial by Imbrian impact debris and Cayley plains material.



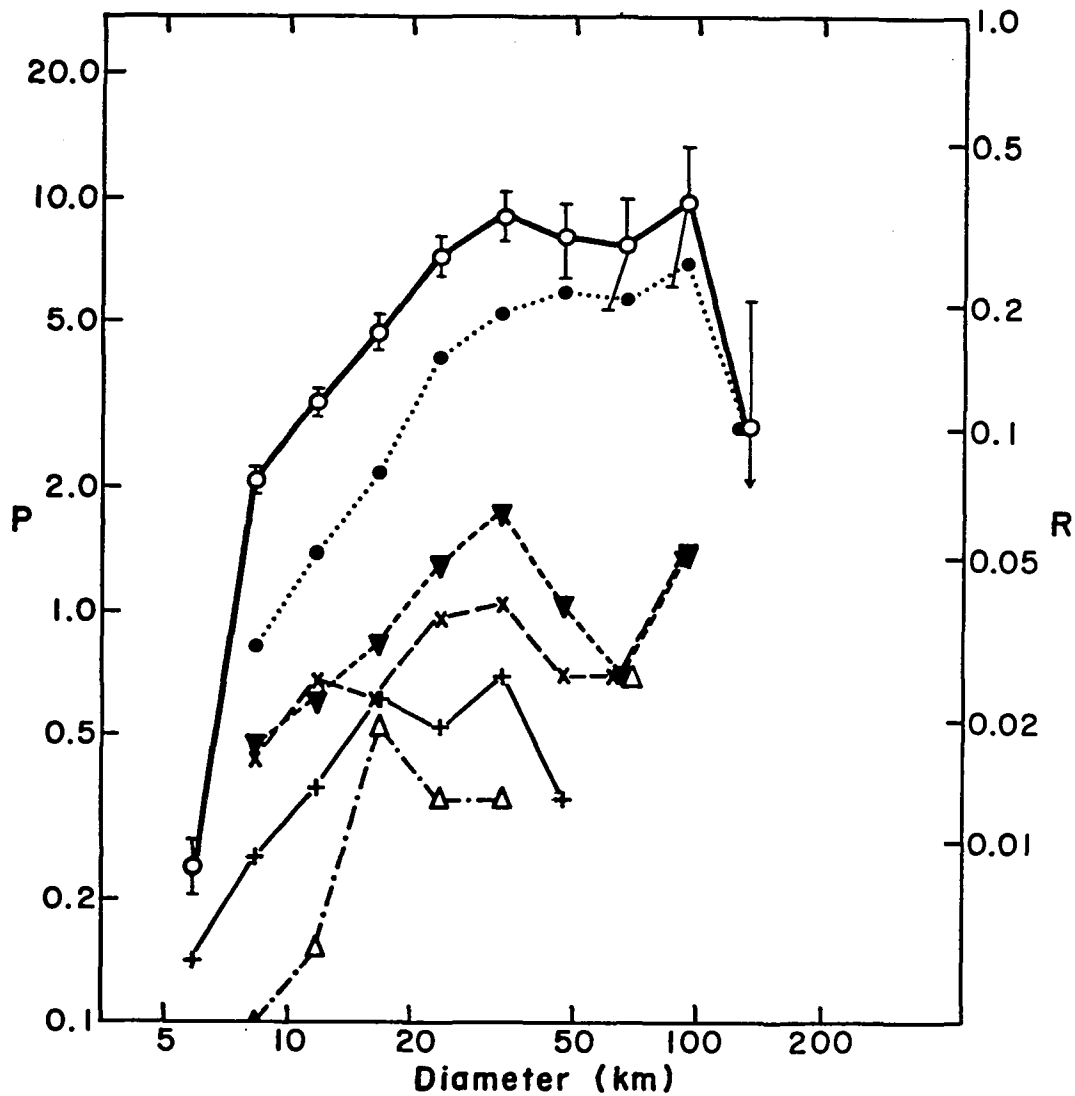


Fig. 54. Cuvier Region (S123) Crater Coverage

Pre-Imbrian Plains are most abundant in this sector. Note the steeper area plot, dominance of C3 and C2 craters, absence of C5 craters, and deficiency of 7-10 km craters relative to the Clavius sector statistics. Differences between the S123 statistics and those of Werner indicate a different mode of crater degradation and resurfacing, possibly burial by volcanic flows which leave rims of large craters intact.

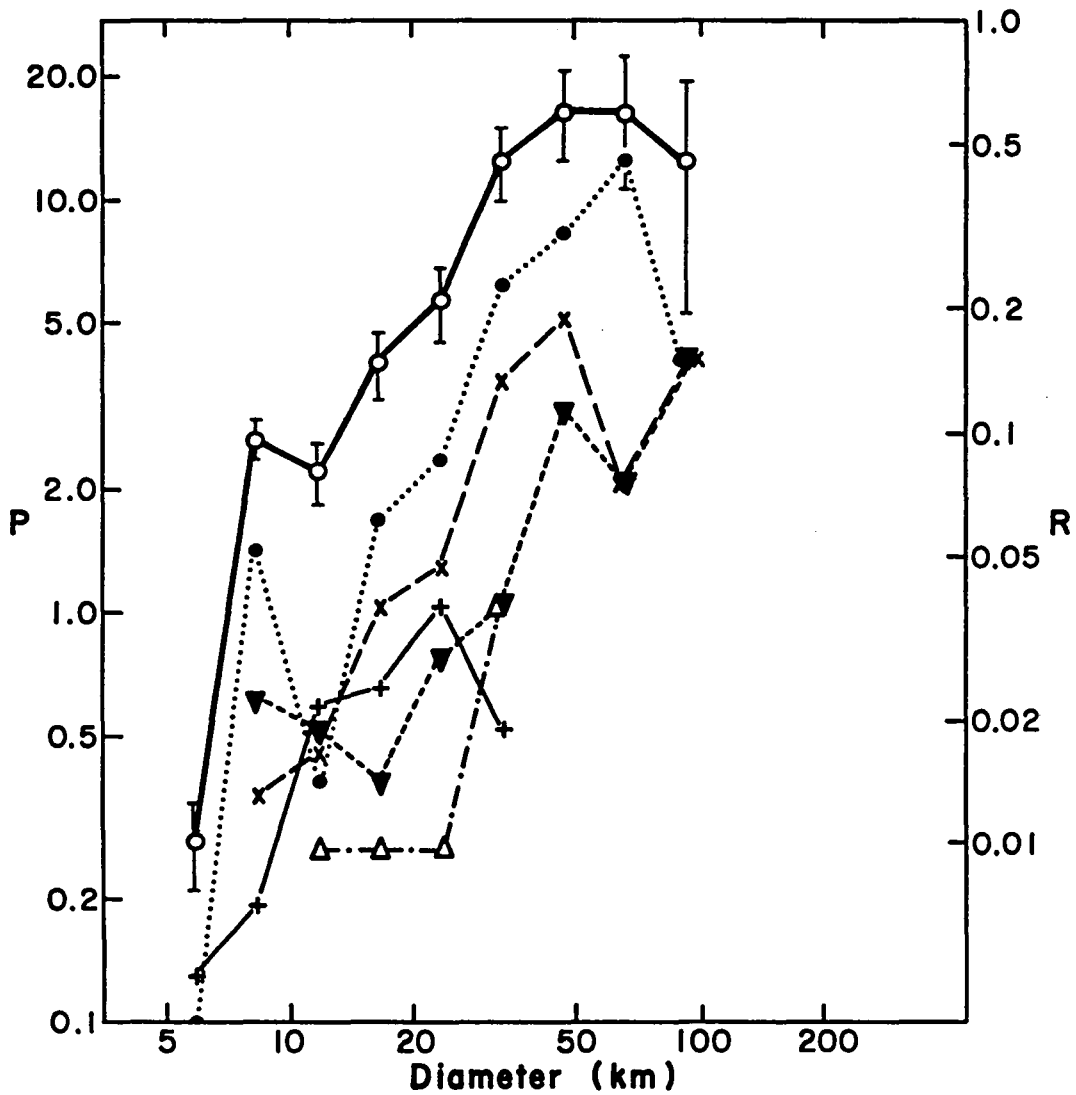


Fig. 55. Jacobi Region (S0) Crater Coverage

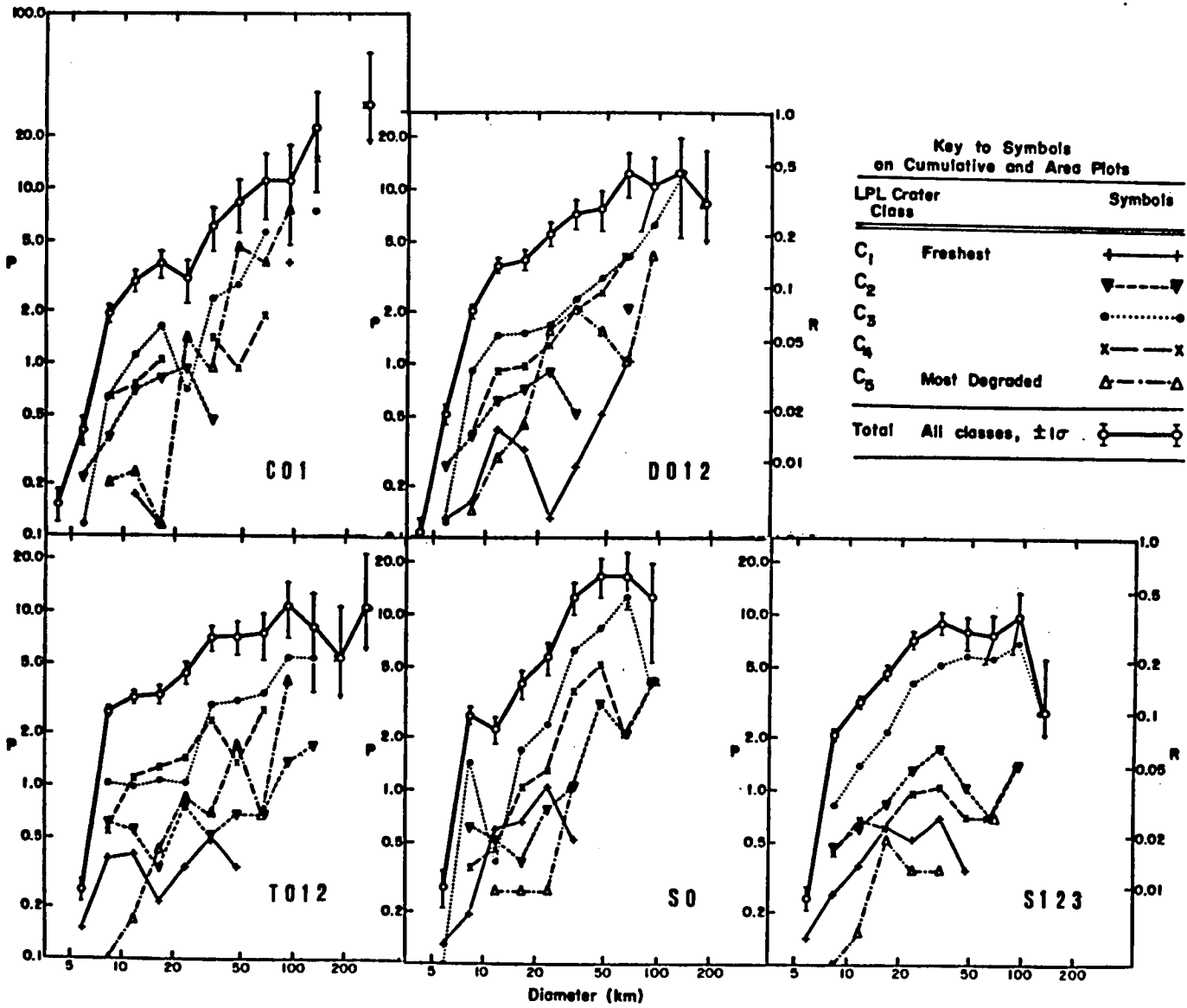
This sector lies between S123 and T012 and exhibits statistics somewhat intermediate to those of its neighbors. Note however, the area plot's steep slope and the apparently greater coverage by 33 to 80 km craters relative to the Clavius and Cuvier regions.

11-19 km secondaries from Nectaris have been added. The abundance of large degraded craters formed by a nearby basin impact, seen in the C and D blocks, is not obvious in the plains region, S123 (Fig. 56). The absence of large degraded craters may instead indicate that the area was once affected by a direct basin impact in pre-Nectarian times, (Sec. 2; see also Wilhelms et al., 1979).

Oberbeck et al. (1977) argue that the apparent deficiency of small craters with respect to large ones (or the "increase in the frequency distribution slopes," Oberbeck and Aggarwal, 1977) is not due to erasure of small craters by flooding, but is an intrinsic property of the bombarding population. They claim that one of the most primitive areas of the Moon (based on its distance from young basins) is the region near the central meridian, the area designated S0 in this study. By removing obvious and suspected basin secondaries from crater statistics in the pre-Imbrian plains region (S123), they derive the equivalent of a steeper area plot, as in S0. In other words, they reject pre-mare highland volcanism as the mechanism which removed the small  $\leq 50$  km diameter craters from the southern highlands.

Geologic analysis of the southern highlands indicated that the pre-Imbrian plains formed a P3 surface emplaced in mid to late Class 3 time, and that the Nectaris event occurred in early C3 time. If so, the originally freshest secondaries of Nectaris may be C3 or older. If the P3 plains embayed the ejecta blankets of C3 craters, secondary fields of those craters may have been lost, but rims of 11 to 19 km

Fig. 56. Regional Crater Coverage in the Lunar Southern Highlands  
 A composite of statistics in each sector, arranged according to their  
 relative location on the lunar nearside (see Fig. 50). Data derived  
 from the LPL Catalog of Lunar Craters (Wood and Andersson, 1978a).



secondaries may not have been buried. This implies that many of the observed small-crater densities must consist of secondaries of C1 and C2 craters. C3 secondaries may survive volcanic burial if they were emplaced in elevated regions (on crater rims); they would not survive substantial ballistic deposition in those areas. Since C1 and C2 craters greater than 40 km only cover 0.3% to 3% of the intercrater S123 region, it is not certain whether they are abundant enough to produce the 5% coverage by 1 - 4 km craters.

#### Crater Statistics on Divided Sectors

In a third phase of cratering analyses of the southern highlands, three regions around Manzinus, Cuvier, and Werner (Strom, 1977) were divided into heavily cratered and non-heavily cratered areas. Diameter and degradation class data were collected for large ( $\geq 7$  km) craters. The division into heavily (HC) and non-heavily (NHC) cratered areas is acknowledged as artificial and is noted in the large transition diameter where coverage of large craters on the HC region begins to exceed that of the NHC regions. When statistics of all three provinces are combined (Figs. 57 and 58), one notes that small crater densities for NHC regions exceed those of the HC regions to 20 km diameter. Class 3 craters dominate throughout all diameter ranges. Class 1 craters have similar densities on HC and NHC areas, indicating that plains emplacement occurred prior to C1 time. The transition diameter for the Class 5 craters is larger than that of other classes,

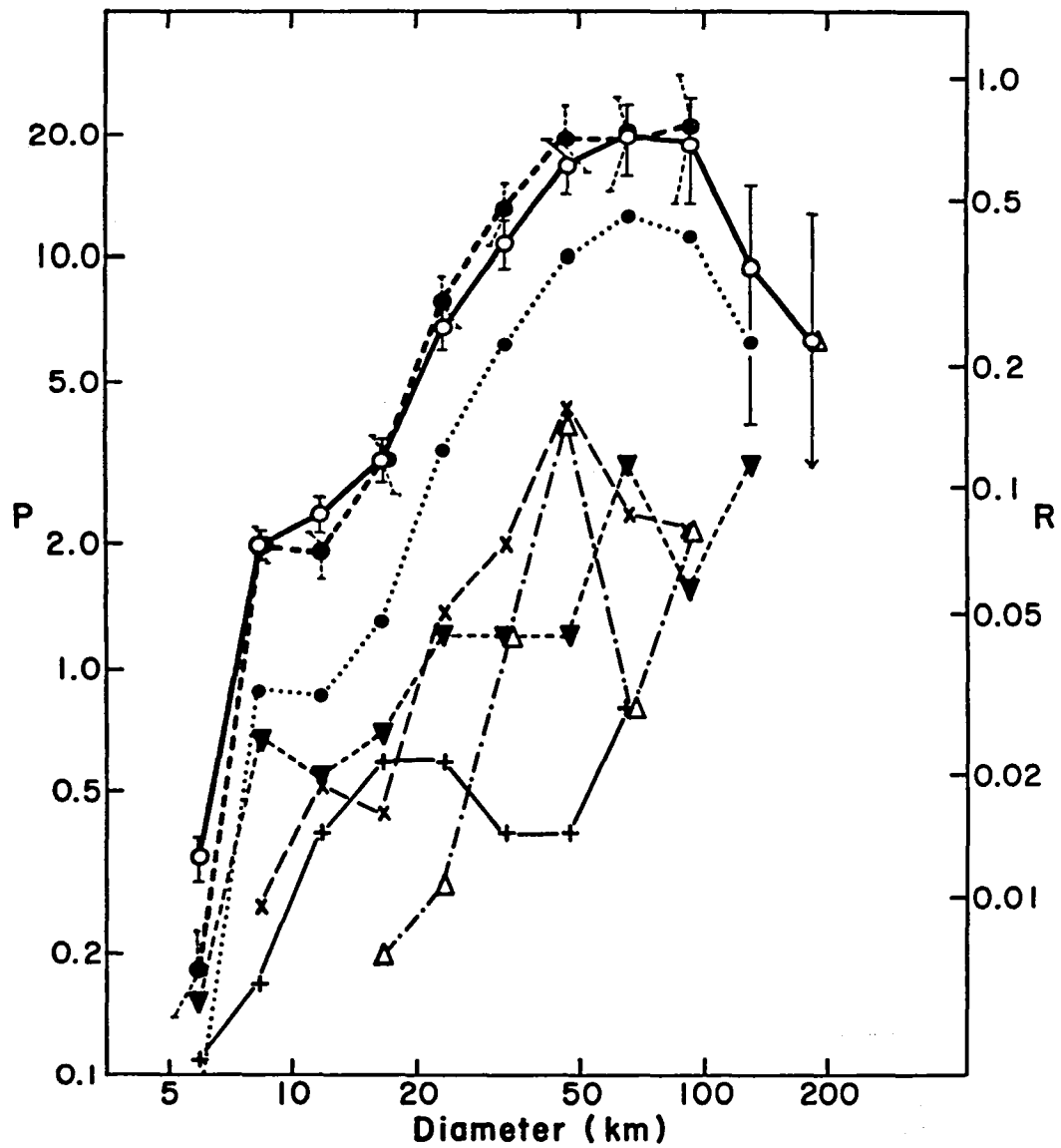


Fig. 57. Crater Coverage of Heavily Cratered Regions of Southern Highlands

Crater coverage within heavily cratered regions of the Werner, Cuvier, and Manzinus areas described by Strom (1977). Thick dashed line denotes total HC coverage within Cuvier and Manzinus sectors only. Note the similarity to S0 sector statistics (Fig. 55).

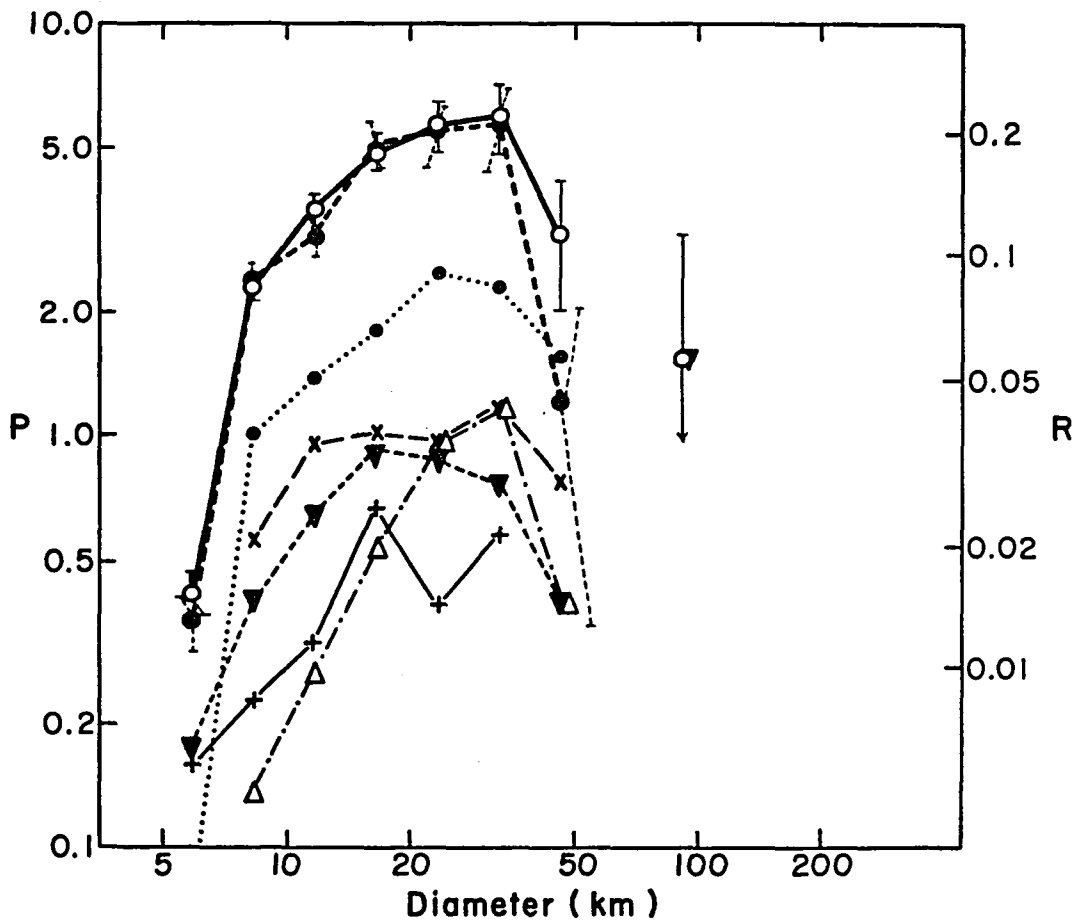


Fig. 58. Crater Coverage of Non-Heavily Cratered Regions of Southern Highlands

Statistics from regions lying outside of clusters of large craters ("NHC") in the Werner, Cuvier, and Manzinus sectors (Strom, 1977). Thick dashed line denotes total NHC coverage statistics of Manzinus and Cuvier sectors only. Note similarity to S123 statistics (Fig. 54).

perhaps because of the proximity weathering effects within the clusters of large craters and the greater "visibility" of severely degraded craters on the plains. Survival of C5 craters on either terrain is biased toward higher diameters.

Major differences among crater abundances on the Werner, Cuvier, and Manzinus regions occur for degraded Class 4 and 5 craters. As noted by Strom (1977), the Manzinus area shows a severe lack of C5 craters on both HC and NHC units when compared to Werner. Fresh craters of 10 to 40 km diameter are more abundant on the plains (NHC) of the Werner areas, than on the plains of Cuvier regions relative to their HC populations. Imbrium secondaries are expected in the Werner area and the northern part of the Cuvier region. Fresh craters are nearly equally abundant on both divisions of the Manzinus region. The Werner area has a higher abundance of large degraded C5 craters than either Manzinus or Cuvier; C3 craters make up less of its total crater density and are not as depleted at lower diameters on its HC unit compared to other regions.

This analysis suggests that volcanic processes affected the Manzinus region, which includes the southern quarter of the S block, and generally supports Strom's hypothesis that the style of degradation in the plains units is unlike the degradation in areas near recent basin impacts.



## Discussion

The change in lunar crater production with time is approached similarly by Strom (1977) and Wilhelms et al. (1978) using different age classifications of craters. Strom (1977) employs the correlation of a crater's degradation class with general age, using crater distributions on marker horizons (e.g. Orientale ejecta blanket, or the mare surface) to tie degradation class to absolute ages. Fig. 59a and Fig. 60a reproduce his analyses of lunar and mercurian populations. Fig. 59a from Strom (1977) presents area plots for the highlands, the total population, and that of each class, 1 through 5. From Tables 3 and 4 of the preceding chapter, one notes that Class 1 craters are Imbrium age and younger, Class 2 later pre-Imbrian to Imbrian, Class 3, late pre-Imbrian, Class 4, middle pre-Imbrian, and Class 5 early pre-Imbrian (Wood, 1979; Wood and Andersson, 1978a). A change occurs in the populations, from a peaked distribution weighting coverage by very large craters in earliest times, to a horizontally distributed (constant coverage with diameter) population appearing in C2 time (Whitaker and Strom, 1976).

Wilhelms et al. (1978) present crater statistics for primary craters greater than 20 km in diameter as a function of geologic age. By attempting removal of secondaries from the data and avoidance of all confusing resurfacing episodes (proximity weathering, volcanic flooding), the density of primary craters of Copernican through

Fig. 59. Comparison of Crater Coverage of Lunar Highlands  
Using Degradation Classes and Time Stratigraphic Systems

Area plot of lunar highland data reprinted from Strom (1977) on left (Fig. 59a) and adapted from Wilhelms et al. (1978) on right (Fig. 59b). Raw data from Strom (1977 ; Fig. 49) has been smoothed out and broken into Classes 1-5 and post-mare craters. Wilhelms et al.'s data is plotted in P(D) format (Fig. 41,42), divided into time stratigraphic units listed in Fig. 41. Wilhelms et al.'s data include selected primaries and secondaries; Strom's data include all craters larger than 7 km on the nearside highlands (see text).

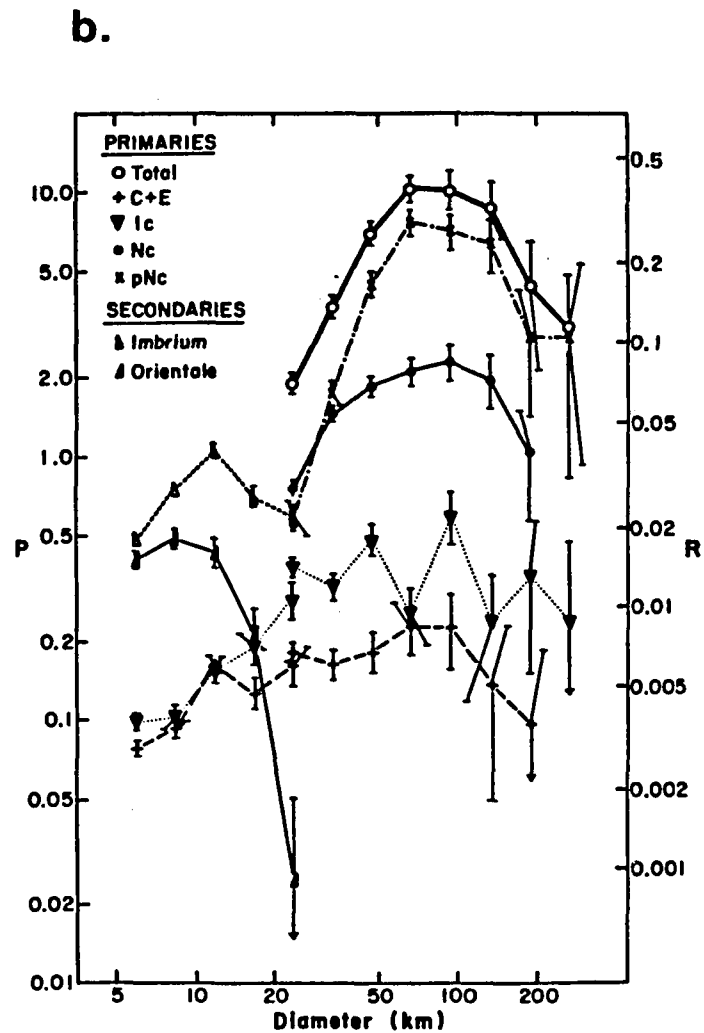
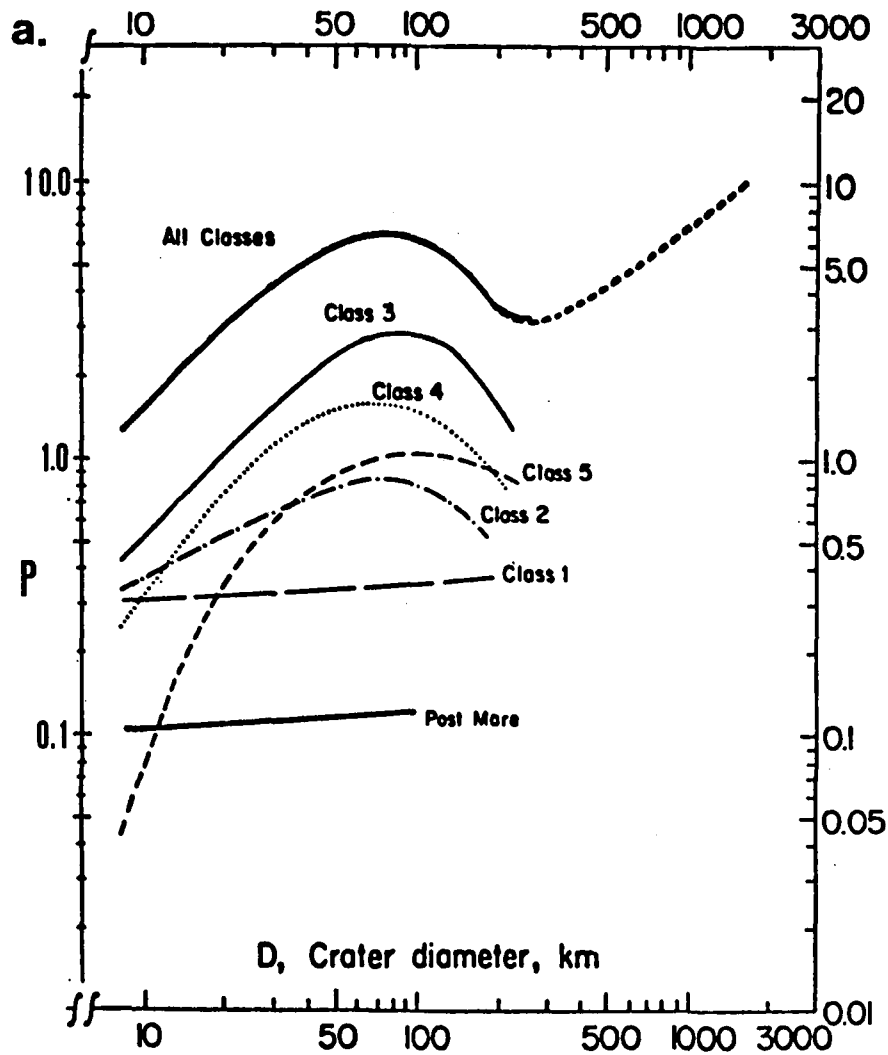
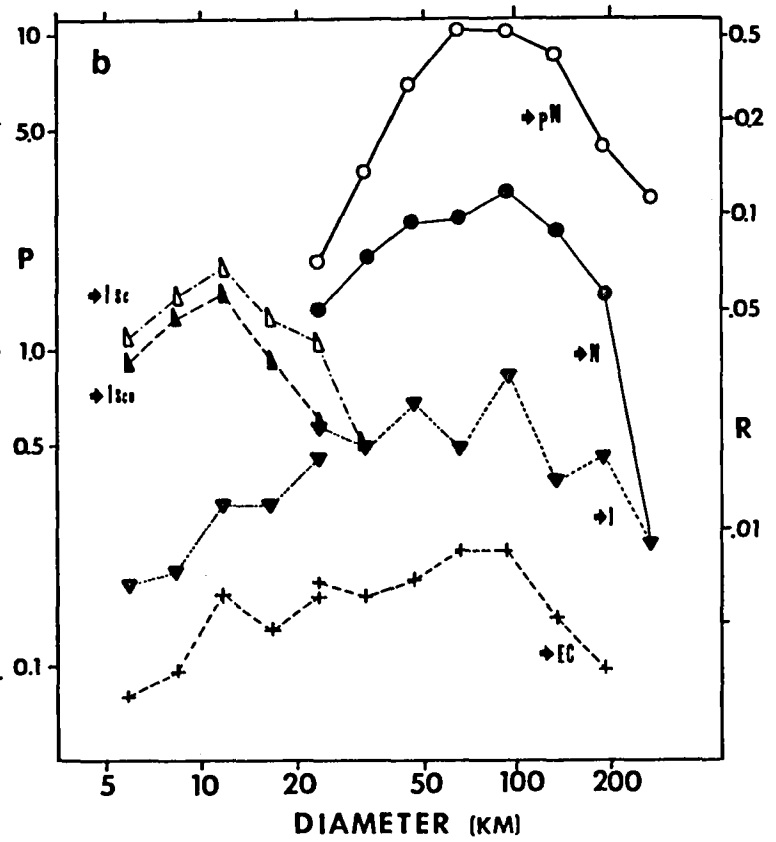
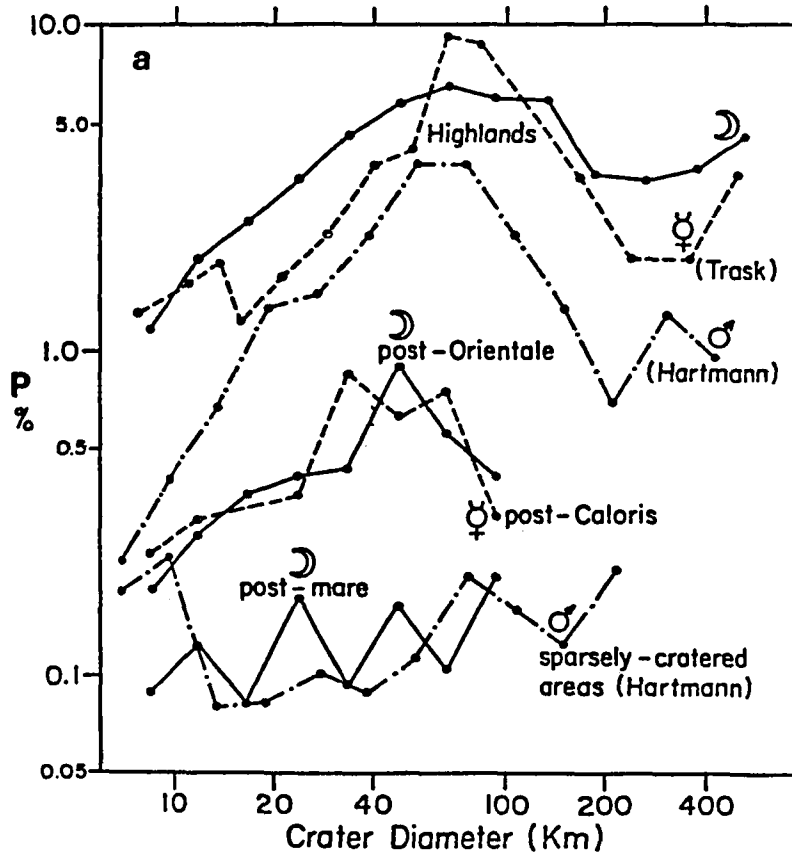


Fig. 60. Comparison of Accumulated Crater Coverage on Surfaces of Different Age on the Moon With Mars and Mercury

Crater densities on different planetary surfaces (from Strom, 1977; Fig. 60a, left) are compared to those on surfaces of different age on the Moon (from Wilhelms et al., 1978; Fig. 60b, right). P(D) values shown in Fig. 59b have been summed up to the surface "age," e.g., the "N" surface includes coverage by Nectarian (N), Imbrian (I), and Copernican and Eratosthenian (C + E) craters. Imbrian and Orientale secondary craters are included in curves marked with arrows to Isc and Isco, respectively. Crater densities of Mercury's south polar regions from Trask's data in Strom (1977) show a bump at 10-15 km which may be due to abundant secondary craters.



pre-Nectarian age was determined. Densities of smaller craters, 5-20 km diameter primaries of Imbrian to Copernican age and secondaries of Imbrium and Orientale, complete their observations. Area plots of their results (Figs. 41, 42 and 59b) are strikingly similar to Strom's (1977) degradation class area plots. The correlation of geologic age with degradation class is clearly seen. The more positively sloped age profiles of Wilhelms et al.'s data are in part due to the greater degradation with age for smaller craters. Strom's Class 3 plot (late pre-Imbrian to Imbrian) may include part of Wilhelms et al.'s Nectarian population at large diameters and part of the Imbrian population at smaller diameters, thus making the curve appear less steep.

Both authors agree that the change in size-frequency distribution of the crater population indicates either a change in the size-frequency distribution of the bombarding population or the shifting dominance of two different groups of impacting objects, the older dominated by large objects which produce 50-150 km diameter craters and basins over a period of .4 to .6 aeons, and a younger group of less numerous objects which are smaller, producing constant coverage by craters, over a time span of 3.9 ae. (Whitaker and Strom, 1976; Wilhelms et al., 1978).

Basin secondaries may be a large part of the small crater population if Wilhelms et al.'s data are correct.

Fig. 60 compares the crater densities in the four lunar time-stratigraphic periods (Wilhelms et al., 1978; Fig. 60b) with the

densities on various planetary surfaces (Strom, 1977; Figs. 60a and 49). Malin (1976a) suggests that the surfaces of these planets began to record impacts at different times in their thermal history. The two graphs imply that the martian highlands have recorded a cumulative Nectarian population, while the mercurian surface has recorded a pre-Nectarian population, replete with "secondary hump" at about 15 km. Similarities occurring in the younger populations are displayed in Fig. 60a (Strom, 1977). Revised statistics of Woronow, Strom, and Gurnis (1980) show even greater similarities in magnitude and slope of the total crater populations, suggesting that the highland surfaces of all three planets solidified at the same time and record the same impacting population; this heavy bombardment ended about 4.0 b.y. ago on all bodies. Because different fluxes could bombard each planet, and their surfaces solidify at different times, and because no absolute ages are available for Mercury or Mars, it may be premature to speculate that the coincidence of area plot statistics implies similar surface ages and surface bombardments (Chapman, 1976). The next section details the mercurian crater statistics compiled in this research; relative and absolute ages of the planetary surfaces are discussed in Chapter 7.

#### Summary of Lunar Crater Statistics

The data generally support the hypothesis that the lunar intercrater plains are an old volcanic surface, and that the high

densities of small craters are probably secondaries. There are some ambiguities. If the lunar surface is partitioned into regions like Strom's (1977), the data strongly imply that volcanic processes formed the intercrater plains of the Manzinus area, an area south of Nectaris, and out of range of many of its secondaries. Other regional divisions (e.g., S123, S0) indicate addition of Nectarian secondaries, and slight volcanic resurfacing with respect to the Clavius area. In support of an origin not related to deposition of basin ejecta and basin-destruction, there is no overabundance of C4 and C5 craters in the lunar intercrater regions. The S123 region is more representative of the lunar intercrater plains as defined by Trask and Guest (1975) than is the Manzinus area. Small crater statistics do not indicate substantial losses of small craters; to the contrary, they indicate additions due to secondaries of moderate-size craters. Differential preservation within more consolidated plains units may support a volcanic origin.

On a regional scale, the lunar intercrater plains lack craters of 40 km diameter and larger, indicating possible reduction of crater densities by an ancient impact in this area. Such an event would reset the cratering record and reduce the coverage relative to an older surface (not necessarily the Clavius Quadrangle!).

Thus the cratering record of this region indicates that a variety of processes may have affected it. Volcanism is likely to have



reduced small to intermediate-size crater densities, but subsequent cratering produced many secondaries less than about 1/25-th the size of the primaries. The Nectaris impact has injected larger (8-18 km) secondaries into the region. Consolidated materials may better preserve small craters in the plains. An ancient basin-forming impact may have reduced all crater densities in the area, i.e., resurfaced the area, prior to the Nectaris event or volcanic flooding of the surface.

#### Cratering Histories of the Intercrater Plains of Mercury

The crater statistics of mercurian surfaces will be compared to the various models of sections 2 and 3 and to those behaviors displayed by the lunar crater statistics of the preceding section. The selected regions are described below. Statistical data of the geologic map are briefly summarized in a later section. The data, as will be seen, are remarkably similar to selected area and regional statistics of the lunar southern highlands.

#### Statistics of Selected Areas

Description. A pervasive dichotomy on the mercurian surface is that between clusters of large craters and the intercrater plains. Four regions of overlapping large craters, designated heavily cratered areas (HCA), and four adjacent regions of intercrater plains (ICP) were selected for crater density studies. Tables in Appendix D provide imagery data and the crater statistics for each area. Fig. 61 illustrates the area boundaries.

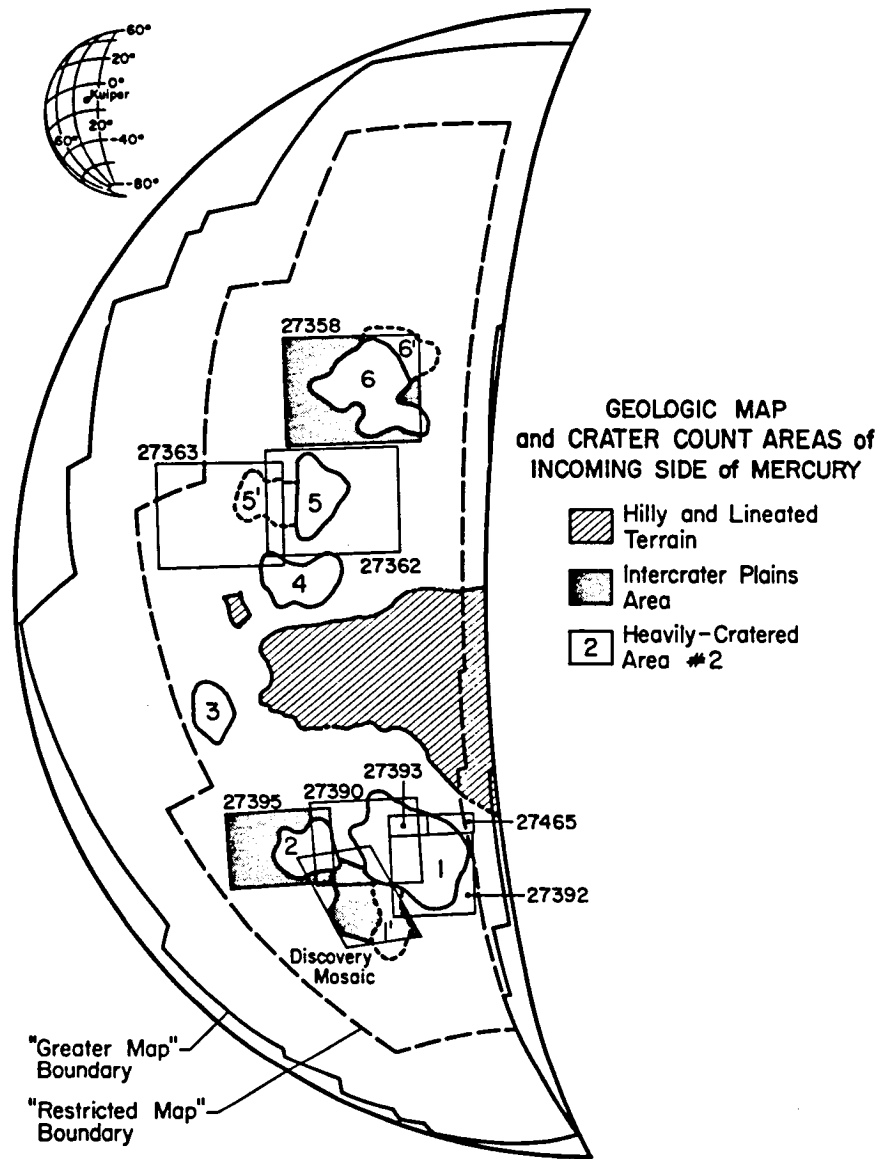


Fig. 61. Review of Selected Area Boundaries on Mercury

Reprint of Fig. 10. Areas described in text.

Area 1 (HCA 1) contains the crater Sōtatsu and its neighbors. Area 2 (HCA 2) consists of the Andal crater complex. Areas 5 and 5' (HCA 5 and HCA 5') include craters east and west of Kuiper and Murasaki. Area 6 + 6' (HCA 66') encloses the crater Lu Hsun and large craters east of it. The lower diameter limit within these regions varies from 2.5 km to 3.5 km; resolution (2.2 TV lines) is usually one half the limiting crater size ("cut-off diameter"), about 1.4 km.

The intercrater areas sampled include the plains east (DSE) and west (DSW) of Discovery Scarp, the area east of the Andal complex (ICP 2), and the area east of the Lu Hsun complex (ICP 6). Craters greater than 2 km diameter were counted east and west of Discovery Scarp to detect any relative age variation across the scarp trace. The ICP 2 area was divided into eight subsections roughly corresponding to mapped plains (Fig. 63); statistics were collected on each area. Craters of 2-2.4 km diameter and greater were sampled. Resolution varied from 0.8 km in the center of the Discovery Scarp mosaic (Fig. 8) to 1.4 km elsewhere.

Heavily Cratered Area Statistics. Individual and combined heavily cratered areas display a typical V-shaped area plot. As shown in Fig. 62, the area plot of combined HCA's is much like an area plot of lunar selected areas displaced to higher diameters. Equally high coverage occurs for craters less than 10 km or greater than 40 to 56 km in diameter. Over diameters of 20 to 160 km, the slope of the HCA

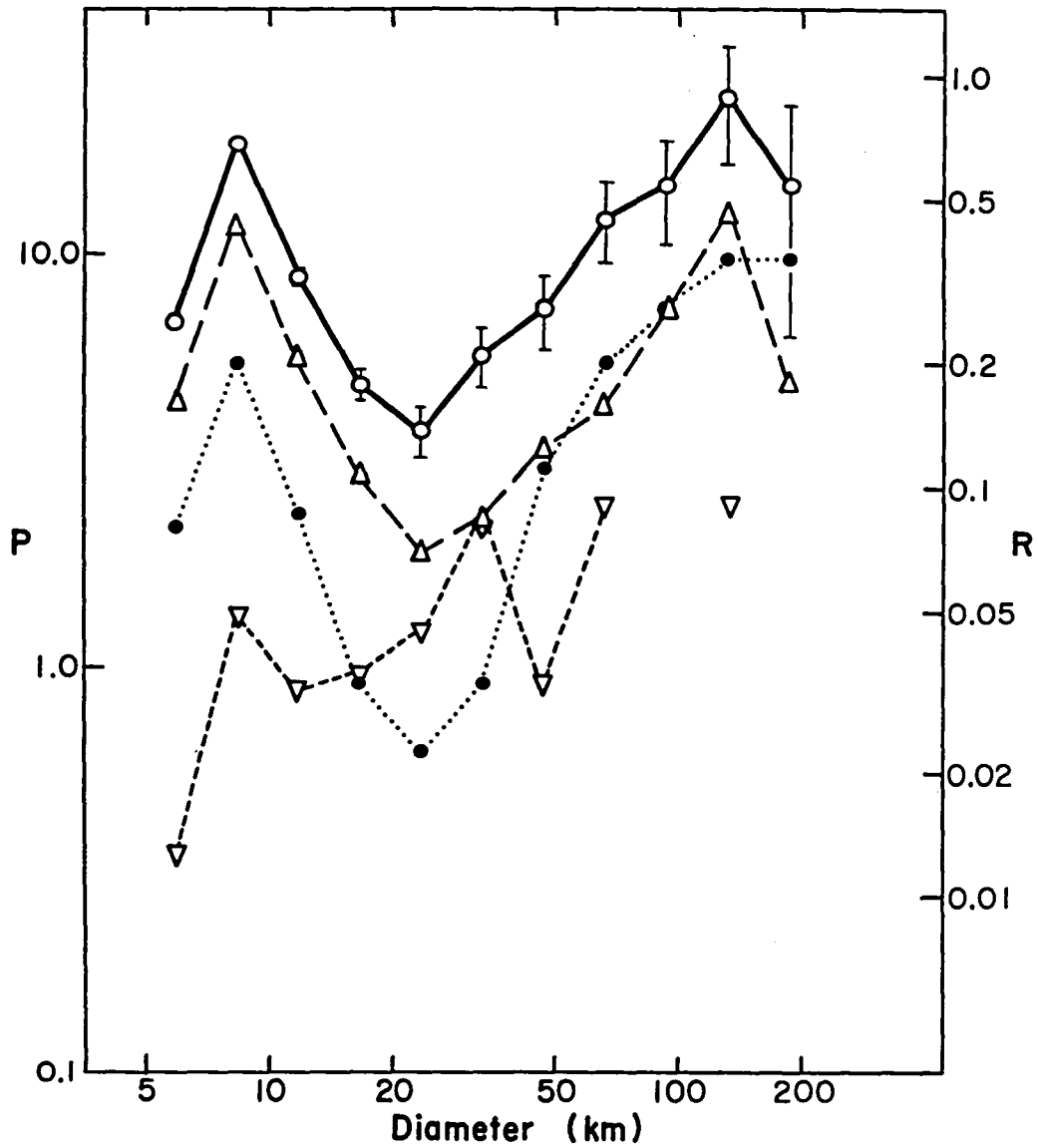


Fig. 62. Heavily Cratered Areas of Mercury: Crater Coverage Within Selected Regions

Data from Areas HCA 1, 2, 5, 5', and 66' used (Table D25 of Appendix D). Symbols of Caloris System format (Fig. 46) are: open triangles, pre-Caloris craters (C5-C4); solid circles, Caloris age (C3); and inverted open triangles, post-Caloris craters (C1 and C2).

combined plot is represented by a slope index of -2.0. The opposite leg of the V, over diameters of 7 to 20 km, is represented by slope index of -5.0.

The "description" of this curve or the intercrater curve may bias its interpretation. One may cite a decrease in production, or increased obliteration, of 14 to 40 km craters in the neck of the V. Or, one may postulate an addition of small craters ( $D < 20$  km) to the upwardly sloping curve of  $D > 20$  km. Interpretation of the first suggests a bimodal production population, or a horizontally distributed one which suffered unique destruction of 14 to 40 km craters. The latter hypothesis is not likely. The second description suggests a lunar-like production population to which excess numbers of small craters, very likely secondaries, have been added. Whether the large crater distribution represents the bombarding population or a crater population previously altered by obliteration processes is not evident.

The major tasks are to distinguish crater additions and crater obliteration from the production population. Crater overlap, proximity weathering, and production of secondaries will strongly affect crater statistics within a selected region which is bounded by the continuous ejecta blankets of its craters. The sequence of events is very important, for statistics may be dictated by the largest, youngest crater in the cluster. This effect is averaged in the combined HCA plot. Furthermore, the resurfacing or flooding of large old crater floors is

equally effective in producing uncratered areas, and to a lesser extent, in reducing the intermediate size crater population. Many processes thus will eliminate or severely degrade the smaller craters--overlap, proximity weathering, ejecta deposition, flooding of crater floors--but primarily overlap by a large crater is likely to eliminate the 100 km craters which dominate the clusters. Larger, basin-size craters may also be affected by isostatic equilibrium over their lifetimes (Schaber et al., 1977).

At large diameters, pre-Caloris impact craters dominate the lunar-like crater statistics; the area plot's steep slope is similar to that of the lunar intercrater region S123. The more abrupt decline of C3 craters of 14 to 40 km relative to C4 and C5 craters complicates any interpretation. The decline may simply be due to degradation of intermediate size C3 craters by larger C3 and C2 craters. Or it may be a tectonic-type degradation, in which a catastrophic event obliterates C3 craters, or degrades them to C4 or C5, prior to C2 emplacement. If P3 age volcanism eliminates craters of 14 to 40 km (as it appears to do in the Victoria Quadrangle), it should eliminate smaller craters as well, and be so registered in the statistical data.

The preferred interpretation of the small-crater statistics of the HCA (and ICP) regions is a contribution by secondary craters. (Endogenic craters are rare; only a few collapse pits of 14 km have been identified.) Individual HCA and ICP regions show up to 6% additional coverage by craters in chains or clusters typical of

secondaries. The influx is greatest at 5-7 km diameters. From Section 3, one finds that primaries of the size corresponding to 5-7 km secondaries are abundant in the HCA regions. Preservation of secondaries on Mercury, and the formation of degraded secondaries contribute to the dominance of degraded states at 5-14 km. Volcanic plains will not embay secondaries emplaced on the large crater rims or elevated plateaus common in the crater clusters.

Are the HCA (and ICP) statistics consistent with volcanism? They are not consistent if the volcanism was recent (Class 2 or 1), extensive, and covered older cratered plains (the floor of a C4 basin for example) within the sampled region. However, the statistics are consistent with volcanism if it occurred (1) early in the heavy bombardment, (2) within smaller craters, (3) to very shallow depths, and (4) if it was followed by extensive (secondary) cratering, forming small craters. Again, differential preservation of craters on consolidated (volcanic) surfaces may enhance the lifetime of small secondaries and small primaries. Other studies have concluded that Mercury's surface, both plains and heavily cratered regions, is more consolidated than the lunar terra (Cintala et al., 1977; Pike et al., 1980).

Are changes in the bombarding population indicated? A bimodal population of projectiles, very large bodies and much smaller debris, may characterize the early, heavy bombardment of the pre-Caloris and

Caloris eras. Secondaries may contribute to the small crater populations, but are not responsible for its entirety. Following the Caloris event--which may have signalled the end of a heavy bombardment--the projectile population appears to lose its larger members and much of its smaller debris, thereby leaving a signature of reduced, but nearly constant, coverage over a broad range of crater diameters.

Intercrater Plains Statistics. The curves of the intercrater areas are similar in form and magnitude to those of the heavily cratered areas, but peaks and minima occur at slightly different diameter ranges, due to the general age of the plains surface, proximity to large primaries, or inclusion of field craters.

The small crater coverage in individual intercrater units increases slightly with average age of the unit. Lower densities of small craters occur on ICP 2, dominated by P3 and P2 plains, than on ICP 6, dominated by P4 and P5 units. Crater coverage east and west of Discovery Scarp differed little, reaffirming that average relative age of plains does not change across the scarp, i.e. that it is primarily a tectonic structure (Strom et al., 1975b). Degradation class coverage suggests that the western plains consists of older units, consistent with geologic mapping. Younger plains of the ICP 2 region (Fig. 63) appear to contain higher densities of very degraded craters. This puzzling occurrence suggests that some younger surfaces were formed by shallow burial of older topography. Limited volcanism or sporadic ballistic deposits may incompletely resurface these areas.



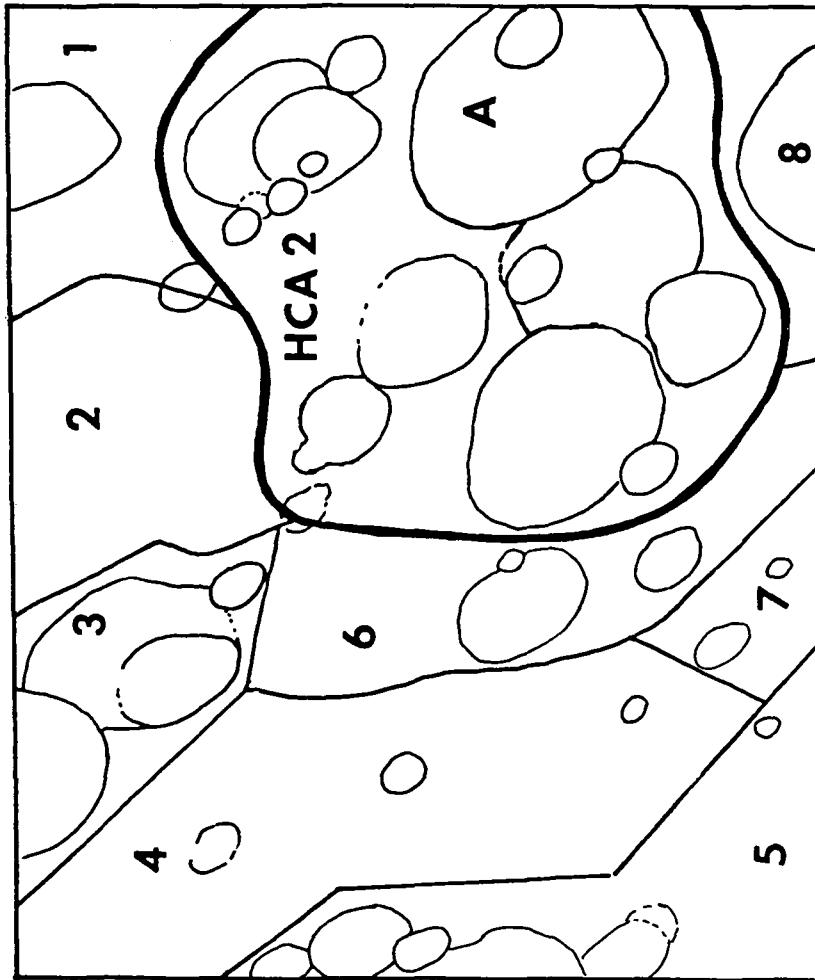


Fig. 63. Selected Area 2: HCA 2 and ICP 2 in Andal (A) Region

- a. Heavily cratered area (HCA 2) is outlined above and illustrated in Fig. 63b. ICP 2 forms the rest of the photograph area. The intercrater plains were divided into eight regions shown in the sketch map. (See Appendix D for statistical data.) Geologic mapping shows that Region 2 contains mainly P2 materials, Region 4 consists of P3 materials, and Region 6 contains P4 materials. Schubert lies immediately to the west.

FDS 27395. North to left, as shown. Andal is 90 km in diameter.

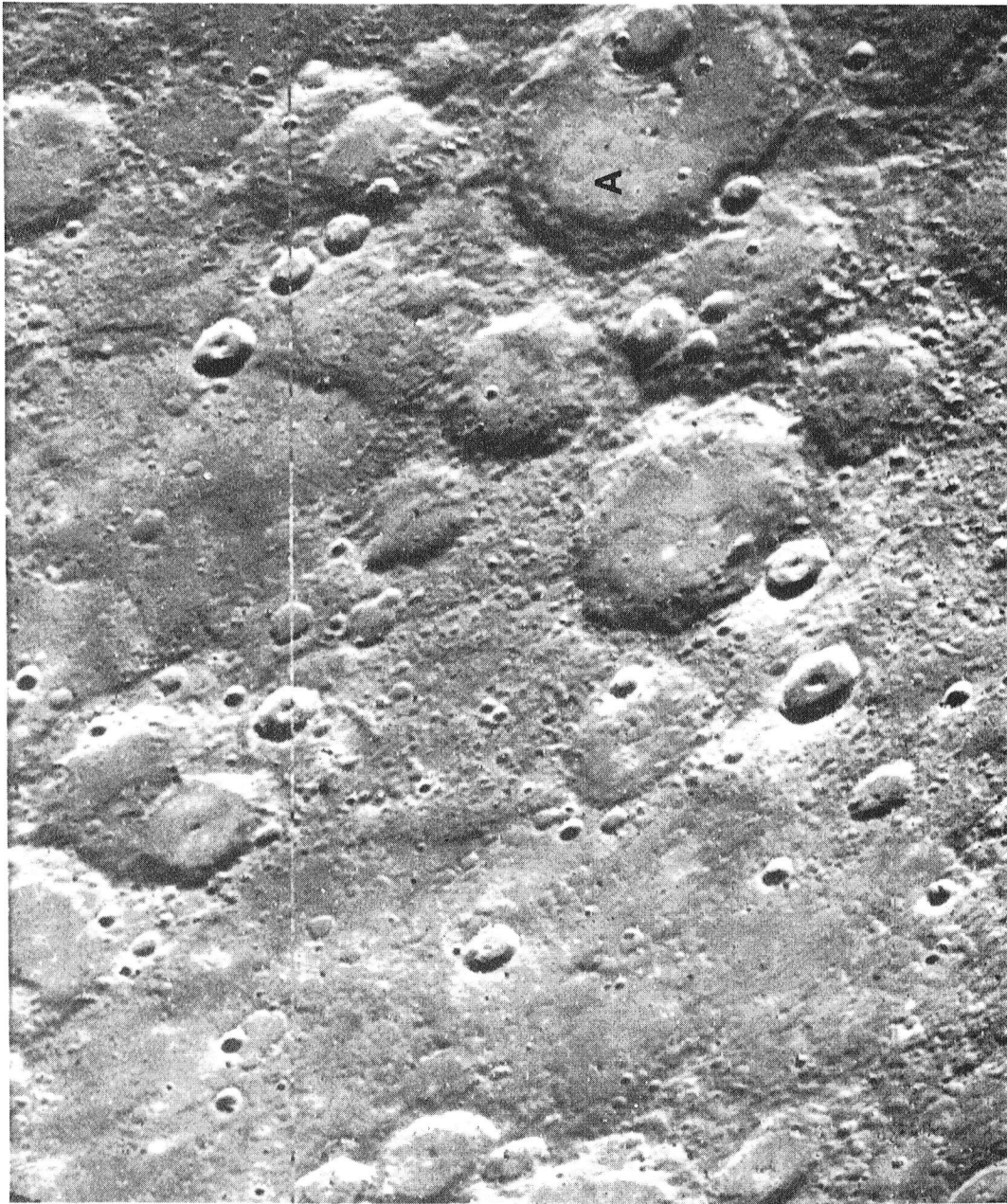


Fig. 63. Selected Area 2: HCA 2 and ICP 2 in Andal (A) Region  
--Continued

b. FDS 27395. North at left.

The area plot of the combined intercrater plains statistics (Fig. 64) nearly duplicates that of the heavily cratered regions, except that the plains lack the larger structures. A great many of the small, degraded craters, about as many as in the heavily cratered regions, are recognized as possible secondary craters, aligned in chains and clusters. Many of the chains can be traced to a probable primary source in the HCA clusters; the source craters are not distant. The intercrater regions have higher densities of intermediate size C5 craters than do the HCA clusters. This can be explained by a greater visibility of this size feature due to the lack of obliteration by overlap on the intercrater surface.

The absence of large craters on the plains, partly a product of definition, may be attributed to direct basin impacts in the earliest phases of Mercury's bombardment history, followed by plains-forming volcanism. C5' structures are common under the intercrater plains. Large crater densities are thus reduced at the C5' site. Volcanism following the impact destroys later structures and then better preserves subsequent small impact craters. Because the characteristic signature of volcanism is not observed over the diameter range of 5 to 20 km, these craters may either be too large to be buried by volcanic plains, or they were emplaced after the resurfacing event.

Because the heavily cratered and the intercrater plains areas' distributions are so similar, they may represent the same population.

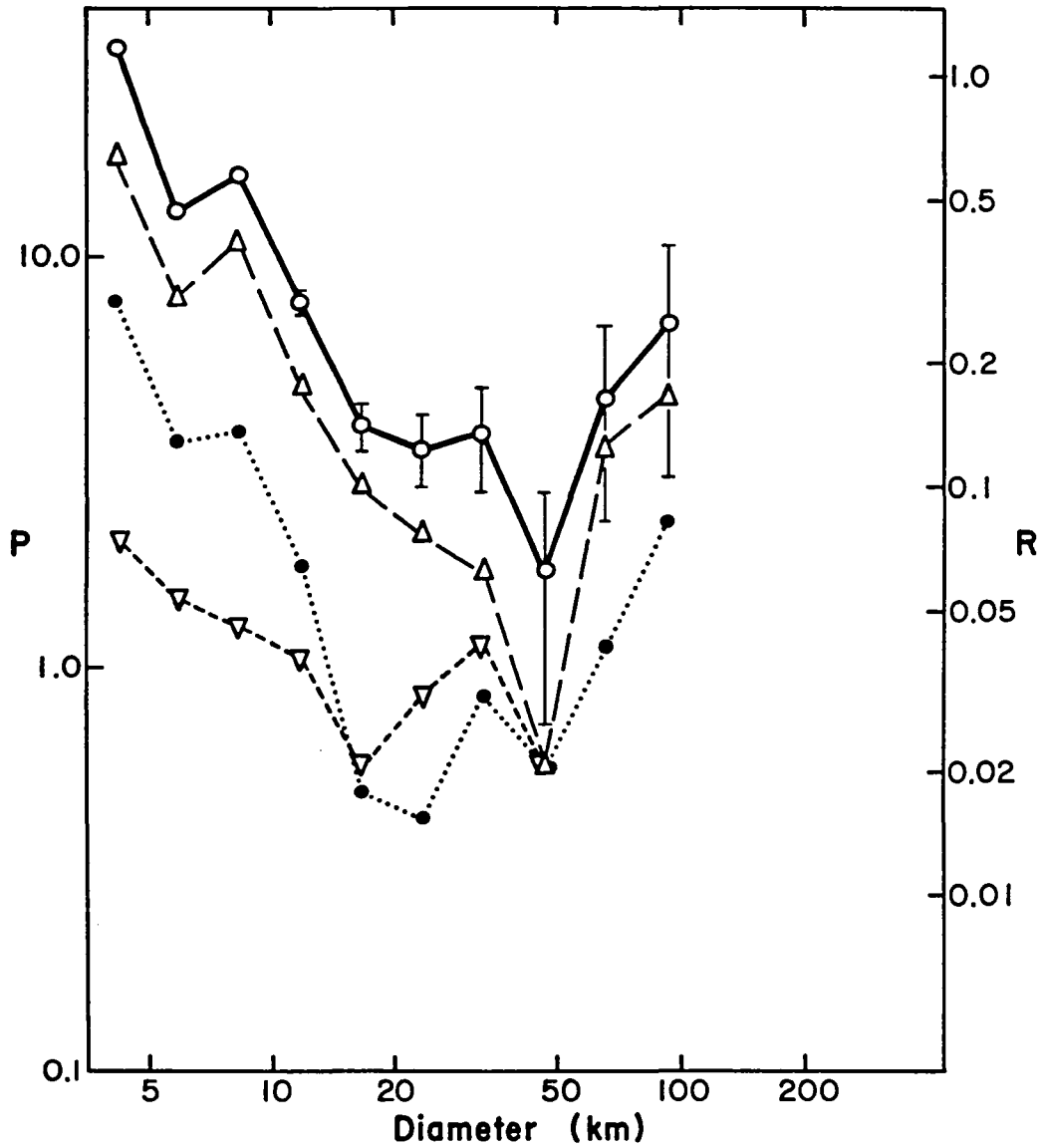


Fig. 64. Intercrater Plains of Mercury: Crater Coverage Within Selected Regions

Symbols in Caloris system format as explained in Fig. 62. Data from ICP regions of Discovery Scarp East and West, ICP 2, and ICP 6 (see Table D26 of Appendix D).

The younger plains and some intercrater plains may lie within ancient basins and sites of volcanic resurfacing, while the seeds of the heavily cratered clusters and the older plains lie on that C5' basin's rim (or exterior to it) where they are better preserved. The paradoxical conclusion is that the heavily cratered areas occur in the intercrater regions of the C5' basins, while some of the intercrater plains are the floors, or intracrater regions, of the C5' basins.

Combined Statistics of the Selected Regions. The combined statistics better represent the cratered surface of Mercury (Guest and Gault, 1976). All the features of the combined area plot (Fig. 65) have been described above. The statistics are affected by volcanic resurfacing on the plains, crater overlap in the crater clusters, and direct basin impacts during the early bombardment. The latter essentially formed the ICP--HCA dichotomy. Direct basin impacts, however, must have had "peripheral effects," yet the age of these impacts and the restricted range of ejecta on Mercury may have reduced associated crater degradation, plains formation, and small crater eradication.

For such great numbers of secondaries and small craters to accumulate, significant basin cratering and plains resurfacing must have been completed before many of the smaller craters (and their secondaries) formed (Trask, 1976 a,b; Trask and Guest, 1975). Changes in the external impacting population may be involved too, as has been established for the Moon (Whitaker and Strom, 1976; Strom, 1979). A

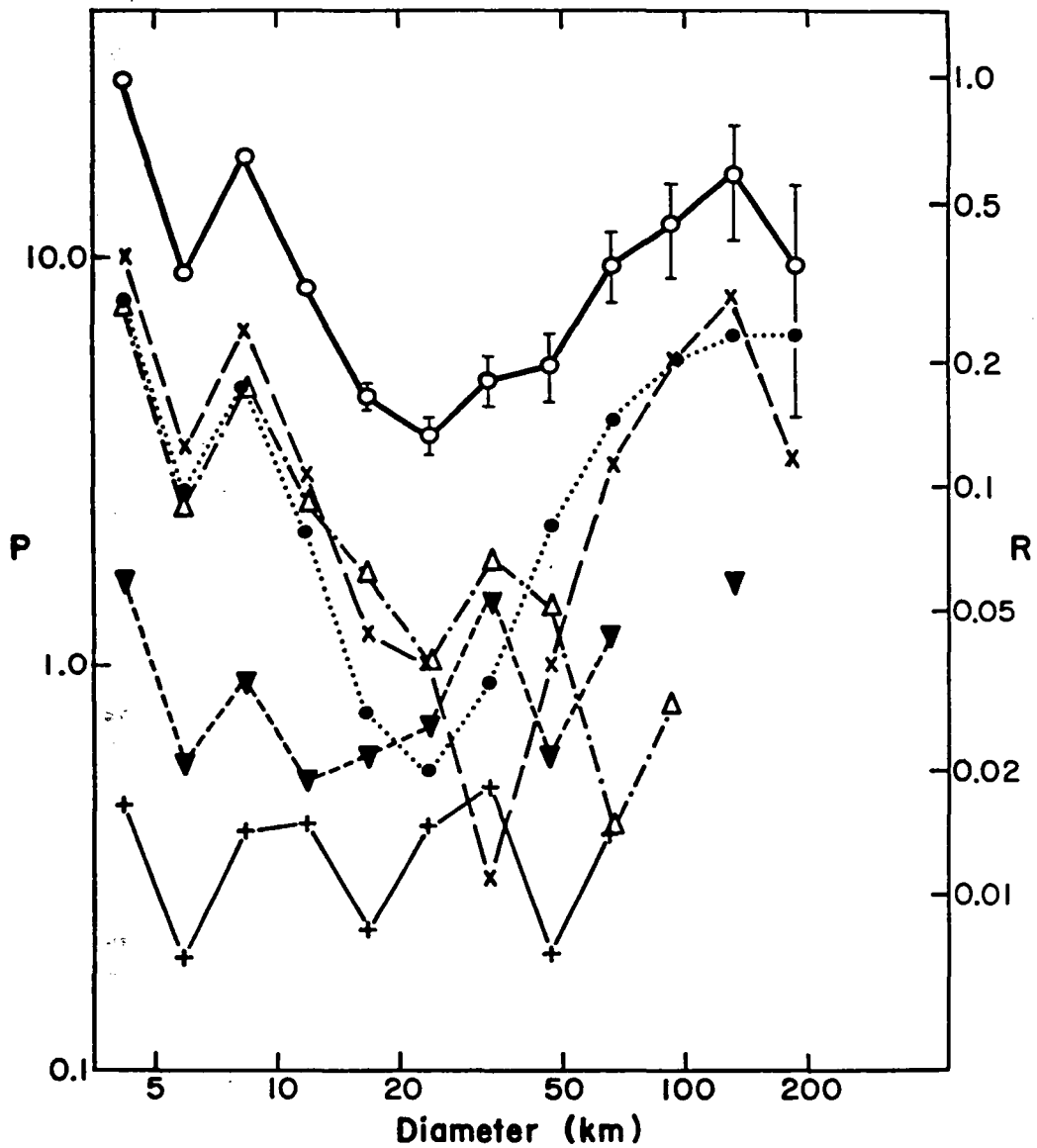


Fig. 65. Selected Regions of Mercury: Crater Coverage by Degradation Class

Symbols defined in Fig. 46. In this combined data of ICP and HCA regions, note the roughly constant horizontal slope of the youngest craters C1 and C2, contrasted with the "V-shaped" Caloris and pre-Caloris population statistics (C3-C5).

change in the diameter-frequency distribution may have followed the C3 period (see Fig. 66 where Caloris era format is used; see also O'Donnell, 1978).

The data from selected areas is also presented in the standard cumulative curve format (Fig. 67). Breaks in slope, often very subtle, are interpreted to represent obliteration events, such as lava flows, or different responses to subsurface structure (Neukum and Horn, 1976; Greeley and Gault, 1970; Schultz et al., 1977). This type of presentation does not make the alternative interpretations any clearer. The major questions still focus on what produced the fluctuations of crater density. (Such a task is difficult when working with the total crater statistics. It may be even more difficult when working with subjective degradation classes containing fewer craters.)

#### Statistics of the Geologic Map Area

Method. Following completion of the geologic mapping of the first quadrant of Mercury, data for crater frequency distributions of the map area were collected. The data recorded include diameter, inner ring diameter, latitude and longitude in  $10^\circ$  bins, degradation state in the five class system with C5' structures, and the principal units on which (or in which) the crater is located. The General Geologic Map area is  $1.0284 \cdot 10^6 \text{ km}^2$ ; the more conservative Restricted Geologic Map area is  $4.985 \cdot 10^7 \text{ km}^2$ .

Data from the Geologic Map. Data from the geologic map for craters over 40 km diameter provides a broader sampling of cratering

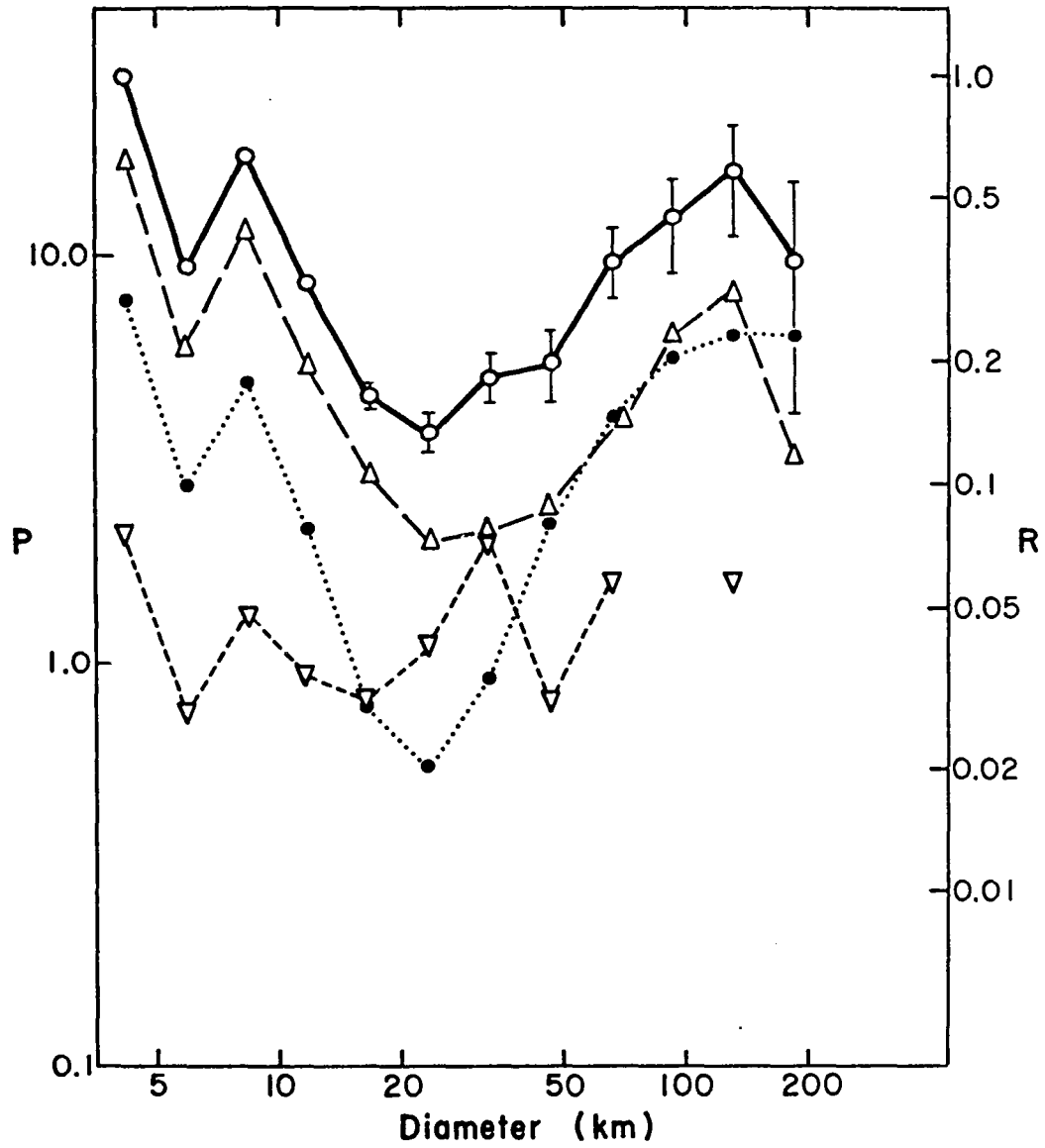


Fig. 66. Selected Regions of Mercury: Coverage Using Caloris System Notation

Combined data from HCA and ICP selected regions. Symbols defined in Fig. 46, 61, and 62.



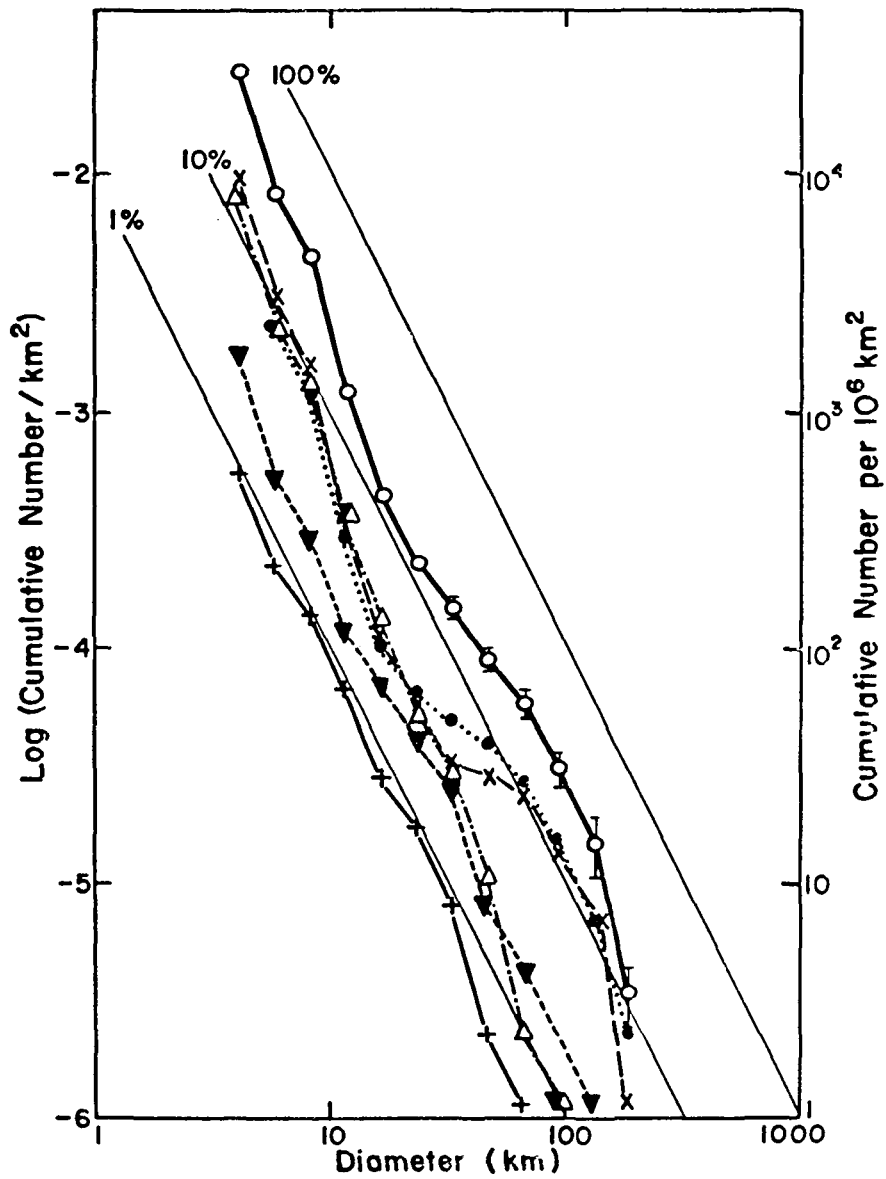


Fig. 67. Cumulative Size Frequency Statistics of Selected Regions of Mercury

Symbols defined in Fig. 46. Lines of -2 slope marked 1%, 10%, and 100% represent percent of "saturation" as defined by Gault (1970). Compare results of O'Donnell (1978).

in the first quadrant, analogous to the statistics of the combined selected regions. A variety of data presentations enables one to determine the average first quadrant diameter/density distribution, regional distributions by quadrangle, the crater coverage in the hilly and lineated area, and the diameter/density distribution on specific mapped units. Information on small diameter craters can be supplied by the selected areas contained within these regions. Changes in the degradation criteria in mapping may shift some of the C4 and C3 craters of selected regions to C3 and C2 classes respectively.

Crater coverage statistics of the general map (Figs. 68, 69, and 70) resemble those of the restricted map (Fig. 71) and the Kuiper and Discovery Quadrangles (Figs. 73, 75, and 76). All present an average over diverse collections of crater and plains units.

In general, coverage increases with increasing diameter to basin sizes. No deficit in basin density is noted if ancient circular depressions are included in the statistics. If these queried structures are omitted, a relatively severe lack of coverage by basins results, consistent with observations by Schaber et al. (1977), Malin (1976a), Wood and Head (1976), Frey and Lowry (1979), and others. The maximum in crater coverage occurs at larger diameters for more degraded craters, even though the magnitude of C2 through C5 coverage does not vary significantly. Fresh C1 craters display constant coverage, at  $3 \pm 1\%$ , at the same magnitude as C1 crater coverage in the combined selected regions over a total diameter range of 5 to 150 km.

C3 craters dominate the statistics from 40 to 158 km diameter. Coverage for all craters of diameters less than 50 km decreases, reflecting the intermediate size crater deficiency noted in the selected regions (due to volcanism?), or reflecting the production population. If the map boundaries are restricted, excluding more plains than craters, the area plot becomes more distinctly peaked and more positively sloped, with fewer basins and fewer 56-80 km craters represented (Fig. 71). All trends remain the same. Slope index of the 40-112 km segment of the general map is -2.3; for the restricted map area, it is -1.9. (The former is similar to the general lunar highland statistics, and the latter is similar to the intercrater plains region of the Moon, S123.) The steeper slopes of the restricted curve may indicate resurfacing events such as volcanism, similar to the proposed volcanism in the S123 region.

The Hilly and Lineated Region. The hilly and lineated region (Fig. 72, total coverage plotted only) exhibits abnormally large coverage by very degraded craters, and sparse coverage by fresher crater classes. Although geologic mapping suggests that the disruption event occurred near the end of the Class 3 formation period, crater statistics suggest an event in early C2 time. Class 3 coverage is normal in this area when compared to statistics for craters outside the disturbed region, but Class 2 coverage falls below that of exterior regions. The area plot is not unusually steep at diameters greater

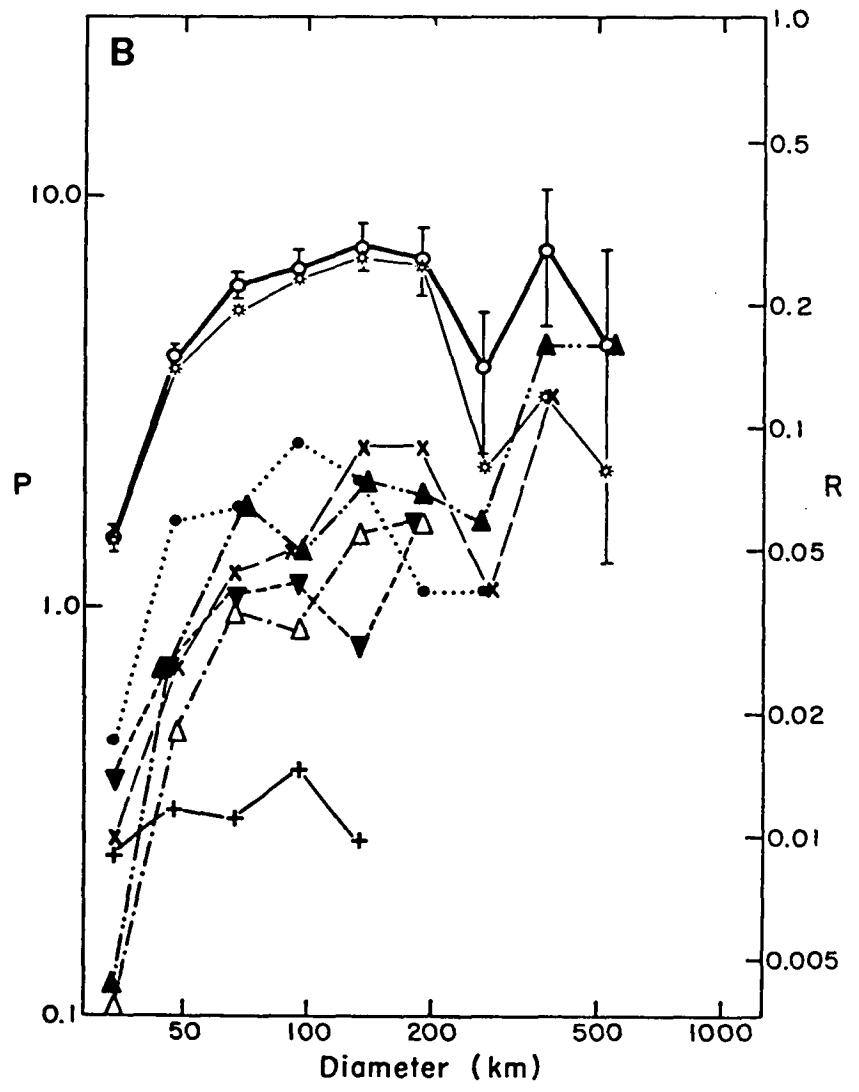
Fig. 68. Geologic Map Crater Coverage (B) and Key to Symbols (A)

Crater coverage displayed by C1 to C5' craters; note that starred total curve omits the queried C5' craters, reducing coverage most severely at basin diameters. Compare absolute coverage and relative densities to those of the lunar surface, Fig. 59a. Data presented in Table D28 of Appendix D.

A

**Key to Symbols  
on Cumulative and Area Plots**

LPL Crater Class		Symbols
C <sub>1</sub>	Freshest	+ — +
C <sub>2</sub>		▽ - - - ▽
C <sub>3</sub>		● ····· ●
C <sub>4</sub>		x — x
C <sub>5</sub>	Most Degraded	△ - · - · △
C <sub>5</sub> + C <sub>5'</sub>		▲ ····· ▲
Total	All classes, ±1σ	○ — ○
Total	Hilly and lineated terrain	⊕ - - - ⊕
Total	All classes except C <sub>5'</sub>	* — *
<hr/>		
Post Caloris	C <sub>1</sub> + C <sub>2</sub>	▽ - - - ▽
Caloris	C <sub>3</sub>	● ····· ●
Pre Caloris	C <sub>4</sub> + C <sub>5</sub>	△ — △
	C <sub>4</sub> + C <sub>5</sub> + C <sub>5'</sub>	▲ - · - · ▲



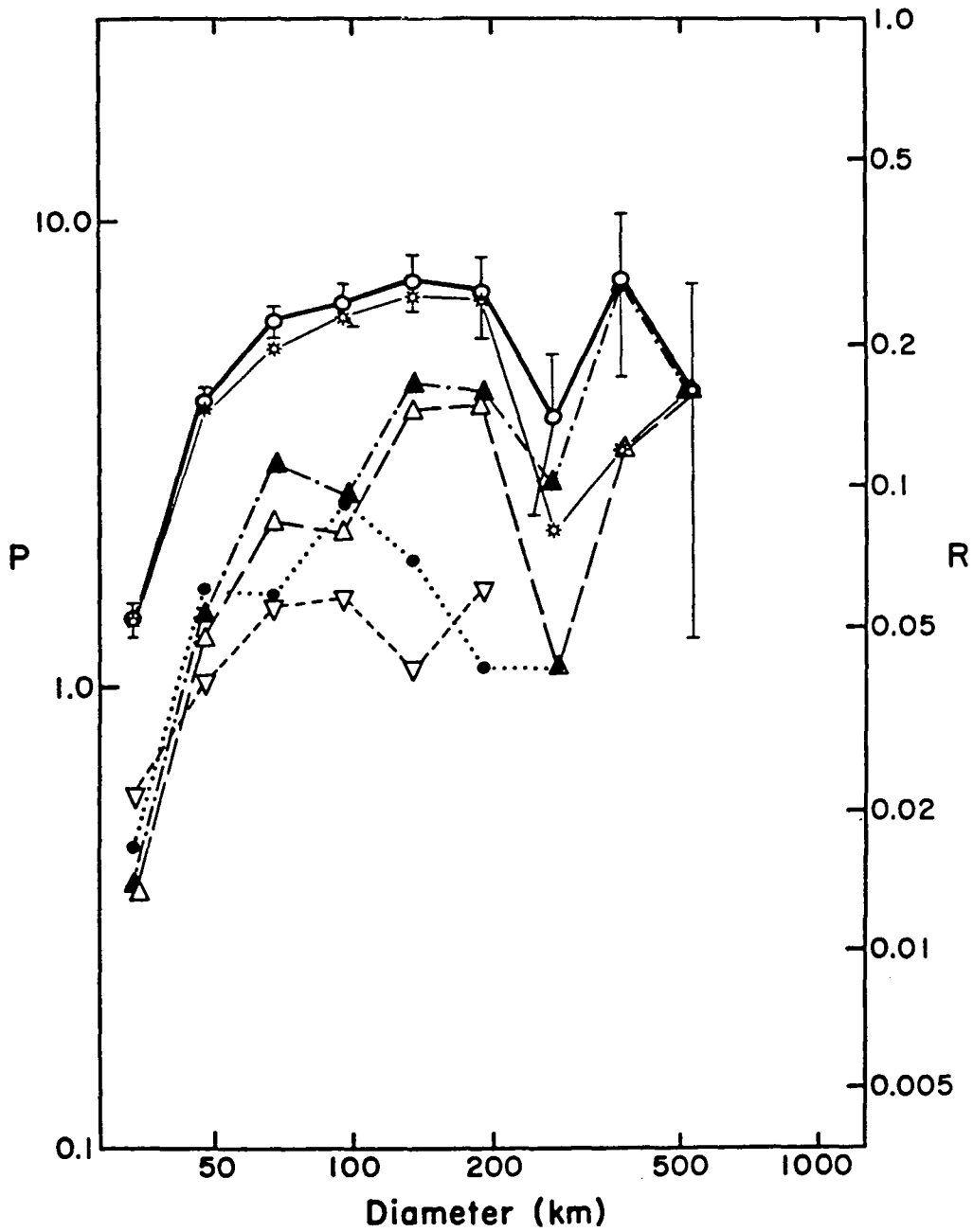


Fig. 69. Crater Coverage of Geologic Map Using Caloris System Notation

Symbols in Fig. 68. Note the dominance of coverage by pre-Caloris craters and the significant contribution of C5' craters to surface coverage. Area =  $1.0284 \cdot 10^7 \text{ km}^2$ .

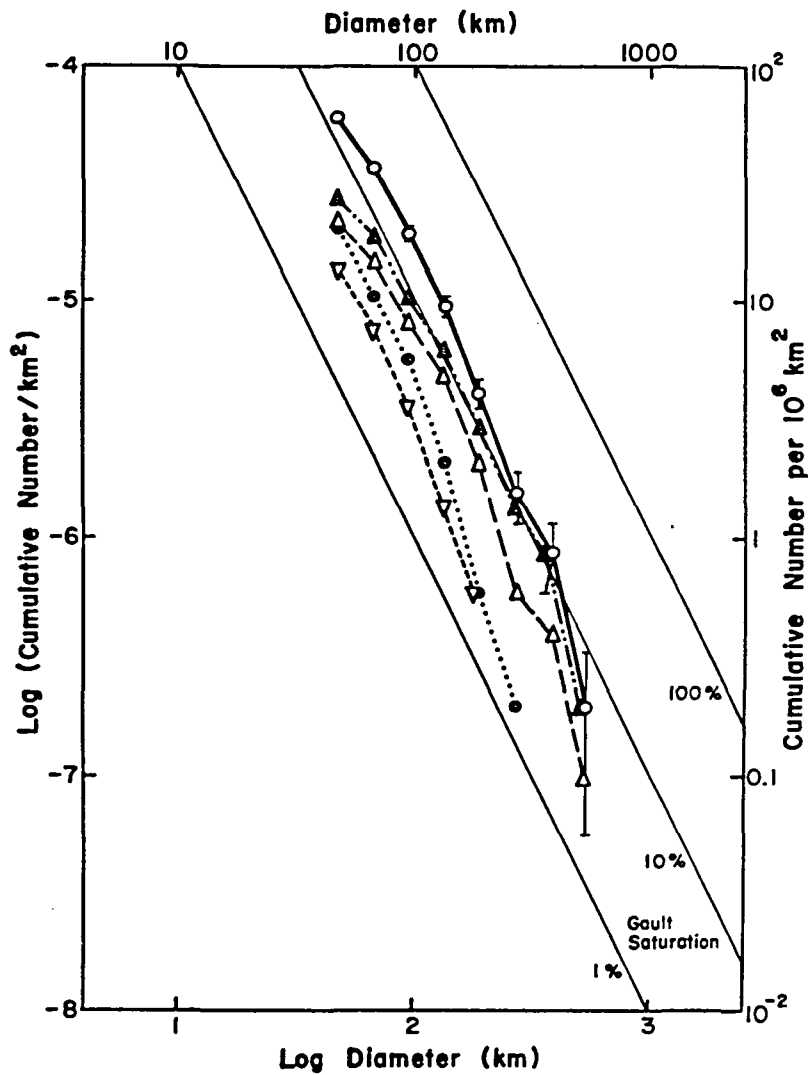


Fig. 70. Cumulative Size-Frequency Plot of Geologic Map Statistics Using Caloris System Notation

Gault (1970) saturation lines of -2 slope shown for comparison with statistics of Fig. 67, selected regions of Mercury.

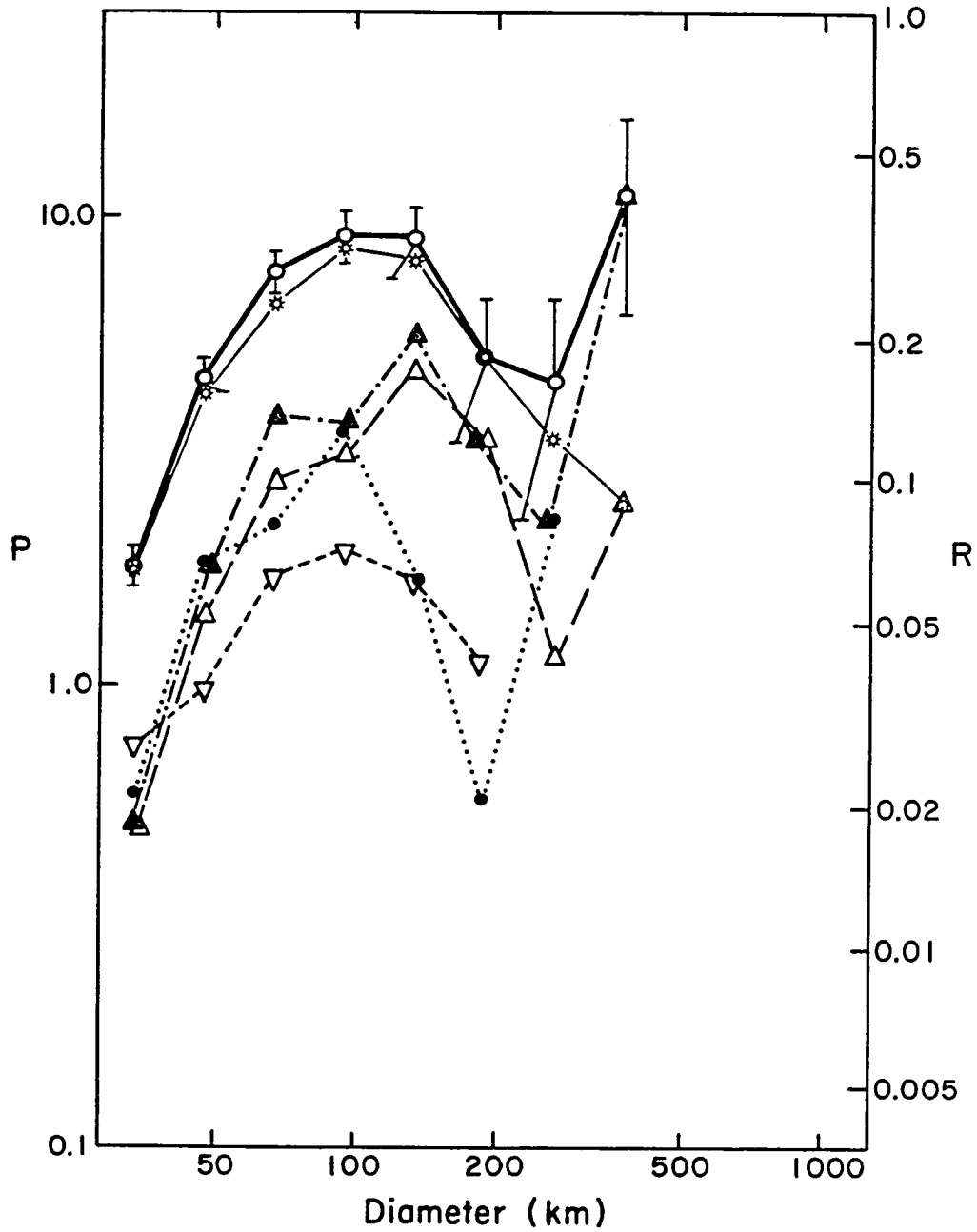


Fig. 71. Crater Coverage of Restricted Geologic Map Using Caloris System Notation

Conservative map boundaries exclude some basins, peaking up coverage by 60-150 km craters. Surface area =  $4.985 \cdot 10^6 \text{ km}^2$ ; data given in Table D30 of Appendix D. Compare with Fig. 69.



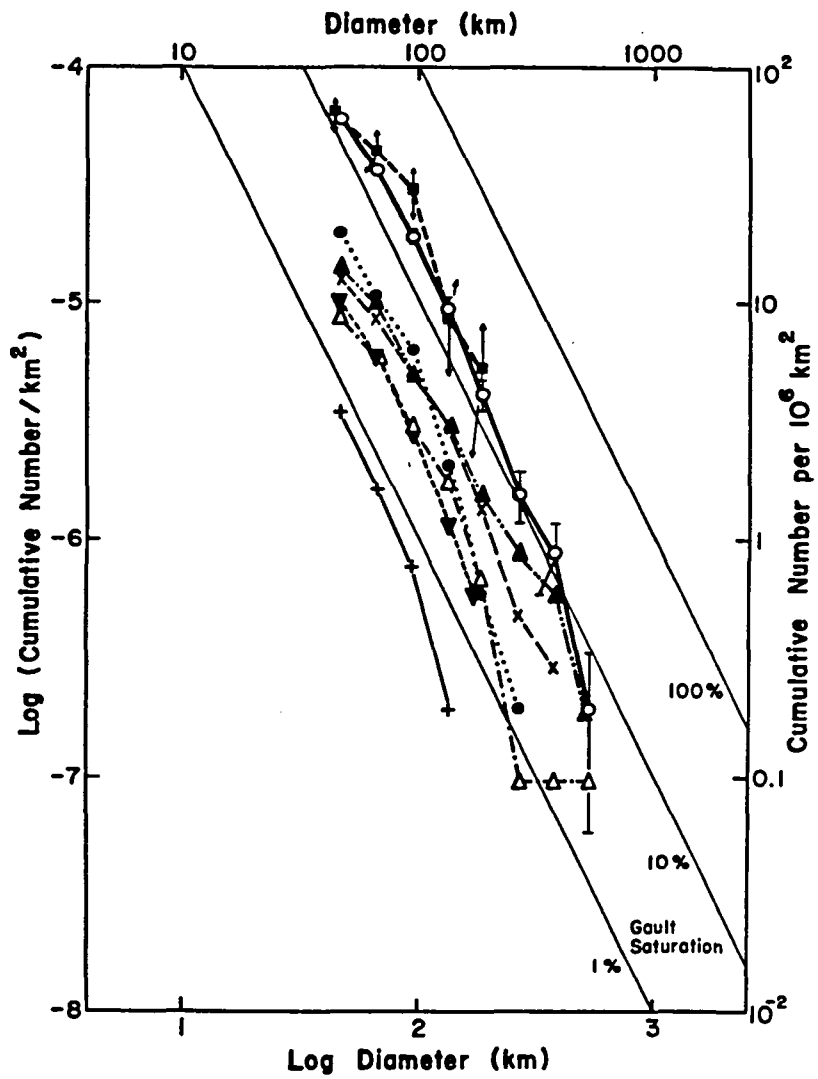


Fig. 72. Cumulative Size-Frequency Data of Geologic Map and Hilly and Lineated Region

Data for geologic map presented by crater class on cumulative plot. Heavily dashed line represents total cumulative frequency of craters in hilly and lineated region ( $5.7438 \cdot 10^5 \text{ km}^2$ ). Symbols in Fig. 68. Data for the hilly and lineated region given in Table D29 of Appendix D.

than 40 km (compared to the restricted area), suggesting that craters were degraded rather than completely obliterated, or that exterior regions were affected in a similar manner. A variety of questions and uncertainties remain in the interpretation of this area plot. The signature of the disturbance appears to be the severe (tectonic) degradation of craters as large as 100 km, boosting the population of C5 classes and depleting somewhat C3 classes (Sec. 2). Timing of the event determines which classes of craters are depleted. Guest and Gault (1976; see also Gault, Guest, and Schultz, 1976) propose that the hilly and lineated terrain formation severely degraded craters as large as 80-90 km in diameter, and obliterated all existing craters less than 20-30 km in diameter.

Quadrangle Data. Cratering data from the Victoria and Bach Quadrangles (Figs. 73, 74, and 77) may provide some examples of regional resurfacing and its effect on crater populations. Unusually high densities of fresh craters are noted in the Victoria H-2 Quadrangle, where P3 plains cover a great part of the mapped area (and bury 30 to 60 km craters). Degraded craters provide only sparse coverage at 40-56 km, but are more common at large sizes. De Hon (1978) has proposed that part of this area is the site of an ancient basin. Direct basin impacts and later volcanism are consistent with the statistics of the Victoria Quadrangle. The Bach Quadrangle also shows a domination by C3 craters, but relatively higher degraded C4

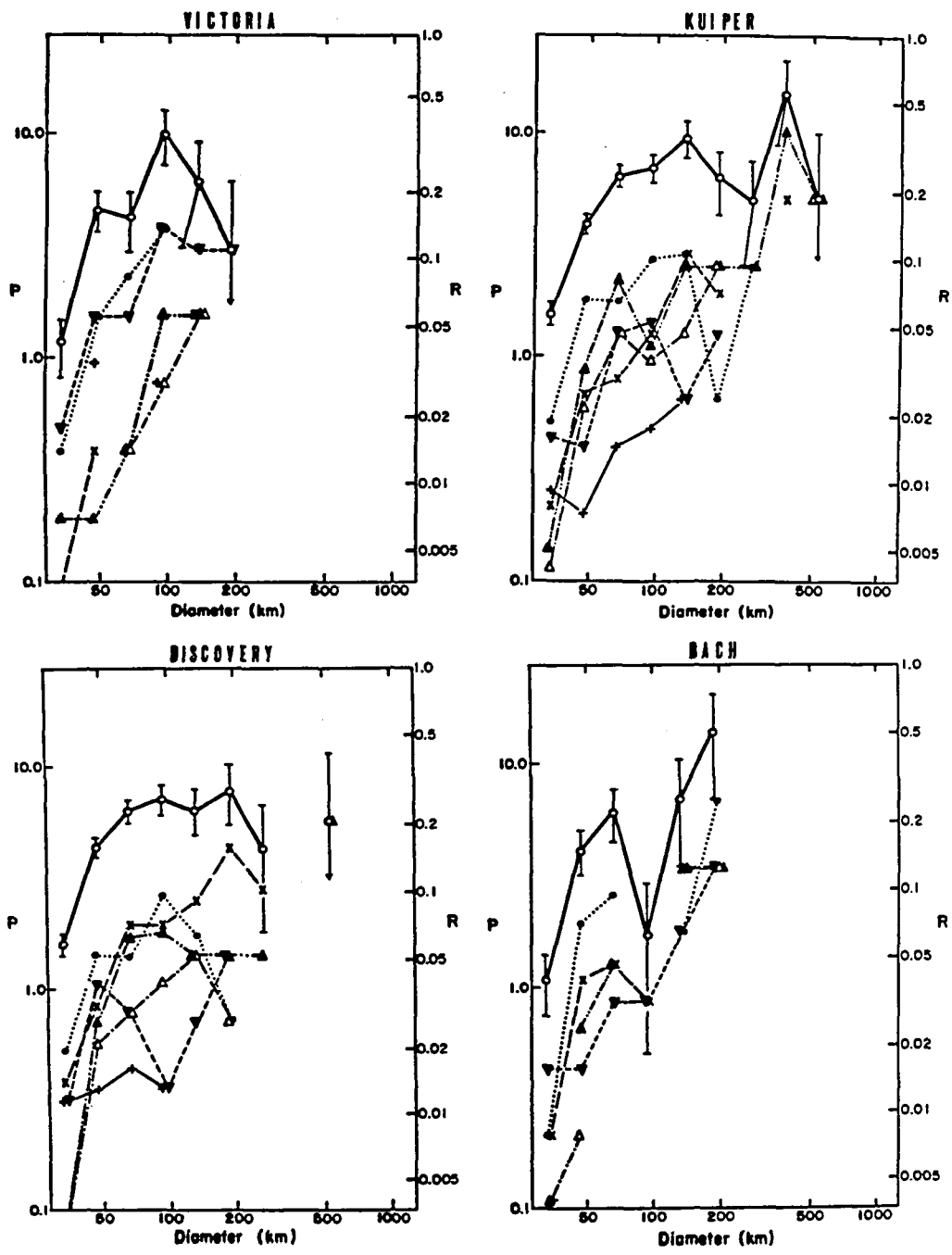


Fig. 73. Crater Coverage of Quadrangles of Mercury's First Quadrant

Similar coverage statistics are displayed by the four quadrangles of the first quadrant: H-2 Victoria, H-6 Kuiper, H-11 Discovery, and H-15 Bach. Variations may be due to the extent of diversity of units within the sampled areas.

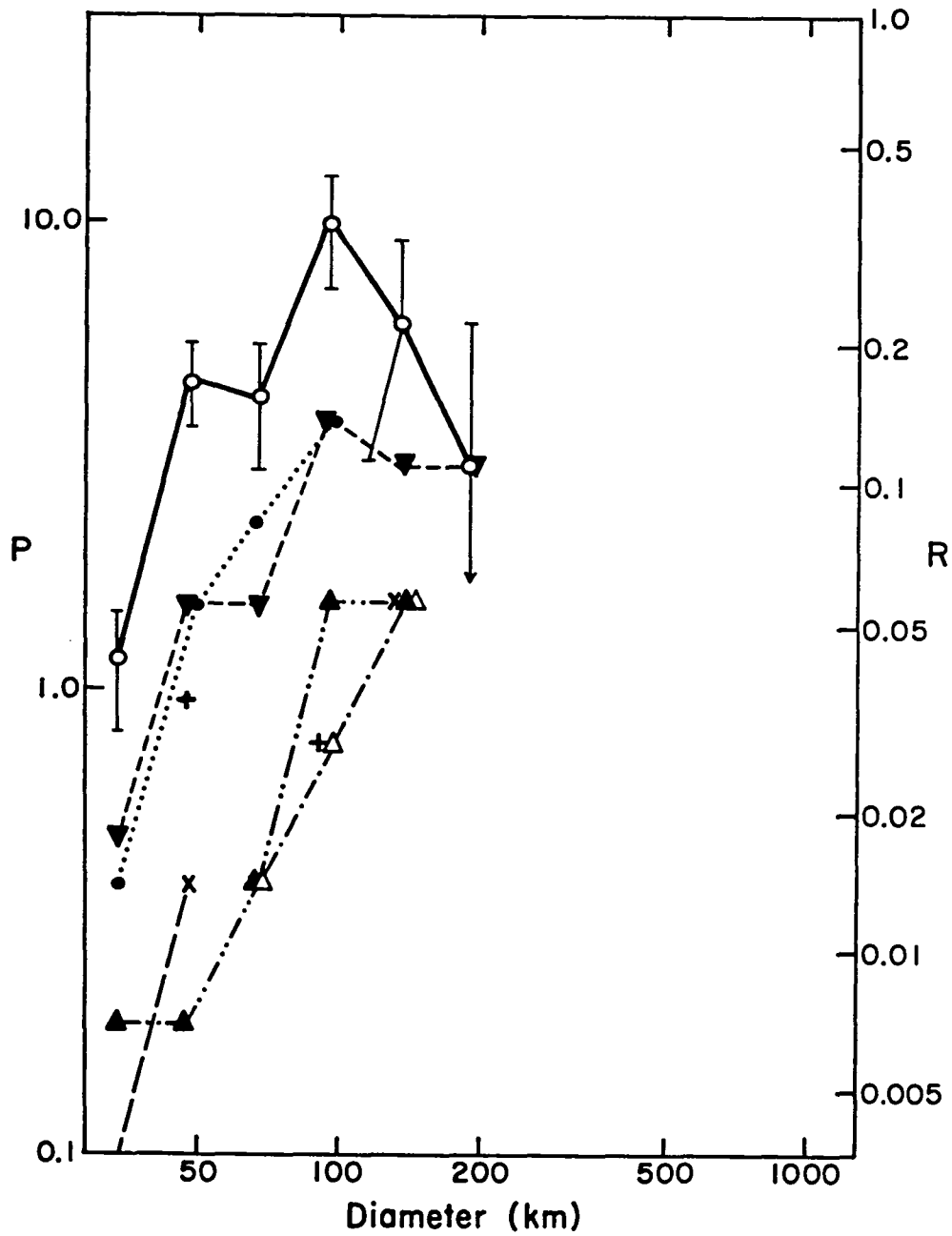


Fig. 74. Crater Coverage of Victoria Quadrangle (H-2)

Fresher craters appear to dominate coverage in the sampled half of the Victoria Quadrangle.  $A = 9.1564 \cdot 10^5 \text{ km}^2$ . See Table D34, Appendix D.

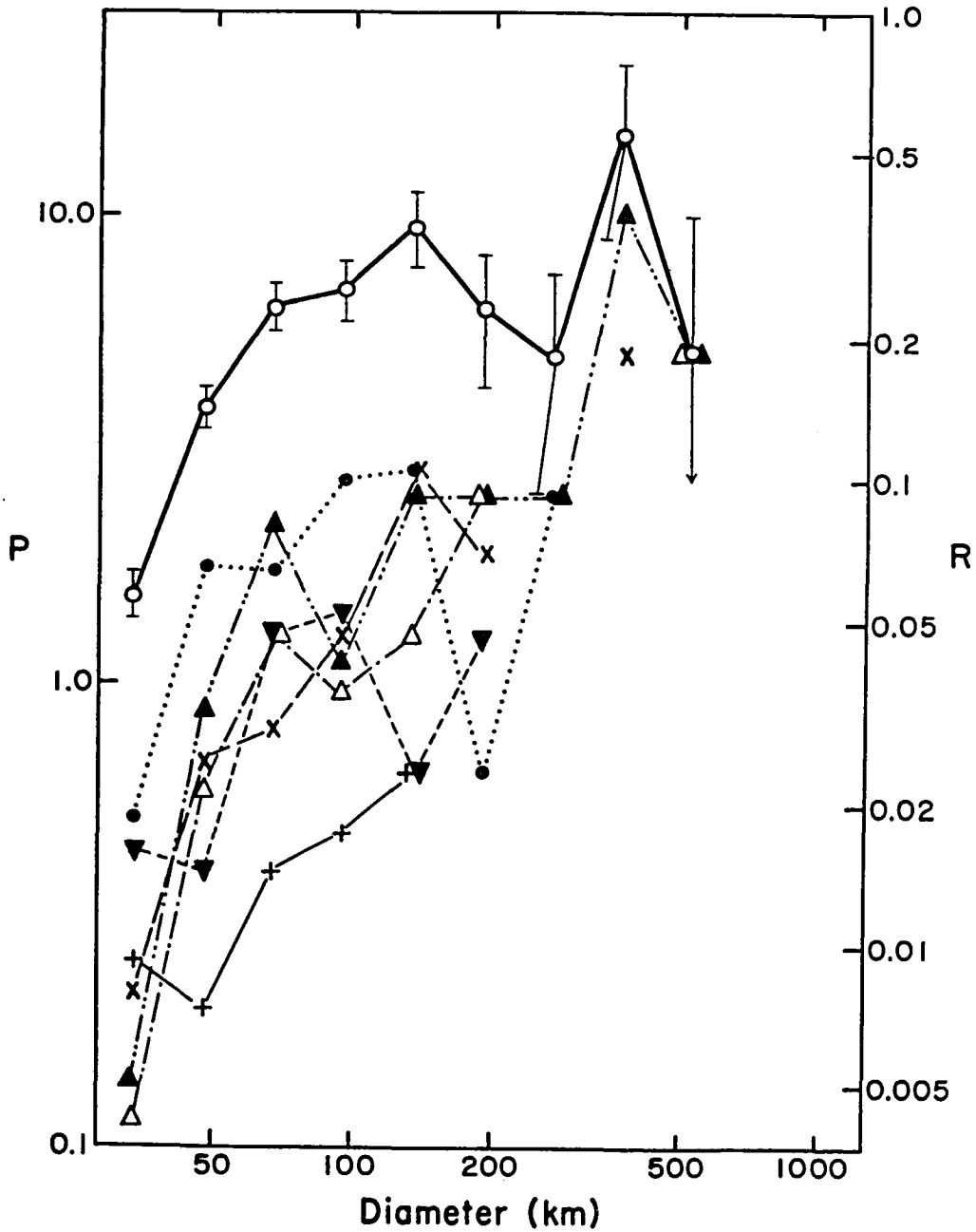


Fig. 75. Crater Coverage of Kuiper Quadrangle (H-6)

A large sampling of diverse units, basins, and craters causes the H-6 statistics to mimic those of the general map, Fig. 68.  $A = 4.4327 \cdot 10^6$  km<sup>2</sup>. See Table D33 of Appendix D. The largest basins include Homer and its two neighbors to the south and west, and numerous C5' depressions.

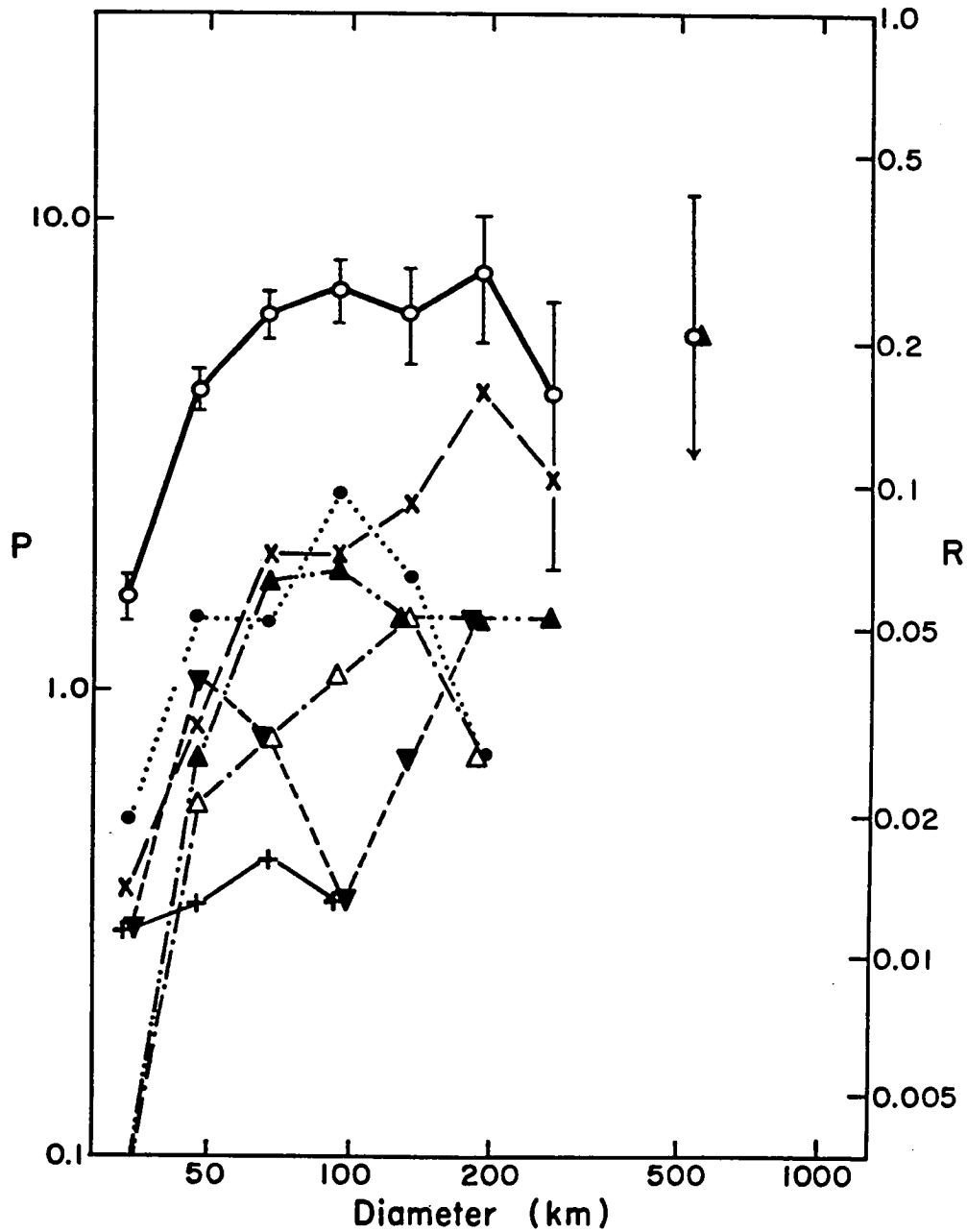


Fig. 76. Crater Coverage of Discovery Quadrangle (H-11)

Again note similarity to general map statistics, Fig. 68. A large, diverse area,  $A = 3.9197 \cdot 10^6 \text{ km}^2$ , was sampled. See Table D32, Appendix D. The largest basin represented is that surrounding the rayed crater Copley, Fig. 28.

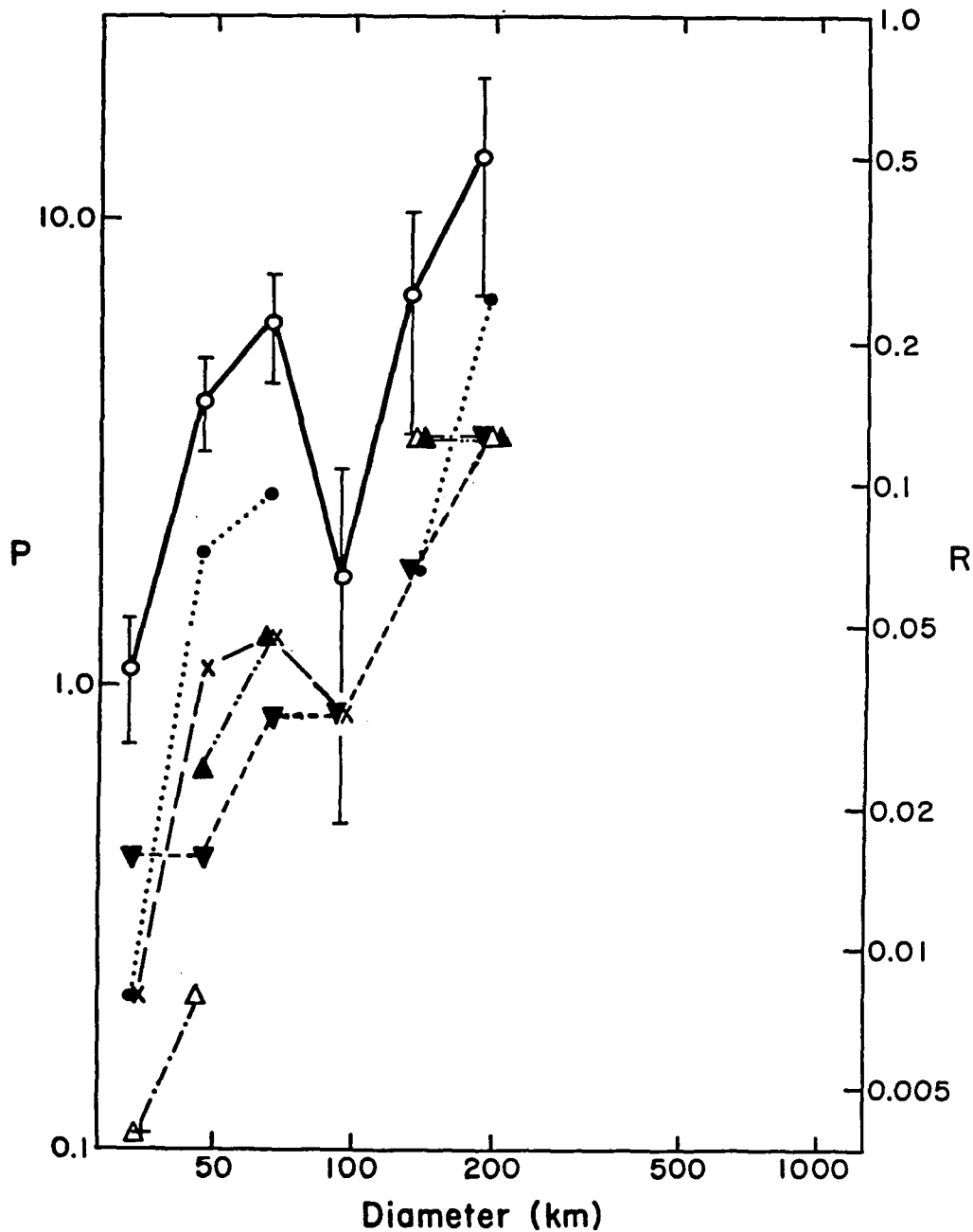


Fig. 77. Crater Coverage of Bach Quadrangle (H-15)

The half of the Bach Quadrangle sampled in these statistics is dominated by P5 plains and a sizeable region of P3 materials. The lack of 100 km and C1 craters is partly due to the 70°S latitude northern limit of this region.  $A = 8.0998 \cdot 10^5 \text{ km}^2$ ; statistics given in Table D31, Appendix D.

crater abundances, without severe losses at smaller diameters. The spectrum reflects greater coverage by older plains units (P5 and P4) and multiple resurfacing episodes.

All crater distributions demonstrate that pre-Caloris bombardment (C5, C4, and C3) greatly exceeds post-Caloris bombardment. This intense cratering flux occurs during P5, P4, and P3 plains formation episodes. The end of the heavy bombardment may extend into the beginning of the C2 period; plains formation during that era continues, but is less than in the preceding Class 3 period.

The distribution of craters on different ages of surfaces illustrates that magnitude of coverage decreases with time, and its maximum shifts toward smaller diameters on younger units. The specificity of coverage by craters over 40 km diameter--and of the projectiles responsible for the impacts--may increase (become more restricted) as the population evolves to the present. The greatest coverage is exhibited by craters which lie in or underneath the older intercrater plains surface. The P5 plains are therefore not interpreted as primordial, because the large number of structures embayed or buried by those plains must yet cover an older surface.

#### Discussion and Summary of Mercurian Crater Statistics

As in the lunar statistics, the mercurian crater size-frequency data collected in this study are more complex and less transparent than the study of Strom (1977) in which he establishes



that volcanic plains emplacement probably affected the mercurian intercrater plains as well as the lunar intercrater region. Volcanism is consistent with some of the regional statistics found here (including the Woronow et al., 1980, study), and is consistent, with a few conditions, with the selected area statistics. However, other processes have affected the crater distributions. Ballistic deposition of ejecta may be indicated by the combination of small crater losses, abundant C4 and C5 craters, and C5 craters partly covered by younger plains material. Direct basin impacts are postulated to decrease overall crater abundances within some circular areas (C5' depressions) later filled by intercrater plains. Magma may intrude into such locally thin crustal regions and further reduce crater densities.

In addition, tectonic destruction is indicated in the hilly and lineated region. Differential preservation may be a factor in some selected areas if the craters are small enough to be strength dominated (Schultz et al., 1977; Pike et al., 1980). The high numbers of small craters--many of which are secondaries--may be preserved in more consolidated intercrater and smooth plains (Cintala et al., 1977), as well as preserved by factors noted earlier, such as higher ejection angles and higher ejection velocities (Scott, 1977). Gravity effects have been noted only in reference to the restricted ejecta blanket distribution on Mercury (Gault et al., 1975). Its control over other morphological factors may be minimal (Malin and Dzurisin, 1977, 1978).

The size-frequency distribution of impacting objects appears to shift from larger to smaller sizes with time to the present. The loss of basin producing objects seems well established. The relative increase in small bodies producing craters of 40-100 km may be due to decreasing activity of plains emplacement, crater destruction, or ballistic deposition. A heavy bombardment is represented by C5' to C3 craters. According to the arguments of Strom (1977), Wilhelms et al. (1978), and Woronow et al. (1980), this bombardment occurred prior to 4.0 b.y. ago, and may have been common to the Moon and Mars. The revised mercurian statistics of Woronow et al. show a progressive loss of craters of smaller diameters relative to the lunar highlands; this loss probably resulted from plains emplacement.

Returning to Fig. 60, one notes that a lunar-like post mare population does not seem to be recorded on Mercury's observed surface. The sparsely cratered plains of the Moon and Mars exhibit the -3 distribution of the same magnitude coverage over diameters of 8 to 150 km. The C1 population of Mercury exhibits the same slope and slightly higher magnitude (equal to C1's on the Moon). The largest expanse of young plains on Mercury, however, records a highland-type, post-Oriente population; the Caloris plains are thus interpreted as older than the lunar mare. The distribution of rayed craters on Mercury (Allen, 1977) supports this conclusion. Further comparisons of relative ages of mercurian and lunar surfaces are given in the next chapter.

The major preferred interpretation of Mercury's cratering history restates the conclusions of the geologic study, namely, that volcanism has probably eliminated smaller craters from the surface, direct impacts have resurfaced large circular regions and degraded some peripheral landforms, and that secondary cratering from the surviving large craters, usually clustered around the rims of ancient depressions, has produced the high density of small 5-15 km craters which superpose the plains' surface.

## CHAPTER 4

### GEOLOGIC MAP ANALYSES: CORRELATION OF GEOLOGIC AND CRATERING HISTORIES

Geologic map analyses are expanded in this chapter, beginning with a discussion of particular regions which may illustrate volcanic and ballistic plains emplacement on Mercury. Major attention is focused on the surface history of Mercury through discussion of the areal distribution of plains and craters and the paleogeologic maps of the first quadrant. A summary of the lunar intercrater plains formation similarly interrelates the information from the Moon's geologic and cratering histories. The derived "igneous chronologies" set constraints on the thermal models discussed in Chapter 6.

#### Specific Areas Illustrating Volcanic and Ballistic Plains Emplacement Mechanisms

The areas of Renoir basin, Chekov, and a large crater west of Shevchenko present strong evidence for volcanic emplacement of plains material. Tentative examples of ballistically deposited plains material occur between the Kuiper and Imhotep complexes, east of Schubert, east of Handel, and possibly surrounding Ma Chih-Yuan. The evidence for ballistic emplacement is poorer, and suggests that this process is supplemented by volcanism and mass wasting. The best example of each process, Renoir and Kuiper-Imhotep (stereo images in Figs. 78 and 79), is discussed in more detail; a brief discussion of the other regions

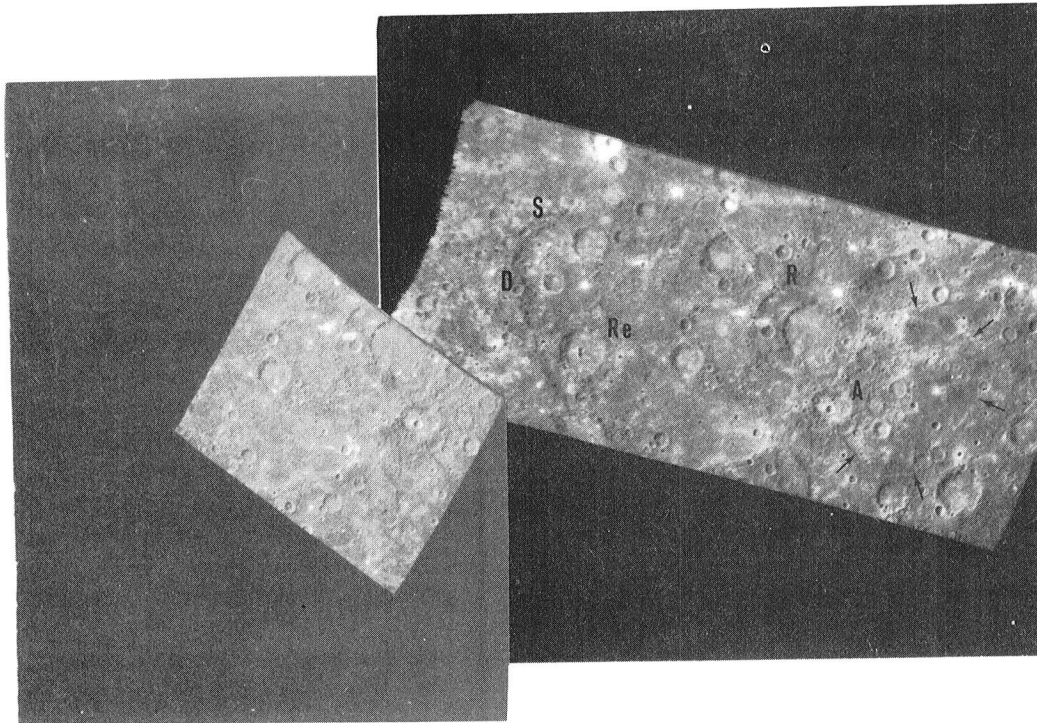


Fig. 78. Renoir Area Volcanic Features--Stereo Pair

The superposition relationships of smooth plains, the small crater (A) to Renoir's southeast, and Renoir (R) are illustrated above. Although severely degraded, crater A appears to be superposed on Renoir's rim. Note the vertical relief of the pitted lobe. The dark material near the inner rim does not correspond well with mapped geologic units; compare with Fig. 9 (xviii-xix).

The arcuate scarp to the south bounds materials lifted above regions containing Renoir secondary sculpture. To the east and west, this depressed region has been embayed by P2 and P3 plains materials. See also Fig. 25b.

Note the large 300 km C5' basin west of Renoir visible in the right hand picture. Its rim consists of inward facing scarps which trend along the global lineament directions. Simeiz Vallis (S), an arcuate valley atop the rim crest of large C4 basin (D) to Renoir's west, may be associated with the collapse of the C4 basin's rim. The C4 and C5' basins appear to have outer scarps located a half radius beyond the primary rims. The crater Repin (Re), located north of the "ponded" smooth plains, also has an exterior depression (moat?) encircling its rim.

Left: FDS 166649. Right: FDS 27301. North at top. Renoir is 220 km diameter; Repin is 95 km in diameter.

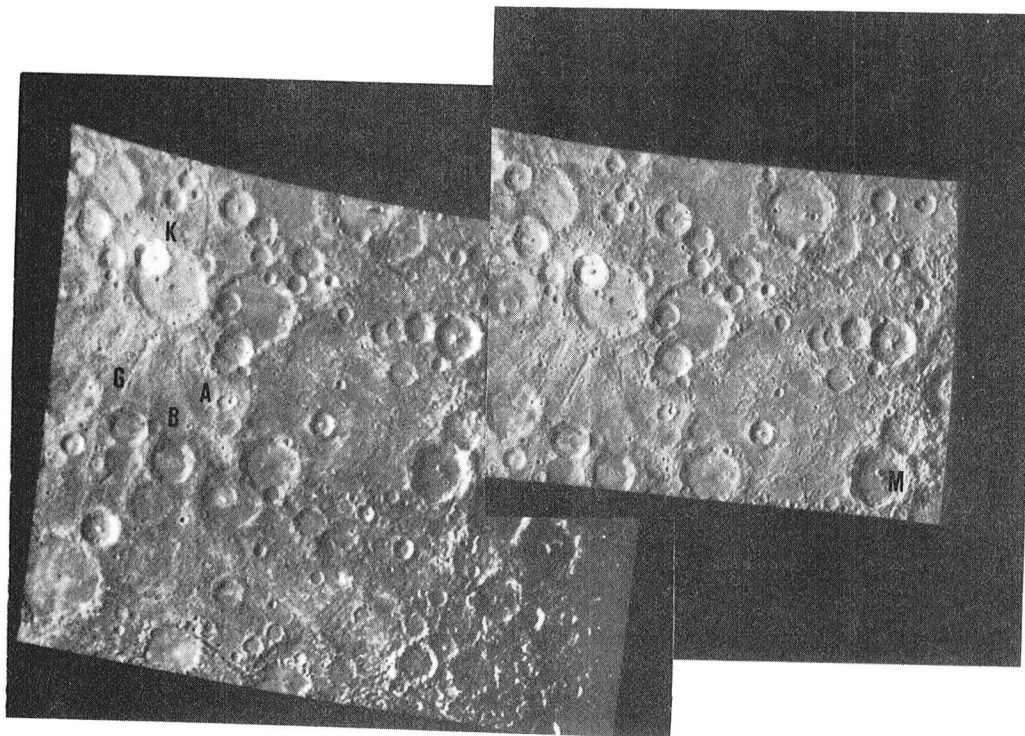


Fig. 79. Kuiper - Imhotep Area Plains: Tentative Examples of Ballistic Emplacement

In this stereo view, complexes of large craters are separated by regions of irregular plains which may consist of ejecta deposits from the surrounding craters. Ancient circular depressions occupy almost all regions now covered by plains. Two distinct features displayed in Fig. 13b are designated A and B. A larger C5' basin may underlie both A and B, its west rim visible as a curved ridge east of Goldstone Vallis (G). The latter is probably a secondary chain of Murasaki; other sculpture visible under the plains material appears to be part of a different radial system (from a large crater nearly destroyed by Murasaki?).

Plains here do not necessarily occupy topographically lower regions. Younger plains material is distributed between the two younger C2 craters, although the southern crater has been embayed by some P2 plains. Older plains units lie beneath the younger plains between the older craters. Large C5' structures flank this zone to east and west, suggesting that the cratering history of this region has been quite severe.

Stereo pair FDS 166478 (Left) and FDS 27304 (Right). North at top. Kuiper is 60 km in diameter; Mahler (M) on right is 100 km in diameter.

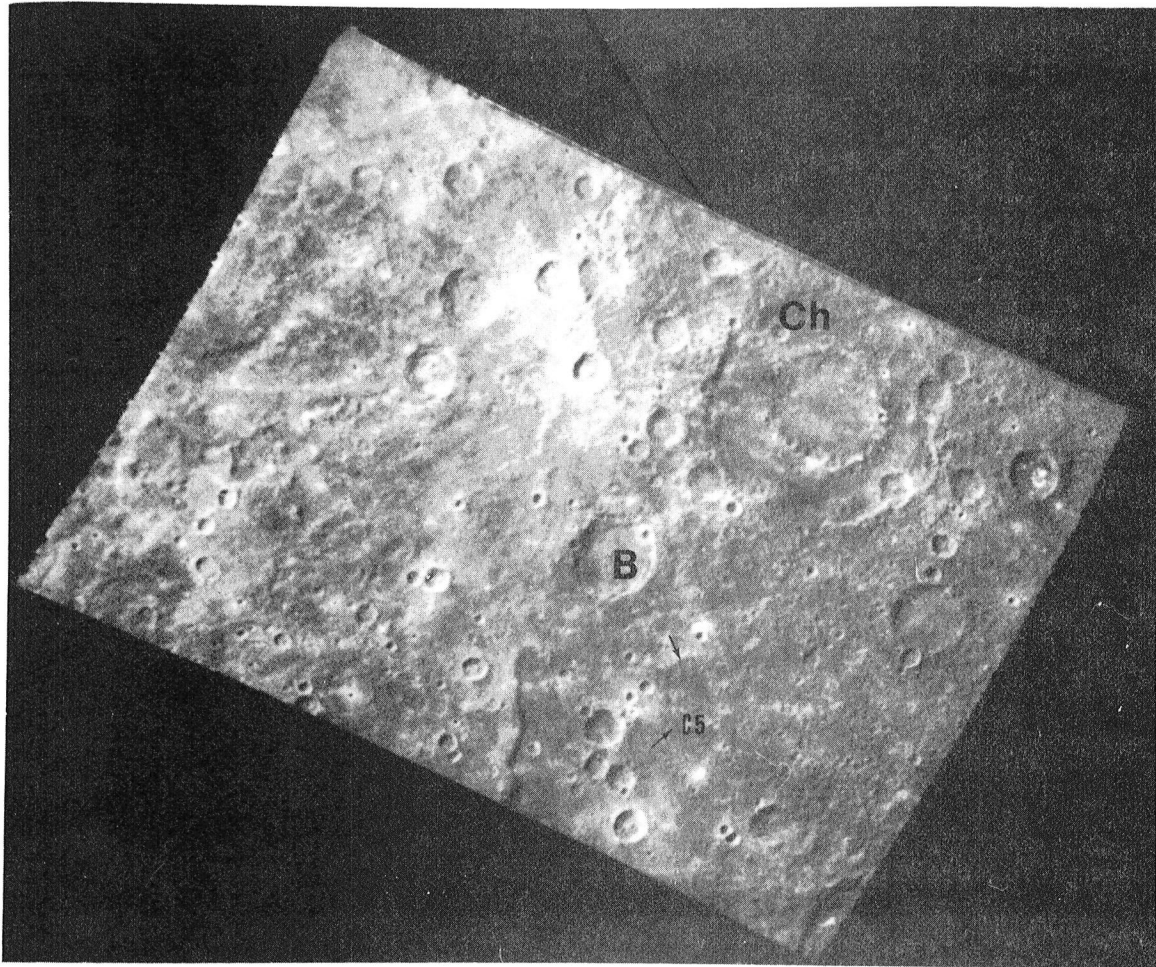


Fig. 80. C4 Basin Chekov Embayed by P4 Plains

The C4, 180 km diameter basin Chekov is embayed by P4 intercrater materials along its southern rim. Pitted and hummocky materials lie within the outer scarp of the basin and also bury a C5 crater south of the basin. The other half of the C5 crater is filled with and surrounded by P3 plains. The C4 crater (B) just southwest of Chekov appears to have dark materials on its rim to either side of a trench along the rim's crest.

The ridge oriented north-south at the lower center of the image is Astrolabe Rupes. It is mapped as P4 material which was thrust upward in Class 3 time, then flooded by P3 materials. The entire region to the west of the scarp may contain materials within a large basin (C5'), roughly centered on the rayed crater Copley (see Fig. 28). Volcanic activity is indicated for the P4, P3, and tentative P1 materials of this region.

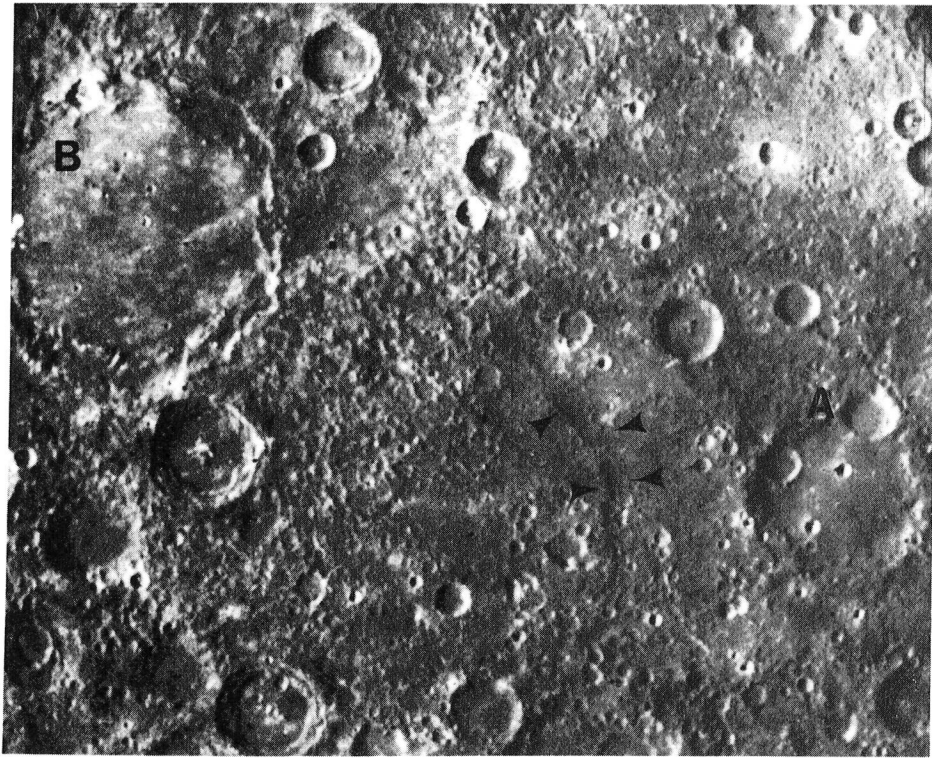
Rectified image FDS 166601. North at top. Chekov is 180 km in diameter.

Fig. 81. Multiple Flow Units in Crater West of Shevchenko

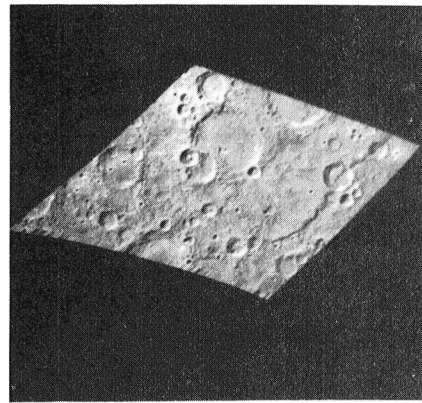
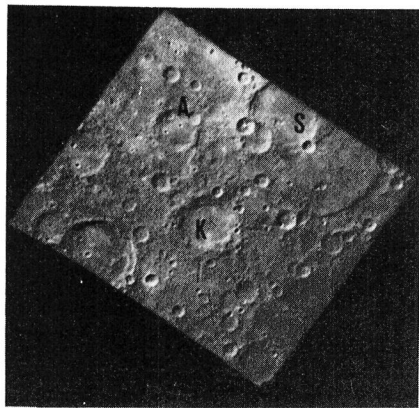
Crater (A) is best interpreted to be embayed by a succession of plains materials, some of which are volcanic. The lowermost, roughest material is P4 impact melt filling the C4 crater, or part of the P4 deposit overlying the crater's western ejecta blanket. The P3 deposit forms part of the P3 plains unit exterior to the crater; these plains fill the western half of the crater, and embay the southern rim and adjacent areas. P2 material later filled the crater's northern sections. The east-west wedge or dome shape may be due to the thickness of the deposits or to later tectonic uplift. It is not understood why the usual relation of younger plains occupying lower levels is reversed inside the crater but normal outside of the crater. Fault blocks may form the multilayered floor, but volcanism is the preferred interpretation.

- a. FDS 166669. North at top. P2 material fills a sinuous depression which seems to open northward into a crater-like depression. The "graben" may be a remnant of intercrater plains formation, but few constraints exist on its age, other than its formation prior to P2 plains emplacement.
- b. Stereo pair FDS 166613 (Left) and FDS 27399 (Right). North at top right corner. Shevchenko (S) is 130 km in diameter. Khansa, although only 90 km to the southeast, does not appear to have ejected debris into the P4 unit within crater A.





a.



b.

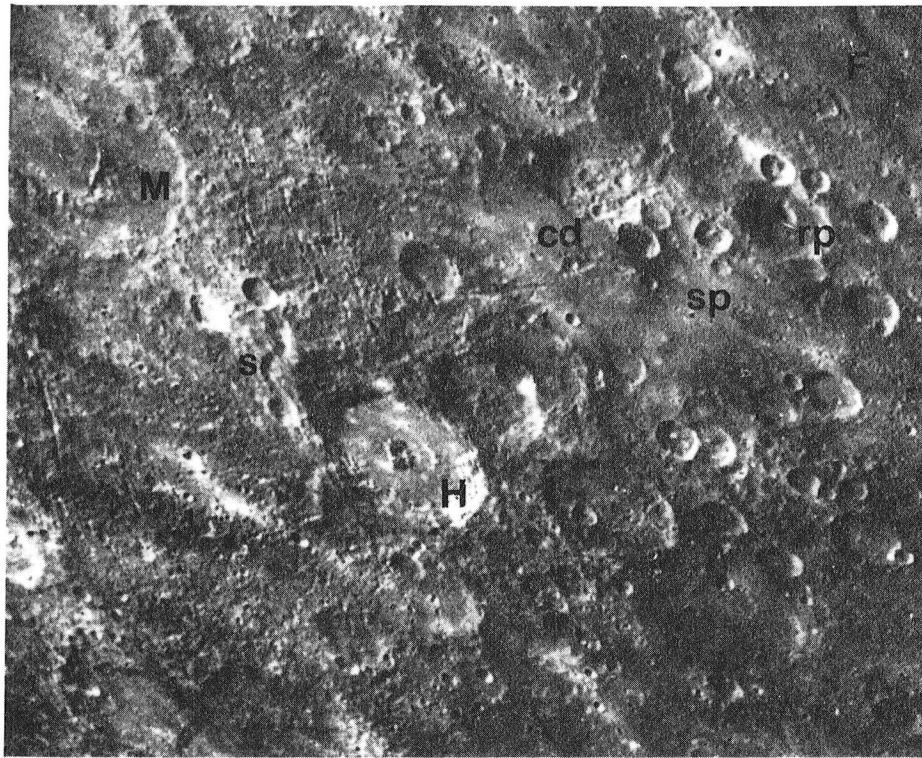
Fig. 82. Hawthorne Area--Volcanic Features?

Possible volcanic landforms near Hawthorne lie just off the geologic map, south of Ma Chih-Yuan in the H-12 Quadrangle (see Fig. 28). The smooth area in right center may be asymmetrically deposited ray crater material, because its thickness appears to increase away from the dark-floored ray crater. Thinner deposits, as determined by the subjacent topography, may occur at the edges of the smooth area, where darker material dominates. The rays partly superpose a rimless, scalloped-edged depression, termed a caldera depression (cd) in Fig. 82a.

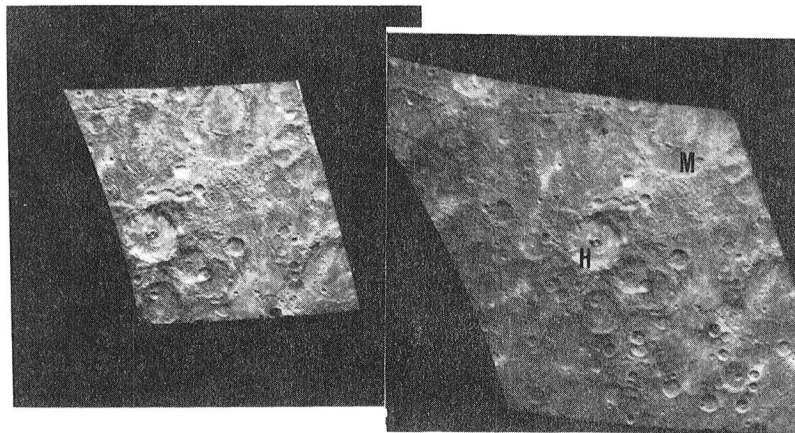
The sinuous trench near Hawthorne has raised edges, is nearly 10 km in width, and is headed by a small crater at one end, while superposed by a similar size crater at its other end. The rimless pit north of the rayed crater is elongated linearly along a fault trace. Like the pit within the C2 crater transected by Antoniadi Dorsum (Fig. 21), this one also lies within a crater, and is associated with tectonic features.

Fram Rupes is visible near the top right corner of Fig. 82a. The domical mass lies just off the picture, visible in Fig. 84, southwest of Ma Chih-Yuan. C5' depressions occur north, east, and west of Hawthorne.

- a. FDS 166605. North at top right. Hawthorne is 100 km in diameter.
- b. Stereo pair FDS 166660 (Left) and FDS 166605 (Right). North at right. Michelangelo (M) is 200 km in diameter.



a.



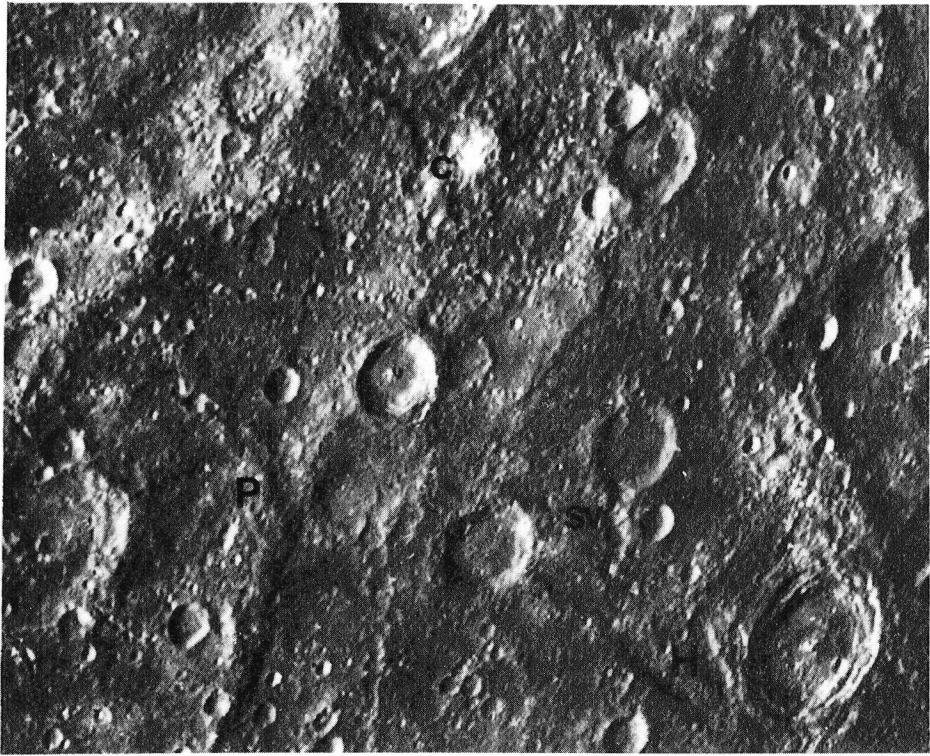
b.

Fig. 83. Hero Rupes Area Volcano-Tectonic Features

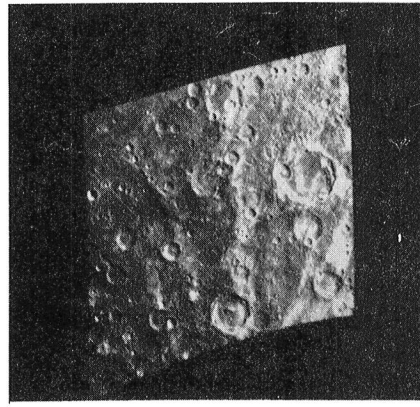
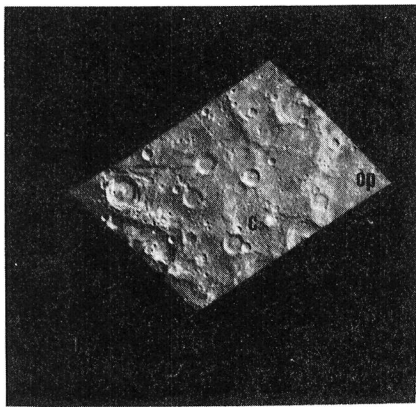
This region lies within the H-12 Quadrangle near the termination of Pourquoi-Pas Rupes and Hero Rupes, near 60 S and 153 W. Structural features include a continuous chain of 5-15 km craters radial to Dostoevskij (390 km diameter), circular depressions (C5 and C5') of various sizes, a series of overlapping 70 km discs of smooth plains, and the features noted at right. The crater chain (which is unusually long and distinct) and the two arcuate scarps appear to converge at the center of the photographed area (Fig. 83a), in a depression (C5'?) partly covered by smooth plains. The flat-floored crater to the west may be transected by the sinuous valley; note the stereo view (Fig. 83b). The massive, pitted, conical peak, nearly 30 km at its base, has been described by Malin (1978), and is interpreted to be a volcanic dome.

Coincident with a bright ray on the east of the stereo image, there appears to be a subdued scarp consisting of the overlapping, smooth spatulate discs noted above. The linear array (of at least 3 circular features) is depressed along its center. It is not possible to specify the origin of this feature, but one speculation is that it is a remnant of planetary expansion flooded by smooth plains.

- a. FDS 166750. North to lower left (direction of the trend of Pourquoi-Pas Rupes); east parallels the trend of Hero Rupes. The central crater is 40 km in diameter. Dostoevskij's crater chain extends 1 D to 2 D from its rim (3R to 5R from its center).
- b. Stereo pair FDS 166750 (Left) and FDS 166836 (Right). North is up. This region can be seen in South Polar Mosaics SP-16, SP-7, and SP-11.



a.



b.

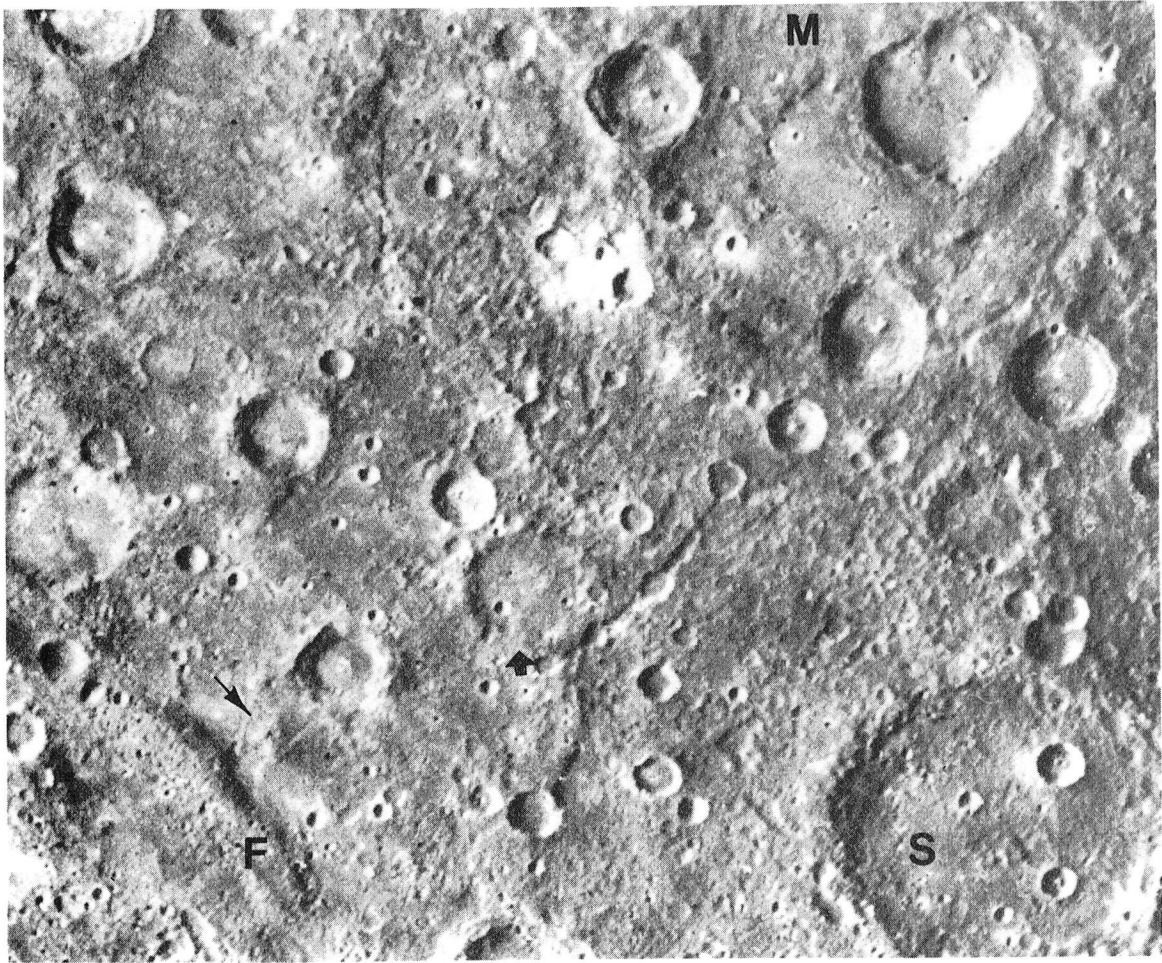


Fig. 84. Ma Chih-Yuan and Perimeter

The C4 basin, Ma Chih-Yuan, 170 km in diameter, may be attaining isostatic equilibrium, based on the shape and relief of its rim and peak ring (compare Rodin, Fig. 21, and Fig. 6 in Scott, 1967). Part of the basin rim has collapsed to form a trough along its crest. The ancient age indicated by the high density of superposed craters and the basin's degradation conflicts with the preservation of basin secondaries in adjacent materials (P5 plains). Beyond 1 - 2 D from the basin center, Ma Chih-Yuan's secondaries are buried by a peripheral ring of P3 plains. The encircling deposits may be ballistically emplaced; however, they also embay a 45 km crater through its breached southern rim (farthest from the basin). Note the domical feature (thin arrow) in the P3 materials, near Fram Rupes (F; lower left). The scarp, dome, and flooded crater suggest a volcanic origin for the P3 plains.

FDS 166666. North at top. Sei (S) is 130 km in diameter.

illustrating volcanic and ballistic processes is presented in Figs. 80 - 85. Please refer to the Geological Terrain Map (Fig. 9, xviii-xix) for detailed stratigraphy of these regions.

#### Volcanic Plains

Renoir. The area of Renoir basin (Fig. 78; see also Fig. 25) exhibits a variety of volcanic and tectonic features. The double-ringed, C3 basin, 220 km in diameter, is an impact structure; sculpturing from its secondaries can be detected to the southwest extending one diameter outward from the rim. P2 and P3 plains fill the interior: P2 plains lie in a deeper inner basin and within depressions in the outer plateau.

A companion crater which appears to lie on top of Renoir's southeast rim is highly degraded. Its basinward rim is thin and crenulated, but intact, unlike the rim farther from the basin. Deposits of smooth material cover the small crater's floor and extend up to the crenulated rim crest on the inner edge; they also flank the outer rim, extending down into the outer ring portion of Renoir, ending in a massive, pitted, and lobate extension at Renoir's inner ring. These deposits may also embay the ejecta blanket of Renoir west of the companion crater. Dzurisin (1977b) detects an albedo difference extending from the small crater to the lobate extension, and along similarly pitted material (here mapped as P3) to the west. Malin (1976b) detects a textural difference.

Fig. 85. C5' Features of the Homer-Handel Area

- a. Vague circular depression C5' denoted by arrows. Irregular depressions to northeast, northwest, and south suggest smaller, very degraded crateriforms. Corner marks denote the boundaries of Fig. 85b. Homer (Ho), Handel, and Lu Hsun (320 km, 150 km, and 95 km in diameter respectively) may have contributed ejecta deposits as well as secondary crater-forming materials to this circular depression. P5 material (which records secondaries from C4 basin Homer) apparently covers this C5' feature. Handel and Lu Hsun are C2 in age.

FDS 27317. North at top right.

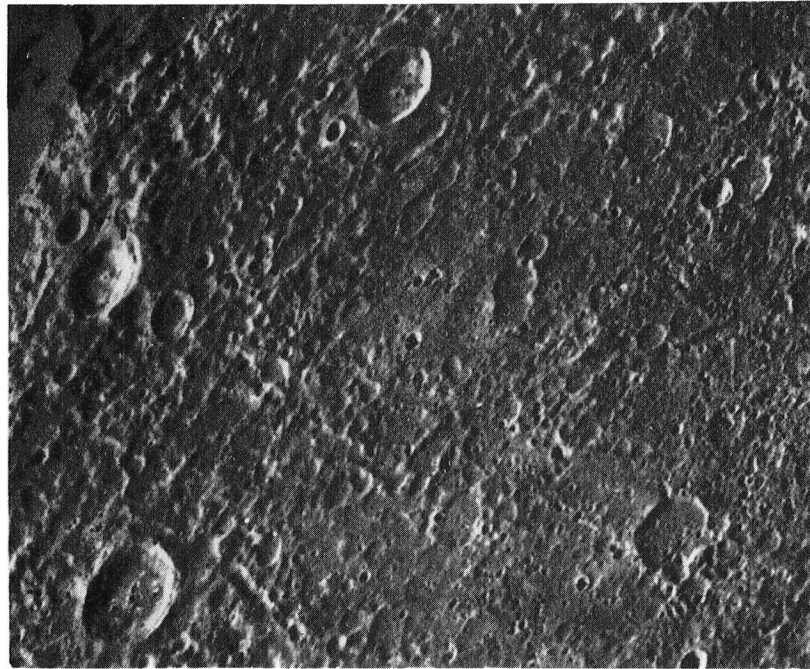
- b. High resolution image of the large depression. Note that features radial to Handel (west) and Homer (southwest) are overlain by smooth material in the depressed regions of the C5' feature. In addition to nearby volcano-tectonic features (a dome and contact zone, Figs. 22 and 24), the superposed P2 material suggests that its origin may be volcanic.

FDS 27440. North at top right. The crater at lower left is approximately 32 km in diameter. The entire area is mapped in Fig. 24, an excerpt from Fig. 9 (in pocket).





a.



b.

Within the inner basin, two circular rims of 30 km diameter are noted; the one closer to the basin center has less topographic relief. These features are best interpreted as the result of volcanic processes. The hummocky P3 material may be impact melt of Renoir; the two "ghost rings" are craters which impacted the basin's central depression, prior to plains emplacement. The delayed embayment, the albedo change associated with the lobate escarpment, and the mantled rim of the crater to the southeast are the major arguments for volcanism. The smooth P2 plains may have several source vents: the basin center, the northeast basin rim, and the exterior rim flank where impacted by the C3 crater. The hummocky lobe of material can be interpreted as a pitted volcanic extrusion, or *décollement* thrust fault.

The plains embaying Renoir are apparently shallow--800 to 1000 m deep (De Hon et al., 1980)--and only partly bury the two 30 km craters. Further infilling would eliminate both the craters and the basin's ring. Renoir illustrates part of the process of intercrater plains formation as proposed in Chapter 3: direct basin impact, followed by volcanism interior to that basin, resulting in a circular area which lacks intermediate to large craters. The smooth P2 plains are clearly neither impact melts nor ejecta from nearby basins: Renoir is relatively isolated. The emplacement of volcanic plains exterior to Renoir's rim may have been structurally controlled by the

superposed rims of Renoir, the smaller crater, and a C5' basin to the east. A large arcuate scarp may control plains emplacement south of Renoir (see Fig. 25b).

Renoir's companion crater with the crenulated rim may belong to a group of endogenically modified craters described by Schultz (1976b, 1977). His examples, mostly second quadrant craters, often lie on the periphery of plains-flooded basins. Albedo data, color data (e.g. Hapke et al., 1975), apparent floor depth, and crater morphology provide clues for detection of modified craters. (Both Schultz (1976a, 1977) and Malin (1978) discuss the discernibility of possible volcanic landforms using the Mariner 10 imagery.)

#### Ballistic Emplacement

Ballistic emplacement of plains-forming materials is not evident around large fresh craters (e.g. Mozart, 225 km); although the rim materials of the continuous ejecta blanket are somewhat smoothed, no plains appear near the distal end of the satellitic craters. However, around larger and older craters and basins, materials commonly embay secondary crater chains radial to the crater, and appear to be ballistically emplaced ejecta.

Kuiper'-Imhotep. Between heavily cratered regions containing the craters Imhotep and Kuiper, respectively, are plains which may be ballistically emplaced, although the mechanism is uncertain. Patches of plains lie between basins and craters of the same age as the plains

material, and usually outside the satellitic crater fields of those structures. (Refer to map, Fig. 9, in pocket, and Fig. 79.) P3 plains lie between Murasaki (C3, 125 km diameter) and Imhotep (C3, 160 km) but beyond most large secondary crater troughs of the former. P2 plains lie between smaller C2 craters of each area; some of these plains embay the southern C2 crater's ejecta blanket. The plains fill C5' structures, overlying both their raised rims and their interiors (Fig. 13b). Secondaries of Murasaki severely crater these raised areas. It appears that primary crater ejecta has embayed the secondaries, or those of similarly-aged craters. As shown in Figs. 13b and 79, the proposed ballistic deposits are smooth and not confined to depressions.

Color Differences near Renoir and Kuiper-Imhotep. From the color-ratio map of Hapke et al. (1980b), Renoir's outer ring plateau is comprised of bluer-than-average materials. A lobe of these blue materials appears to embay a C5 crater directly north of Renoir. The color boundaries on Hapke et al.'s map, the plains' boundaries mapped here, the albedo boundary of Dzuring (1977b), and the textural boundary of Malin (1976b) all differ in their details, but do show that the deposits of the basin's interior are unlike those of the basin's outer ring. No anomalous color appears to be associated with the companion crater.

The Kuiper and Murasaki region is unusual in its distinctive colors; however, there are no color differences associated with the P2

and P3 deposits postulated to be ballistically emplaced between C2 and C3 craters respectively. As might be expected, they are similar to the surrounding surface in color. However, directly north of the region, Murasaki's red floor contrasts with the much bluer Kuiper, and with the yellower deposits outside the rim of Murasaki. Slightly bluer ray material extends west and south; not all bright ray deposits appear in the color ratio map. Bluer-than-average materials occupy two craters to the south which have tentatively-identified volcanic flows within them (Strom et al., 1975b; Dzurisin, 1978). The C2 craters in question do not impact onto these anomalous units.

Thus, the color-ratio data--in these two examples--support a volcanic origin for Renoir's plains, and a ballistic origin for the plains between the Kuiper and Imhotep complexes. Many of the areas illustrated in the following figures are not included in the Hapke et al. (1980b) data; for those areas which are included, color differences better correspond to ray materials than possible volcanic plains deposits.

#### Discussion of Mapping Bias

The definition of plains in this mapping technique is reviewed and the implications explored in this discussion.

The older age limit of the plains unit is defined as the youngest material which it overlies or embays, and the other age limit is less than the oldest material superposed upon it (Malin, 1975). The

relative age of a plains unit is thus bracketed by the relative ages of the craters which are embayed by or superposed upon the plains material.

Clearly volcanic plains material fits well into this method of classification. Volcanic materials extruded exterior to craters will embay craters of older or similar age classes. While smaller craters may be completely eliminated, the larger craters may simply have their ejecta blankets embayed, or inundated to the rim. In the latter case, age identification must depend on degradation of the remaining rim. Fresher craters will impact the resurfaced area, or distribute their secondary fields upon it. Complications arise if there are too few craters in the plain's locale to constrain its age, or if those craters are either too old or too young to confine the relative age of the plains material. However, neither the plains-forming episode nor the cratering episode will be discrete events over separate intervals. That ambiguity, as well as the likelihood of partial resurfacing and variation in crater degradation states due to proximity weathering, will make the plain's relative age less specific than presupposed in the age-dating technique, even though emplaced as a volcanic unit.

However, plains formation by ballistic deposition could pose even more ambiguities in this mapping strategy; such a plains unit is formed from the ejecta of many craters in multiple events. Material should be distributed over all topographic forms, and only locally

confined to low-lying areas where secondary impacts and seismic shaking promote mass wasting (Trask, 1976a).

On the lunar surface, plains deposits from basins are emplaced at the edge of the continuous ejecta blanket, near the beginning of secondary fields (Scott et al., 1977; Howard et al., 1974), or adjacent and downrange of the secondary clusters (Oberbeck et al., 1974). If the order of secondary cratering and debris surge mantling are the same for Mercury and the Moon, the plains-forming debris surge of a crater may overlie its secondaries, thereby embaying the crater deposits, and may be then classed as material of the same age as the primary. This appears to be true of many craters on the Moon (and Mercury?).

However, for some impacts, including basin impacts (e.g. Orientale), late arriving secondaries crater the continuous ejecta deposits and plains material. Oberbeck (1975) finds that target layering may cause such an effect. Low velocity, strength-dominated impacts into layered targets with incompetent material overlying a consolidated material may produce two ejecta curtains: first a conical ejecta sheet ejected at angles below  $45^\circ$  from the horizontal, followed by high angle ejecta of the firmer substrate. Material from the high angle ejecta is sometimes deposited as fallback (Settle, 1980) or as secondaries on the continuous (or first layer) deposits (Oberbeck, 1975, p. 359; Oberbeck et al., 1977). Similar processes may

occur on Mercury. If so, the material cratered by secondaries around a primary may actually be materials from the crater, but will be mapped and dated as an older surface according to the definition of the plain's age.

However, nearly all the craters mapped here are over 40 km in diameter, and dominated by gravity and not by strength of the target medium. Layering effects will be negligible, and most debris can be expected to be ejected in a thin conical shaped curtain (Gault, Quaide and Oberbeck, 1968; Oberbeck, 1975). If a velocity dispersion occurs in the ejected material, due to target inhomogeneities or an atmosphere, newly deposited debris may be re-excavated by target ejecta, producing a net effect of less local material excavation. This is the major argument of the thick ejecta cone model of Schultz (1978), which is used by Schultz and Mendell (1978) in infrared "maps" of lunar ejecta blankets.

If the deposits are constrained to lie between the continuous ejecta deposits and the point of maximum areal density of secondaries, they must fall between  $1.88 R$  and  $2.5 R$  from the primary crater center (Gault et al., 1975; Mougini-Mark, 1978). The formation of a plains surface through deposition of ejecta so narrowly constricted to the crater's continuous ejecta deposits is a far more irregular and ill-defined process than flooding of a region by volcanic materials.

In mapping Mercury, crater materials are mapped only to the continuous ejecta blanket. One assumes that the secondary craters



simply excavate and rework local materials, without depositing significant quantities of primary ejecta (Morrison and Oberbeck, 1975, 1978). Some support for this conclusion comes from the color data on Mercury and the distinctiveness of ejecta deposits. However, one may be eliminating or weakening the possible mode of plains formation through ballistic deposition with the above assumptions, some of which are based on ideal lunar and terrestrial experimental craters.

The mapping bias is twofold: volcanic plains are more easily interpreted, and ballistic deposits are eliminated from the initial assumptions.

#### Areal Coverage by Craters and Plains on Mercury

Within the geologic map and each quadrangle, areas of plains units interior to craters and exterior to craters were tabulated and their percentage of the map or quadrangle area was calculated. These figures are compared to the cumulative crater densities ( $N/km^2$ ) for all craters greater than or equal to 40 km in diameter, and to their cumulative coverage, the summation of the P(D) factors for the same set of craters. The latter value is an upper limit to the area occupied by craters over 40 km; no factor has been included for possible crater overlap or ejecta blanketing. The mechanism of plains formation may be reflected by the areal distribution of craters and plains. One might expect that flood-type volcanism is not correlated with the current bombardment, whereas ballistic deposits should be strongly

correlated. As will be seen, interrelation of volcanism and cratering, as well as ballistic deposition and cratering, can be more complex.

#### Unit Coverage over the Entire Geologic Map

Figure 86 compares the area of plains located interior and exterior to craters to the cumulative number density of craters of that age, displayed in a manner similar to that of Trask (1977). "Interior" plains are not differentiated by the age of the crater in which they are located; i.e. P3 plains noted as "interior" may lie within C3 or C4 craters. In general, the area of plains units exterior to craters decreases with time to the present with the exception of a slight increase in plains production in the Class 3 period. The area of exposed plains materials located interior to craters increases with time, up to the Class 2 period. The P2 plains located interior to craters exceed in area those exterior to craters, while the P1 materials are primarily found interior to craters. The cumulative crater frequency ( $N/km^2$ ) changes as well over the five periods, apparently increasing from Class 5 to 4 to 3, and then decreasing after C3 time. The addition of C5' craters to the C5 population is dashed in Fig. 86 because the ancient depressions are queried. Plains burying these units were marked as "exterior" units, rather than "interior" units; they are continuous over the C5' rims. The surge in C3 crater density is partially due to larger numbers of "small" craters relative to the older crater populations as seen in

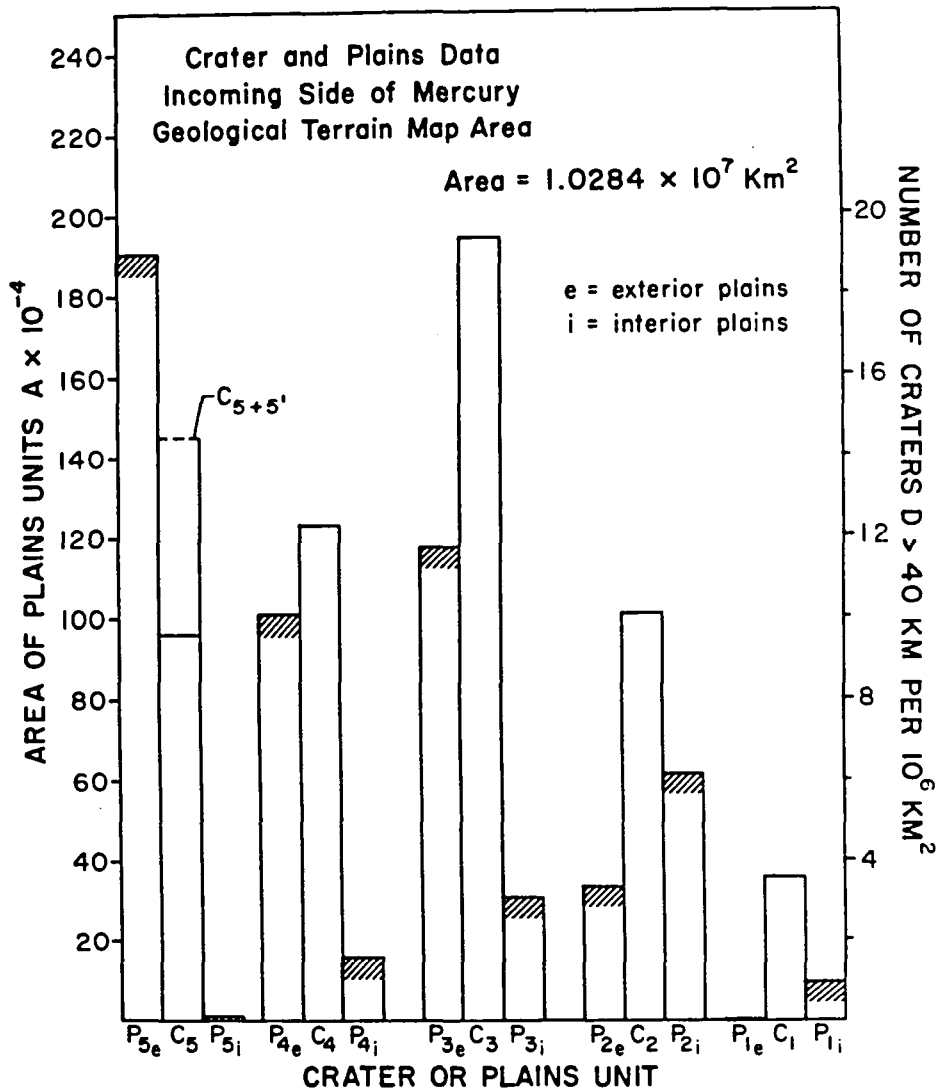


Fig. 86. Area of Plains Units and Number Densities of Craters Within Boundaries of the General Geologic Map

Histogram displays the area of plains units of a given class lying exterior ( $P_e$ ) and interior ( $P_i$ ) to craters plotted to either side of the number of craters over 40 km of the same class per  $10^6 \text{ km}^2$ .  $C_5'$  craters (queried) are often buried by  $P_5$  plains. Many "smaller" craters (40-70 km) may be included within the  $C_3$  population.

the coverage statistics and in Chapter 3. No clear pattern relating plains area and crater densities is indicated in Fig. 86.

A better comparison is made between plains coverage and crater coverage. The latter, weighted by crater diameter squared, represents the maximum percent area covered by craters of all diameters  $\geq 40$  km. Table 8 lists brief unit descriptions and the percent of mapped area covered by craters and plains. Fig. 87 presents the same information in histogram form for the general geologic map and the restricted area map. Because very little change occurs in the two sets of data, the general map figures are considered representative and used in the following analyses.

If C5' craters are included, crater coverage decreases with age for each younger class, in contrast to crater areal density ( $N/km^2$ ). Craters of more recent periods are smaller, cover less area, and, at least in the C3 era, are more numerous. Greater percentages of basins contribute to the coverage of older craters, as was noted in more detail in area plots of Chapter 3.

Plains coverage is similar to that described above for Fig. 86. Interior plains make up an increasingly larger part of the sample, partially because the plains which fill younger craters are less subject to crater overlap and obliteration unlike older landforms, which are also buried by plains deposits. Impact melt comprises some of the interior plains, but cannot account for all the P2 plains interior to craters: many P2 deposits fill older, more degraded craters. Very

Table 8: Description of the Geological Map of Mercury's First Quadrant

Era	Plains/Crater Class	Brief Description of Materials	% of mapped area covered <sup>a,d</sup>
Post-Caloris	P1	Very smooth plains material	0.95 (0.01,0.94) <sup>b</sup>
	C1	Fresh and/or rayed craters	1.3 <sup>c</sup>
	P2	Smooth plains material where thick, rougher where thin, burying rough topography	9.3 (3.3,6.0)
	C2	Moderately fresh craters	5.4
Caloris	P3	Moderately smooth to hummocky plains	14.4 (11.4,3.0)
	C3	Moderately subdued craters, rounded rims	10.0
Pre-Caloris	P4	Moderately rough to hilly intercrater plains	11.3 (9.8,1.5)
	C4	Subdued, dissected craters	12.5
	P5	Very rough, knobby and pitted plains	18.6 (18.5,0.1)
	C5	Highly subdued craters	7.6
	C5'	Ancient circular depressions; vague rims	10.5
	Hilly and Lineated	Hilly and lineated material, large massive hills and troughs	0.06

a. Total mapped area  $A = 1.0284 \cdot 10^7 \text{ km}^2$

b. In parentheses are % area of exterior and interior plains, respectively

c. Crater area percentage =  $\sum(\pi D^2 N \cdot 100) / (4A)$  for each crater class over all diameter bins of geometric mean bin size  $D \geq 40 \text{ km}$ ,  $N$  craters per bin.

d. From Leake (1980a).

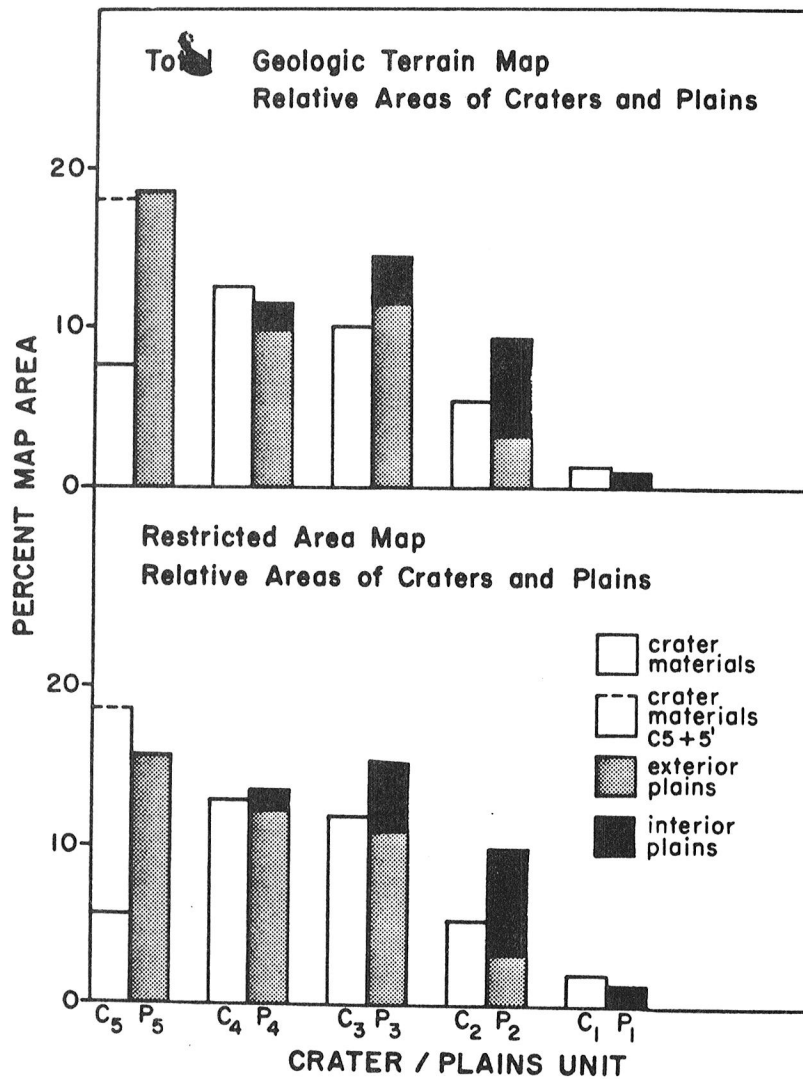


Fig. 87. Coverage by Plains and Craters of the Geologic Map

Histogram of percentage coverage by plains and craters of Mercury's first quadrant. Area covered by general map is  $1.0284 \cdot 10^7 \text{ km}^2$ ; Restricted map encloses  $4.985 \cdot 10^6 \text{ km}^2$  (see Fig. 61). Plains coverage equals plains area divided by total map area. (Plains comprise 55% and 56% of the general and restricted map areas respectively.) Crater coverage is the sum of coverage P(D) for all craters in diameter bins of  $D \geq 40 \text{ km}$ , and constitutes an upper limit to the area occupied by craters, as crater overlap is not adjusted for. (See formula in Table 8.) Note that the restricted and general map histograms are so similar that the general map data is used to draw further conclusions.

little P5 material is noted interior to C5 craters because they are usually embayed by younger materials.

Exterior plains coverage does not appear to be well correlated with the relative crater coverage, although both are of the same general magnitude and decrease in more recent eras if one includes coverage by the C5' craters. P5 plains cannot be a product of the C5' if the latter are often buried by P5 materials, unless in situ erosion by small craters converts the C5' form to intercrater plains (Malin, 1976b).

Crater clustering, burial of older plains by younger units, the absence of mapped plains in the smaller 40 km craters, and continuous ejecta blanket area affect the relative coverage in ways not recorded in Fig. 87. Clustering of large craters decreases actual crater coverage. Burial of older plains by younger units implies that plains production in older eras is underestimated. This forms a strong argument for volcanism because of the enormous volumes of plains generated in ancient times. Yet, since C5 craters are also underestimated, and since cratering was greater at earlier times, ballistic deposition should also have been greater. However, pre-C5 ballistic deposition may not be the source of the existing, exposed plains. Continuous ejecta blankets are excluded from the mapped plains units because they are included with the crater materials on the geologic map; they also are not included in the calculated crater coverage, but can be modelled as demonstrated below.

Various models were constructed to test the relation between crater and plains production. The cumulative area of crater plus continuous ejecta deposits (Gault et al., 1975) was calculated and then compared to plains coverage or to the area actually occupied by crater materials (the map area minus total plains coverage). The latter comparison yields an estimate of the degree of overlap of crater materials within the specified area. In a similar manner, the amount of interior plains was estimated using an approximate floor-to-rim diameter ratio, and then compared to the coverage by interior plains. An estimate of clustering and infill of older craters by younger plains can be obtained.

Estimates can be made of the amount of material ejected beyond the continuous ejecta blanket. Appendix E presents the estimated thickness of deposits assuming the material simply blankets that surface to a uniform depth. This "plains depth" is then compared to the rim heights of mercurian craters which may be buried by the deposits. Assumptions and models include: areal distribution of terrestrial ejecta deposits (Oberbeck, 1975), hemispherical crater volume, and rim heights and depths of fresh mercurian craters (Cintala, 1979b; Malin and Dzurisin, 1977, 1978). From such simple models, craters of 43 and 317 km diameter deposit enough material (0.2 km and 0.4 km respectively) to bury craters of 5 and 10 km beyond a range of two primary radii of the crater center. Studies by Croft (1978), Morrison and



Oberbeck (1978), and Malin and Dzurisin (1977, 1978) may refine the estimate of crater volume ejected and those of Ahrens and O'Keefe (e.g. 1978) can better define ejecta depths. The ratio of local materials excavated by secondaries to the primary ejecta should then be calculated (Morrison and Oberbeck, 1978) and compared to the assumption that local materials dominate ejecta beyond the continuous deposits. If the estimated ejecta depths are reasonable, then the plains producing potential of mercurian craters is substantial. However, it is more likely to be an overestimate because of the simplified assumptions and models used.

Plains deposits may be more extensive than the observed coverage if younger units embay older plains materials. If the plains do not bury any C5 craters or younger craters which are now recognized, the P5 through P1 coverage exterior to craters is 43%, 24.5%, 14.7%, 3.3%, and 0.01% of the map surface, respectively. Assuming only C5 craters contribute P5 plains material, C4 craters contribute P4 material, and so forth, the ratios of plains-to-crater coverage, not counting overlapped craters (which increase the amount of exposed plains), have the estimated values shown in Table 9.

Table 9: Ratios of Plains to Crater Coverage

1 Age	2 Cumulative ext. Plains Coverage <sup>a</sup>	3 Crater Coverage	4 Ratio #2/#3	5 Plains Coverage <sup>a</sup> (int. & ext.)	6 Ratio #5/#3
5	43.0%	7.6%	5.7	18.6%	2.4
4	24.5	12.5	2.0	11.3	0.9
3	14.7	10.0	1.5	14.4	1.4
2	3.3	5.4	0.6	9.3	1.7
1	0.01	1.3	0.01	0.95	0.7

a. Exterior plains ("ext."); Interior plains ("int.")

From the values of cumulative plains coverage divided by crater coverage (Column 4), it appears that the mechanism of plains production changes with time. If the plains are ballistically emplaced, these figures imply that the craters of the ancient past, age 5, were able to produce 500 times more material than fresh craters of age 1. Since the resurfacing potential of craters and basins is apparently small, based on the lack of significant target materials outside the continuous ejecta blanket and the survival of craters beneath the continuous ejecta deposits of some basins, a solely ballistic ejecta origin for the intercrater plains is unlikely. Even if ancient craters are buried by plains material, there appears to be a

contribution to ballistic ejecta deposits which was greater in the earliest history of the planet. This contribution is postulated to be volcanic.

The decrease in plains coverage with time indicates that volcanic activity declined in recent ages. Volcanically produced plains material may be correlated with the crater flux if craters and basins tap subsurface reservoirs.

## Unit Coverage of the Quadrangles

Regional variations in plains emplacement and crater coverage are noted when statistical data are presented for the four major quadrangles comprising the geologic map (Fig. 88). Part of the variations are due to the smaller areal sampling of the Bach and Victoria regions; the larger quadrangles, Discovery (H-11) and Kuiper (H-6), have comparable but unique distributions of plains as well as craters. The variations reinforce the conclusion that plains and crater coverage are not related. In particular, it does not appear that plains form strictly by ballistic emplacement of crater ejecta.

Most of the quadrangles exhibit a decrease in plains coverage with time, with P5 deposits the most extensive. P5 plains usually exceed, by a factor of 2, the C5 coverage. If the existing exterior P4 and P3 materials cover older P4 and P5 materials, the older inter-crater plains unquestionably dominate the surface in all quadrangles. Plains emplacement during the heavy bombardment of C4 and C5 craters is uncorrelated with area covered by those craters. In each quadrangle, P3 coverage increases relative to P4 coverage, but by different extents and interior/exterior modes. The great expanse of P3 plains in the Victoria quadrangle has noticeably affected the crater statistics (Chapter 3). Each quadrangle displays a different ratio of exposed P3 to C3 units, including the large H-6 and H-11 regions.

The apparent increase in P3 production may be relative only, for P3 material covers P5 or P4 units, or C5' - C4 craters, or lies in

Percentage of Quadrangle Area Covered by Craters and Plains

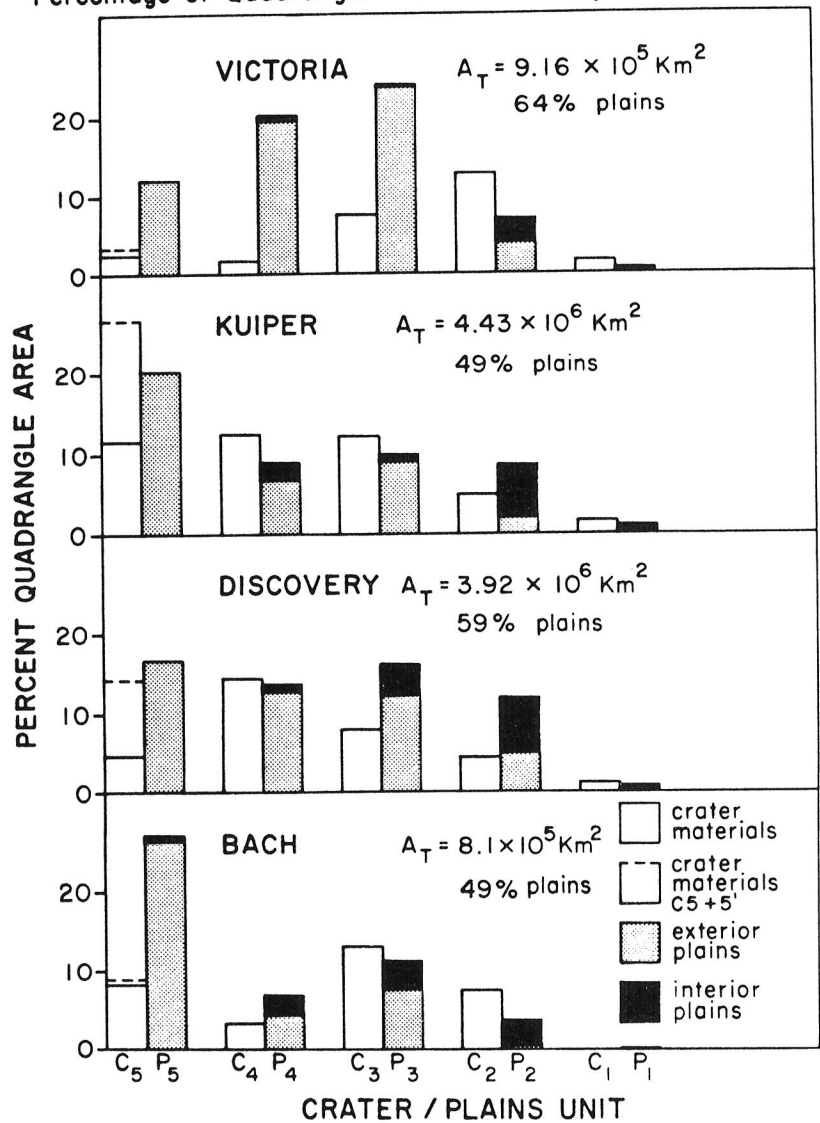


Fig. 88. Percentage of Quadrangle Area Covered by Craters and Plains

Outer boundaries of General Map used. Plains and crater coverage are computed as described in text and Fig. 87. Mapped areas of Victoria and Bach comprise only half their total quadrangle, unlike the nearly complete sampling of Kuiper and Discovery. Note the similarities of plains and crater distribution within the larger quadrangles in contrast to that on the smaller sampled regions. P3 plains, for instance, dominate the Victoria region; P5 plains dominate the Bach region.

basins and crater depressions of some ancient era. P3 exposures increase due to decreases in coverage by the younger craters and plains.

Younger plains, often designated smooth plains, are more often located interior to craters than in exterior positions. Measurements of floor diameter of fresh craters suggests that the ratio of interior plains to crater area is 0.5 to 0.36; this figure most likely represents the impact melt material. The P2-C2 relation in the Bach Quadrangle appears to be that expected for P2 impact melts filling C2 craters, as in this model. Elsewhere, P2 material within craters often exceeds the calculated floor areas of the existing C2 craters and must therefore fill older craters, as observed. The most significant feature of young plains in the four quadrangles is that plains production exterior to craters has decreased markedly.

The emplacement of smooth plains material is correlated with crater coverage only insofar as the production of impact melts which usually fill the younger craters, and which are not overlapped by even younger materials. Because the relationship of plains to crater coverage in the post-Caloris periods of Class 1 and Class 2 is not duplicated in earlier periods, one may surmise that the style (or mechanism) of plains formation changes with time as noted above. Alternatively, the intensity of plains formation may fall with time.

Thus the percentage of quadrangle area covered by plains represents primarily emplacement of volcanic materials; secondly,

inevitable contributions from ejecta deposition, especially during the heavy bombardment; and thirdly, impact melts. Crater coverage affects plains production directly through the impact mechanism, and indirectly through the production of vents which allow subsurface magmas to gain access to the surface. The mode of emplacement changes from positions exterior to craters to positions interior to craters; not all the plains interior to craters are impact melts. These conclusions are supported in the following analyses of the paleogeologic maps.

#### Paleogeologic Maps of Mercury's First Quadrant

##### The Caloris Connection

The hilly and lineated unit (Fig. 19) forms a critical link between the relative ages established on the first and second quadrants of Mercury. Rather than designate this area as a separate unit or deposit, as was done by Trask and Guest (1975), it was treated as a region disturbed by some distinct event. To determine the relative age of this disturbance, plains and crater map units were continued into this region from the surrounding area. Sections of rims of Class 3 craters are modified where they extend into the hilly and lineated area; exterior to this boundary the rims are intact (Fig. 89). Class 1 and 2 craters superposed on this surface are unmodified; the distal edges of their continuous ejecta blankets reflect the hummocky topography beneath. As can be seen in Fig. 90, smooth plains in this zone

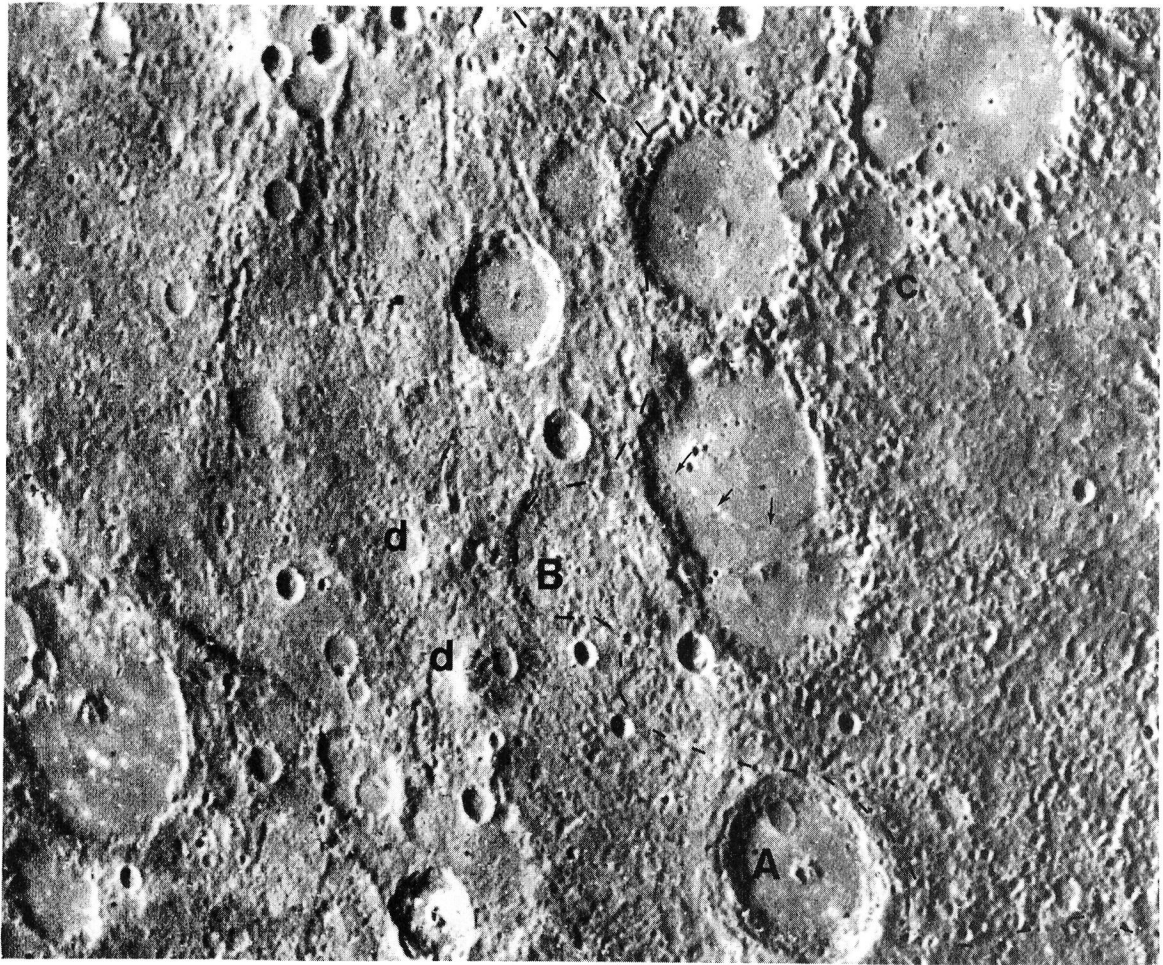


Fig. 89. West Edge of the Hilly and Lineated Area

The rough boundary of the hilly and lineated area determined by Trask and Guest (1975) is outlined by dashes. A C3 crater A is cut by this boundary; its rim and ejecta blanket are disturbed to the east, yet intact to the west. The crater to the north, joined by a plateau of continuous ejecta blanket materials, may be the same age, but lies entirely within a linear array of 3 - 4 domes (see Fig. 19). Nearby are two very old C5 craters designated as B and C. B lies near the domes; C is filled and surrounded by smooth plains lying in between the remnants of rougher topography. Post-event, smooth P2 plains fill larger older craters such as Petrarch (Fig. 19). The scarp in the oblong crateriform (arrows) may be a volcanic flow front (Strom et al., 1975b).

FDS 27379. North at top. Crater A is about 75 km in diameter.



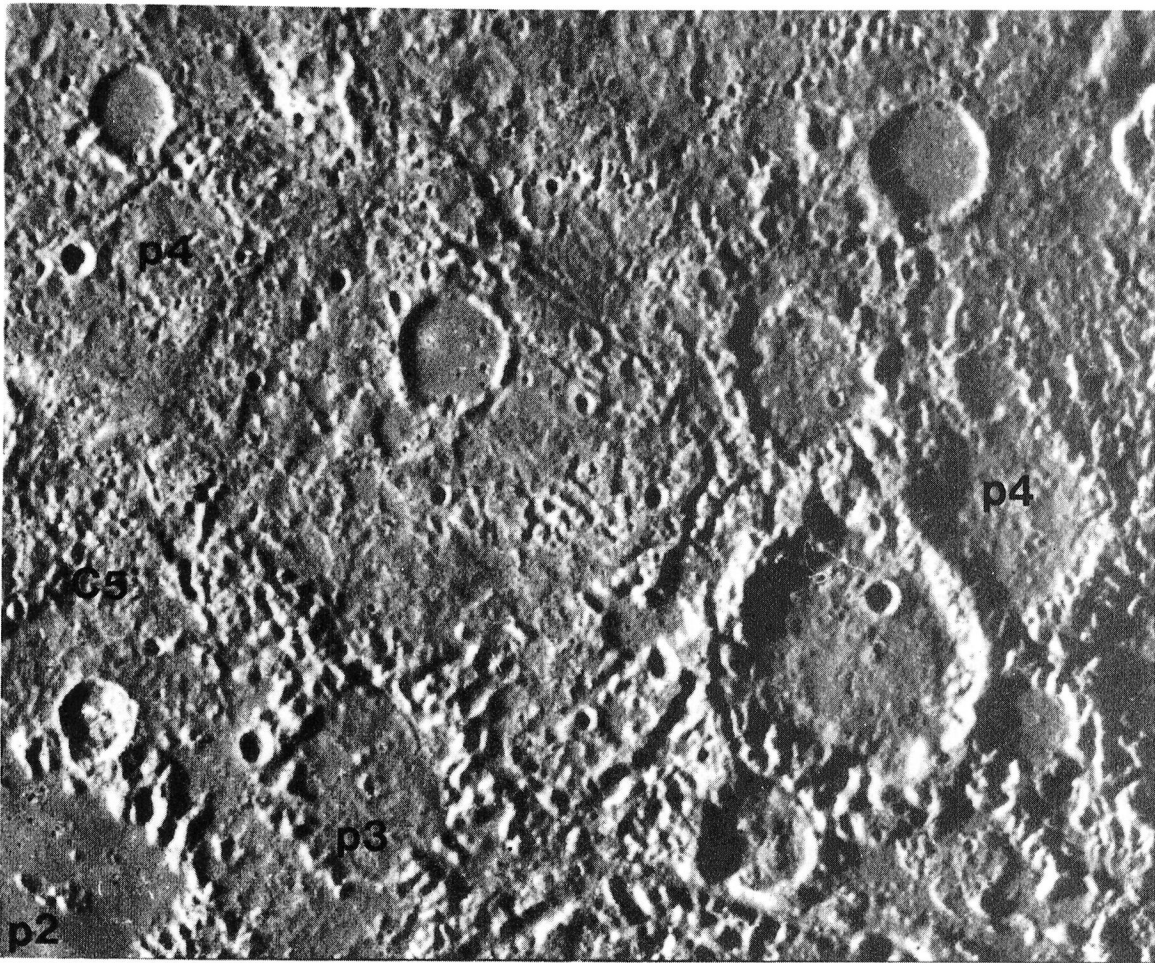


Fig. 90. Craters and Plains Units Within the Hilly and Lineated Terrain

In general, Class 1 and Class 2 units formed after the disruption event; Classes 3, 4, and 5 formed before the event. Note the hummocky P3 plains, as if they were sifted on top of jumbled debris, and the very smooth, relatively uncratered P2 surface. Massive P4 materials extend downward to the rim of the C5 crater beneath Petrarch; three parallel troughs roughly radial to this crater may be covered by the P4 plains. Some areas also are filled with massive, less blocky, smooth plains. Note the P4 plains within craters to the northeast.

FDS 27423. See also Fig. 19. Note the large crater at right; its diameter is approximately 70 km.

are undisturbed and fill older, heavily disrupted craters such as Petrarch. These stratigraphic relations suggest that the disturbance occurred sometime between the formation of Class 2 and Class 3 craters. Crater diameter-frequency studies of the hilly and lineated area also suggest a disturbance in the late C3 period, or possibly early C2 period.

Independently, geologic mapping of the Caloris basin quadrangles (H-3 and H-8) by McCauley et al. (1978) indicates that the Caloris impact occurred between the formation periods of (LPL) Class 2 and 3 craters within the error of classification. Substantiating this result, Woronow (in Strom, 1977) finds very few Class 3 craters on the smooth plains of the Caloris basin and periphery. (Watkins, 1980, supports this.) Wood et al. (1977) find two cratering episodes marked by different degradation styles which are demarcated by the end of the heavy bombardment episode, between Classes 2 and 3. From crater surveys using the Brown University Mercury Crater Library (Cintala et al., 1976), the rim and ejecta facies of Caloris might be as young as early Class 2 period. Watkins' (1980) evidence indicates that plains emplacement after the Caloris impact obliterated many craters on the Caloris ejecta facies.

This agreement of relative ages of the Caloris impact and hilly and lineated terrain formation lends support to the proposal by Schultz and Gault (1975a,b; 1976) that the hilly and lineated terrain was formed by seismic waves which were generated by the Caloris impact

and focused on its antipodal area (Hughes, App, and McGetchin, 1977; different formation mechanisms are postulated by Moore et al., 1974, and Wilhelms, 1976a).

The "Caloris Connection" is then the probable cause-effect relationship between the impact forming the Caloris basin and the disturbance forming the hilly and lineated terrain. From cratering data there is only minor ambiguity in the date of the Caloris event, being either late Class 3 or early Class 2 periods. Despite this ambiguity, the Caloris event at the end of the Class 3 period was used as a "time horizon" to date the crater and plains units relative to the Caloris event. "Paleogeologic" maps were constructed by grouping units of Class 1 and 2 as "Post-Caloris" features, Class 3 craters and plains as "Caloris" features, and units of Classes 4, 5, and 5' as "Pre-Caloris" features. This dating nomenclature has been used previously in analysis of cratering data. Details of the construction of the paleogeologic maps are given in Appendix F. The reconstruction of the paleogeologic map ("paleomap") essentially presents the material laid down within that time period, and is not strictly a "snapshot" of the geology at the ends of the Class 4, Class 3 and Class 1 periods. The plains represented on the maps better correspond to the cumulative plains coverage discussed in the previous section.

## The "Post Caloris" Surface

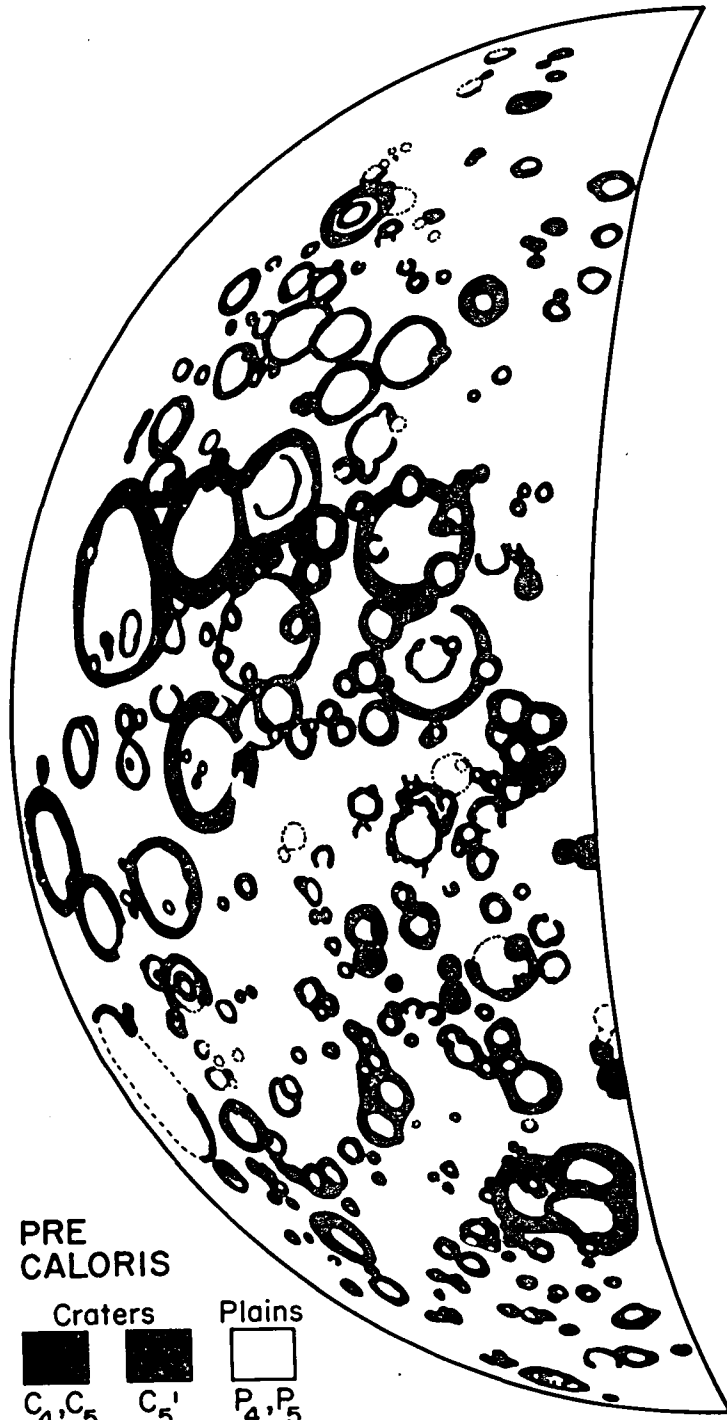
The Post-Caloris surface is sparsely populated by both craters and plains as shown in Fig. 91. Relatively few large craters are included, and these are randomly distributed over the surface. Crude clusters of the post-Caloris craters (e.g., the Lu Hsun--Donne area and the Sōtatsu--Andal area) roughly correspond to concentrations of central peak craters in studies by Carusi et al.(1977). Absences of craters occur east of Ts 'ai Wen-chi, south and west of Titian, along the western limb of Bramante and perhaps within the hilly and lineated boundaries. Fewer of the large fresh craters occur near the limb, where large expanses of post-Caloris plains material lie within the C5' depressions.

The plains distribution indicates several regularities. All craters, except the smallest of about 40 km diameter, which are mapped as one unit, have plains-covered floors. These are likely to be impact melts. Most plains lie in depressed regions, including crater interiors. The small, circular patches of plains material on the map are usually young plains filling older craters. They occur both adjacent to or far from younger craters, so origins as ballistic fill or volcanic intrusion respectively may both be possible. Irregular areas of plains material occur in two modes, one adjacent to young craters and another isolated from young craters, both within depressed regions. The former type, illustrated between Handel and Lu Hsun (Figs. 22b and 85), may contain ballistically deposited materials, especially since

Fig. 91. Paleogeologic Maps of Mercury's First Quadrant

- a. Pre-Caloris surface, consisting of Class 4, 5, and 5' units. Queried ancient circular depressions are a darker shade. Rims of mapped C5' structures and buried craters are marked with dashed lines and dash-dot lines respectively. Pre-Caloris plains, not shaded, are hypothesized to occupy most of the surface. Appendix F explains the construction of these maps.
- b. "Caloris" surface, consisting of Class 3 craters and plains. Note location of plains exterior to basins, surrounding smaller craters, and isolated from C3 craters and basins, sometimes within much older crater-depressions. Actual age of "Caloris" units may pre-date the Caloris impact, since the latter event is proposed to occur near the end of the Class 3 period. Extensive plains emplacement must have extended into this Caloris era. See text.
- c. Post-Caloris surface, consisting of Class 1 and 2 units. Basins are few and craters and plains are sparsely distributed. Many plains units lie far from young craters, and as above, are sometimes confined to older depressions. A few post-Caloris plains lie between craters of a similar age, suggesting ballistic emplacement. Isolated exposures are likely to be volcanic.

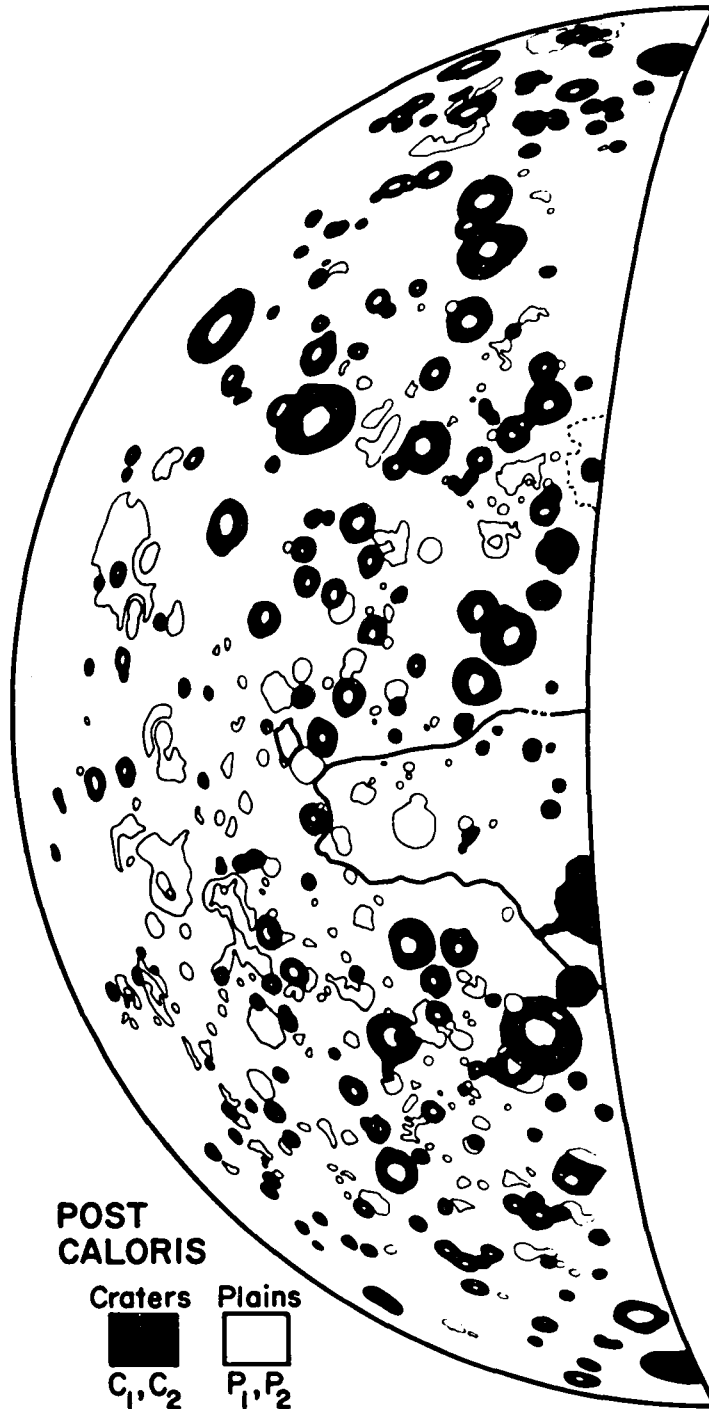
Hilly and lineated region is marked by a heavy line in (b) and (c).



a.



b.



c.



the associated craters are large. The irregular, isolated post-Caloris plains are probably volcanic deposits. They are noted especially in the limb region, enclosed within the ancient circular depressions. Often these materials are physically separated from younger craters by older plains units, and therefore are unlikely to be ballistically deposited. Most of the post-Caloris plains within the hilly and lineated area are located within older, degraded craters far from young post-Caloris craters. These exposures are also interpreted to be volcanic materials. The two largest expanses of smooth plains occur within the C5' depressions; the areal extent is great enough so that fairly large impacts have occurred on the plains' surface.

Further information on the post-Caloris surface is obtained from the various crater statistics discussed in Chapter 3, plains and crater morphologies, specific examinations of plains distribution, analysis of tectonic events, and analyses of the albedo and color of the post-Caloris materials. These topics are summarized below.

Summary of Post-Caloris Data. Craters from 40 to 120 km in diameter cover 6.7% of the mapped surface; plains cover 10%. Plains occur within floors of craters of the same age or older, and exterior to craters at varying distances from fresher craters and basins. Many plains are isolated, irregular in plan, remote from fresh crater units, and interspersed with older materials. The more-circular exposures fill older craters and ancient depressions. These low lying

units; sometimes associated with volcanic landforms, are interpreted to be volcanic in origin. Other exposures of plains are interpreted to be impact related--as impact melt, or as deposits of ballistically emplaced ejecta. Albedo of the plains material may be bright (0.23) or dark (0.13), with no apparent transition between the two (Dzurisin, 1977b).

This era is also marked by continued tectonic activity including scarp formation, ridge formation, and some faulting constrained within crater floors. The seismic disturbance forming the hilly and lineated terrain at the onset of this era may have contributed to mass wasting and degradation, forming subdued areas which are later embayed and buried by smooth deposits. Because most scarps transect smooth plains material and because P1 plains exterior to craters of the first quadrant of Mercury are very rare, it is likely that most plains formation occurred early in this era, shortly after the Caloris impact. Smooth plains formation around the Caloris basin is much more extensive, but also appears to be distinct from the basin event, and continues throughout Class 2 and Class 1 periods (Watkins, 1980; Wood et al., 1977).

In the first quadrant, plains and crater formation of the Post-Caloris Era is far less than that of previous eras. Distribution of craters on the post-Caloris surface is apparently random, with minor clustering. Distribution of plains materials is affected by

local topography and may be spatially random (although larger exposures occur in the equatorial area and limb regions of the larger quadrangles). Plains preferentially occupy topographically lower regions such as crater floors, ancient depressions, or channels curbed by continuous ejecta deposits or older plains materials.

Origins of the materials are varied, but as was shown in Chapter 2, the smooth plains are predominantly volcanic, with some additions of ballistic ejecta, impact melt, and mass wasted debris. Although scarp formation is more active early in the Post-Caloris Era, as it progresses into the Class 1 period, fewer plains units are noted exterior to craters. Continued scarp formation and declining plains formation signal the cessation of surface volcanism or the increasing difficulty of magma's access to the surface. Thus, the interpretation that contraction and cooling of the planet caused compressional thrust faults on the surface (Strom et al., 1975b) is consistent with most crater and plains distributions of the Post-Caloris Era.

#### The "Caloris" Surface

The Caloris surface, as illustrated in Fig. 91, comprises the C3 and P3 units, and serves to emphasize that a heavy bombardment by fairly large projectiles and extensive plains production continued into the Class 3 period before ending in the early Post-Caloris Era. Most of these materials were emplaced before the Caloris impact, for that event occurred near the end of the Class 3 period.

The crater distribution is fairly random on the Caloris surface. The basin size craters (150 km - 250 km) are randomly distributed from terminator to limb and from high to low latitudes. That randomness must also characterize the original distribution of smaller craters, before resurfacing and proximity weathering occurred. (Because most of the overlying post-Caloris population consists of smaller, randomly distributed craters, their proximity weathering of older craters may not be as great as that of the Caloris craters on the pre-Caloris units.)

Degradation by superposed larger craters or nearby C3 basins may reduce the contrast in original degradation states of those craters, so that they are mapped as clusters of equally degraded craters. (For instance, the craters Sōtatsu, Lu Hsun, and Ts'ai Wen-chi have affected the degradation states of the craters around them.)

Smaller craters, 40 to 50 km in diameter, appear to have lower densities in the Homer-Handel area. The hilly and lineated area has normal C3 densities. If the paleomaps of the Caloris and post-Caloris surfaces are compared, one notices the greater number of basins of the older surface; smaller craters equally populate either surface.

The distribution of Class 3 plains materials is varied and suggests several origins. Four types of plains are noted on the Caloris surface similar to, but more extensive than, the general exposures of the post-Caloris surface. The paleomap shows that plains

occur (1) interior to Class 3 craters, (2) interior to Class 4, 5, and 5' structures, (3) exterior but adjacent to or between Class 3 craters, and (4) exterior to and isolated from similar age craters. Plains interior to older craters also vary with distance from C3 crater materials. The paleomap does not show which units are hummocky and which are smooth, but often the exposures within mapped craters are smooth. Textures of exterior plains can vary greatly, depending in part on the texture of the underlying unit, and the depth of the overlying deposit. The deposits listed have characteristic shapes, or plans: the first two, confined by crater rims, are circular in plan; the latter two exposures are irregular in plan, asymmetrically distributed around nearby craters, are much greater in area, and sometimes surround smaller members of the Caloris population. As will be discussed below, a volcanic origin is inferred for plains of type 2 and 4, a mixed ballistic and volcanic origin for type 3 plains, and impact melts for type 1. Exterior P3 plains are more extensive than both P2 materials and P3 interior materials, but appear to be deficient east of Homer, north of Sōtatsu, and possibly in the hilly and lineated region; all are areas of severe degradation. However, because neither the Caloris nor post-Caloris plains are unusually abundant in the hilly and lineated area, its formation was not accompanied by local volcanism and flooding in any large amounts exterior to craters. If the Caloris event did not trigger extensive volcanic flooding at the antipode, it is unlikely that it triggered flooding at less stressed areas.

Summary of Caloris Era Data. Plains formation appears extended throughout the Caloris Era, in part continuing the emplacement of intercrater plains, and in part, marking the beginning of the preserved smooth plains. The majority of the Caloris age plains are interpreted to be volcanic. Other exposures have ballistic, impact melt, or mass wasting origins. Volcanic landforms--domes, ridges, and scarps of distinctive albedos--may have been constructed during this period, signalling the closing of various conduits to the surface and related changes in the composition of the magma source. Scarp formation begins early in the C3 period. Not all conduits closed with the onset of scarp formation, for post-Caloris plains emplacement is fairly extensive. Exterior plains production falls by about a factor of four; interior plains production actually doubles. Crater production drops by about half after the Caloris period.

Production of plains and craters is more complex than first noted. Plains emplacement may be related to crater formation in the following ways: (1) crater formation may fracture the crust (creating a locally thinner region) to create conduits for plains-forming materials, (2) craters may become sites for later plains emplacement within depressions, (3) the plains may be ballistic deposits of crater and basin ejecta, and (4) crater and basin impacts may enhance local mass wasting and differential compaction to level the surrounding terrain. P3 interior plains of impact melt origin are directly related

to the number and size of the impacting bodies (see Hawke and Head, 1977). Survival of all these facies depends on superposed materials and subsequent degradation.

#### The "Pre-Caloris" Surface

Large basins 100 to 400 km in diameter and ubiquitous plains characterize the Pre-Caloris surface (Fig. 91), which consists of Class 4, 5, and 5' units. Most of the small craters are C4 in age; they seem to be more numerous in the Discovery and Bach Quadrangles where fewer basins are located. The equatorial latitudes (Kuiper Quadrangle) contain many ancient depressions 200 to 300 km diameter; superposed craters are usually smaller. Compared to other areas of the map, the hilly and lineated region contains no unusual numbers of pre-Caloris structures. (Note that C4, C5 and C5' structures are grouped in pre-Caloris statistics, so that this observation is not contrary to the abundant C5 population indicated by the hilly and lineated crater statistics.)

Plains materials of pre-Caloris age are presumed to underlie all younger material, and so are located wherever identified pre-Caloris crater materials are absent. They also embay recognized pre-Caloris craters, e.g. the south rim of Chekov. Plains interior to pre-Caloris craters were originally impact melts and floor materials.

Summary of Pre-Caloris Era Data. The Pre-Caloris surface is exceptional for its numerous large craters and basins of 100 to 400 km

in diameter, and its widespread plains. The existing intercrater plains cover many of the ancient circular depressions: these craters are not "ballistic" sources of the existing plains material but may be sites of localized extrusions. The remaining craters and basins of C4-C5 ages do not have the resurfacing potential to cover the 30% of the mapped area covered by P4 and P5 plains, compared to the 20% covered by craters greater than 40 km. The widespread plains, volcanic landforms, and evidence of features preserved as lineaments (or ancient graben) suggest a volcanic origin for the pre-Caloris plains.

Within this terrain, small craters and secondaries of C4 basins are preserved. High numbers of small craters 5-10 km in size have formed on this surface, yet the associated brecciation and ejected debris have not erased older features, nor weakened the surface with respect to its mare-like morphological behavior (Cintala et al., 1977). The intercrater plains are not completely flat surfaces however, but rolling and hummocky (as first described by Trask and Guest, 1975). Buried or highly degraded craters are noted in stereo pictures (see Malin, 1976b); the plains share the topographic contours of the ancient basin rims and depressions. The intercrater plains often form a local highland; elevated sites may help preserve P5-P4 units, since the low-lying regions are filled with younger plains. Restriction of ballistic ejecta by gravitational forces has prevented burial of features by ejecta deposits.



The geologic analysis and cratering studies of the previous chapters suggest that volcanism was a major factor in altering the (lunar-like) spectrum of craters caused by impacting projectiles. Most of Mercury's basin size impacts (including those designated C5') seem to have occurred in the earliest stages of heavy bombardment. Inter-crater plains were emplaced during the continuing heavy bombardment represented by craters of the pre-Caloris and Caloris surfaces.

Reduction of densities of intermediate to large craters in the intercrater plains may be attributed to ancient basin-size impacts and subsequent volcanism. The heavily cratered and intercrater regions suffered the same bombardment, but different obliteration mechanisms. Secondary cratering appears to be responsible for the high densities of small craters on the intercrater plains.

Tectonic history of the pre-Caloris surface includes a wide range of activities. Basin-produced seismic disturbances are likely and may affect degradation of surrounding craters (Ronca and Green, 1969; Schultz and Gault, 1975b). Expansion of the planet produced tensional, possibly normal faulting (graben production), and extrusion of molten materials onto the crust (Solomon, 1976), although little or no evidence of that expansion remains (see Chapter 2). Tidal spin-down may produce stresses and strains in equatorial regions. These stresses spread poleward as the planet relaxes to spherical shape (Melosh, 1977a,b; Melosh and Dzurisin, 1978). They may be recorded as lineaments in the intercrater plains, a sort of jointing fabric not

preserved in, or felt by, the younger materials (Strom et al., 1975b; Dzurisin, 1978). Thus the intercrater plains may have formed during the period of planetary expansion and minor tidal heating (Burns, 1976), and were cut by lineaments and then by scarps during the periods of tidal spin-down and the initial cooling of the planet, respectively.

Other observations about the "Pre-Caloris" intercrater plains include identification of domical structures and the lack of albedo variations. The domes appear to be as old as the pre-Caloris surface, but other constructions, such as ridges, are formed in later eras on the intercrater material. The intercrater plains have a moderately high albedo, and do not contrast strikingly with smooth materials, or heavily cratered units. Some albedo differences are noted across scarp contacts of P4 and P3 material, where P3 units are darker, but in general, there is a "lack of photometric contrast between and within intercrater plains, heavily cratered plains, and Caloris plains units," (Dzurisin, 1977b, p. 134). If volcanism contributes to forming all three units, whose materials are then redistributed as crater ejecta, a lack of contrast is likely if the composition of the volcanic materials does not change significantly over that period. The existence of minor areas of albedo and color contrast--across two scarps, in some crater floors, and across some ejecta blankets--may imply that compositional changes are muted by other processes.

## Summary

This part of the chapter attempts to correlate the geologic and cratering histories in Chapters 2 and 3, respectively. Major plains origins were examined first by isolating proposed examples of volcanic and ballistically emplaced materials. Secondly, the relative areas and coverage of craters and plains on Mercury's surface were examined for correlations. Such a comparison may not be able to determine a volcanic versus ballistic origin because cratering and volcanism appear to be complexly related. Although both crater and plains coverage roughly decrease with younger ages to the present, variations within each quadrangle, and variations with respect to successive plains ages and interior-exterior modes challenge plains emplacement strictly as impact ejecta.

Various simple models were tested which estimate the amount of plains-forming ejecta, the amount of material exclusive of continuous deposits and impact melts, and the amount of plains buried by subsequent deposits. Plains-producing potential may in fact be large, but because this is not indicated from observations of craters and basins on Mercury, further refinements of this estimate should be made. It appears likely that both plains production by ballistic deposition and volcanic emplacement were greatest during the early heavy bombardment represented by the C4 and C5 craters. However, the P5 plains which cover C5' craters, C5 craters, and regions exterior to

them, are anomalously extensive. In addition, plains-to-crater-coverage ratios become lower in more recent ages. This does not suggest a change in the physical mechanism of ballistic ejection, but rather an addition of volcanic materials which has decreased since the P5 period.

In a third exploration of the crater and plains history, paleogeologic maps were constructed, maps which present surface units laid down in that era. It is clearly seen that the mode and quantity of plains emplacement changes from vast exterior tracts in pre-Caloris time to plains restricted to the interiors of craters in the post-Caloris period. That change may result from lessening of volcanic plains production.

Similar tests and analyses are applied to the synthesis of lunar geologic and cratering data in the following section. Later chapters discuss remote sensing and chemical data pertinent to intercrater plains formation and the planet's history. A surface history, or "igneous chronology," can be constructed which provides constraints for thermal history modelling.

#### The Lunar Intercrater Plains:

##### Synthesis of Geologic and Cratering History

The surface history of the lunar intercrater plains consists of episodes of cratering, plains formation, and tectonic activity somewhat similar to those of Mercury. Plains surfaces include basaltic

maria, light smooth plains, older light plains, and the disputed pre-Imbrian pitted plains (the intercrater plains of the lunar surface). The geologic and cratering histories of the southern highlands and related terrain have been discussed in Chapters 2 and 3. Origin of the highland pitted plains and some comparisons to Mercury's intercrater plains are discussed below.

### Origins

Cratering and stratigraphic studies indicate a complex origin for the pre-Imbrian plains, one that may involve basin influences to an extent greater than on Mercury. As on Mercury, the primordial-origin hypothesis for the plains can be ruled out because of evidence of buried craters and topographic forms. However, plains and terra within the nearside southern highlands may span a great period of lunar history, from the heavy bombardment of pre-Nectarian time to the quiescent Copernican period. Furthermore, that range in history is not as obscured by the recent Orientale and Imbrium impacts as are other regions of the earth-facing hemisphere. Regions around the Clavius area (not within the plains unit) may represent a basic ancient surface from which the earliest cratering records after crustal solidification can be obtained (Strom, 1977; Oberbeck et al., 1977). The plains themselves "sample" a slightly later part of lunar history, the period around the Nectaris impact.

Volcanic flooding and ballistic erosion and ejecta emplacement are still viable mechanisms for pre-Imbrian (pitted) plains formation.

Volcanic-origin arguments center about stratigraphic relations in the area which indicate an extended, post-Nectaris emplacement, tentative volcanic landforms, including a flow lobe near Mutus, and plains of variable thickness occupying lower topographic levels over a wide tract of southern lunar highlands. As noted in Chapter 3, this region also exhibits crater degradation patterns characteristic of volcanic flooding (Strom, 1977).

However, proximity to the Nectaris basin demands that this area was once greatly affected by that event. Chapter 3, sections 1 and 2 discuss the direct and peripheral effects of basin impacts. Craters less than 50 km may be severely degraded within the extent of the continuous ejecta blanket (Woronow et al., 1979). Beyond that range, for at least a basin diameter, additions of secondary craters from 11 to 19 km will exceed the former primary population. A thinner sheet of ejecta facies, similar to the outer Hevelius Formation of Orientale, may both overlie or underlie these secondaries; pre-impact terrain should be discernible beneath the blanket (Scott, McCauley, and West, 1977). The morphology of this outer facies may vary from lineated to smooth and obviously will lose its distinctive characteristics by erosion over time. The ejecta blanket and secondaries will be emplaced over a time-scale of minutes. Degradation from the basin impact beyond the continuous ejecta blanket should abnormally age existing craters, producing an abundance of C4 and C5 structures, as

illustrated in the Albategnius and Werner regions (Strom, 1977). The areas around Cuvier and Manzinus do not exhibit the peripheral basin degradation patterns.

Stratigraphic dating argues that the plains are post-Nectarian and pre-Imbrian (Scott, 1972; Mutch and Saunders, 1972). But the interval between the Nectaris impact and the pre-Imbrian plains formation is unknown, as was the interval between the Imbrium impact and the Imbrian plains (Cayley-like) formation. Secondaries from Nectaris visible beneath the pIp unit do not necessarily imply a lengthy post-impact interval. Post-basin, pre-plains crateriforms have not been identified, but Nicolai and Spallanzani are possible candidates.

The oldest plains surface mapped to date--the pre-Imbrian plains or Nectarian plains--were emplaced during the heavy bombardment represented by Class 4 and Class 3 cratering periods. This was determined by dating the plains relative to the enclosed craters (Chapter 2) and by correlating the time-stratigraphic sequence with the LPL crater classes (Wood, 1979). Because this "heavy bombardment" period also includes at least 10 basins formed prior to the Nectaris event, and two dozen more following it, the primary dispute is whether the plains are basin and crater ejecta (Wilhelms, 1979).

The basin formation may hold some complexities which are more consistent with the "preservation" of the pitted plains. Craters which

predate the basin forming impact and are located just southwest of the Altai Scarp are not severely damaged--Zagut, for example. Woronow et al.'s (1979) study of Orientale implies that Zagut would be severely deformed if it were located just 150 km from the topographic rim of the basin. One explanation is that the excavation crater of Nectaris is the intermediate rim,  $R = 310$  km; craters nearer the Altai Scarp may have suffered less degradation. If the Rook Formation is the excavation crater of Orientale, this "intermediate ring" theory will not ensure preservation of materials outside the topographic rim. (Compare Schultz' 1979 hypothesis in which the Nectarian rings are "tectonic adjustments" made soon after basin formation, and do not correspond to Orientale-like excavation craters.) If the Nectaris impact was oblique, secondary craters and ejecta facies and associated destruction may be less in the uprange zone of the projectile's trajectory. From the discussion in Chapters 2 and 3, an oblique impact from the southwest forming the Nectaris basin implies that (1) fewer Nectarian secondaries impact the intercrater region, (2) ejecta facies are confined within  $1.5 R$  to  $2.0 R$  from the basin center (almost inside the northernmost limit of the pre-Imbrian plains), and that (3) there is less destruction to existing craters (Gault and Wedekind, 1978). If such corrections are warranted, the lunar intercrater plains were subjected to less basin influence than many other regions of the lunar highlands.



## Similarities and Contrasts of the Lunar to Mercurian Intercrater Plains

There are several similarities and contrasts of the lunar intercrater area with the mercurian intercrater plains which should be emphasized. On both planets there are episodes of plains emplacement during the ongoing cratering of the surface. Intercrater plains--lunar pIp or mercurian P5-P3 units--are emplaced during a heavy bombardment characterized by many basin-forming impacts. Smoother plains, flat-lying and less cratered, are emplaced in periods of less intense bombardment--on the Moon, early to late Imbrian (Ip) or younger (e.g., the mare units, Im, Em) and on Mercury, the post-Caloris units, P2 and P1. A major difference is that the age of the lunar intercrater plains appears restricted to Class 3 period. Terra surfaces (e.g., ridged pre-Imbrian terra), defined as heavily cratered, flat-to-rolling plains, may be analogous to P4 units, widening the lunar intercrater plains age "spectrum."

The observed areal distribution of these units is not uniform; later deposits and impacts markedly alter the smooth plains exposures, especially on the Moon. Both planets show asymmetries with respect to large young basins (Caloris and Imbrium). Older units are absent there, and younger units (e.g. mare), postdating the basins, are concentrated in deep basin interiors.

In areas unaffected by young basin events, plains production appears to decrease with time to the present. This occurs for the

southern highlands, where pIp exposures are greater than Ip and Im exposures, and in Mercury's first quadrant, where pre-Caloris plains are more extensive than Caloris plains, and the latter are more extensive than post-Caloris plains. The second quadrant of Mercury would probably show that post-Caloris plains are more than or equally as extensive as existing intercrater units. The lunar farside, in a similar manner, contains more Imbrian plains than Imbrian-Nectarian plains. The Nectarian plains of the farside are the least abundant (Gifford and El-Baz, 1979).

Plains distribution is also similar on the two planets with respect to elevation of the surface. Younger plains usually lie within depressions, enclosed, or curbed by higher relief structures, such as crater rims, fault scarps, and ejecta masses. Older intercrater plains occupy higher areas which block further embayment by volcanic materials. Often the intercrater plains (P5-P3) occupy shallow C5' depressions on Mercury; the lunar pIp unit and the farside Np units may lie within similar ancient basin sites, and were emplaced in regions of thinner planetary crust during episodes of post-basin volcanism.

Plains regions on both planets show lesser densities of large craters and higher densities of small craters, less than 10 km in diameter, compared to terra. Small crater coverage on pre-Imbrian plains may exceed that on older terra units, because the craters are

better preserved by consolidated subsurface layers (of volcanic materials?) which may overlies a widespread lunar megaregolith. Secondary craters form a large percentage of the high coverage by small craters, on both the heavily cratered terrains and the surrounding intercrater plains.

Loss of large craters on lunar plains is not consistent with degradation by nearby basin impacts, but perhaps with direct impacts at some ancient time. Crater deficiencies on Mercury are also linked with the presence of the C5' structures. Schaber et al. (1977) suggest that Mercury may have had an early period of a low viscosity crust, in which large structures were lost through isostatic equilibration; on the average, however, Mercury's viscosity is the same as the Moon's.

Mercury's surface is unlike the lunar highlands in morphologic preservation of large craters: Cintala et al. (1977) propose that Mercury's megaregolith is not as deep nor widespread as the lunar megaregolith. Pike et al. (1980) agree that the mercurian surface is "harder" and more consolidated, but argue that it may still represent a megaregolith of 2 km depth.

Other differences between the plains regions on the two planets concern the (1) extent of intercrater plains exposure; (2) light plains distribution; (3) details of recorded crater populations--e.g. duration of heavy bombardment, (4) dearth of 15-40 km and  $D \geq 225$  km craters on Mercury, and the lack of 3-14 km craters on the

plp of the Moon; and (5) extent of basin influences (secondaries, ejecta deposits, and megaregolith formation).

Tectonic histories differ also. The lunar surface lacks great scarps, interpreted as thrust faults, indicative of planetary contraction of Mercury. Both planets have lineament systems of great age; the lunar system is more pronounced than that on Mercury. The differing tectonic fabric may indicate a difference in the progress or magnitude of thermal evolution of each body (Chapter 6).

Comparisons between lunar and mercurian intercrater plains, among lunar light plains, lunar maria, and mercurian smooth plains, and between highland terra and the heavily cratered terrain of Mercury, provide further information into processes responsible for emplacement of the intercrater plains of the Moon. The principle difference is that the lunar area is not as free from basin influences (and therefore not as primitive) as earlier studies had implied. More extensive compositional data may provide definitive clues for the origin of the pre-Imbrian plains.

## CHAPTER 5

### REMOTE SENSING AND PHYSICAL DATA OF MERCURY AND THE MOON

Imagery data from Mariner 10 and Lunar Orbiter IV form the major base of observations thus far analyzed. But a variety of other information aids in constraining the composition and structure of the Moon and Mercury, and in particular, provides input to the problem of the nature and origin of their intercrater plains. This information for Mercury is remotely sensed from Earth or from the Mariner 10 spacecraft. Lunar data includes, of course, ground truth information from the Apollo landing sites. Since neither intercrater region was sampled, lunar and mercurian data are similar in type and limitations.

Constraints on surface and interior composition and structure are reviewed below. Albedo and color data detected by the Mariner 10 spacecraft were reviewed in the Geologic Mapping section of Chapter 2. Other summaries of physical data are found in Strom (1979), Ferrari and Bills (1979), Gault et al. (1977), and Morrison (1970).

#### Remote Sensing Observations of Mercury

The composition and microstructure of Mercury's uppermost soil layer appears to be globally homogeneous, as determined by polarimetry and infrared data (Dollfus and Geake, 1975; Chase et al., 1974, 1976). Together with albedo and ultraviolet information, these data are

consistent with a silicate, lunar-like surface whose upper centimeters form a fine, powdery regolith (e.g. see Morrison, 1970; and Matson, Johnson, and Veeder, 1977).

#### Spectrophotometric Measurements

The closest analog to the mercurian soil over the wavelengths 0.33 to 1.06  $\mu\text{m}$  is that of the mature highland soil of the Apollo 16 site (McCord and Adams, 1972; Vilas and McCord, 1976). An anorthositic crust would be consistent with the planet's lunar-like albedo (Adams and McCord, 1977). However, recent evaluations indicate a mafic crust (basic to ultrabasic) would also be consistent with the observations (Hapke and Rava, 1980). By analogy with the mature Apollo 16 soils, the FeO content of Mercury's soil is estimated to be less than 6% (McCord and Adams, 1972; Vilas and McCord, 1976). Hapke (1977) constrains the lowermost FeO content to 3%, based on models of darkening process efficiencies. Submicroscopic metallic Fe<sup>0</sup> in concentrations less than 2% provides Mercury with its reddened spectrum. From these data, Hapke concludes that the surface is poor in iron metal, FeO, and Ti. A greater abundance of Fe<sup>0</sup> and Ti would reduce the albedo below observed levels.

Spectral bands are so indistinct as to make identification of any mineral species difficult. The presence of pyroxene on Mercury's surface has not been confirmed by all observers (namely Vilas and McCord, 1976). McCord and Clark (1979) claim detection of a pyroxene

feature, suggesting low-Ca, low-Fe orthopyroxene (pigeonite?) or low-Fe olivine. Tepper et al. (1977) report a high-Ca pyroxene (augite and diopside), and conclude that the surface is diopside-rich. McCord and Clark (1979) conclude that Mercury's surface contains the products of "familiar processes leading to basaltic surface volcanism," (p. 790). This opinion is supported by the other groups noted (Tepper et al., 1977; Adams and McCord, 1977; McCord and Adams, 1972).

Based on the longitudes on Mercury's surface sampled by these various observers, pyroxene detection may be position dependent. A more complete longitudinal sampling is needed. Differences in average reflectivity of the third and fourth quadrants of Mercury (Vilas and McCord, 1976) may imply a difference in composition between the hypothesized Caloris smooth plains and the intercrater plains which dominate each quadrant. Hapke et al.'s (1980a,b) color map of Mercury supports a chemical dichotomy between the Caloris smooth plains and intercrater plains of the first and second quadrants. Higher resolution multispectral photometry is clearly necessary to resolve these ambiguities. Improvement in spatial resolution may aid in determining the spectral signature of recently excavated (ray) materials.

In summary, spectroscopic data appear to confirm the existence of pyroxene on Mercury's surface, and with it, the great likelihood of basaltic volcanism, because FeO is not initially condensed on the planet's surface (Lewis, 1972). Color and albedo variations are not striking, but do not support subtle chemical variations between

morphological provinces such as intercrater plains and smooth plains around Caloris. Mercury's surface appears similar to a mature lunar highland soil, but contains less FeO, Fe metal, and Ti; its higher albedo and reddened spectrum imply anorthositic or mafic materials. Processes must subdue or disguise many of the older compositional variations, otherwise, one must conclude that the ancient surface and source regions for the plains materials (whether volcanic or ballistic) are homogeneous in composition.

#### Thermal Infrared Data

Thermal infrared data indicate that the mercurian soil behaves as if it were lunar soil exposed to the higher insolation received at Mercury's heliocentric distance (Morrison, 1970; Hämeen-Anttila, Pikkarainen, and Camichel, 1970). Although solar insolation is usually modelled as the effective black body temperature of the planet ( $440^{\circ}$  K for Mercury, compared to  $270^{\circ}$  K for the Moon), Mercury's highly eccentric orbit and high inclination cause temperatures on its surface to vary  $600^{\circ}$  K, uniquely dependent on the longitude (Table 1). In the 176 day insolation cycle, temperatures fall to  $100^{\circ}$  K (Murdock and Ney, 1973), and rise to maxima in the range of  $590^{\circ}$  K to  $725^{\circ}$  K (Soter and Ulrichs, 1967). Thermoelastic stresses (Liu, 1972), thermal magnetic resonance, and outgassing (Kumar, 1976) may be affected by such temperature cycles. McKinnon (1980) suggests that Mercury's crustal thickness varies with latitude (and longitude?) due to the



impressed surface temperatures. (Thicker crust may be expected at the north and south poles.)

Thermal inertia measurements of materials of Mercury's dark side hemisphere are characteristic of low density, porous material near the evening terminator and more consolidated, rockier materials approaching the western rim of the Caloris basin (Chase et al., 1974, 1976). Anomalies with greater thermal contrast, such as those detected outside the Caloris rim, may result from impacts into a consolidated surface, namely, the young smooth plains; lesser contrasts would result from impacts into a highly cratered megaregolith, perhaps like the ancient intercrater plains (Thompson et al., 1979). Albedo maps and radar altimetry profiles suggest that the intercrater plains extend across the observed evening terminator, and that smooth plains encircle the western rim of Caloris (Camichel and Dollfus, 1968; Murray et al., 1972; Zohar and Goldstein, 1974). Further investigation of the unimaged hemispheres of Mercury have been made using Doppler delay range maps and radar altimetry profiles (Zohar and Goldstein, 1974).

#### Orbital Data and Implications

Klaassen (1975, 1976) has refined measurements showing that Mercury rotates three times in two revolutions about the sun (Table 1). The 3:2 resonance of spin to orbital periods suggests that the planet was slowed from more rapid rotation (10-20 hours) by solar

tides (Burns, 1976). Heating of the planet through dissipation of energy during the relaxation of the oblate spheroid (the "tidal spin-down") may have been minimal according to Solomon (1976), but it may have produced stresses which fractured the crust in predictable patterns (Melosh and Dzurisin, 1978; Burns, 1976; Melosh, 1977a,b; Pechmann and Melosh, 1979). Peale and Boss (1977) argue that if the planet had a molten core, passed through the 2:1 resonance, and was captured into the 3:2 resonance, without acquiring higher order, less stable resonance configurations, then the viscosity of the possible core can be constrained to a broad set of values similar to viscosities in the Earth's molten core. However, if Mercury was initially a solid body, there are no constraints on its initial obliquity and spin.

#### Magnetic Field

Analyses by Ness et al. (1974, 1975a,b) and supporting data from other experiments aboard Mariner 10 (particles and fields, electron densities, plasma densities) confirm that Mercury possesses an intrinsic magnetic field. An active regenerative dynamo or a magnetized shell are the two mechanisms consistent with the observations. Since Mercury is protected from the solar wind by its magnetic field, and since polar darkening is not observed, solar wind darkening cannot be the primary mechanism by which albedo features are altered or their contrasts reduced (Hapke, 1977). If Mercury's

magnetic field is produced by an active regenerative dynamo, the planet must have a partially molten iron core of sufficient thermal energy to support convective motions (Ness et al., 1974, 1975a,b; Stevenson, 1975). Gubbins (1977) and Stevenson (1975) find that, at present, Mercury rotates fast enough to satisfy criteria for regenerative dynamos, and that Coriolis forces "control core dynamics."

A molten core of high conductivity--composed of iron, the heaviest, most common element available in the early solar nebula--implies that Mercury differentiated, consistent with its silicate, FeO-poor surface, detected by spectroscopic studies, and its high density (see Table 1). Reynolds and Summers (1969) estimate that the radius of the iron core would be 0.75 to 0.80 the radius of Mercury (implying a 600 km thick silicate mantle). The question to be addressed by modellers of thermal histories is whether this core is molten, how much of it is molten, and whether there is an energy source to produce convective activity.

Mercury's magnetic field can also be produced by remanent magnetization within a spherical shell (Stephenson, 1976). Although this does not imply a presently molten core, it does not exclude differentiation and core formation. Various conditions must be satisfied (concerning iron content of the shell, shell thickness, and thickness of the sub-shell with temperatures above the Curie

temperature of the remanence-carrying mineral), which Ness argues are unreasonable for Mercury (Stephenson, 1976; Ness, 1978). The debate on the source of the magnetic field is closely linked to the planet's thermal history, discussed in Chapter 6. Most thermal models are based on the dynamo interpretation of Mercury's field, and on the silicate-rich, FeO-poor, basaltic-type surface interpretation of the spectrophotometric data.

Thus the implications of Mercury's physical data and remotely sensed observations with respect to the origin of the intercrater plains seem to be that (1) Mercury is a differentiated planet; (2) it has a presently convecting, molten, iron core; (3) it has undergone tidal spin-down and its associated stress history; (4) there may have been local thermal stresses (Liu, 1972); and (5) the composition of Mercury's crust, mantle, and core are consistent with the above. Finally, the physical data and imagery analyses suggest that Mercury has a thermal history of global resurfacing through volcanism, and associated global tectonism.

#### Remote Sensing Observations of the Moon

Remote sensing observations and lunar sample ages provide some support to the assumptions and tentative conclusions reached in Chapters 2, 3, and 4, regarding (1) the age of the Nectaris and Imbrium impacts, (2) the thickness of the crust and its relation to lunar basins and plains emplacement, (3) the chemical distinctiveness of the pitted plains and smooth plains units, and (4) possible plains origins.

## Age and Petrologic Data From the Apollo 16 Site

The age of the Nectaris event is less certain than that of Imbrium or Orientale, and is quite important in estimating the intensity of bombardment during the Nectarian and pre-Nectarian periods, and in constraining the duration of emplacement of the pre-Imbrian plains. Maurer et al. (1978) use rock composition, crystal history, and shock history to determine the sequence of basin events as recorded at the Apollo 16 site. They reason that basin impact ages can be determined by geochronological dating of rocks affected by those impacts.

From this data, the authors determine two ages and magnitudes of cratering. In the earliest episode, over 4.1 b.y. ago, craters of moderate size, less than 200 km in diameter, were formed. These impacts apparently reset the Ar exposure age (gas retention age) but did not excavate deeper than the "feldspathic, anorthositic highland crust." The next cratering episode (visible at the Apollo 16 site), occurring from 3.9 b.y. to 4.0 b.y., was dominated by basin events. Excavations penetrated to deeper crustal levels, reset the Ar ages of affected rocks, and produced a wider variety of crystal textures and compositions, including excavated KREEP basalts. Using further assumptions, they date the Imbrium event at 3.88 b.y., and the Nectaris event at 3.98 b.y.; Humorum, South Serenitatis, and Crisium formed in the 100 m.y. interval between the Nectaris and Imbrium impacts.

The 3.98 b.y. age of Nectaris is much younger than prior determinations. Geological mappers place the Nectaris event in the early middle pre-Imbrian period, about 4.1 b.y. according to Wood's (1979) chronology (Offield and Pohn, 1969; Wilhelms and McCauley, 1971; Scott, 1972). Schaeffer and Husain (1974), using Ar exposure ages and estimates of ejecta debris depths from each basin impact (like the Maurer et al. group, 1978), set the Nectaris event at  $4.25 \pm 0.05$  b.y. and the Imbrian event at  $3.95 \pm 0.05$  b.y. These two dates had been accepted as the standard ages for these events. As noted in Chapter 2, the age of the P3 intercrater surface (4.0 b.y. in Wood's 1979 chronology) is nearly contemporary with the Nectaris impact as dated by Maurer et al. (1978). This does not imply that the two units (plains and Nectaris basin ejecta) are related. Maurer et al.'s study constrains the time of emplacement of pre-Imbrium plains to a 100 m.y. interval which nearly overlaps the time of mare basalt emplacement, and falls within the estimated ages of KREEP basalt genesis 4.3 to 3.85 b.y., reported by Ryder (1976), Ryder and Spudis (1979), and others. Maurer et al.'s study does not answer the question of whether the pre-Imbrian plains deposit is part of the highland KREEP basalt volcanism.

#### Compositional Data

Highland areas are, by definition, high in elevation, high in albedo, and overlie a thick lunar crust. Compositionally, they are

high in Al/Si, low in Mg/Si, low in Fe, and usually lower in radiogenic elements, U, Th, and K than the mare regions (Clark et al., 1978; Hubbard, 1979; Arnold, Metzger, and Reedy, 1977; Haines, Parker, and Metzger, 1977; Metzger et al., 1977). Adams and McCord (1977) estimate 5.5% FeO occurs in the Descartes highlands of the Apollo 16 site, near the Cayley plains material. The generally high albedo of the area and the returned samples indicate an anorthositic composition. Variations in color and albedo contrast in the highlands are few (Whitaker, 1972). Smooth light plains which show no spectral contrast with surrounding highland material are likely to be Cayley plains materials of locally derived brecciated debris (Conca and Hubbard, 1979).

Exceptions to this dominant spectral pattern have been noted recently and attributed to highland basalts, i.e., to highland volcanism (Haines, Etchegaray-Ramirez, and Metzger, 1978; Bielefeld et al., 1976). KREEP volcanism may have occurred during the Pre-Nectarian to Imbrian eras (e.g. Hawke and Head, 1978). KREEP basalts, richer in Mg, K, Th, and Fe than mare basalts or highland materials, may form a widespread layer under the eastern and western maria (Andre, Wolfe, and Adler, 1979b), may underlie Imbrian-Nectarian plains near Balmer (Haines et al., 1978; Hawke, Spudis, and Clark, 1979), and may form the Apennine Bench Formation (Spudis, 1978). Duration of emplacement is extensive: from 4.3 aeons (as dated in KREEP samples and constrained by granulitic impactites, Warner et al., 1977) to 3.8 aeons,

prior to emplacement of Mare Imbrium (Ryder and Spudis, 1979; Spudis, 1979; Metzger et al., 1979, Haines et al., 1978). Smooth plains which appear spectrally distinct may be chemically distinct as well. The light plains--Imbrian plains to Nectarian plains--probably have a variety of origins, including pre-mare highland volcanism (Andre et al., 1979a; Conca and Hubbard, 1979; Charette et al., 1977; and El-Baz and Wilhelms, 1975).

Studies by Pieters (1979), Seeger, Potter, and Wolfe (1979), and Seeger (1979) confirm that the pre-Imbrian pitted plains unit is distinct from younger plains units and distinct from Nectaris ejecta. Only minor amounts of the Janssen Formation "signature" are included in the pIp unit (Seeger, 1979), suggesting that the pIj unit may underlie the pIp, and may be exposed by subsequent excavations, consistent with the geologic analysis of Scott (1972). Pieters (1979) suggests that this common, FeO rich highland soil may be volcanically derived, even though it is not a mare basalt, as determined by its orthopyroxene and plagioclase composition. This material was not sampled in the Apollo missions. Recognition of other, possibly widespread, pre-Imbrian basaltic materials strengthens the argument for ancient highland volcanism as the source of the lunar intercrater plains.

Longer wavelength data. Longer wavelength data indicate a surface uniformly cooler than the mare, with temperature contours



paralleling the mare-highland boundaries (Keihm and Gary, 1979; Gary and Keihm, 1978; Shorthill and Saari, 1965; and Raine et al., 1975). The highlands appear to be more pulverized than the mare, forming a brecciated zone (a megaregolith) of 2 km depth. Small craters of the highlands eject fewer blocks than small craters on the mare (Thompson et al., 1979).

One may conclude that the uppermost layers of the intercrater plains are local breccias and ejecta deposits, similar to those comprising many Cayley plains. However, beneath this layer may be another of distinct composition related to the episode of KREEP basalt emplacement prior to the Imbrian period. KREEP-rich light plains are detected by compositional variations from local deposits; so too, the pre-Imbrian plains may have been detected by Pieters and Seeger. Because of the greater age of this intercrater unit, deeper amounts of local debris may cover the KREEP-rich deposits (cf. Hawke et al., 1979).

#### Physical Data

Physical data indicate that (1) the southern highland crust, determined to be 50 to 80 km in depth (Bills and Ferrari, 1977; Thurber and Solomon, 1978), is thin enough to be consistent with KREEP volcanism because the KREEP basalts are emplaced beneath a crust of less than 60 km (Spudis, 1979); (2) craters of Imbrian age may be locally intruded by magma (Dvorak and Phillips, 1978); and (3) near-side and farside Nectarian plains are found in topographically low

areas, such as basins or lowermost fault blocks (Gifford and El-Baz, 1979; Scott, 1972; Mutch and Saunders, 1972). Neither an anomalously thin crust, nor a mascon feature appears to be located beneath the pitted plains region, within the latitudinal confines of the data.

Magnetic data are not inconsistent with the formation of a small lunar core, and possibly indicate that the surface field increased in Imbrium time and has decreased since. The field appears to be relatively high during the pre-Nectarian era (Russell et al., 1977; Srnka and Mendenhall, 1979). Apparently the core formed during the rapid melting of the Moon, after crustal formation. More recent data suggest that the magnetic fields detected in lunar orbit result from surficial sources only; these sources most likely are Fe<sup>o</sup>-rich breccias magnetized in impact cratering events. The strongest fields are located over high-albedo swirl features near the antipodes of major recent basins (Hood, Coleman, and Wilhelms, 1979).

## CHAPTER 6

### THERMAL HISTORIES OF MERCURY AND THE MOON

#### Thermal Histories of Mercury

To determine a planet's thermal history, a wide range of data is necessary. These data include remote sensing results, photogeologic evidence, magnetic field and remanent magnetization data, composition and ages of samples, and physical parameters of the planet and its orbit. Few of these data form unambiguous constraints for thermal models of Mercury. Toksöz, Hsui, and Johnston (1978) provide a general list of constraints set by the data (Table 10). They define the "igneous chronology" as the "time history of the differentiation and igneous activity," (p. 293). "Igneous Chronology" is used here in the sense of the apparent igneous or relative chronology of geologic events, such as plains formation (through whatever mechanism) relative to the crater production and tectonic history (lineament and scarp formation).

The preceding chapters summarize much of the available data used as constraints for thermal modelling. The "igneous chronology" and tectonic features are discussed in Chapters 2 and 4. More complete discussions of Mercury's thermal history appear in Gault et al. (1977), Ness (1978), Toksöz et al. (1978), Solomon (1976, 1977b, 1978a), Siegfried and Solomon (1974), Fricker, Reynolds, and Summers (1974), Fricker et al. (1976), and Strom (1977, 1979).

Table 10: Data Needed to Constrain Thermal History Models

Data	Constraint
Moment of inertia	Interior structure; core
Uncompressed Density	Pressure and density gradients
Seismic data	Subcrustal layers and molten zones
Magnetic field	Presence of molten core, dynamo; remanently magnetized shell; paleofield
Surface heat flow	Radioactive materials, differentiation
Electrical conductivity	Composition, density, and temperature gradients
Imagery: Igneous Chronology	Surface record of igneous activity (volcanism), crust and lithospheric growth, core formation
Imagery: tectonic features	Global stresses (expansion/contraction) local to regional stresses (basin loading and dynamical thermal activity)
Imagery: Cratering*	Indirect dating mechanism for igneous chronology, basin events
Spectrophotometry*	Composition and small scale structure of surface.

\* Added to Toksöz et al.,'s (1978) list, pp. 293-294.

## Compositional Constraints of Mercury's Surface and Interior

Equilibrium nebular condensation theory predicts that Mercury contains minerals which condensed at average temperatures of  $1400^{\circ}\text{K}$  and pressures of  $\sim 10^{-3}$  atm (Lewis, 1972). Predicted components formed by cooling to those temperatures are mostly high temperature refractories, iron-nickel, and Mg-rich silicates. These include: perovskite  $\text{CaTiO}_3$ , melilite  $\text{Ca}_2\text{MgSi}_2\text{O}_7$  (which may re-equilibrate at  $1450^{\circ}\text{K}$  to form diopside), spinel  $\text{MgAl}_2\text{O}_4$ , diopside  $\text{CaMgSi}_2\text{O}_6$ , forsterite  $\text{Mg}_2\text{SiO}_4$ , and possibly pyroxene  $\text{MgSiO}_3$  (at  $1349^{\circ}\text{K}$ ). Fe-Ni condenses at  $1475^{\circ}\text{K}$ . Anorthite  $\text{CaAl}_2\text{Si}_2\text{O}_8$  forms from spinel at  $1362^{\circ}\text{K}$ . The lower temperature minerals are included within the temperature range allowed by Lewis (1972),  $1550^{\circ}\text{K}$  to  $1300^{\circ}\text{K}$ ; pressures may be as great as  $10^{-2}$  atm according to Lewis' Figure 2 (1972). Rare earth elements are expected to condense out with perovskite, melilite, and diopside in solid solution. The incompatible refractories uranium and thorium will enter the refractory compounds. In later re-equilibration U and Th will enter the Mg-silicates (Grossman and Larimer, 1974).

Goettel (1976) used Lewis' theory to predict the following composition for Mercury at  $T = 1400^{\circ}\text{K}$  and  $P = 10^{-3}$  atm.

Refractory condensates:	15.43%
$\text{Al}_2\text{O}_3$ 5.81%;    CaO    5.31%;    MgO    1.04%	
$\text{SiO}_2$ 3.02%; $\text{TiO}_2$ 0.25%	
FeNi alloy	65.07%
$\text{Mg}_2\text{SiO}_4$ (Forsterite)	19.52%

Lewis' model assumes equilibrium condensation and homogeneous accretion of planetesimals in the immediate locale of Mercury in its orbit. Goettel (1976) claims that the above composition will not change much if gas/solid equilibrium is not active. However, should mixing of high and low temperature condensates or fractionation processes occur (e.g. Weidenschilling, 1978), the following changes may be expected in the following order:

- (1) Replacement of  $Mg_2SiO_4$  (olivine) with  $MgSiO_3$  (pyroxene)
- (2) Addition of K and Na
- (3) Addition of FeS
- (4) Addition of FeO

It thus appears likely, comparing these expected changes with spectrophotometric data (which suggest FeO and pyroxene), that mixing or fractionation processes have occurred to a limited degree on Mercury, as concluded by Ringwood (1979). Endogenic processes may have generated some of these minerals, so some caution is necessary in the conclusion that they are "primordial." The more volatile components are not likely to be abundant; Mercury's silicate chemistry may be modelled by mixing high temperature refractories with a small amount of anhydrous chondritic material, as Seitz and Kushiro (1974) have done with Allende meteorite in modelling Earth's mantle.

Condensation and Accretion. A planet's thermal history begins with condensation and accretion. These processes determine the planet's initial temperature, its initial composition, and the physical distribution of its components, especially the heat-producing elements. The accepted (but sometimes challenged) models are equilibrium condensation and homogeneous accretion, discussed above (see e.g. Grossman and Larimer, 1974; Lewis, 1972; and Goettel, 1976).

In this model, heat producing elements U and Th occur in the Mg-silicates, homogeneously distributed throughout the body prior to differentiation. Initial temperatures used in thermal models vary from the planet's present effective temperature ( $440^{\circ}$  to  $350^{\circ}$  K), to its condensation temperature  $1400^{\circ}$  K (Lewis, 1972). More rapid accretion rates increase surface temperatures; larger impacting bodies may deposit heat at greater depths, possibly initiating melting of the planet.

Condensation rates (fast or slow cooling) determine whether different chemical species have time to equilibrate. A fractional condensation occurs if condensates are removed from equilibration from the solar gas, usually by condensing, accreting, and being buried in layers of primitive aggregates. One expects U and Th to enter the high temperature refractories, perovskite and melilite, rather than magnesium silicates. If inhomogeneous accretion then occurs, these refractory rich materials are buried at the core of the planetesimal,

covered by Fe-Ni and then by the silicates (see Cordell, 1977). Had equilibrium condensation occurred, followed by inhomogeneous accretion, the heat producing elements may occur in the silicate mantle, not in the core of the body. Other processes, such as iron-silicate fractionation and magnetic field interactions, may have affected Mercury's composition, as argued by Weidenschilling (1978) and Alfvén and Arrhenius (1976). Mixing of planetesimals accreted at different solar distances introduces low temperature condensates, like K, S, and FeO, to Mercury; substances such as these are invoked to maintain a molten, convecting core. Ringwood (1979) considers that Mercury is composed of a small amount of low temperature condensates (FeO, K, and S) plus a large proportion of the high temperature refractories and Fe-Ni.

A large number of initial states can be produced by combinations of the condensation, accretion, and fractionation hypotheses. These include:

(1) A cool homogeneous body of iron and silicates with radioisotopes (U, Th) distributed throughout the silicates (e.g. Solomon, 1976).

(2) A hot body, whose temperatures cause melting and differentiation (possibly during accretion) so that iron metal sinks to lower layers of the molten material, and U and Th differentiate to the crust. In this process, an iron core will form (Fricker et al., 1974).

(3) A cool heterogeneous body with a refractory core, iron mantle, silicate upper mantle, with U and Th in the uppermost silicates.



(4) A Ca-Al rich refractory core with U, Th within it, surrounded by FeNi, with an upper mantle or crust of Mg silicates (Cordell, 1977). This configuration may be unstable.

(5) A cool (or hot) homogeneous mixture of low temperature condensates and high temperature condensates, with the latter predominant (e.g., Kaula, 1976).

Thermal history models accommodate the initial conditions by beginning with a body of the observed mass and density and of composition regulated by position in the solar system. If other information is known--the moment of inertia, seismic, or compositional data--the interior structure can be approximated; otherwise a homogeneous, self-gravitating sphere is assumed. (Some models begin with a differentiated body.) Initial temperatures on Mercury have been set to the (a) effective temperature of a reflecting surface ( $344^{\circ}$  K), (b) temperature of the solar nebula at that distance and pressure ( $1400^{\circ}$  K, condensation temperature), (c) melting temperature of the body, assuming a rapid, hot accretion,  $2000^{+}$  K, (d) present surface temperatures, assuming a cold accretion ( $100^{\circ}$  to  $700^{\circ}$  K), or (e) a temperature based on other information. Radioactive element content of the bodies varies from chondritic ratios, to lunar, to terrestrial, as listed in Table I, Toksöz et al. (1978). Although the (Th/U) ratio is nearly equal for the solar system bodies (3.5-4.0), the (K/U) ratio varies widely because K is a volatile element and U a refractory. (In mineral

melts, both are incompatible.) At Mercury, (K/U) is expected to be zero. Other heat source densities and model parameters are listed in Table II of Ness (1978, p. 541).

#### Basic Thermal Evolution Models

The earliest thermal evolution of a planet is dependent on its initial temperature and the heat source strength; this determines the likelihood of core formation. Later evolution and the planet's present condition are governed primarily by its size (Toksöz et al., 1978; Walker, Stolper, and Hays, 1979). The observations for Mercury apparently require (1) very early core formation, prior to the end of heavy bombardment, and (2) a presently molten core, required by the active dynamo interpretation of the magnetic field data (Ness et al., 1975a,b). Satisfying these constraints and others presents the greatest challenge to thermal history models. Both constraints are, moreover, model dependent, as described earlier.

The models of Toksöz et al. (1978) and Solomon (1976, 1977b, 1978a) best fit the constraints set by previous authors, as summarized by Gault et al. (1977), Strom (1979), and Ness (1978). Earlier models of Majeve (1969), Siegfried and Solomon (1974), and Fricker et al. (1974) have been improved with better constrained melting curves and heat source densities. For example, Majeve (1969) used chondritic values of K, U, and Th; the planet did not melt and differentiate. Recent modelling omits K as a heat source, based on Lewis' (1972)

condensation sequences, and scales U and Th to the amount of silicates in the planet, based on lunar, chondritic, or terrestrial values. The iron melting curve of Higgins and Kennedy (1971) is improved by that of Liu and Basset (1975). Fricker et al. (1976) suggested that separate melting relations for the iron core and the silicate mantle be used after differentiation. Toksöz et al. (1978) use the diopside melting curve of Boyd and England (1963) to approximate the refractory-rich mantle of Mercury. For smaller bodies (the Moon), the basalt melting curve of Ringwood and Essene (1970) is commonly used (Toksöz et al., 1978).

Thermal conductivity values have also become more sophisticated. Siegfried and Solomon (1974) averaged silicate and iron conductivities, with a resulting conductivity similar to that measured in mesosiderites and pallasites, the stony-iron meteorites. Fricker et al. (1974, 1976) separate these conductivities after differentiation, with the result that the low conductivity of the silicate mantle insulates the high conductivity core, reinforcing the discontinuity of their melting temperatures at the boundary. Toksöz et al. (1978) include the radiative and electrical conductivity with the lattice conductivity term. Other complexities include the inclusion of convection, (Schubert, Cassen, and Young, 1979; Turcotte, Cooke, and Willeman, 1979), solid state creep or convection (Tozer, 1972, 1974; Meissner and Lange, 1977), and different distributions of heat sources

(Daly and Richter, 1978; Schubert, Stevenson, and Cassen, 1980; Stevenson et al., 1980; Horedt, 1980; Kaula 1979a; Gubbins, 1977; and Liu, 1972). Some of these models are reviewed in Appendices G and H.

Variations between the Toksöz et al. (1978) and Solomon (1977b) models centers on the time of initiation of core formation and the subsequent events.

The "Toksöz" model. The Toksöz et al. (1978) model of Mercury begins with surface temperatures of  $1400^{\circ}\text{C}$  (base temperature  $1400^{\circ}\text{K}$ ), U heat source abundance of 44 ppb., and rapid initiation of partial melting to a depth of  $\sim 900$  km. (See Figs. 10 and 12 of Toksöz et al., 1978.) The core separation begins at 0.5 b.y. as melting advances to deeper levels in the homogeneous planet; the energy released from these processes raises the temperature  $600^{\circ}\text{C}$  to  $700^{\circ}\text{C}$  globally. By 1.5 b.y. core separation is complete and cooling begins. Solid state convection within the partial melt zone keeps the planet "active" for another 1 b.y. This zone, located at the  $1200^{\circ}\text{C}$  isotherm, descends in depth from 100 km at 1 b.y. to 150 km at 2 b.y., to 200 km at 2.5 b.y. At present, the base of the lithosphere, defined as the  $1000^{\circ}\text{C}$  isotherm, extends to 250 - 300 km depth; solid mantle continues to 500 km depth, consistent with the  $3/4 R$  radius of the core-mantle boundary. The core remains partially molten only when a heat source abundance of  $H \geq 1.5 \cdot 10^{-8}$  ergs/cm<sup>3</sup>/sec is included; if  $H = 0$ , the core would be solid. The minimum heat source abundance is equivalent to 2 ppb U remaining in the core (Toksöz et al., 1978, p. 303).

Mercury's internal energy and activity may have peaked at 0.8 b.y., during the surge of thermal energy produced in core formation. Tectonic activity lasts 2 b.y. after planet formation. Energy within the planet starts to decrease more rapidly at 2.5 b.y., after the cooling of lithosphere and mantle, and cessation of solid state creep. According to Toksöz et al.'s (1978) Fig. 18, the duration of activity on Mercury exceeds that of the Moon. Unless this applies only to the scarp formation activity, it contradicts Solomon's (1977b, 1978a) prediction that the youngest plains on Mercury's surface should be older than those on the Moon. Strom (1977, 1979) appears to support Solomon's conclusion based on the crater population recorded on the Caloris smooth plains.

Intercomparisons of planetary energy output shows that the time of peak energy output (thermal evolution) occurs in the order Moon, Mercury, Venus, and Mars, with the value and rate of decrease in energy greatest for the Moon, followed by Mercury and Mars. Venus has had nearly constant activity since its core separation, 1 b.y. following accretion. Venus and Mars may still be active (with partial melt zones), but Mercury and the Moon are currently inactive.

The "Solomon" models. Solomon's 1976 model is very similar to Toksoz et al. (1978) model. Solomon's (1976) initial conditions are a nearly flat temperature gradient with  $T(\text{center}) = 1400^\circ \text{K}$ . Core formation occurs from 1.2 to 1.8 b.y., accompanied by radial increase of 17 km, and heat generation equivalent to  $700^\circ \text{K}$  increase in temperature.

The major part of core formation occurs between 1.4 to 1.6 b.y. The upward differentiation of heat sources contributes to rapid heat loss; the core is solid ~1.5 b.y. after it separates completely. The radial contraction due to lithospheric cooling is 2 km. Core solidification brings the total radial decrease to 17 km.

The "thermo-tectonic" models of Solomon (1977a,b; 1978a,b) are directly applicable to the parallel history of volcanism and tectonism on Mercury. The basic model is simple. Radioactive materials (or another heat source) within a homogeneous body cause melting and differentiation of iron and silicates, often leading to core formation. The body expands from the thermal expansion, redistribution of iron and silicates, and phase changes in core and mantle. During this extensional tectonics period, extrusion of volcanic materials occurs through opened vents. Following core formation, the planet cools, and enters a compressional tectonics stage, during which contraction of the lithosphere closes off source vents, ending the phase of volcanism.

Solomon (1977b, 1978a) predicts that the intercrater plains formed during core formation-expansion episode, and that scarp formation occurred during the cooling and contraction of the planet, accompanied by the cessation of volcanism.

Apparent inconsistencies in this model are (1) the lack of global scale tensional features on the surface, (2) the approximate

limit of radial contraction of 2 km (Strom et al., 1975b), and (3) the probability of a molten core at the present (Ness, 1978). The conclusions of this research and earlier observations (e.g., Strom et al., 1975a,b) suggest in addition that scarp formation is concurrent with smooth plains formation, that the average viscosity of the surface is  $10^{26.5}$  poise, similar to that of the Moon's (Schaber et al., 1977), and that the compositions of Mercury's old and young plains do not differ substantially (Hapke et al., 1975, 1980a,b; Hapke, 1977; Dzurisin, 1977b).

Solomon (1977b), addressing these constraints, argues that the extrusion of intercrater plains materials during the core formation period and the heavy bombardment erased the tensional features. Therefore, the age of the oldest visible plains surface must be younger than the extensional tectonic period, confining differentiation and core formation to a period prior to the end of the heavy bombardment. From arguments noted earlier, it is assumed that Mercury's heavy bombardment, like the Moon's, ended about 4.0 b.y. ago, setting a span of 0.6 b.y. for core formation on Mercury. To ensure such rapid core formation (as compared to Toksöz et al.'s or Solomon's earlier models), Solomon starts with a high initial temperature ( $T_c = 1600^\circ\text{K}$ ). Radioactive elements (uranium concentration of 38 ppb) become concentrated in the upper 80 km of the crust. The ( $700^\circ\text{K}$ ) increase in global temperature is accompanied by global tensional

stresses and fractures, and magmatic extrusions through the vents. Radial increase of this model (Fig. 8 in Solomon, 1977b, p. 141) is 7km.

Following core formation the planet cools and compressional stresses dominate as the radius of the planet decreases. Compressional stresses are greatest, and produce the most pronounced contraction, about 400 m.y. after "core segregation." A tangential stress factor  $\Delta\sigma_t \div \Delta t$  can be computed which measures the change in thermoelastic tangential stress with time (Solomon, 1977b, p. 138). This factor (defined in Appendix I) is positive for tension and negative for compression. Solomon comments that this factor is negative to 40 km depth, i.e. implying a global compression. From 40 to 120 km depth, the factor is positive, indicating subsurface tensional pressures which persist for "several billions of years," (p. 142, Solomon, 1977b). This creates a favorable mechanism for extrusion of molten materials after the onset of scarp formation (Solomon, 1977b; Leake, 1980b), consistent with smooth plains formation during the P3 through P1 episodes.

Craters of 40 km or larger are likely to have fractured the crust to 40 km depth (Roddy, 1977; Croft, 1978). Magma may be extruded into the tensional layer; Solomon notes, (1977b, p. 142), "...thermal stress will readily permit upwards propagation of magma to shallow



crustal levels, from which it can travel to the surface if fluid pressure exceeds lithostatic or if the overlying crust is weakened by impacts." Because the radius decrease is apparently confined to 2 km, only 60% or less of the core can be solidified at present. Although this is consistent with the conclusion of a molten, convecting core-dynamo producing Mercury's intrinsic magnetic field (Ness et al., 1974, 1975b), it nevertheless requires extra heat sources in the core.

The other two constraints, those of Schaber et al. (1977) and Hapke and Rava (1980) and others, are met by Solomon's model to some extent. Core formation prior to 4.0 b.y. ago is consistent with an average viscosity of  $10^{26.5}$  poise only if Mercury's current crustal viscosity is higher than average (for about 4 b.y.). Values of  $10^{27}$  poise are predicted for Mercury at a depth of 100 km at the present, decreasing to  $10^{21.5}$  poise at 400 km depth (Meissner and Lange, 1977).

Compositional changes within extruded lava flows are expected for extended fractionation times, as may occur on large bodies with active volcanism (Walker et al., 1979); these changes may also be correlated with the source depth (Stolper, 1980). Further discussion is given in the Implications section of the next chapter. The lack of striking compositional differences may imply that Solomon's subcrustal tensional layer is too deep, that the tensional conditions were shorter in duration than "several billions of years," or that compressional stresses above or below the tensional layer were too great

to overcome, or that his model is wrong. Otherwise, the onset of scarp formation may signal the deepening of the source region of the young plains extruded during that time. Only a few smooth plains deposits are chemically distinct from older plains units (as, for example, the red unit on Murasaki's floor, Hapke et al., 1980b).

In most models with reasonable heat source concentrations, a cool initial temperature, efficient differentiation of radiogenic isotopes to subcrustal silicates, and efficient separation of silicates from iron, the core begins to form at least 1 b.y. after planet formation, is completed in another half billion years, and has solidified about 1-2 billion years before the present. In models with 30 ppb Uranium concentration in the silicates, scaled to estimated lunar abundances, core separation and melting do not occur. The planet's internal temperatures rise, but do not reach the Fe-liquidus in 4.6 b.y. Models with 44 ppb U, scaled to chondritic meteorites, do melt for all initial surface temperatures (Siegfried and Solomon, 1974). Efficient differentiation of these heat sources causes most models to cool before the present. Methods proposed to keep the core molten are summarized below.

The preferred models of Solomon (1977a,b; 1978a), according to Strom (1979), show (1) rapid core formation, prior to 4.0 b.y. ago, (2) greatest cooling and contraction rates shortly after core formation, (3) less severe contraction over the remaining history, (4) a

molten core, or molten and convecting outer core at present, and (5) volcanic extrusions during early compression and cooling of Mercury.

Some relaxation of these requirements may be indicated by this study. Since ancient tensional features other than Caloris and the hilly and lineated area have been tentatively identified, the requirement of rapid core formation and obliterating bombardment may be eased slightly (only slightly--these features are rare and not regional). Because scarps of period 2 are more numerous than those of period 3, the greatest contractive phase need not follow immediately after core formation ends. Compositional homogeneity may require that the proposed tensional layer be shallower or more shortlived than "several billions of years."

Toksöz' general model fits most of these revised constraints, but may still be too sluggish to have intercrater plains formation coincident with heavy bombardment, unless the heavy bombardment on Mercury was nearly the same magnitude as on the Moon, but more prolonged, or occurred a half billion years later. Both authors show that accelerated core formation results from high initial temperatures, especially near the surface, or from external heat sources (see also Appendices G and H).

Volcanism during compression results from subcrustal tensional forces. Global compression is locally exceeded by impact-related stresses: The reduction in area of smooth plains from Class 3 to

Class 2 to Class 1 periods results from these competing stresses. Solomon (1978a) predicts that "Global compression would act to shut off volcanism associated with local stress systems faster than for a planet under global tension. Thus the time duration of smooth plains emplacement is predicted to be short for Mercury compared to that for volcanic plains on Mars or the Moon," (Solomon, 1978a, p. 462). This would also be more consistent with reduced compositional differences on the mercurian surface (similar to the lack of compositional variety on the lunar highlands).

Keeping the Core Molten. The presence of a molten core is not directly constrained by the intercrater plains research conducted here, nor demanded by the detection of an intrinsic magnetic field at Mercury. But, as noted in Chapter 5, an active dynamo may be the most plausible source of this field (Ness et al., 1975, a,b, 1976; cf. Stephenson, 1976; Russell, 1980).

There are various proposals to keep the core molten. Heat sources may be retained in the core if differentiation was inefficient. Mixing or fractionation during accretion may inject volatiles which act as impurities, lowering the melting temperature (as S in a Fe-FeS melt), or as heat sources (as K-40; Weidenschilling, 1978; Ringwood, 1979). Solomon (1976) estimates that 20% of Mercury's U and Th must remain in its core to maintain a molten state at present. Toksöz et al. (1978) estimate that the necessary heat source abundance

is  $1.5 \cdot 10^{-8}$  ergs  $\text{cm}^{-3}\text{s}^{-1}$ , satisfied by 2 ppb U (see also Cassen, 1977). A sulfur content of 3% by mass would lower the melting point, percolate through denser materials, and maintain rigorous convection within a thin, molten layer according to Stevenson et al. (1980; cf. Stevenson, 1980). An addition of 156 ppm K-40 to the core materials would also keep it molten (Toksöz and Johnston, 1977). However, inefficient differentiation of radioisotopes is "implausible" (Solomon, 1976), and mixing of volatiles K and S into Mercury's high temperature accretion zone is not likely to introduce the substantial quantities noted above (Goettel, 1976; personal communication, 1981).

Other energy sources are gravitational heating, tidal energy, cooling of the inner core, and more exotic, extinct radionuclides. Gravitational heating over the age of the planet would keep the core molten, but produce an extended period of tensional tectonics not observed on Mercury's surface (Solomon, 1976; Strom et al., 1975b). Tidal energy and precessional heating are "insufficient" according to Solomon (1976; compare Burns, 1976) and Gubbins (1977). Cooling of the inner core provides a more viable mechanism for heating an outer core. Fricker et al. (1974, 1976) find that the silicate mantle has a melting point  $200^\circ$  K higher than that of iron at the temperature and pressure of the core-mantle boundary. They postulate that the low conductivity of the silicate mantle insulates the iron core, such that an outer molten layer  $\sim 500$  km thick forms. Extra heat sources are

needed to keep this layer superadiabatic. Gubbins' (1977) mechanism (and that of Stevenson et al., 1980) will sustain convection of the outer core using the heat from the cooling of the inner core. Fields produced by weak convective motions in Mercury's interior could be amplified by ambient fields--perhaps remanent magnetic fields near Mercury's surface (Levy, 1979). Extinct nucleotide Fe-60 has been suggested as a possible source of heat for the early core (Kohman and Robinson, 1980; Herndon and Rowe, 1973), but its half life has not yet been determined.

An alternative model for the intrinsic field--a remanently magnetized shell--could require that the core was once molten and conducting. Should iron be inefficiently segregated from silicates, the general conductivity of the upper mantle would rise, allowing a thicker shell at sub-Curie point temperatures to be remanently magnetized (Solomon, 1976). This theory however, implies fairly shallow, high-Fe deposits which would be excavated by basin impacts. Albedo, color, and spectrophotometric data do not support such high-Fe deposits.

In summary, relaxations of compositional constraints, namely the presence of volatiles, may enable the core to remain molten and convecting up to the present. The core may be insulated by density and conductivity discontinuities at the core-mantle boundary. Late or extended core formation may keep it molten at present, but heat

sources within the core or unusual initial heat distributions are required. Some of the scenarios are inconsistent with observations. Of course, most photogeologic constraints used by Solomon, Toksöz, and others are themselves model dependent. Observations of mass and density distributions are not yet accurate enough to probe the structure of Mercury's interior (Data such as  $J_2$ ,  $C/MR^2$ , and obliquity are not well constrained; see Ferrari and Bills, 1979.) Orbiters and landers, magnetic probes, and orbital chemical data would aid in answering these dilemmas.

Results of this analysis describe a planet much like other terrestrial bodies, possibly sharing the following characteristics:

- (1) Early global melting and high initial temperatures;
- (2) Volcanic extrusions during core separation and melting;
- (3) Tectonic forces accompanying the volume changes during core separation and heating, involving thermal expansion and mass redistribution, followed by contraction with cooling;
- (4) Global heavy bombardment early in history;
- (5) Subsurface tensional forces proceeding during lessening bombardment;
- (6) Local stresses leading to local, short duration, volcanic episodes;
- (7) Cooling of the planet's lithosphere and/or core.

Many of these processes, namely the late thermal histories, are dependent on the size of the body. Toksöz et al. (1978), Solomon (1977a,b, 1978a,b), Walker et al. (1979), Stolper (1980), and others correlate composition, tectonic activity, core size, age of last plains emplacement, and extent of highland area to planet's size and mass. Heliocentric distance of the planet may determine its initial composition and volatile content: this will affect source region chemistry, heat source complement, and melting temperatures of core and mantle. The earlier thermal histories may depend on conditions which are shared throughout the inner solar system: radiogenic heat sources, high temperature phases of the sun, processes in the solar nebula, and an early, intense accretional bombardment. Initial high temperatures and global melting are apparently common occurrences among the terrestrial planets (Hostetler and Drake, 1980).

#### Lunar Thermal Evolution: Some Comparisons

No attempt is made here to explain the complexities of lunar thermal evolution, especially where it involves the Moon's origins, although such considerations may be necessary to model the earliest stages of thermal history (Ringwood, 1979; Ringwood and Kesson, 1977). Chapters 3, 4, and 5 review the pertinent constraints; here, the models of Toksöz et al. (1978), Solomon and Chaiken (1976), and Solomon (1977b, 1978a,b) are used to compare the genesis of the



intercrater plains and mare in the Moon's thermal history. Further comparisons are made to Mercury's thermal history.

#### Lunar Thermal Evolution

Both Mercury and the Moon qualify as 'one plate' planets in Solomon's (1978a) thermo-tectonic models. He and Toksöz et al. (1978) use as constraints evidence for volcanism, composition and age of volcanic rocks, lunar heat flow measurements, tectonic features, and the relative ages of these events recorded in the impact bombardment. The major constraint for the Solomon models is that the total change in lunar radius since 3.9 b.y. ago is  $\pm 1$  km or less; in addition, the age of the magma ocean is at least 4.4 b.y., and the age of mare volcanism is 3.9 to 3.2 b.y. (Solomon and Chaiken, 1976).

Lunar evolution begins with a high initial temperature, which causes global melting to a depth  $Z_0$ ; heat sources U, Th, and K are differentiated upward to the crustal layers. The interior of the Moon remains cool and undifferentiated. Mechanisms for melting the early Moon are similar to those noted for Mercury.

The  $\Delta R$  constraint on the change in lunar volume restricts global melting to 200 to 300 km in Solomon's model (1977b), less than the 500 km depth originally proposed (e.g. Taylor and Jäkes, 1974) and used by Toksöz et al. (1978). As the planet ages, the near molten 200-300 km zone begins to cool while the cool interior heats due to its homogeneously distributed heat sources. Although no mention of a

core is made by Toksöz or Solomon, its radius is restricted to 400 km by the moment of inertia and has little effect on volcanism at the lunar surface (except possibly in remanent magnetization recorded by cooling lavas; Russell et al., 1977; Stephenson, Runcorn, and Collinson, 1975). Solomon's models prohibit the total melting proposed by Russell's group.

Solomon (1978a) notes that changes in the lunar stress regime have a decided effect on mare volcanism; for a positive tangential stress factor, stresses are tensional, conducive to volcanism and open vents. This factor remains positive in the Moon for a longer period than on Mercury. The beginning of negative stress factors,  $\frac{\Delta\sigma_t}{\Delta t} < 0$ , signals the closure of vents and the cessation of volcanism. Local tensional stresses under the margins of large basins may allow late extrusions when the global compressional forces are exceeded, analogous to the subcrustal tensional stress factors during Mercury's compressional period which allow smooth plains volcanism. Volcanism on the Moon during the Moon's global expansion period is consistent with the age of the pre-mare KREEP volcanics and with the age of the (possibly associated) lunar intercrater plains.

Pre-mare and mare volcanism both occur primarily in the tensional stress regime, during different stages of the heavy bombardment. In contrast, intercrater and smooth plains volcanism on Mercury occur during its expansional and contraction phases respectively.

The difference in timing of volcanism and tectonism may explain the difference in areal extent of the mare basalts versus the smooth plains on the first quadrant of Mercury. The former were emplaced in a tensional regime, the latter in a compressional period. Yet if the lunar intercrater plains were emplaced during the early phases of the lunar tensional regime, one wonders why they are not greater in expanse or in age variation (for instance, P3 through P5 units). Subsequent degradation (basin events as well as continued heavy bombardment), crustal thickness variations, and available magma sources may have limited the formation and exposures of the pIp material.

Age of volcanic materials of one planet relative to the other is also linked to the planetary "energy" cycle. In Solomon's (1978a) model the Moon reaches a peak volume at a time later than on Mercury, because of its protracted tensional episode (Solomon, 1978a). The youngest "large scale plains volcanism" on the Moon is expected to be younger than comparable volcanism on Mercury. That is, the lunar mare basalts are younger than the mercurian (P3) intercrater plains, and the youngest of the mare basalts (at the mare borders) are probably younger than the mercurian smooth plains (P1 and P2), where both of the latter episodes occur under compressional regimes, and the former under tensional regimes.

Toksöz et al. (1978) support many (but not all) of these conclusions in their latest model of lunar thermal history. Heat source abundances are  $K/U = 2000$ ,  $Th/U = 3.5$ , and  $U = 35$  ppb--values which indicate a depletion in volatiles and a  $K/U$  ratio similar to differentiated achondrites (the eucrites). Radioactive heat sources are concentrated near the crust following differentiation. Solid state creep (as advocated by Tozer, 1972, as a means of heat transfer) is included in the Toksöz model.

Initial conditions are a partially molten zone to 500 km depth (on the Ringwood and Essene, 1970, basalt solidus), and a cool interior, of central temperature  $500^{\circ}C$ . The first 0.5 to 1.0 b.y. are critical, because the pre-Imbrian plains may have formed 0.4-0.6 b.y. after planet formation. As the near surface regions cool, the partial melt zone moves deeper into the lithosphere and is less accessible, except by basin impacts (see McGetchin, Head, and Schultz, 1979); at 4.2 b.y., the partial melt zone occurs below 80 km depth; at 4.0 b.y., it lies below 120 km depth. The bottom of the lithosphere occurs 30 to 40 km above the partial melt zone. (See Fig. 8, Toksöz et al., 1978, p. 300.) Accessibility of magma sources will decrease as the crust thickens; the latter varies with the frequency and location of basin events. It seems likely that a period of pre-mare volcanism is consistent with the Toksöz model also, especially because the planet is most active in its earliest stages, following the cooling of the magma

ocean. Maurer et al. (1978) however, imply that a hiatus occurred in lunar volcanic activity, from 4.2 to 4.12 b.y., which is not predicted by either the Solomon or Toksöz models.

The early rise and rapid decline of the Moon's thermal energy is in part due to its small size and high surface-to-volume ratio. The peak in its activity corresponds to "large scale magmatic activity as evidenced by mare basin filling," (Toksöz et al., 1978, p. 311). At 3.6 b.y., the Moon's energy begins to decrease, after maintaining a plateau of high energy from 4.6 b.y. ago.

#### Comparisons with Mercury

It is interesting to compare the energy histories of the Moon and Mercury, as illustrated in Fig. 18 of Toksöz et al. (1978, p. 311). The surge in Mercury's energy curve due to core formation occurs about the time of the lunar pre-mare volcanism, implying that some mare basalts may be older surfaces than the Mercurian smooth plains, which are formed later in Mercury's 2 b.y. active period in the Toksöz model. The rate of decrease in lunar energy is more abrupt than for Mercury (unless Mercury's core has solidified).

Morrison and Warner (1978) theorize that planet size and the depth of the feldspar stability field (to 12 kb) regulate the amount of terra formed in the planets. Larger planets have thinner, more mobile crusts. Lateral motions of the Moon's crust did not occur because of its thick lithosphere, estimated to be 250 km early in

history by Morrison and Warner. More complex models for the formation of the lunar crust are presented by Herbert, Drake, and Sonett (1978), and Schubert et al. (1979). Walker et al. (1979) speculate that the variety of basalts on the Moon will be less than on Mercury (if such basalts exist), because the duration of volcanism is shorter, allowing less time for severe fractionation. Their reasoning fits the Toksöz model better than the Solomon model. The disagreement in the two thermal chronologies of Mercury and the Moon will be discussed shortly.

In summary, few constraints can be added to the lunar thermal history models, for they are already consistent with pre-mare and mare volcanism. In fact, these two volcanic periods may be a single ongoing phase in lunar evolution, separated by the intense late bombardment and basin events. The activity, distinct from the original magma ocean, occurs when the crust is fairly stable and has reached a high enough viscosity to record craters and basins. Bombardment may act to initiate the volcanic extrusions by fracturing (and heating?) the crust to the depths of the partially molten zone. The duration of volcanism, or subcrustal melting, determines the variety of basalts. Upward differentiation of U, Th, and K during the magma ocean period provides a concentration of heat sources to prolong the basalt fractionation period.

Peak Evolution of the Moon and Mercury. The "Solomon" and "Toksöz" models map out different sequences of peak evolutionary

activity of Mercury with respect to the Moon. A variety of constraints cause this variation. Solomon's (1977b) requirement that core formation and expansion in Mercury occur prior to 4.0 b.y. ago biases his evolutionary sequence to Mercury--Moon--Mars, with the age of the youngest plains volcanism decreasing in the same order. Toksöz et al. (1978) do not accelerate core formation in Mercury, except to require that the planet have high initial temperatures. The sequence of peak evolutionary activity which they determine is Moon-Mercury--Mars; activity on Mercury is predicted to last nearly a billion years longer than lunar activity.

Were one to restrict heavy bombardment on Mercury to continue until just after core formation in the Toksöz model, the date of this final bombardment would be 3.8 to 3.6 b.y. ago, fully 0.2 to 0.4 b.y. after the recorded end of heavy bombardment on the Moon. Because the bombarding populations are so similar in diameter-density distributions on the two planets (Strom, 1977; Woronow et al., 1980), this temporal offset is difficult to reconcile. One possibility is that both planets may have suffered a heavy bombardment 4.0 b.y. ago, but cratering on Mercury continued 0.3 b.y. longer, possibly due to its closer heliocentric position, or to a local population.

If one fixes the bombardment period to end 3.9 to 4.0 b.y. ago, one would expect to observe global tensional features on Mercury, (because it has not yet reached its peak energy), and smooth Caloris-age plains younger than lunar mare basalts. The time evolution of the

Toksöz model for Mercury therefore seems to present more problems and inconsistencies than that of Solomon, if the impact fluxes on the Moon and Mercury are similar, and if global tensional features on Mercury were indeed obliterated.



## CHAPTER 7

### DISCUSSION OF THE NATURE, ORIGIN, AND ROLE OF THE INTERCRATER PLAINS OF MERCURY AND THE MOON

The first section of this final chapter summarizes the nature and origin of the intercrater plains of Mercury and the Moon as determined through geologic mapping, crater statistics, and remotely sensed data analyzed in this research. Some implications of these results regarding scarp formation, absolute ages, and terrestrial planet surfaces follow the summaries. In the last section, I attempt to define the "role" of the intercrater plains and outline future work which might lead to a better understanding of these units and terrestrial planet evolution.

#### Summaries of Results

The intercrater plains of both Mercury and the Moon form flat-to-gently-rolling surfaces between larger craters and crater clusters. High densities of small (1-10 km diameter) craters occur on these plains; many of the small craters are elongated, breached, and occur in chains or clusters, characteristic in morphology to secondary craters (Trask and Guest, 1975). Intercrater plains form a major, widespread unit on Mercury; on the Moon, they are restricted to the

southern nearside highlands, southwest of the Nectaris basin, and to ancient basin interiors, such as Lomonosov-Fleming, on the farside.

### Mercury

A geologic mapping strategy developed by Malin (1975), in which the plains are dated relative to the degradation ages of superposed and embayed craters, establishes that the intercrater materials mapped by Trask and Guest (1975) span a range of relative ages P3 to P5, indicating emplacement over an extended period of time, concurrent with the period of heavy bombardment responsible for C5 to C3 craters and basins.

From geologic mapping, the intercrater plains are interpreted as primarily volcanic flows, severely disrupted by repeated impacts of primary and secondary projectiles, by mass wasting, and by seismic disturbances. Ballistic deposits are interbedded with, and must overlie, much of this surface. The flat expanses of plains, their widespread distributions, occurrences within depressions, embayment of craters and basins, and association with tentative volcanic landforms (domes, and some ridges and scarps) form the bases of this conclusion. The higher elevations of many intercrater surfaces preserve them from embayment by later volcanic flows, but not from ballistically emplaced ejecta. The preservation of discernible C4 secondaries of 10-15 km on the plains attests to the minimal deposition of impact ejecta. The embayment of the C5' craters by the oldest plains unit (P5) suggests

that this plains unit is not a primordial surface. Instead, it must overlie a still older surface.

The distribution and morphology of the younger plains units also suggest a volcanic origin for those exposures within older craters or depressions isolated from younger basins. Many of the smooth plains around Caloris, equivalent in texture to the P2 and P1 units, are also interpreted as volcanic (e.g. Strom et al., 1975b; Trask and Strom, 1976). Impact melt materials within craters of the same age, and impact ejecta distributed between large, young craters of similar ages, are two other sources of the P1, P2, and some P3 units of the first quadrant.

Studies of Mercury's tectonic history suggest that the intercrater plains were emplaced during the tidal spin-down on Mercury, as evidenced by the confinement of joint-like lineaments to P5 to P3 units. Although thermal models also suggest that the P4 and P5 plains formed during early global expansion, few tensional features which are globally distributed have been identified. Rift-like features (within and exterior to craters) may have been eliminated by subsequent impacts of the ongoing bombardment and by the plains deposits themselves. As the planet cools, it contracts radially, causing the formation of scarps (high angle reverse faults or thrust faults) during the early C3 period, near the end of intercrater plains emplacement. Scarp formation continues throughout the younger plains-forming eras.

Crater statistics of selected regions and mapped areas support the above hypotheses. The lunar-like crater size-frequency distribution on Mercury has fewer 15-40 km craters, consistent with their obliteration by volcanic plains deposits. An apparent lack of basins of  $D \geq 400$  km on Mercury reduces the volume of ballistically distributed materials. The ancient circular depressions C5', if included, minimize this basin deficit, but imply that most basins (ejecta sources) precede much of the plains emplacement (especially P4 and P3 units) on Mercury.

The heavily cratered areas and intercrater plains apparently record nearly identical small crater abundances, but differ in abundances of craters larger than 40 km. An early, direct basin-forming impact and subsequent volcanism localized to that (C5') basin's interior may reduce large crater densities in circular areas of the intercrater plains. The high density of 5-15 km craters consists largely of secondary craters from C1-C3 craters and basins and from C4 basins. The preservation of C4 secondaries may also be a result of high ejection angles, higher ejection velocities, or a more consolidated surface. Crater morphology studies (e.g. Cintala et al., 1977) suggest that the intercrater plains and Mercury's smooth plains are more similar in physical properties to the consolidated lunar mare basalts than to the megaregolith of the lunar highlands.

A heavy and uniform bombardment is indicated by the combined C3 to C5 crater densities relative to C1 and C2 abundances. Regional

variations in the first quadrant's crater statistics occur when a particular plains unit dominates the area sampled. In general, the older intercrater plains were emplaced during the heavy bombardment.

Both cratering and geologic dating of the hilly and lineated region indicates it was formed in late C3 or early C2 period, concurrently with the Caloris basin, and was the result of seismic waves created by the impact and focused on the antipodal zone. By grouping the craters and plains of the first quadrant in "eras" relative to the Caloris impact (using it as a "marker horizon"), paleogeologic maps were compiled. These maps show that the ubiquitous plains distribution on the Pre-Caloris surface (Class 4, 5, and 5' units) lessens somewhat during the heavy bombardment of the Caloris Era (Class 3 units preceding the Caloris impact), and becomes increasingly localized to basin and crater interiors during the Post-Caloris Era, represented by the Class 1 and 2 units. As noted earlier, those plains interior to older craters or depressions within the older plains, and isolated from younger basins, are interpreted to be volcanic.

The paleogeologic maps and measurements of existing plains areas confirm that plains formation on the first quadrant of Mercury generally decreases with time, greatly declining after the C3 cratering period. The percentage area of craters also declines with age, although not in the matching proportions which might suggest plains formations by ejecta deposition alone. Arguments against widespread

intercrater plains-forming ejecta deposits include the limited extent of continuous and discontinuous ejecta deposits of mercurian craters (compared to lunar craters), limited destructive resurfacing potential, and the large areas of plains relative to craters and their uncorrelated areal variations between quadrants. There appears to be a lack of "source basins" for the intercrater and smooth plains. Resurfacing by ballistic deposition is apparently supplemented by or exceeded by another source of intercrater plains material, and this source is most likely volcanic.

The color and albedo of Mercury's surface places constraints on the composition and origin of the intercrater plains. The similarity in albedo of Mercury's major surface units suggests a similarity in composition or prolonged activity of a process which homogenizes albedo variations. Color variations are less than those on the Moon, and usually uncorrelated with geologic unit contacts or topography.

The exceptions to those generalities suggest compositional differences probably associated with volcanism, both ancient and more recent events. Albedo differences across scarps, or within plains which embay an older basin, and color differences which are most extreme in the youngest units support a volcanic origin for at least some plains units. A slight color difference (and possible spectral variation) between the Caloris smooth plains and the intercrater plains suggests more FeO-rich material around the Caloris basin.

Because this compositional difference is rarely present between first quadrant smooth and intercrater plains, sources of Caloris materials may be distinct from sources of most first quadrant smooth plains.

Other remote sensing data suggest that Mercury has differentiated. It has a silicate surface low in FeO, Fe metal, and Ti, and is possibly anorthositic, like the lunar highlands, although a mafic surface is also consistent with the data. Infrared, ultraviolet, polarimetric, and radar data are characteristic of lunar soils and regolith. This evidence, contrasted with Mercury's high density and postulated Fe-rich composition, suggests that the planet has differentiated. The magnetic field supports planetary differentiation at some period in history, and may suggest a currently molten iron core. Temperature variations impressed on Mercury's surface due to its unique orbit and rotation may cause thermal stresses in the crust, variations in lithospheric thicknesses, or losses of remanent magnetization in surface units.

The three major competing theories for the origin of Mercury's plains are (a) a primordial surface remaining after global melting and solidification, (b) basin ejecta and melt deposits, and (c) volcanic deposits. From the evidence presented above, it is very unlikely that the oldest intercrater plains P4 and P5 represent a primordial surface. They are more likely a complex assortment of primarily volcanic deposits formed during planetary differentiation and expansion,

interbedded with the impact ejecta of the heavy bombardment, and mixed with mass wasted debris from impact and tectonic events. The plains surface is reworked by small primary and basin-secondary impacts.

A chronological summary of Mercury's history gathered from the above data and analyses is presented in Appendix J.

#### The Moon

The Pre-Imbrian plains of the lunar nearside southern highlands form the "intercrater plains unit" analogous to those covering Mercury. The Pre-Imbrian Plains (pIp) were emplaced during the period of heavy bombardment, following the Nectaris impact and preceding the Imbrian event. Some of the pre-Imbrian units may pre-date the Nectaris impact. Emplacement does not appear to be instantaneous or uniform, nor primordial, for older terrains are partially exposed under the pIp blanket. Some doubt remains about the ages of the plains with respect to the "embedded" craters; in particular, it is difficult to determine how much material was emplaced before, during, and after the Nectaris event. Maurer et al. (1978) severely narrow the time of emplacement to 0.1 b.y. between the Nectaris and Imbrium events. Other dates for the basin impact provide an emplacement interval from 4.25 b.y. ago to 3.9 b.y., or a 350 m.y. interval (Schaeffer and Husain, 1974).

When the LPL degradation classes are used to date the lunar plains, one finds that the expanse of pIp intercrater plains is interpreted to be a P3 surface. The lunar intercrater plains are less diverse in age than plains on Mercury. The P3 to P4 Janssen Formation



(the Nectaris ejecta blanket), the P2-P3 age Imbrian plains (Ip), and P2-P1 mare surfaces to the north form the spectrum of relative ages of lunar nearside surfaces. The plains of the nearside southern highlands decrease in areal extent from pre-Imbrian to Imbrian periods, whereas production of farside plains appears to increase with younger ages. Most of the exposures on the farside (Np units) are within old craters and basin remnants, not in extensive tracts such as the pIp units. (The Lomonosov--Fleming exposure of Np units is quite large.)

Photogeologic studies of the lunar intercrater plains reveal (1) high proportions of small craters, some of which are secondaries, (2) different ages of intercrater plains exposures, (3) buried and partly embayed craters, (4) crater chains which are secondary and related to major basins, (5) structurally controlled emplacement of cratered plains materials, and (6) flow lobes near Mutus.

Crater statistical data show that densities of small craters on the pIp units are greater than densities on older terra units (Mutch and Saunders, 1972). This may indicate that the pIp form a more consolidated surface (possibly underlain by a megaregolith which includes Nectaris ejecta). As noted by Strom (1977), the style of degradation as displayed in the pIp (Manzinus area) size-frequency distribution is unlike that nearer the Imbrium basin: fewer large craters appear to be degraded to classes 4 or 5, yet a loss of smaller craters of the more degraded classes is noted to increase with

decreasing diameter. This type of degradation is similar to that of flooded basins.

The intercrater plains region displays high densities of 1-10 km craters and apparently lacks craters over 40 km when compared to the region surrounding Clavius. As suggested by photogeologic studies, the small crater excesses may be due to secondary cratering from craters formed following the plains emplacement, as determined by studies of Langrenus and Copernicus. The slight deficiency of large craters in the intercrater region may have resulted from an ancient basin impact. The plains occupy a relatively "circular" area, and are structurally confined to lower topographic regions. The nearside and farside Nectarian plains exposures may thus be similar in distribution and origin.

The intercrater plains region is located from 1.6 to 3.6 R (Altai scarp) from the center of Nectaris, 4.0 to 5.5 R from Imbrium and 5.0 to 6.6 R (Cordillera Scarp) from Orientale. The Nectaris basin, as expected, has a noticeable influence on the southern highlands in its deposits of 8 to 18 km secondary craters, some of which are embedded in the intercrater plains. Basin influences are more critical on the Moon because of the greater resurfacing and destructive capabilities of lunar ejecta, and also because there are more large basins on the Moon than Mercury. As noted above, the youngest basins are quite distant, and their influence minimal. But, in addition, the Nectaris basin, which has clearly affected a region east of

the intercrater plains, may have been formed by an oblique impact, and thus caused less damage to the area southwest of the basin--the intercrater plains area (Wilhelms, 1980).

Volcanic features are not common in the intercrater plains regions, similar to their apparent absence on Mercury. However, areas containing evidence for pre-Imbrian volcanism include the Apennine Bench Formation, INp regions near Balmer on the eastern limb, older plains of Mare Australe (Whitford-Stark, 1979), and the highland domes of the western mare (Head, 1976a; Spudis, 1979). Such volcanism appears to occur in areas of thin lunar crust, and continues and overlaps with emplacement of the mare basalts. Estimates of crustal depth of 60 to 80 km do not exclude the intrusion of KREEP basalts into the intercrater highlands region. Bouguer anomalies around unity imply that some compensation other than infilling by breccias or by mantle intrusions may have occurred here (Dvorak and Phillips, 1978).

Tectonic activity after the Imbrium impact is slight and includes formation of graben and ridges radial and concentric to the major basins (Hartmann, 1963, 1964). Lineaments, fault scarps, and other linear features often trend along the lunar grid pattern (Strom, 1964); no global system of compressive thrust faults is found on the lunar surface.

Composition of the pre-Imbrian plains and the southern highlands is predominantly anorthositic. Slightly younger plains (INp rather than Np) near the eastern limb-crater Balmer have high thorium

contents, indicating a subsurface KREEP or MKFM (Medium-K, Fra Mauro) basalt. Most Imbrian plains' (Ip) compositions match those of the surrounding highlands, supporting interpretations of locally derived impact debris. No striking variations in color (UV/IR), albedo, infrared, cm, or radio wavelength data occur in the southern highlands intercrater region. Recent attempts to study compositional variations in the highlands with spectrophotometry are as yet inconclusive. The pre-Imbrian plains material is a common rock unit in the highland area, although it may not have been sampled in the Apollo missions. Pieters (1979) indicates that, although the pIp unit is not a mare basalt, its plagioclase and orthopyroxene composition does not rule out a volcanic, high iron basalt. Seeger's (1979) results suggest that the pre-Imbrian plains, the Janssen unit, and the Imbrium plains are all chemically distinct.

In summary, the lunar intercrater plains display a range in ages if one includes among the plains surfaces the pre-Imbrian plains, the Imbrian light plains, and the maria. No primordial surface is indicated. Although a complete resolution of this problem has yet to be made, the origin of the lunar intercrater plains appears to be related to KREEP volcanism in the shallow crustal areas of the highlands. Geologic evidence--embayment and transection relationships, tentatively identified volcanic flow lobes, the areal distributions of the plains--and the crater statistical data support a volcanic origin

for the intercrater plains. Basin influences are decidedly more severe than on Mercury; the Nectaris impact may have deposited loosely consolidated material which is now overlain by the pIp unit. Nectarian secondaries occur in this region. Local impacts subsequent to pIp emplacement have covered the regions with highland-like regolith. Continuing remote sensing studies and the resolution of the mercurian intercrater units' origin should reduce the uncertainties noted here.

A synopsis of the lunar chronology regarding the emplacement of the intercrater plains is given in Appendix K.

The products of this research which clarify the nature and origin of the intercrater plains are: (1) Geologic terrain map of Mercury's first quadrant, including the hilly and lineated terrain (Chapter 2), (2) Paleogeologic maps of Pre-Caloris, Caloris, and Post-Caloris surfaces (Chapter 4), (3) Plains coverage within each era for Mercury (Chapter 4), (4) Crater diameter-density distributions and crater coverage for selected local areas and regions used in mapping of Mercury and the Moon (Chapter 3), (5) Crater statistics for the secondary crater fields of Copernicus and Langrenus on the Moon (Chapter 3), (6) Determination of the onset and duration of scarp formation relative to ages of craters and plains on Mercury (Chapters 2 and 7), and (7) Incorporation of remote sensing data into the geologic and cratering syntheses (Chapter 5).

## Implications for Terrestrial Planet Evolution

Many of the implications of this research involve better understanding of apparently simple mechanisms which are in reality quite complex. The link between crater and plains production is one such relation which has been discussed throughout the text. Thermo-tectonic models are another concept of deceptive simplicity introduced in the preceding chapter. The constraints applied often dictate the outcome of the model. Because intercrater plains formation is an intermediate process in thermal history, the heat sources and initial temperatures (which govern the initial evolution) and the size of the planet (which governs later evolution) may not directly apply. Furthermore, one must determine the extent to which bombardment controls a planet's thermal history, as opposed to the extent to which thermal evolution and plains production merely produce surfaces which record various stages of impact bombardment. Given these uncertainties, as well as those within the remote sensing interpretations, the results of this work are applied to the problem of the source depth of magmas forming the intercrater and smooth plains and the problem of the relative and absolute ages of the plains on Mercury and the Moon.

### Scarp Formation and Magma Source Depth

The onset of scarp formation roughly divides the expansion--extrusion phase of Mercury's thermal history from the contraction-cooling phase. From evidence given earlier, smooth plains

of a volcanic nature are formed during the scarp formation period. This is mechanically possible if surface compressional forces are exceeded by magma pressures from a partially molten zone beneath the compressional layer. Solomon (1977b) predicts such tensional forces will exist for about two billion years after core separation at depths of 40 to 120 km. Because the isotherm for partial melt zones retreats deeper into the mantle as cooling continues, plains formed at different times by this mechanism should have different source region depths. The implication is that the younger smooth plains were formed at greater depths and in different source regions.

Surface composition may be governed by conditions in the upper fifth of Mercury's 600 km silicate mantle. Walker et al. (1979) maintain that the most voluminous basalts on a planet's surface must have compositions governed by dry, low pressure "crystal/liquid equilibria" relations, i.e., by processes occurring at less than 10 kb (to 80 km depth on Mercury, 250 km depth on the Moon). The most voluminous mercurian plains are the intercrater plains, formed when the planet expanded due to core segregation. Morrison and Warner (1978) link terra formation to planet size and the resultant stability depth of feldspar at pressures less than 12 kb. Smaller planets have deeper regions of feldspar stability, and thus usually have thicker, less mobile, less active crusts. However, because core separation is a global process, involving formation of 600 km of silicate mantle, low

pressure relations for terra and intercrater plains may not be the only process governing their composition.

Stolper (1980) outlines the source depth compositions for 0-10 kb, 10-25 kb, and pressures greater than 25 kb for the terrestrial planets (see Table 11). These pressures (0, 10, and 25 kb) correspond to the surface, 80, and 220 km depths on Mercury; or the surface, 250, and 600 km depths on the Moon. The source region of the smooth plains must be at depths greater than or equal to 40 to 120 km, or at pressures of 5-14 kb (Meissner and Lange, 1977; Solomon, 1977b). Thus for the youngest plains, source region chemistry may change from spinel-plagioclase-wehrlite (ol+di+sp+pl) to spinel lherzolite (ol+di+sp+en), a change of plagioclase (pl), to enstatite (en) within a melt of olivine (ol), spinel (sp), and diopside (di). The composition of extruded materials is not certain; neither of these systems has been adequately modeled (with the exception of work by Seitz and Kushiro, 1974). The expected change in spectral signatures (plagioclase to enstatite) should also be investigated further.

The correlation is intriguing for two reasons: the lack of observed color variations and the implied similarity of the 10-25 kb source regions of the terrestrial planets.

The first quadrant shows few color variations which correlate with geologic units (Hapke, 1977; Hapke et al., 1980a,b; Dzurisin, 1977b), but the second quadrant shows a rough correlation of color



Table 11: Mineral Assemblages of Planet Groups\*

Pressure Range	Mineral Assemblages of:	
	Mercury and Mars	Earth, Moon, Venus, and EPB#
0 - 10 kb	Spinel-plagioclase- wehrlite = ol + sp + di + pl#	Plagioclase lherzolite = ol + di + pl + en
10 - 25 kb	Spinel lherzolite = ol + en + di + sp	Spinel lherzolite = ol + en + di + sp
25 kb	Spinel-garnet- wehrlite = ol + di + ga + sp	Garnet-lherzolite = ol + en + di + ga

\* Adapted from Stolper (1980; Fig. 1).

# Symbols: ol = olivine; sp = spinel; di = diopside; pl = plagioclase;  
en = enstatite; ga = garnet; EPB = Eucrite Parent Body.

with the smooth plains of the Caloris basin and the surrounding planitia compared to the intercrater plains. This may imply that smooth plains production of the incoming quadrant tapped shallower, less chemically distinct, source levels than plains of the Caloris region. Plains production may have been "shut off" by cooling and compressional stresses at an earlier date on the intercrater plains-dominated quadrant. The first quadrant is severely lacking in large basins (especially young ones) which could tap deeper levels. (This compositional difference could also reflect the excavated materials from the deeply penetrating impact.)

A second note is that deeper source regions of Mercury are accessible by studying products from deep (10-25 kb) source regions on Mars, the Moon, or Earth. Observation of young flows on the Tharsis volcanoes, where source depth can be estimated from the volcano height, may provide analogs to smooth plains on Mercury, allowing for changes in FeO and volatiles in the martian magmas. Stolper (1980) finds that Mars and Mercury have the same source region chemistries (ignoring volatiles and FeO) at all three depth zones. The Moon, Earth, Venus, and eucrite parent bodies share a different set of compositions. But both groups have spinel lherzolite at 10-25 kb depth. Thus tools for studying and testing Mercury's composition are in our back yard, or on the Moon or Mars.

Similar correlations in composition and source region depth are still being applied to the Moon, with the result that the problem was found to be much more complex than simple increase of source depth with cooling (Lucchitta and Boyce, 1979; Solomon and Toksöz, 1973). But on Mercury, scarp formation may be a marker of changing source depths for volcanic materials. More work is necessary in geochemical modeling, spectrophotometric recognition of these materials, thermal histories, and dating the intercrater and smooth plains units. These analyses, if carried out, would also test and further constrain Solomon's (1977b, 1978a) models and hypotheses.

#### Relative and Absolute Ages of the Intercrater Plains

Several references to the relative and absolute ages of the mercurian and lunar surfaces have been made throughout the text. Geologic mapping (Chapter 2) shows that the age of formation of intercrater plains surfaces differs: mercurian intercrater plains are emplaced from Class 5 through mid Class 3 periods; lunar intercrater (pre-Imbrian plains) are emplaced during the Class 3 period. Thus the younger mercurian intercrater plains have a degradation age similar to the age of the lunar intercrater plains. Lunar C3 craters are 3.9 to 4.0 b.y. old, using the LPL crater age classification and Wood's (1979) chronology. An older lunar P3 surface may be implied if Nectaris' age is 4.25 ae (Schaeffer and Husain, 1974) rather than ~398 ae (Maurer et al., 1978). The age of the mercurian P3 surface

would be the same if the bombarding fluxes and attendant degradation were similar.

Various studies (Chapter 3) do suggest that the recorded populations on highlands of the Moon, Mercury, and Mars are similar, and in production, rather than saturation (Strom, 1977; Woronow, 1977c; and Woronow et al., 1980). Lesser densities of small craters on Mercury and Mars relative to the lunar surface population may have resulted from the emplacement of intercrater plains, or regional erosion on Mars (Gurnis, 1980). Woronow et al. (1980) argue that the highland surfaces record the same bombarding population which ended about 4.0 b.y. ago, throughout the inner solar system.

Solomon (1977b) uses this constraint in his thermal models of Mercury (Chapter 6); high initial temperatures are required for the early global melting and differentiation which leads to intercrater plains production during the heavy bombardment. Hostetler and Drake (1980) argue that if the Moon formed a global magma ocean, then the other terrestrial planets underwent early global melting too. Accretional heating--a process tied to bombardment--is a major cause of the solar system-wide planetary melting. The similar highland production populations of Mercury, the Moon, and Mars, and the similar formation ages of their solid surfaces, suggest to Gurnis (1980) and Woronow et al. (1980) that the flux responsible for the heavy bombardment was the same within the inner solar system, therefore enabling us to date and compare the absolute ages of the terrestrial planets' surfaces.

However, the crater statistics of Mercury and the Moon gathered in this study are more complex and argue for more caution in stating that the bombarding populations are the same. The heavy bombardment on Mercury does not seem to be as temporally peaked as on the Moon (cf. Chapman, 1976). Figures in Chapter 3 illustrate this complexity. The total population recorded in the restricted map area is very similar to the basic crater coverage on the southern lunar highlands, so the conclusions of Strom (1977) and others are accepted cautiously.

Strom (1977) compared post-Caloris crater statistics with post-Oriente crater statistics and found them essentially the same, indicating that some of the youngest plains of Mercury (P1 and P2) may record the same bombardment as Oriente, which formed 3.85 b.y. ago. Post-mare densities are apparently not recorded in Mercury's youngest plains, implying that the post-mare population did not impact Mercury, or that the youngest mercurian surfaces are older than the lunar mare, and record a cumulative bombardment from 3.85 b.y. ago. The latter interpretation is consistent with Solomon's (1977b) model of Mercury and not consistent with the extended activity predicted by Toksöz et al. (1978), nor with substantial extended activity from Solomon's subsurface tension mechanism.

The mercurian smooth plains may be as old as the oldest lunar mare (3.9 b.y.) if the results of Watkins (1980) on crater density in

the Caloris regions and the results of De Hon et al. (1980) on crater densities of smooth plains in the Kuiper Quadrangle are representative of smooth plains' crater densities. This point is questioned because of the small areas and limited diameter ranges of the sampled craters. Statistics in this study which show that C1 crater densities on Mercury over a diameter range of 7 to 150 km are the same slope (horizontal) and magnitude (0.3% coverage) as the C1 population on the Moon may not be sufficient to claim a recent bombardment similar to the post-mare phase, because of the differential degradation (and age) of small and large craters (Woronow, 1979a).

The above arguments suggest that the mercurian P5 and P4 plains were emplaced (very approximately) 4.2 and 4.1 b.y. ago, the P3 plains about 4.0 b.y. ago, and the P2-P1 plains, 3.9 to 3.8 b.y. ago. Younger surfaces (such as the interiors of fresh craters or modified craters) probably exist, but do not comprise a great observed expanse.

Whitaker and Strom (1976) propose that two populations of objects bombarded the Moon, one which delivered the heavy bombardment, and which may have been a remnant accretional population; and a second group of objects characteristic of the quiescent cratering phase subsequent to mare basin filling. This later population may comprise fragments of planetesimals similar to the asteroid population; although this group of bodies may not have cratered Mercury, it does appear to have cratered the northern plains of Mars, as well as the lunar mare. Two populations, rather than one evolving population, are therefore suggested as sources for inner solar system bombardment.

The aim of comparative studies of basins and crater populations is to determine their flux and perhaps their source(s). We have no absolute ages for any geologic unit on Mercury, except by analogy with the Moon as stated in the above arguments. Reasonable hypotheses can be derived. Frey and Lowry (1979) examine basin populations on Mercury and the Moon, concluding, with several assumptions, that the sources of Mercury's large projectile population are Mars-crossing objects (Shoemaker, Helin, and Gillette, 1976). Sources of impacting bodies, still at the center of much observation and dynamical research (e.g. Shoemaker et al., 1979; Wetherill, 1975, 1978; Hartmann, 1977; Kaula, 1979b; Schultz and Srnka, 1980) include: early planetesimals, accretional remnants, comets, various groups of asteroids (the Apollos, Amors, main belt objects), outer solar system objects, local heliocentric populations, and orbiting debris clouds. All of these objects may contribute to the planet's accretion and later bombardment history.

The recent data from the Galilean and Saturnian satellites indicates increased complexity of this task of source determination. The Galilean satellites Callisto and Ganymede do not exhibit the same production population as that of the terrestrial planets. Strom et al. (1980) postulate that these satellites were bombarded by objects from a different source. A determination of such sources would enable us to evaluate the extent of mixing in accretion (in the inner and outer solar system), and the size and space distribution of early solar system objects. Strom (1979) gives a summary of some recent studies.

Summary of Surface Histories as Shaped or  
Recorded by the Intercrater Plains

Little mention has been made of the Earth, Venus, Mars, the martian moons, asteroids, or the Galilean satellites--the other rocky bodies (with and without volatiles) in our solar system. All of the inner solar system bodies bear evidence of cratering. Earth has the poorest collection of craters because of its mobile, dynamic surface and persistent erosion. Tectonism and volcanism also appear to be major geologic processes on most of these bodies. Intercrater plains surfaces--produced by thermo-tectonic evolution usually coincident with heavy bombardment--occur in various forms and origins on the terrestrial planets. These surfaces present clues for the thermal evolution of the body; they record and disguise crater populations by the resurfacing inherent in their formation; and their compositions may provide clues to low pressure source regions.

Deimos may be the ballistic deposition "endmember" for intercrater plains. Deimos' intercrater plains are certainly not volcanic, but an extensive regolith, the depth of which may be a function of size, density, and gravity of the moonlet (Thomas, 1978; Cintala et al., 1978; Housen and Davis, 1978; Housen et al., 1979).

Many of Mars' surface features are the result of protracted expansion over most of its history. This expansion has been conducive to extensive volcanism: during the heavy bombardment, highland volcanism produced the intercrater plains surfaces in the highlands and



bordering the plains (Malin, 1977; Greeley and Spudis, 1978). Much later volcanism produced extensive basalt flows and volcanic constructs which characterize the northern lowlands (see the color-ratio data of Soderblom et al., 1978). Huge rift valleys like Vallis Marineris are also products of such expansion. It is not clear why rifting is so localized; it may be a function of age and mass distributions or convection within the planet. High volatile contents in the crust and aeolian erosion further affect the nature and origin of these intercrater surfaces.

The Moon exhibits minor expansion and contraction as grabens and rilles respectively; total thermo-tectonic activity produces less than 1 km change in the lunar radius. Intercrater plains form well after crustal formation, and may be related to KREEP volcanism (4.3 to 3.9 b.y.) and to mare volcanism (3.9 to 3.0 b.y.?). The plains deposits are less extensive, more sporadic in emplacement, and contain higher amounts of ballistically emplaced materials than on Mercury. Their composition--if unique (as suggested by Pieters, 1979, and Seeger, 1979)--is masked by ejecta from the local anorthositic highlands. These intercrater plains record most of the heavy bombardment.

Plate tectonics distinguishes geologic activity on the Earth from all the terrestrial planets. Craters are preserved in the cratonic shields, Earth's ancient granitic crust. Volcanism and tectonics are much more diverse and complex processes, and not simply coupled

with heating and cooling episodes. Continental flood basalts may be an analog to intercrater plains on Earth (without the craters). As Strom (1979) notes, basaltic volcanism on Earth has the unique function of producing the oceanic basins.

Venus has ancient cratered surfaces, rolling plains uplands, volcanic constructs, basins, lowlands, rift systems, but thus far, no evidence of plate tectonics (Masursky et al., 1977, 1980; Malin and Saunders, 1977; Pettengill, Nozette, and Ford, 1980). The rolling plains plateau of Venus covers 65% of its surface and has many intercrater plains features: craters, rolling topography, evidence of volcanism. Ejecta deposition may be a major source of plains materials; ejecta distribution is more widespread because particles are lofted into the dense atmosphere and transported by venusian winds (Cutts, Thompson, and Lewis, 1980; Warner, 1980; Greeley et al., 1980). An equatorial blanket of such deposits may cover the lowland regions. Evidence for sorting in rock sizes appeared in the Venera 9 and 10 photographs. Tectonism on Venus is implied by rift valleys, lineated ridges, and mountain chains. Volcanism has occurred in Beta and Aphrodite Terra and in the lowland regions. Application of thermo-tectonic models should be made with caution since it is uncertain that Venus is a one-plate planet. The craters preserved on its surface suggest no plate tectonic-like activity, but the planet's size places it in the transition zone between Mars and Earth.

Mercury may be the other endmember in intercrater plains origin, i.e. primarily volcanic. These plains form as a result of core separation, and their early formation allows them to record much of the heavy bombardment and be "tapped" by that bombardment. Mercury is unique in that it exhibits compressional stresses over a major portion of its history. Plains formation continues into the period of scarp formation, indicating availability of sources, subsurface tensional regimes, and pressures exceeding the surface compression. Source regions are predicted to become deeper and possibly more fractionated with time; these chemical changes should be exhibited in the youngest plains. Compositional studies can further constrain these models.

#### The Role of the Intercrater Plains

The "role" of the intercrater plains is that they comprise an intermediate product of the thermo-tectonic-ballistic evolution which is shared by most of the terrestrial bodies. Thermo-tectonic models applicable to one-plate planets predict such a surface may form during expansion and heating of the body. Because high initial temperatures characteristic of most terrestrial planets lead to early melting (partial or total), the intercrater plains are usually very old units, formed over a span of time during the heavy bombardment. Mercury's intercrater plains surface may be among the oldest in the solar system. Resurfacing processes such as intercrater plains formation, whether volcanic or ballistic, destroy information about smaller

craters, and begin the recording process at different times. Basin impacts destroy information about larger and older craters. Heavy bombardment or a high temperature phase, or some process synchronous throughout the solar system, may produce the remarkable age similarities seen in the highlands and intercrater plains of Mercury, the Moon, and Mars. The high densities of small craters, which were originally used to define such surfaces, are a result of the surfaces' age and the cumulative secondary craters of the large crater population, and more importantly, of the more consolidated nature of this primarily volcanic surface.

#### Future Work

The intent of this research has been to determine the origin of the intercrater plains of Mercury and the Moon. With respect to that task, much more research could be done. On Mercury in particular, one needs systematic crater statistics for the plains units used in mapping, a thorough analysis of the color and albedo "problems," mapping of the remaining observed surface in a manner similar to that used here, and refinement of thermal models which incorporate the results of this research. A "molten core" still remains a problem. Lunar history is still being unraveled, and the southern highlands have only recently been the focus of concentrated research.

Many advances are being made. Geologic maps of Mercury's quadrangles will soon be available. A project is underway to achieve

higher resolution spectrophotometry of Mercury's surface. Higher resolution radar data exist which will reveal Mercury's third and fourth quadrants. Spectrophotometry of the southern lunar highlands is proceeding.

In the course of this research a whole host of other problems and unknowns in Mercury's history have been uncovered. One unknown involves the formation of transition size craters and the source of the inner deposits. Another involves the distribution of basins and craters of different morphology (e.g., terraced craters, or double to triple-ringed basins). A few of the other perplexing features on Mercury are the rim-troughs of old basins, sinuous valleys (near Hawthorne, Petrarch, Simeiz Vallis, Bramante, and others), a row of overlapping 80 km, spatulate depressions extending several hundreds of kilometers, and breached "lava lakes." The full extent of ballistic impact ejecta distribution has yet to be adequately modeled and adjusted for conditions on Mercury. Ejection mechanisms themselves are unclear regarding the sequence of formation of secondary craters versus deposition of material, especially within layered substrates. Cometary impacts on Mercury and the Moon may spread ejecta to greater distances, but excavate to shallower depths.

There is definitely much more to be studied: Mercury is far from being a dull body, and deserves much more attention. In particular, the latest data on the Galilean and Saturnian satellites

present to researchers bodies of mercurian and lunar size but with far different masses, compositions, and geologic and cratering histories. The intercrater plains study conducted here may help strengthen this newly expanded field of comparative planetology.

## APPENDIX A

### DESCRIPTION OF UNITS

#### TO ACCOMPANY THE GEOLOGIC TERRAIN MAP OF MERCURY'S FIRST QUADRANT

- P1: Materials of very smooth plains. Few to no superposed craters at moderate resolution. Albedo may be high (0.22 - 0.44, Dzurisin, 1977b) or low (0.13). Usually found as floor material in C1 craters, less often in C2 and C3 craters.  
Interpreted as impact melt in C1 craters; as volcanic material within older craters. May include mass wasted materials from steeper slopes and later volcanic alterations.  
Type Area: Interior plains of Hitomaro ( $-16^{\circ}$ ,  $16^{\circ}$ W).
- C1: Materials of very fresh and/or rayed craters. Crisp rims and interior forms (central peaks, peak rings, terraces), and very few to no superposed craters. Ejecta blankets distinct.  
Interpreted as young impact craters surrounded by ballistically emplaced deposits. Satellitic craters interpreted as secondary crater materials.  
Type Area: Hitomaro ( $-16^{\circ}$ ,  $16^{\circ}$ W).
- P2: Materials of smooth, sparsely cratered plains filling irregular depressions or crater interiors. Often rough where they appear to overlie hummocky and ridged topography. Albedos 0.13 to 0.23.

Interpreted as impact melt in C2 craters, as volcanic materials in exterior locations and within older craters. Similar to P1 materials which have undergone more degradation by cratering, ejecta deposition, and mass wasting. Includes ballistic ejecta component from large craters.

Type Area: Plains east of Andal ( $-47^{\circ}$ ,  $33^{\circ}$ W) and east of Handel ( $2^{\circ}$ ,  $28^{\circ}$ W); also within Andal.

C2: Materials of moderately fresh craters. Distinct but modified rims, interior features, and secondary crater fields. Terracing common. No rays. Basin size examples have discontinuous rims.

Interpreted as in C1, but degraded by subsequent impacts, tectonic processes (scarp formation), and plains formation (P2).

Type Area: Mahler ( $-19^{\circ}$ ,  $19^{\circ}$ W).

P3: Materials of moderately smooth to hummocky plains. Low to moderate densities of 1-15 km craters often forming chains and clusters. Occur in depressed regions, interior and exterior to craters. Often cut by scarps and ridges. Albedos not distinctive, averaging 0.17 - 0.21 (Dzurisin, 1977b).

Interpreted as volcanic extrusions in large expanses exterior to craters, and in coeval or older craters. Includes impact melt in C3 craters and accumulations of impact ejecta of nearby basins and craters.

Type Area: Plains east of Schubert ( $-43^{\circ}$ ,  $48^{\circ}$ W).



- C3: Materials of moderately subdued craters. Rounded rims, indistinct interior forms and discontinuous deposits, except around basin size objects.
- Interpreted as C1 type craters but more degraded by subsequent craters, plains formation, scarp formation, and mass wasting.
- Type Area: Crater pair west of Ibsen, ( $-25^{\circ}$ ,  $44^{\circ}$  W) and ( $-26^{\circ}$ ,  $47.5^{\circ}$  W); Brunelleschi ( $-8.5^{\circ}$ ,  $22.5^{\circ}$  W).
- P4: Materials of rough to hilly intercrater plains. High and uniform densities of small ( $\leq 15$  km) superposed craters, many elongated and aligned in chains. Form raised, plateau-like areas, flat to gently rolling. Albedos average 0.17.
- Interpreted to be volcanic flows from fissures subsequently buried by flows. Very rarely impact melt in C4 craters or basins. Interbedded with ballistic ejecta deposits.
- Type Area: West of Vostok Rupes ( $-38^{\circ}$ ,  $23^{\circ}$  W), east of Equiano.
- C4: Materials of subdued craters. Rounded and crater-pitted rims of usually low relief. Satellitic crater fields and radial chains visible around a few basin size ( $D > 150$  km) craters only. Greater numbers of superposed craters (10 - 30 km) than on C3. Outer rim often extended and shelf-like, or cut by trough parallel to rim crest.

Interpreted as modified impact craters, but more degraded than above. Isostatic equilibration may cause uplift of floor and subsidence of loaded rim. Impact scouring and tectonic processes may create rim trough. Landslides in pre-existing topography may extend rim materials.

Type Area: Kenkō (-21°, 16.5°W) and Ma Chih-Yuan (-59°, 72°W).

P5: Materials of very rough, knobby, and pitted intercrater plains. Form gently rolling to level surfaces between and around larger craters, with a high density of small 1 - 15 km craters. Smaller superposed craters elongated, in chains and clusters, as on P4 material. Plains bury and/or embay vague circular depressions. Albedos average 0.18, with rays 0.22.

Interpreted as volcanic flows, severely disrupted by repeated impacts of primary and secondary projectiles, and by mass wasting and tectonic processes. Sources (vents) of volcanic material buried by plains or destroyed by subsequent cratering. Ballistic deposits interbedded with, and must overlie, much of these plains. Not primordial.

Type Area: East of Homer and Handel (2°, 31°W); east of Rodin (23°, 13°W); and north of Po Ya (-44°, 20°W).

C5: Materials of highly subdued to indistinct craters. Dissected, pitted, and/or collapsed rims of usually low relief. No interior facies, except rarely on basin size craters. No remaining satellitic crater fields. Exterior rim contacts indistinct and queried when adjacent to P5 materials. Usually filled with younger plains material.

Interpreted as ancient, degraded impact craters. Degradation processes noted above.

Type Area: Crater north of Handel (6°5 , 31°5 W).

C5': Vague Circular Depressions (also Ancient Circular Depressions).

Materials of vague circular depressions, nearly unrecognizable landforms. Sometimes bounded by inward facing scarps. Interior often has fewer large craters than the exterior, and is filled with P5 or younger plains materials. Large depressions sometimes double-ringed, with deeper central depression.

Interpreted as ancient impact basins and craters which were formed before and during major intercrater plains formation and during the continuing early heavy bombardment by large objects. Scarp-like rims may form later as tectonic adjustment of crust. C5' features buried by intercrater plains.

Type Area: Two crateriforms south of Murasaki (-21° , 47°W), and depression east of Handel at (2°5 , 27°5 W).

Buried Craters: Materials of raised circular forms of undetermined age within plains or crater materials.

Interpreted as craters buried by crater ejecta and plains materials.

Type Area: Within P3 material east of Antoniadi Dorsum (29°, 25°W).

Dome Material: Material forming domes or small plateaus, often subdued and cratered, occurring on plains or on crater rims. Some domes have rimless summit depressions; another group of 3 to 4 domical features is aligned north-south.

Interpreted to be volcanic domes at centers of volcanic activity, overlying central vents or fissures. Remnants of plains formation, with more viscous material.

Type Area: Dome on crater rim and unit contact northwest of Lu Hsun (4°, 25°W).

Rimless Depressions: Materials forming rimless depressions or pits.

Circular to irregular in plan, steep inner slope, hummocky to flat floor, located along fault, scarp trace, contact, or summit of dome. Commonly within crater floor.

Interpreted as collapse depressions due to movement along fault, shallow volcanic calderas, or compaction of porous breccia lens deposits beneath crater cut by scarp.

Type Area: On floor of C2 crater (27°, 19.5°W).

Hilly and Lineated Area: Materials of the above units divided by

troughs of 10 km width. Form linear valleys and massive angular hills or knobs, of 5 - 10 km horizontal dimensions, and of 0.1 to 1.8 km height (Trask and Guest, 1975, p. 2471). Bases of hills and valleys locally filled with smooth units. Most craters and plains severely degraded; smooth plains or hummocky plains can be found in craters with dissected rims. Normal craters superposing the area are of Classes 2 and 1. Youngest crater partially displaying the area's characteristics is late C3 in age.

Interpreted as craters and plains disrupted by seismic event associated with Caloris impact, antipodal to this area (Schultz and Gault, 1975a,b, 1976). Disruptive event was apparently sudden, and occurred in late C3 period or early C2 period.

Hummocky plains formed initially as smooth materials which were then disrupted; smooth plains were deposited after the event.

Tensional stresses formed linear valleys along the global lineament directions. Smooth facies in valleys are mass wasted materials from steep slopes of hills.

Type Area: Area around Petrarch,  $-24^{\circ}$  to  $-40^{\circ}$  latitude,  $10^{\circ}$ W to  $37^{\circ}$ W longitude.

## APPENDIX B

### AREAL MEASUREMENT OF MERCURY'S FIRST QUADRANT

This appendix contains discussions of various linear and areal measurements of Mercury's first quadrant which were used in geological map preparation, map analysis, and statistical surveys of crater densities. Accuracy of each method rests on the determination of the scale of the photograph, i.e., the conversion factor between distances on the planet (in km) and distances on the photograph (in cm). Measurement errors arise due to uncertainty in Mercury's radius, poor resolution, poor coverage, high sun angle illumination in the limb regions, planetary curvature, limited precision in measuring instruments, and inaccuracies in the printed map scales. Estimates are given for these errors.

#### Limiting Diameter and Scale

Detail within the geological terrain map is limited to features larger than about 40 km, or 5 mm on the base photomosaic. Plains-filled, linear troughs of widths less than 40 km but lengths greater than 40 km were included. As a consequence of this reduction in detail, crater outlines are smoothed out, circular, and cartoon-like, rather than lobate or rayed. Detail within the convoluted unit boundaries of the hilly and lineated area remains slightly greater

than that of the rest of the map. Failure to include features of 40 km or greater because of scale factor errors across the photograph of the planet's disk is not expected to be significant.

The scale across the photomosaic, roughly 1 to 7,700,000, is preserved in this perspective projection (similar to orthographic) for distances measured parallel to the limb (or its tangent). The scale was first determined by measurements of features near the center of the disk, approximately near the center of the hilly and lineated area, where foreshortening is not a problem. The pixel and line sizes (given in SEDR volumes in kilometers) were converted to km/pixel and then km/mm by determining the average pixel length. (The 1 cm eye-piece scale and 30 cm ruler described below were used to measure the length of 100 pixel elements marked along the edge of the Mariner 10 image.) This method of scale determination is informally called the "pixel-photoscale method."

Other scale determinations were used to verify that derived from pixel size. For instance, published crater diameters were ratioed to their diameters in the photomosaic measured parallel to the limb; a similar scale was obtained. Another verification applied the network of control points (Davies and Batson, 1975). When these points formed lines parallel to the limb, the calculated distance and resultant picture scale were nearly equal to those derived in the pixel photoscale method at the center of the disk. In a few instances, irregularities in the photomosaic cause crater diameters to

be too long or too short. (Near the east limb at  $0^{\circ}$  N,  $60^{\circ}$ W, the mosaic is not joined correctly; a large 60 km crater there appears twice, offset by a small amount laterally.)

There is a slight ambiguity in rim to rim diameter due to curvature of the surface (chord length versus arc length over the sphere), but the correction is minimal for craters less than 700 km. Although errors in linear dimensions due to scale and curvature are not great, some uncertainties result from the loss of resolution toward the limb, principally in recognition of craters and plains and determinations of their boundaries for measurement. Appendix C contains a short discussion of scale factors used in measurements of the selected regions.

#### Map Boundaries and Area

In order to determine the extent of the area mapped (Fig. 10, text), the boundaries of the map region were transferred onto the USGS Shaded Relief Maps. The terminator position marks that boundary where features of 40 km or greater could no longer be distinguished. This boundary extends roughly along the  $10^{\circ}$  (West) meridian in the northern half of the mosaic and along the  $12^{\circ}$  to  $17^{\circ}$  meridian in the southern half. The enclosed map area was extended to the South Pole, following the  $140^{\circ}$  meridian to latitude  $-72^{\circ}$  and then in staggered latitude-longitude blocks to the limb zone of the planet. Areas were included if coverage and resolution were adequate. The map extent is slightly greater than that used by Trask and Guest (1975) and others (e.g. Murray et al., 1974b; Wood et al., 1977), who set conservative limits



on the region of discriminability. The southern limb area limits reflect the use of second encounter, south polar photography (Strom et al., 1975a). The northern limb limit was extended only slightly more than that of Trask and Guest; high sun angles, poorer resolution and coverage argued for such caution. The limit of coverage to the north was about the  $45^{\circ}$  latitude.

#### Map Areas

Using the shaded relief maps, areas were marked off in swaths of latitude and longitude zones and computed from formulas for the area on a sphere of radius 2439 km. The areal extent of the general geologic map is  $1.0284 \cdot 10^7 \text{ km}^2$ , about one seventh of the planet's surface. A  $\pm 1$  km uncertainty in Mercury's radius translates into a  $\pm 8 \cdot 10^3 \text{ km}^2$  uncertainty in the general map area. The more conservative map extends from  $70^{\circ}$  S to  $30^{\circ}$  N, slightly inward from the terminator on the east and inward to the  $60^{\circ}$  or  $50^{\circ}$  meridians on the west, enclosing  $4.985 \cdot 10^6 \pm 4 \cdot 10^3 \text{ km}^2$ .

Hilly and Lineated Area. The area of the hilly and lineated zone was computed using latitude and longitude of bounding points (in Davies et al., 1978, Atlas) for the surface area on a sphere. The area enclosed was irregular, but was approximated by reducing it to a grid of square degrees (or fraction thereof) where appropriate. The eastern (terminator) boundary was adjusted to the general map area and the restricted map area. The resulting areas are, respectively,  $5.744 \cdot 10^5 \pm 5 \cdot 10^2 \text{ km}^2$  and  $4.776 \cdot 10^5 \pm 4 \cdot 10^2 \text{ km}^2$ .

Selected Regions. Areas marked "Heavily Cratered Areas" and "Intercrater Plains" were used for the small-crater statistical studies. These regions were measured initially by the pixel-photoscale method and later by the latitude-longitude grid method. Errors in areal measurements using the latter method stem from uncertainty in Mercury's radius, and the approximation of irregular areas by a square degree grid. Further error may occur in averaging scale factors over 5 or 10 degree latitude intervals. Errors in the pixel photoscale factors are discussed in Appendix C.

Areas of the Plains Surfaces. The areas covered by the various plains units were measured by planimeter after transferring the geologic map from the 16" by 24" photomosaic onto the six quadrangle maps of the incoming side. Plains boundaries were reproduced as on the 1:7,700,000 scale map but with slightly more definition and occasional inclusion of features smaller than the 40 km cutoff size. Unit boundaries and designations were further reviewed and corrected if necessary. Where the shaded relief maps overlap in latitude, the plains and crater units were duplicated as accurately as possible, given the different map projections in each quadrangle. The area of each plains unit, too complex to be marked off on a latitude-longitude grid, was measured with a planimeter. Because the scale changed across the map with latitude, measurements were made in 5 or 10 degree swaths between the mapped latitudes, up to the longitudinal boundary of the restricted map and then to the general map boundary.

Plains exterior and interior to the craters were measured and recorded separately. Many of the ancient depressions which are covered with plains material were considered part of the "exterior" plains. If the rim of a breached crater was nearly closed, the terrain was considered "interior;" if the crater rim was less than half complete, the plains were considered exterior to the crater. Many plains fill craters much older than themselves; this value can be estimated (or modelled) but was not recorded in the planimeter measurements (described below). Although measurements were not made of the exposed cratered area, that information also can be derived by the same procedures. A crude estimate can be made of the total area occupied by craters merely by subtracting the exterior plains area from the total map area, and by modelling the crater area using the collected crater statistics. Results of the distribution of plains and crater coverage are discussed in Chapter 4 of the text.

In some cases differences were noticed in the latitude and longitude of control points included within the overlapped strip of the shaded relief maps (Davies and Batson, 1975). These gaps were determined and the area included within them was added to the appropriate quadrangle.

Planimeter Measurements. The planimeter measures the area encircled by the movements of a small wheel on a flat, level surface; the area in arbitrary units is read from a micrometer dial on the moving "cursor." The planimeter was calibrated on known areas of

simple shapes (a 6 x 5 cm rectangle and a 3 cm radius circle): a conversion factor to square centimeters was computed and checked for consistency before each round of measurements. Accuracy of the boundary tracing of the user, reproducibility of the planimeter's recorded area, and the accuracy when measuring more complexly shaped areas were also checked at regular intervals. From calibration trials, the conversion from units to square centimeters was  $63.48 \pm 0.70 \text{ cm}^2 / \text{unit}^2$  for 130 trials of mixed shapes. Translating this figure into square kilometers on Mercury's surface depended upon the scale of the shaded relief map at that latitude.

The printed scales bounding each  $5^\circ$  latitude strip were measured (with a 1 mm ruled 30 cm ruler and a 0.2 mm ruled 1 cm eyepiece scale), averaged, squared, and multiplied by the area in square centimeters. When compared to the areas determined by latitude and longitude, the arithmetic average differed by 1.5% to less than 0.5% for the Lambert Conformal Projections (Discovery, Victoria, and Michelangelo quadrangles) and the Equatorial Mercator Projections (Kuiper and Beethoven quadrangles), but differed by nearly 10% in the Polar Stereographic Projection of the Bach Quadrangle. In the latter (H-15) quadrangle, errors due to the  $\text{cm}^2$ -to- $\text{km}^2$  scale conversion were greater than the planimeter unit-to- $\text{cm}^2$  conversion. The opposite was true in other middle latitude projections. Symmetry and slowly changing scales enable scale factors in some regions to be averaged over a  $10^\circ$  (not  $5^\circ$ ) latitude strip (as in Discovery and Michelangelo

from  $-30^{\circ}$  to  $-60^{\circ}$  and in Kuiper and Beethoven from  $-20^{\circ}$  to  $+20^{\circ}$  about the equator). Latitudes duplicated by adjacent shaded relief maps could provide a check on the map scales of different projections of the same area. Generally, the scales were the same; accuracy of the planimeter was good enough to consider its error no higher than the map scale error in this region.

A final error estimate combines that due to measured scales with that due to planimeter measurements (Table B1). The map's restriction in detail and smooth unit boundaries probably exceeds the above errors, estimated to be less than 10%, and usually less than 1.5%. Also, the increased difficulty in recognizing and measuring crater and plains units in the limb region cause the uncertainty in plains area on the general map to be greater than that of the restricted map. Error estimates for areas measured by latitude-longitude formulas, using the shaded relief maps to provide the reference grid, are slightly less ( $\sim 1\%$ ) than those of areas measured by planimeter ( $\sim 1.5\%$  to  $10\%$ ). The latter errors include those due to approximation of regions not bounded by square degrees, errors in the reference grid, and the uncertainty in Mercury's radius.

Table B1: Uncertainties and Estimated Errors  
in Linear and Areal Measurements

Factor	Estimated Uncertainty
Radius of Mercury, $R_M$	$2439 \pm 1$ km
Errors in latitude, longitude due to uncertainty in $R_M$	$< \pm 0.01\%$
Shaded Relief Map: Position	
Stated error between image on base mosaic and computed control point positions (Davies and Batson, 1975)	$< 2$ km for H-2, H-6, H-15 $< 5$ km for H-11
Observed error in regions of overlap ( $20^\circ$ - $25^\circ$ lat, and $-65^\circ$ to $-70^\circ$ lat)	$\sim \pm 0.3^\circ$ lat., lon.
Measuring Instruments	
1 cm scale eyepiece	precision 0.2 mm accuracy $\pm 0.1$ mm
30 cm ruler	precision 1.0 mm accuracy $\pm 0.5$ mm
Planimeter	precision 0.001 unit <sup>2</sup> accuracy $\pm 0.001$ unit <sup>2</sup>
Protractor	precision $1^\circ$ accuracy 0.5
Diameters, Lengths (L)	
Errors due to instruments' uncertainties, for	
L ~ 1 mm	$\pm 10\%$
L ~ 1 cm	$\pm 1\%$ (eyepiece)
L ~ 1 cm	$\pm 5\%$ (ruler)
L > 5 cm	$\pm 1\%$
On the Shaded Relief Map base, L is 5, 50 and 250 km respectively.	
On the General Map, L is 7.7, 77.4, and 287 km respectively.	

Table B1: Uncertainties and Estimated Errors--Continued

Factor	Estimated Uncertainty
<b>Scales of Shaded Relief Maps</b>	
H-2 and H-11	1: 4 623 000 at 22.5° latitude
H-6	1: 5 000 000 at 0° latitude
H-15	1: 4 290 000 at -65° latitude
Uncertainty due to instruments	~1%
Uncertainty due to interpolation between marked values at 5 degree intervals	< 5%
Uncertainty due to using average scale across 5° latitude interval	< 5%
Error in average scale versus latitude-longitude calculation for area	<1.7% in H-2, H-6, H-11 ~10% in H-15
Planimeter Calibration 130 trials of varied shapes (includes errors in reading vernier dial, repeatability, and complex shapes) Resulting error at scale of Shaded Relief Maps:	63.45 ± 0.70 cm <sup>2</sup> /unit <sup>2</sup> ± 1.1%  + 1750 km <sup>2</sup> at 0° lat.
<b>Areas: Boundaries and values (Shaded Relief Maps)</b>	
Errors due to latitude - longitude	0.3° lat., lon.
or	153 km <sup>2</sup> at ± 20° lat.
	69 km <sup>2</sup> at ± 65° lat.
Errors due to transfer of map from base mosaic to Shaded Relief Map	< 10%
Error in mapping at terminator and limb	< 10% (estimate)
Error in 1 x 1 grid round-off estimates	± 1812 km at 0° lat. ± 16 km at poles
This error is less than 0.4% of the Hilly and Lineated, Restricted, and General Map regions.	
<b>Combined error estimates (measuring device, planimeter, scale, and radius of Mercury)</b>	
Victoria H-2	~1.3%
Kuiper H-6	~1.8%
Discovery H-11	~1.3%
Bach H-15	~12.2%

## APPENDIX C

### MEASUREMENT AND ERRORS OF CRATER STATISTICS

The collection of cratering data from planetary imagery has been described in the text. Further clarification of techniques, errors in measurement or degradation assignment, and statistical formulas is presented here. Section 1 contains a discussion of base map photograph preparation, measurement of crater diameters and sampled area, and instruments used. Section 2 contains a discussion of possible uncertainties, such as sun angle, scale factors, degradation classification, and biases in crater recognition. A third section presents the mathematical formulas used in crater statistics compiled in Appendix D.

#### Section 1: Materials and Techniques

##### Data Sources

Negative prints of 20" by 24" Lunar Orbiter IV imagery and positive prints of Mariner 10 imagery were used for most crater measurements. Hard copy prints were obtained through the Space Imagery Center of the Lunar and Planetary Laboratory (LPL) of the University of Arizona, Tucson, and the photographic services at LPL. Additional specially processed images, stereo pairs, and photomosaics were obtained from the Image Processing Lab of the Jet Propulsion Laboratory (JPL/IPL), Pasadena, California.



## Measurement Techniques

Base Photograph. The photographs were covered by transparent acetate which could be marked with pencil; grids of some small size were drawn on the counting area. Crater parameters within each square were measured directly on the photograph surface with instruments described below and tabulated on a prepared data sheet. Crater rims (circled in pencil on acetate) were numbered for identification to prevent recounting the crater.

Crater Diameters. Crater diameters were measured from rim to rim as outlined in the Catalog of Lunar Craters (Wood and Andersson, 1978a). On most of the lunar images, the distance between the sharply shadowed sunward rims, parallel to the sun's azimuthal direction, was taken as the best approximation to the crater's rim-to-rim diameter. However, often on the Mercury imagery, the crater appeared foreshortened near the picture edges or in oblique viewing angles; in those cases the long axis of the crater was measured, parallel to the limb of the planet. Shadows defining the rim ansae tend to disappear in the mid-disk limb regions, increasing the uncertainty of the diameter measurement. Two measurements were recorded for truly elliptical craters and for large craters with irregular and ill-defined rims, but the average diameter was used in the crater statistics.

Measured Areas. Determination of the areas over which the craters were sampled was critical to later statistical studies. If the area was rectangular and described by one scale factor, as on most

lunar photos, simple measurements of the length of the bounding sides, multiplied by the scale factor squared, gave an area in  $\text{km}^2$  with approximate accuracy better than 1%-5%. Irregular areas could be blocked off into geometrical shapes, measured, and the  $\text{cm}^2$  value converted to  $\text{km}^2$  with the appropriate scale factors. (Errors in the scale factors, as discussed shortly, are critical because the term is squared.) Lunar count areas were only part of a high resolution photograph, so errors due to change in scale factor with distance from the principal point, or with foreshortening and tilt, were insignificant. Changes in scale factor across the Mariner 10 images may be more significant for the lower resolution, oblique photos containing limb regions, but not for the higher resolution coverage near the center of the disk. Other methods of determining the count surface area are described in Appendix B.

Instruments. The same measuring devices were used to determine crater diameters, scale factors, and areas of counted regions on both planets. For craters less than 1.0 cm on the hard-copy photo, a magnifying eyepiece, 1-cm scale with 0.2 mm divisions was used with an estimated accuracy of  $\pm 0.1$  mm for sharp rimmed craters. Craters as small as 1.0 mm were measured in some lunar areas; maximum error is  $\sim 10\%$ . Craters larger than 1 cm on the photo were measured with a precision 30 cm ruler of 1 mm divisions, with an estimated accuracy of 0.5 mm; maximum error of a "1 cm" crater is 5%. Sharp rimmed craters of larger diameters within the range of each instrument will have smaller maximum errors, but the error associated with more degraded landforms is greater.

## Section 2: Discussion of Errors

In general, diameters of lunar craters measured on Orbiter IV imagery are judged to be more accurate than those on Mariner 10 imagery because of higher resolution, different imaging systems, and lower, more uniform sun angles. Orbiter IV imagery has a resolution of 100 m, as compared to Mariner 10 imagery of  $\sim 1$  km for most of the photos used in this study. Scale factors for lunar imagery appear to be more easily determined (and precise) than Mariner 10 figures. Crater degradation and rough topography limit the accuracies on either surface.

### Sun Angle

Varying sun angle illumination may be one factor contributing to inaccuracies in diameter measurements. In Orbiter IV imagery, the sun angle is  $\sim 22^\circ$  from the horizontal near  $42^\circ$  latitude and  $\sim 10^\circ$  at  $72^\circ$  latitude, and approximately constant over the measured area (Table C1). Sun angle illumination on Mercury's incoming side varies from  $0^\circ$  to  $90^\circ$ . Changes in sun angle affect diameter measurements as well as crater recognition and apparent morphology (Young, 1975; Schultz, 1976a, 1977). The effects on crater diameter and recognition by the imaging system (vidicon TV image as opposed to photographic image) and by resolution are outlined by Schultz (1976a, 1977) and discussed in Chapter 2 of the text.

Table C1: Lunar Orbiter IV Photographic Data from Wood and Andersson (1978a)

LO IV High Resolution <sup>ç</sup>	Spacecraft altitude (km)	Latitude at center of photo	Scale at center (km/mm)	Scale at corner (km/mm)	Nominal ground resolution at center	Range of sun elevations
Equatorial	2700	$\pm 14^{\circ}$	.62	.63	.06	$15^{\circ} - 23^{\circ}$
Temperate	2900	$\pm 42^{\circ}$	.66	.68	.06	$14^{\circ} - 24^{\circ}$
Polar	3500	$\pm 72^{\circ}$	.80	.83	.08	$0^{\circ} - 24^{\circ}$
Sunset	5500 (N) 5800 (S)	$\pm 34^{\circ}$	1.3	1.5 <sup>#</sup>	.12	$0^{\circ} - 50^{\circ}$

# At limb

ç Photographs all 20" by 24" glossies, transparencies, positives, and negatives.

## Scale Factors

Lunar Orbiter IV Photos. Scale variations over the standard Lunar Orbiter IV photos have been calculated by Andersson and are reproduced in Table C1 below (from Wood and Andersson, 1978a). Interpolations of scale factors for varying spacecraft altitudes or principal point latitudes were made using a fit to a quadratic curve. Published diameters (Wood and Andersson, 1978a) and measured diameters were ratioed across the photograph and averaged to ascertain the effective scale factor. Agreement was usually satisfactory. Instrumental errors are of the same order (1% - 3%) as the published errors in the diameter of small, 3.5 - 7.0 km, craters. Wood and Andersson (1978a) state an accuracy of 0.1 km (about the limit of resolution) for small craters, and an internal accuracy of 2% to 5% for catalog data. The appropriate scale for the portion of the photo used for counting was then applied to all measurements. Calculations of crater diameter in kilometers were completed after the values in mm were recorded, tabulated, and binned. A conversion table of mm to km was prepared for each photograph before measuring the small craters, after calculation of the photo scale.

Mariner 10 Mercury Images. Scale factors derived from Mariner 10 imagery proved to be a problem. Initially these factors were derived by dividing the published pixel size, or resolution per pixel, given in km, by the measured and averaged pixel size in mm. (Tick marks of 5, 10, and 100 pixels and TV lines appear on the Mariner 10

images.) Although some differences in pixel width and line width occur, the initial scale factor was based on pixel width. The scale of the Discovery mosaic was derived from the measured and published size of the crater Rameau ( $D = 55$  km, Murray et al., 1974b). Foreshortening, for a true perspective projection from great distances, is not expected to seriously affect the dimensions parallel to the limb. For the large photomosaic of Mercury's first quadrant, variations in scale by 1% to 2% occur depending on the slant range of the individual pictures and the processing of the scale across the mosaic. Most of the higher resolution, closer-range photos used here were targeted closer to the disk center, and thus not as affected by foreshortening.

However, scales computed along the horizontal axis of the Mariner 10 images may not be valid for measurements made at angles to that axis, i.e. parallel to the limb. Therefore, a precise scale was determined for the center of the first quadrant mosaic and used to recompute the scale factors for the images in the mosaic. If this revision is correct, the former pixel scale factors could be too high by 10% to 20%. Relative densities in one area are not expected to change, for both crater diameter and measured areas are affected by the  $\text{km}^2$  factor. However, a shift in the number of craters per bin could occur for those craters of diameters approximately equal to the boundaries of the bin. The net shift should be toward lower diameters. After rebinning the data according to the revised scales, minor shifts in bin populations to lower diameters were noted, but did not change any of the conclusions drawn (Chapter 3).

Table C2 below lists the areas of the selected regions as determined by the pixel-photoscale method, the revised mosaic-scale method, and the latitude-longitude grid method. The variations in the first value could be attributed to failure to use a spherical triangle approximation of the photo area, or similarly, using a horizontally directed scale (km/pixel) for features foreshortened at an oblique angle. The latitude-longitude grid method is the most accurate of the methods used.

#### Degradation Class

Although a detailed discussion of degradation class criteria appears in Chapter 2, some particular problems are reviewed here. The LPL system, based on criteria of rim sharpness and continuity (Wood and Andersson, 1978a), was applied to selected regions of the Moon and Mercury. A slightly modified LPL system was used in mapping the first quadrant of Mercury. In both systems, Class 1 craters are fresh and/or rayed, and Class 5 craters are highly subdued. The slight modification of degradation class criteria between the crater count project on the selected areas and the geologic mapping produced conflicting results in degradation class densities. In general, over half the large (greater than 40 km) craters of the selected areas were assigned to the same degradational class in mapping. However, a large percentage was reassigned to fresher crater units by a change of one crater class. The shift in class was most common for C3 and C4 craters which

Table C2: Areas of Selected Regions

Selected Region	Areas (km <sup>2</sup> )		
	Using Pixel Size Scale	Using Revised Mosaic Scale	Using Lat. Long. of Shaded Relief Maps
Area 1 HCA	$1.6559 \cdot 10^5$	$1.3495 \cdot 10^5$	$1.7294 \cdot 10^5$
Disc. Scarp ICP	$6.4275 \cdot 10^4$	$6.422 \cdot 10^4$	$7.1575 \cdot 10^4$
Area 2 HCA	$8.5226 \cdot 10^4$	$5.1302 \cdot 10^4$	$6.4654 \cdot 10^4$
Area 2-ICP	$1.397 \cdot 10^5$	$8.3171 \cdot 10^4$	$1.2696 \cdot 10^5$
Area 55'	$1.3628 \cdot 10^5$	$9.1228 \cdot 10^4$	$1.0784 \cdot 10^5$
Area 6(6')	$1.7595 \cdot 10^5$	$1.3196 \cdot 10^5$	$1.3222 \cdot 10^5$
Area 6 ICP	$1.0175 \cdot 10^5$	$7.6309 \cdot 10^4$	$1.4777 \cdot 10^5$
Area 6	$1.5400 \cdot 10^5$	$1.155 \cdot 10^5$	$1.2266 \cdot 10^5$
Area 3*			$5.0529 \cdot 10^4$
Area 4*			$5.9553 \cdot 10^4$

\* Areas not sampled in small-crater statistics.



were then mapped as C2 and C3 craters respectively. In effect, many of the selected regions when mapped appear younger than when analyzed by the crater-diameter frequency relation. The large C4 population decreases slightly in the map statistics; the C2's increase. Table C3 presents these changes for the general map for craters over 40 km.

Roughness of the terrain also affects the assessment of degradation classes. Nowhere is this more clearly illustrated than in the hilly and lineated area of Mercury (Fig. 19, text). The high relief terrain appears to affect superposed craters by mass wasting from topographic highs and by differential erosion along lines of pre-existing weakness (cf. Mutch and Saunders, 1972). For all lunar and mercurian crater statistics, information on the background unit could prove helpful in evaluating uncertainties in diameter and degradation class.

#### Biases in Crater Counts

A bias appeared to be introduced by setting a lower size limit for the counted craters prior to measurement; craters of the "cut-off diameter" size were recognized more easily. This recognition may be just the result of the increasingly larger numbers of small craters on the planet surface. In two adjacent areas of the southern lunar highlands, the larger area with the higher  $D_{\min}$  has higher densities of 4.2 km craters than the smaller region with the smaller  $D_{\min}$ . Crater recognition sometimes appeared to change with the time spent counting craters. The possibility of "missed" craters makes it advisable that a

Table C3. Degradation Class Shift

Degradation classes of craters  $\geq 40$  km in selected regions of Mercury when measured, compared to their classes when mapped.

		Classes as Mapped					Total
		C1	C2	C3	C4	C5	
Classes as Measured	C1	4					4
	C2	5	10	3			8
	C3		14	22	3		39
	C4			12	19	3	31
	C5				4		7
Total		9	24	37	26	3	99

Of 99 craters in HCA and ICP areas:

58 remain in the same class,

35 are reclassified to one fresher unit when mapped,

6 are reclassified to one more degraded unit when mapped.

recount of a certain area be conducted to establish statistically the average number of craters miscounted or unrecognized. Repeatability of diameter values and degradation class assignments could be tested in such a recount exercise. Greeley and Gault (1970) performed such studies in an extensive crater survey involving many crater counters. Recounting the same area on a different photograph, or at different sun angles could establish the effect of those variables on crater statistics (Young, 1975). Such tests were not conducted in this survey, but may be valuable in future study.

### Section 3: Mathematical Formulas for Crater Statistics

The statistical formulas which follow are presented in the report of the Crater Analysis Techniques Working Group (1978, p. 16-17). Let  $D$  be the crater diameter, and  $\bar{D}$  the geometric mean of a diameter interval from  $D_1$  to  $D_2$ , where  $D_2 = 2^{\frac{1}{2}} \cdot D_1$ ; thus  $\bar{D} = (D_1 \cdot D_2)^{\frac{1}{2}}$ , or  $D_1 \cdot 2^{\frac{1}{4}}$ . If  $N$  is the number of craters with diameters  $D$  such that  $D_1 \leq D < D_2$  over an area  $A$  of crater sampling, then the various statistical functions are:

Differential Size Frequency Distribution  $F(D)$

$$dF(D) = dN = bD^a dD \quad \text{where } N = dD^a. \quad \text{Note that}$$

$(d \log N)/(d \log D)$  equals the "slope"  $a$ .

Cumulative Size Frequency Distribution  $C(D)$

$$C(D) = \frac{1}{A} \int_{D_{\max}}^D F(D) dD$$

Relative Size Frequency Distribution  $R(D)$

$R(D) = F(D)/S(D)$  where  $S(D)$  is a differential reference distribution,  $S(D) = D^{-3}$ .

$$\begin{aligned} R(D) &= \Delta N / (\Delta D \cdot A \cdot D^{-3}) &&= \frac{\Delta N}{\Delta D} \frac{1}{D^{-3} A} \\ &= \frac{(C(D_2) - C(D_1))}{D^{-3} \cdot (D_2 - D_1)} \\ &= \frac{\bar{D}^3 \cdot N}{A \cdot (D_2 - D_1)} \end{aligned}$$

Area Plot  $P(\bar{D})$

$$P(\bar{D}) = \frac{\pi \bar{D}^2 \cdot N \cdot 100}{4 \cdot A} = 0.0365 R(\bar{D})$$

## APPENDIX D

### CRATER STATISTICAL DATA

The tables presented below list, for each area A, the total number of craters N within a bin of mean diameter  $\bar{D}$  and the number of craters of each degradational type (C1-C5, C5') within that bin. Rim-to-rim diameters were measured at arbitrary azimuths for rectified photos or photos taken at vertical incidence (most lunar photos), and at azimuths paralleling a local tangent to the limb for oblique images.

Although not presented here, additional information was gathered for some regions, including (1) diameter of crater floor, (2) shadow length of sunward crater wall, (3) presence of crater in a chain or cluster of craters, (4) background unit if known, (5) position relative to significant objects, and (6) presence of a central peak, peak ring, fault, or scarp. These data are available on request.

The support data included with each table provide necessary information on the materials used, the area measured, and the method. Information on materials includes image identification, type of processing, source of photo, and the photo scale (km/mm). Information about the area measured includes the region's boundaries or exact location (center coordinates or a finding chart) and its dimensions in  $\text{km}^2$ . Included as data on the method are the measurement technique and instruments used to measure diameter and regional area, estimates of

instrument accuracy and errors, comments on the area's subdivisions, the lower diameter limit ("cut-off diameter") of measured craters, and any necessary notes on degradation classes or the surface itself. Criteria for the latter are discussed and illustrated in Chapter 2. More quantitative morphologic parameters for Mercury and the Moon are not presented here but have been published by Malin and Dzurisin (1977, 1978), Smith and Hartnell (1978), Carusi et al. (1976a,b), Caputo et al. (1976a,b), Wood et al. (1977), Wood and Andersson (1978a,b,c), Pike (1976, 1977a,b) and others.

Abbreviations used in the following tables are listed below.

LPL	<u>L</u> unar and <u>P</u> lanetary <u>L</u> aboratory, University of Arizona, Tucson, Arizona.
JPL	<u>J</u> et <u>P</u> ropulsion <u>L</u> aboratory, California Institute of Technology, Pasadena, California.
IPL	<u>I</u> mage <u>P</u> rocessing <u>L</u> aboratory, Jet Propulsion Laboratory, Pasadena, California.
USGS	<u>U</u> nited <u>S</u> tates <u>G</u> eological <u>S</u> urvey
SEDR	<u>S</u> upplementary <u>E</u> xperimenter <u>D</u> ata <u>R</u> ecords
FDS	<u>F</u> light <u>D</u> ata <u>S</u> ystem
LO IV	<u>L</u> unar <u>O</u> rbiter <u>I</u> V
Pixel	<u>P</u> icture <u>E</u> lement
H-11	<u>H</u> ermes Quadrangle <u>11</u> , Discovery Quadrangle
HCA	<u>H</u> eavily <u>C</u> ratered <u>A</u> rea
ICP	<u>I</u> nter <u>C</u> rater <u>P</u> lains

Table D1: Lockyer G Region of Lunar Southern Highlands ("Area 1")

	Pre-Imbrian Pitted Plains Area = $4.085 \cdot 10^3 \text{ km}^2$						Pre-Imbrian Terra and Craters Area = $5.327 \cdot 10^3 \text{ km}^2$					
Diameter Bin (km)	N(bin)	N(Degradation Class)					N(bin)	N(Degradation Class)				
		1	2	3	4	5		1	2	3	4	5
0.62 -- 0.88	142	11	21	71	31	9	181	30	17	66	54	14
0.88 -- 1.24	265	22	42	105	70	26	184	9	18	49	74	34
1.24 -- 1.75	232	19	33	90	51	39	157	7	13	59	54	24
1.75 -- 2.47	65	9	19	13	12	12	73	3	10	30	19	10
2.47 -- 3.5	27	2	10	6	2	7	32	6	5	7	4	10
3.5 -- 4.95	8	2	2	1	1	2	11	1	2	2	2	4
4.95 -- 7.0	3	1	0	0	0	2	7	1	0	1	1	4
7.0 -- 9.9	3	1	1	0	0	1	3	2	0	1	0	0
9.9 -- 14.0	0	0	0	0	0	0	4	1	0	2	0	1
14.0 -- 19.8	0	0	0	0	0	0	2	0	0	1	0	1
19.8 -- 28.0	0	0	0	0	0	0	3	1	0	2	0	0
28.0 -- 39.6	1	0	0	0	1	0	1	0	0	1	0	0

Supporting Data for Table D1 Lockyer G Region

Source. Lunar Orbiter IV 88--H2, negative print, full size (20" by 24"), prepared from positive transparency at the Lunar and Planetary Lab, using the facilities of the Space Imagery Center and the photography lab.

Measuring Devices. Hand lens eyepiece with 1 cm scale, precision 0.2 mm, accuracy  $\pm$  0.1 mm; and a ruler, 30 cm, precision 1 mm, accuracy  $\pm$  0.5 mm.

Location. Principal Ground Point of LO IV 88: (24.94° E, 42.69° S). Southeast corner of the H2 photo used, bounded by the coordinates: (27.5° E, 43.0° S), (31.2° E, 42.5° S), (34.0° E, 47.0° S), (31.5° E, 47.5° S). Pre-Imbrian Pitted Plains mapped by Scott (1972) marked as the pIp region; Pre-Imbrian Terra and larger craters for the non-pIp region. Areas measured in  $\text{cm}^2$ , converted to  $\text{km}^2$  using the scale factor.

Scale. Scale determined to be 0.686 km/mm by measurement of catalogued craters within the area (i.e. using the known diameters recorded in Wood and Andersson, 1978a). Scale assumed to be constant over the area of data collection.

Cut Off Diameter. 1.0 mm, or about 0.7 km.

Degradation Classes. LPL scheme: Class 1 freshest, Class 5 most degraded. Explained further, with examples and criteria, in text, Chapter 2, and Fig. 6.



Table D2: Spallanzani Region of Lunar Southern Highlands ("Area 2")

Diameter Bin (km)	Pre-Imbrian Pitted Plains Area = $2.0188 \cdot 10^4$ km <sup>2</sup>						Pre-Imbrian Terra and Craters Area = $7.4825 \cdot 10^3$ km <sup>2</sup>					
	N(bin)	N(Degradation Class)					N(bin)	N(Degradation Class)				
		1	2	3	4	5		1	2	3	4	5
1.24 -- 1.75	13	6	1	5	0	1	1	1	0	0	0	0
1.75 -- 2.47	299	46	55	120	58	19	66	4	16	20	24	2
2.47 -- 3.5	271	42	37	87	57	48	89	16	14	32	20	9
3.5 -- 4.95	76	14	13	17	15	16	31	7	9	4	4	7
4.95 -- 7.0	28	4	6	5	5	8	13	3	1	4	3	2
7.0 -- 9.9	20	2	4	5	2	7	3	2	0	1	0	0
9.9 -- 14.0	5	0	0	3	1	1	7	1	2	1	1	2
14.0 -- 19.8	8	1	2	5	0	0	7	0	0	5	0	2
19.8 -- 28.0	2	0	0	2	0	0	4	0	1	3	0	0
28.0 -- 39.6	0	0	0	0	0	0	1	0	1	0	0	0

## Supporting Data for Table D2 Spallanzani Region

Source. Lunar Orbiter IV 88--H2, negative print, full size (20" by 24"), prepared at Lunar Planetary Lab from positive transparency from the Space Imagery Center.

Measuring Devices. Hand lens eyepiece with 1 cm scale, precision 0.2 mm, accuracy  $\pm 0.1$  mm; and a ruler, 30 cm, precision 1 mm, accuracy  $\pm 0.5$  mm.

Location. Principal Ground Point of LO IV 88: (24.94° E, 42.69° S). Lower third of that photo used, southwest part, bounded by coordinates: (19.5° E, 45.5° S), (27.5° E, 43.0° S), (31.5° E, 47.5° S), (22.0° E, 50.5° S). Pre-Imbrian Pitted Plains region mapped by Scott (1972) marked off as the pIp area; Pre-Imbrian Terra and remaining craters for the non-pIp region. Both areas measured, converted from  $\text{cm}^2$  to  $\text{km}^2$  using the photo scale factor. This region is adjacent to Area 1 described in Table D1. (See also Fig. 44.)

Scale. Scale of 0.686 km/mm determined from measurements of catalogued craters in the photo area (Wood and Andersson, 1978a). Scale assumed to be constant over the area of data collection.

Cut Off Diameter. 2.55 mm or 1.75 km.

Degradation Classes. LPL scheme: Class 1 craters freshest, Class 5 most degraded; applied to all sizes of craters. See text, Chapter 2, and Fig. 6.

Table D3: Ascelpi Region of Lunar Southern Highlands ("Area 3")

$$\text{Area} = 3.63 \cdot 10^4 \text{ km}^2$$

Diameter Bin (km)	Number of Craters in Bin	Number within Degradation Classes				
		1	2	3	4	5
1.24 -- 1.75	347	30	55	119	93	49
1.75 -- 2.47	402	49	80	122	101	48
2.47 -- 3.5	241	44	29	56	69	43
3.5 -- 4.95	97	16	8	23	23	25
4.95 -- 7.0	61	6	7	23	8	17
7.0 -- 9.9	24	1	7	4	4	8
9.9 -- 14.0	28	2	5	8	6	7
14.0 -- 19.8	16	3	2	7	0	4
19.8 -- 28.0	6	0	3	3	0	0
28.0 -- 39.6	4	0	2	2	0	0
39.6 -- 56.0	3	0	1	2	0	0

Supporting Data for Table D3 Ascelpi Region

Source. Lunar Orbiter IV 82-H3, negative print, full size (20" by 24"), prepared from a positive transparency at the Lunar and Planetary Lab. Space Imagery Center and photography lab facilities used.

Measuring Devices. Hand lens eyepiece with 1 cm scale, precision of 0.2 mm, accuracy  $\pm 0.1$  mm; and ruler, 30 cm, precision of 1 mm, accuracy of  $\pm 0.5$  mm.

Supporting Data Table D3--Continued

Location. Principal Ground Point of LO IV 82 is (32.47° E, 72.37° S); spacecraft altitude 3502.94 km. Northern part of photograph used, west to Pitiscus. Bounding coordinates are: (21.0° E, 51.5° S), (30.25° E, 51.5° S), (30.0° E, 57.0° S), (20.0° E, 59.8° S). No Pre-Imbrian Pitted Plains mapped in this region; units were undifferentiated in the counting statistics. Region illustrated in Fig. 33a; boundaries shown in Fig. 44.

Scale. Scale of 0.822 km/mm determined from measurements of catalogued craters on the photo. Scale assumed to be constant over this region.

Cut Off Diameter. 1.5 mm, or 1.24 km.

Degradation Classes. LPL scheme: C1 freshest, C5 most degraded. Fig. 6, Chapter 2 illustrates the degradation classes.

Table D4: Mutus Region of Lunar Southern Highlands ("Area 4")

$$\text{Area} = 1.0135 \cdot 10^4 \text{ km}^2$$

Diameter Bin (km)	Number of Craters in Bin	Number within Degradation Classes				
		1	2	3	4	5
0.62 -- 0.88	360	24	29	177	115	15
0.88 -- 1.24	438	35	44	201	130	26
1.24 -- 1.75	310	23	61	115	89	22
1.75 -- 2.47	114	13	21	35	32	13
2.47 -- 3.5	69	16	6	16	20	11
3.5 -- 4.95	20	5	1	3	8	3
4.95 -- 7.0	9	1	0	4	2	2
7.0 -- 9.9	10	1	0	2	3	4
9.9 -- 14.0	4	0	0	1	1	2
14.0 -- 19.8	3	0	0	1	1	1
19.8 -- 28.0	2	0	0	0	1	1

Supporting Data for Table D4 Mutus Region

Source. Lunar Orbiter IV 82--H3, negative print, full size (20" by 24"), prepared from positive transparency at the Lunar and Planetary Lab, using the photography lab and Space Imagery Center facilities.

Measuring Devices. Hand lens eyepiece with 1 cm scale, precision 0.2 mm, accuracy  $\pm 0.1$  mm; and a ruler, 30 cm, precision 1 mm, accuracy  $\pm 0.5$  mm.

Supporting Data Table D4 --Continued

Location. Principal Ground Point of LO IV 82 is (32.47° E, 72.37° S). Southeast corner of photo used, east of Mutus in the "Flow Lobe" area noted by Strom (1977). Bounding coordinates are: (36.5° E, 61.5° S), (41.5° E, 61.0° S), (43.0° E, 65.0° S), (36.0° E, 65.2° S).

Scale. Scale of 0.822 km/mm determined by measurements of catalogued craters (Wood and Andersson, 1978a); scale assumed constant over the region sampled.

Cut Off Diameter. 1.0 mm, or 0.82 km.

Degradation Classes. LPL scheme used: Class 1 freshest, Class 5 most degraded; applied to all craters. See Fig. 6 and text of Chapter 2 for details.

Table D5: Jacobi Region of Lunar Southern Highlands ("Area 5")

Diameter Bin (km)	Southern ("ABC") Region Area = $1.1567 \cdot 10^4$ km <sup>2</sup>						Northern ("DEF") Region Area = $1.0282 \cdot 10^4$ km <sup>2</sup>					
	N(bin)	N(Degradation Class)					N(bin)	N(Degradation Class)				
		1	2	3	4	5		1	2	3	4	5
0.88 -- 1.24	229	30	24	62	89	24	327	28	22	90	141	44
1.24 -- 1.75	245	16	31	64	99	34	358	19	21	122	132	60
1.75 -- 2.47	135	13	26	46	33	18	236	21	42	92	53	30
2.47 -- 3.5	52	12	9	11	13	7	75	16	31	17	6	6
3.5 -- 4.95	18	5	4	6	2	1	27	10	9	3	3	2
4.95 -- 7.0	15	3	4	4	3	1	17	3	2	4	4	4
7.0 -- 9.9	4	1	0	2	0	1	10	0	0	5	1	4
9.9 -- 14.0	5	1	2	2	0	0	5	1	1	1	0	2
14.0 -- 19.8	4	2	0	0	1	1	2	0	0	0	1	1
19.8 -- 28.0	3	0	1	1	1	0	1	0	0	0	0	1
28.0 -- 39.6	1	0	1	0	0	0	1	0	0	1	0	0
39.6 -- 56.0	3	0	0	2	1	0	1	0	0	0	1	0

Supporting Data for Table D5 Jacobi Region

Source. Lunar Orbiter IV 112--H1, negative print, full size (20" by 24"), prepared from positive transparency at Lunar Planetary Lab. Facilities of Space Imagery Center, photography lab used.

Measuring Devices. Hand lens eyepiece with 1 cm scale, precision 0.2 mm, accuracy  $\pm 0.1$  mm; and a ruler, 30 cm, precision 1 mm, accuracy  $\pm 0.5$  mm.

Location. Principal Ground Point of LO IV 112 is ( $1.35^{\circ}$ W,  $42.58^{\circ}$ S), from altitude of 2986.04 km. The western part of this photograph was divided in two halves: the northern part (named DEF) contains Imbrian-pre-Imbrian terra (IpIt), Imbrian cratered plains (Ipc), and craters; the southern half, named ABC, contains the IpIt unit and craters. The Ipc unit is mapped as pre-Imbrian plains by Wilhelms and McCauley (1971). The bounding coordinates of the entire area are: ( $0.0^{\circ}$ E,  $55.13^{\circ}$ S), ( $7.5^{\circ}$ E,  $55.0^{\circ}$ S), ( $15.5^{\circ}$ E,  $60.1^{\circ}$ S), ( $9.0^{\circ}$ E,  $62.5^{\circ}$ S). The endpoints of the line dividing the ABC southern block and the DEF northern block are: ( $3.5^{\circ}$ E,  $59.3^{\circ}$ S) and ( $9.5^{\circ}$ E,  $57.7^{\circ}$ S). The region is illustrated in Figs. 33b and 44.

Scale. Scale of 0.717 km/mm determined from measurement of catalogued craters within the area (Wood and Andersson, 1978a). Scale assumed to be constant over the area.

Cut Off Diameter. 1.2 mm, or 0.88 km.

Degradation Classes. LPL scheme: Class 1 freshest, Class 5 most degraded; applied to all craters. See Fig. 6, Chapter 2.



Table D6: Combined Southern Highlands Statistics

Diameter Bin (km)	N(bin)	N(Degradation Class)					Surface Area (km <sup>2</sup> )
		1	2	3	4	5	
0.62 -- 0.88	683	65	67	314	200	38	1.9547·10 <sup>4</sup>
0.88 -- 1.24	1443	124	150	507	504	154	4.1396·10 <sup>4</sup>
1.24 -- 1.75	1649	114	214	569	524	228	7.7696·10 <sup>4</sup>
1.75 -- 2.47	1390	158	269	478	332	152	1.0537·10 <sup>5</sup>
2.47 -- 3.5	856	154	141	232	191	141	1.0537·10 <sup>5</sup>
3.5 -- 4.95	288	60	48	59	58	60	1.0537·10 <sup>5</sup>
4.95 -- 7.0	153	22	20	45	26	40	1.0537·10 <sup>5</sup>
7.0 -- 9.9	77	10	12	20	10	25	1.0537·10 <sup>5</sup>
9.9 -- 14.0	58	6	10	18	9	15	1.0537·10 <sup>5</sup>
14.0 -- 19.8	42	6	4	19	3	10	1.0537·10 <sup>5</sup>
19.8 -- 28.0	21	1	5	11	2	2	1.0537·10 <sup>5</sup>
28.0 -- 39.6	9	0	4	4	1	0	1.0537·10 <sup>5</sup>
39.6 -- 56.0	7	0	1	4	2	0	1.0537·10 <sup>5</sup>

Supporting Data for Table D6 Combined Statistics

Source. Combined crater statistics from the previous tables were used in Table D6. These areas are: LO IV 88 H2, Lockyer G, Area of  $9.412 \cdot 10^3$  km<sup>2</sup>; LO IV 88 H2, Spallanzani, Area of  $2.767 \cdot 10^4$ ; LO IV 82 H3, Ascelpi, Area of  $3.630 \cdot 10^4$  km<sup>2</sup>; LO IV 82 H3, Mutus, Area of  $1.014 \cdot 10^4$  km<sup>2</sup>; and LO IV 112 H1, Jacobi, Area of  $2.185 \cdot 10^4$  km<sup>2</sup>.

Other Data. Specified in Tables D1 through D5.

Table D7: Southern Highlands Pre-Imbrian Pitted Plains

Diameter Bin (km)	N(bin)	N(Degradation Class)					Surface Area (km <sup>2</sup> )
		1	2	3	4	5	
0.62 -- 0.88	142	11	21	71	31	9	4.085·10 <sup>3</sup>
0.88 -- 1.24	265	22	42	105	70	26	4.085·10 <sup>3</sup>
1.24 -- 1.75	232	19	33	90	51	39	4.085·10 <sup>3</sup>
1.75 -- 2.47	364	55	74	133	70	31	2.427·10 <sup>4</sup>
2.47 -- 3.5	298	44	47	95	59	55	2.427·10 <sup>4</sup>
3.5 -- 4.95	84	16	15	18	16	18	2.427·10 <sup>4</sup>
4.95 -- 7.0	31	5	6	5	5	10	2.427·10 <sup>4</sup>
7.0 -- 9.9	23	3	5	5	2	8	2.427·10 <sup>4</sup>
9.9 -- 14.0	5	0	0	3	1	1	2.427·10 <sup>4</sup>
14.0 -- 19.8	8	1	2	5	0	0	2.427·10 <sup>4</sup>
19.8 -- 28.0	2	0	0	2	0	0	2.427·10 <sup>4</sup>
28.0 -- 39.6	1	0	0	0	1	0	2.427·10 <sup>4</sup>

Supporting Data for Table D7 Combined pIp Statistics

Source. Combined pre-Imbrian pitted plains data from Tables D1 and D2. Areas and Cut Off Diameters specified above and in the proper tables. Methods previously specified.

Table D8: Southern Highlands Non-Pre-Imbrian Pitted Plains

Diameter Bin (km)	N(bin)	N(Degradation Class)					Surface Area (km <sup>2</sup> )
		1	2	3	4	5	
0.62 -- 0.88	541	54	46	243	169	29	1.546·10 <sup>4</sup>
0.88 -- 1.24	1178	102	108	402	434	128	3.731·10 <sup>4</sup>
1.24 -- 1.75	1417	95	181	479	473	189	7.361·10 <sup>4</sup>
1.75 -- 2.47	1026	103	195	345	262	121	8.109·10 <sup>4</sup>
2.47 -- 3.5	558	110	94	137	132	86	8.109·10 <sup>4</sup>
3.5 -- 4.95	204	44	33	41	42	42	8.109·10 <sup>4</sup>
4.95 -- 7.0	122	17	14	40	21	30	8.109·10 <sup>4</sup>
7.0 -- 9.9	54	7	7	15	8	17	8.109·10 <sup>4</sup>
9.9 -- 14.0	53	6	10	15	8	14	8.109·10 <sup>4</sup>
14.0 -- 19.8	34	5	2	14	3	10	8.109·10 <sup>4</sup>
19.8 -- 28.0	19	1	5	9	2	2	8.109·10 <sup>4</sup>
28.0 -- 39.6	8	0	4	4	0	0	8.109·10 <sup>4</sup>
39.6 -- 56.0	7	0	1	4	2	0	8.109·10 <sup>4</sup>

Supporting Data for Table D8 Combined Non-pIp Statistics

Source. Regional statistics combined for this table include: pIt of Lockyer G area, pIt of the Spallanzani area, all of Ascelpi, all of Mutus, and all of Jacobi. Sources, locations, measuring devices, and other data are given in the previous tables.

Table D9: Boundaries and Areas for Sectors of Southern Highlands

Crater statistics bounded within the following sectors are compiled within the Lunar and Planetary Laboratory Catalog of Lunar Craters (Wood and Andersson, 1978a).

Sector Name	LPL Catalog Boundaries*			Surface Area (km <sup>2</sup> )
	Xi	Eta	Zeta	
D012	0.0 to 0.3	-0.7 to -0.4	~ 0.9 to 0.7	3.3577·10 <sup>5</sup>
C01	0.0 to -0.2	-0.7 to -0.4 -0.5	0.9 to 0.7	1.8736·10 <sup>5</sup>
T012	0.0 to -0.3	-0.97 to -0.7	0.2 to 0.7	5.0780·10 <sup>5</sup>
S0	0.0 to 0.1	-0.97 to -0.7	~ 0.2 to 0.7	1.6787·10 <sup>5</sup>
S123	0.1 to 0.4	-0.97 to -0.7	~ 0.2 to 0.7	4.9624·10 <sup>5</sup>

\* Boundaries illustrated in Fig. 50 of text, Chapter 3.

Table D10: Crater Statistics of Divided Sectors Combined

Diameter Bin (km)	Heavily Cratered Areas Area = $4.4198 \cdot 10^5 \text{ km}^2$						Non Heavily Cratered Areas Area = $4.4907 \cdot 10^5 \text{ km}^2$					
	N(bin)	N(Degradation Class)					N(bin)	N(Degradation Class)				
		1	2	3	4	5		1	2	3	4	5
7.0 -- 9.9	163	14	55	72	21	1	192	19	33	83	46	11
9.9 -- 14.0	96	16	22	35	21	2	147	13	27	57	39	11
14.0 -- 19.8	65	12	14	26	9	4	102	14	19	37	21	11
19.8 -- 28.0	69	6	12	34	14	3	59	4	9	26	10	10
28.0 -- 39.6	55	2	6	31	10	6	31	3	4	12	6	6
39.6 -- 56.0	42	1	3	25	11	1	8	0	1	4	2	1
56.0 -- 79.2	25	1	4	16	3	1	0	0	0	0	0	0
79.2 -- 112.0	12	0	1	7	2	2	1	0	1	0	0	0
112.0 - 158.4	3	0	1	2	0	0	0	0	0	0	0	0
158.4 - 224.0	1	0	0	0	0	1	0	0	0	0	0	0

Table D11: Crater Statistics of Divided Sectors, Werner Area

Diameter Bin (km)	Heavily Cratered Areas Area = $1.7548 \cdot 10^5 \text{ km}^2$						Non Heavily Cratered Areas Area = $1.6030 \cdot 10^5 \text{ km}^2$					
	N(bin)	N(Degradation Classes)					N(bin)	N(Degradation Classes)				
		1	2	3	4	5		1	2	3	4	5
7.0 -- 9.9	65	5	20	27	12	1	64	6	13	26	16	3
9.9 -- 14.0	49	6	12	18	12	1	66	7	15	24	15	5
14.0 -- 19.8	26	3	6	11	5	1	34	5	8	6	8	7
19.8 -- 28.0	21	1	4	8	6	2	23	1	2	6	6	8
28.0 -- 39.6	15	1	0	6	4	4	12	1	0	4	2	5
39.6 -- 56.0	12	1	0	4	6	1	6	0	0	4	1	1
56.0 -- 79.2	10	1	2	4	2	1	0	0	0	0	0	0
79.2 -- 112.0	4	0	0	2	0	2	1	0	1	0	0	0
112.0 - 158.4	3	0	1	2	0	0	0	0	0	0	0	0
158.4 - 224.0	1	0	0	0	0	1	0	0	0	0	0	0

Table D12: Crater Statistics of Divided Sectors, Manzinus Area

Diameter Bin (km)	Heavily Cratered Areas Area = $1.2894 \cdot 10^5 \text{ km}^2$						Non Heavily Cratered Areas Area = $8.0882 \cdot 10^4 \text{ km}^2$					
	N(bin)	N(Degradation Classes)					N(bin)	N(Degradation Classes)				
		1	2	3	4	5		1	2	3	4	5
7.0 -- 9.9	25	0	11	13	1	0	23	2	4	11	6	0
9.9 -- 14.0	17	3	4	5	5	0	16	2	3	8	3	0
14.0 -- 19.8	14	5	5	3	1	0	12	2	2	4	3	1
19.8 -- 28.0	16	2	0	10	4	0	12	1	1	8	2	0
28.0 -- 39.6	16	1	3	9	2	1	2	0	0	1	1	0
39.6 -- 56.0	14	0	1	10	3	0	0	0	0	0	0	0
56.0 -- 79.2	5	0	1	3	1	0	0	0	0	0	0	0
79.2 -- 112.0	5	0	1	3	1	0	0	0	0	0	0	0

Table D13: Crater Statistics of Divided Sectors, Cuvier Area

Diameter Bin (km)	Heavily Cratered Areas Area = $1.3756 \cdot 10^5$ km <sup>2</sup>						Non Heavily Cratered Areas Area = $2.0788 \cdot 10^5$ km <sup>2</sup>					
	N(bin)	N(Degradation Classes)					N(bin)	N(Degradation Classes)				
		1	2	3	4	5		1	2	3	4	5
7.0 -- 9.9	73	9	24	32	8	0	105	11	16	46	24	8
9.9 -- 14.0	30	7	6	12	4	1	65	4	9	25	21	6
14.0 -- 19.8	25	4	3	12	3	3	56	7	9	27	10	3
19.8 -- 28.0	32	3	8	16	4	1	24	2	6	12	2	2
28.0 -- 39.6	24	0	3	16	4	1	17	2	4	7	3	1
39.6 -- 56.0	16	0	2	12	2	0	2	0	1	0	1	0
56.0 -- 79.2	10	0	1	9	0	0	0	0	0	0	0	0
79.2 -- 112.0	3	0	0	2	1	0	0	0	0	0	0	0



## Supporting Data for Tables D10-D13, Divided Sectors

Sources. Lunar Orbiter IV photographs, 20" by 24" positives and negative prints, Lunar Orbiter IV Atlases SP-206 (Bowker and Hughes, 1971) and SP-241 (Gutschewski et al., 1971), geologic maps (e.g. Cummings, 1972), the LPL Catalog of Lunar Craters (Wood and Andersson, 1978a), and charts from the System of Lunar Craters (Arthur et al., 1966).

Measuring Devices. Hand lens eyepiece and ruler, as previously described.

Location. The Werner, Cuvier, and Manzinus sectors are described in Strom (1977). The Werner area corresponds to region D012 described in Table 9. The Cuvier sector includes the northern two thirds of S0, S1, S2, S3 regions, while Manzinus comprises the southern third. These sectors were divided into heavily cratered regions (clusters of large craters) and non-heavily cratered regions (plains, terra, and isolated larger craters). Using finding charts from the lunar catalogs, the craters were located and assigned to Heavily Cratered (HC) or Non-Heavily Cratered (NHC) units.

Scale. Scales were determined for each photo or atlas picture needed to cover the three sectors. Scales of the atlas pictures usually given. Those for LO IV photos computed from the size of measured catalogued craters.

Cut Off Diameter. Statistics in the LPL Catalog are complete above 7 km diameter.

Degradation Classes. LPL classes 1 through 5 specified in the Catalog.

Supporting Data for Table D11, Werner Divided Sector

Sources. Lunar Orbiter IV prints: 88 H2, 88 H3, 112 H2, 100 H2, Atlas photos: LO IV 107 H3, 107 H2, 100 H3, 95 H3, 101 H1, 96 H1, 89 H1.

Location. Same as D012 region. LPL coordinates in Table D9. See also Fig. 50, and Strom (1977).

Supporting Data for Table D12, Manzinus Divided Sector

Sources. Lunar Orbiter IV prints: 82 H2, 82 H3; Atlas photos: 106 H2, 70 H2, 70 H3 (LO IV).

Location. See Strom (1977). S0, S123 regions with Eta from -0.97 to -0.93.

Supporting Data for Table D13, Cuvier Divided Sector

Sources. Lunar Orbiter IV prints: 82 H3, 94 H3, 112 H1, 107 H3, 100 H2, 88 H2, 118 H2, and geologic map of Clavius area (Cummings, 1972). Portions of LO IV 88 H3, and 112 H2 also used.

Location. See Strom (1977). S0, S123 regions with Eta from -0.93 to -0.7 on the meridian ( $X_i = 0$ ). Total area determined from bounding latitudes and longitudes of each sector. HC and NHC regions were blocked off, measured, and converted to  $\text{km}^2$  using the appropriate scale factor of the photo.

Table D14: Langrenus Secondary Study, Rings L0.5 to L1.0

	L0.5 (0.5 R -- <sub>3</sub> 1.0 <sub>2</sub> R) Area = $0.364 \cdot 10^3 \text{ km}^2$						L1.0 (1.0 R -- <sub>3</sub> 1.5 <sub>2</sub> R) Area = $3.211 \cdot 10^3 \text{ km}^2$					
Diameter Bin (km)	N(bin)	N(Degradation Classes)					N(bin)	N(Degradation Classes)				
		1	2	3	4	5		1	2	3	4	5
0.88 -- 1.24	8	0	0	4	3	1	25	0	0	4	14	7
1.24 -- 1.75	19	0	0	6	12	1	52	0	1	11	19	21
1.75 -- 2.47	8	0	1	4	2	1	39	0	1	7	8	23
2.47 -- 3.5	3	0	0	2	1	0	30	0	0	0	8	22
3.5 -- 4.95	1	0	0	1	0	0	16	0	0	1	5	10
4.95 -- 7.0	0	0	0	0	0	0	9	0	0	0	6	3

Table D14: Langrenus Secondary Study--Continued, Rings L1.5 to L2.0

	L1.5 (1.5 R -- 3.0 R) Area = $5.135 \cdot 10^3 \text{ km}^2$						L2.0 (2.0 R -- 2.5 R) Area = $6.918 \cdot 10^3 \text{ km}^2$					
Diameter Bin (km)	N(bin)	N(Degradation Classes)					N(bin)	N(Degradation Classes)				
		1	2	3	4	5		1	2	3	4	5
0.88 -- 1.24	28	0	2	5	10	11	33	0	1	0	18	14
1.24 -- 1.75	71	0	1	2	9	59	104	1	4	14	51	34
1.75 -- 2.47	81	1	1	4	12	63	126	2	2	17	66	39
2.47 -- 3.5	42	0	1	1	6	34	69	2	0	16	34	18
3.5 -- 4.95	42	0	0	2	16	24	37	0	4	16	13	4
4.95 -- 7.0	12	0	1	1	3	7	8	0	0	7	0	1
7.0 -- 9.9	0	0	0	0	0	0	4	0	1	0	1	2
9.9 -- 14.0	0	0	0	0	0	0	0	0	0	0	0	0
14.0 -- 19.8	0	0	0	0	0	0	0	0	0	0	0	0
19.8 -- 28.0	0	0	0	0	0	0	0	0	0	0	0	0
28.0 -- 39.6	1	0	0	1	0	0	1	0	0	1	0	0

Table D14: Langrenus Secondary Study--Continued, Rings L2.5 to L3.0

Diameter Bin (km)	L2.5 (2.5 R -- 3.0 R) Area = $9.153 \cdot 10^3 \text{ km}^2$						L3.0 (3.0 R -- 3.5 R) Area = $10.908 \cdot 10^3 \text{ km}^2$					
	N(bin)	N(Degradation Classes)					N(bin)	N(Degradation Classes)				
		1	2	3	4	5		1	2	3	4	5
0.88 -- 1.24	62	9	2	7	23	21	61	2	4	11	24	20
1.24 -- 1.75	145	6	1	11	70	57	172	9	9	15	65	73
1.75 -- 2.47	113	0	3	16	62	32	111	4	8	33	30	35
2.47 -- 3.5	72	1	4	23	31	13	48	1	9	8	15	15
3.5 -- 4.95	35	3	15	5	6	6	24	1	11	3	3	6
4.95 -- 7.0	11	1	4	4	0	2	8	3	2	3	0	0
7.0 -- 9.9	5	1	2	1	1	0	1	1	0	0	0	0
9.9 -- 14.0	0	0	0	0	0	0	0	0	0	0	0	0
14.0 -- 19.8	0	0	0	0	0	0	0	0	0	0	0	0
19.8 -- 28.0	0	0	0	0	0	0	0	0	0	0	0	0
28.0 -- 39.6	0	0	0	0	0	0	0	0	0	0	0	0
39.6 -- 56.0	1	0	0	1	0	0	0	0	0	0	0	0

Table D14: Langrenus Secondary Study--Continued, Rings L3.5 to L4.0

	L3.5 (3.5 R -- 4.0 R) Area = $12.75 \cdot 10^3 \text{ km}^2$						L4.0 (4.0 R -- 4.5 R) Area = $12.09 \cdot 10^3 \text{ km}^2$					
Diameter Bin (km)	N(bin)	N(Degradation Classes)					N(bin)	N(Degradation Classes)				
		1	2	3	4	5		1	2	3	4	5
0.88 -- 1.24	87	5	3	19	29	32	79	4	9	25	32	9
1.24 -- 1.75	197	8	9	41	70	69	157	5	18	50	41	44
1.75 -- 2.47	90	3	11	19	31	26	47	4	1	16	13	12
2.47 -- 3.5	28	3	1	4	6	14	8	0	1	2	1	4
3.5 -- 4.95	5	2	1	0	1	1	7	1	3	1	0	2
4.95 -- 7.0	1	0	0	0	0	1	0	0	0	0	0	0
7.0 -- 9.9	1	1	0	0	0	0	0	0	0	0	0	0
9.9 -- 14.0	1	1	0	0	0	0	1	0	0	0	0	1

438

Table D14: Langrenus Secondary Study--Continued, Rings L4.5 to L5.0

	L4.5 (4.5 R -- 5.0 R) Area = $12.99 \cdot 10^3 \text{ km}^2$						L5.0 (5.0 R -- 5.5 R) Area = $6.555 \cdot 10^3 \text{ km}^2$					
Diameter Bin (km)	N(bin)	N(Degradation Classes)					N(bin)	N(Degradation Classes)				
		1	2	3	4	5		1	2	3	4	5
0.88 -- 1.24	75	1	2	22	27	22	24	1	0	8	8	7
1.24 -- 1.75	112	4	7	33	35	33	49	0	3	10	15	21
1.75 -- 2.47	37	4	5	7	7	14	19	2	3	4	8	2
2.47 -- 3.5	9	1	1	0	0	7	5	1	0	2	2	0
3.5 -- 4.95	2	1	0	0	0	1	1	1	0	0	0	0
4.95 -- 7.0	2	1	1	0	0	0	0	0	0	0	0	0

Table D14: Langrenus Secondary Study--Continued, Ring L5.5

L5.5 (5.5 R -- 6.0 R) Area = $3.535 \cdot 10^3 \text{ km}^2$						
Diameter Bin (km)	N(bin)	N(Degradation Classes)				
		1	2	3	4	5
0.88 -- 1.24	14	0	0	7	5	2
1.24 -- 1.75	16	0	0	7	6	3
1.75 -- 2.47	4	0	1	2	1	0
2.47 -- 3.5	1	0	0	1	0	0
3.5 -- 4.95	0	0	0	0	0	0
4.95 -- 7.0	2	2	0	0	0	0

Support Data for Table D14, Langrenus Secondary Study

Source. Lunar Orbiter IV 53 H3, glossy print, 20" by 24".

Measuring Devices. Hand lens eyepiece with 1 cm scale, precision 0.2 mm, accuracy  $\pm 0.1$  mm; ruler, 30 cm, precision 1 mm, accuracy  $\pm 0.5$  mm; simple protractor, accuracy 1 degree.

Location. Principal ground point is ( $43.52^\circ \text{ E}$ ,  $71.01^\circ \text{ S}$ ). Southeast corner of photo contains the northwest quarter of Langrenus (Diameter 136 km, center located at ( $60.9^\circ \text{ E}$ ,  $8.9^\circ \text{ S}$ )).

Scale. Scale of 0.636 km/mm determined by measurement of cataloged craters. Scale assumed constant over the photograph.

Cut Off Diameter. 1.8 mm or 1.14 km.



Table D15: Langrenus Secondary Crater Study: Ring Totals

Diameter Bin (km)	Total N of craters $D \geq 1.14$ km within each ring $nR$ to $(n+0.5)R$ Areas of each section listed in last row										
	0.5	1.0	1.5	2.0	2.5	3.0	3.5	4.0	4.5	5.0	5.5
0.88 -- 1.24	8	25	28	33	62	61	87	79	75	24	14
1.24 -- 1.75	19	52	71	104	145	172	197	157	112	49	16
1.75 -- 2.47	8	39	81	126	113	111	90	47	37	19	4
2.47 -- 3.5	3	30	42	69	72	48	28	8	9	5	1
3.5 -- 4.95	1	16	42	37	35	24	5	7	2	1	0
4.95 -- 7.0	0	9	12	8	11	8	1	0	2	0	2
7.0 -- 9.9	0	0	0	4	5	1	1	0	0	0	0
9.9 -- 14.0	0	0	0	0	0	0	1	1	0	0	0
14.0 -- 19.8	0	0	0	0	0	0	0	0	0	0	0
19.8 -- 28.0	0	0	0	0	0	0	0	0	0	0	0
28.0 -- 39.6	0	0	1	1	0	0	0	0	0	0	0
39.6 -- 56.0	0	0	0	0	1	0	0	0	0	0	0
Area $\cdot 10^3$ km <sup>2</sup>	0.364	3.211	5.135	6.918	9.153	10.908	12.75	12.09	12.99	6.555	3.535

Supporting Data for Tables D14 and D15, Langrenus Secondary Study

Source. Lunar Orbiter IV 53 H3 glossy print, 20" by 24".

Measuring Devices. Hand lens eyepiece with 1 cm scale, precision 0.2 mm, accuracy  $\pm 0.1$  mm; ruler, 30 cm, precision 1 mm, accuracy  $\pm 0.5$  mm; simple protractor, precision, accuracy both 1 degree.

Location. Principal ground point of LO IV 53 is  $56.82^{\circ}$  E longitude,  $14.81^{\circ}$  S latitude. (Slant distance of spacecraft 2740.47 km.) Southeast corner of photo contains the northwest quarter of Langrenus. The center of Langrenus (136 km diameter) is located at ( $60.9^{\circ}$  E,  $8.9^{\circ}$  S).

Scale. Scale of 0.636 km/mm determined by measurements of cataloged craters on the photo. Scale assumed constant over the entire photograph.

Cut Off Diameter. 1.8 mm or 1.14 km.

Degradation Classes. LPL classification used, C1 freshest, C5 most degraded. Langrenus classed as C2 crater by Arthur et al. (1966).

General. The region around Langrenus was marked off into 0.5 R (R = 68 km) sections starting 0.5 R inward from the rim. The rim visible on the photo was fitted with a circle of radius approximately 68 km given the photo scale, 0.636 km/mm. Using the estimated center of Langrenus, circles of radii  $(n/2)R$  were marked onto an acetate sheet. Area of each ring was calculated by measuring the angles subtended and miscellaneous forms, then converted to  $\text{km}^2$  using the scale above. Diameter and degradation class of craters as large as the cut off diameter and larger were measured. The LO IV 53 H3 photo includes the Langrenus secondaries northwest of the primary on Mare

Supporting Data, Tables D14 and D15--Continued

Fecunditatis. No attempt was made to eliminate obvious small and large primaries from this study. Most of the craters in the diameter range 5-14 km are primaries; the three larger craters Langrenus B, C, and D are older primaries partially inundated by mare flooding.

Supporting Data for Tables D16 and D17, Copernicus Secondary Study

Source. Lunar Orbiter IV 121 H2 and 121 H3 used; both 20" by 24" glossy prints. Lunar Orbiter V M145 used for high resolution of ray area. Other information obtained from charts of Arthur et al. (1963) and Wood and Andersson (1978a).

Measuring Devices. As described in Langrenus study.

Location. Principal Ground Point of LO IV 121 is (16.79°W, 13.81°N). Center of Copernicus located at (20.0°W, 9.7°N). See illustration in text, Fig. 37.

Scale. Scale of 0.612 km/mm for LO IV 121 H2 and 0.621 km/mm for LO IV 121 H3 determined by measurements of cataloged craters. Scales assumed constant over the photograph.

Cut Off Diameter. 2.45 km (4 mm) out to 4 R from center of Copernicus; 1.84 km (3 mm) out to 6 R from center, and 1.22-1.24 km (2 mm) beyond that radii.

LO V M145 Scale and Cut Off Diameter. Ray area located 4 R to 5 R from center of Copernicus. Scale of photograph was 198 m/mm and cut off diameter was 3 mm or 594 m.

Degradation Classes. LPL classes C1 through C5 used as described in the text.

General. Annuli of one radius width ( $R = 47.5$  km) marked off from rim of Copernicus as illustrated in Fig. 37 of text. A0 designates center of crater; A1 the ring from 1R to 2 R; A4 the ring from 4 R to 5 R, and so forth. Data were taken in increments of theta (azimuth) around the annulus, and on equaradial bands about Eratosthe -

Supporting Data, Tables D16 and D17--Continued

nes or Pytheas within each Copernican annulus, so that effects of secondaries from those craters could be determined. Total area sampled was  $1.069 \cdot 10^5 \text{ km}^2$ . Areas of each annulus are given in Table D16.

Table D16: Areas of Copernican Annuli and Sampled Areas

Annuli	Span in Range R = 47.5 km	Area $\text{km}^2$	Cut Off Diameter	LO # Photo	Scale km/mm
A0	0 -- 1 R	$5.23 \cdot 10^3$	2.45	IV-121 H2	0.612
A1	1 R -- 2 R	$8.442 \cdot 10^3$	2.45	IV-121 H2	0.612
A2	2 R -- 3 R	$1.153 \cdot 10^4$	2.45	IV-121 H2	0.612
A3	3 R -- 4 R	$1.493 \cdot 10^4$	2.45	IV-121 H2	0.612
A4	4 R -- 5 R	$1.663 \cdot 10^4$	1.84	IV-121 H2	0.612
A5	5 R -- 6 R	$1.342 \cdot 10^4$	1.84	IV-121 H2 121 H3	0.612 0.621
A6	6 R -- 7 R	$1.275 \cdot 10^4$	1.22- 1.24	IV-121 H2 121 H3	0.612 0.621
A7	7 R -- 8 R	$1.227 \cdot 10^4$	1.22- 1.24	IV-121 H2 121 H3	0.612 0.621
A8	8 R -- 9 R	$1.166 \cdot 10^4$	1.22- 1.24	IV-121 H3	0.621
A9	9 R -- 10 R	$1.168 \cdot 10^4$	1.22- 1.24	IV-121 H3	0.621
East ray/ West ray	4 R -- 5 R	$4.152 \cdot 10^3$ $2.165 \cdot 10^3$	0.594	V-M145	0.198

Table D17: Secondary Study of Copernicus, Annuli Totals

Diameter Bin (km)	Total number of craters within bin, within each annulus											
	A0	A1	A2	A3	A4	A5	A6	A6	A7	A7	A8	A9
1.24 -- 1.75	1	0	2	0	28	9	2	75	26	156	119	148
1.75 -- 2.47	4	8	2	2	248	148	93	21	11	63	31	23
2.47 -- 3.5	7	95	286	257	123	56	30	6	1	10	2	3
3.5 -- 4.95	1	39	52	60	24	5	1	0	0	3	0	1
4.95 -- 7.0	0	9	11	11	3	2	2	0	0	0	0	0
7.0 -- 9.9	0	2	2	0	0	0	0	0	0	0	0	1
9.9 -- 14.0	0	1	0	0	0	0	0	0	0	0	0	0
Area · 10 <sup>3</sup> km <sup>2</sup>	5.230	8.442	11.534	14.93	16.63	13.42	5.849	6.902	0.773	11.50	11.66	
							12.75		12.27		11.68	

Table D18: Area 1 -- Heavily Cratered Area

FDS 27390, 27392, 27393 Area $1.6559 \cdot 10^5 \text{ km}^2$						
Diameter Bin (km)	N(bin)	N(Degradation Classes)				
		1	2	3	4	5
4.95 -- 7.0	278	3	19	106	100	49
7.0 -- 9.9	597	13	35	216	224	109
9.9 -- 14.0	112	7	11	19	41	34
14.0 -- 19.8	34	3	6	5	7	13
19.8 -- 28.0	15	1	1	2	9	2
28.0 -- 39.6	12	1	5	3	0	3
39.6 -- 56.0	10	0	2	5	0	3
56.0 -- 79.2	4	0	0	1	2	1
79.2 -- 112.0	4	0	0	2	2	0
112.0 -- 158.4	3	0	0	1	2	0
158.4 -- 224.0	2	0	0	1	1	0

Supporting Data for Table D18, Area HCA 1 on Mercury

Source. Flight Data System (FDS) images 27390, 27392, 27393, and 27465 from Mariner 10 first encounter at Mercury. Mariner 10 photographs processed at Jet Propulsion Laboratory with computer enhancement (high pass filter). Additional copies printed at LPL. All supporting data given in Mariner SEDR volumes.

Location. General area of HCA 1 is bounded by latitudes  $-41^\circ$  to  $-55^\circ$ , and longitudes  $15^\circ \text{ W}$  to  $33^\circ \text{ W}$  (see Fig. 10 of text). The center

Table D18: Area 1 -- Heavily Cratered Area, High Resolution

FDS 27465 Area $8.804 \cdot 10^3 \text{ km}^2$						
Diameter Bin (km)	N(bin)	N(Degradation Classes)				
		1	2	3	4	5
1.24 -- 1.75	97	0	1	29	41	26
1.75 -- 2.47	218	0	8	59	108	42
2.47 -- 3.5	119	0	2	39	55	23
3.5 -- 4.95	77	1	1	23	32	17
4.95 -- 7.0	59	0	1	18	30	10
7.0 -- 9.9	24	1	0	5	13	5
9.9 -- 14.0	6	0	0	2	1	3
14.0 -- 19.8	2	0	1	0	0	1
19.8 -- 28.0	1	0	0	0	0	1
28.0 -- 39.6	1	0	0	0	0	1

Supporting Data--Continued

of each image is given in Table D24.

Scale. Scale determined for each photo by the ratio of size of pixels in mm (measured along the base of the photo) to the published "Resolution" or pixel size (PIX SZ) in km/pixel. Each Mariner photo is 832 pixels by 700 TV lines. Tick marks of 5 pixels occur at photo base.

Measuring Devices. Hand lens eyepiece of 1 cm scale, precision of 0.2 mm, accuracy  $\pm 0.1$  mm; ruler, 30 cm, precision 1 mm, accuracy  $\pm 0.5$  mm. Crater diameters measured parallel to limb.



Table D19: Area 2 -- Heavily Cratered Area and Surrounding Inter crater Plains

Diameter Bin (km)	Heavily Cratered Area Area = $8.523 \cdot 10^4$ km <sup>2</sup>						Inter crater Plains Area Area = $1.397 \cdot 10^5$ km <sup>2</sup>					
	N(bin)	N(Degradation Classes)					N(bin)	N(Degradation Classes)				
		1	2	3	4	5		1	2	3	4	5
4.95 -- 7.0	487	5	24	141	197	120	893	38	81	261	262	251
7.0 -- 9.9	325	10	24	88	125	78	342	21	37	87	83	111
9.9 -- 14.0	91	1	8	26	29	27	77	11	10	15	19	22
14.0 -- 19.8	19	2	5	2	3	7	18	4	2	1	1	10
19.8 -- 28.0	6	0	3	1	1	1	7	1	0	0	1	5
28.0 -- 39.6	6	1	0	1	1	3	5	1	1	1	0	2
39.6 -- 56.0	1	0	1	0	0	0	2	1	0	0	0	1
56.0 -- 79.2	4	0	0	2	2	0	3	0	0	0	3	0
79.2 -- 112.0	1	0	0	0	1	0	2	0	0	0	1	1
112.0 - 158.4	3	0	0	3	0	0	0	0	0	0	0	0

Supporting Data for Table D19, Area HCA 2 and ICP 2

Source. FDS 27395, 27386. Original prints and negatives prepared from real time transmissions of Mariner 10 data; hard copy produced at JPL/IPL, with copies made at LPL in Tucson.

Measuring Devices. As described above.

Location. General boundaries of HCA 2 are  $-44^{\circ}$  to  $-48^{\circ}$  latitude and  $35^{\circ}$ W to  $46^{\circ}$ W longitude. Boundaries of ICP 2 are  $-40^{\circ}$  to  $-50^{\circ}$  latitude, and  $33.5^{\circ}$ W to  $57.5^{\circ}$ W longitude. Region illustrated in Fig. 10 of text. Areas and locations of image centers given in Table D24.

Scale. Scale (Table D24) derived from measured pixel width, mm/pixel, ratioed to the published resolution, or km/pixel. Scale assumed to be constant across the image. (This assumption may be unsatisfactory for images containing the limb.)

Cut Off Diameter. For HCA 2, 2.4 to 2.5 mm (5.6 km); for ICP 2, 2 mm or 4.7 km cut off diameter was used.

Degradation Classes. The mercurian degradation classes correspond to those of the Moon (C1 to C5) in general characteristics. More subtle differences noted in Chapter 2 of text, Sections 1 and 2.

Note. Much of the general data in this section applies to all selected area supporting information. Table D24 lists cut off diameters, scales, areas, location of center of image, and resolution or pixel scale. Fig. 10 of text illustrates the selected area location on Mercury's first quadrant.

Table D20: Area 2 Intercrater Plains Within Eight Subregions

Diameter Bin (km)	N(bin)	Number Within Each Region of Intercrater Plains								N(bin) without sec.*
		1	2	3	4	5	6	7	8	
4.95 -- 7.0	893	98	83	74	161	151	185	49	92	714
7.0 -- 9.9	342	32	29	42	74	64	62	11	28	263
9.9 -- 14.0	77	9	5	6	26	13	12	1	5	67
14.0 -- 19.8	18	2	3	2	2	1	5	1	2	17
19.8 -- 28.0	7	0	1	0	4	0	0	0	2	7
28.0 -- 39.6	5	1	0	1	1	1	0	1	0	5
39.6 -- 56.0	2	0	0	0	0	1	1	0	0	2
56.0 -- 79.2	3	0	0	1	0	1	1	0	0	3
79.2 -- 112.0	2	0	0	2	0	0	0	0	0	2
Area · 10 <sup>4</sup> km <sup>2</sup>	13.971	1.280	1.922	1.578	3.822	2.285	1.658	0.543	0.882	13.971

\* Total number of craters in bin without those arranged in chains or clusters (i.e. secondaries).

Supporting Data for Table D20, Subregions of Area ICP 2

Source. FDS 27395, as described above.

Measuring Devices. Described above.

Location. Area surrounding HCA 2 divided into 8 subregions along rough plains boundaries. The dominant plains and crater units of each region are listed below, as determined in subsequent geologic mapping. Areas of each subdivision are given in Table D20. Total area is  $1.397 \cdot 10^5 \text{ km}^2$ . See the accompanying figure (Fig. D1) corresponding to Fig. 63 of text.

Scale, Cut Off Diameter, Degradation Classes. As described above and in Table D24.

Subregion	Major Units Mapped
1	C3 > P4 >> P3
2	P2 >> P4 > P5
3	C4 > C5 ~ P4
4	P3 >> P2 ~ P4
5	C3, C2 >> P3 ~ P2
6	P4 >> P3 > C4
7	P4
8	C4 >> P3

Table D21: Discovery Scarp Area -- Inter crater Plains

Diameter Bin (km)	West of Discovery Scarp Area = $3.520 \cdot 10^4 \text{ km}^2$						East of Discovery Scarp Area = $2.908 \cdot 10^4 \text{ km}^2$					
	N(bin)	N(Degradation Classes)					N(bin)	N(Degradation Classes)				
		1	2	3	4	5		1	2	3	4	5
3.5 -- 4.95	689	11	32	160	256	230	614	11	45	211	220	127
4.95 -- 7.0	183	1	14	36	67	64	173	5	19	57	51	41
7.0 -- 9.9	41	2	2	7	10	20	28	0	1	13	10	4
9.9 -- 14.0	13	2	0	1	4	6	7	1	0	2	2	2
14.0 -- 19.8	3	0	0	0	0	3	5	0	1	1	1	2
19.8 -- 28.0	3	0	0	1	1	1	3	2	0	0	0	1
28.0 -- 39.6	4	0	0	2	0	2	3	0	1	0	1	1
39.6 -- 56.0	1	0	0	1	0	0	0	0	0	0	0	0
56.0 -- 79.2	1	0	0	1	0	0	0	0	0	0	0	0

Supporting Data for Table D21, Discovery Scarp ICP Area

Source. Mosaic of Discovery Scarp made by JPL for images FDS 27386, 27393, 27397-9, and 528881-4. Reproduction from negative made at LPL.

Location. General boundaries are  $31^{\circ}$  W to  $45^{\circ}$  W longitude, and  $-47^{\circ}$  to  $-57^{\circ}$  latitude. Locations of centers of each photo are listed below, as found in the Mariner 10 SEDR volumes, encounters 1 and 3.

Measuring Devices. As described above.

Scale. Derived scale of 1.7187 km/mm; determined from published diameter of 55 km for Rameau, a crater in the center of the mosaic. Resolution varies across the photo (Fig. 8, text). Scale factor is assumed to remain constant across the mosaic.

Cut Off Diameter, Degradation Classes. As described above.

FDS No.	Location of Center	Pixel Size*	TV Line Size*
27386	( $36^{\circ}26$ W, $-45^{\circ}77$ )	.62	.56
27393	( $20^{\circ}00$ W, $-47^{\circ}37$ )	.52	.51
27397	( $18^{\circ}29$ W, $-55^{\circ}05$ )	.50	.56
27398	( $31^{\circ}41$ W, $-55^{\circ}61$ )	.53	.56
27399	( $45^{\circ}18$ W, $-54^{\circ}41$ )	.60	.60
528881	( $36^{\circ}91$ W, $-49^{\circ}69$ )	.37	.36
528882	( $46^{\circ}54$ W, $-52^{\circ}99$ )	.41	.43
528883	( $30^{\circ}97$ W, $-50^{\circ}42$ )	.33	.34
528884	( $38^{\circ}69$ W, $-53^{\circ}41$ )	.36	.38

\* In km.

Table D22: Area 5 and 5', Kuiper Region -- Heavily Cratered Area

Diameter Bin (km)	Area 5 $6.7045 \cdot 10^4 \text{ km}^2$						Area 5' $6.9240 \cdot 10^4 \text{ km}^2$					
	N(bin)	N(Degradation Classes)					N(bin)	N(Degradation Classes)				
		1	2	3	4	5		1	2	3	4	5
4.95 -- 7.0	246	0	4	71	99	72	(20	2	0	2	11	5)*
7.0 -- 9.9	196	0	9	39	84	64	290	0	12	76	116	74
9.9 -- 14.0	86	0	3	30	36	17	54	2	3	15	17	17
14.0 -- 19.8	17	0	1	5	6	5	24	0	5	2	7	10
19.8 -- 28.0	5	0	0	3	1	1	7	1	0	0	1	5
28.0 -- 39.6	2	0	1	0	0	1	5	1	0	2	0	2
39.6 -- 56.0	6	0	0	3	2	1	1	0	0	0	0	1
56.0 -- 79.2	4	0	1	3	0	0	2	1	0	1	0	0
79.2 -- 112.0	0	0	0	0	0	0	1	0	0	1	0	0
112.0 -- 158.4	1	0	0	0	1	0	1	0	0	0	1	0
158.4 -- 224.0	0	0	0	0	0	0	1	0	0	1	0	0

Supporting Data for Table D22, HCA 5+5'

Source. FDS 27362 for Heavily Cratered Area 5 (HCA 5); FDS 27362 and 27363 for HCA 5'. Data obtained as noted above.

Measuring Devices. As described above.

Location. Kuiper Area HCA 5 is bounded by longitudes  $23.5^{\circ}$ W to  $29.5^{\circ}$ W, and by latitudes  $-7.5^{\circ}$  to  $-15.0^{\circ}$ . HCA 5', further to the west, is bounded by longitudes  $29^{\circ}$ W to  $37^{\circ}$ W, and by latitudes  $-8^{\circ}$  to  $-15.0^{\circ}$ . Center of each frame given in Table D24.

Scale. See Table D24. Determined as described above, and assumed to be constant over the picture (HCA region).

Cut Off Diameter. 2.5 mm (6.5 km) for FDS 27362, and 2.2-2.4 mm (or 7.05-7.69 km) for FDS 27363.

Degradation Classes. As described above.

\* Incomplete data set within diameter bin.



Table D23: Area 66' -- Heavily Cratered Area and Surrounding Inter crater Plains

Diameter Bin (km)	Heavily Cratered Area 66' Area = $1.7595 \cdot 10^5 \text{ km}^2$						Inter crater Plains 66' Area $1.0175 \cdot 10^5 \text{ km}^2$					
	N(bin)	N(Degradation Classes)					N(bin)	N(Degradation Classes)				
		1	2	3	4	5		1	2	3	4	5
4.95 -- 7.0	249	2	6	79	114	48	201	3	3	39	91	66
7.0 -- 9.9	535	4	24	156	230	121	478	4	4	102	175	190
9.9 -- 14.0	116	6	4	31	45	30	120	3	3	32	39	43
14.0 -- 19.8	32	0	3	10	10	9	28	0	1	5	13	9
19.8 -- 28.0	16	2	8	2	2	2	11	1	2	2	4	2
28.0 -- 39.6	12	1	6	0	1	4	1	0	1	0	0	0
39.6 -- 56.0	6	0	0	2	3	1	0	0	0	0	0	0
56.0 -- 79.2	6	0	2	2	2	0	1	0	0	0	1	0
79.2 -- 112.0	6	0	0	3	3	0	1	0	0	1	0	0
112.0 - 158.4	2	0	1	0	1	0	0	0	0	0	0	0

Supporting Data for Table D23, HCA 66' and ICP 6

Source. FDS 27358. Processing as described above.

Measuring Devices. As described above.

Location. Center of photo at (25°68 W, -0°05). See Fig. 10. HCA 66' includes, but lies east of, Lu Hsun. The ICP region includes the C5' basin northeast of Homer (Fig. 85, text), although the basin was not recognized when these statistics were compiled.

Scale. Scale of 2.754 km/mm derived from the image's pixel length and the published resolution or pixel size (km/pixel). Pixel Size = 0.74; TV Line Size = 0.64. Resolution 0.745 km/pixel.

Cut Off Diameter. 2.4 mm or 6.6 km.

Degradation Classes. LPL classes C1 through C5, modified for Mercury as described above and in text Chapter 2.

Area and Units Included. HCA 6 Area =  $1.54 \cdot 10^5 \text{ km}^2$ . HCA 6' area =  $2.195 \cdot 10^4 \text{ km}^2$ . Total HCA 66' is  $1.7595 \cdot 10^5 \text{ km}^2$ . ICP 6 has an area of  $1.0175 \cdot 10^5 \text{ km}^2$ . Major units within the heavily cratered area are C2, C3, C4, C1, and some P3 plains interior to craters. The inter-crater plains sector is comprised mainly of P2, P5, P4, and P3 units.

Table D24: Supporting Data for Selected Regions of Mercury

Selected Area Name	FDS No.	Location of Center (Long., Lat.)	Resolution Pixel Size (km/pixel)	Derived Scale (km/mm)	Cut Off Diameter		Area (km <sup>2</sup> )
					mm	km	
HCA 1	27390	(30°46 W, -45°61)	0.577	2.715	2.4	6.5	9.698 · 10 <sup>4</sup>
HCA 1	27392	(16°76 W, -49°88)	0.517	1.86	3.6	6.7	5.483 · 10 <sup>4</sup>
HCA 1	27393	(20°00 W, -47°37)	0.527	1.894	3.5	6.5	1.378 · 10 <sup>4</sup>
HCA 1	27465	(17°97 W, -44°23)	0.199	0.751	2	1.5	8.804 · 10 <sup>3</sup>
HCA 2	27395	(44°68 W, -44°43)	0.65	2.342	2.4	5.6	8.144 · 10 <sup>4</sup>
HCA 2	27386	(36°26 W, -45°77)	0.62	2.232	2.0	4.5	3.784 · 10 <sup>3</sup>
ICP 2	27395	(44°68 W, -44°43)	0.65	2.342	2.0	4.7	1.397 · 10 <sup>5</sup>
Dis. Sc. E	Mosaic	Rameau (38°W, -54°)	variable	1.719	2.0	3.4	2.908 · 10 <sup>4</sup>
Dis. Sc. W	Mosaic	Rameau (38°W, -54°)	variable	1.719	2.0	3.4	3.52 · 10 <sup>4</sup>
HCA 5	27362	(27°28 W, -10°50)	0.726	2.63	2.5	6.5	6.704 · 10 <sup>4</sup>
HCA 5'	27362	(27°28 W, -10°50)	0.726	2.63	2.5	6.5	2.243 · 10 <sup>4</sup>
HCA 5'	27363	(40°47 W, -10°14)	0.87	3.204	2.2	7.0	4.681 · 10 <sup>4</sup>
HCA 66'	27358	(25°68 W, -0°05)	0.745	2.754	2.4	6.6	1.760 · 10 <sup>5</sup>
ICP 66'	27358	(25°68 W, -0°05)	0.745	2.754	2.4	6.6	1.018 · 10 <sup>5</sup>

Table D25: Combined Statistics for Heavily Cratered Regions

Diameter Bin (km)	N(bin)	N(Degradation Classes)					Surface Area (km <sup>2</sup> )
		1	2	3	4	5	
4.95 -- 7.0	1260	10	53	397	510	289	$4.938 \cdot 10^5$
7.0 -- 9.9	1943	36	104	575	779	446	$5.6305 \cdot 10^5$
9.9 -- 14.0	459	16	29	121	168	125	$5.6305 \cdot 10^5$
14.0 -- 19.8	126	5	20	24	33	44	$5.6305 \cdot 10^5$
19.8 -- 28.0	49	4	12	8	14	11	$5.6305 \cdot 10^5$
28.0 -- 39.6	37	4	12	6	2	13	$5.6305 \cdot 10^5$
39.6 -- 56.0	24	0	3	10	5	6	$5.6305 \cdot 10^5$
56.0 -- 79.2	20	1	3	9	6	1	$5.6305 \cdot 10^5$
79.2 -- 112.0	12	0	0	6	6	0	$5.6305 \cdot 10^5$
112.0 - 158.4	10	0	1	4	5	0	$5.6305 \cdot 10^5$
158.4 - 224.0	3	0	0	2	1	0	$5.6305 \cdot 10^5$

Supporting Information

Sources, Measuring Devices, Locations, and so forth are given in the preceding tables, Table D24 in particular. Cut Off Diameters vary, but statistics are complete above 7.0 km.

Table D26: Combined Statistics for Intercrater Plains Regions

Diameter Bin (km)	N(bin)	N(Degradation Classes)					Surface Area (km <sup>2</sup> )
		1	2	3	4	5	
3.5 -- 4.95	1303	22	77	371	476	357	6.4276 · 10 <sup>4</sup>
4.95 -- 7.0	1450	47	117	393	471	422	3.0572 · 10 <sup>4</sup>
7.0 -- 9.9	889	27	44	209	278	325	3.0572 · 10 <sup>4</sup>
9.9 -- 14.0	217	17	13	50	64	73	3.0572 · 10 <sup>4</sup>
14.0 -- 19.8	54	4	4	7	15	24	3.0572 · 10 <sup>4</sup>
19.8 -- 28.0	24	4	2	3	6	9	3.0572 · 10 <sup>4</sup>
28.0 -- 39.6	13	1	3	3	1	5	3.0572 · 10 <sup>4</sup>
39.6 -- 56.0	3	1	0	1	0	1	3.0572 · 10 <sup>4</sup>
56.0 -- 79.2	5	0	0	1	4	0	3.0572 · 10 <sup>4</sup>
79.2 -- 112.0	3	0	0	1	1	1	3.0572 · 10 <sup>4</sup>
112.0 - 158.4	0	0	0	0	0	0	3.0572 · 10 <sup>4</sup>

Supporting Information

Supporting data is given in the previous tables and text. Note that cut off diameters vary from 3.4 km to 6 km (Table D24), such that the 7.0 km to 9.9 km bin is generally complete. Location of intercrater regions shown in Fig. 10 of text.

Table D27: Combined Selected Area Statistics

Diameter Bin (km)	N(bin)	N(Degradation Classes)					Surface Area (km <sup>2</sup> )
		1	2	3	4	5	
3.5 -- 4.95	1303	22	77	371	476	357	$6.4275 \cdot 10^4$
4.95 -- 7.0	2710	57	170	790	981	711	$7.995 \cdot 10^5$
7.0 -- 9.9	2832	63	148	784	1057	771	$8.6877 \cdot 10^5$
9.9 -- 14.0	676	33	42	171	232	198	$8.6877 \cdot 10^5$
14.0 -- 19.8	180	9	24	31	48	68	$8.6877 \cdot 10^5$
19.8 -- 28.0	73	8	14	11	20	20	$8.6877 \cdot 10^5$
28.0 -- 39.6	50	5	15	9	3	18	$8.6877 \cdot 10^5$
39.6 -- 56.0	27	1	3	11	5	7	$8.6877 \cdot 10^5$
56.0 -- 79.2	24	1	3	10	9	1	$8.6877 \cdot 10^5$
79.2 -- 112.0	15	0	0	7	7	1	$8.6877 \cdot 10^5$
112.0 - 158.4	10	0	1	4	5	0	$8.6877 \cdot 10^5$
158.4 - 224.0	3	0	0	2	1	0	$8.6877 \cdot 10^5$

Supporting Information

Source. FDS Mariner 10 pictures: 27390, 27392, 27393, 27465, 27386, 27395, 27362, 27363, 27358, and the Discovery Scarp Mosaic.

Location. See Fig. 10 in text. Other information given in the individual tables used in this compilation. Details of imagery given in Table D24.

Table D28: General Geologic Map Crater Statistics

$$\text{Area} = 1.0284 \cdot 10^7 \text{ km}^2$$

Diameter Bin (km)	Number of Craters in bin	N(Degradation Classes)					5'
		1	2	3	4	5	
28.0 -- 39.6	174	29	45	55	32	12	2
39.6 -- 56.0	241	19	43	95	42	29	13
56.0 -- 79.2	180	9	32	51	36	29	23
79.2 -- 112.0	100	6	17	37	20	13	7
112.0 - 158.4	56	2	6	15	18	11	4
158.4 - 224.0	26	0	6	4	9	6	1
224.0 - 316.8	7	0	0	2	2	0	3
316.8 - 448.0	7	0	0	0	3	0	4
448.0 - 633.6	2	0	0	0	0	1	1

Supporting Data for Table D28, General Geologic Map

Source. Geologic map base--a 24" by 18" photomosaic of the incoming side (first quadrant) of Mercury, "Perspective Projection," assembled by JPL, reproduced at the Lunar and Planetary Lab. Composed of 70 medium to high resolution Mariner 10 pictures; limb areas and northern latitudes west of 40°W to 50°W received poorer, low resolution coverage.

Location. Outer boundary of Fig. 10 in text. Total area mapped and used for crater statistics was  $1.0284 \cdot 10^7 \text{ km}^2$ . The hilly and lineated region comprises  $5.7438 \cdot 10^5 \text{ km}^2$  (Table D29).

Supporting Data for Table D28--Continued

Measuring Devices. Hand lens eyepiece with 1 cm scale, precision 0.2 mm, accuracy  $\pm$  0.1 mm; and ruler, 30 cm scale, precision 1 mm, accuracy  $\pm$  0.5 mm. Accuracy of diameter of sharp, fresh crater better than that of more degraded, less distinct crater especially C5 and C5'. Measurements of larger FDS photos or the Shaded Relief Maps helped verify measurements on the photomosaic.

Scale. Scale of 7.74 km/mm (or 1:7,740,000 on the Perspective Projection) determined from measured diameter of craters near the center of Mercury's disk which were previously determined by the pixel width in mm and km method described above. Changes in scale across the photo are minimal if craters are measured parallel to the limb. See Appendix C.

Cut Off Diameter. Craters over 40 km were measured and compiled. Some smaller ones are recorded. 40 km corresponds to 5 mm on the photomosaic.

Degradation Classes. Classes C1 (freshest) through C5 (most degraded) and C5' (vague circular depression, queried) used in the geologic mapping. Degradation classes correspond to those used in previous tables; Chapter 2, Sections 1 and 3 describe the degradation criteria.

Note. These supporting data apply to all the following tables. Areas of each surface are given in the respective crater statistics.



Table D29: Hilly and Lineated Area of General Geologic Map

$$\text{Area} = 5.7438 \cdot 10^5 \text{ km}^2$$

Diameter Bin (km)	Number of Craters in bin	N(Degradation Classes)					5'
		1	2	3	4	5	
28.0 -- 39.6	15	2	2	6	5	0	0
39.6 -- 56.0	11	1	0	4	2	3	1
56.0 -- 79.2	8	0	2	2	1	2	1
79.2 -- 112.0	12	0	0	2	4	4	2
112.0 - 158.4	2	0	0	2	0	0	0
158.4 - 224.0	3	0	1	0	1	1	0

Supporting Data for Table D29, Hilly and Lineated Area

Source. Mariner 10 photomosaic of incoming side, as described above.

Location. Region bounded by the hilly and lineated terrain shown as diagonal-line area of Fig. 10.

Other Data. See supporting data of Table D28 above.

Table D30: Restricted Area Geologic Map Crater Statistics

$$\text{Area} = 4.9852 \cdot 10^6 \text{ km}^2$$

Diameter Bin (km)	Number of Craters in Bin	N(Degradation Classes)					
		1	2	3	4	5	5'
28.0 -- 39.6	103	19	23	33	20	6	2
39.6 -- 56.0	131	8	20	52	19	21	11
56.0 -- 79.2	109	8	16	31	24	15	15
79.2 -- 112.0	65	5	9	25	15	7	4
112.0 - 158.4	32	2	4	6	13	4	3
158.4 - 224.0	9	0	2	1	3	3	0
224.0 - 316.8	4	0	0	2	1	0	1
316.8 - 448.0	5	0	0	0	1	0	4
448.0 - 633.6	0	0	0	0	0	0	0

Supporting Data for Table D30, Restricted Area Map

Location. See the footprint map, Fig. 10. A more restricted area was outlined to approximate the "Discriminability Limits" cited or used by other authors (Murray et al., 1974a,b; Trask and Guest, 1975; and Wood et al., 1977). Boundaries were moved inward from the terminator, limb, and north and south latitudes as described in text, Chapter 2, Section 2.

Other Data. See supporting data of Table D28 above.

Table D31: Bach Quadrangle Statistics

$$\text{Area} = 8.0998 \cdot 10^5 \text{ km}^2$$

Diameter Bin (km)	Number of Craters in Bin	N(Degradation Classes)					5'
		1	2	3	4	5	
28.0 -- 39.6	10	1	4	2	2	1	0
39.6 -- 56.0	19	0	2	9	5	1	2
56.0 -- 79.2	14	0	2	6	3	3	0
79.2 -- 112.0	2	0	1	0	1	0	0
112.0 - 158.4	4	0	1	1	0	2	0
158.4 - 224.0	4	0	1	2	0	1	0

Supporting Data for Table D31, Bach Quadrangle

Location. Shaded Relief Map H-15 Quadrangle from latitudes  $-90^\circ$  to  $-70^\circ$ . Craters greater than 40 km were sampled on the corresponding area of the photomosaic.

Other Data. See supporting data for Table D28.

Table D32: Discovery Quadrangle Statistics

$$\text{Area} = 3.9197 \cdot 10^6 \text{ km}^2$$

Diameter Bin (km)	Number of Craters in Bin	N(Degradation Classes)					
		1	2	3	4	5	5'
28.0 -- 39.6	72	14	13	24	17	4	0
39.6 -- 56.0	98	8	24	32	19	13	3
56.0 -- 79.2	71	5	9	16	22	9	10
79.2 -- 112.0	40	2	2	15	11	6	4
112.0 - 158.4	18	0	2	5	7	4	0
158.4 - 224.0	11	0	2	1	6	1	1
224.0 - 316.8	3	0	0	0	2	0	1
316.8 - 448.0	0	0	0	0	0	0	0
448.0 - 633.6	1	0	0	0	0	0	1

Supporting Data for Table D32, Discovery Quadrangle

Location. Shaded Relief Map H-11, Latitudes  $-70^\circ$  to  $-25^\circ$ .

This area corresponds to the sampled area of the photomosaic.

Other Data. See Table D28, supporting data.

Table D33: Kuiper Quadrangle Statistics

$$\text{Area} = 4.4327 \cdot 10^6 \text{ km}^2$$

Diameter Bin (km)	Number of Craters in Bin	N(Degradation Classes)					5'
		1	2	3	4	5	
28.0 -- 39.6	79	13	22	26	11	6	1
39.6 -- 56.0	99	5	10	45	17	15	7
56.0 -- 79.2	81	5	16	22	10	16	12
79.2 -- 112.0	44	3	9	17	8	6	1
112.0 - 158.4	30	2	2	9	9	4	4
158.4 - 224.0	10	0	2	1	3	4	0
224.0 - 316.8	4	0	0	2	0	0	2
316.8 - 448.0	6	0	0	0	2	0	4
448.0 - 633.6	1	0	0	0	0	1	0

Supporting Data for Table D33, Kuiper Quadrangle

Location. Area bounded between  $-25^\circ$  and  $+25^\circ$  latitude on the Shaded Relief Map H-6 sampled on the photomosaic.

Other Data. See Table D28, supporting data.

Table D34: Victoria Quadrangle Statistics

$$\text{Area} = 9.1564 \cdot 10^5 \text{ km}^2$$

Diameter Bin (km)	Number of Craters in Bin	N(Degradation Classes)					
		1	2	3	4	5	5'
28.0 -- 39.6	12	0	5	4	1	1	1
39.6 -- 56.0	24	5	8	8	2	0	1
56.0 -- 79.2	11	0	4	6	0	1	0
79.2 -- 112.0	13	1	5	5	0	1	1
112.0 -- 158.4	4	0	2	0	1	1	0
158.4 -- 224.0	1	0	1	0	0	0	0

## Supporting Data for Table D34, Victoria Quadrangle

Location. Area bounded between latitudes  $+25^\circ$  to  $+45^\circ$  on Shaded Relief Map H-2 corresponds to the sampled region of the photomosaic.

Other Data. See supporting data for Table D28. Craters on the photomosaic which fall into the Michelangelo and Beethoven Quadrangles (H-12 and H-7, respectively) are very few and not recorded in this set of tables. For more information, and for statistics of the quadrangles bounded within the Restricted Area Map, please notify the author. Areas in which crater statistics were compiled are the same areas in which plains areal measurements were made, using a planimeter on the base Shaded Relief Maps.

## APPENDIX E

### ESTIMATED THICKNESS OF EJECTA DEPOSITS COMPARED TO CRATER RIM HEIGHTS

Using Gault et al.'s (1975) formula for the radial extent of the continuous ejecta blanket on Mercury,

$$R_{cb} / D_r = 0.44 - 10^{-3} \cdot D_r$$

where  $R_{cb}$  is the width of the continuous ejecta blanket, one calculates that area of the continuous deposits varies from 2.24 to 0.64 times the crater's area for those of diameter 40 km to 300 km. Because crater boundaries on the geologic map include the detectable continuous ejecta blanket, plains exterior to these deposits must consist of farther-flung ejecta (of that or other craters), or volcanic deposits flooding the intervening areas. Ejecta models are explored here.

Oberbeck (1975) notes that 50% of terrestrial craters' (explosion or lab impact) ejecta is deposited in the continuous ejecta blanket within two radii from the crater center, and the other 25% (lab impact) to 40% (explosion) is deposited between two to four radii from the crater center. These limits are close to those observed for mercurian craters; the edge of the continuous ejecta blanket lies approximately 1.88R from the primary center and the zone of greatest areal density of secondaries lies 2.5R from the center

(Gault et al., 1975). Oberbeck's model can be tentatively applied to mercurian crater deposits, as follows.

If 50% of the ejected volume falls within a distance of  $2R$  to some average depth (cylindrical disk model), then the 40% of the ejecta which falls within  $4R$ , over four times the area, has an average depth one-fifth that of the continuous ejecta blanket. Accumulation of such deposits from many craters would be substantial. However, plains forming materials are not noted at the edge of the continuous ejecta blanket nor at the distal edge of secondary swarms. Target ejecta on Mercury must therefore be more greatly dispersed to escape detection, or, as Gault et al. (1975) have shown, be more closely confined and contained within the continuous ejecta blanket and rim of the crater.

Based on rim heights and crater depths determined by Cintala (1979a,b) for fresh, small, mercurian craters, the thickness of plains materials necessary to embay an intact 5 km diameter crater is at least 0.2 km. To completely fill this crater, 0.85 km thickness is required, or 0.6 km to fill the crater level with the surrounding surface. To bury a 10 km crater, 0.4 km plains thickness is necessary to embay the crater rim, 1.7 km to fill the crater to the rim crest, or 1.2 km to fill it level with the surface (the apparent depth of the crater, after Pike, 1977b). Of course, if the 5 and 10 km craters are older, shallower, or breached, as might be expected of some secondary craters, the plains thickness necessary to fill those crateriforms is less. Burial of fresh 5 to 10 km craters by one primary in its  $2R-4R$



zone implies a continuous ejecta blanket depth of 3 km to 6 km or greater (much too high for normal craters); embayment of the rims of small craters requires lesser continuous ejecta blanket heights, 1 to 2 km, averaged over the disk annulus. Note that secondary cratering may extensively damage the rims of existing craters, enough so that they are more readily filled by the primary crater's later ejecta deposits.

If the volume of a primary crater is represented as the volume of a segment of a sphere of radius  $R$  and depth  $R_a$  (the apparent depth), all of which is ejected in impact, the calculated primary radius for an ejecta blanket depth of 1 km is 44 km, and for an ejecta blanket depth of 6 km is 264 km, using the following formulas:

$$V = (1/6) \pi R_a (3R + R_a^2) \quad \text{Volume of spherical segment;}$$

$$0.5V = \pi(4R^2 - R^2) \cdot t_{ej} \quad \text{Volume of cylindrical ejecta blanket.}$$

Using Cintala's (1979b) relation that  $R_a = 0.133D_r$  for Mercury's fresh unmodified craters, ejecta thickness  $t_{ej} = 0.0227 R$ . The thickness beyond  $2R$  to  $4R$ , where, at most, 40% of the crater volume is deposited, is

$$t = t_{ej}/5 = 0.00454 \cdot R$$

This implies that deposit depths of 0.2 and 0.4 km, sufficient to embay the 5 and 10 km craters, are produced by craters of diameters 97 km and 194 km.

However, the calculated ejecta heights should not exceed the observed crater rim height. If Cintala's (1979b) relation of rim height of craters greater than 18 km is used,  $R_e = 0.268 D_r^{0.349}$  (where  $R_e$  is rim height), and if the ejected volume forms an annulus as thick as the rim height to a distance of  $2R$ , and  $1/5$  that to  $4R$ , craters of 43 km and 317 km diameter could bury 5-10 km craters respectively at a range of  $2R-4R$ . These diameters are quite likely to be underestimates. Radial exponential decay of continuous ejecta deposit's depth (McGetchin, Settle, and Head, 1973; and Cintala, 1979b) would predict that much larger craters (220 km and 1602 km) are necessary to produce such ejecta depths. Such calculations suggest a reduced plains-forming potential of mercurian craters relative to lunar craters.

## APPENDIX F

### CONSTRUCTION OF THE PALEOGEOLOGIC MAPS

Construction of the paleogeologic maps is complex only for older units. The Post Caloris surface was easily derived from the geologic map simply by plotting all Class 1 and 2 features. To construct the Caloris surface, Class 3 craters were plotted onto the map, as well as all Class 3 plains. However, if P3 plains were adjacent to P2 units, and appeared continuous with other exposures of P3 material, the P2 unit was assumed to overlie the C3 and P3 material. The younger superposed craters were "ignored" with respect to the Class 3 surface. The boundaries of P3 materials were then continued under the superposed units, using a minimum of reasonable assumptions. For instance, if P2 and P4 plains were adjacent units, no P3 plains were presumed to lie under the P2 material. Similarly, all C3 craters were considered to have some deposits of impact melt after formation, even if they are mapped containing younger units. C3 craters which were superposed with younger units, C1 or C2 craters, and perhaps P2 plains, were redrawn as if later materials had not been emplaced, i.e. in their post impact, pre-degradation states.

This reconstruction of the geologic map essentially presents the materials laid down within that time period, and is not strictly a "snapshot" of the geology at the ends of the Class 4, Class 3, and Class 1 periods.

The older units were similarly drawn. Crater rims of C4 and C5 craters were left incomplete if buried by P4 or P5 material. A dot-dash line designates visibly buried rims. Ancient circular depressions, C5', were marked distinctly to emphasize (1) their queried nature, (2) their burial by intercrater plains. P4 and P5 plains were grouped together, and presumed to underlie all P3, P2 and P1 materials; therefore, the intercrater plains overlie all areas not specifically covered by crater materials. The C4 and C5 structures are also presumed to be filled with impact melt, or material synchronous with the impact. Basin and crater rims were reconstructed "under" the superposed materials of Classes 3, 2, and 1. The shapes and interiors of craters and basins were not adjusted for degradation. Although it is probable that continuous ejecta blankets were once larger, and that the floor diameter was once smaller, basins and craters were left in their degraded plans, since reconstruction involved too many assumptions. Some rims of ancient depressions are marked as heavy dashed lines, indicating ambiguous, indistinct, or interpolated information. No allowances were made in the hilly and lineated terrain to correct for the unusually severe degradation there.

## APPENDIX G

### THERMAL MODELS OF MERCURY

Recent and more complex thermal models of Mercury and the terrestrial planets are discussed or noted in this appendix. These models isolate a particular aspect of the planet's thermal history in an attempt to understand that parameter. Included among these topics are thermal conductivity, convection, radiogenic sources of heat, other heat sources, and the problem of the molten core and regenerative dynamo. Much material has been omitted, especially more detailed models of lunar history. Early papers on thermal models which might prove useful are: Anderson and Phinney (1967); Wood (1967); Lubimova (1969); Reynolds and Summers (1969); Tozer (1967, 1972, 1974); Johnston, McGetchin, and Toksöz (1974); Cassen and Reynolds (1974); and Sonett, Colburn, and Schwartz (1975).

#### Thermal Conductivity

The transport of heat occurs through radiation, convection, and conduction. The slowest process of the three, and that which therefore controls many thermal models, is conduction. The homogenous planet, a mixture of silicates and metal, is well represented in melting and conductivity by ferrobaltic substances. Mercury's internal temperature and pressure, determined by the distribution of mass, can be modelled without the many extrapolations to high T and P necessary for earth's interior.

Siegfried and Solomon (1974) use iron and silicate conductivity values to model the core and mantle respectively. Silicate inclusions within an iron melt, or iron inclusions within a silicate melt (similar to the stony-iron meteorites) are used to simulate the core-mantle boundary area, assuming a continuous compositional transition across the boundary. Conductivity and melting curves are estimated for these mixtures, using the melting curves of iron from Higgins and Kennedy (1971) and of diopside (a reasonable, high temperature silicate) of Boyd and England (1963).

Fricker et al. (1976) re-evaluate the problem of a molten core in Mercury, using improved iron phase curves of Liu and Bassett (1975). Assuming early melting and core separation, they find that the melting temperatures of the silicates at the temperature and pressure of the core-mantle boundary is  $200^{\circ}$  C higher than that of iron. The lower conductivity of the mantle causes this discontinuity to be a "barrier" to heat transfer, if there is no solid mantle convection. The silicate mantle insulates the iron core. The thermal gradient at the boundary decreases, and the temperature of iron rises above the melting temperature in a 500 km thick outer core. If this barrier is absent, core solidification could occur in less than 2 billion years; its presence, however, ensures a molten outer core today (and a solid inner core). Although the model meets the condition for a molten core, the temperature gradient is subadiabatic, so convection--also necessary for a dynamo--is probably inhibited. For

the outer core to be convective, some form of energy must drive fluid motion in that region (possibly Gubbins' 1977 mechanism?). Fricker et al. (1974) note that Mercury's radiogenic sources are less than the earth's or the Moon's if scaled to the silicates present in each planet. Thus high initial heat is necessary for core separation. Possible initial heat sources are high accretion temperatures and/or rates, short lived radioisotopes, electrical unipolar induction, and Hayashi or T-Tauri phases of the sun (Sonett and Herbert, 1977).

#### Core Formation Mechanisms

Stevenson (1980) explores a different method of core formation. He finds that the Elsasser-drop model and sinking-layer model, which are ultimately governed by conductivity, are too slow for the rapid core formation usually required in thermal history scenarios. A "catastrophic asymmetry" model predicts melting proceeding downward as the cool, buoyant regions of the inner, primitive core break away and "raft" upward beneath the molten convecting mantle. The fluid layer of iron in which the inner homogenous core floats is churned up by this motion helping to produce or maintain a dynamo field. A layer only a few kilometers thick is required. With this model, the magnetic field at the surface would decline as the molten source layer moved further inward.

### Convection

Subsolidus convection, and viscosity  $\nu(T)$  control the thermal histories modelled by Schubert et al. (1979): they assume a hot initial state with no internal heat sources. Their calculations may be applicable to the lower mantle, after total melting and upward differentiation of radiogenic sources. Calculations for Mercury show that subsolidus convection ends at 1.62 b.y. with the growth of a lithosphere 246 km thick. At 0.6 b.y., the crust is 100 km thick. The growth of the lithosphere may be impeded by such processes as vigorous convection (which might follow the separation of the core), or the disruption and heat produced by heavy bombardment. Since both of these processes end near 0.6 b.y. (from Solomon, 1977b, and others), the 100 km thickness may be an overestimate. Viscosity increases rapidly over this period for Mercury. Values of  $10^{21.8}$  cm<sup>2</sup> /sec are predicted for 0.6 b.y., with lower values prior to that time and higher values afterward. The mercurian and lunar viscosities are both  $10^{22}$  cm<sup>2</sup> /sec at 1.2 b.y. after formation of both bodies. Schaber et al. (1977) find average viscosities of similar but higher values for the Moon and Mercury at the present, consistent with the variation in viscosities noted above. (Core viscosities calculated by Peale and Boss, 1977, constrained by Mercury's spin-orbit resonance, are a separate problem. They predict that Mercury's core must have had viscosities like that of the Earth's core to be captured into the 3:2 spin-orbit resonance.)



Tozer (1972) argues that solid state creep controls the internal state of large terrestrial planets; its influence changes with size of the body. The capacity for viscous dissipation and chemical differentiation increases with radius of the planet; the largest planets have not ceased this quasi-static evolution. Convective cores may become hotter and smaller with time.

Convection is modelled by Turcotte et al. (1979) by using uniformly heated, self gravitating spheres. Heat is generated by "radioactive heat and transient heating or cooling" by whole mantle convection. Two scales of convection occur, one involving surface plates of the body, the second involving materials beneath that surface cell. Turcotte et al. (1979) neglect the differentiation of radiogenic elements and contributions of heat from the core. Internal temperatures regulate viscosity as expressed in the Rayleigh numbers. Initial temperatures of  $1400^{\circ}$  K in Mercury decrease only to  $1200^{\circ}$  K after 4.5 aeons. Due to the decay of radioactive heat sources, the viscosity rises and the Rayleigh number decreases within this once-fluid layer of 610 km. The slight decrease in temperature may not be likely to affect the extent or type of volcanism in that planet. However, they acknowledge that neglecting the heat input of the core of Mercury is a poor approximation.

As others have concluded (e.g. Hsui and Toksöz, 1977), Turcotte et al. (1979) find that initial conditions have little effect on present thermal evolution of the planet. The Earth and Venus are

affected by  $T_0$  for the first 500 m.y., the Moon, for 2 b.y., and Mercury is probably intermediate in the duration of influence of its  $T_0$ . Meissner and Lange (1977) parameterized convection and solid state creep within the terrestrial planets. They find that creep halts when temperatures fall below about  $0.65 T_m$ , where  $T_m$  is the melting temperature in the silicates which varies with pressure and depth.  $0.65 T_m$  becomes a "steady state" temperature of planetary mantles. Planets with similar mantle compositions--and thus similar behavior of minerals with pressure-dependent melting temperatures  $T_m(P)$ --may behave similarly, with temperature gradients scaled inversely with gravity or planet size. They expect Mercury to have a lithosphere of ~250 km depth at the present, where  $T(P) = 1000^\circ + K$ , or  $0.7 T_m$ . The lithosphere's viscosity above 100 km depth is presently greater than  $10^{25}$  poise, similar to present lunar viscosities (see also Schaber et al., 1977). Viscosities are  $10^{21}$  poise at 100-400 km depth; between 400 to 1000 km depth viscosity varies from  $10^{20}$  to  $10^{22}$  poise.

#### Radiogenic Sources and Heat Output

Because of the slow nature of conduction, and the inefficiency of true convection, heat flow from a planet's surface is not in equilibrium or "steady state" balance with heat production in the interior. Turcotte et al. (1979) found that present heat flows of the terrestrial planets are 7-12% greater than values determined by the

steady state approximation. Daly and Richter (1978) also caution that convection with decaying heat sources is not sufficient to "result in equilibrium between heat production and heat flow." Surface heat losses reflect earlier heat source densities of greater (or lesser) magnitude, so that present calculations may overestimate (or underestimate) radiogenic sources. As Schubert et al. (1979) explain, a low heat flow is observed for a cool, primitive planet just beginning to warm up internally from radiogenic sources; while an evolved planet with decaying heat sources in its interior appears to have a higher heat flow from the surface. Schubert et al. (1980) find that earth's radiogenic heat is only 65-85% of its heat loss; the 15 to 35% difference is called "secular cooling." Lunar radiogenic heat, correcting for the imbalance suggested by Daly and Richter (1978), is only 70-80% of its surface heat loss. In fact, the primordial heat (accretion or condensation) component may be as high as 1/3 to 1/4 the present heat flux of the earth and other planets (Schubert et al., 1979). In most of the Toksöz and Solomon models discussed in the text, this imbalance is ignored, and steady state conditions are assumed to hold. The relation between the surface heat flow and the surface activity (volcanism and tectonism) may be important: prior to core formation, surface heat flow activity may be less than predicted; while it might be greater than predicted after the core forms and heat sources differentiate upward. Extended surface activity may occur while the heat sources decay.

This effect may have some bearing on estimated temperatures in the core. Despite these caveats, as noted by Solomon (1976, 1977b), Toksöz et al. (1978), Fricker et al. (1974, 1976), and Stevenson (1975), the core may need internal heat sources to sustain convection within its liquid shell layers. Once the radiogenic heat sources have been partitioned into the shallow crustal silicates, the core cools fairly rapidly. High heat flows from the planet's surface may not imply a molten core.

#### Other Heat Sources

Horedt (1980) explores three different types of gravitational heating for planets: accretional heat, adiabatic compression, and core formation. Core formation is the most dramatic heat source for the larger terrestrial planets, although accretional heating is important for bodies of all sizes early on. Kaula (1979a) examines accretional heating by impacts of planetesimals on the earth and moon. Growth times of 50 m.y. for the earth raises temperatures high enough to vaporize the outer layers of proto-earth if more than 12% of the heat energy of impacts is retained, possibly as hot fall-back ejecta. Heating may increase with growth time, contrary to some models where heating is negligible if distributed over long periods. In this case, Kaula (1979a) notes that larger planetesimals are likelier to impact earth after lengthier periods of time; larger objects bury their heat deeper in the target planet, where it may be retained. According to Kaula's (1979a) model, the Moon does not melt during accretion, even

if the presence of the earth "focuses" objects onto the Moon's surface. Heat sources such as cooling of an inner core are cited by Gubbins (1977) as sufficient to keep the temperature gradient superadiabatic in the outer molten core. Tidal heating is dismissed as a viable heat source for the core by many authors (e.g. Burns, 1976).

Stevenson et al. (1980) argue that the core and mantle thermal histories are coupled through the temperature dependence of rheology. Alloys may be necessary to depress the melting temperature of iron; otherwise, temperatures below that melting point occur in the deep mantle. Stevenson et al. (1980) assume radiogenic heat sources are absent from the core. If the core formed by differentiation, rather than heterogeneous accretion (as discussed by Cordell, 1977), then core convection is driven by cooling the fluid from above, and adding heat from below as the inner core becomes solid (see also Gubbins, 1977). Impurities of lighter elements percolating through this core material will aid convection. They suggest that just 3% sulfur by mass could decrease the melting point, and act as the percolating light element.

Heating by tidal action is discussed by Liu (1972) who predicts two thermal bulges on Mercury at the hot poles,  $0^\circ$  and  $180^\circ$  W longitude. The bulges raised by differential solar insolation are acted on as a tidal bulge, and further heat may be released. Thermal stress may be as great as  $4 \cdot 10^8$  dynes  $\text{cm}^{-2}$ . This heat, dissipated probably in Mercury's upper crustal layers, may cause local heating

(volcanism) or tectonic activity, but is unlikely to directly affect the core. Liu's (1972) work must be re-evaluated with different physical parameters, specifically, a silicate density of 3.0 to 1.5 g cm<sup>-3</sup> (brecciated rock) instead of the mean density of 5.3 g cm<sup>-3</sup> used in his calculations. Burns (1976) notes that tidal stresses may raise temperatures by 100° C, dissipated mainly at the poles. The effects of such an increase in temperature are debatable.

Mercury's surface temperature may reach 725° K at 0° and 180° longitude on the equator every 176 days. No one (other than Liu, 1972) has determined whether that periodic thermal imprint is communicated to the mantle, although Stevenson et al. (1980) note that the 770° K surface temperature on Venus is communicated to its mantle. Convection in Mercury's silicate mantle may once have been affected, and possibly manifested in, lithospheric and crater morphologic differences. (The Caloris basin and hilly and lineated areas lie near the hot poles, but off the equator.) Radioactive heat sources may have differentiated to shallower levels near the hot poles, contributing to a thinner lithosphere there than at the warm poles. McKinnon (1980) finds that polar--equatorial asymmetries in lithospheric thickness may be more pronounced than warm pole-hot pole differences. The evidence is inconclusive. A basic uncertainty in equatorial heat input is the duration of the 3:2 resonance which is responsible for longitudinal differences in thermal insolation. If Mercury's spin was greater in the past, longitudinal temperature

excursions would be less pronounced, and closer to Mercury's effective reflectance temperature. Tidal spin-down could dissipate more heat in polar regions, off-setting latitudinal heat differences (Burns, 1976). If thermal stresses had occurred, one might expect evidence of loss of large craters by isostatic relaxation. If tidal spin-down formed the lineaments registered in the intercrater plains, then the hot pole/warm pole phase may have persisted since the time of heavy bombardment. Crater morphology may change with longitude as lithospheric thicknesses vary.

#### The Problem of a Molten Core and Regenerative Dynamo

Stevenson (1975) outlined four necessary, but "probably not sufficient," requirements for a regenerative dynamo. The first requirement of the regenerative dynamo is a molten core, or molten, highly conductive layer; the second is an energy source to drive convection in the molten layer; the third is a magnetic Reynolds number greater than unity (in which the time scale for convection is much more rapid than the time scale for decay of the magnetic field); and the fourth is the influence of Coriolis forces to drive the Cowling fluid motions. These conditions may be alternately satisfied in Mercury's core or mantle, but not all are satisfied in the core. Stevenson (1975) concluded that a regenerative dynamo in Mercury was unlikely.

It has been noted that various studies appear to relax some of these conditions. Gubbins (1977) asserts that Coriolis forces dominate in Mercury's interior, despite its slow rotation, and that

planetary cooling may provide adequate energy to drive convection. Levy (1979) finds that an ambient field may be amplified by weak convection (insufficient for regenerative behavior on its own), thus creating a dynamo-like field exterior to the planet. Yet most thermal histories thus far reviewed lead to the conclusion that internal heat sources are necessary for Mercury's core to be molten at present (Cassen, 1977; Hsui and Toksöz, 1977; Toksöz et al., 1978; Solomon, 1976, 1977b; Siegfried and Solomon, 1974).

Stephenson (1976) found that the intrinsic field could reflect a remanent magnetization locked within a cool ( $T < T(\text{Curie})$ ) shell. Shell thicknesses of 20 to 200 km are possible with iron contents as small as  $\sim 3$  wt %  $\text{Fe}^0$ . Solomon (1976) concedes that inefficient differentiation could leave Fe within the silicate mantle, thus increasing electrical conductivity, allowing a thicker layer to be below the Curie temperature. Others (Ness, 1978) disagree with Stephenson's conditions, arguing that the required shell is too thick and the Fe content too high. Iron contents slightly higher than that of lunar ferrobasalts may be necessary.  $\text{FeO}$  on Mercury's surface is apparently restricted to 3% to 6% (Hapke, 1977). Further discussion can be found in Chapter 6 of the text.



## APPENDIX H

### ALTERNATIVE THERMAL HISTORIES

A differentiated, once active Mercury is based on the following interpretations: (1) the observed magnetic field represents an active dynamo; (2) the high density of the planet results from a high iron content, presumably in the core; (3) the silicate surface layers indicate a 600 km thick lithosphere formed by differentiation; (4) the intercrater plains are volcanic materials; (5) regional tensional features were destroyed by volcanism and impacts; (6) scarps are compressional faults produced in a global contraction; (7) young plains include volcanic materials extruded for limited times during surface cooling; and (8) the heavy bombardment involved the same population of objects, at the same time, as on the Moon.

Although all the above conclusions are the most reasonable, competing interpretations may spell out a simpler history for Mercury. The magnetic field may be due to remanent magnetization of an iron-rich shell, magnetized by an ancient dynamo or external field. Mercury's high density also is represented by a homogeneous mixture of 65% iron and 35% silicates and refractories. The silicate surface layers may be superficial (meteoritic debris), with composition and albedo variations recently disguised (by a late heterogeneous accretion?). The intercrater plains may be dominated by ballistically

emplaced materials, breccias, as argued by Wilhelms (1976b). In fact plains formation solely by ballistic mechanisms excludes surface volcanism. Regional tensional features may not have occurred if the planet never expanded (Cordell, 1977); on the other hand, regional tensional features may yet be identified. Most scarps are tectonic. Two are well identified thrust faults; others are high angle faults which, in a few cases, may be normal faults, as proposed by Scott et al. (1980) and Dzurisin (1977a). A global distribution of scarps may be imprinted on the tectonic fabric of tidal spin down, which will also generate compressional faults in equatorial areas (Melosh and Dzurisin, 1978). Young plains may also be impact melts or other impact generated debris, deposited in low-lying landforms. The young plains show slight compositional variations primarily around the Caloris basin. And finally, Mercury's heavy bombardment may comprise a different population occurring at a later time, or the same population recorded later on the surface, or combined populations, one of which is unique to Mercury.

Various combinations of these alternative scenarios are presented below. Many contradict the evidence, but other scenarios are remotely possible and warrant further study and more data.

As noted earlier, various initial conditions are possible if condensation and accretion are "non-standard" or if fractionation and mixing processes occur. Weidenschilling's (1978) metal-silicate fractionation hypothesis affects Mercury's composition, but does not

affect the planets' mode of accretion. Differentiation is affected if other heat sources or alloying elements are introduced into the system. It may be possible that silicate-rich fragments accreted later than the iron-rich materials, in a heterogeneous accretion. Some influx of silicate materials drifting into Mercury's accretion zone from farther radial distances could contribute low temperature condensates, which are accreted in either mode.

Cordell (1977) builds a scenario for Mercury based on inhomogeneous accretion, eliminating the need for rapid core formation and significant global expansion. A (rapid) hot accretion creates a global magma ocean of the upper mantle silicates. U and Th are trapped in a refractory core which melts and subsequently melts the surrounding Fe-Ni mantle. Because these phases are already at high temperature and pressure, little volume increase is expected from element redistributions. To keep the core molten and drive the dynamo, 20% of the U and Th must remain trapped in the core. The rest of the U and Th migrate to crustal regions, causing intercrater plains volcanism. Since expansion of the planet is minimal, there are no large rift valleys--tensional features--to be erased by crater and plains formation. Scarp formation begins after the surface and lithosphere cool.

Strom (1979) describes an alternative scenario where melting, core formation, expansion, and initial plains formation (resurfacing) substantially precede the recorded heavy bombardment. Intercrater

plains (some of which are remnants of the early resurfacing) are emplaced throughout that bombardment via the mode of ballistic deposition of brecciated ejecta and impact melts. The early core formation presumably forms an ancient dynamo, which magnetizes crustal layers as they cool. Energy sources in the core were not sufficient to keep it molten. Scarp formation follows crustal cooling, primarily during the early bombardment. Younger plains are also emplaced ballistically, like the lunar Cayley plains.

This research indicates that Mercury's surface began to record impacts very early in history, and that impacts occurred throughout plains formation without a substantial low viscosity surface. Some rifts may be evident, as remnants, within the intercrater plains. The new data presented above on the onset of scarp formation (i.e., in the P3 period during late intercrater plains formation and late heavy bombardment) and its duration (through the P1 period) argue against Strom's (1979) alternative model.

High initial temperatures are attainable through several mechanisms, many of which have been discussed in the literature (e.g. Sonett et al., 1975). These include rapid accretion, short lived radionuclides, unipolar induction, electrical heating, and high temperature or high magnetic field phases of the early sun. Other mechanisms are tidal friction, gravitational heating, and core formation. Each process causes early melting, and perhaps the creation of a magma ocean; both events would certainly contribute to resurfacing the

planet. Impacting objects would not be recorded on this surface until it cooled substantially.

Although a primordial surface is ruled out by observations of ancient circular depressions buried by plains, this observation may not necessarily exclude an incompletely differentiated planet. In support of this, Schaber et al. (1977) note that viscosities on Mercury have been high ( $10^{26.5}$  poise) for 4.0 b.y. Scarp formation may occur through tidal relaxation, or cooling of a deep-lying partially molten zone. Only a heat source abundance less than 30.4 ppb U fails to melt the body; insufficient or marginal abundances may have been enough to raise a subcrustal layer, still Fe-rich, above the Curie point, to cool in an ambient magnetic field. Following cold accretion, as discussed by Sharpe and Strangway (1976), Mercury's crust or core may have acquired the field of an external magnetic source. However, if Fe were that close to the surface (within the Curie isotherm), greater compositional variations around basin impacts may be expected, but are not observed.

It is important to note that better determination of Mercury's magnetic field, its moment of inertia, and its surface heat flow could easily distinguish between many of these models. Sharpe and Strangway (1976) show that the latter two parameters differ greatly in the cold accretion and hot accretion core formation models. (Siegfried and Solomon, 1974, and Kozlovskaya, 1969, also demonstrate this.) Russell et al. (1977) have shown that magnetic field analyses of the Moon better define its internal history.

Alternatives to an active dynamo are a Fe-rich shell magnetized by an ancient dynamo, as discussed in Appendix G and in the text, and a low temperature core magnetized by an external paleofield. An ancient dynamo is quite consistent with predictions of a core which solidifies 1.5 to 2.0 b.y. following its formation. Solid state convection in the mantle would hasten core cooling. Ness (1978), however, objects to the amount of Fe required in the shell, the shell's thickness, and the strength of the dynamo field. Core formation is not expected to be an inefficient process with respect to Fe left in the mantle or heat sources left in the core. Concurrent with core dynamo processes, the surface units or subsurface layer must be cooling through the Curie isotherm. Since this form of remanence is a second order effect, field intensities of 1-10 gauss are required (Stephenson, 1976). Magnetization by an external field requires that the planet's surface layers cool in the presence of a stable external field. Thermal events subsequent to field decay (e.g. impacts) may destroy the TRM field.

A ballistic plains origin demands no volcanic episodes; the only molten materials are impact melts and hot ejecta sheets. Impact erosion from much smaller impacts or secondary craters from basins, may subdue cratered terrain to mimic the intercrater plains (Malin, 1976b; Trask, 1976a,b). However Mercury's cratering history, the contemporaneous areas of craters and plains, the reduced ejecta distribution relative to the Moon, and the lack of similar plains on the

Moon except in a specific area, argue against plains production by impact ejecta. Since ancient basin-sized depressions appear to be embayed by the intercrater plains, and since fewer, younger, large basins occur in the vicinity of these structures, ballistic materials necessary to create the second generation of plains material are insufficient.

Another alternative thermal history worth exploring concerns the link between heavy bombardment and surface volcanism. Although the surfaces of Mercury and the Moon do not record the major accretion of the planet (i.e., the surfaces are not primordial), they record a very heavy bombardment which, on Mercury, ends near the onset of scarp formation in period 3, and on the Moon, ends about 3.9 b.y. ago with the last of the basin impacts. Heavy bombardment accompanies highland and intercrater plains volcanism. Accretional bombardment has been suggested as one mechanism for producing the magma ocean (Ahrens and O'Keefe, 1978; cf. Kaula, 1979a). The later "terminal" bombardment may also inject heat into the crust, and create excavated areas and hot, insulated areas which disturb the local isotherms (Bastin, 1974). Bastin's "liquefaction" theory for the lunar Cayley plains involves in situ formation by subsurface heating and relaxation of topographic relief. Differential insulation by crater ejecta blankets and regolith variations cause lateral thermal gradients which aid in the spread of these flat-lying regions. Ahrens and O'Keefe (1978) discuss impact ejecta heat distribution more fully.

Furthermore, cratering fractures the crust to a depth equal to the crater diameter. Should molten zones exist beneath that surface, the number of conduits through which magma may rise increases with time as the cratering continues. Global compressional stresses of "one plate planets" may close these vents if the planet cools and contracts. Thus plains formation may be tied to impact cratering through heat production and fracturing of the crust. Concurrent heavy bombardment and intercrater plains production occur on Mercury, the Moon, Mars, and possibly the Gallilean satellites Callisto and Ganymede. (Basin rings and crustal thickness are discussed in McKinnon, 1980.) Plains formation by impact ejecta, impact erosion, and liquefaction exclude the need for volcanism on the surface. Observations of Mercury's intercrater plains indicate that the most attractive mechanism is formation by volcanic extrusions.

In each of these models, it is important to note how they satisfy such constraints as the nearly uniform color and albedo of Mercury's surface. A homogeneous, undifferentiated object would not be expected to exhibit major changes in color and albedo due to crater excavations. However, it would be expected to show higher Fe concentrations than observed. Color variations in initial surface melts depend on the duration of melting and fractionation in the source region and in the access of highly fractionated materials to the surface. Before further interpretations are made, it would be wise to



obtain higher resolution multicolor spectrophotometry of Mercury's surface. Albedo and two-color ratios may not be adequately diagnostic of surface composition.

In summary, alternative scenarios of Mercury's thermal history involve different internal distributions of accreted materials, including U- and Th-rich materials, variations of early melting, and different modes of plains and scarp formation. Arguments in this paper strongly favor plains formation by volcanism, lack of a primordial surface, and possible identification of remnant tensional features. Studies of remote sensing data which suggest a modestly homogeneous surface of silicates strongly imply core separation. Better constraints on timing of these events and the volume and nature of plains production enable us to reject Strom's (1979) alternative hypothesis. Rejection of Cordell's (1977) hypothesis is more difficult, but is based on tentative identification of tensional rifts and evidence for an anorthositic crust. In general, the better hypotheses for thermal histories of Mercury are those of Toksöz and Solomon, modified by the observations of onset and duration of scarp formation and later plains formation by volcanism.

## APPENDIX I

### TANGENTIAL STRESS FACTOR

Solomon (1977b, p. 138) notes that radial and tangential stress in the crust are a result of "non-uniform thermal expansion or contraction" acting over a time interval  $\Delta t = t_2 - t_1$  and associated with a temperature change  $\Delta T(r) = T(r, t_2) - T(r, t_1)$ . The change in radial thermoelastic stress is given by

$$\Delta \sigma_r(r) = \frac{2E}{3(1-\nu)} (I(R) - I(r))$$

and the change in the tangential thermoelastic stress is given by

$$\Delta \sigma_t(r) = \frac{E}{3(1-\nu)} \cdot (2I(R) + I(r) - \Delta T(r) \cdot \alpha(r))$$

where  $I(r)$  is the expression

$$I(r) = \frac{1}{r} \int_0^r \alpha(r) \Delta T(r) r^2 dr$$

Other parameters are:  $E$ , Young's modulus, assumed to be spatially uniform and of value  $10^{12}$  dyn/cm<sup>2</sup>;  $\nu$ , Poisson's ratio, also assumed to be spatially uniform and equal to 0.25; and  $\alpha(r)$ , the thermal expansion coefficient. The tangential stress factor used by Solomon (1977b, p. 138) is actually the rate of change of tangential stress, or  $\Delta \sigma_t / \Delta t$ . If stress is tensional, the stress factor  $\Delta \sigma_t / \Delta t$  is positive, and if compressional, the factor is negative.

## APPENDIX J

### CHRONOLOGY OF SURFACE HISTORY OF MERCURY

The following chronology of Mercury's history is similar to, but not as detailed as, those reported by Dzurisin (1978), Strom (1979), and Gault et al. (1977), but follows their basic guidelines.

(1) Condensation and Accretion. The initial phases of Mercury's history are condensation and accretion. Unlike Cordell's hypothesis (1977), equilibrium condensation followed by homogeneous accretion are likely starting conditions (Lewis, 1972). Metal-silicate fractionation or mixing of high and low temperature condensates (Weidenschilling, 1978) may introduce other heat producing (K-40) or alloying (S) elements to Mercury's refractory, iron-nickel, and magnesium silicate-rich composition (Goettel, 1976). FeO may have been incorporated with more oxidized planetisimals; however, it is believed to be a product of later differentiation in Mercury's crust.

(2) Heating. A second, or concurrent, stage is heating of the planet. Rapid accretion, external heat sources (like an active T-Tauri solar phase), or extinct radionuclides (Fe-60?) contribute to high initial temperatures, on the surface or throughout the planet, which lead to melting, differentiation, and formation of an iron core.

(3) Planetary Expansion During Heavy Bombardment. The redistribution of silicate and iron within a formerly homogeneous

Mercury is likely to cause substantial expansion and tensional stresses in addition to higher temperatures. Plains extrusions follow. Emplacement of these intercrater plains occurs during an ongoing heavy bombardment of Mercury by large planetesimals. The graben and fissures formed during planetary expansion are destroyed in the bombardment and embayed by the plains materials which they conduct to the surface. A few of the later-forming tensional features may still exist in the P5 and P4 plains.

(4) Tidal Spin - Down and Lineament Formation. Mercury's initially high rotation rate (10 to 20 hours; see references in text) was slowed by solar tides and eventually assumed a value  $2/3$  that of its orbital period. The relaxation of the tidal bulge, or tidal spin-down, may produce lineaments by faulting or jointing in the newly emplaced and stressed plains units, and may also exert some control over the vents through which plains are extruded. Because of tidal spin-down, tensional features due to expansion may be more numerous in middle to high latitudes; small numbers of isolated great rifts are not expected, contrary to what Cordell (1977) has suggested in analogy to Mars.

(5) P5 Plains Emplacement. The earliest recorded plains are not part of the primordial surface. The C5' depressions may have formed as impacts into the recently cooled, high viscosity surface. P5 plains surround and bury many of the C5' structures. Thermal heterogeneities in the crust and subsurface partially-molten areas may

have caused extended plains formation, or induced isostatic relaxation of basins and craters in particular areas. The P5 plains are the most widespread unit and probably formed during the surge of energy associated with core formation (Toksöz et al., 1978).

(6) P4 Plains Emplacement. Plains emplaced in the Class 4 period are slightly less widespread; thermal heterogeneities may remain. Bombardment is still heavy; many 200-300 km basins form during this period. Lineament formation continues. Dome formation may occur during intercrater plains emplacement P5 through P3.

(7) Peak Planetary Volume in P3 Period. Peak planetary volume is reached in this period, marking the completion of core formation. Plains emplacement is slightly less extensive than the P5 units and has become localized to depressions, interior and exterior to clusters of craters. Crater clusters appear to be preserved in part because they are at higher elevation; in addition, their massive continuous ejecta blankets act to channel exterior deposits, and protect the cluster from external embayment by volcanic plains. Subsequent craters have left the imprint of their secondaries on Class 5, 4, and 3 plains and craters, out to distances of 1-2 diameters from the primary craters' rims.

(8) Scarp Formation. Scarp formation begins early in the Class 3 period following core formation as the planet's lithosphere starts to cool. Plains formation continues because of availability of molten material, subsurface tensional forces which allow pooling of

magma, and impact cratering or tidal fracturing which provides conduits through the surficial compressional zone. Lithostatic pressures and magma pressures are able to overcome the initially weak compressional stress. The scarps are thrust faults or high angle reverse faults, which, in their entirety, imply a radial contraction of Mercury of 2 km or less (Solomon, 1977b; Strom et al., 1975b). Ridges form during the Class 3 and 2 periods, possibly as the last extrusions along fissure vents, or as "squeeze ups" of material in fissures during the compressional era.

(9) Caloris Basin Formation, Late Class 3. The Caloris basin formed late in the C3 period or early C2 period, creating the hilly and lineated area when its seismic waves were focused at the basin's antipodal area. The degree of destruction of pre-existing terrain within the hilly and lineated area depends on the age of the material, the consolidation of that material prior to the disturbance, and the distance of the affected zone from the epicenter of the focused seismic waves. The Caloris basin forms extensive deposits of rim materials, ejecta facies, and secondary crater fields. Hummocky plains are also formed around the basin rim at the time of impact.

(10) Scarp Formation and P2 Plains Formation. Scarp formation continues and plains formation decreases as the planet's lithosphere continues to cool and as source regions retreat from the surface. Scarps are most numerous in the Class 2 period, while plains become increasingly confined to local depressions (e.g., the C5'), and

to interiors of older craters and basins of the first quadrant. Many P2 exposures are impact melts; some are ballistic deposits overlying rough topography. Those which are isolated from young basins and which occur in older structures are interpreted as volcanic. Cratering intensity decreases. Tidal spin-down has ceased by this time, for the associated lineaments are not recognized in the P2 and P1 plains.

(11) Smooth Plains Formation In and Around Large Basins.

Large basin-forming impacts, like that which formed Beethoven, the Copley basin, the North-polar basin, Caloris, and others, have fractured the crust and created sufficiently deep conduits for extrusion of material from deep-lying molten zones local to the basin. The Caloris basin has lengthened smooth plains activity on the second quadrant of Mercury, regionally reversing the decreasing plains formation trend noted for the first quadrant.

(12) Late or Local Tectonic Stress. In the late P2 period or C1 period, the Caloris basin appears to have undergone a subsidence, forming ridges radial and concentric to the basin center; the subsidence may be associated with local plains formation as magma withdraws from cavities beneath the basin floor (Dzurisin, 1977a). Subsequent isostatic compensation and uplift produced tensional features (fractures) in radial and concentric patterns on the basin floor. If normal faults did form on the first quadrant during the Class 2 and 1 periods, they too are likely to be local--perhaps local adjustments to

retreat or exhaustion of magma chambers. Scott et al.'s (1980) suggestion of a late tensional regime is not well documented by the controversial identifications of normal faults in the first quadrant.

(13) Quiescent Class 1 Period. The last stage of the planet is marked by greatly reduced crater fluxes and reduced plains and scarp formation. Scarps transect some C1 craters, indicating late compressional stresses. Most smooth P1 plains form as impact melts in C1 craters; a few exposures occur in older craters and are interpreted as volcanic. Bright young units occur on the floors of young craters; Dzurisin (1977b) interprets these as possible chemical alteration products. Ray craters make up a sizeable sample of the C1 craters (Allen, 1977); their blue rays cross all types of terrain and are rarely embayed by plains.

(14) Present Conditions. Although cooling and contraction of the lithosphere are complete, the core remains molten as an active dynamo, producing the magnetic fields detected by Mariner 10. The plains produced since core formation (P3-P1) should record its magnetic activity. Only ~23% of the core volume (or 60% of core radius;  $r/R_c = 0.6$ ) may have cooled and contributed to Mercury's 2 km radial decrease. Color Homogenization: Cratering during the Class 2 and Class 1 periods is probably not enough to distribute ballistic materials and homogenize any color differences. Some color variations are located in the younger plains materials, whereas older plains appear more homogeneous. This effect may be a chemical-compositional one, or simply related to decreased impact fluxes.



## APPENDIX K

### CHRONOLOGY OF SURFACE HISTORY OF THE MOON

The scenario for the lunar surface highlights the formation of its intercrater plains. The sequence of events is quite similar to those sequences proposed by lunar mappers (e.g. Scott, 1972).

(1) Ancient crust solidification about 4.4 b.y. ago; anorthositic highlands (plagioclase rockbergs of Herbert et al., 1977) dominate the surface.

(2) Ongoing heavy bombardment and accretion act to mix the crust with subsurface materials and with the incoming projectiles.

(3) During the magma ocean stage, radioactive elements are concentrated just beneath the crust. As the crust founders and is cratered, these minerals are more evenly distributed.

(4) Long-term tensional stresses are produced by the magma ocean genesis, although actual increase in the Moon's radius is small.

(5) As the crust cools, partial melt zones move deeper into the planet; fractionated basalts are concentrated under the chilled crust.

(6) The heavy bombardment and heat sources remelt much of the upper crust and excavate fractionated basalts. The initial extrusions of partial melts (LKFM basalts?) may have produced some intercrater plains possibly localized in an ancient basin southwest of Nectaris.

(7) Ancient basin impacts locally reduce large crater and small crater densities in the area.

(8) The Nectaris impact excavates some KREEP rich materials. The Janssen Formation is emplaced as the Nectaris ejecta blanket, and may fill surrounding depressions with smoother materials at its distal edges. The impact appears to do little structural damage to the large craters southwest of the basin in the intercrater plains region. Secondaries of Nectaris occur on Zagut, Hommel, Dove, and Nearch. This may be a consequence of oblique impact of the Nectaris projectile from the southwest.

(9) Large amounts of pre-Imbrian plains are formed by local melting of the highland crust and extrusions along fissures and vents which trend along the lunar grid direction or which are localized to an ancient basin. Plains are deposited sporadically over time in topographic lows and embay the Janssen Formation. Adjustment of fault blocks may elevate some regions, so that different thicknesses of materials build up (Mutch and Saunders, 1972). Small craters are buried by the plains; large craters are embayed or surrounded, their rims intact.

(10) Ongoing heavy bombardment ejects and deposits local anorthositic highland materials onto these pitted plains units, disguising most compositional variations.

(11) The Imbrium impact ejects secondary swarms onto the northernmost reaches of the pre-Imbrian plains. Craters of this

period and the Imbrium basin help form the Cayley plains units from the brecciated ejecta deposits which are then concentrated in topographic lows.

(12) As partial melting continues, the mare basalts are extruded; higher FeO contents may result from greater duration of fractionation. The Moon is still under global expansion and tension, so open vents and available source materials combine to aid emplacement of widespread mare basalts. Grabens form. The occurrence of ridges and graben around major basins depends on the combination of global and basin-local stresses.

(13) Global contraction (cooling) begins around 3.3 b.y.; late-stage basalts are emplaced at basin margins where fractures penetrate to subsurface tensional zones.

The lunar intercrater plains may be linked with early KREEP volcanism, the LKFM basalt source region, and the first stages of mare volcanism. Ages of KREEP bracket the possible ages of the pre-Imbrian plains, and overlap the initial stages of mare basalt emplacement. Both plains are extruded under the same tensional tectonic regime.

## LIST OF REFERENCES

- Adams, J. B., and T. B. McCord, Mercury: Evidence for an anorthositic crust from reflectance spectra, Bull. Amer. Astron. Assoc., 9, 457, 1977.
- Aggarwal, H. R., and V. R. Oberbeck, Monte Carlo simulation of lunar megaregolith and implications, Proc. Lunar Planet. Sci. Conf. 10th, 2689-2705, 1979.
- Ahrens, T. J., and J. D. O'Keefe, Energy and mass distributions of impact ejecta blankets on the Moon and Mercury, Proc. Lunar Planet. Sci. Conf. 9th, 3787-3802, 1978.
- Alfvén, H., and G. Arrhenius, Evolution of the Solar System, NASA SP-345, 599 pp., Washington, D. C., 1976.
- Allen, C. C., Rayed craters on the Moon and Mercury, Phys. Earth Planet. Interiors, 15, 179-188, 1977.
- Allen, C. C., Large lunar secondary craters: Size-range relationships, Geophy. Res. Lett., 6(1), 51-54, 1979.
- Anderson, D. L., and R. A. Phinney, Early thermal history of the terrestrial planets, in Mantles of the Earth and Terrestrial Planets, edited by S. K. Runcorn, pp. 113-126, Interscience Publ., London, 1967.
- Andre, C. G., T. A. Maxwell, F. El-Baz, and I. Adler, Chemical diversity of the lunar light plains from orbital X-ray data, in Papers Presented to the Conf. on the Lunar Highlands Crust, pp. 1-2, Lunar Planet. Inst., Houston, Texas, 1979a.
- Andre, C. G., R. W. Wolfe, and I. Adler, Are early magnesian-rich basalts widespread on the Moon? Proc. Lunar Planet. Sci. Conf. 10th, 1739-1751, 1979b.
- Arnold, J. R., A. E. Metzger, and R. C. Reedy, Computer generated maps of lunar composition from gamma-ray data, Proc. Lunar Sci. Conf. 8th, 945-948, 1977.

- Arthur, D. W. G., A. P. Agnieray, R. A. Horvath, C. A. Wood, and C. R. Chapman, The system of lunar craters, Quadrant I, Comm. Lunar Planet. Lab., 2 (30), 71-78, 1963.
- Arthur, D. W. G., A. P. Agnieray, R. A. Horvath, C. A. Wood, and C. R. Chapman, The system of lunar craters, Quadrant II, Comm. Lunar Planet. Lab., 3(40), 1-59, 1964.
- Arthur, D. W. G., A. P. Agnieray, R. H. Pellicori, C. A. Wood, and T. Weller, The system of lunar craters, Quadrant III, Comm. Lunar Planet. Lab., 3 (50), 61-146, 1965.
- Arthur, D. W. G., R. H. Pellicori, and C. A. Wood, The system of lunar craters, Quadrant IV, Comm. Lunar Planet. Lab., 5(1), 1-208, 1966.
- Bastin, J. A., A new theory for the formation of the maria and Cayley-type lunar regions, The Moon, 10, 143-162, 1974.
- Beals, C. S., and R. W. Tanner, Crater frequencies on lava covered areas related to the Moon's thermal history, The Moon, 12, 63-90, 1975.
- Bielefeld, M. J., R. C. Reedy, A. E. Metzger, J. I. Trombka, and J. R. Arnold, Surface chemistry of selected lunar regions, Proc. Lunar Sci. Conf. 7th, 1661-1676, 1976.
- Bills, B. G., and A. J. Ferrari, A lunar density model consistent with topographic, gravitational, librational and seismic data, Jour. Geophys. Res. 82(8), 1306-1314, 1977.
- Bowker, D. E., and J. K. Hughes, Lunar Orbiter Photographic Atlas of the Moon, NASA SP - 206, 1971.
- Boyd, F. R., and J. L. England, Effect of pressure on the melting of diopside,  $\text{CaMgSi}_2\text{O}_6$ , and albite,  $\text{NaAlSi}_3\text{O}_8$ , in the range up to 50 kilobars, Jour. Geophys. Res., 68, 311-323, 1963.
- Burns, J. A., Consequences of tidal slowing of Mercury, Icarus, 28, 453-458, 1976.
- Camichel, H., and A. Dollfus, La Rotation et la Cartographie de la Planete Mercure, Icarus, 8, 216-226, 1968.
- Caputo, C., R. Casacchia, G. Caverretta, M. Parotto, A. Carusi, and M. Fulchignoni, Mercury cratering I: A catalogue of large craters (belt from  $+60^\circ$  to  $-60^\circ$  of latitude), Geologica Romana, 15, 435-449, 1976a.

- Caputo, C., M. Parotto, A. Carusi, and M. Fulchignoni, Mercury cratering IV: A comparison between different physiographic provinces, Geologica Romana, 15, 467-470, 1976b.
- Carusi, A., M. Fulchignoni, C. Caputo, and M. Parotto, Mercury cratering II: Distribution pattern of diameters, areas, and perimeters of craters having a radius of  $> 10$  km, Geologica Romana, 15, 451-455, 1976a.
- Carusi, A., M. Fulchignoni, M. Poscolieri, C. Caputo, R. Casacchia, M. Coradini, and M. Parotto, Mercury cratering: Statistical recognition of physiographic units and their evolution, Proc. Lunar Sci. Conf. 8th, 3565-3574, 1977.
- Carusi, A., M. Fulchignoni, M. Poscliere, C. Caputo, R. Casacchia, and M. Parotto, Mercury cratering III: A catalogue of large polar craters, some statistical considerations, Geologica Romana, 15, 457-465, 1976b.
- Cassen, P., Planetary magnetism and the interiors of the Moon and Mercury, Phys. Earth Planet. Interiors, 15, 113-120, 1977.
- Cassen, P., and R. T. Reynolds, Convection in the Moon: Effect of variable viscosities, Jour. Geophys. Res., 79, 2937-2944, 1974.
- Chapman, C. R., Chronology of terrestrial planet evolution: The evidence from Mercury, Icarus, 28, 523-536, 1976.
- Charette, M. P., S. R. Taylor, J. B. Adams, and T. B. McCord, The detection of soils of Fra Mauro basalt and anorthositic gabbro composition in the lunar highlands by remote spectral reflectance techniques, Proc. Lunar Sci. Conf. 8th, 1049-1061, 1977.
- Chase, S. C. Jr., E. D. Miner, D. Morrison, G. Münch, G. Neugebauer, and M. Schroeder, Preliminary infrared radiometry of the night side of Mercury from Mariner 10, Science, 185(4146), 142-145, 1974.
- Chase, S. C., Jr., E. D. Miner, D. Morrison, G. Münch, and G. Neugebauer, Mariner 10 infrared radiometer results: Temperatures and thermal properties of the surface of Mercury, Icarus, 28, 565-578, 1976.
- Cintala, M. J., Small fresh crater morphometry: A preliminary assessment of the effects of gravitational acceleration and impact velocity, NASA Tech. Memo. 80339, 176-178, 1979a.

- Cintala, M. J. Mercurian crater rim heights and some interplanetary comparisons, Proc. Lunar Planet. Sci. Conf. 10th, 2635-2650, 1979b.
- Cintala, M. J., J. W. Head, and J. Veverka, Characteristics of the cratering process on small satellites and asteroids, Proc. Lunar Planet. Sci. Conf. 9th, 3803-3830, 1978.
- Cintala, M. J., C. A. Wood, S. U. Grenander, M. E. Dibner-Dunlap, T. A. Mutch, and J. W. Head, Mercury crater analysis: An automated data gathering and handling system, (Abstract) in Papers Presented to the Conference on Comparisons of Mercury and the Moon, p. 5, The Lunar Science Institute, Houston, Texas, 1976.
- Cintala, M. J., C. A. Wood, and J. W. Head, The effects of target characteristics on fresh crater morphology: Preliminary results for the Moon and Mercury, Proc. Lunar Sci. Conf. 8th, 3409-3425, 1977.
- Clark, P. E., E. Eliason, C. G. Andre, and I. Adler, A new color correlation method applied to XRF Al/Si ratios and other lunar remote sensing data, Proc. Lunar Planet. Sci. Conf. 9th, 3015-3027, 1978.
- Conca, J., and N. Hubbard, Evidence for early volcanism in Mare Smythii, Proc. Lunar Sci. Conf. 10th, 1727-1737, 1979.
- Cordell, B. M., Tectonism and the Interior of Mercury, Ph. D. Dissertation, U. Arizona, Tucson, Arizona, 1977.
- Crater Analysis Techniques Working Group, Standard techniques for presentation and analysis of crater size-frequency data, NASA Tech. Memo. 79730, 1978.
- Croft, S. K., Lunar crater volumes: Interpretation by models of impact cratering and upper crustal structure, Proc. Lunar Planet. Sci. Conf. 9th, 3711-3733, 1978.
- Cummings, D., Geologic map of the Clavius Quadrangle of the Moon, (LAC 126), U.S. Geol. Survey Misc. Geol. Inv. Map I-706, 1972.
- Cutts, J. A., T. W. Thompson, and B. H. Lewis, Radar craters on Venus: A steady state population, Bull. Amer. Astron. Soc., 12(3), 690, 1980.

- Daly, S. F., and F. M. Richter, Convection with decaying heat sources: A simple thermal evolution model, Lunar Planet. Sci. Conf. IX, Abstr., 213-214, 1978.
- Davies, M. E., and R. M. Batson, Surface coordinates and cartography of Mercury, Jour. Geophys. Res., 80, 2417-2430, 1975.
- Davies, M. E., S. E. Dwornik, D. E. Gault, and R. G. Strom, Atlas of Mercury, NASA SP-423, 1978.
- De Hon, R., Multiring basins in the Kuiper Quadrangle, NASA Tech. Memo. X-3364, 242-244, 1976.
- De Hon, R. A., In search of ancient astroblemes: Mercury, NASA Tech. Memo. TM-79729, 150-152, 1978.
- De Hon, R. A., D. H. Scott, and J. R. Underwood, Jr., Plains forming materials of the Kuiper Quadrangle of Mercury, NASA Tech. Memo. 81776, 34-36, 1980.
- De Hon, R. A., J. R. Underwood, Jr., and D. H. Scott, Geology of the Kuiper Quadrangle of Mercury, NASA Tech. Memo. TM X-3511, 242-244, 1977.
- Dollfus, A., and J. E. Geake, Polarimetric properties of the lunar surface and its interpretation: Part 7--Other solar system objects, Proc. Lunar Sci. Conf. 6th, 2749-2768, 1975.
- Dvorak, J., and R. J. Phillips, Lunar Bouguer gravity anomalies: Imbrian age craters, Lunar Planet. Sci. Conf. IX, Abstr., 270-272, 1978.
- Dzurisin, D., Scarps, ridges, troughs, and other lineaments on Mercury, Part I, Ph. D. Dissertation, Cal. Inst. of Technology, Pasadena, Cal., 1977a.
- Dzurisin, D., Geologic significance of photometric variations of Mercury, Part II, Ph. D. Dissertation, Cal. Inst. of Technology, Pasadena, Cal., 1977b.
- Dzurisin, D., The tectonic and volcanic history of Mercury as inferred from studies of scarps, ridges, troughs, and other lineaments, J. Geophys. Res., 83(B10), 4883-4906, 1978.
- El-Baz, F., and D. E. Wilhelms, Photogeological, geophysical, and geochemical data on the east side of the Moon, Proc. Lunar Sci. Conf. 6th, 2721-2738, 1975.



- Ferrari, A. J., and B. G. Bills, Planetary geodesy, Rev. Geophys. Space Phys., 17(7), 1663-1676, 1979.
- Frey, H., and B. L. Lowry, Large impact basins on Mercury and relative crater production rates, Proc. Lunar Planet. Sci. Conf. 10th, 2669-2687, 1979.
- Fricker, P. E., R. T. Reynolds, and A. L. Summers, On the thermal evolution of the terrestrial planets, The Moon, 9, 211-218, 1974.
- Fricker, P. E., R. T. Reynolds, A. L. Summers, and P. M. Cassen, Does Mercury have a molten core? Nature, 259, 293-294, 1976.
- Gaffney, E. S., Effects of gravity on explosion craters, Lunar Planet. Sci. Conf. IX, Abstr., 365-367, 1978.
- Gary, B. L., and S. J. Keihm, Interpretation of ground based microwave measurements of the Moon using a detailed regolith properties model, Proc. Lunar Planet. Sci. Conf. 9th, 2885-2900, 1978.
- Gault, D. E., Saturation and equilibrium conditions for impact cratering on the lunar surface: Criteria and implications, Radio Sci., 5, 273-291, 1970.
- Gault, D. E., J. A. Burns, P. Cassen, and R. G. Strom, Mercury, Ann. Rev. Astrophys., 15, 97-126, 1977.
- Gault, D. E., J. E. Guest, J. B. Murray, D. Dzurisin, and M. C. Malin, Some comparisons of impact craters on Mercury and the Moon, Jour. Geophys. Res., 80(17) 2444-2460, 1975.
- Gault, D. E., J. E. Guest, and P. H. Schultz, Caloris age changes in Mercury's crater population, NASA Tech. Memo. X-3364, 183-185, 1976.
- Gault, D. E., W. L. Quaide, and V. R. Oberbeck, Impact cratering mechanics and structures, in Shock Metamorphosism of Natural Materials, edited by B. M. French and N. M. Short, pp. 87-99, Mono Book Corp., Baltimore, 1968.
- Gault, D. E., and J. A. Wedekind, Experimental hypervelocity impact into quartz sand II. Effects of gravitational acceleration, in Impact and Explosion Cratering, edited by D. J. Roddy, R. O. Pepin and R. B. Merrill, pp. 1231-1260, Pergamon Press, New York, 1977.

- Gault, D. E., and J. A. Wedekind, Experimental studies of oblique impact, Proc. Lunar Planet. Sci. Conf. 9th, 3843-3875, 1978.
- Gifford, A. W., and F. El-Baz, Distribution and ages of light colored plains on the Moon, in Papers Presented to the Conf. on the Lunar Highlands Crust, pp. 21-23, Lunar Planet, Inst., Houston, Texas, 1979.
- Goettel, K. A., Geochemical constraints on the composition of Mercury and the Moon, paper presented to Conf. on comparisons of Mercury and the Moon, Lunar Sci. Inst., Houston, Texas, 1976.
- Goettel, K. A., personal communication, Lunar and Planetary Lab, U. Arizona, Tucson, AZ., Feb. 1981, (Dr. Kenneth Goettel).
- Greeley, R., and D. E. Gault, Precision size-frequency distributions of craters for 12 selected areas of the lunar surface, The Moon, 2, 10-77, 1970.
- Greeley, R., and D. E. Gault, Endogenic craters on basaltic lava flows. Size frequency distributions, Proc. Lunar Planet. Sci. Conf. 10th, 2919-2933, 1979.
- Greeley, R., and P. D. Spudis, Volcanism in the cratered terrain hemisphere of Mars, Geophys. Res. Lett., 5(6) 453-455, 1978.
- Greeley, R., B. R. White, R. Leach, R. Leonard, J. Pollack, and J. D. Iversen, Venus aeolian processes of saltation studies and the venusian wind tunnel, NASA Tech. Memo. TM 82385, 275-277, 1980.
- Grossman, L., and J. W. Larimer, Early chemical history of the solar system, Rev. Geophys. Space Physics, 12, 71-101, 1974.
- Gubbins, D., Speculations on the origin of the magnetic field in Mercury, Icarus, 30, 186-191, 1977.
- Guest, J. E., and D. E. Gault, Crater populations in the early history of Mercury, Geophys. Res. Lett., 3, 121-123, 1976.
- Gurnis, M., Ancient crater populations on Mars, Bull. Amer. Astron. Soc., 12(3), 677, 1980.
- Gutschewski, G., D. C. Kinsler and E. Whitaker, Atlas and Gazateer of the Near Side of the Moon, NASA Spec. Publ. 241, 538 pp, 1971.

- Haines, E. L., M. I. Etchegaray-Ramirez, and A. E. Metzger, Thorium concentrations in the lunar surface, II: Deconvolution modeling and its application to the regions of Aristarchus and Mare Smythii, Proc. Lunar Planet. Sci. Conf. 9th, 2985-3013, 1978.
- Haines, E. L., R. E. Parker, and A. E. Metzger, Distribution of radioactive elements in the lunar crust, Bull. Amer. Astron. Soc., 9(4), 1, 529-530, 1977.
- Hale, W., Orientations of central peaks in lunar craters: Implications for regional structural trends, in Papers Presented to the Conf. on Lunar Highlands Crust, pp. 36-38, Lunar Planet. Inst. Houston, Texas, 1979.
- Hale, W., and J. W. Head, Lunar central peak basins: Morphology and morphometry in the crater to basin transition zone, NASA Tech. Memo. 80339, 160-162, 1979a.
- Hale, W., and J. W. Head, Central peaks in lunar craters: Morphology and morphometry, Proc. Lunar Planet. Sci. Conf. 10th, 2623-2633, 1979b.
- Hämeen-Anttila, K. A., T. Pikkarainen, and H. Camichel, Photometric studies of the planet Mercury, The Moon, 1, 440-448, 1970.
- Hapke, B., Interpretation of optical observations of Mercury and the Moon, Phys. Earth Planet. Interiors, 15, 264-274, 1977.
- Hapke, B., C. Christman, B. Rava, and J. Mosher, A color-ratio map of Mercury, Lunar Planet. Sci. Conf. XI, Abstr., 394-395, 1980a.
- Hapke, B., C. Christman, B. Rava, and J. Mosher, A color ratio map of Mercury, Proc. Lunar Planet. Sci. Conf. 11th, 187-821, 1980b.
- Hapke, B., G. E. Danielson, K. Klaasen, and L. Wilson, Photometric observations of Mercury from Mariner 10, Jour. Geophys. Res., 80(17), 2431-2443, 1975.
- Hapke, B., and B. Rava, Mariner 10 color ratio data and the surface of Mercury, NASA Tech. Memo. 82385, 431, 1980.

- Hartmann, W. K., Radial structures surrounding lunar basins I: The Imbrium system, Comm. Lunar Planet. Lab., 2(24), 1-16, 1963.
- Hartmann, W. K., Radial structures surrounding lunar basins II: Orientale and other systems; conclusions, Comm. Lunar Planet. Lab., 2(36), 175-192, 1964.
- Hartmann, W. K., Secondary volcanic impact craters at Kapoho, Hawaii and comparisons with the lunar surface, Icarus, 7, 66-75, 1967.
- Hartmann, W. K. Ancient lunar mega regolith and subsurface structure, Icarus, 18, 634-636, 1973.
- Hartmann, W. K., Relative crater production rates on planets, Icarus, 31, 260-276, 1977.
- Hawke, B. R., and J. W. Head, Impact melt on lunar crater rims, in Impact and Explosion Cratering, edited by D. J. Roddy, R. O. Pepin, and R. B. Merrill, pp. 815-841, Pergamon Press, New York, 1977.
- Hawke, B. R., and J. W. Head, Lunar KREEP volcanism: Geologic evidence for history and mode of emplacement, Proc. Lunar Planet. Sci. Conf. 9th, 3285-3309, 1978.
- Hawke, B. R., P. D. Spudis, and P. E. Clarke, Geochemical anomalies on the lunar eastern limb and farside, in Papers Presented to the Conf. on the Lunar Highlands Crust, pp. 56-58, Lunar Planet. Inst., Houston, Texas, 1979,
- Head, J. W., Stratigraphy of the Descartes region Apollo 16: Implications for the origin of samples, The Moon, 10, 77-99, 1974.
- Head, J. W., Processes of lunar crater degradation: Changes in style with geologic time, The Moon, 12, 299-329, 1975.
- Head, J. W., Lunar volcanism in space and time, Rev. Geophys. Space Phys., 14, 265-300, 1976a.
- Head, J. W., The significance of substrate characteristics in determining morphology and morphometry of lunar craters, Proc. Lunar Sci. Conf. 7th, 2913-2929, 1976b.
- Herbert, F., M. J. Drake, and C. P. Sonett, Geophysical and geochemical evolution of the lunar magma ocean, Lunar Planet. Sci. Conf. IX, Abstr., 494-496, 1978.

- Herbert, F., M. J. Drake, C. P. Sonett, and M. J. Wiskerchen, Some constraints on the thermal history of the lunar magma ocean, Proc. Lunar Sci. Conf. 8th, 573-582, 1977.
- Herndon, J. M., and M. W. Rowe, Thermal models of inhomogeneously accreted meteorite parent bodies, Nature Physical Sci., 244, 40-41, 1973.
- Higgins, G. and G. C. Kennedy, The adiabatic gradient and the melting point gradient in the core of the Earth, J. Geophys. Res., 76, 1870-1878, 1971.
- Hood, L. L., P. J. Coleman, and D. E. Wilhelms, Lunar nearside magnetic anomalies, Proc. Lunar Planet. Sci. Conf. 10th, 2235-2257, 1979.
- Horedt, G. P., Gravitational heating of planets, Phys. Earth Planet. Interiors, 21, 22-30, 1980.
- Hostetler, C. J., and M. J. Drake, On the early global melting of the terrestrial planets, Proc. Lunar Planet. Sci. Conf. 11th, 1915-1929, 1980.
- Housen, K., and D. R. Davis, Ejecta distribution patterns on Phobos and Deimos, Bull. Amer. Astron. Soc., 10, (3), Part II, 593, 1978.
- Housen, K. R., R. Greenberg, C. R. Chapman, and L. L. Wilkening, A comparison of regolith evolution on asteroids and the Moon, Lunar Planet. Sci. Conf. X, 579-581, 1979.
- Howard, K. E., D. E. Wilhelms, and D. H. Scott, Lunar basin formation and highlands stratigraphy, Rev. Geophys. Space Phys., 12(3), 309-327, 1974.
- Hsui, A. T., and M. N. Toksöz, Thermal evolution of planetary size bodies, Proc. Lunar Sci. Conf. 8th, 447-461, 1977.
- Hubbard, N., Regional chemical variations in lunar basaltic lavas, Proc. Lunar Planet. Sci. Conf. 10th, 1753-1774, 1979.
- Hughes, H. G., F. N. App, and T. R. McGetchin, Global seismic effects of basin-forming impacts, Phys. Earth Planet Inter., 15, 251-263, 1977.
- Johnston, D. H., T. R. McGetchin, and M. N. Toksöz, The thermal state and internal structure of Mars, Jour. Geophys. Res., 79(26), 3959-3971, 1974.

- Kaula, W. M., Comments on the origin of Mercury, Icarus, 28, 429-433, 1976.
- Kaula, W. M., Thermal evolution of Earth and Moon growing by planetesimal impacts, Jour. Geophys. Res., 84(B3), 999-1008, 1979a.
- Kaula, W. M., Equilibrium velocities of a planetesimal population, Icarus, 40, 262-275, 1979b.
- Keihm, S. J., and B. L. Gary, Comparison of theoretical and observed  $\lambda$  3.55 cm wavelength brightness temperature maps of the full Moon, Proc. Lunar Planet. Sci. Conf. 10th, 2311-2319, 1979.
- Klaasen, K. P., Mercury rotation period determined from Mariner 10 photography, Jour. Geophys. Res., 80(17), 2415-2416, 1975.
- Klaasen, K. P., Mercury's rotation axis and period, Icarus, 28, 469-478, 1976.
- Kohman, T. P., and M. S. Robinson, Iron-60 as a heat source and chronometer in the early solar system, Bull. Amer. Astron. Soc., 12(3).
- Kozlovskaya, S. V., On the internal constitution and chemical composition of Mercury, Astrophys. Lett., 4, 1-3, 1969.
- Kuiper, G. P., Consolidated Lunar Atlas Photographic Reproductions Pt. I, Pt. II (with R. Strom, E. Whitaker, J. Fountain, and S. Larson), Suppl. nos. 3 and 4, Contri. Lunar Planet Lab., 4, 1967.
- Kumar, S., Mercury's atmosphere: A perspective after Mariner 10, Icarus, 28, 579-591, 1976.
- Leake, M., Intercrater plains of Mercury, NASA Tech. Memo. TM-81776, 31-33, 1980a.
- Leake, M., Onset of scarp formation on Mercury, Bull. Amer. Astron. Soc., 12(3), 677, 1980b.
- Levy, E. H., Planetary dynamo amplification of ambient magnetic fields, Proc. Lunar Planet Sci. Conf. 10th, 2335-2342, 1979,
- Lewis, J. L., Metal/silicate fractionation in the solar system, Earth Planet. Sci. Lett., 15, 286-290, 1972.

- Liu, Han-Shou, Thermal elastic deformation of the planet Mercury, Jour. Geophys. Res., 77, 6482-6485, 1972.
- Liu, L., and W. A. Bassett, The melting of iron up to 200 kilobars, J. Geophys. Res., 80, 3777-3782, 1975.
- Lubimova, E. A., Thermal history of the Earth, in The Earth's Crust and Upper Mantle, edited by Pembroke Hart, pp. 63-77, American Geophys. Union Mono. #13, Washington, D.C., 1969.
- Lucchitta, B., Geologic Map of the North Side of the Moon, U.S. Geol. Survey Misc. Inv. Ser. Map I-1062, 1978.
- Lucchitta, B. K., and J. M. Boyce, Altitude--age relationships of the lunar maria, Proc. Lunar Planet. Sci. Conf. 10th, 2957-2966, 1979.
- Majeva, S. V., The thermal history of the terrestrial planets, Astrophys. Lett., 4, 11-16, 1969.
- Malin, M. C., Comment on the nature of the intercrater plains on Mercury, paper presented at the First International Colloquium on Mercury, Pasadena, Ca., 25-27, 1975.
- Malin, M. C., Comparison of large crater and multiringed basin populations, Proc. Lunar Sci. Conf. 7th, 3589-3602, 1976a.
- Malin, M. C., Observations of intercrater plains on Mercury, Geophys. Res. Lett., 3, 581-584, 1976b.
- Malin, M. C. Intercrater plains and the early history of Mars, Bull. Amer. Astron. Soc., 9(3), 448, 1977.
- Malin, M. C. Surfaces of Mercury and the Moon: Effects of resolution and lighting conditions on the discrimination of volcanic features, Proc. Lunar Planet. Sci. Conf. 9th, 3, 3395-3409, 1978.
- Malin, M. C., and D. Dzurisin, Landform degradation on Mercury, the Moon and Mars: Evidence from crater depth/diameter relationships, Jour. Geophys. Res., 82(2), 376-388, 1977.
- Malin, M. C., and D. Dzurisin, Modification of fresh crater landforms: Evidence from the Moon and Mercury, Jour. Geophys. Res., 83, 233-243, 1978.
- Malin, M. C., and R. S. Saunders, Surface of Venus: Evidence of diverse landforms from radar observations, Science, 196, 987-990, 1977.

- Matson, D. L., T. V. Johnson, and G. J. Veeder, Soil maturity and planetary regoliths: The Moon, Mercury and the asteroids, Proc. Lunar Sci. Conf. 8th, 1001-1011, 1977.
- Masursky, H., W. M. Kaula, G. E. McGill, G. H. Pettengill, R. J. Phillips, C. T. Russell, G. Schubert, and I. I. Shapiro, The surface and interior of Venus, Space Sci. Rev., 20, 431-449, 1977.
- Masursky, H., G. Schaber, M. Strobell, and A. Dial, Geology of Venus, Bull. Amer. Astron. Soc., 12(3), 690, 1980.
- Maurer, P., P. Eberhardt, J. Geiss, N. Grögler, A. Stettler, G. M. Brown, A. Peckett, and U. Krähenbühl, Pre-Imbrian craters and basins: Ages, comparisons, and excavation depths of Apollo 16 breccias, Geochim. Cosmochim. Acta, 42, 1687-1720, 1978.
- McCauley, J. F., J. E. Guest, N. J. Trask, G. G. Schaber, R. Greeley, D. E. Gault, and H. E. Holt, Stratigraphy of the Caloris Basin, NASA Tech. Memo. TM-79729, 75-77, 1978.
- McCord, T. B., and J. B. Adams, Mercury: surface composition from the reflectance spectrum, Science, 178 (4062), 745-747, 1972.
- McCord, T. B., and R. N. Clark, The Mercury soil: Presence of Fe<sup>2+</sup>, Lunar Planet. Sci. Conf. X, Abstr., 789-791, 1979.
- McGetchin, T. R., J. W. Head, and P. H. Schultz, Lunar basins and holes in sea ice or a magma ocean, NASA Tech. Memo. TM-80339, 168-170, 1979.
- McGetchin, T. R., M. Settle, and J. W. Head, Radial thickness variations in impact crater ejecta: Implications for lunar basin deposits, Earth Planet. Sci. Letters, 20, 226-236, 1973.
- McKinnon, W. B., Aspects of ring tectonics: Mercury, Ganymede, and beyond, in Papers Presented to the Conf. on Multiring Basins: Formation and Evolution, pp. 56-58, Lunar Planet. Inst., Houston, Texas, 1980.
- Meissner, R., and M. Lange, An approach for calculating temperatures and viscosities in terrestrial planets, Proc. Lunar Sci. Conf. 8th, 551-562, 1977.
- Melosh, H. J., Global tectonics of a despun planet, Icarus, 31, 221-243, 1977a.



- Melosh, H. J., Tectonic patterns: Implications for planetary history, Bull. Amer. Astron. Soc., 9(4), Part I, 541, 1977b.
- Melosh, H. J., Crater modification by gravity. A mechanical analysis of slumping, in Impact and Explosion Cratering, edited by D. J. Roddy, R. O. Pepin, and R. B. Merrill, pp. 1245-1260, Pergamon Press, New York, 1977c.
- Melosh, H. J., and D. Dzurisin, Mercurian global tectonics: A consequence of tidal despinning? Icarus, 35, 227-236, 1978.
- Metzger, A. E., E. L. Haines, M. I. Etchegaray-Ramirez, and B. R. Hawke, Thorium concentrations in the lunar surface: III. Deconvolution of the Apennines region, Proc. Lunar Sci. Conf. 10th, 1701-1718, 1979.
- Metzger, A. E., E. L. Haines, R. E. Parker, and R. G. Radocinski, Thorium concentrations in the lunar surface. I: Regional values and crustal content, Proc. Lunar Planet. Sci. Conf. 8th, 949-999, 1977.
- Moore, H. J., C. A. Hodges, and D. H. Scott, Multiringed basins--illustrated by Orientale and associated features, Proc. Lunar Sci. Conf. 5th, 1, 71-100, 1974.
- Morrison, D., Thermophysics of the planet Mercury, Space Science Reviews, 11, 271-307, 1970.
- Morrison, D. M., and J. L. Warner, Planetary tectonics: II: A gravitational effect, Lunar Planet. Sci. Conf. IX, Abstr., 769-771, 1978.
- Morrison, R. H., and V. R. Oberbeck, Geomorphology of crater and basin deposits--emplacement of the Fra Mauro Formation, Proc. Lunar Sci. Conf. 6th, 2503-2530, 1975.
- Morrison, R. H., and V. R. Oberbeck, A composition and thickness model for lunar impact craters and basin deposits, Proc. Lunar Planet. Sci. Conf. 9th, 3763-3785, 1978.
- Mouginis-Mark, P. J., Spatial distribution and morphology of secondary craters, Lunar Planet. Sci. Conf. IX, Abstr., 772-774, 1978.
- Murdock, T. L., and E. P. Ney, Mercury: The dark side temperature, Science, 170, 535-537, 1973.

- Murray, B. C., M. J. S. Belton, G. E. Danielson, M. E. Davies, D. Gault, B. Hapke, B. O'Leary, R. G. Strom, V. Suomi, and N. Trask, Mariner 10 pictures of Mercury: First results, Science, 184, 459-461, 1974a.
- Murray, B. C., M. J. Belton, G. E. Danielson, M. E. Davies, D. E. Gault, B. Hapke, B. O'Leary, R. G. Strom, V. Suomi, and N. Trask, Mercury's surface: Preliminary description and interpretation from Mariner 10 pictures, Science, 185, 169-179, 1974b.
- Murray, J. B., A. Dollfus, and B. Smith, Cartography of the surface markings of Mercury, Icarus, 17, 576-584, 1972.
- Murray, B. C., R. G. Strom, N. J. Trask, and D. E. Gault, Surface history of Mercury: Implications for terrestrial planets, Jour. Geophys. Res., 80(17), 2508-2514, 1975.
- Mutch, T. A., and R. S. Saunders, Geologic map of the Hommel Quadrangle of the Moon, U.S. Geol. Surv. Misc. Inv. Ser. Map I-702, (LAC 127), 1972.
- Ness, N. F., Mercury: Magnetic field and interior, Space Sci. Rev., 21, 527-553, 1978.
- Ness, N. F., K. W. Behannon, R. P. Lepping, and Y. C. Whang, The magnetic field of Mercury, Jour. Geophys. Res., 80, 2708-2716, 1975a.
- Ness, N. F., K. W. Behannon, R. P. Lepping, and Y. C. Whang, The magnetic field of Mercury confirmed, Nature, 255, 204-205, 1975b.
- Ness, N. F., K. W. Behannon, R. P. Lepping, and Y. C. Whang, Observations of Mercury's magnetic field, Icarus, 28, 479-488, 1976.
- Ness, N. F., K. W. Behannon, R. P. Lepping, Y. C. Whang, and K. H. Schatten, Magnetic field observations near Mercury: Preliminary results from Mariner 10, Science, 185(4146), 150-160, 1974.
- Neukum, G., and P. Horn, Effects of lava flows on lunar crater populations, The Moon, 15, 205-222, 1976.

- Neukum, G., G. König, and J. Arkani-Hamed, A study of lunar impact crater size distributions, The Moon, 12, 201-229, 1975a.
- Neukum, G., B. König, H. Fechtig, and D. Storzer, Cratering in the Earth-Moon system: Consequences for age determination by crater counting, Proc. Lunar Sci. Conf. 6th, 2597-2620, 1975b.
- Newburn, Ray, Frontispiece data of Proc. Lunar Planet. Sci. Conf. 9th, 3, front inside cover, 1978.
- Oberbeck, V. R., The role of ballistic erosion and sedimentation in lunar stratigraphy, Rev. Geophys. Space Phys., 13(2), 337-362, 1975.
- Oberbeck, V. R., and H. R. Aggarwal, Topographic analysis of lunar secondary craters of Copernicus and implications, Proc. Lunar Sci. Conf. 8th, 3521-3537, 1977.
- Oberbeck, V. R., F. Hörz, R. H. Morrison, W. L. Quaide, and D. E. Gault, On the origin of the lunar smooth plains, The Moon, 12, 19-54, 1975.
- Oberbeck, V. R., and R. H. Morrison, Laboratory simulations of the herringbone pattern associated with lunar secondary crater chains, The Moon, 9, 415-455, 1974.
- Oberbeck, V. R., and R. H. Morrison, Candidate areas of in situ ancient lunar materials, Proc. Lunar Sci. Conf. 7th, 2983-3005, 1976.
- Oberbeck, V. R., R. H. Morrison, F. Hörz, W. L. Quaide, and D. E. Gault, Smooth plains and continuous deposits of craters and basins, Proc. Lunar Sci. Conf. 5th, 1, 111-136, 1974.
- Oberbeck, V. R., and W. L. Quaide, Genetic implications of lunar regolith thickness variations, Icarus, 9, 446-465, 1968.
- Oberbeck, V. R., W. L. Quaide, R. E. Arvidson, and H. R. Aggarwal, Comparative studies of lunar, martian, and mercurian craters and plains, Jour. Geophys. Res., 82(11), 1681-1697, 1977.
- O'Donnell, W. P., Crater production and erosion on Mercury, NASA Tech. Memo. TM 79729, 144-146, 1978.

- Offield, T. W., and H. A. Pohn, Lunar crater morphology and relative age determinations of lunar geologic units, Part 2: Applications, Interagency Report: Astrogeology 13, U.S. Geological Survey, Reston, Va., 1969.
- Peale, S. J., and A. P. Boss, A spin-orbit constraint on the viscosity of a mercurian liquid core, Jour. Geophys. Res., 82, 743-749, 1977.
- Pechmann, J. B., and H. J. Melosh, Global fracture patterns of a despun planet: application to Mercury, Icarus, 38, 243-250, 1979.
- Pettengill, G. H., S. Nozette, and P. G. Ford, The radar reflectivity of Venus, Bull. Amer. Astron. Soc., 12(3), 690, 1980.
- Pieters, C. M., Highland basalts? Spectral data for a southern highlands plains unit, Lunar Planet. Sci. Conf. X, Abstr., 981-983, 1979.
- Pike, R. J., Crater dimensions from Apollo data and supplemental sources, The Moon, 15, 463-477, 1976.
- Pike, R. J., Size dependence in the shape of fresh impact craters on the Moon, in Impact and Explosion Cratering, edited by D. J. Roddy, R. O. Pepin, and R. B. Merrill, pp. 489-509, Pergamon Press, New York, 1977a.
- Pike, R. J. Apparent depth/diameter relations for lunar craters, Proc. Lunar Sci. Conf. 8th, 3427-3436, 1977b.
- Pike, R. J., D. J. Roddy, and D. W. G. Arthur, Gravity and target strength: Controls on the morphologic transition from simple to complex impact craters, NASA Tech. Memo. TM-81776, 108-110, 1980.
- Pohn, H. A., Geologic map of the Tycho Quadrangle of the Moon, U.S. Geol. Surv. Misc. Geol. Inv. Map I-713, (LAC-112), 1972.
- Pohn, H. A., and T. W. Offield, Lunar crater morphology and relative age determination of lunar geologic units, Part I: Classification, Interagency Report: Astrogeology 13, U.S. Geological Survey, Reston, Va., 1969.
- Raine, W. L., W. F. Fountain, J. A. Fountain, M. W. Segewitz, J. V. Swearingen, and M. K. White, Thermal study of the unilluminated surface of the waning moon, The Moon, 12, 407-447, 1975.

- Reynolds, R. T., and A. L. Summers, Calculations on the composition of the terrestrial planets, Jour. Geophys. Res., 74, 2494-2511, 1969.
- Ringwood, A. E., Origin of the Earth and Moon, Springer Verlag, New York, Inc., New York, 295 pp., 1979.
- Ringwood, A. E., and E. Essene, Petrogenesis of lunar basalts and the internal constitution of the Moon, Science, 167, 607-610, 1970.
- Ringwood, A. E., and S. E. Kesson, Composition and origin of the Moon, Proc. Lunar Sci. Conf. 8th, 371-398, 1977.
- Roddy, D. J., Large-scale impact and explosion craters: comparisons of morphological and structural analogs, in Impact and Explosion Cratering, edited by D. J. Roddy, R. O. Pepin, and R. B. Merrill, pp. 185-246, Pergamon Press, N.Y., 1977.
- Ronca, L. B., and R. R. Green, Statistical geomorphology of the lunar surface, Boeing Scientific Research Laboratories Document D1-82-0888, May, 1969.
- Rowan, L. C., Geologic map of the Rupes Altai Quadrangle of the Moon, U.S. Geol. Survey Misc. Inv. Series Map I-690, 1971.
- Russell, C. T., Planetary magnetism, Rev. Geophys. Space Phys., 18(1), 77-106, 1980.
- Russell, C. T., H. Weiss, P. J. Coleman, Jr., L. A. Soderblom, D. E. Stuart-Alexander, and D. E. Wilhelms, Geologic-magnetic correlations on the Moon: Apollo subsatellite results, Proc. Lunar Sci. Conf. 8th, 1171-1185, 1977.
- Ryder, G., Pre-mare volcanism, Lunar Sci. Conf. VII, Abstr., 755-757, 1976.
- Ryder, G., and P. Spudis, Volcanism prior to termination of heavy bombardment: Evidence, characteristics and concepts, in Papers Presented to the Conf. on the Lunar Highlands Crust, pp. 132-134, Lunar Planet. Inst., Houston, Texas, 1979.
- Schaber, G. G., J. M. Boyce, and N. J. Trask, Moon-Mercury: Large impact structures, isostasy and average crustal viscosity, Phys. Earth Planet. Interiors, 15, 189-201, 1977.

- Schaeffer, O. A., and L. Husain, Chronology of lunar basin formation, Proc. Lunar Sci. Conf. 5th, 2, 1541-1555, 1974.
- Schubert, G., P. Cassen, and R. E. Young, Subsolidus convective cooling histories of terrestrial planets, Icarus, 38, 192-211, 1979.
- Schubert, G., D. Stevenson, and P. Cassen, Whole planet cooling and the radiogenic heat source contents of the Earth and Moon, Jour. Geophys. Res., 85(B5), 2531-2538, 1980.
- Schultz, P. H., Comparison of lunar and planetary imagery, NASA Tech. Memo. TM X-3364, 73-75, 1976a.
- Schultz, P. H., Floor fractured craters on the Moon, Mars, and Mercury, NASA Tech. Memo. TM X-3364, 159-160, 1976b.
- Schultz, P. H. Moon Morphology, Interpretations based on Lunar Orbiter Photography, Univ. of Texas Press, Austin and London, 1976c.
- Schultz, P. H., Endogenic modification of impact craters on Mercury, Phys. Earth Planet. Interiors, 15, 202-219, 1977.
- Schultz, P. H., Ejecta dynamics of large scale impacts, Lunar Planet. Sci. Conf. IX, Abstr., 1024-1026, 1978.
- Schultz, P. H., Evolution of intermediate-age impact basins on the Moon, in Papers Presented to the Conf. on the Lunar Highlands Crust, pp. 141-142, Lunar Planet. Inst., Houston, Texas, 1979.
- Schultz, P. H., and D. E. Gault, Seismically induced modification of lunar surface features, Proc. Lunar Sci. Conf. 6th, 2845-2862, 1975a.
- Schultz, P. H., and D. E. Gault, Seismic effects from major basin formations on the Moon and Mercury, The Moon, 12, 159-177, 1975b.
- Schultz, P. H., and D. E. Gault, On the origin of the hilly and lineated terrain on Mercury, Geologica Romana, 15, 479-480, 1976.
- Schultz, P. H., R. Greeley, and D. Gault, Interpreting statistics of small lunar craters, Proc. Lunar Sci. Conf. 8th, 3539-3564, 1977.
- Schultz, P. H., and W. Mendell, Orbital infrared observations of lunar craters, and possible implications for impact ejecta emplacement, Proc. Lunar Planet. Sci. Conf. 9th, 2857-2883, 1978.

- Schultz, P. H., and L. J. Srnka, Cometary collisions on the Moon and Mercury, Nature, 284, 22-26, 1980.
- Scott, D. H., Geologic map of the Maurolycus Quadrangle, U.S. Geol. Surv. Misc. Inv. Map I-695, (LAC 113), 1972.
- Scott, D. H., Moon-Mercury: Relative preservation states of secondary craters, Phys. Earth Planet. Interiors, 15, 173-178, 1977.
- Scott, D. H., J. F. McCauley, and M. West, Geologic Map of the West side of the Moon, U.S. Geol. Surv. Misc. Inv. Map I-1034, 1977.
- Scott, D. H., J. R. Underwood, Jr., and R. A. De Hon, Normal faults on Mercury: Examples in the Kuiper Quadrangle, NASA Tech. Memo. TM 81776, 1980.
- Scott, R. F., Viscous flow of craters, Icarus, 7, 139-148, 1967.
- Seeger, C. R., Geological content of the Skylab Multispectral Scanner data, in Papers Presented to the Conf. on the Lunar Highlands Crust, pp. 145-147, Lunar Planet. Inst., Houston, Texas, 1979.
- Seeger, C. R., A. E. Potter, and R. H. Wolfe, Jr., Geochemical characterization of the lunar nearside using the Skylab S-192 Multispectral Scanner data, Lunar Planet. Sci. Conf. X, Abstr., 1098-1100, 1979.
- Seitz, M. G., and I. Kushiro, Melting relations of the Allende meteorite, Science, 183, 954-957, 1974.
- Settle, M., The role of fallback ejecta in the modification of impact craters, Icarus, 42, 1-19, 1980.
- Settle, M., and J. W. Head, III, The role of rim slumping in the modification of impact craters, J. Geophys. Res., 84(B6), 3081-3096, 1979.
- Sharpe, H. N., and D. W. Strangway, The magnetic field of Mercury and models of thermal evolution, Geophys. Res. Lett., 3(5), 285-288, 1976.
- Shoemaker, E., Interpretation of lunar craters, in Physics and Astronomy of the Moon, edited by Z. Kopal, pp. 283-359, Academic Press, New York, 1962.

- Shoemaker, E. M., E. F. Helin, and S. L. Gillett, Populations of planet crossing asteroids, Geologica Romana, 15, 205-222, 1976.
- Shoemaker, E. M., J. G. Williams, E. F. Helin, and R. F. Wolfe, Earth crossing asteroids: Orbital classes, population and fluctuation of population in late geologic time, NASA Tech. Memo. TM 80339, 3-5, 1979.
- Shorthill, R. W., and J. M. Saari, Non uniform cooling of the eclipsed Moon: A listing of thirty prominent anomalies, Science, 150 (3693), 210-212, 1965.
- Siegfried, R. W., and S. C. Solomon, Mercury: Internal structure and thermal evolution, Icarus, 23, 192-205, 1974.
- Smith, E. I., Comparisons of crater morphology-size relationship for Moon, Mars, and Mercury, Icarus, 28, 543-550, 1976.
- Smith, E. I., and J. A. Hartnell, Crater size-shape profiles for the Moon and Mercury: Terrain effects and interplanetary comparisons, The Moon and Planets, 19, 479-511, 1978.
- Soderblom, L. A., K. Edwards, E. M. Eliason, E. M. Sanchez, and M. P. Charette, Global color variations on the martian surface, Icarus, 34, 446-464, 1978.
- Solomon, S., Some aspects of core formation in Mercury, Icarus, 28, 509-521, 1976.
- Solomon, S. C., Put up or shut up: What do we really know about terrestrial planetary interiors? Bull. Amer. Astron. Soc., 9(4), Part I, 542, 1977a.
- Solomon, S. C., The relationship between crustal tectonics and interior evolution in the Moon and Mercury, Phys. Earth Planet. Interiors, 15, 135-145, 1977b.
- Solomon, S. C., On volcanism and thermal tectonics on one plate planets, Geophys. Res. Lett., 5(6), 461-463, 1978a.
- Solomon, S. C., The thermal model/density model game, in Planetary Interiors: An Interim report, papers presented to a special session of the Ninth Lunar and Planetary Science Conference, pp. 6-8, LPI Contribution #313, 1978b.



- Solomon, S. C., and J. Chaiken, Thermal expansion and thermal stress in the Moon and terrestrial planets: Clues to early thermal history, Proc. Lunar Sci. Conf. 7th, 3229-3243, 1976.
- Solomon, S. C., and M. N. Toksöz, Internal constitution and evolution of the Moon, Phys. Earth Planet. Int., 7, 15-38, 1973.
- Sonett, C. P., D. S. Colburn, and K. Schwartz, Formation of the lunar crust: An electrical source of heating, Icarus, 24(2), 231-255, 1975.
- Sonett, C. P., and F. Herbert, Pre main sequence heating of planetoids, in Comets, Asteroids, Meteorites--Interrelationships, evolution, and origins, I. A. U. Coll. #39, edited by A. H. Delsemme, pp. 429-437, Publ. U. Toledo, Toledo, Ohio, 1977.
- Soter, S. and J. Ulrichs, Rotation and heating of the planet Mercury, Nature, 214, 1315-1316, 1967.
- Spudis, P. D., Composition and origin of the Apennine bench formation Proc. Lunar Planet. Sci. Conf. 9th, 3379-3394, 1978.
- Spudis, P. D., The extent and duration of lunar highland volcanism, NASA Tech. Memo. TM 80339, 270-272, 1979.
- Srnka, L. J., and M. H. Mendenhall, Models of an early lunar dynamo, Proc. Lunar Planet Sci. Conf. 10th, 2343-2355, 1979.
- Stephenson, A., Crustal remanence and the magnetic moment of Mercury, Earth Planet. Sci. Lett., 28, 454-458, 1976.
- Stephenson, A., S. K. Runcorn, and D. W. Collinson, On changes in the intensity of the ancient lunar magnetic field, Proc. Lunar Sci. Conf. 6th, 3049-3062, 1975.
- Stevenson, D. J., Core formation dynamics and primordial planetary dynamos, Lunar Planet. Sci. Conf. XI, Abstr., 1088-1090, 1980.
- Stevenson, D. J., Dynamo generation in Mercury, Nature, 256, 634, 1975.
- Stevenson, D. J., G. Schubert, P. Cassen, and R. T. Reynolds, Core evolution and magnetism of the terrestrial planets, Lunar Planet. Sci. Conf. XI, Abstr., 1091-1093, 1980.

- Stolper, E., Mineral assemblages in planetary interiors: Predictions based on estimates of planetary composition, Lunar Planet. Sci. Conf. XI, Abstr., 1100-1102, 1980.
- Strom, R. G., Analysis of lunar lineaments, I: Tectonic maps of the Moon, Comm. Lunar Planet. Lab., 2(39), 205-216, 1964.
- Strom, R. G., Origin and relative age of lunar and mercurian intercrater plains, Phys. Earth Planet. Interiors, 15, 156-172, 1977.
- Strom, R. G., Mercury: A post Mariner 10 assessment, Space Sci. Rev., 24, 3-70, 1979.
- Strom, R. B., M. C. Malin, and C. C. Allen, Geology of the Bach Quadrangle (H-15) of Mercury, preprint, 1978.
- Strom, R. G., B. C. Murray, M. J. S. Belton, G. E. Danielson, M. E. Davies, D. E. Gault, B. Hapke, B. O'Leary, N. Trask, J. E. Guest, J. Anderson, and K. Klaasen, Preliminary imaging results from the second Mercury encounter, Jour. Geophys. Res., 80(17), 2345-2356, 1975a.
- Strom, R. G., N. J. Trask and J. E. Guest, Tectonism and volcanism on Mercury, Jour. Geophys. Res., 80(17), 2478-2507, 1975b.
- Strom, R. G., A. Woronow, and M. C. Gurnis, Cratering record of Ganymede and Callisto, NASA Tech. Memo. TM 82385, 499-501, 1980.  
(See also J. Geophys. Res., 86(A10), 8659-8674, 1981.)
- Stuart-Alexander, D. E., Geologic map of the Rheita Quadrangle of the Moon, U.S. Geol. Surv. Misc. Inv. Map I-694, (LAC 114), 1971.
- Stuart-Alexander, D. E., Geologic map of the central far side of the Moon, U.S. Geol. Surv. Misc. Geol. Inv. Map I-1047, 1978 and Interagency Report: Astrogeology 79, U.S. Geological Survey, Reston, Va., 1976.
- Stuart-Alexander, D.E., and D. E. Wilhelms, The Nectarian System, A new lunar time-stratigraphic unit, Jour. Research U.S. Geol. Surv., 3(1), 53-58, 1975.
- Taylor, S. R., and P. Jäkes, The geochemical evolution of the Moon, Proc. Lunar Sci. Conf. 5th, 2, 1287-1305, 1974.

- Tepper, L., B. Hapke, J. Woodman, and M. Perry, Mercury: Detection of a 1000 nm ferrous band, Bull. Amer. Astron. Soc., 9(4), Part 1, 532, 1977.
- Thomas, Peter C., The morphology of Phobos and Deimos, Doctoral Thesis, Cornell Univ., New York, 1978.
- Thompson, T. W., W. J. Roberts, W. K. Hartmann, R. W. Shorthill, and S. H. Zisk, Blocky craters: Implications about the lunar megaregolith, The Moon and Planets, 21(3), 319-342, 1979.
- Thurber, C. H., and S. C. Solomon, An assessment of crustal thickness variations on the lunar near side: Models, uncertainties and implications for crustal differentiation, Proc. Lunar Planet. Sci. Conf. 9th, 3481-3497, 1978.
- Toksöz, M. N., A. T. Hsui, and D. H. Johnston, Thermal evolution of the terrestrial planets, The Moon and Planets, 18, 281-320, 1978.
- Toksöz, M. N., and D. H. Johnston, The evolution of the Moon and the terrestrial planets, in The Soviet-American Conference on Cosmochemistry of the Moon and Planets, (J. H. Pomeroy and N. J. Hubbard, eds.), NASA Special Publications SP-370, Part I, 295-327, 1977.
- Tozer, D. C., Some aspects of thermal convection theory for the earth's mantle, Geophys. Journ., 14, 395-402, 1967.
- Tozer, D. C., The present thermal state of the terrestrial planets, Phys. Earth Planet. Interiors, 6, 182-197, 1972.
- Tozer, D. C., Internal evolution of planetary objects, The Moon, 9, 167-182, 1974.
- Trask, N. J., Cratering history of the heavily cratered terrain on Mercury, Geologica Romana, 15, 471-476, 1976a.
- Trask, N. J., History of basin development on Mercury, in Conf. on Comparisons of the Moon and Mercury, p. 36, Lunar Sci. Inst., Houston, Texas, 1976b.
- Trask, N. J., The distribution of plains according to relative age in the Discovery Quadrangle of Mercury, contributed to P.G.P.I. Mercury Mapping meeting, St. Louis, May 1977. (See also Geological Society of America.)

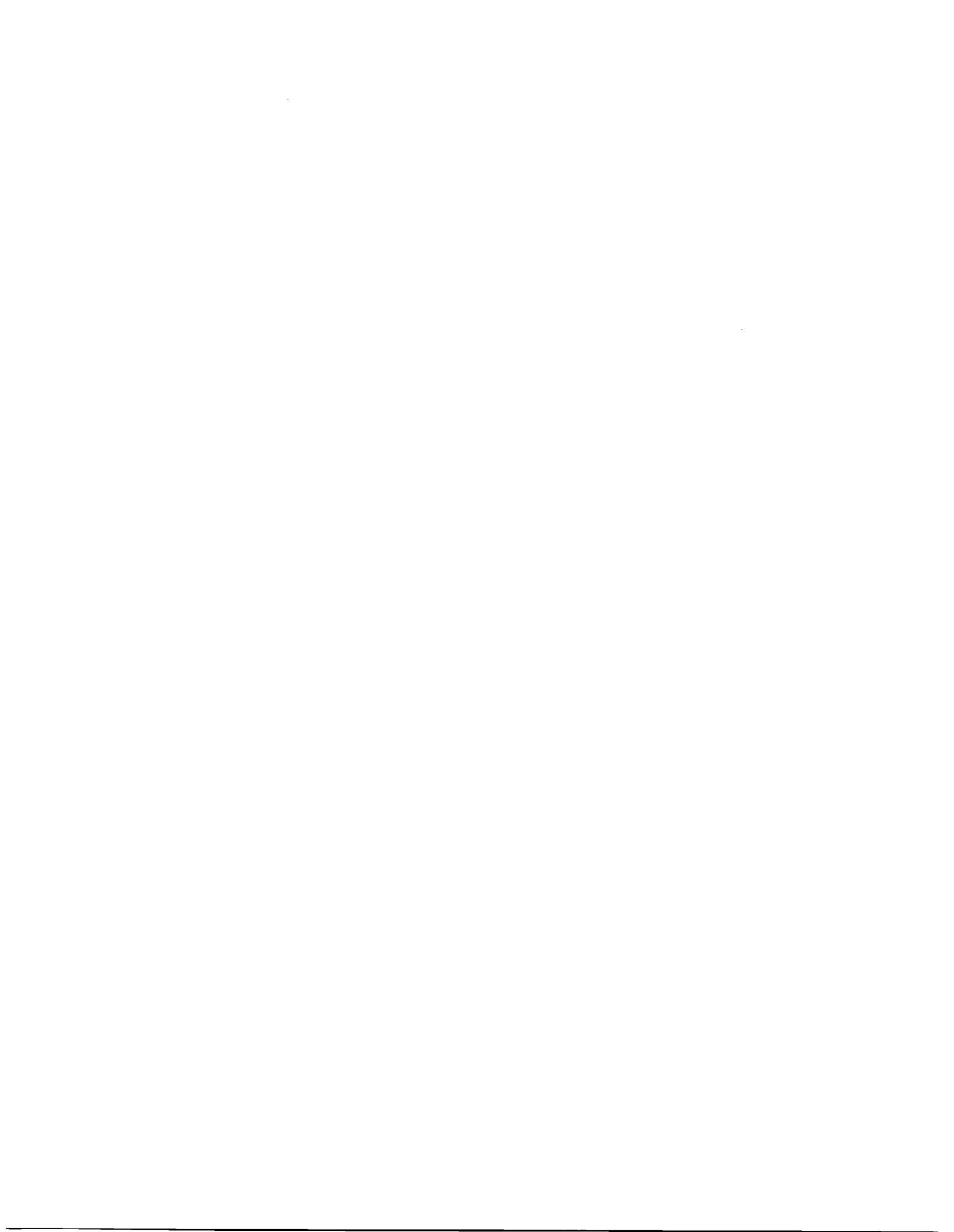
- Trask, N. J. and J. E. Guest, Preliminary geologic terrain map of Mercury, Jour. Geophys. Res., 80(17), 2461-2477, 1975.
- Trask, N. J., and R. G. Strom, Additional evidence of mercurian volcanism, Icarus, 28, 559-563, 1976.
- Turcotte, D. L., F. A. Cooke, and R. J. Willeman, Parameterized convection within the Moon and the terrestrial planets, Proc. Lunar Planet. Sci. Conf. 10th, 2375-2392, 1979.
- Vilas, F., and T. B. McCord, Mercury: Spectral reflectance measurements (0.33-1.06  $\mu\text{m}$ ) 1974/75, Icarus, 28, 593-599, 1976.
- Walker, D., E. M. Stolper, and J. F. Hays, Basaltic volcanism: The importance of planet size, Proc. Lunar Planet. Sci. Conf. 10th, 1995-2015, 1979.
- Warner, J. L., Venus: Do sediments cover lowlands? Bull. Amer. Astron. Soc., 12(3), 691, 1980.
- Warner, J. L., W. C. Phinney, C. E. Bickel, and C. H. Simonds, Feldspathic granulitic impactites and pre-final bombardment lunar evolution, Proc. Lunar Sci. Conf. 8th, 2051-2066, 1977.
- Watkins, J. A., Relative ages of the smooth plains and Caloris related terrain of Mercury, NASA Tech. Memo. TM 81776, 37-39, 1980.
- Weidenschilling, S. J., Iron/Silicate fractionation and the origin of Mercury, Icarus, 35, 99-111, 1978.
- Wetherill, G. W., Late heavy bombardment of the Moon and terrestrial planets, Proc. Lunar Sci. Conf. 6th, 1539-1561, 1975.
- Wetherill, G. W., Dynamical evidence regarding the relationship between asteroids and meteorites, in Asteroids: An Exploration Assessment, edited by D. Morrison, and W. C. Wells, NASA Conf. Publ. 2053, 17-36, 1978.
- Whitaker, E. A., Lunar color boundaries and their relationship to topographic features: A preliminary survey, The Moon, 4(314), 348-355, 1972.
- Whitaker, E. A., and R. G. Strom, Populations of impacting bodies in the inner solar system, Lunar Sci. Conf. VII, Abstr., 933-934, 1976.

- Whitford-Stark, J. L., Charting the southern seas: The evolution of the lunar mare Australe, Proc. Lunar Planet. Sci. Conf. 10th, 2975-2994, 1979.
- Wilhelms, D. E., Geologic mapping of the second planet, Interagency Report, Astrogeology 55, U.S. Dept. Interior Geological Survey, Reston, Va., 1972.
- Wilhelms, D. E., Mercurian volcanism questioned, Icarus, 28, 551-558, 1976a.
- Wilhelms, D. E. Secondary impact craters of lunar basins, Proc. Lunar Sci. Conf. 7th, 2883-2901, 1976b.
- Wilhelms, D. E., Relative ages of lunar basins, NASA Tech. Memo. TM 80339, 135-137 1979.
- Wilhelms, D. E., Irregularities of lunar basin structure, NASA Tech. Memo. TM 81776, 25-27, 1980.
- Wilhelms, D. E., and F. El-Baz, Geologic map of the east side of the Moon, U.S. Geol. Surv. Misc. Inv. Series Map I-948, 1977.
- Wilhelms, D. E., C. A. Hodges, and R. J. Pike, Nested crater model of lunar ringed basins, in Impact and Explosion Cratering, edited by D. J. Roddy, R. O. Pepin, and R. B. Merrill, pp. 539-562, Pergamon Press, New York, 1977.
- Wilhelms, D. E., K. A. Howard, and H. G. Wilshire, Geological map of the south side of the Moon, U.S. Geol. Surv. Misc. Inv. Ser. Map I-1162, 1979.
- Wilhelms, D. E., and J. F. McCauley, Geologic map of the near side of the Moon, U.S. Geol. Surv. Misc. Inv. Series Map I-703, 1971.
- Wilhelms, D. E., V. R. Oberbeck and H. R. Aggarwal, Size frequency distribution of primary and secondary lunar impact craters, Proc. Lunar Planet. Sci. Conf. 9th, 3735-3762, 1978.
- Wood, C. A., Crater degradation through lunar history, Lunar Planet. Sci. Conf. X, Abstr., 1373-1375, 1979.
- Wood, C. A., and L. E. Andersson, The Lunar and Planetary Laboratory Catalog of Lunar Craters: Part I: Nearside, NASA TM 79328, in preparation, 1978a.

- Wood, C. A., and L. Andersson, Lunar crater morphometry: New data, Lunar Planet. Sci. Conf. IX, Abstr., 1267-1269, 1978b.
- Wood, C. A., and L. Andersson, New morphometric data for fresh lunar craters, Proc. Lunar Planet. Sci. Conf. 9th, 3669-3689, 1978c.
- Wood, C. A., and A. W. Gifford, Crater distributions and the evolution of the lunar farside highlands, NASA Tech. Memo. TM 81776, 111-113, 1980.
- Wood, C. A., and J. W. Head, Comparisons of impact basins on Mercury, Mars, and the Moon, Proc. Lunar Sci. Conf. 7th, 3629-3651, 1976.
- Wood, C. A., J. W. Head, and M. Cintala, Crater degradation on Mercury and the Moon, Clues to surface evolution, Proc. Lunar Sci. Conf. 8th, 3503-3520, 1977.
- Wood, J., The early thermal history of the planets: Evidence from meteorites, in Mantles of the Earth and Terrestrial Planets, edited by S. K. Runcorn, pp. 3-14, Interscience Publ., London, 1967.
- Woronow, A., Crater saturation and equilibrium: A Monte Carlo simulation, Jour. Geophys. Res., 82, 2447-2456, 1977a.
- Woronow, A., A size frequency study of large martian craters, Jour. Geophys. Res., 82(36), 5807-5820, 1977b.
- Woronow, A., Large impact crater production in the inner solar system, NASA Tech. Memo. TM X-3511, 87-90, 1977c.
- Woronow, A., Lunar and Martian crater classes, Lunar Planet. Sci. Conf. X, (Abstr.), 1385-1387, 1979a.
- Woronow, A., Lunar and martian crater classes, NASA Tech. Memo. TM 80339, 157-159, 1979b.
- Woronow, A., R. G. Strom, and M. C. Gurnis, Cratering record in the inner solar system, NASA Tech. Memo, TM 82385, 174-176, 1980.
- Woronow, A., R. G. Strom, and E. Rains, Effects of the Orientale impact on the pre-existing crater population, NASA Tech. Memo. TM 80339, 152-153, 1979.

Young, R. A., Mare crater size frequency distributions: Implications for relative surface ages and regolith development, Proc. Lunar Sci. Conf. 6th, 2645-2663, 1975.

Zohar, S., and R. M. Goldstein, Surface features on Mercury, Astron. Journ., 79(1), 85-91, 1974.





**SECTION II**



These abstracts were prepared by the 1981 participants in the Planetary Geology Undergraduate Research Program. Each summer, the NASA-sponsored program matches qualified undergraduates with Principal Investigators who supervise their research projects. Students whose findings are included in this publication are:

Carlos A. Atallah, senior, University of California at Davis.  
Hosted by Dr. Stephen Saunders, JPL, Pasadena, CA.

Steven E. Heckendorn, senior, Wittenburg University, OH.  
Hosted by Dr. Duwayne M. Anderson, State University of New York at Buffalo.

Maureen Kilcoyne O'Toole, junior at the University of Massachusetts. Hosted by Dr. Elliot Morris, USGS, Flagstaff, AZ.

Lynn M. Reding, senior, James Madison University, VA. Hosted by Dr. Ronald Greeley, NASA Ames Research Center, Moffett Field, CA.

Henry Schuver, senior, Western Washington University. Hosted by Dr. Charles A. Wood, Johnson Space Center, TX.

Alejo Verdes, senior at Hunter College, NY. Hosted by Dr. Elliot Morris.

Stephen J. Wetzel, sophomore, Franklin and Marshall College, PA.  
Hosted by Dr. James Head, Brown University.

The papers of Dennis Rashka, Ellen Sugarman, and Mary Mei-ling Yang will appear in a future edition of this publication.



PLANET-CROSSING ASTEROID SURVEY

Carlos A. Atallah

NASA Planetary Geology  
Undergraduate Research Program  
Division of Geological and  
Planetary Sciences  
Jet Propulsion Laboratory  
CALIFORNIA INSTITUTE OF TECHNOLOGY

Address:

Department of Geology  
University of California  
Davis, CA 95616

## THE PLANET-CROSSING ASTEROID SURVEY

### INTRODUCTION:

The planet-crossing asteroid survey is a continuing systematic search of the sky for fast-moving, planet-crossing objects and for slower main belt asteroids. This project has been in operation since 1973 under the direction of Eugene M. Shoemaker and Eleanor F. Helin of the California Institute of Technology. The purpose of this search is to discover new objects and obtain and refine orbits for new and previously known asteroids, giving new insight into their populations, their origin, their collision frequency with other bodies of the solar system, and their role in the cratering history of the terrestrial planets (ref. 1). Moreover, knowledge of the population of earth-crossing asteroids could be of interest for future exploration with spacecraft, and perhaps they may ultimately become a source for raw materials (ref. 2 & 3).

### METHODOLOGY:

There are currently two programs of search: the first one is carried out by using photographic exposures obtained, on a monthly basis, with the 18" Schmidt telescope at Mount Palomar Observatory. Generally, a pair of exposures is taken of a predetermined region of the sky. These exposures are then developed and inspected at the observatory. The major emphasis of this effort is to search for fast-moving asteroids. They are somewhat easy to identify due to their characteristically long trails displayed on the plate as a result of their close proximity to the earth. However, a discovery of this sort is relatively rare. Orbits are determined for new high motion objects found on this films. As many as 25 new asteroids, mostly main-belt objects, are found in any film. During the August

1981 observing runs no fast-moving asteroids were discovered, although a new long-period comet, 1981 d, was discovered and 2100 Ra-Shalom was photographed to improve its orbit.

The second project involves the use of the 48" Schmidt telescopes at Palomar Mountain Observatory in California, and Siding Springs Observatory, New South Wales, Australia. The photographic plates obtained with these telescopes cover a 42 square degree region of the sky. One can find from 100 to 400 asteroids on each plate taken near the ecliptic plane. During June, July and August of 1979, E.F. Helin and S.J. Bus obtained a total of 14 plates using these telescopes. The plates were obtained using fixed field centers of each of the three lunations. Therefore, some objects were lost due to their motion out of the field of view during the observing run. Nevertheless, 109 asteroids were measured and preliminary orbits were determined by S.J. Bus.

#### RESEARCH:

Using the ephemerides computed from the orbits and the 48" Palomar Schmidt log book I determined the number of objects that might have appeared in plates taken in years other than 1979. Thus, new positions could be calculated aiding the refinement of the preliminary orbits of these asteroids, eventually leading to their permanent number designation. From these 109 asteroids, 35 were potentially on 97 plates taken at Palomar between the years 1976 and 1981. Unfortunately, only 27 plates were readily available and the number of tentative asteroids was reduced to 10. Furthermore, upon examination of the films, only 6 objects were found to be in the region predicted by their ephemerides. The remaining 4 objects were not found in their predicted positions primarily due to less than

optimal film quality or the faintness of the object. The position of the 6 objects identified were measured to one arcsecond precision and they have been reported to Brian Marsden of the Smithsonian Astrophysical Observatory.

#### ACKNOWLEDGEMENTS:

I am very grateful to E.F. Helin and S.J. Bus for their patience and help during my learning experience, and to R.S. Dunbar for the many instructive discussions and help in the revision of the original report. I also wish to thank R.S. Saunders for his help with living arrangements.

#### REFERENCES:

1. Helin, E.F. and Shoemaker, E.M.: The Palomar Planet-Crossing Asteroid Survey, 1973-1978. *Icarus* 40, 321-328 (1979).
2. Gaffey, M.J., Helin, E.F. and O'Leary, B.: An Assessment of Near-Earth Asteroid Resources. in: *Space Resources and Space Settlements*, NASA SP-428, 191-204 (1977).
3. Shoemaker, E.M., and Helin, E.F.: Near Earth Asteroids, Search and Rescue; Towing Asteroids Into Earth Orbits for Exploration and Exploitation. *Transcripts of the Presentations of the Eighth Lunar Science Conference*, Johnson Space Center, Houston, Texas, 16 March 1977.



POSSIBLE APPLICATIONS OF TIME DOMAIN REFLECTOMETRY  
IN PLANETARY EXPLORATION MISSIONS

by

Steve Heckendorn\*

\*I wish to thank Dr. Duwayne M. Anderson, my host for this program, for his guidance and helpful suggestions. I also wish to thank Dr. Michael W. Smith of the Geotechnical Science Laboratories, Geography Department at Carleton University, Ottawa, Canada for his helpful telephone conversation.

POSSIBLE APPLICATIONS OF TIME DOMAIN REFLECTOMETRY  
IN PLANETARY EXPLORATION MISSIONS

Steve Heckendorn	Faculty of Natural Sciences	Buffalo, NY
	and Mathematics	14260
Planetary Geology	State University of New York	U.S.A.
Undergraduate Research	at Buffalo	
Program		

Through several experimenters (Chernyak, Nikodem, Thomas, Lundien, Cihlar and Ulaby, Hipp, Hoekatra and Delaney, Chudobiak, Topp, Davis, and Annan) it has been shown that a time domain reflectometry technique can be used to determine free volumetric liquid water content in a soil, and since Patterson and Smith (1981) have demonstrated the application of this technique to frozen soils, the possibility of using it for planetary exploration has been opened. A time domain reflectometer, (TDR), is used along with a coaxial transmission line or a balanced parallel transmission line which is more apt to field use. With the two rods, or parallel probes, of known length inserted into a soil, the TDR sends electromagnetic waves through the transmission lines where some of the energy of the pulses is reflected back to the TDR. The TDR output is commonly displayed on an oscilloscope and then photographed or plotted on an x-y recorder. From the output of the TDR, which shows the reflection coefficient versus distance, the apparent dielectric constant,  $K_a$ , can be determined. This physical property, the dielectric constant, of the soil can give one the volumetric water content because  $K_a$  is primarily dependent on it.(6) The reason is the substances' dielectric constant values, which are 87.7 for water at 0°C and around 3.0 for dry soil and most geologic materials. The method also works in frozen ground since water-ice has a value very close to dry soils, approximately 3.

Figure 1 shows a typical TDR trace for a wet soil. One arrives at the volumetric water content,  $\theta_v$ , by first finding the one-way travel time of an electromagnetic wave in the probe. This is accomplished by converting the

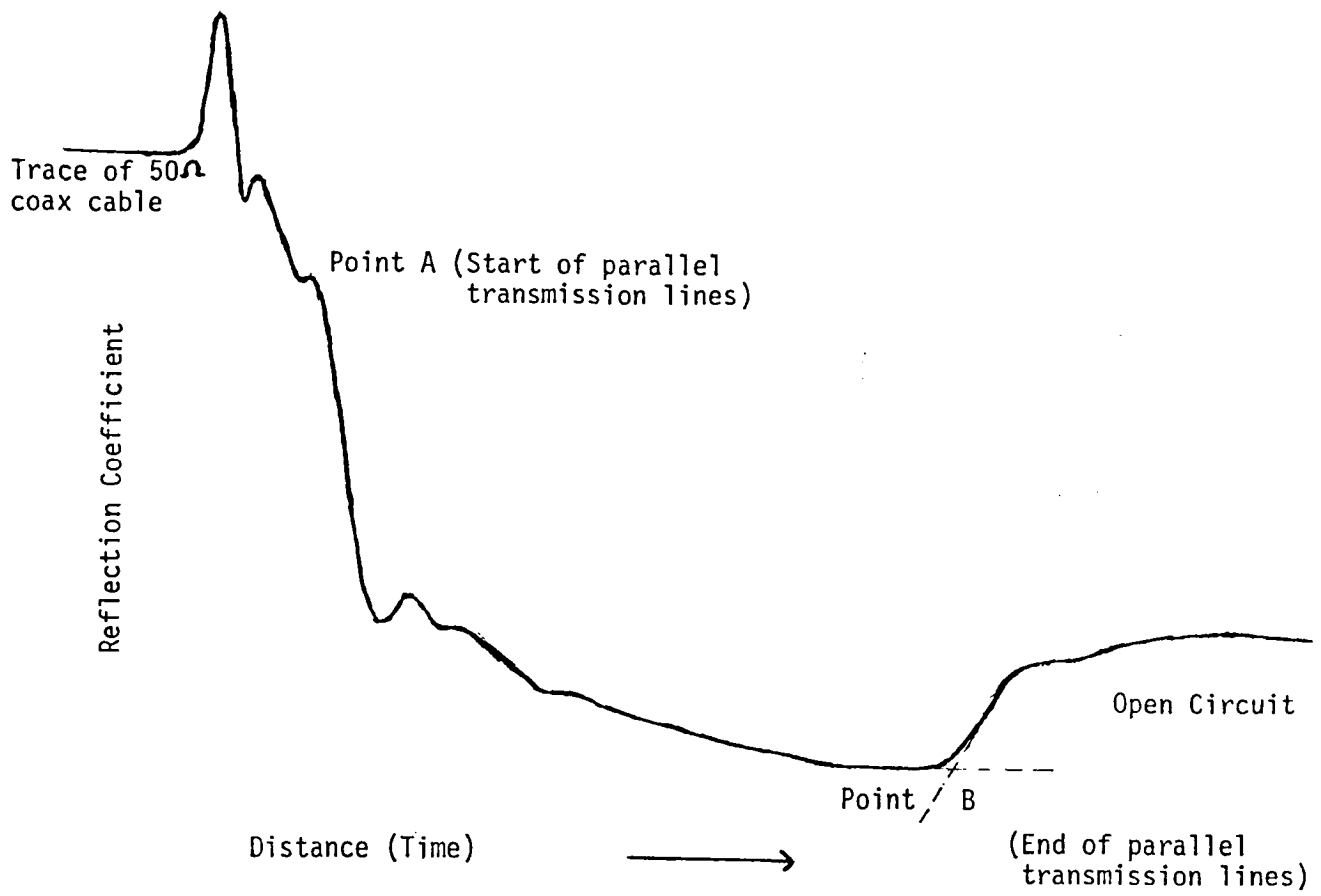


Figure 1. Typical TDR trace for a wet soil (8)

distance axis to a time axis by dividing the horizontal scale setting (in cm/DIV) by 30 cm/nsec (the speed of light in cm/nanosecond). (8) Then points A and B are located (See Fig. 1), and the number of horizontal divisions between them is counted.

The number of divisions times the time per division gives one the travel time. All the values for the following equation are now known and the  $K_a$  can be determined.

$$K_a = \left( \frac{c \times t}{L} \right)^2$$

c = the speed of light  
t = the travel time  
L = the transmission line length

Topp et al. have determined the empirical relationship between  $K_a$  and  $\theta_v$  by fitting a third-degree polynomial equation to their data and getting

$$K_a = 3.03 + 9.3 \theta_v + 146.0 \theta_v^2 - 76.7 \theta_v^3$$

or

$$\theta_v = 5.3 \times 10^{-2} + 2.92 \times 10^{-2} K_a - 5.5 \times 10^{-4} K_a^2 + 4.3 \times 10^{-6} K_a^3$$

or a tabulated table can be used to get  $\theta_v$  from the  $K_a$ . (10)

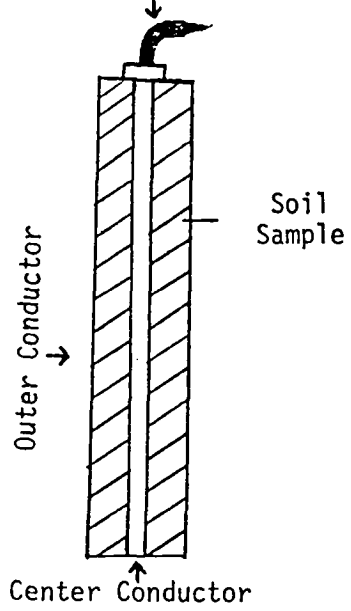
I became familiar with the TDR technique by using it on samples, and then I listed all of the advantages and disadvantages I thought it has, especially if it were to be applied for remote sensing exploration. I used a Tektronix 1502 for my TDR instrument and two extreme soil types for my samples, a local sandy soil and Wyoming Bentonite. Two types of probes, or transmission lines, were used. One is a coaxial line with a length of 15 cm and of cylindrical shape. (See Fig. 2). The soil samples were placed in between the inner and outer conductors. The other probe is a parallel transmission line with a 20cm line length. (See Fig. 2). This probe was

COAXIAL LINE

PARALLEL TRANSMISSION LINE

Coaxial Line to TDR

Coaxial Line to TDR



Head Connector

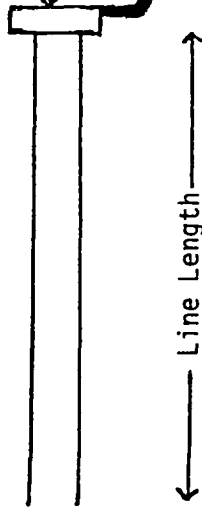


Figure 2. Probe Configurations (6)

quickly and physically implanted by hand into an open container holding the sample.

I manually added the same amount of soil and water, (to the best of my ability, using a top loading balance and a graduated cylinder), to three coaxial lines. I was convinced of the technique's precision when I obtained almost the exactly same shaped output for all three and arrived at the same water content value for each to the best of the resolution of the oscilloscope on the instrument.

I got expected values with the local sandy soil from dry to saturated water contents. With the Wyoming Bentonite, which is 90% montmorillonite and absorbs water nearly five times its weight, there was an appreciable amount of signal loss to the point that there was none of the wave being reflected back. The output resembled that of a shorted cable. This is probably due to the clay's electrical properties. Since there was no open circuit rise at the end of the trace, it was impossible to locate point B and determine the water content. I believe that none of the experimenters of this technique have ever used a sample with greater than 80% clay content. A sample with an extremely large salt content, which might be found on Mars, may give the same results. This problem could be dealt with by either using a shorter length probe, at the sacrifice of resolution, or possibly by increasing the signal strength.

Once, I froze a pure Wyoming Bentonite and water sample with the parallel probe inserted in it for 24 hours at  $-10^{\circ}\text{C}$ . An inner core of the sample, where the probe was inserted, was not frozen; however, the output was very much like a typical trace. (See Fig. 3) This allowed me to fix a point B, but I am not sure about the accuracy of the measurement. As the sample defrosted, the end rise of the trace degenerated back to the unfrozen trace which I previously described for the clay. When a sample of local sandy soil and water was frozen in a coaxial line and then allowed to defrost,



Figure 3. Montmorillonitic Clay

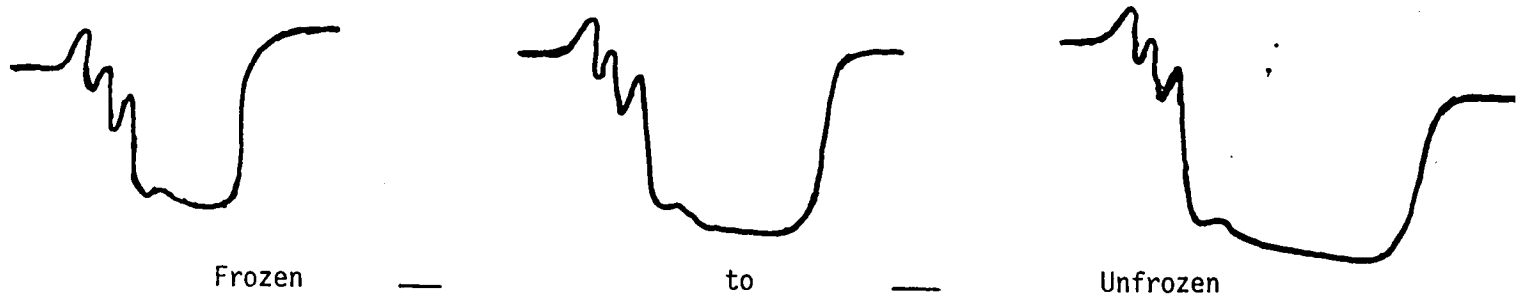


Figure 4. Sandy Soil

the shape of the trace continually changed relative to itself, but always resembled a typical trace and a water content measurement was possible. (See Fig. 4) The distance between points A and B increased as the amount of unfrozen water increased. Patterson and Smith have shown the promise of using the TDR technique for determining the unfrozen water content in frozen soils. (6)

I will first mention many of the attractive advantages to this technique. The commercially available Tektronix TDR is a rugged portable instrument which without its panel cover, handle, and knobs has the approximate dimensions of 12 cm in height, 26 cm in width, and 31 cm in length. Its performance requirements state an operating temperature range from  $-15^{\circ}\text{C}$  to  $+55^{\circ}\text{C}$  and a non-operating range from  $-62^{\circ}\text{C}$  to  $+85^{\circ}\text{C}$  with the batteries removed.

(3) It consumes little power, and the requirements for the probe are simple. Once the probe is installed, the TDR technique gives immediate, in-situ, and easily attainable measurements. It can be used for several or different seasonal readings. The TDR gives an average value over the probe length with a probable maximum error of  $\pm 2\frac{1}{2}\%$  in volumetric water content. (6) The parallel transmission lines can be used with known discontinuities along its length to give a vertical profile of water content versus depth. (2) This technique has been used on different soil types, ranging from sandy loam to clay, and has been found that it is not critically dependent on soil type, bulk density, temperature, or solute content. Due to the TDR using a frequency range of 1MHz to 1GHz, an increase in solute content will cause an increase in signal attenuation but not an appreciable change in the measured value. (9)

No one has found a significant temperature dependence, but not one has studied extremely low temperature measurements. As the temperature gets lower, will the dielectric constant of water change enough to require recalibration of the water content to  $K_a$  relationship? The soil type



encountered on an exploration mission will probably not pose a problem unless it deviates significantly from the range of typical terrestrial soils, such as having an extremely high clay or salt content, which may cause signal loss.

There are some possible problems associated with the installation of the probe. The probe should be implanted so as to cause a minimal disturbance to the soil. If an air gap is present between the transmission line and the surrounding soil, the measured value for the apparent dielectric constant will be lower than the true dielectric constant. The deviation between the two increases as the value for the constant increases. (1) If a gap between the soil and the probe is filled with water, the water content will be overestimated. Though, the error is much less than for an air-gap. (1) Next, the deviation of the transmission lines from being parallel should be small compared to the signal wave length in the soil. (2) An externally applied voltage greater than 5V can damage the sampling gate or tunnel diode of a Tektronix TDR. (3)

A definite disadvantage and a major source of uncertainty lies in determining the points A and B of a TDR trace, for the reason of the individuality of each trace. It could pose a difficult task to systematize the locating of the points in order for a machine to do. Otherwise, a remote sensing device would have to digitize the shape of each trace for the whole trace to be sent back.

The TDR technique seems to be less effective with low or high water content extremes. A measurement of volumetric water content below 5%, which may likely occur on a planetary mission, can easily result in a large amount of error for three reasons. First, the resolution of the trace for such small values will be poor. Next, the standard error of estimate is 1.3% over the complete range of water contents. (10) The smaller values would

have a greater percent of error. Plus, measurements for low water content would be more sensitive to the differences in the soil dielectrics. Greater precision and accuracy would require calibration for the particular soil that is under investigation.

Several things would have to be studied and evaluated before applying the TDR technique to a planetary mission. A material would have to be selected for the transmission line conductors that would be physically strong enough for installation and would minimize physical and thermal disturbance to the soil. Determination of the optimum method of installation is needed. The probe could be installed from a surface penetrator or soft lander by using a spring or explosive with or without the aid of pilot holes. The TDR technique may be particularly well suited for use with surface penetrators, elongated missile-shaped instrument carriers. A TDR instrument could probably withstand the hard landing of a penetrator into a solid planetary body. Once a penetrator has come to rest in the sub-surface, the probe could be implanted into the regolith through two small holes in the side of a penetrator. A length for the probe would have to be chosen. Lengths from 6 cm to 200 cm have been used. (8 + 2) The shortness of a transmission line is restricted by the system's resolution, and the length by the signal attenuation and the ability to fix point B. Samples at very low temperatures and with low water content must also be examined.

The Time Domain Reflectometry technique for determining volumetric water content in a soil holds great promise as a non-destructive, terrestrial field method. As for applying the technique to planetary exploration missions, it still holds promise, but there is some question as to its effectiveness under these conditions. Measurements at low temperatures and with low water content will have to be studied, and it must be decided how points A and B are to be determined.

## References

1. Annan, A.P. Time-Domain Reflectometry-Air-Gap Problem for Parallel Wire Transmission Lines. In Report of Activities, Part B, Geol. Serv. Can., Paper 77-1B, pp. 59-62, 1977.
2. Davis, J. L. Relative Permittivity Measurements of a Sand and Clay Soil in situ. Geol. Serv. Can., Paper 75-1C, pp. 361-365.
3. Instruction Manual for the 1502 Time Domain Reflectometer, Tektronix, 1980.
4. Mars Science Working Group. A Mars 1984 Mission. NASA TM-78419, July 1977.
5. Murphy, James P., Ray T. Reynolds, Maxwell B. Blanchard, and Uel S. Clanton. Surface Penetrators for Planetary Exploration: Science Rationale and Development Program. NASA Technical Memorandum 81251, March 1981.
6. Patterson, D. E., and M. W. Smith. The Measurement of Unfrozen Water Content by Time Domain Reflectometry: Results from Laboratory Tests. Can. Geotech. J., Vol. 18, pp. 131-144, 1981.
7. Smith, M. W. Electromagnetic Detection of Soil Water: Use of Time Domain Reflectometry on Frozen Soils. Proc. of the Third Colloquium on Planetary Water, pp. 182-185, 1980.
8. Smith, Michael W. Personal Communication, 1981.
9. Topp, G.C., J.L. Davis, and A.P. Annan. Electromagnetic Determination of Soil Water Content: Application of TDR to Field Measurements. Proc. of the Third Colloquium on Planetary Water, pp. 176-181, 1980.
10. Topp, G.C., J.L. Davis, and A.P. Annan. Electromagnetic Determination of Soil Water Content: Measurements in Coaxial Transmission Lines. Water Resources Res., Vol. 16, pp. 574-582, 1980.
11. Topp, G.C., J.L. Davis, and A.P. Annan. Electromagnetic Determination of Soil Water Content Using TDR: II Applications to Wetting Fronts and Steep Gradients. Submitted to Soil Science Society Amer. Jour., 1980.
12. Topp, G.C., J.L. Davis, and A.P. Annan. Electromagnetic Determination of Soil Water Content Using TDR: I Laboratory Simulations of Field Installations. Submitted to Soil Science Society Amer. Jour., 1980.

ASSESSING THE VOLCANIC PROBABILITY  
OF MARTIAN LANDFORMS  
MAUREEN M. O'TOOLE  
PLANETARY GEOLOGY INTERN  
U.S.G.S., FLAGSTAFF CENTER  
BRANCH OF ASTROGEOLOGIC STUDIES  
JUNE-JULY 1981

It is known that volcanism has been a very important process on Mars. Large volcanic constructs such as Olympus Mons, Arsia Mons and Elysium Mons have been identified and studied by the planetary community. More difficult to identify are smaller volcanoes that are not clearly associated with major volcanic provinces such as Tharsis and Elysium. This paper provides a scheme to aid in assessing the probability that landforms are volcanic in nature.

Eight types of known volcanic features and associations are described in table 1. Each is assigned a point value based on the degree to which it is thought to be characteristic of volcanoes. Fewer points are allotted to features that may be ambiguous in that non-volcanic processes such as erosion, tectonics and meteorite impact could have produced similar features. The classic volcanic combination of general volcanic shape, summit depression and lobate flanks receives extra points because they mutually enhance the probability of volcanic origin.

It is recognized that this point system is completely subjective and can neither positively identify nor eliminate martian landforms as being volcanoes. However it does provide a means for quantifying confidence levels in volcano identification and for the comparison of these features. The table also provides an easy method for referencing descriptive information.

Table 2. shows how some well known martian volcanoes were rated using this system. The large shield volcanoes of the Tharsis Region have very high scores, with Olympus Mons receiving the maximum possible score of 21 points and Arsia Mons 19 points. Elysium Mons, a composite volcano with a single, circular summit crater, accumulated 18 points. Tyrrhena Patera, an old, eroded volcano with degraded flows has 12 points.

Using this system to evaluate possible volcanoes in other areas, I found cratered cones, domes and shields which were assigned as few as 4 or 5 points. More complex landforms received as many as 16 points. Features having low point scores may or may not be volcanoes and alternate origins should be considered before identifying them as such.

It is hoped that this point system will be useful in the evaluation of the volcanic probability of martian landforms when studying and mapping the martian surface.

Table 1.

Landform Name:

Location:

Characteristic	Description	amt.	pts.	Comments
I FORM A. MAP OUTLINE	1-Circular	2		
	2-Elongate	1		
	3-Irregular	1		
B. CROSS SECTION	1-Gentle slopes, low relief	1		
	2-Steep slopes, high relief	1		
	3-Steep sides, flat top	1		
II SUMMIT DEPRESSION	1 Circular	1		
	2-Slot-shaped	2		
	3 Irregular, coalescing	3		
III LOBATE FLANKS A. DEGRADED FLOWS	Tongue-like extentions of material around base of feature, lava flows Eroded, fractured, cratered	1		
	B. FRESH FLOWS	Evidence of channels and tubes, buries other features	4	
IV COMBINATION OF I, II, III	Feature has general volcanic form, summit crater and lobate flanks	3		
V RADIAL PATTERN ON FLANKS	Radial pattern of possible lava flows, tubes and channels	1		
VI POSSIBLE VOLCANO-TECTONIC FEATURES	Concentric fractures of grabens associated with the landform itself	1		
VII STRATAGRAPHIC POSITION	Feature appears to be younger than surrounding material and features	1		
VIII RELATION TO REGIONAL STRESSES	1-Located on prominent fracture	2		
	2-located on intersection of two or more fractures	3		
IX RELATION TO OTHER POSSIBLE VOLCANOES	Landform is in close proximity to or in a linear pattern with other similar features	1		
ADDITIONAL COMMENTS AND MEASUREMENTS	TOTALS			

Table 2.  
Landform Name: see below

Location:

Characteristic	Description	amt.	A.	B.	C.	D.
I FORM A. MAP OUTLINE	1-Circular	2	2	2	2	2
	2-Elongate	1				
	3-Irregular	1				
B. CROSS SECTION	1-Gentle slopes, low relief	1	1	1		1
	2-Steep slopes, high relief	1			1	
	3-Steep sides, flat top	1				
II SUMMIT DEPRESSION	1 Circular	1		1	1	
	2-Slot-shaped	2				
	3-Irregular, coalescing	3	3			3
III LOBATE FLANKS A. DEGRADED FLOWS	Tongue-like extentions of material around base of feature, lava flows Eroded, fractured, cratered	1	1	1	1	1
	B. FRESH FLOWS	Evidence of channels and tubes, buries other features	4	4	4	4
IV COMBINATION OF I,II,III	Feature has general volcanic form, summit crater and lobate flanks	3	3	3	3	3
V RADIAL PATTERN ON FLANKS	Radial pattern of possible lava flows, tubes and channels	1	1	1	1	1
VI POSSIBLE VOLCANO-TECTONIC FEATURES	Concentric fractures of grabens associated with the landform itself	1	1	1	1	1
VII STRATAGRAPHIC POSITION	Feature appears to be younger than surrounding material and features	1	1	1	1	
VIII RELATION TO REGIONAL STRESSES	1-Located on prominent fracture	2			2	
	2-located on intersection of two or more fractures	3	3	3		
IX RELATION TO OTHER POSSIBLE VOLCANOES	Landform is in close proximity to or in a linear pattern with other similar features	1	1	1	1	
ADDITIONAL COMMENTS AND MEASUREMENTS	TOTALS A. Olympus Mons B. Arsia Mons C. Elysium Mons D. Tyrrhena Patera	max. 21	21	19	18	12

THE EFFECTS OF VARYING SURFACE ROUGHNESS  
ON AERODYNAMIC AND AEOLIAN PROCESSES

Lynn M. Reding

1981  
Planetary Geology  
Summer Intern

Space Sciences Division  
National Aeronautics and Space Administration  
Ames Research Center  
Moffett Field, California

Aeolian processes on Earth and Mars have been studied with wind tunnel simulations. Geologic applications have been made to soils, sand and snow movement, and with the aid of recent Viking images, investigations have included aeolian transport of surface material on Mars. The effects that various roughness elements have on an aeolian process is of great significance and application to the study of material transport. Previous tests conducted at the MARSWIT facility dealt with a surface lacking non-erodible rough surface elements. A floor with pebbles  $\sim 1$ cm in diameter and spaced 1cm apart was used for this study. The object was to perform a preliminary investigation of the effects of varying surface roughness on aerodynamic and aeolian processes.

A boundary layer survey was conducted over the rough surface. Profiles were made with various sand bed heights. The rough surface profiles did not resemble that of a smooth surface but were still found to be turbulent. The boundary layer profiles were used to determine friction velocity ratios,  $V^*/V_\infty$ . This value was determined for various sand depths and was found to increase as roughness increased. The straight log-height v. s. velocity plot confirmed the assumption inferred from the profile that the boundary layer was in fact turbulent. Next, wind friction threshold speeds,  $V^*t$ , were determined for 350  $\mu\text{m}$  and 95  $\mu\text{m}$  sand beds. The beds were superimposed over the pebble surface and  $V^*t$  values were determined for various heights of the bed as it was allowed to erode.  $V^*t$  was found to increase with increasing surface roughness (Fig. 1). Values for  $V^*t$  where the roughness height was zero, and  $V^*t$  determined for the smooth MARSWIT surface revealed similar values. Finally, particle flux,  $q$  ( $\text{gm}/\text{cm}^2/\text{sec}$ ) as a function of height above the pebble base, and total flux  $Q$ , ( $\text{gm}/\text{cm}/\text{sec}$ ), were determined for both sand sizes. The sand beds were 75 percent of a full bed or 7.5mm thick.  $q$  decreased



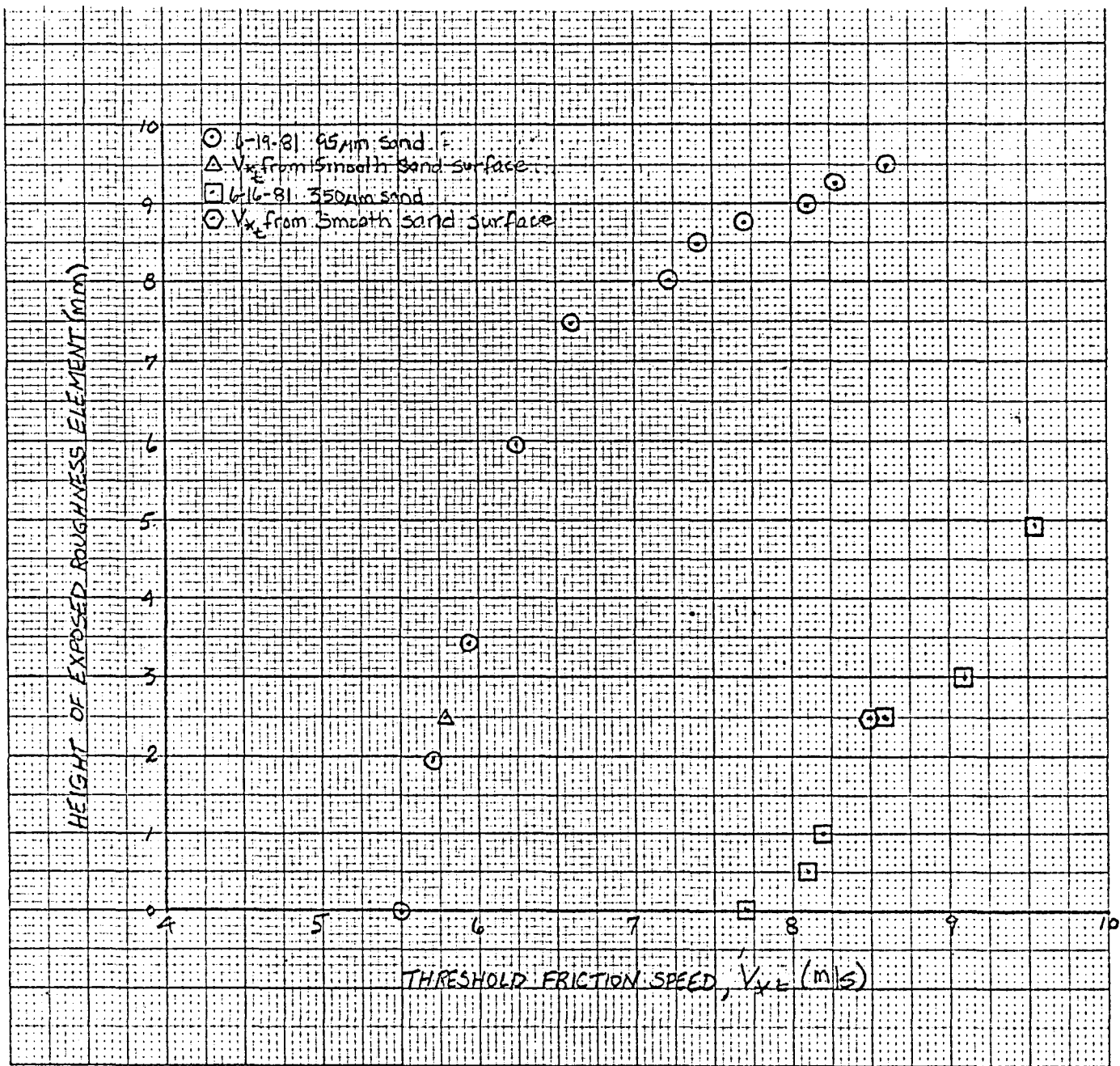


Fig. 1 - Threshold friction speed as a function of surface roughness. 95µm and 350µm sand sizes used.  $V_{*t}$  values for smooth surface from Greeley unpublished data, 1981 are also included.

with height,  $Q$  increased with free-stream velocity,  $V_{\infty}$ . Interpolating both sets of data showed  $Q$  for the smooth surface to be slightly less than  $Q$  for the rough. Tables 1 and 2 are compiled charts of boundary layer and flux data.

The results obtained in the rough surface wind tunnel may be applied to geologic and possibly Martian analogues. Understanding the effects of wind on various sand surfaces enables prediction and control not only of sand movement, but snow, soil and dust as well. Erosion rates, ripple formation and migration and other aeolian related processes are also better understood through tests of this nature. Applications of this knowledge may be applied to the study of such geologic areas as flat farmlands, desert sands, snow fields and even the rugged surface of Mars.

Fundamental to understanding the aeolian regime on the Martian surface is the knowledge of wind characteristics and parameters on a geologic surface. Knowing the effects that surface roughness has on geologic aeolian parameters, one may extrapolate the data to apply to the Martian surface. In conjunction with theoretical considerations, actual simulations of Martian conditions are informative and aid in the understanding of the aeolian process which occur on the surface of the planet. Therefore, wind tunnel experiments using the rough surface at Martian atmospheric conditions, are also planned for the future.

TABLE I  
BOUNDARY LAYER SURVEY DATA

run	$V_{\infty}$ (m/s)	$H_{\infty}$ (mm)	$V_*/V_{\infty}$	$C_f$	k	roughness (mm)	sand size ( $\mu\text{m}$ )
6-11-81-A	8.49	221	.100	.020	4	10	---
6-12-81-A	4.40	350	.0955	.018	"	"	---
6-12-81-B	4.31	232	.100	.020	"	"	---
6-15-81-A	10.19	240	.102	.021	"	"	---
6-15-81-B	11.39	252	.098	.019	"	"	---
6-16-81-A	7.70	180	.080	.013	1.3	1	350
6-17-81-B	9.80	234	.071	.011	1.3	6	"
6-17-81-A	12.80	240	.073	.011	0	0	95
6-19-81-B	4.20	152	.080	.013	1.1	2.5	"
6-19-81-C	5.70	180	.084	.014	1.6	7.5	"
6-19-81-D	8.14	216	.090	.016	2.6	10	"

TABLE II  
BOUNDARY LAYER SURVEY DATA

run	$V_{\infty}$ (m/s)	$Q$ (gm/cm/sec)	roughness (mm)	sand size ( $\mu\text{m}$ )
6-30-81-B	7.20	$3.5 \times 10^{-4}$	2.5	350
6-30-81-C	8.34	$7.5 \times 10^{-4}$	"	"
6-30-81-D	8.78	$8.6 \times 10^{-4}$	"	"
7-2-81-D	8.96	$3.6 \times 10^{-4}$	"	"
7-7-81-B	9.26	$8.4 \times 10^{-4}$	"	"
7-2-81-A	9.32	$1.3 \times 10^{-3}$	"	"
7-7-81-A	9.49	$3.2 \times 10^{-3}$	"	"
7-1-81-A	9.55	$1.3 \times 10^{-2}$	"	"
7-1-81-B	9.60	$5.6 \times 10^{-3}$	"	"
6-23-81-A	5.50 <sup>Δ</sup>	$2.0 \times 10^{-3}$	"	95
6-29-81-D	5.99	$1.6 \times 10^{-3}$	"	"
6-30-81-A	6.42	$1.2 \times 10^{-2}$	"	"
6-29-81-C	6.99	$2.1 \times 10^{-2}$	"	"
6-23-81-C	7.50	$2.8 \times 10^{-2}$	"	"
6-29-81-A	7.87	$5.0 \times 10^{-2}$	"	"
6-23-81-B	8.59	$8.3 \times 10^{-2}$	"	"
6-22-81-B	9.49	$2.7 \times 10^{-1}$	"	"
4-81*	9.0 <sup>Δ</sup>	0	0	350
4-81*	5.5 <sup>Δ</sup>	0	0	95

Δ V\* valves

\* Greeley unpublished data, 1981

## REFERENCES

- Bagnold, R. A., The Physics of Blown Sand and Desert Dunes, 265 pp., Methuen, London, 1941.
- Chepil, W. S., Dynamics of Wind Erosion: I. Nature of Movement of Soil by Wind, Soil Science 60, 305-320, 1945.
- Greeley et al., unpublished data, 1981.
- Malone, K. A., Flux of Windblown Particles on Mars, Planetary Geology Summer Intern Report, NASA Ames, 55 pp., 1980.
- Schlichting, H., Boundary-Layer Theory, translated from German by J. Kestin, 748 pp. McGraw-Hill Book Company, New York, 1968.
- White, B. R., Plane Bed Thresholds of Fine-Grained Sediments, Nature, 228, 152-153, 1970.

## Introduction

Direct knowledge of extraterrestrial volcanoes is limited to photos of the volcanoes' morphology. An understanding of the parameters that influence the morphology of terrestrial volcanoes will expand our ability to understand extraterrestrial volcanoes.

## Composition of Lava

There are many variables that influence the morphology of terrestrial volcanoes, however one parameter has generally been accepted as the most important. It has long been known that an increase in the percentage of silica in a lava increases its viscosity. From this it has been assumed that highly viscous, siliceous lavas build steep sided volcanoes, and low silica, less viscous lavas build gently sloped volcanoes. From an analysis of 45, mostly composite and some shield volcanoes, I have found no correlation between the amount of silica and slope of the volcanoes (Fig. 1). I have used the mean silica value for chemical analysis of each volcano listed in the Catalogue of Active Volcanoes. For the slope of the volcanoes I used height and flank width measurements by Pike (1978), so slope values are of the average geometric slope. It is easy to see why a simple correlation between silica abundance in lavas and the slope of volcanoes does not hold true. The amount of silica is considered an important influence on morphology because silica effects a lava's viscosity. However, there are other parameters that also influence a lava's viscosity. The amount of volatiles and temperature of a lava have an important influence on viscosity and may override the influence of silica on viscosity.

I have compared height, flank width, slope and volume of 45 composite volcanoes to various compositional parameters that influence lava viscosity such as silica,  $\text{SiO}_2$ , potassium,  $\text{K}_2\text{O}$ , alkali ratio,  $\frac{(\text{Na}_2\text{O} + \text{K}_2\text{O})^2}{\text{SiO}_2 - 43}$ , average serial index  $\frac{\text{Fe}_2\text{O}_3}{\text{FeO}}$ , and iron ratio,  $\frac{\text{Al}_2\text{O}_3}{\text{FeO}}$ , an indicator of the amount of water vapor contained in the lava). I found only weak correlations between volcano morphology and these chemical parameters.

## Physical Processes

I believe physical processes involved in cone building are more important than chemical compositions of the cones' lavas. Correlation between lava compositions and volcano morphology is limited because chemical analyses can only be made of surface lavas whereas the morphology of a volcano may be the result of earlier buried lavas possibly of another composition. The strongest argument against a simple relationship between chemical content and volcano morphology is the number of cone building processes that are not directly related to the chemical content of lavas. Ash fall, ash flows, mud flows, avalanche, flank eruptions, parasitic cones and caldera collapse all effect volcano morphology. It has been suggested that the percentage of pyroclastics that make up a cone effect its morphology. Volcanoes with a high percentage of pyroclastic material are expected to have high slopes because pyroclastics are deposited near their repose angle of  $\sim 30^\circ$ . Some data support the theory that the rate of effusion of lava from a vent determines how far that lava will flow

(Walker, 1973; Malin, 1980). It has been inferred that the effusion rate influences the morphology of the entire volcano. It is apparent that many parameters influence the morphology of a volcano and no single parameter alone controls morphology. A technique, called factor analysis, could assess the individual parameters that influence morphology.

### Difficulties in Investigating Volcanic Morphology

The biggest problems in studying volcanic morphology are the lack of data, and ambiguity of data that are available. No data are available on the amounts of pyroclastics in a cone to test the theory that pyroclastics increase the slope of a cone. Several workers have suggested the lower slopes of some volcanoes consist almost wholly of lahar, avalanche and ash flow deposits (Crumpler, 1978). Thus only the upper portion of the cone results directly from deposition of lava and pyroclastic, but no data are available to document this. For only a handful of eruptions has the rate of effusion of lava been determined. It has also been suggested the effusion rate changes radically during an eruption. For some eruptions the effusion rate reaches a maximum shortly after the eruption begins and decreases rapidly to a lower rate that continues until the eruption ends (Scandone, 1979). Since a low effusion rate produces short lava flows a long period of low effusion rate eruptions may cause short compound lava flows to pile upon one another at the vent, forming a steep, high angled cone. However there are not enough data available to test this theory.

Ambiguity in determining volcano morphology centers on the definition of quantities being measured. The flank width of a volcano is a very important measurement of a volcano's morphology. The flank width determines the elevation of the base of the volcano and thus determines the height, average geometric slope and the volume of the volcano. There is no obvious or genetic definition of the edge of a volcano. Pike (1978) defines flank width as the distance from "rim crest to edge of edifice." Measurements of flank width are made from topographic maps and defined by a break in slope between volcano topography and surrounding terrain. Definition of the edge of a volcanic edifice is confused by lava flows that extend beyond the nominal radius of the volcano. One volcano (Kefildyngja) in Iceland has a radius of ~10 km but has a recent lava flow that is 85 km long! Perhaps the edge of a volcano should be considered the maximum radius where all radiating lava flows are in contact with their neighbors such that they all contribute to the volume of a cone. However, such a measurement would be nearly impossible to make on all but a few well mapped volcanoes.

### Lava Flow Lengths

Data on the primary factors that influence volcano morphology are not available. Data on the lengths of lava flows are available and the length of lava flows strongly reflect the effusion rate (Walker, 1973). However, the length of lava flows may also be related to the volume of lava produced during the eruption, the temperature of the erupted lava, the composition and the volatile content of the lava. I averaged the lengths of historic lava flows for each of 17 composite and shield volcanoes and plotted the average length of lava flows against the geometric slope of the volcanoes (Fig. 2). I found a good correlation between the length of lava flows and the slope of volcanoes, considering that a number of volcanic processes other than lava flows possibly contribute to the morphology of a volcano. None-the-less, the data in Figure 2 suggest that the effusion rate of a volcano, as indicated by lengths of lava

flows, influences ultimate volcano shape to a remarkable degree.

### Discussion

Because many of the factors that influence volcano morphology have not been measured in the past and are difficult to determine I see the major developments in understanding volcanic morphology resulting from experimental modeling of volcanoes. In experimental simulation individual parameters can be isolated and varied to observe their influence on morphology.

### References

Crumpler, L. S. (1978) Mt. Taylor Composite Volcano, New Mexico: Geology of the North and West Flanks. Geol. Soc. Am. Abst. with Prog. 10, 101.  
Malin, M. (1980) Lengths of Hawaiian Lava Flows. Geology 8, 306-308.  
Pike, R. J. (1978) Volcanoes on the Inner Planets: Some Preliminary Comparisons of Gross Topography. Proc. Lunar Planet. Sci. Conf. 9th, 3239-3273.  
Scandone, R. (1979) Effusion Rate and Energy Balance of Paricutin Eruption (1943-1952), Michoacan, Mexico. J. Volc. Geoth. Res. 6, 49-59.  
Walker, G. P. L. (1973) Lengths of Lava Flows. Phil. Trans. R. Soc. Lond. A.-274, 107-118.

### CONE SLOPE VS. SILICA CONTENT

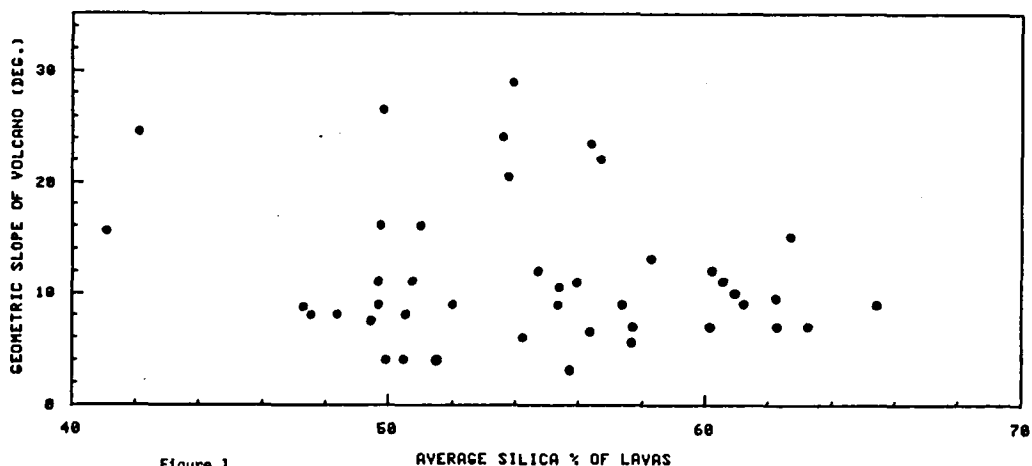


Figure 1 .

### CONE SLOPE VS. LAVA FLOW LENGTH

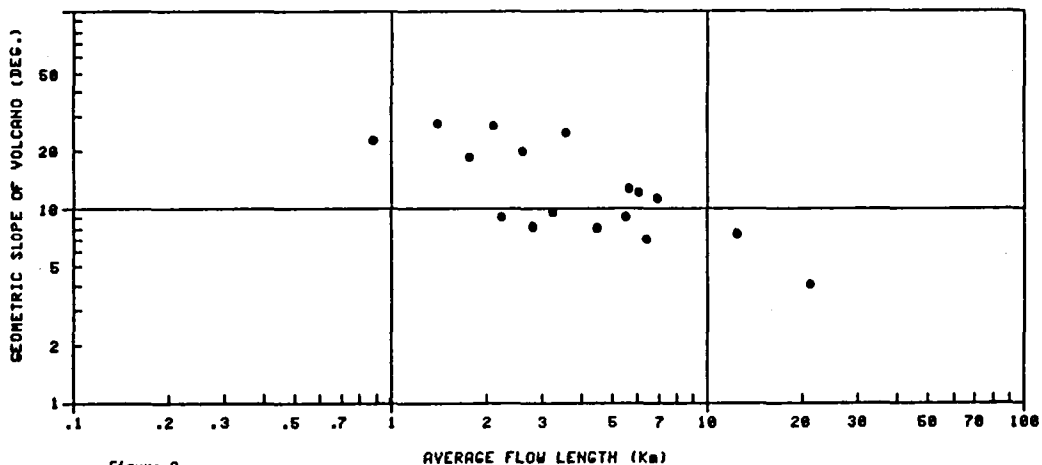


Figure 2.

## Two Methods for Determining Volumes for Explosion and Impact Craters

Alejo N. Verdes  
NASA Intern, U.S. Geological Survey  
2255 North Gemini Drive, Flagstaff, Arizona 86001

INTRODUCTION. Dimensional data for impact and explosion craters is important in a number of studies of cratering mechanics. The research described in this paper deals with the development and testing of two techniques designed to determine apparent and rim crest volumes of impact and explosion craters with a high level of accuracy (1). One example of the use of this data is the calculations of cratering efficiency, i.e., the apparent volume divided by the total energy and normalized to volume per ton of TNT-energy. Two techniques were employed to collect the volume data. One method involves a measurement of diameters across the crater profile, calculation of thin-disk volumes, and summation of the total thin-disk volume increments obtained from the crater bottom to the original ground level. The second method was to digitize the detailed topographic map of the crater and utilize a sequence of computer programs to calculate the crater volumes. The point of using these two methods is to compare the accuracy of the two techniques, their relative cost, and the time to complete the volume calculations with each technique.

BACKGROUND. In 1973, the Defense Nuclear Agency conducted a series of explosive cratering trials at Yucca Flat, Nevada called Pre-Mine Throw IV. Two of the trials were conducted using a 7.1-ton and a 100-ton TNT sphere. Both explosions yielded large bowl-shaped craters. The 100-ton explosion produced a crater with a diameter of 25.0 m measured at the rim crest, and the 7.1-ton explosion produced a crater with a diameter of 17.2 m measured at the rim crest. The charges were detonated lying tangent on the surface above flat-lying dry playa sediments. The craters had similar morphologic as well as structural similarities (1). With respect to morphology, both craters



shared the following similarities: a) bowl-shapes, b) small flat floors, c) irregular rim crests, d) ejecta blankets, and e) talus-covered lower walls. Both craters shared the following structural similarities: a) breccia lens, b) disrupted zones below the breccia, c) uplifted rims, d) overturned layers in the ejecta, and e) faulting, fractured and uplifted rim strata.

PRIMARY METHOD. Taking the algebraic expression  $V=\pi R^2 H$ , the volume for a cylindrical shape may be calculated. A crater may be viewed as an inverted, truncated, conical projection. The diameter of the crater floor ( $D_{cf}$ ) and the diameter of the crater rim crest ( $D_{rc}$ ) are shown in Figure 1. In this technique, volumes are summed from thin-disks from the floor of the crater to the rim crest with each disk projecting slightly beyond the crater walls (see Fig. 1). The disks intersect the crater walls at each  $D^n$  measurement (Fig. 1). Two right triangles appear sharing one point (in Fig. 1 at x or y). The triangle outside the slope wall is omitted since it is approximately equal to the triangle within the wall. The small error in volume due to the  $R^2$  effect for the base of each disk triangle of volume is reduced by keeping the H interval as small as is practical. In the specific case of Pre-Mine Throw IV, each disk has an H value of 0.1 meter. The diameter used in each disk is measured halfway between the disk top and bottom (Figs. 1, 2). Referring to Fig. 1, line  $\overline{ab}$  is considered the disk top, while line  $\overline{cd}$  is the disk bottom. D is defined as a diameter, while n is one specific diameter being measured. The horizontal distance between point x and point y is the numerical value used for a  $D^n$  measurement. Each disk has a constant H value, and from the  $D^n$  value,  $R^2$  is obtained. Using the formula  $V=\pi R^2 H$ , a volume is computed for that specific disk. The summation of all the disks constitutes the total volume of the crater. Figure 2 shows the stack of disks used in this technique.

DIGITIZED METHOD. The second method involves the use of an Electrak digitizer. This system consists of a digitizing board and support hardware, which records x and y coordinates with a Z value for every contour line of the topographic map inside the crater. This hardware allows the systematic production of a digitized assemblage of positional data for each contour line. Using the appropriate software, a plotter was used to aid in the necessary editing of information from the digitized contour map. In this case a Calcomp plotter was used to edit errors to produce the corrected copy shown in Figure 3. From the edited tape, further corrections were made using display hardware (DeAnza system) which assigns color values to specific Z values. This system also allows visual depth perception of the digitized data sheets. This is the "fine-tune" stage, where any remaining errors are eliminated, thus allowing the final software programs to be processed for the volume calculations. In this phase of the computer data reduction, the computer assigns the final Z values to the existing contour lines. This is accomplished by averaging the distances between two existing Z values and adding a topographic line, thereby numerically increasing the number of contour lines available for the volume calculations. The final product may once again be displayed for corrections. A shading program is used to contour relief for viewing purposes. This program incorporates different sun angles and creates a "shading" effect. A histogram of the interpellated file is also generated, giving a pixel count of all the Z values. Manual calculations of volumes are then compiled using the map scale.

RESULTS. For the Pre-Mine Throw IV 100-ton crater, four different profiles were measured and the 7.1-ton crater had two profiles measured. The results of the volume calculations for both craters are listed below.

$V_{ap}$  = volume apparent, from crater floor to the original ground level.

$V_{ag}$  = volume above original ground level to rim crest.

$V_{rc}$  = total volume from crater floor to rim crest.

#### 7.1-TON CRATER PROFILES

Volume	090°E,270°W	360°N,180°S	AVERAGE VOLUMES
$V_{ap}$	21.37m <sup>3</sup>	22.72m <sup>3</sup>	22.15m <sup>3</sup>
$V_{ag}$	9.98m <sup>3</sup>	12.75m <sup>3</sup>	11.37m <sup>3</sup>
$V_{rc}$	31.35m <sup>3</sup>	35.47m <sup>3</sup>	33.41m <sup>3</sup>

#### 100-TON CRATER PROFILES

Volume	045°NE	360°N	135°SE	090°E	AVERAGE VOLUMES
$V_{ap}$	522.56m <sup>3</sup>	555.85m <sup>3</sup>	518.89m <sup>3</sup>	522.88m <sup>3</sup>	530.05m <sup>3</sup>
$V_{ag}$	476.08m <sup>3</sup>	515.96m <sup>3</sup>	460.69m <sup>3</sup>	502.04m <sup>3</sup>	488.69m <sup>3</sup>
$V_{rc}$	998.64m <sup>3</sup>	1071.81m <sup>3</sup>	979.58m <sup>3</sup>	1024.92m <sup>3</sup>	1018.74m <sup>3</sup>

The results of the first digitized volume for the 100-ton crater gave the following results for the crater as listed below:

$$V_{ap} = 555.39\text{m}^3$$

$$V_{ag} = 643.37\text{m}^3$$

$$V_{rc} = 1198.76\text{m}^3$$

CONCLUSIONS. We are still in the process of reviewing the results of the two techniques used to determine the crater volumes. The digitizing technique is expected to give the most accurate results, however the data reduction of the

second digitized data base of the 100-ton crater is not yet reduced. The best comparison between the two techniques is to compare the apparent volumes that are calculated from the crater floor to the original ground level, i.e, the  $V_{ap}$ . This avoids comparisons of volume data taken from the very irregular topography of the rim crest. The  $V_{ap}$  values are certainly the most important volume data for examining cratering processes, such as the determination of cratering energy efficiencies, and the data reduced to date clearly shows that both techniques give comparable  $V_{ap}$  values. The apparent volumes differ only by about 5% and indicate both techniques give comparable result for  $V_{ap}$ . After the second digitized map values are completed, a much better determination can be made regarding the accuracy, cost, and time for each technique.

REFERENCES. (1) Roddy, David J. (1976) Large-scale impact and explosion craters: Comparisons of morphological and structural analogs, Impact and Explosion Cratering, p. 185-246.

ACKNOWLEDGEMENTS. The author wishes to thank Dr. David J. Roddy for being my mentor and showing me new worlds, Christopher E. Isbell, Janet M. Wilkerson, and Tammy Rock for their professional help and personal assistance in this program, and the staff of the US Geological Survey at Flagstaff.

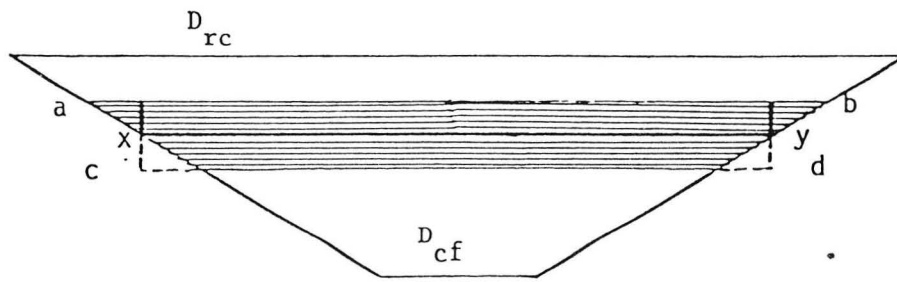


FIG 1

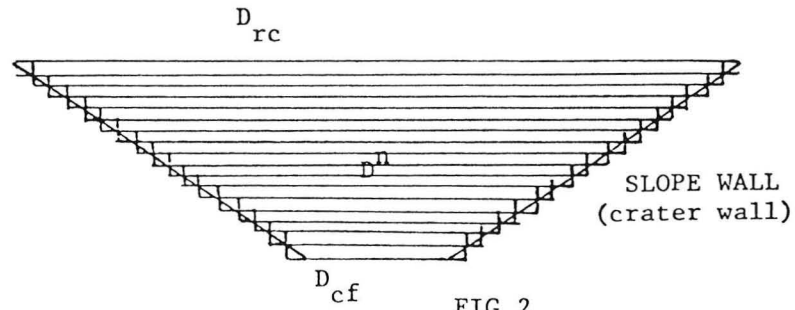


FIG 2

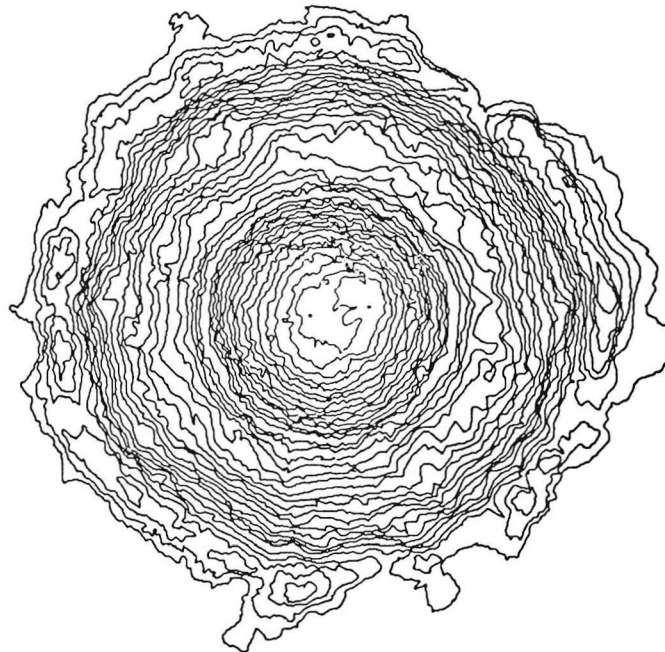


FIG. 3

DX002/1 CRATER #1  
 NEG #150RAS 9TRACK 16BIT \*800BPI FILE 1 NL 750 NS 1000  
 30-JUL-81 09:27:18 U.S.G.S. FLAGSTAFF IMAGE PROCESSING FACILITY

EJECTA DISTRIBUTION AROUND A SMALL LUNAR CRATER

Stephen J. Wetzel  
 NASA PGUR Intern, Brown University  
 July 1981

The ejecta deposit surrounding a one-half kilometer lunar crater was examined with the goal of finding a pattern to its distribution. The unnamed crater selected for the study was taken from Lunar Orbiter III, frame 153 H2. A 19.125 x 18.750 inch enlargement (covering an area of 2.250 x 2.206 kilometers) was digitized. Conversion of the raw data into a coordinate system based upon the subspacecraft point was accomplished by an angular translation, photographic length contraction correction and photographic scaling. Based upon this corrected data, many forms of final data expression were possible. Figure 1 explains the three phases of data reduction.

Figure 1: Three phases of data reduction

<u>Raw Data</u>	<u>Semi-reduced Data</u>	<u>Data For Analysis</u>
Crater data:	Crater data:	Crater data:
5 sets of 3 rim points	Average center	Average center
Block data:	Block data:	Block data:
Block number	Block number	Quality factor
Number of axes	Number of axes	Number of axes
Quality factor	Quality factor	Magnitude of length axis
2 endpoints per axis	2 endpoints per axis	Distance from crater center to midpoint of length axis
2 framelet strip prints for photo orientation	All data in lunar-based coordinates	Magnitude of width axis
All data in digitizing board coordinates		Distance from crater center to midpoint of width axis
		Bearing from north
		Ratio: length/width

Once the data existed in the final reduced form, the blocks were grouped according to size. The size ranges were based upon a  $5\log_2 L$  scale, where L is the block length in meters. In this manner, small size ranges were established in the lower block sizes where many blocks occurred, and larger bin sizes were used for the larger blocks.

The total size--frequency distribution resulted in a very clean normal distribution where block sizes 1.74 -5.27 clearly dominated. More specifically, the size bins from 2.64 - 3.48 meters together comprised one-third of the block population, as is displayed in Table 1.

Table 1: Size-Frequency Data for Total Population

<u>Size Bin Number</u>	<u>Size Ranges</u>	<u>Size Variation</u>	<u>Percentage of Total Number of Blocks</u>
1	up to 1.00m		1.48
2	1.00- 1.15	.15	0.67
3	1.15- 1.32	.17	0.79
4	1.32- 1.52	.20	1.76
5	1.52- 1.74	.22	3.01
6	1.74- 2.00	.26	4.55
7	2.00- 2.30	.30	9.47
8	2.30- 2.64	.34	12.36
9	2.64- 3.03	.39	16.89
10	3.03- 3.48	.45	16.06
11	3.48- 4.00	.52	13.11
12	4.00- 4.59	.59	8.54
13	4.59- 5.28	.69	4.39
14	5.28- 6.06	.78	2.61
15	6.06- 6.96	.90	1.31
16	6.96- 8.00	1.04	1.09
17	8.00- 9.19	1.19	0.59
18	9.19-10.56	1.37	0.44
19	10.56-12.13	1.57	0.32
20	12.13-13.93	1.80	0.16
21	13.93-16.00	2.07	0.08
22	16.00-18.38	2.38	0.12
23	18.38-21.11	2.73	0.04
24	21.11-24.25	3.14	0.02
25	24.25-27.86	3.61	0.02
26	27.86-32.00	4.14	0.06
27	32.00-		0.04

In examining size-frequency plots for individual 50 meter range groupings extending 200-1700 meters from the crater center, a secondary peak appeared at block sizes just less than the dominant 2.64-3.48 meter peak in ranges less than 400 meters, but with increasing range this secondary peak disappeared and at ranges just greater than 450 meters reappeared as a minor peak at block sizes larger than 3.48 meters.

A range-frequency plot resulted in a concentration of blocks within the 250-550 (1.0 - 2.2 R) range followed by a gradual decrease as range increased.

Incremental plots, comparing the number of blocks in a size range divided by the change in block length within the size range versus the size range itself, became useful. In the incremental plot of the total population (shown on the right), a smooth curve resulted with the exception of a slope change at block size 3.6 meters, suggesting a resolution drop-off at this point. The incremental plots of individual 50 meter range groups showed a decrease of larger blocks with increasing range. The incremental plot of the 600-650 meter range group indicated a lack of both large and small block sizes. It consisted of blocks approximately 1 - 8 meters.

A slope  $b$  value (see Hartmann, 1969), although having a correlation coefficient of 0.705, was calculated to be 0.337.

Admittedly, this data has a somewhat tentative nature since only one-half of the area around the crater was examined. Other problems included the fact that the crater latitude, longitude, and diameter were interpolated from the Lunar Orbiter Postmission Photo Support Data. The Lunar Orbiter photos, although of good quality, lost precision in their mosaicking process. It is estimated that meters to a few tens of meters of the lunar surface have been lost between some of the framelets.

The true ramifications of the study will not become evident until this and a few other craters have been completed. It is interesting to note the normal distribution of the total block frequency, indicating a single rock formation rather than several of varying strengths and fracturing tendencies

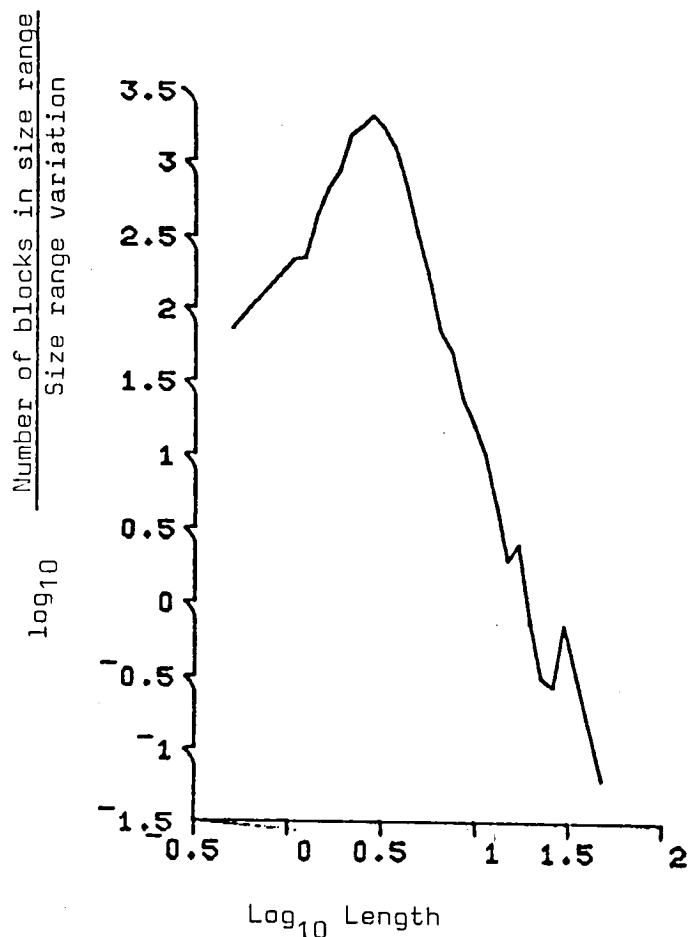


Figure 2: Incremental Plot for Total Block Population



was impacted. The calculated  $b$  value of 0.337 indicates a very simple level of fracturing (Hartmann, 1969).

As work on the project continues at Brown University, many more far-reaching conclusions may be revealed. The possibilities are numerous. Perhaps substrate thickness and strength will be more clearly defined. Depth of penetration, impact velocity, and volume of ejected blocks may become known. Other projectile characteristics and perhaps an absolute age for the crater could conceivably be determined.

## REFERENCES

- Cintala, Mark J., Head, James W., and Wilson, Lionel. (1979). "The Nature and Effects of Impact Cratering on Small Bodies." In Asteroids. Ed. T. Gehrels. Tucson: University of Arizona Press, pp. 579-600.
- Gault, Donald E., Quaide, William L., and Oberbeck, Verne R. (1968). "Impact Cratering Mechanics and Structures." In Shock Metamorphism of Natural Materials. Ed. B. M. French and N. M. Short. Baltimore: Mono Book Corp, pp. 87-99.
- Hansen, Thomas P. (1970). Guide to Lunar Orbiter Photographs. NASA Publication SP-242.
- Hartmann, William K. (1969). "Terrestrial, Lunar, and Interplanetary Rock Fragmentation." Icarus 10, 201-213.
- Head, James W. (1976). "The Significance of Substrate Characteristics in Determining Morphology and Morphometry of Lunar Craters." Proc. Seventh Lunar Sci. Conf. 3, 2913-2929.
- Kosofsky, L. J., and El-Baz, Farouk. (1970). The Moon as Viewed by Lunar Orbiter. NASA Publication SP-200.
- NASA Publication Cr-66469. (1967). Lunar Orbiter III: Postmission Photo Supporting Data. Washington, D.C.
- Oberbeck, Verne R. and Quaide, William L. (1968). "Genetic Implications of Lunar Regolith Thickness Variations." Icarus 9, 446-465.
- Quaide, William L. and Oberbeck, Verne R. (1968). "Thickness Determinations of the Lunar Surface Layer From Lunar Impact Craters." Journal of Geophysical Research 73, 5247-5270.
- Settle, Mark and Head, James W. (1977). "Radial Variation of Lunar Crater Rim Topography." Icarus 31, 123-135.
- Settle, Mark, Cintala, Mark J., and Head, James W. (1979). "Emplacement of Fahrenheit Crater Ejecta at the Luna-24 Site." The Moon and the Planets 20, 281-300.







1. Report No. NASA TM-84894		2. Government Accession No.		3. Recipient's Catalog No.	
4. Title and Subtitle  Advances in Planetary Geology				5. Report Date September 1982	
				6. Performing Organization Code EL-4	
7. Author(s)  Alex Woronow, Editor				8. Performing Organization Report No.	
				10. Work Unit No.	
9. Performing Organization Name and Address Office of Space Science and Applications Earth and Planetary Exploration Division Planetary Geology Program				11. Contract or Grant No.	
				13. Type of Report and Period Covered Technical Memorandum	
12. Sponsoring Agency Name and Address National Aeronautics and Space Administration Washington, DC 20546				14. Sponsoring Agency Code	
15. Supplementary Notes					
16. Abstract  Advances in Planetary Geology is a new series intended to serve the planetary geology community with a form for quick and thorough communications. There are no set lists of acceptable topics or formats, and submitted manuscripts will not undergo a formal review. All submissions should be in a camera-ready form, preferably single spaced, and submitted to the Editor.					
17. Key Words (Suggested by Author(s))  Planetary Geology Planetology			18. Distribution Statement  Unclassified-Unlimited  Category 91		
19. Security Classif. (of this report) Unclassified		20. Security Classif. (of this page) Unclassified		21. No. of Pages 586	22. Price* A25



National Aeronautics and  
Space Administration

SPECIAL FOURTH CLASS MAIL  
BOOK

Postage and Fees Paid  
National Aeronautics and  
Space Administration  
NASA-451



Washington, D.C.  
20546



Postage and Fees Paid  
National Aeronautics and  
Space Administration  
NASA-451



Official Business  
Penalty for Private Use, \$

National Aeronautics and  
Space Administration

Official Business  
Penalty for Private Use \$300

Washington, D.C.  
20546

SPECIAL FOURTH CLASS MAIL  
BOOK

8 13 10, J, 821015 S00008ASR  
NASA  
LANGLEY RESEARCH CENTER  
ATTN: TECHNICAL LIBRARY, MS 185  
HAMPTON VA 23665



POSTMASTER If Undeliverable (Section 158  
Postal Manual) Do Not Return